

DESIGN AND DEVELOPMENT OF HIGH TEMPERATURE  
NICKEL-BASED SUPERALLOYS

A THESIS SUBMITTED TO  
THE GRADUATE SCHOOL OF NATURAL AND APPLIED SCIENCES  
OF  
MIDDLE EAST TECHNICAL UNIVERSITY



BY

RASİM ERİŞ

IN PARTIAL FULFILLMENT OF THE REQUIREMENTS  
FOR  
THE DEGREE OF MASTER OF SCIENCE  
IN  
METALLURGICAL AND MATERIALS ENGINEERING

JULY 2017



Approval of the thesis:

**DESIGN AND DEVELOPMENT OF HIGH TEMPERATURE  
NICKEL-BASED SUPERALLOYS**

submitted by **RASİM ERİŞ** in partial fulfillment of the requirements for the degree of **Master of Science in Metallurgical and Materials Engineering Department, Middle East Technical University** by,

Prof. Dr. Gülbin Dural Ünver  
Dean, Graduate School of **Natural and Applied Sciences**

Prof. Dr. C. Hakan Gür  
Head of Department, **Metallurgical and Materials Eng.**

Prof. Dr. M. Vedat Akdeniz  
Supervisor, **Metallurgical and Materials Eng. Dept., METU**

Prof. Dr. Amdulla O. Mekhrabov  
Co-Supervisor, **Metallurgical and Materials Eng. Dept., METU**

**Examining Committee Members:**

Prof. Dr. Macit Özenbaş  
Metallurgical and Materials Eng. Dept., METU

Prof. Dr. M. Vedat Akdeniz  
Metallurgical and Materials Eng. Dept., METU

Prof. Dr. Amdulla O. Mekhrabov  
Metallurgical and Materials Eng. Dept., METU

Prof. Dr. C. Hakan Gür  
Metallurgical and Materials Eng. Dept., METU

Assoc. Prof. Dr. Ziya Esen  
Materials Science and Eng. Dept., Çankaya University

**Date:** 07.07.2017



**I hereby declare that all information in this document has been obtained and presented in accordance with academic rules and ethical conduct. I also declare that, as required by these rules and conduct, I have fully cited and referenced all material and results that are not original to this work.**

Name, Last name : Rasim Eriş

Signature :

## ABSTRACT

### DESIGN AND DEVELOPMENT OF HIGH TEMPERATURE NICKEL-BASED SUPERALLOYS

Eriş, Rasim

M.S., Department of Metallurgical and Materials Engineering

Supervisor: Prof. Dr. M. Vedat Akdeniz

Co-Supervisor: Prof. Dr. Amdulla O. Mekhrabov

July 2017, 289 pages

Remarkable high temperature mechanical properties of nickel-based superalloys are related with the arrangement of ternary alloying elements in  $L1_2$ -type ordered  $\gamma'$ -Ni<sub>3</sub>Al intermetallics. Therefore, in this thesis, high temperature site occupancy preference and energetic-structural characteristics of atomic short range ordering of ternary alloying X elements (X = Co, Cr, Hf, Mo, Nb, Pt, Re, Ru, Ta and W, respectively) in Ni<sub>75</sub>Al<sub>21.875</sub>X<sub>3.125</sub> alloy systems have been studied by combining the statistico-thermodynamical theory of ordering and electronic theory of alloys in the pseudopotential approximation. Simulations have shown that, all ternary alloying element atoms (except Pt) tend to occupy Al sublattice sites of Ni<sub>3</sub>Al intermetallics, whereas Pt atoms prefer to substitute for Ni sublattice sites. However, in contrast to other X elements, sublattice site occupancy characteristics of Re atoms seem to be both composition and temperature dependent. Distribution of Re atoms at both Al and Ni sublattice sites above critical temperatures,  $T_c$ , may lead to localized supersaturation of the parent Ni<sub>3</sub>Al phase and makes possible formation of topologically close-packed (TCP) phases. In order to validate these results, site occupancy tendencies of afore

mentioned alloying X elements have also been determined by performing first-principles *ab initio* calculations at 0 Kelvin and similar results have been obtained. Furthermore, by making use of charge density difference (CDD), electron localization function (ELF) and density of states (DOS) methods, the effects of alloying X elements on the bonding nature of Ni<sub>3</sub>Al-X phases have been simulated.

Superior mechanical properties of nickel-based superalloys strongly depend on microstructural characteristics of these materials (i.e.  $\gamma'$  volume fraction, size & size distribution, orientation and shape). For this purpose, Ni<sub>80</sub>Al<sub>15</sub>X<sub>5</sub> alloy systems (X = Al, Co, Cr, Hf, Mo, Nb, Ta, Ti and W, respectively) have been produced and characterized by various techniques. In the light of all theoretical and experimental data, it has been concluded that better micro-hardness properties of nickel-based superalloys can be obtained by appropriate alloying element additions and heat treatment procedures which lead to  $\gamma'$  precipitates having higher lattice parameter, higher volume fraction, smaller size and correspondingly optimum  $\delta$  parameter.

**Keywords:** Ni<sub>3</sub>Al Intermetallics, Site Preference, Atomic Short Range Ordering Characteristics, First-principles *Ab Initio* Calculations, Microstructural Evolution

## ÖZ

### YÜKSEK SICAKLIK UYGULAMALARINDA KULLANILAN NİKEL ESASLI SÜPER ALAŞIMLARIN TASARIMI VE GELİŞTİRİLMESİ

Eriş, Rasim

Yüksek Lisans, Metalurji ve Malzeme Mühendisliği Bölümü

Tez Yöneticisi: Prof. Dr. M. Vedat Akdeniz

Ortak Tez Yöneticisi: Prof. Dr. Amdulla O. Mekhrabov

Temmuz 2017, 289 sayfa

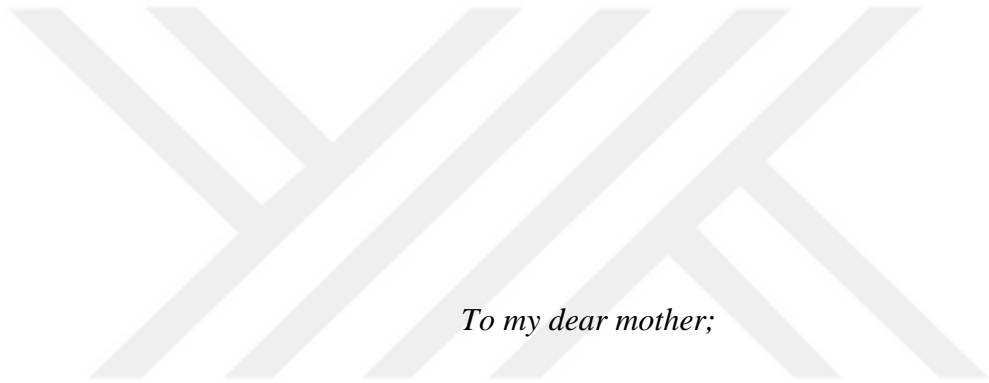
Yüksek sıcaklık uygulamalarında kullanılan nikel esaslı süper alaşımların dikkat çekici mekanik özellikleri, alaşım elementlerinin mikroyapı içinde yer alan  $L1_2$ -tipi düzenli  $\gamma'$ - $Ni_3Al$  intermetaliklerinde yerleştiği kafes-altı pozisyonlar ile ilişkilidir. Dolayısıyla, bu tezde, X alaşım elementlerinin ( $X = Co, Cr, Hf, Mo, Nb, Pt, Re, Ru, Ta$  ve  $W$ )  $Ni_{75}Al_{21.875}X_{3.125}$  alaşım sistemlerindeki kafes-altı pozisyonlara yerleşim tercihleri, istatistik-termodinamik teori ve alaşımların elektronik teorisinin pseudopotansiyel yaklaşımı ile birleştirilmesiyle incelenmiştir. Mevcut simülasyonlara göre, X alaşım element atomlarının tümü (Pt hariç)  $Ni_3Al$  intermetaliklerinin Al pozisyonlarına yerleşme eğilimi gösterirken, Pt atomları Ni pozisyonlarını doldurmayı tercih etmektedir. Ancak, diğer elementlerden farklı olarak, Re atomlarının kafes-altı pozisyonlara yerleşme eğilimi hem alaşım kompozisyonuna hem de sıcaklığa bağlı görünmektedir. Re atomlarının kritik sıcaklıkların üzerinde hem Al'a hem de Ni'e yönelmesi  $Ni_3Al$  fazının lokalize bir şekilde doygunluğa ulaşmasına ve topolojik açıdan yakın paketlenmiş (TCP) fazların çökmesine neden olabilir. Bu sonuçları doğrulamak için, yukarıda bahsedilen X alaşım elementlerinin  $Ni_3Al$  fazı

içindeki kafes-altı pozisyonlara yerleşme eğilimleri “first-principles *ab initio*” hesaplamaları ile 0 Kelvin’de araştırılmış ve sonuçların çoğunlukla tutarlılık gösterdiği görülmüştür. Ayrıca, “charge density difference (CDD)”, “electron localization function (ELF)” ve “density of states (DOS)” gibi bazı metodlar kullanılarak, X alaşım elementlerinin Ni<sub>3</sub>Al-X fazlarındaki bağ yapma özellikleri simüle edilmiştir.

Nikel esaslı süper alaşımların gelişmiş mekanik özellikleri, bu malzemelerin mikroyapısal özelliklerine ( $\gamma'$  çökeltilerinin hacimce fraksiyonuna, boyut & boyut dağılımına, oryantasyonuna ve şekline) bağlıdır. Bu amaçla, Ni<sub>80</sub>Al<sub>15</sub>X<sub>5</sub> alaşım sistemleri (X = Al, Co, Cr, Hf, Mo, Nb, Ta, Ti ve W) üretilmiş ve çeşitli tekniklerle karakterize edilmiştir. Tüm teorik ve deneysel verilerin ışığında, nikel esaslı süper alaşımlar için daha iyi mikro-sertlik değerlerinin yüksek örgü parametre sabiti ve yüksek hacim fraksiyonuna sahip, düşük boyuttaki Ni<sub>3</sub>Al çökeltilerine ve dolayısıyla optimum  $\delta$  parametresine neden olan uygun alaşım elementi ilaveleri ve ısıl işlem prosedürleri ile elde edilebileceği sonucuna varılmıştır.

**Anahtar Sözcükler:** Nikel Alüminidler, Pozisyon Tercihi, Kısa Mesafeli Atomik Düzen Özellikleri, “First-principles *Ab Initio*” Hesaplamaları, Mikroyapı Gelişimi





*To my dear mother;*

## ACKNOWLEDGEMENTS

First of all, I would like to express my sincerest gratitude to my supervisors Prof. Dr. M. Vedat Akdeniz and Prof. Dr. Amdulla O. Mekhrabov for their perpetual interest, guidance, encouragement, immense knowledge and limitless patience. My supervisors consistently allowed this paper to be my own work, but steered me in the right direction whenever they thought I needed it. Besides my supervisors, I would like to thank the rest of thesis committee for their insightful questions and comments which encourage me to expand my thesis research from various perspectives.

I would like to acknowledge Asst. Prof. Dr. Mehmet Yıldırım of the Department of Metallurgical and Materials Engineering at Selçuk University. Words cannot express my appreciation with him. He played a major role in determining my thesis topic and always treated me like a mentor. Secondly, I would like to thank my labmates for their contributions in Novel Alloys Design and Development Laboratory, NOVALAB. In addition, I am thankful for the Department of Metallurgical and Materials Engineering at METU since I always had opportunity to use some facilities easily. Hereby, I must acknowledge Research Associate Serkan Yılmaz, Laboratory Technicians Nilüfer Özel and Yusuf Yıldırım for their help in Microscopy and Microanalysis, XRD and Heat Treatment Laboratories, respectively. I would also like to thank METU Central Laboratory for ICP-MS measurements.

Last but not the least, I would like to thank my family and friends standing by me throughout my education life.

This work was supported through TÜBİTAK, the national scholarship programme for the graduate students (2211) and the program for the participation in scientific activities abroad (2224-A).

## TABLE OF CONTENTS

ABSTRACT .....	v
ÖZ .....	vii
ACKNOWLEDGEMENTS .....	x
TABLE OF CONTENTS .....	xi
LIST OF TABLES .....	xviii
LIST OF FIGURES .....	xxii
LIST OF SYMBOLS AND ABBREVIATIONS .....	xxxix
CHAPTERS	
1. INTRODUCTION.....	1
1.1 Aim and Motivation.....	1
1.2 Contribution of the Thesis.....	2
2. NICKEL-BASED SUPERALLOYS.....	5
2.1 Historical Background of Nickel-based Superalloys.....	5
2.2 Mechanical Properties of Nickel-based Superalloys .....	7
2.3 Strengthening Mechanisms .....	8
2.3.1 Precipitation Hardening .....	8
2.3.2 Solid Solution Strengthening .....	9
2.3.3 Coherency-type Strengthening.....	9
2.3.4 Grain Boundary Strengthening .....	10
2.4 General Microstructural Features .....	10
2.4.1 $\gamma'$ -Ni <sub>3</sub> Al Precipitates .....	11
2.4.2 $\gamma$ Matrix Phase-Ni Solid Solution .....	13

2.4.3 $\gamma''(\delta)$ -Ni <sub>3</sub> (Al,Nb) Phase .....	14
2.4.4 Topologically Close-packed (TCP) Phases .....	15
2.5 Idealization of Microstructural Characteristics .....	16
2.5.1 Volume Fraction of $\gamma'$ Precipitates .....	17
2.5.2 Size & Size Distribution of $\gamma'$ Precipitates .....	17
2.5.3 Orientation of $\gamma'$ Precipitates .....	18
2.5.4 Shape of $\gamma'$ Precipitates and Lattice Misfit Parameter ( $\delta$ ) ...	18
2.5.5 Channel Width of $\gamma$ Matrix Phase .....	20
2.5.6 APB and SF Energy .....	21
2.5.7 $\gamma$ - $\gamma'/\gamma$ Phase Transformation (Solvus) Temperature .....	22
2.6 Coarsening Behaviour of $\gamma'$ Precipitates .....	23
2.7 Compositions of Nickel-based Superalloys .....	24
2.7.1 Effects of Alloying Elements .....	24
2.7.1.1 Ni Addition .....	24
2.7.1.2 Al Addition .....	24
2.7.1.3 Co Addition .....	26
2.7.1.4 Cr Addition .....	26
2.7.1.5 Hf Addition .....	26
2.7.1.6 Mo Addition .....	27
2.7.1.7 Nb Addition .....	27
2.7.1.8 Pt Addition .....	27
2.7.1.9 Re Addition .....	27
2.7.1.10 Ru Addition .....	28
2.7.1.11 Ta Addition .....	28
2.7.1.12 Ti Addition .....	29

2.7.1.13 W Addition .....	29
2.7.2 Phase Preferences of Alloying Elements .....	29
2.7.3 Site Preferences of Alloying Elements .....	31
2.7.3.1 SRO Parameter Calculations .....	31
2.7.3.2 First-principles Ab Initio Calculations .....	31
3. HIGH TEMPERATURE SITE PREFERENCE AND ATOMIC SHORT RANGE ORDERING CHARACTERISTICS OF TERNARY ALLOYING ELEMENTS IN $\gamma'$ -Ni <sub>3</sub> Al INTERMETALLICS .....	33
3.1 Introduction .....	33
3.2 Theory .....	35
3.3 Partial Ordering Energy & Partial SRO Parameters .....	37
3.4 Site Occupancy Characteristics of Ternary Alloying Elements and Theoretical Explanation of Possible TCP Phase Formation .....	45
3.5 Conclusions .....	51
4. SITE OCCUPANCY CHARACTERISTICS OF TERNARY ALLOYING ELEMENTS IN $\gamma'$ -Ni <sub>3</sub> Al INTERMETALLICS: FIRST-PRINCIPLES AB INITIO CALCULATIONS AT 0 KELVIN .....	53
4.1 Introduction .....	53
4.2 Methodology .....	53
4.3 Point Defect Formation Enthalpies in Ni <sub>3</sub> Al Phase .....	55
4.4 Anti-site Formation-based Formalism .....	57
4.5 Site Preferences of Ternary Alloying Elements at 0 Kelvin .....	57
4.6 Theoretical Lattice Parameter Calculations of Ni <sub>3</sub> Al-X Phases .....	58
4.7 Atomistic Level Simulations of Ni <sub>3</sub> Al-X Phases .....	61

4.7.1 Charge Density Difference (CDD) .....	61
4.7.2 Electron Localization Function (ELF) .....	71
4.7.3 Density of States (DOS).....	73
4.8 Conclusions.....	86
<b>5. PRODUCTION, CHARACTERIZATION AND MICROSTRUCTURAL &amp; MECHANICAL DEVELOPMENT OF Ni<sub>80</sub>Al<sub>20</sub> AND Ni<sub>80</sub>Al<sub>15</sub>X<sub>5</sub> ALLOY SYSTEMS.....</b>	<b>89</b>
5.1 Introduction.....	89
5.2 Experimental Procedure.....	89
5.2.1 Raw Materials .....	89
5.2.2 Production of the Samples.....	90
5.2.2.1 Arc Melting.....	90
5.2.2.2 Suction Casting .....	91
5.2.3 ICP-MS Measurements .....	92
5.2.4 Heat Treatment .....	92
5.2.5 Characterization Techniques .....	93
5.2.5.1 X-ray Diffraction (XRD) .....	93
5.2.5.2 Differential Scanning Calorimetry (DSC) .....	93
5.2.5.3 Field Emission Scanning Electron Microscopy (FESEM) .....	93
5.2.5.4 Micro-hardness Measurements .....	95
5.3 Characterization of Ni <sub>80</sub> Al <sub>20</sub> Alloys .....	95
5.3.1 Phase Analysis.....	96
5.3.2 Determination of Lattice Parameters of $\gamma'$ Precipitates in Ni <sub>80</sub> Al <sub>20</sub> Alloys .....	99

5.3.3 Thermal Properties .....	101
5.3.4 Microstructural Investigation.....	102
5.3.5 Energy Dispersive Spectroscopy (EDS) Measurements ...	114
5.3.6 Micro-hardness Measurements .....	114
5.3.7 Effects of Heat Treatment Procedures on the Microstructural and Mechanical Properties of Ni <sub>80</sub> Al <sub>20</sub> Alloys .....	118
5.3.8 Conclusions.....	120
5.4 Characterization of Ni <sub>80</sub> Al <sub>15</sub> X <sub>5</sub> Alloy Systems .....	123
5.4.1 Phase Analysis .....	123
5.4.2 Determination of Lattice Parameters of $\gamma'$ Precipitates in Ni <sub>80</sub> Al <sub>15</sub> X <sub>5</sub> Alloy Systems .....	124
5.4.3 Thermal Properties .....	124
5.4.4 Microstructural Investigation.....	127
5.4.4.1 As Cast Microstructures.....	127
5.4.4.2 Pre-aged Microstructures .....	134
5.4.4.3 Aged Microstructures.....	136
5.4.5 Energy Dispersive Spectroscopy (EDS) Measurements ...	140
5.4.6 Micro-hardness Measurements .....	141
5.4.7 Effects of Alloying X Element Additions and Heat Treatment Procedures on the Microstructural Characteristics and Mechanical Properties of Ni <sub>80</sub> Al <sub>15</sub> X <sub>5</sub> Alloy Systems .....	142
5.4.7.1 Effects of Alloying X Elements on the Mechanical Properties .....	143
5.4.7.2 Effects of Heat Treatment Procedures on the	

Microstructural Characteristics.....	149
5.4.7.2.1 Volume Fraction of $\gamma'$ Precipitates.....	150
5.4.7.2.2 Size & Size Distribution of $\gamma'$ Precipitates .....	150
5.4.7.2.3 Orientation of $\gamma'$ Precipitates .....	151
5.4.7.2.4 Shape of $\gamma'$ Precipitates.....	151
5.4.8 Conclusions .....	153
6. CONCLUSIONS .....	155
7. FUTURE SUGGESTIONS .....	161
REFERENCES .....	163
APPENDICES	
A. BINARY PHASE DIAGRAM OF Ni-Al SYSTEM.....	183
B. TERNARY PHASE DIAGRAMS OF Ni-Al-X SYSTEMS .....	185
C. XRD PATTERNS OF Ni <sub>80</sub> Al <sub>15</sub> X <sub>5</sub> ALLOY SYSTEMS.....	195
D. DETERMINATION OF LATTICE PARAMETERS OF $\gamma'$ PRECIPITATES IN Ni <sub>80</sub> Al <sub>15</sub> X <sub>5</sub> ALLOY SYSTEMS .....	205
E. DSC HEATING AND COOLING CURVES OF Ni <sub>80</sub> Al <sub>15</sub> X <sub>5</sub> ALLOY SYSTEMS .....	209
F. FESEM MICROGRAPHS OF Ni <sub>80</sub> Al <sub>15</sub> X <sub>5</sub> ALLOY SYSTEMS ....	215
G. EDS PHASE ANALYSIS AND DETERMINATION OF PHASE PARTITIONING COEFFICIENTS OF ALLOYING X ELEMENTS IN Ni <sub>80</sub> Al <sub>15</sub> X <sub>5</sub> ALLOY SYSTEMS .....	245
H. MICRO-HARDNESS VALUES OF Ni <sub>80</sub> Al <sub>15</sub> X <sub>5</sub> ALLOY SYSTEMS .....	255
I. MICRO-HARDNESS VARIATIONS OF Ni <sub>80</sub> Al <sub>15</sub> X <sub>5</sub> ALLOY	



SYSTEMS.....	259
J. $\gamma'$ PRECIPITATE VOLUME FRACTIONS OF $\text{Ni}_{80}\text{Al}_{15}\text{X}_5$ ALLOY SYSTEMS.....	265
K. $\gamma'$ PRECIPITATE SIZE & SIZE DISTRIBUTION AND ORIENTATION CHARACTERISTICS OF $\text{Ni}_{80}\text{Al}_{15}\text{X}_5$ ALLOY SYSTEMS.....	269
L. COMPARISON OF MICROSTRUCTURAL CHARACTERISTICS AND MECHANICAL PROPERTIES OF $\text{Ni}_{80}\text{Al}_{15}\text{X}_5$ ALLOY SYSTEMS.....	277
CURRICULUM VITAE .....	287

## LIST OF TABLES

### TABLES

<b>Table 2.1</b> Physical properties of Ni <sub>3</sub> Al intermetallics (Adapted from [24]).....	12
<b>Table 2.2</b> Physical properties of Ni solid solution/Ni.....	14
<b>Table 2.3</b> Lattice misfit parameters ( $\delta$ ) and $\gamma'$ precipitate morphologies of related alloys (Adapted from [54]) .....	20
<b>Table 2.4</b> Compositions of well-known commercial nickel-based superalloys (wt.%) (Adapted from [2]) .....	25
<b>Table 3.1</b> Partial ordering energies of Ni-X and Al-X atomic pairs at first coordination sphere, $R_1$ , in Ni <sub>75</sub> Al <sub>21.875</sub> X <sub>3.125</sub> alloy systems.....	41
<b>Table 3.2</b> Partial SRO parameters of Ni-Al, Ni-X and Al-X atomic pairs of Ni <sub>75</sub> Al <sub>21.875</sub> X <sub>3.125</sub> alloy systems at elevated temperatures.....	42
<b>Table 3.3</b> Site occupancy preferences of ternary alloying X elements (X = Co, Cr, Hf, Mo, Nb, Pt, Re, Ru, Ta and W) in Ni <sub>75</sub> Al <sub>21.875</sub> X <sub>3.125</sub> alloy systems and the comparison of the current work results with other theoretical first-principles calculations and experimental methods. (*): APFIM studies, (**): ALCHEMI works, (a): at 0 Kelvin, (b): at lower service temperatures (i.e. < T <sub>c</sub> ), (c): at higher service temperatures (i.e. > T <sub>c</sub> ) and (d): in the studied temperature range (i.e. 800 °C-1250 °C).....	47
<b>Table 3.4</b> Partial SRO parameters of Ni-Al, Ni-Ru and Al-Ru atomic pairs of Ni-rich Ni <sub>75</sub> Al <sub>21</sub> Ru <sub>4</sub> alloy at elevated temperatures ( $W_{\text{Ni-Al}}(R_1) = 7.1 \times 10^{-3}$ at. u., $W_{\text{Ni-Ru}}(R_1) = 30.645 \times 10^{-3}$ at. u. and $W_{\text{Al-Ru}}(R_1) = 25.198 \times 10^{-3}$ at. u.) .....	49
<b>Table 4.1</b> Formation enthalpies of exchange anti-site defects .....	56
<b>Table 4.2</b> Total energy and energy change parameters, $E_{\text{Ni} \rightarrow \text{Al}}^{\text{X}}$ , of Ni <sub>32-x-y</sub> Al <sub>x</sub> X <sub>y</sub> systems where X = Co, Cr, Hf, Mo, Nb, Pt, Re, Ru, Ta, Ti and W, respectively.....	59
<b>Table 4.3</b> Lattice parameters of Ni <sub>24</sub> Al <sub>7</sub> X and Ni <sub>23</sub> Al <sub>8</sub> X systems where X = Co, Cr, Hf	

Mo, Nb, Pt, Re, Ru, Ta, Ti and W, respectively.....	60
<b>Table 5.1</b> Purities of alloying X elements (wt.%).....	90
<b>Table 5.2</b> Verification of alloy compositions by ICP-MS technique.....	92
<b>Table 5.3</b> A series of heat treatment steps applied to Ni <sub>80</sub> Al <sub>15</sub> X <sub>5</sub> alloy systems (X = Al, Co, Cr, Hf, Mo, Nb, Ta, Ti and W).....	94
<b>Table 5.4</b> Lattice parameter determination of $\gamma'$ precipitates in Ni <sub>80</sub> Al <sub>20</sub> alloys.....	100
<b>Table 5.5</b> EDS phase analysis of Ni <sub>80</sub> Al <sub>20</sub> alloys.....	115
<b>Table 5.6</b> Micro-hardness values of Ni <sub>80</sub> Al <sub>20</sub> alloys .....	116
<b>Table 5.7</b> Comparison of microstructural characteristics and mechanical properties of Ni <sub>80</sub> Al <sub>20</sub> alloys .....	121
<b>Table 5.8</b> Melting/solidification temperatures of heating/cooling curves of as cast (fast cooled) Ni <sub>80</sub> Al <sub>15</sub> X <sub>5</sub> alloy systems where X = Al, Co, Cr, Hf, Mo, Nb, Ta, Ti and W, respectively.....	126
<b>Table 5.9</b> Atomic radius of alloying X elements from the biggest to the smallest where X = Hf, Ta, Nb, W, Mo, Ti, Cr and Co, respectively (Adapted from [136]).....	143
<b>Table D.1</b> Lattice parameter determination of $\gamma'$ precipitates in Ni <sub>80</sub> Al <sub>15</sub> X <sub>5</sub> alloy systems where X = Co, Cr, Hf and Mo, respectively .....	205
<b>Table D.2</b> Lattice parameter determination of $\gamma'$ precipitates in Ni <sub>80</sub> Al <sub>15</sub> X <sub>5</sub> alloy systems where X = Nb, Ta, Ti and W, respectively .....	206
<b>Table D.3</b> Lattice parameter determination of Ni <sub>5</sub> Hf phase in Ni <sub>80</sub> Al <sub>15</sub> Hf <sub>5</sub> alloys..	207
<b>Table G.1</b> EDS phase analysis and determination of phase partitioning coefficients of X = Co atoms in Ni <sub>80</sub> Al <sub>15</sub> Co <sub>5</sub> alloys .....	246
<b>Table G.2</b> EDS phase analysis and determination of phase partitioning coefficients of X = Cr atoms in Ni <sub>80</sub> Al <sub>15</sub> Cr <sub>5</sub> alloys.....	247
<b>Table G.3</b> EDS phase analysis and determination of phase partitioning coefficients of X = Hf atoms in Ni <sub>80</sub> Al <sub>15</sub> Hf <sub>5</sub> alloys .....	248
<b>Table G.4</b> EDS phase analysis and determination of phase partitioning coefficients of	

X = Mo atoms in Ni <sub>80</sub> Al <sub>15</sub> Mo <sub>5</sub> alloys .....	249
<b>Table G.5</b> EDS phase analysis and determination of phase partitioning coefficients of X = Nb atoms in Ni <sub>80</sub> Al <sub>15</sub> Nb <sub>5</sub> alloys.....	250
<b>Table G.6</b> EDS phase analysis and determination of phase partitioning coefficients of X = Ta atoms in Ni <sub>80</sub> Al <sub>15</sub> Ta <sub>5</sub> alloys .....	251
<b>Table G.7</b> EDS phase analysis and determination of phase partitioning coefficients of X = Ti atoms in Ni <sub>80</sub> Al <sub>15</sub> Ti <sub>5</sub> alloys .....	252
<b>Table G.8</b> EDS phase analysis and determination of phase partitioning coefficients of X = W atoms in Ni <sub>80</sub> Al <sub>15</sub> W <sub>5</sub> alloys.....	253
<b>Table H.1</b> Micro-hardness values of Ni <sub>80</sub> Al <sub>15</sub> X <sub>5</sub> alloy systems where X = Co, Cr, Hf and Mo, respectively .....	256
<b>Table H.2</b> Micro-hardness values of Ni <sub>80</sub> Al <sub>15</sub> X <sub>5</sub> alloy systems where X = Nb, Ta, Ti and W, respectively .....	257
<b>Table L.1</b> Comparison of microstructural characteristics and mechanical properties of Ni <sub>80</sub> Al <sub>15</sub> Co <sub>5</sub> alloys .....	278
<b>Table L.2</b> Comparison of microstructural characteristics and mechanical properties of Ni <sub>80</sub> Al <sub>15</sub> Cr <sub>5</sub> alloys.....	279
<b>Table L.3</b> Comparison of microstructural characteristics and mechanical properties of Ni <sub>80</sub> Al <sub>15</sub> Hf <sub>5</sub> alloys.....	280
<b>Table L.4</b> Comparison of microstructural characteristics and mechanical properties of Ni <sub>80</sub> Al <sub>15</sub> Mo <sub>5</sub> alloys .....	281
<b>Table L.5</b> Comparison of microstructural characteristics and mechanical properties of Ni <sub>80</sub> Al <sub>15</sub> Nb <sub>5</sub> alloys .....	282
<b>Table L.6</b> Comparison of microstructural characteristics and mechanical properties of Ni <sub>80</sub> Al <sub>15</sub> Ta <sub>5</sub> alloys.....	283
<b>Table L.7</b> Comparison of microstructural characteristics and mechanical properties of Ni <sub>80</sub> Al <sub>15</sub> Ti <sub>5</sub> alloys .....	284

**Table L.8** Comparison of microstructural characteristics and mechanical properties of  
Ni<sub>80</sub>Al<sub>15</sub>W<sub>5</sub> alloys .....285



## LIST OF FIGURES

### FIGURES

- Figure 2.1** Development of high temperature mechanical properties of superalloys from the 1940s to 2010s (Adapted from [1]) ..... 5
- Figure 2.2** Equiaxed (left), columnar (middle) and single-crystal (right) forms of turbine blades (Adapted from [1])..... 6
- Figure 2.3** The crystal structure of L1<sub>2</sub>-type ordered  $\gamma'$ -Ni<sub>3</sub>Al precipitates in which Al atoms (blue) and Ni atoms (green) occupy corner and face-centered sites, respectively ..... 12
- Figure 2.4** The crystal structure of FCC-type disordered  $\gamma$  matrix phase-Ni solid solution in which Al and Ni atoms randomly occupy any sites ..... 13
- Figure 2.5** FESEM micrograph showing  $\delta$  phase (white plates) within V207M exposed to heat treatment at 950 °C for 35 minutes (Adapted from [37]) ..... 14
- Figure 2.6** FESEM micrograph showing TCP phase precipitation at 1100 °C for 1000 hr exposure time (Adapted from [16])..... 16
- Figure 3.1** Solubility limits of alloying X elements affecting the extent of  $\gamma'$  phase field in ternary phase diagram of Ni-Al-X systems at 1000 °C (Adapted from [84])..... 34
- Figure 3.2** Partial ordering energies of Ni-X (solid curves) and Al-X (dashed curves) atomic pairs as a function of interatomic distance in Ni<sub>75</sub>Al<sub>21.875</sub>X<sub>3.125</sub> alloy systems where X = (a) Co, (b) Cr, (c) Hf, (d) Mo and (e) Nb, respectively. (1 at. u. (energy) = 2 Ry = 27.2 eV; and 1 at. u. (length) = 0.529177 Å)..... 39
- Figure 3.3** Partial ordering energies of Ni-X (solid curves) and Al-X (dashed curves) atomic pairs as a function of interatomic distance in Ni<sub>75</sub>Al<sub>21.875</sub>X<sub>3.125</sub> alloy systems where X = (a) Pt, (b) Re, (c) Ru, (d) Ta and (e) W, respectively. (1 at. u. (energy) = 2 Ry = 27.2 eV; and 1 at. u. (length) = 0.529177 Å) ..... 40

**Figure 3.4** The variation of partial SRO parameters of (a) Ni-Re and (b) Al-Re atomic pairs of  $Ni_{75}Al_{25-x}Re_x$  alloys with increasing temperature where  $x = 1-4$  at.% .....48

**Figure 3.5** The variation of critical temperatures,  $T_c$ , with respect to Re content at which occupancy preferences of Re atoms in  $L1_2$ -type ordered  $Ni_3Al$  intermetallics showing alteration and lead to phase instability of the parent  $\gamma'$  precipitates and possible formation of TCP phases .....50

**Figure 4.1** Optimum values of plane wave cut-off energy and  $1/K$  spacing .....54

**Figure 4.2** 32 atoms  $2 \times 2 \times 2$  supercells of (a)  $Ni_{25}Al_7$  and (b)  $Ni_{23}Al_9$  systems in which (a) Ni (green) and (b) Al (blue) anti-sites located at the centres, respectively .....55

**Figure 4.3** Lattice parameter variations of  $Ni_{24}Al_7X$  (shown in spheres) and  $Ni_{23}Al_8X$  (indicated by triangles) systems where  $X = Hf, Ta, Nb, W, Mo, Ti, Re, Cr, Ru, Co$  and  $Pt$ , respectively.....60

**Figure 4.4** CDD characteristics of centrally located alloying X elements (light blue) at either (a,c,e) Al or (b,d,f) Ni sites of 32 atoms  $2 \times 2 \times 2$  model of  $Ni_3Al$  phase for (a,b) (010), (c,d) (110) and (e,f) (111) planes, respectively .....62

**Figure 4.5** (010) plane CDD characteristics of centrally located alloying X elements at Al sites of  $Ni_3Al$  phase where  $X = Al, Co, Cr, Hf, Mo, Nb, Pt, Re, Ru, Ta, Ti$  and  $W$ , respectively (1: NN Ni and 2: NN Al atoms) .....64

**Figure 4.6** (010) plane CDD characteristics of centrally located alloying X elements at Ni sites of  $Ni_3Al$  phase where  $X = Ni, Co, Cr, Hf, Mo, Nb, Pt, Re, Ru, Ta, Ti$  and  $W$ , respectively (1: NN Ni and 2: NN Al atoms) .....65

**Figure 4.7** (110) plane CDD characteristics of centrally located alloying X elements at Al sites of  $Ni_3Al$  phase where  $X = Al, Co, Cr, Hf, Mo, Nb, Pt, Re, Ru, Ta, Ti$  and  $W$ , respectively (1: NN Ni and 2: NN Al atoms) .....66

**Figure 4.8** (110) plane CDD characteristics of centrally located alloying X elements at Ni sites of  $Ni_3Al$  phase where  $X = Ni, Co, Cr, Hf, Mo, Nb, Pt, Re, Ru, Ta, Ti$  and  $W$ , respectively (1: NN Ni atoms) .....67

<b>Figure 4.9</b> (111) plane CDD characteristics of centrally located alloying X elements at Al sites of Ni <sub>3</sub> Al phase where X = Al, Co, Cr, Hf, Mo, Nb, Pt, Re, Ru, Ta, Ti and W, respectively (1: NN Ni and 2: NN Al atoms) .....	68
<b>Figure 4.10</b> (111) plane CDD characteristics of centrally located alloying X elements at Ni sites of Ni <sub>3</sub> Al phase where X = Ni, Co, Cr, Hf, Mo, Nb, Pt, Re, Ru, Ta, Ti and W, respectively (1: NN Ni and 2: NN Al atoms) .....	69
<b>Figure 4.11</b> ELF contour plots of centrally located alloying X elements (light blue) at either (a,c,e) Al or (b,d,f) Ni sites of 32 atoms 2 x 2 x 2 model of Ni <sub>3</sub> Al phase for (a,b) (010), (c,d) (110) and (e,f) (111) planes, respectively.....	72
<b>Figure 4.12</b> (010) plane ELF contour plots of centrally located alloying X elements at Al sites of Ni <sub>3</sub> Al phase where X = Al, Co, Cr, Hf, Mo, Nb, Pt, Re, Ru, Ta, Ti and W, respectively (1: NN Ni and 2: NN Al atoms) .....	74
<b>Figure 4.13</b> (010) plane ELF contour plots of centrally located alloying X elements at Ni sites of Ni <sub>3</sub> Al phase where X = Ni, Co, Cr, Hf, Mo, Nb, Pt, Re, Ru, Ta, Ti and W, respectively (1: NN Ni and 2: NN Al atoms) .....	75
<b>Figure 4.14</b> (110) plane ELF contour plots of centrally located alloying X elements at Al sites of Ni <sub>3</sub> Al phase where X = Al, Co, Cr, Hf, Mo, Nb, Pt, Re, Ru, Ta, Ti and W, respectively (1: NN Ni and 2: NN Al atoms) .....	76
<b>Figure 4.15</b> (110) plane ELF contour plots of centrally located alloying X elements at Ni sites of Ni <sub>3</sub> Al phase where X = Ni, Co, Cr, Hf, Mo, Nb, Pt, Re, Ru, Ta, Ti and W, respectively (1: NN Ni atoms) .....	77
<b>Figure 4.16</b> (111) plane ELF contour plots of centrally located alloying X elements at Al sites of Ni <sub>3</sub> Al phase where X = Al, Co, Cr, Hf, Mo, Nb, Pt, Re, Ru, Ta, Ti and W, respectively (1: NN Ni and 2: NN Al atoms) .....	78
<b>Figure 4.17</b> (111) plane ELF contour plots of centrally located alloying X elements at Ni sites of Ni <sub>3</sub> Al phase where X = Ni, Co, Cr, Hf, Mo, Nb, Pt, Re, Ru, Ta, Ti and W, respectively (1: NN Ni and 2: NN Al atoms) .....	79
<b>Figure 4.18</b> pDOS diagrams of (a) Al-p/Ni-d and (b-f) X-d/Ni-d states showing p-d and d-d hybridizations between centrally located Al(X) and their NN Ni atoms along	



<110> directions where X = Co, Cr, Hf, Mo and Nb, respectively.....	82
<b>Figure 4.19</b> pDOS diagrams of (a-f) X-d/Ni-d states showing d-d hybridizations between centrally located X and their NN Ni atoms along <110> directions where X = Pt, Re, Ru, Ta, Ti and W, respectively .....	83
<b>Figure 4.20</b> pDOS diagrams of (a) Ni-d/Al-p and (b-f) X-d/Al-p states showing d-p hybridizations between centrally located Ni(X) and their NN Al atoms along <110> directions where X = Co, Cr, Hf, Mo and Nb, respectively.....	84
<b>Figure 4.21</b> pDOS diagrams of (a-f) X-d/Al-p states showing d-p hybridizations between centrally located X and their NN Al atoms along <110> directions where X = Pt, Re, Ru, Ta, Ti and W, respectively .....	85
<b>Figure 5.1</b> Edmund Bühler arc melting unit used for the production of samples.....	91
<b>Figure 5.2</b> Copper mold and cylindrical rods produced by arc melting and suction casting techniques.....	91
<b>Figure 5.3</b> Setaram Setsys–16/18 DSC used for thermal analysis measurements....	95
<b>Figure 5.4</b> XRD patterns of (a) fast and (b) slow cooled as cast Ni <sub>80</sub> Al <sub>20</sub> alloys .....	97
<b>Figure 5.5</b> XRD patterns of (a) as cast (fast cooled) Ni <sub>80</sub> Al <sub>20</sub> alloys, (b) partially-solutionized at 1150 °C for 3 hr and subsequently aged at 800 °C for (c) 4 hr (d) 16 hr (e) 64 hr and (f) 256 hr, respectively .....	97
<b>Figure 5.6</b> XRD patterns of (a) as cast (fast cooled) Ni <sub>80</sub> Al <sub>20</sub> alloys, (b) homogenized at 1250 °C for 24 hr and partially-solutionized at 1150 °C for 3 hr and subsequently aged at 800 °C for (c) 4 hr (d) 16 hr (e) 64 hr and (f) 256 hr, respectively .....	98
<b>Figure 5.7</b> XRD patterns of (a) as cast (fast cooled) Ni <sub>80</sub> Al <sub>20</sub> alloys, (b) primarily aged at 800 °C for 3 hr and subsequently aged at 800 °C for (c) 4 hr (d) 16 hr (e) 64 hr and (f) 256 hr, respectively .....	98
<b>Figure 5.8</b> XRD patterns of (a) as cast (fast cooled) Ni <sub>80</sub> Al <sub>20</sub> alloys, (b) homogenized at 1250 °C for 24 hr and primarily aged at 800 °C for 3 hr and subsequently aged at 800 °C for (c) 4 hr (d) 16 hr (e) 64 hr and (f) 256 hr, respectively.....	99
<b>Figure 5.9</b> DSC (a) heating and (b) cooling curves of as cast (fast cooled) Ni <sub>80</sub> Al <sub>20</sub>	

alloys (at a rate of 20 °C/minutes) ..... 101

**Figure 5.10** FESEM micrographs of as cast Ni<sub>80</sub>Al<sub>20</sub> alloys showing (a) fine and (c) coarse dendritic ( $\gamma$ - $\gamma'$ ) and interdendritic ( $\gamma'$ ) regions due to (a) fast and (c) slow cooling rates, respectively. Micrographs (b,d) show dendrite-interdendrite interface regions of (a,c) where (b) fine and (d) coarse  $\gamma'$  precipitates exist ..... 102

**Figure 5.11** FESEM micrographs showing (a) as cast (fast cooled), (b) partial solution heat treated (at 1150 °C for 3 hr) microstructures and temporal evolution of  $\gamma'$  precipitates in Ni<sub>80</sub>Al<sub>20</sub> alloys as aging time at 800 °C is (c) 4 hr, (d) 16 hr, (e) 64 hr and (f) 256 hr, respectively ..... 106

**Figure 5.12** FESEM micrographs showing (a) as cast (fast cooled), (b) partial solution heat treated (at 1150 °C for 3 hr) microstructures and temporal evolution of  $\gamma'$  precipitates in Ni<sub>80</sub>Al<sub>20</sub> alloys as aging time at 800 °C is (c) 4 hr, (d) 16 hr, (e) 64 hr and (f) 256 hr, respectively ..... 107

**Figure 5.13** FESEM micrographs showing (a) as cast (fast cooled), (b) homogenized and partial solution heat treated (at 1250 °C for 24 hr and 1150 °C for 3 hr) microstructures and temporal evolution of  $\gamma'$  precipitates in Ni<sub>80</sub>Al<sub>20</sub> alloys as aging time at 800 °C is (c) 4 hr, (d) 16 hr, (e) 64 hr and (f) 256 hr, respectively ..... 108

**Figure 5.14** FESEM micrographs showing (a) as cast (fast cooled), (b) homogenized and partial solution heat treated (at 1250 °C for 24 hr and 1150 °C for 3 hr) microstructures and temporal evolution of  $\gamma'$  precipitates in Ni<sub>80</sub>Al<sub>20</sub> alloys as aging time at 800 °C is (c) 4 hr, (d) 16 hr, (e) 64 hr and (f) 256 hr, respectively ..... 109

**Figure 5.15** FESEM micrographs showing (a) as cast (fast cooled), (b) primarily aged (at 800 °C for 3 hr) microstructures and temporal evolution of  $\gamma'$  precipitates in Ni<sub>80</sub>Al<sub>20</sub> alloys as aging time at 800 °C is (c) 4 hr, (d) 16 hr, (e) 64 hr and (f) 256 hr, respectively. .... 110

**Figure 5.16** FESEM micrographs showing (a) as cast (fast cooled), (b) primarily aged (at 800 °C for 3 hr) microstructures and temporal evolution of  $\gamma'$  precipitates in Ni<sub>80</sub>Al<sub>20</sub> alloys as aging time at 800 °C is (c) 4 hr, (d) 16 hr, (e) 64 hr and (f) 256 hr, respectively ..... 111

<b>Figure 5.17</b> FESEM micrographs showing (a) as cast (fast cooled), (b) homogenized and primarily aged (at 1250 °C for 24 hr and 800 °C for 3 hr) microstructures and temporal evolution of $\gamma'$ precipitates in Ni <sub>80</sub> Al <sub>20</sub> alloys as aging time at 800 °C is (c) 4 hr, (d) 16 hr, (e) 64 hr and (f) 256 hr, respectively .....	112
<b>Figure 5.18</b> FESEM micrographs showing (a) as cast (fast cooled), (b) homogenized and primarily aged (at 1250 °C for 24 hr and 800 °C for 3 hr) microstructures and temporal evolution of $\gamma'$ precipitates in Ni <sub>80</sub> Al <sub>20</sub> alloys as aging time at 800 °C is (c) 4 hr, (d) 16 hr, (e) 64 hr and (f) 256 hr, respectively .....	113
<b>Figure 5.19</b> Micro-hardness (Vickers) comparison of fast cooled (left) and slow cooled (right) as cast Ni <sub>80</sub> Al <sub>20</sub> alloys .....	117
<b>Figure 5.20</b> Micro-hardness (Vickers) comparison of heat treated Ni <sub>80</sub> Al <sub>20</sub> alloys. Black sphere denotes to fast cooled as cast sample, whereas sample groups (1-4) are represented in 1: blue, 2: red, 3: green and 4: purple spheres, respectively.....	117
<b>Figure 5.21</b> $\gamma'$ precipitate volume fraction variation of the second sample group of Ni <sub>80</sub> Al <sub>20</sub> alloys as aging time at 800 °C is (a) 4 hr, (b) 16 hr, (c) 64 hr and (d) 256 hr, respectively.....	118
<b>Figure 5.22</b> Size & size distribution and orientation of $\gamma'$ precipitates of the second sample group of Ni <sub>80</sub> Al <sub>20</sub> alloys as aging time at 800 °C is (a,e) 4 hr, (b,f) 16 hr, (c,g) 64 hr and (d,h) 256 hr, respectively .....	119
<b>Figure 5.23</b> FESEM micrographs showing as cast (fast cooled) microstructures of ternary Ni <sub>80</sub> Al <sub>15</sub> X <sub>5</sub> alloy systems where X = (a) Co, (b) Cr, (c) Hf, (d) Mo, (e) Nb, (f) Ta, (g) Ti and (h) W, respectively .....	128
<b>Figure 5.24</b> FESEM micrographs of as cast (fast cooled) Ni <sub>80</sub> Al <sub>15</sub> Nb <sub>5</sub> alloys showing (a) 3D dendrites, (b) the traces of a peritectic reaction, (c) SEI and (d) BSE micrographs demonstrating peritectic phases and Nb segregation in single $\gamma'$ phase .....	130
<b>Figure 5.25</b> FESEM micrographs of as cast (fast cooled) Ni <sub>80</sub> Al <sub>15</sub> Ti <sub>5</sub> alloys showing (a) the traces of a peritectic reaction, (b) peritectic phases (c) bigger and (d) smaller faceted $\gamma'$ precipitates around and in ( $\gamma + \gamma'$ ) phase regions, respectively .....	131

<b>Figure 5.26</b> FESEM micrographs showing different eutectic morphologies of as cast (fast cooled) $\text{Ni}_{80}\text{Al}_{15}\text{Hf}_5$ alloys: (a,b) lamellar, (c,d,e) rod-like and (f) feathery-like .....	132
<b>Figure 5.27</b> FESEM micrographs showing (a) partially-solution heat treated (at 1150 °C for 3 hr) and (b) homogenized and partially-solution heat treated (at 1250 °C for 24 hr and 1150 °C for 3 hr) microstructures of $\text{Ni}_{80}\text{Al}_{15}\text{Hf}_5$ alloys.....	135
<b>Figure 5.28</b> FESEM micrographs showing homogenized and partially-solution heat treated (at 1250 °C for 24 hr and 1150 °C for 3 hr) microstructures of $\text{Ni}_{80}\text{Al}_{15}\text{Ta}_5$ alloys containing both (a) dendritic regions and (b) grains within the same sample .....	136
<b>Figure 5.29</b> FESEM micrographs showing homogenized and partial solution heat treated (at 1250 °C for 24 hr and 1150 °C for 3 hr) and aged (at 800 °C for 256 hr) microstructures of $\text{Ni}_{80}\text{Al}_{15}\text{X}_5$ alloy systems where X = (a) Co, (b) Cr, (c) Mo and (d) Nb, respectively .....	137
<b>Figure 5.30</b> FESEM micrographs showing $\text{Ni}_{80}\text{Al}_{15}\text{Ta}_5$ alloys aged at 800 °C for (a,e) 4 hr, (b,f) 16 hr, (c,g) 64 hr and (d,h) 256 hr subsequent to either (a-d) partial solution heat treatment (at 1150 °C for 3 hr) or (e-h) homogenization and partial solution heat treatment (at 1250 °C for 24 hr and 1150 °C for 3 hr), respectively. ....	138
<b>Figure 5.31</b> Phase partitioning coefficients of alloying X elements (X = Co, Cr, Hf, Mo, Nb, Ta, Ti and W) in $\text{Ni}_{80}\text{Al}_{15}\text{X}_5$ alloy systems homogenized, partially solutionized and aged for 64 hr. First two columns (white and black) represent two individual measurements, whereas third and fourth columns (gray and pattern filled) are for their average values and standard deviations, respectively .....	141
<b>Figure 5.32</b> Atomic radius of alloying X elements (represented in black spheres) and micro-hardness values of as cast $\text{Ni}_{80}\text{Al}_{15}\text{X}_5$ alloy systems (shown in white marks) where X = Hf, Ta, Nb, W, Mo, Ti, Cr and Co, respectively.....	144
<b>Figure 5.33</b> Atomic radius of alloying X elements (represented in black spheres) and phase preferences of these alloying elements where X = Hf, Ta, Nb, W, Mo, Ti, Cr and Co, respectively .....	145

**Figure 5.34** Lattice parameter variations of Ni<sub>3</sub>Al-X phases; theoretically determined ones in Ni<sub>24</sub>Al<sub>7</sub>X (indicated in white spheres) and Ni<sub>23</sub>Al<sub>8</sub>X (represented by triangles) systems where alloying X elements occupy either Al or Ni sublattice sites, respectively and experimentally determined lattice parameters of γ' precipitates in as cast Ni<sub>80</sub>Al<sub>15</sub>X<sub>5</sub> alloy systems (shown in black spheres) where X = Hf, Ta, Nb, W, Mo, Ti, Al, Cr and Co, respectively ..... 146

**Figure 5.35** Experimentally determined lattice parameters of γ' precipitates (Ni<sub>3</sub>Al-X) (represented in black spheres) and micro-hardness values of as cast Ni<sub>80</sub>Al<sub>15</sub>X<sub>5</sub> alloy systems (shown in white marks) where X = Hf, Ta, Nb, W, Mo, Ti, Al, Cr and Co, respectively ..... 147

**Figure 5.36** XRD patterns of as cast (fast cooled) Ni<sub>80</sub>Al<sub>15</sub>X<sub>5</sub> alloy systems where X = (a) Hf, (b) Ta, (c) Nb, (d) W, (e) Mo, (f) Ti, (g) Al, (h) Cr and (i) Co, respectively ..... 148

**Figure 5.37** FESEM micrographs showing (a) elongated, (b) cuboidal, (c) cubic and (d-f) irregular (agglomerated/elongated) shapes of γ' precipitates of the second sample groups of Ni<sub>80</sub>Al<sub>15</sub>X<sub>5</sub> alloy systems aged at 800 °C for 256 hr where X = (a) Co, (b) Cr, (c) Mo, (d) Nb, (e) Ta and (f) Ti, respectively ..... 152

**Figure A.1** Binary phase diagram of Ni-Al system (Adapted from [137]) ..... 183

**Figure B.1** Isothermal (900 °C) ternary phase diagram of Ni-Al-Co system (Adapted from [138]) ..... 185

**Figure B.2** Isothermal (1000 °C) ternary phase diagram of Ni-Al-Cr system (Adapted from [139]) ..... 186

**Figure B.3** Isothermal (1160 °C) ternary phase diagram of Ni-Al-Hf system (Adapted from [140]) ..... 187

**Figure B.4** Isothermal (1000 °C) ternary phase diagram of Ni-Al-Hf system (Adapted from [140]) ..... 188

**Figure B.5** Partial reaction sequence of Ni-Al-Hf system (Adapted from [141]) ... 189

**Figure B.6** Isothermal (1000 °C) ternary phase diagram of Ni-Al-Mo system (Adapted from [142]) ..... 190

<b>Figure B.7</b> Isothermal (1027 °C) ternary phase diagram of Ni-Al-Nb system (Adapted from [143]).....	191
<b>Figure B.8</b> Isothermal (1000 °C) ternary phase diagram of Ni-Al-Ta system (Adapted from [144]).....	192
<b>Figure B.9</b> Isothermal (900 °C) ternary phase diagram of Ni-Al-Ti system (Adapted from [145]).....	193
<b>Figure B.10</b> Isothermal (900 °C) ternary phase diagram of Ni-Al-W system (Adapted from [146]).....	194
<b>Figure C.1</b> XRD patterns of (a) as cast (fast cooled) Ni <sub>80</sub> Al <sub>15</sub> Co <sub>5</sub> alloys, (b) partially-solutionized at 1150 °C for 3 hr and subsequently aged at 800 °C for (c) 4 hr (d) 16 hr (e) 64 hr and (f) 256 hr, respectively .....	196
<b>Figure C.2</b> XRD patterns of (a) as cast (fast cooled) Ni <sub>80</sub> Al <sub>15</sub> Co <sub>5</sub> alloys, (b) homogenized at 1250 °C for 24 hr and partially-solutionized at 1150 °C for 3 hr and subsequently aged at 800 °C for (c) 4 hr (d) 16 hr (e) 64 hr and (f) 256 hr, respectively .....	196
<b>Figure C.3</b> XRD patterns of (a) as cast (fast cooled) Ni <sub>80</sub> Al <sub>15</sub> Cr <sub>5</sub> alloys, (b) partially-solutionized at 1150 °C for 3 hr and subsequently aged at 800 °C for (c) 4 hr (d) 16 hr (e) 64 hr and (f) 256 hr, respectively .....	197
<b>Figure C.4</b> XRD patterns of (a) as cast (fast cooled) Ni <sub>80</sub> Al <sub>15</sub> Cr <sub>5</sub> alloys, (b) homogenized at 1250 °C for 24 hr and partially-solutionized at 1150 °C for 3 hr and subsequently aged at 800 °C for (c) 4 hr (d) 16 hr (e) 64 hr and (f) 256 hr, respectively .....	197
<b>Figure C.5</b> XRD patterns of (a) as cast (fast cooled) Ni <sub>80</sub> Al <sub>15</sub> Hf <sub>5</sub> alloys, (b) partially-solutionized at 1150 °C for 3 hr and subsequently aged at 800 °C for (c) 4 hr (d) 16 hr (e) 64 hr and (f) 256 hr, respectively .....	198
<b>Figure C.6</b> XRD patterns of (a) as cast (fast cooled) Ni <sub>80</sub> Al <sub>15</sub> Hf <sub>5</sub> alloys, (b) homogenized at 1250 °C for 24 hr and partially-solutionized at 1150 °C for 3 hr and subsequently aged at 800 °C for (c) 4 hr (d) 16 hr (e) 64 hr and (f) 256 hr, respectively .....	198

**Figure C.7** XRD patterns of (a) as cast (fast cooled) Ni<sub>80</sub>Al<sub>15</sub>Mo<sub>5</sub> alloys, (b) partially-solutionized at 1150 °C for 3 hr and subsequently aged at 800 °C for (c) 4 hr (d) 16 hr (e) 64 hr and (f) 256 hr, respectively .....199

**Figure C.8** XRD patterns of (a) as cast (fast cooled) Ni<sub>80</sub>Al<sub>15</sub>Mo<sub>5</sub> alloys, (b) homogenized at 1250 °C for 24 hr and partially-solutionized at 1150 °C for 3 hr and subsequently aged at 800 °C for (c) 4 hr (d) 16 hr (e) 64 hr and (f) 256 hr, respectively.....199

**Figure C.9** XRD patterns of (a) as cast (fast cooled) Ni<sub>80</sub>Al<sub>15</sub>Nb<sub>5</sub> alloys, (b) partially-solutionized at 1150 °C for 3 hr and subsequently aged at 800 °C for (c) 4 hr (d) 16 hr (e) 64 hr and (f) 256 hr, respectively .....200

**Figure C.10** XRD patterns of (a) as cast (fast cooled) Ni<sub>80</sub>Al<sub>15</sub>Nb<sub>5</sub> alloys, (b) homogenized at 1250 °C for 24 hr and partially-solutionized at 1150 °C for 3 hr and subsequently aged at 800 °C for (c) 4 hr (d) 16 hr (e) 64 hr and (f) 256 hr, respectively.....200

**Figure C.11** XRD patterns of (a) as cast (fast cooled) Ni<sub>80</sub>Al<sub>15</sub>Ta<sub>5</sub> alloys, (b) partially-solutionized at 1150 °C for 3 hr and subsequently aged at 800 °C for (c) 4 hr (d) 16 hr (e) 64 hr and (f) 256 hr, respectively .....201

**Figure C.12** XRD patterns of (a) as cast (fast cooled) Ni<sub>80</sub>Al<sub>15</sub>Ta<sub>5</sub> alloys, (b) homogenized at 1250 °C for 24 hr and partially-solutionized at 1150 °C for 3 hr and subsequently aged at 800 °C for (c) 4 hr (d) 16 hr (e) 64 hr and (f) 256 hr, respectively.....201

**Figure C.13** XRD patterns of (a) as cast (fast cooled) Ni<sub>80</sub>Al<sub>15</sub>Ti<sub>5</sub> alloys, (b) partially-solutionized at 1150 °C for 3 hr and subsequently aged at 800 °C for (c) 4 hr (d) 16 hr (e) 64 hr and (f) 256 hr, respectively .....202

**Figure C.14** XRD patterns of (a) as cast (fast cooled) Ni<sub>80</sub>Al<sub>15</sub>Ti<sub>5</sub> alloys, (b) homogenized at 1250 °C for 24 hr and partially-solutionized at 1150 °C for 3 hr and subsequently aged at 800 °C for (c) 4 hr (d) 16 hr (e) 64 hr and (f) 256 hr, respectively.....202

**Figure C.15** XRD patterns of (a) as cast (fast cooled) Ni<sub>80</sub>Al<sub>15</sub>W<sub>5</sub> alloys, (b) partially-

solutionized at 1150 °C for 3 hr and subsequently aged at 800 °C for (c) 4 hr (d) 16 hr (e) 64 hr and (f) 256 hr, respectively .....	203
<b>Figure C.16</b> XRD patterns of (a) as cast (fast cooled) Ni <sub>80</sub> Al <sub>15</sub> W <sub>5</sub> alloys, (b) homogenized at 1250 °C for 24 hr and partially-solutionized at 1150 °C for 3 hr and subsequently aged at 800 °C for (c) 4 hr (d) 16 hr (e) 64 hr and (f) 256 hr, respectively .....	203
<b>Figure E.1</b> DSC (a) heating and (b) cooling curves of as cast (fast cooled) Ni <sub>80</sub> Al <sub>15</sub> Co <sub>5</sub> alloys (at a rate of 20 °C/minutes) .....	210
<b>Figure E.2</b> DSC (a) heating and (b) cooling curves of as cast (fast cooled) Ni <sub>80</sub> Al <sub>15</sub> Cr <sub>5</sub> alloys (at a rate of 20 °C/minutes) .....	210
<b>Figure E.3</b> DSC (a) heating and (b) cooling curves of as cast (fast cooled) Ni <sub>80</sub> Al <sub>15</sub> Hf <sub>5</sub> alloys (at a rate of 20 °C/minutes) .....	211
<b>Figure E.4</b> DSC (a) heating and (b) cooling curves of as cast (fast cooled) Ni <sub>80</sub> Al <sub>15</sub> Mo <sub>5</sub> alloys (at a rate of 20 °C/minutes) .....	211
<b>Figure E.5</b> DSC (a) heating and (b) cooling curves of as cast (fast cooled) Ni <sub>80</sub> Al <sub>15</sub> Nb <sub>5</sub> alloys (at a rate of 20 °C/minutes) .....	212
<b>Figure E.6</b> DSC (a) heating and (b) cooling curves of as cast (fast cooled) Ni <sub>80</sub> Al <sub>15</sub> Ta <sub>5</sub> alloys (at a rate of 20 °C/minutes) .....	212
<b>Figure E.7</b> DSC (a) heating and (b) cooling curves of as cast (fast cooled) Ni <sub>80</sub> Al <sub>15</sub> Ti <sub>5</sub> alloys (at a rate of 20 °C/minutes) .....	213
<b>Figure E.8</b> DSC (a) heating and (b) cooling curves of as cast (fast cooled) Ni <sub>80</sub> Al <sub>15</sub> W <sub>5</sub> alloys (at a rate of 20 °C/minutes) .....	213
<b>Figure F.1</b> FESEM micrographs of (a) as cast, (b) partial solution heat treated microstructures and temporal evolution of γ' precipitates in Ni <sub>80</sub> Al <sub>15</sub> Co <sub>5</sub> alloys as aging time is (c) 4 hr, (d) 16 hr, (e) 64 hr and (f) 256 hr, respectively .....	216
<b>Figure F.2</b> FESEM micrographs of (a) as cast, (b) partial solution heat treated microstructures and temporal evolution of γ' precipitates in Ni <sub>80</sub> Al <sub>15</sub> Co <sub>5</sub> alloys as aging time is (c) 4 hr, (d) 16 hr, (e) 64 hr and (f) 256 hr, respectively .....	217



**Figure F.3** FESEM micrographs of (a) as cast, (b) homogenized/partial solution heat treated microstructures and temporal evolution of  $\gamma'$  precipitates in  $\text{Ni}_{80}\text{Al}_{15}\text{Co}_5$  alloys as aging time is (c) 4 hr, (d) 16 hr, (e) 64 hr and (f) 256 hr, respectively.....218

**Figure F.4** FESEM micrographs of (a) as cast, (b) homogenized/partial solution heat treated microstructures and temporal evolution of  $\gamma'$  precipitates in  $\text{Ni}_{80}\text{Al}_{15}\text{Co}_5$  alloys as aging time is (c) 4 hr, (d) 16 hr, (e) 64 hr and (f) 256 hr, respectively.....219

**Figure F.5** FESEM micrographs of (a) as cast, (b) partial solution heat treated microstructures and temporal evolution of  $\gamma'$  precipitates in  $\text{Ni}_{80}\text{Al}_{15}\text{Cr}_5$  alloys as aging time is (c) 4 hr, (d) 16 hr, (e) 64 hr and (f) 256 hr, respectively .....220

**Figure F.6** FESEM micrographs of (a) as cast, (b) partial solution heat treated microstructures and temporal evolution of  $\gamma'$  precipitates in  $\text{Ni}_{80}\text{Al}_{15}\text{Cr}_5$  alloys as aging time is (c) 4 hr, (d) 16 hr, (e) 64 hr and (f) 256 hr, respectively .....221

**Figure F.7** FESEM micrographs of (a) as cast, (b) homogenized/partial solution heat treated microstructures and temporal evolution of  $\gamma'$  precipitates in  $\text{Ni}_{80}\text{Al}_{15}\text{Cr}_5$  alloys as aging time is (c) 4 hr, (d) 16 hr, (e) 64 hr and (f) 256 hr, respectively.....222

**Figure F.8** FESEM micrographs of (a) as cast, (b) homogenized/partial solution heat treated microstructures and temporal evolution of  $\gamma'$  precipitates in  $\text{Ni}_{80}\text{Al}_{15}\text{Cr}_5$  alloys as aging time is (c) 4 hr, (d) 16 hr, (e) 64 hr and (f) 256 hr, respectively.....223

**Figure F.9** FESEM micrographs of (a) as cast, (b) partial solution heat treated microstructures and temporal evolution of  $\gamma'$  precipitates in  $\text{Ni}_{80}\text{Al}_{15}\text{Hf}_5$  alloys as aging time is (c) 4 hr, (d) 16 hr, (e) 64 hr and (f) 256 hr, respectively. ....224

**Figure F.10** FESEM micrographs of (a) as cast, (b) partial solution heat treated microstructures and temporal evolution of  $\gamma'$  precipitates in  $\text{Ni}_{80}\text{Al}_{15}\text{Hf}_5$  alloys as aging time is (c) 4 hr, (d) 16 hr, (e) 64 hr and (f) 256 hr, respectively .....225

**Figure F.11** FESEM micrographs of (a) as cast, (b) homogenized/partial solution heat treated microstructures and temporal evolution of  $\gamma'$  precipitates in  $\text{Ni}_{80}\text{Al}_{15}\text{Hf}_5$  alloys as aging time is (c) 4 hr, (d) 16 hr and (e) 64 hr, respectively. ....226

**Figure F.12** FESEM micrographs of (a) as cast, (b) homogenized/partial solution

heat treated microstructures and temporal evolution of  $\gamma'$  precipitates in  $\text{Ni}_{80}\text{Al}_{15}\text{Hf}_5$  alloys as aging time is (c) 4 hr, (d) 16 hr and (e) 64 hr, respectively. .... 227

**Figure F.13** FESEM micrographs of (a) as cast, (b) homogenized/partial solution heat treated microstructures and temporal evolution of  $\gamma'$  precipitates in  $\text{Ni}_{80}\text{Al}_{15}\text{Hf}_5$  alloys as aging time is (c) 4 hr, (d) 16 hr and (e) 64 hr, respectively. .... 228

**Figure F.14** FESEM micrographs of (a) as cast, (b) partial solution heat treated microstructures and temporal evolution of  $\gamma'$  precipitates in  $\text{Ni}_{80}\text{Al}_{15}\text{Mo}_5$  alloys as aging time is (c) 4 hr, (d) 16 hr, (e) 64 hr and (f) 256 hr, respectively ..... 229

**Figure F.15** FESEM micrographs of (a) as cast, (b) partial solution heat treated microstructures and temporal evolution of  $\gamma'$  precipitates in  $\text{Ni}_{80}\text{Al}_{15}\text{Mo}_5$  alloys as aging time is (c) 4 hr, (d) 16 hr, (e) 64 hr and (f) 256 hr, respectively ..... 230

**Figure F.16** FESEM micrographs of (a) as cast, (b) homogenized/partial solution heat treated microstructures and temporal evolution of  $\gamma'$  precipitates in  $\text{Ni}_{80}\text{Al}_{15}\text{Mo}_5$  alloys as aging time is (c) 4 hr, (d) 16 hr, (e) 64 hr and (f) 256 hr, respectively. .... 231

**Figure F.17** FESEM micrographs of (a) as cast, (b) homogenized/partial solution heat treated microstructures and temporal evolution of  $\gamma'$  precipitates in  $\text{Ni}_{80}\text{Al}_{15}\text{Mo}_5$  alloys as aging time is (c) 4 hr, (d) 16 hr, (e) 64 hr and (f) 256 hr, respectively. .... 232

**Figure F.18** FESEM micrographs of (a) as cast, (b) partial solution heat treated microstructures and temporal evolution of  $\gamma'$  precipitates in  $\text{Ni}_{80}\text{Al}_{15}\text{Nb}_5$  alloys as aging time is (c) 4 hr, (d) 16 hr, (e) 64 hr and (f) 256 hr, respectively ..... 233

**Figure F.19** FESEM micrographs of (a) as cast, (b) partial solution heat treated microstructures and temporal evolution of  $\gamma'$  precipitates in  $\text{Ni}_{80}\text{Al}_{15}\text{Nb}_5$  alloys as aging time is (c) 4 hr, (d) 16 hr, (e) 64 hr and (f) 256 hr, respectively ..... 234

**Figure F.20** FESEM micrographs of (a) as cast, (b) homogenized/partial solution heat treated microstructures and temporal evolution of  $\gamma'$  precipitates in  $\text{Ni}_{80}\text{Al}_{15}\text{Nb}_5$  alloys as aging time is (c) 4 hr, (d) 16 hr, (e) 64 hr and (f) 256 hr, respectively. .... 235

**Figure F.21** FESEM micrographs of (a) as cast, (b) homogenized/partial solution heat treated microstructures and temporal evolution of  $\gamma'$  precipitates in  $\text{Ni}_{80}\text{Al}_{15}\text{Nb}_5$

alloys as aging time is (c) 4 hr, (d) 16 hr, (e) 64 hr and (f) 256 hr, respectively.....	236
<b>Figure F.22</b> FESEM micrographs of (a) as cast, (b) partial solution heat treated microstructures and temporal evolution of $\gamma'$ precipitates in $\text{Ni}_{80}\text{Al}_{15}\text{Ta}_5$ alloys as aging time is (c) 4 hr, (d) 16 hr, (e) 64 hr and (f) 256 hr, respectively .....	237
<b>Figure F.23</b> FESEM micrographs of (a) as cast, (b) partial solution heat treated microstructures and temporal evolution of $\gamma'$ precipitates in $\text{Ni}_{80}\text{Al}_{15}\text{Ta}_5$ alloys as aging time is (c) 4 hr, (d) 16 hr, (e) 64 hr and (f) 256 hr, respectively .....	238
<b>Figure F.24</b> FESEM micrographs of (a) as cast, (b) homogenized/partial solution heat treated microstructures and temporal evolution of $\gamma'$ precipitates in $\text{Ni}_{80}\text{Al}_{15}\text{Ta}_5$ alloys as aging time is (c) 4 hr, (d) 16 hr, (e) 64 hr and (f) 256 hr, respectively.....	239
<b>Figure F.25</b> FESEM micrographs of (a) as cast, (b) homogenized/partial solution heat treated microstructures and temporal evolution of $\gamma'$ precipitates in $\text{Ni}_{80}\text{Al}_{15}\text{Ta}_5$ alloys as aging time is (c) 4 hr, (d) 16 hr, (e) 64 hr and (f) 256 hr, respectively.....	240
<b>Figure F.26</b> FESEM micrographs of (a) as cast, (b) partial solution heat treated microstructures and temporal evolution of $\gamma'$ precipitates in $\text{Ni}_{80}\text{Al}_{15}\text{Ti}_5$ alloys as aging time is (c) 4 hr, (d) 16 hr, (e) 64 hr and (f) 256 hr, respectively .....	241
<b>Figure F.27</b> FESEM micrographs of (a) as cast, (b) partial solution heat treated microstructures and temporal evolution of $\gamma'$ precipitates in $\text{Ni}_{80}\text{Al}_{15}\text{Ti}_5$ alloys as aging time is (c) 4 hr, (d) 16 hr, (e) 64 hr and (f) 256 hr, respectively .....	242
<b>Figure F.28</b> FESEM micrographs of (a) as cast, (b) homogenized/partial solution heat treated microstructures and temporal evolution of $\gamma'$ precipitates in $\text{Ni}_{80}\text{Al}_{15}\text{Ti}_5$ alloys as aging time is (c) 4 hr, (d) 16 hr, (e) 64 hr and (f) 256 hr, respectively.....	243
<b>Figure F.29</b> FESEM micrographs of (a) as cast, (b) homogenized/partial solution heat treated microstructures and temporal evolution of $\gamma'$ precipitates in $\text{Ni}_{80}\text{Al}_{15}\text{Ti}_5$ alloys as aging time is (c) 4 hr, (d) 16 hr, (e) 64 hr and (f) 256 hr, respectively.....	244
<b>Figure I.1</b> Micro-hardness (Vickers) comparison of heat treated $\text{Ni}_{80}\text{Al}_{15}\text{Co}_5$ alloys. Black sphere denotes to fast cooled as cast sample, whereas sample groups (1-2) are represented in 1: open spheres and 2: open triangles, respectively .....	260

**Figure I.2** Micro-hardness (Vickers) comparison of heat treated Ni<sub>80</sub>Al<sub>15</sub>Cr<sub>5</sub> alloys. Black sphere denotes to fast cooled as cast sample, whereas sample groups (1-2) are represented in 1: open spheres and 2: open triangles, respectively ..... 260

**Figure I.3** Micro-hardness (Vickers) comparison of heat treated Ni<sub>80</sub>Al<sub>15</sub>Hf<sub>5</sub> alloys. Black sphere denotes to fast cooled as cast sample, whereas first sample group is represented in open spheres ..... 261

**Figure I.4** Micro-hardness (Vickers) comparison of heat treated Ni<sub>80</sub>Al<sub>15</sub>Mo<sub>5</sub> alloys. Black sphere denotes to fast cooled as cast sample, whereas sample groups (1-2) are represented in 1: open spheres and 2: open triangles, respectively ..... 261

**Figure I.5** Micro-hardness (Vickers) comparison of heat treated Ni<sub>80</sub>Al<sub>15</sub>Nb<sub>5</sub> alloys. Black sphere denotes to fast cooled as cast sample, whereas sample groups (1-2) are represented in 1: open spheres and 2: open triangles, respectively ..... 262

**Figure I.6** Micro-hardness (Vickers) comparison of heat treated Ni<sub>80</sub>Al<sub>15</sub>Ta<sub>5</sub> alloys. Black sphere denotes to fast cooled as cast sample, whereas sample groups (1-2) are represented in 1: open spheres and 2: open triangles, respectively ..... 262

**Figure I.7** Micro-hardness (Vickers) comparison of heat treated Ni<sub>80</sub>Al<sub>15</sub>Ti<sub>5</sub> alloys. Black sphere denotes to fast cooled as cast sample, whereas sample groups (1-2) are represented in 1: open spheres and 2: open triangles, respectively ..... 263

**Figure I.8** Micro-hardness (Vickers) comparison of heat treated Ni<sub>80</sub>Al<sub>15</sub>W<sub>5</sub> alloys. Black sphere denotes to fast cooled as cast sample, whereas first sample group is represented in open spheres ..... 263

**Figure J.1**  $\gamma'$  precipitate volume fraction variation of the second sample group of Ni<sub>80</sub>Al<sub>15</sub>Co<sub>5</sub> alloys as aging time at 800 °C is (a) 4 hr, (b) 16 hr, (c) 64 hr and (d) 256 hr, respectively ..... 266

**Figure J.2**  $\gamma'$  precipitate volume fraction variation of the second sample group of Ni<sub>80</sub>Al<sub>15</sub>Cr<sub>5</sub> alloys as aging time at 800 °C is (a) 4 hr, (b) 16 hr, (c) 64 hr and (d) 256 hr, respectively ..... 266

<b>Figure J.3</b> $\gamma'$ precipitate volume fraction variation of the second sample group of $\text{Ni}_{80}\text{Al}_{15}\text{Mo}_5$ alloys as aging time at 800 °C is (a) 4 hr, (b) 16 hr, (c) 64 hr and (d) 256 hr, respectively.....	267
<b>Figure J.4</b> $\gamma'$ precipitate volume fraction variation of the second sample group of $\text{Ni}_{80}\text{Al}_{15}\text{Nb}_5$ alloys as aging time at 800 °C is (a) 4 hr, (b) 16 hr, (c) 64 hr and (d) 256 hr, respectively.....	267
<b>Figure J.5</b> $\gamma'$ precipitate volume fraction variation of the second sample group of $\text{Ni}_{80}\text{Al}_{15}\text{Ta}_5$ alloys as aging time at 800 °C is (a) 4 hr, (b) 16 hr, (c) 64 hr and (d) 256 hr, respectively.....	268
<b>Figure J.6</b> $\gamma'$ precipitate volume fraction variation of the second sample group of $\text{Ni}_{80}\text{Al}_{15}\text{Ti}_5$ alloys as aging time at 800 °C is (a) 4 hr, (b) 16 hr, (c) 64 hr and (d) 256 hr, respectively.....	268
<b>Figure K.1</b> Size & size distribution and orientation of $\gamma'$ precipitates of the second sample group of $\text{Ni}_{80}\text{Al}_{15}\text{Co}_5$ alloys as aging time at 800 °C is (a,e) 4 hr, (b,f) 16 hr, (c,g) 64 hr and (d,h) 256 hr, respectively.....	270
<b>Figure K.2</b> Size & size distribution and orientation of $\gamma'$ precipitates of the second sample group of $\text{Ni}_{80}\text{Al}_{15}\text{Cr}_5$ alloys as aging time at 800 °C is (a,e) 4 hr, (b,f) 16 hr, (c,g) 64 hr and (d,h) 256 hr, respectively.....	271
<b>Figure K.3</b> Size & size distribution and orientation of $\gamma'$ precipitates of the second sample group of $\text{Ni}_{80}\text{Al}_{15}\text{Mo}_5$ alloys as aging time at 800 °C is (a,e) 4 hr, (b,f) 16 hr, (c,g) 64 hr and (d,h) 256 hr, respectively.....	272
<b>Figure K.4</b> Size & size distribution and orientation of $\gamma'$ precipitates of the second sample group of $\text{Ni}_{80}\text{Al}_{15}\text{Nb}_5$ alloys as aging time at 800 °C is (a,e) 4 hr, (b,f) 16 hr, (c,g) 64 hr and (d,h) 256 hr, respectively.....	273
<b>Figure K.5</b> Size & size distribution and orientation of $\gamma'$ precipitates of the second sample group of $\text{Ni}_{80}\text{Al}_{15}\text{Ta}_5$ alloys as aging time at 800 °C is (a,e) 4 hr, (b,f) 16 hr, (c,g) 64 hr and (d,h) 256 hr, respectively.....	274

**Figure K.6** Size & size distribution and orientation of  $\gamma'$  precipitates of the second sample group of  $\text{Ni}_{80}\text{Al}_{15}\text{Ti}_5$  alloys as aging time at 800 °C is (a,e) 4 hr, (b,f) 16 hr, (c,g) 64 hr and (d,h) 256 hr, respectively .....275



## LIST OF SYMBOLS AND ABBREVIATIONS

<b>a. u.</b>	Arbitrary unit
<b>at. u.</b>	Atomic unit
<b>at. %</b>	Atomic percent
<b><math>a_{\gamma}</math></b>	Lattice parameter of $\gamma$ matrix phase
<b><math>a_{\gamma'}</math></b>	Lattice parameter of $\gamma'$ precipitates
<b><math>C_i^{\gamma}</math></b>	Concentration of “i” element in $\gamma$ matrix phase
<b><math>C_i^{\gamma'}</math></b>	Concentration of “i” element in $\gamma'$ precipitates
<b><math>E_{APB}</math></b>	Antiphase boundary energy
<b><math>E_f</math></b>	Fermi energy
<b><math>N(E_f)</math></b>	pDOS value at Fermi energy level
<b><math>r_i</math></b>	Atomic radius of “i” element
<b><math>R_1</math></b>	First coordination sphere
<b>t</b>	Time
<b>T</b>	Temperature
<b><math>T_c</math></b>	Critical temperature
<b><math>T_m</math></b>	Melting temperature
<b><math>V_f</math></b>	Volume fraction

<b>wt.%</b>	Weight percent
$W_{\alpha-\alpha'}(\mathbf{R}_1)$	Partial ordering energy of $\alpha-\alpha'$ atomic pairs at $R_1$
$\alpha_{\alpha-\alpha'}(\mathbf{R}_1)$	Partial SRO parameter of $\alpha-\alpha'$ atomic pairs at $R_1$
$\gamma$	Ni solid solution, matrix phase
$\gamma'$	$\text{Ni}_3\text{Al}$ precipitates
$\gamma''$	$\text{Ni}_3(\text{Al,Nb})$ precipitates
$\delta$	Orthorombic $\gamma''$ phase stable at higher temperatures
$\delta$	Lattice misfit parameter
$\eta$	Shape parameter
$\kappa_i$	Phase partitioning coefficient of “i” element
<b>ALCHEMI</b>	Atomic site location by channelling enhanced micro-analysis
<b>APB</b>	Antiphase boundary
<b>APFIM</b>	Atom probe field ion microscopy
<b>APT</b>	Atom probe tomography
<b>BSE</b>	Back-scattered electron image
<b>CALPHAD</b>	Calculation of phase diagrams
<b>CDD</b>	Charge density difference
<b>DFT</b>	Density functional theory
<b>DOS</b>	Density of states
<b>DSC</b>	Differential scanning calorimetry



<b>EDS</b>	Energy dispersive spectroscopy
<b>ELF</b>	Electron localization function
<b>EPMA</b>	Electron probe micro-analysis
<b>FESEM</b>	Field emission scanning electron microscopy
<b>GGA-PBE</b>	Generalized gradient approximation after Perdew-Burke-Ernzerhof
<b>ICP-MS</b>	Inductively coupled plasma-mass spectroscopy
<b>LMTO</b>	Linear-muffin-tin orbital
<b>LRO</b>	Long range order
<b>LSW</b>	Lifshitz-Slyozov-Wagner
<b>NN</b>	Nearest neighbour
<b>pDOS</b>	Partial density of states
<b>RT</b>	Room temperature
<b>SCF</b>	Self-consistent-field
<b>SEI</b>	Secondary electron image
<b>SF</b>	Stacking fault
<b>SRO</b>	Short range order
<b>TCP</b>	Topologically closed-packed
<b>TEM</b>	Transmission electron microscopy
<b>UTS</b>	Ultimate tensile strength
<b>VASP</b>	Vienna ab initio simulation package
<b>XRD</b>	X-ray diffraction



# CHAPTER 1

## INTRODUCTION

### 1.1 Aim and Motivation

High temperature nickel-based superalloys used in aerospace (turbine blades/discs), marine and land-based applications, possess significant ability to maintain their excellent mechanical properties at elevated temperatures. Hence, these materials are always of great interest to improve the operating efficiency of their application areas. Nickel-based superalloys owe their unique class of mechanical-environmental properties (high temperature tensile strength, creep and oxidation-corrosion resistance) to the existence of their two phase microstructure; FCC-type disordered  $\gamma$  matrix phase (Ni solid solution) and L1<sub>2</sub>-type ordered  $\gamma'$  precipitates (Ni<sub>3</sub>Al). In the light of strengthening mechanisms, the relationship between these two constituent phases plays a significant role to obtain afore mentioned excellent mechanical properties. Luckily, thanks to developing techniques, enhancement of high temperature capability and efficiency of these materials is possible by adjusting alloy compositions/microstructures and heat treatment procedures.

Nickel-based superalloys may contain ten to fifteen alloying elements (e.g. Al, Co, Cr, Hf, Mo, Nb, Pt, Re, Ru, Ta, Ti and W). Thus, it is very important to comprehend the role of each individual alloying element (their site occupancy characteristics in Ni<sub>3</sub>Al sublattices, phase preferences and effects on the microstructural features, such as  $\gamma'$  precipitate volume fraction, size & size distribution, orientation and shape). In this thesis, therefore, high temperature and 0 Kelvin sublattice site occupancy preferences of afore mentioned alloying elements have been studied by performing short range order (SRO) parameter calculations and first-principles *ab initio* calculations,

respectively. In addition to first-principles *ab initio* calculations utilized in Vienna *ab initio* simulation package (VASP), simulation methods, such as charge density difference (CDD), electron localization function (ELF) and density of states (DOS) have also been applied to reveal the effects of alloying elements on the bonding characteristics and hybridization types of Ni<sub>3</sub>Al-X intermetallics. In the current work, another alloy design consideration is to determine optimum heat treatment parameters result in better microstructural and mechanical properties which depend on cooling rate (during initial solidification and between heat treatment steps) and time/temperature values of homogenization, solutionizing and aging heat treatments.

This thesis consists of seven chapters. After giving a brief introduction in the first chapter, some basic definitions and useful information related with nickel-based superalloys have been mentioned in Chapter 2. In literature, several studies have focused on the determination of site occupancy characteristics of some certain alloying elements in Ni<sub>3</sub>Al phase. Thus, in Chapters 3-4, similar works have been done by applying SRO parameter calculations and first-principles calculations. In Chapter 4, by performing CDD, ELF and DOS methods, bonding types between two adjacent atoms in Ni<sub>3</sub>Al-X phases and the origin of phase strengthenings have been simulated. In Chapter 5, after production of Ni<sub>80</sub>Al<sub>15</sub>X<sub>5</sub> alloy systems (X = Al, Co, Cr, Hf, Mo, Nb, Ta, Ti and W, respectively) by arc melting & suction casting techniques, heat treatment procedures and characterization techniques have been mentioned and microstructural & mechanical properties of as cast and heat treated Ni<sub>80</sub>Al<sub>15</sub>X<sub>5</sub> alloy systems have been examined in detail. Furthermore, all theoretical and experimental data obtained from previous chapters have been combined and discussed. Lastly, in Chapters 6-7, major contributions of this thesis to the existing literature have been highlighted and future works have been suggested.

## **1.2 Contribution of the Thesis**

In literature, sublattice site occupancy characteristics of alloying elements in Ni<sub>3</sub>Al phase are usually determined by performing first-principles *ab initio* calculations at 0

Kelvin which have also been performed in this thesis. However, high service temperatures of nickel-based superalloys (i.e. ~ 1000 °C) necessitate these calculations to be performed at high temperatures as well. Therefore, in the current work, high temperature site preference behaviours of alloying X elements (X = Co, Cr, Hf, Mo, Nb, Pt, Re, Ru, Ta and W, respectively) in non-stoichiometric (Ni-rich)  $\text{Ni}_{75}\text{Al}_{21.875}\text{X}_{3.125}$  alloy systems have been studied by combining the statistical theory of ordering and electronic theory of alloys in the pseudopotential approximation. Theory proposed for the calculation of partial SRO parameters in ternary intermetallic systems at first coordination sphere (in R space or real space) has been utilized for the first time to evaluate distribution tendencies of constituent atoms in submicro volumes of  $\text{Ni}_3\text{Al}$  phase. According to the signs of partial SRO parameters of atomic pairs, as opposed to the alloying elements preferentially occupying either Al or Ni sublattice sites, both Al and Ni site occupancy behaviour of low soluble Re atoms in  $\text{Ni}_{75}\text{Al}_{25-x}\text{Re}_x$  alloys has been attributed to possible formation of topologically closed packed (TCP) phases above critical temperatures,  $T_c$ .

In experimental investigation part of the thesis, the effects of alloying X elements on as cast and heat treated  $\text{Ni}_{80}\text{Al}_{15}\text{X}_5$  alloy systems (X = Al, Co, Cr, Hf, Mo, Nb, Ta, Ti and W, respectively) have been investigated by means of microstructural characteristics, such as  $\gamma'$  precipitate volume fraction, size & size distribution, orientation and shape. Micro-hardness values of each alloy system have been determined and the results have been correlated with these microstructural characteristics and theoretical CDD, ELF and DOS simulations. In conclusion, in the light of these theoretical simulations and experimental data, improved mechanical properties of nickel-based superalloys have been ascribed to  $\gamma'$ - $\text{Ni}_3\text{Al}$  precipitates having higher lattice parameter, higher volume fraction, smaller size and correspondingly optimum  $\delta$  parameter with  $\gamma$  matrix phase.



## CHAPTER 2

### NICKEL-BASED SUPERALLOYS

#### 2.1 Historical Background of Nickel-based Superalloys

Nickel-based superalloys, whose invention dates back to the 1940s, are commonly used in hot sections of turbine blades, rocket engines, nuclear power and chemical processing plants [1,2]. As shown in Figure 2.1 [1], first superalloys were in wrought forms; however, with evolving process technologies, superalloys have been generated in conventionally cast, directionally solidified and single-crystal forms, respectively.

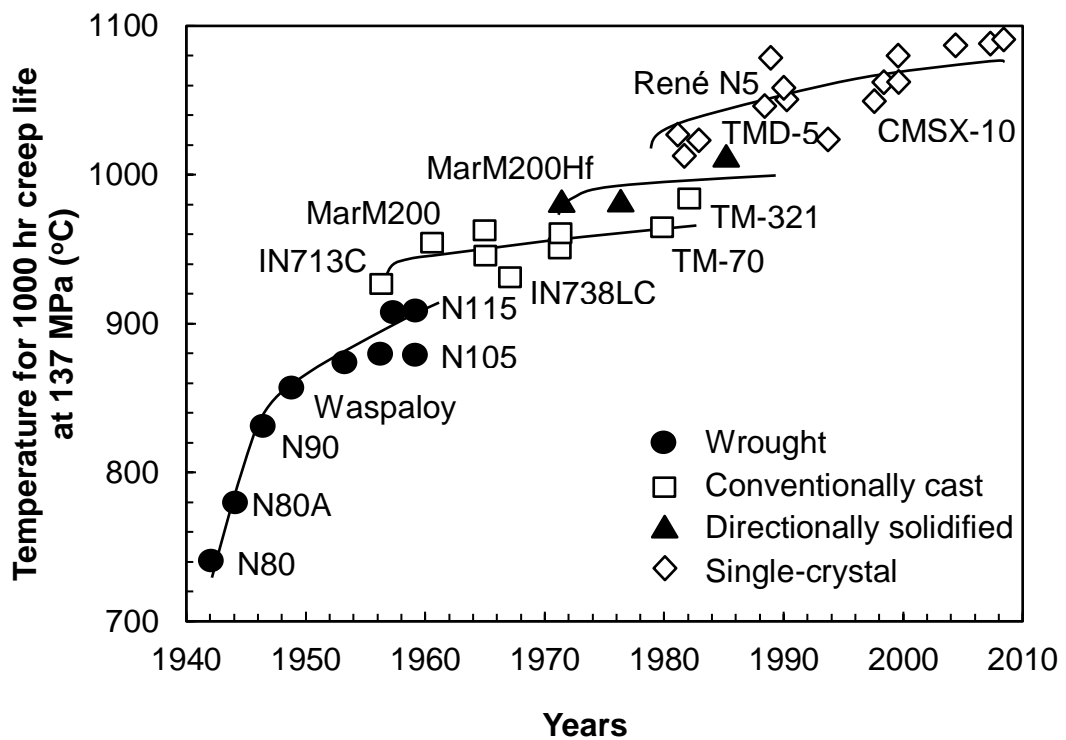


**Figure 2.1** Development of high temperature mechanical properties of superalloys from the 1940s to 2010s (Adapted from [1]).

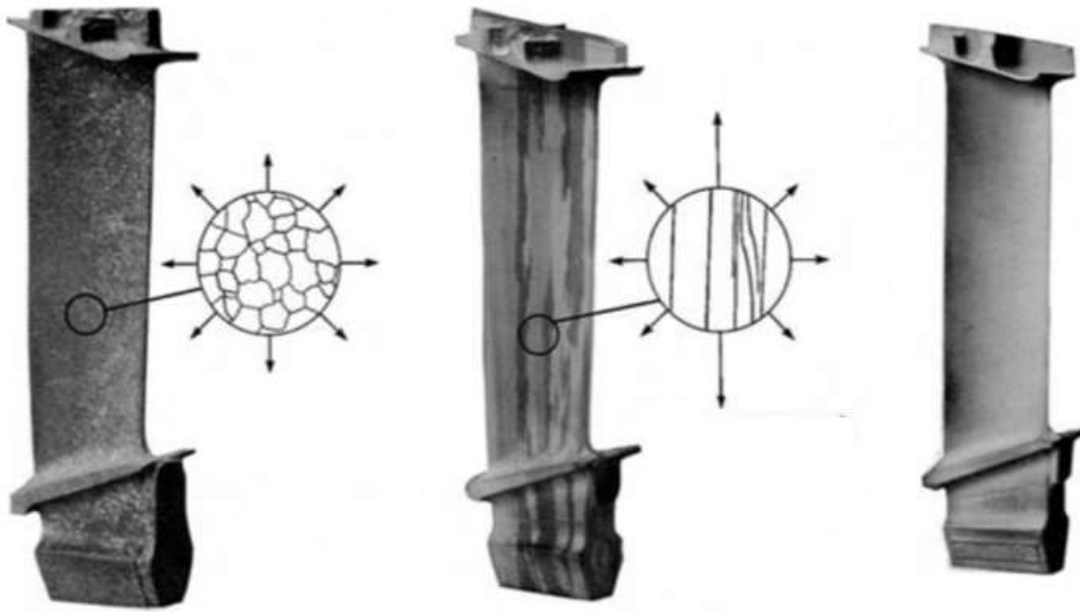


**Figure 2.2** Equiaxed (left), columnar (middle) and single-crystal (right) forms of turbine blades (Adapted from [1]).

The first turbine blades, one of the most commonly used application areas of nickel-based superalloys, were also produced in wrought forms. However, thanks to introduction of enhanced casting techniques, cast turbine blades rather than wrought ones have been preferred. Later, introduction of directional solidification has led to better mechanical properties since microstructures of these materials consisted of columnar grains in which transverse grain boundaries were absent [1]. Starting from the 1980s to middle of the 1990s, in the approximately fifteen year period of alloy processing improvements, physical factors affecting high temperature properties of superalloys have been comprehended and first single-crystal forms of turbine blades have been produced in which grain boundaries were completely removed as illustrated in Figure 2.2 [1]. Due to elimination of grain boundaries within microstructures of single-crystal superalloys, grain boundary strengthening elements, such as carbon and boron were removed and high temperature capability of these materials has enormously been increased. Today, most of the turbine blades are in single-crystal forms since the best creep properties are required in these materials, although columnar and equiaxed form castings of these materials are still used in many practices [1].



## 2.2 Mechanical Properties of Nickel-based Superalloys

Nickel-based superalloys have wide-range of application areas due to their outstanding high temperature mechanical properties (yield strength, creep strength, toughness) and oxidation-corrosion resistance [1,2]. At room temperature (RT), yield strength and ultimate tensile strength (UTS) of nickel-based superalloys mostly change in the interval of 900-1300 MPa and 1200-1600 MPa, respectively [2]. Interestingly, these materials maintain their tensile properties until temperatures slightly greater than 850 °C and a minor improvement in yield strength values of these materials at intermediate temperatures (i.e. < 800 °C), which is called as yield anomaly, is originated from the unusual flow behaviour of  $\gamma'$ -Ni<sub>3</sub>Al precipitates [2]. Depending on different compositions of nickel-based superalloys, the limit of yield anomaly can exceed around 880 °C [1].

Remarkable creep properties of nickel-based superalloys are substantially arised from the fact that  $\gamma'$ -Ni<sub>3</sub>Al precipitates resist shearing at elevated temperatures [2]. Creep deformation generally occurs by the deformation on <110>{111} slip systems in which continuous  $\gamma$  matrix phase is preferred for dislocation glide. On the other hand, <112>{111} slip systems may also be activated by high uniaxial stresses at temperatures < 0.6 T<sub>m</sub> [2]. Since creep properties (including rate controlling processes) are diffusion controlled, alloying elements having low interdiffusion coefficient with nickel atoms are considered to be favourable for creep resistance which can be improved further by orienting grain boundaries along the applied stress direction or, most notably, by removing grain boundaries in the microstructure thoroughly [2].

Because of extreme service conditions of nickel-based superalloys (oxidative-corrosive high temperatures), these materials have to resist environmental degradation. Oxidation-corrosion resistance of these materials are generally enhanced by alloying element additions, such as Cr and Hf which lead to formation of protective layers on superalloys [1]. In general, mechanical properties of nickel-based superalloys are associated with the microstructural characteristics of these materials (i.e. volume

fraction, size & size distribution, orientation and morphology of  $\gamma'$ -Ni<sub>3</sub>Al precipitates within  $\gamma$  matrix phase) [1-3]. However, due to disruption in these microstructural features and high diffusion and coarsening phenomena, strength rapidly decreases above 1000 °C [4,5].

## **2.3 Strengthening Mechanisms**

Strengthening in two phase ( $\gamma$ - $\gamma'$ ) microstructures of nickel-based superalloys is arised from some mechanisms including precipitation hardening, solid solution strengthening, coherency-type strengthening and grain boundary strengthening [1,2]. For this reason, correct understanding of these mechanisms is very important to improve mechanical properties of these materials.

### **2.3.1 Precipitation Hardening**

In precipitation hardening,  $\gamma'$ -Ni<sub>3</sub>Al precipitates restrict the motion of mobile dislocations by means of some interaction mechanisms, such as ordering strengthening, coherency-type strengthening and modulus hardening [6]. While L1<sub>2</sub>-type ordered  $\gamma'$  precipitates interact with dislocations, antiphase boundaries (APB) may form and slow down dislocation motion heading towards  $\gamma'$  precipitates and hence improve mechanical properties (i.e. strength) [6,7]. In other words, by reducing the mobility of dislocations during plastic deformation, coherently distributed  $\gamma'$ -Ni<sub>3</sub>Al precipitates in  $\gamma$  matrix phase-Ni solid solution are the sources of significant order and coherency-type strengthenings [6,8].

In nickel-based superalloys, plastic deformation may occur in different ways; at lower loads, dislocations move within the  $\gamma$  matrix channels. However, if the applied load is sufficiently high, precipitate cutting mechanisms cause deformation to occur in both  $\gamma$  and  $\gamma'$  phases [9]. In precipitate cutting deformation, APBs within  $\gamma'$  precipitates inhibit dislocation motion energy [9]. If temperature is high enough, dislocations become capable of passing  $\gamma'$  precipitates through thermally-activated climb processes [9].

If  $\gamma'$  precipitates are assumed to be perfectly cubic and the interface between  $\gamma$  and  $\gamma'$  phases is perfectly coherent, dislocation glide system becomes  $\langle 110 \rangle \{ 111 \}$ . Thus, intersection shapes between dislocation glide plane and  $\gamma'$  precipitates become triangle or irregular hexagons [10].

### 2.3.2 Solid Solution Strengthening

Besides precipitation hardening, strengthening of relatively soft  $\gamma$  matrix phase is also important to improve mechanical properties [11]. For many alloying elements,  $\gamma$  matrix phase-Ni solid solution has large solid solubility due to electronic structure of Ni. However, there are three criteria need to be met by each alloying element. For a notable solid solution strengthening, alloying elements should have [2,9];

- high amount of solid solubility within  $\gamma$  matrix phase,
- large atomic size to deform/alter the lattice efficiently [2],
- high melting temperature,  $T_m$  [9].

By considering these three criteria, certain amounts of refractory alloying elements (e.g. Mo, Nb, Re, Ru and W) can be added to nickel-based superalloys to designate alloy compositions as solid solution strengtheners [9,12,13]. Unlike Re atoms, Ru atoms cause solid solution strengthening of both  $\gamma$  and  $\gamma'$  phases, whereas Re atoms are the strongest solid solution strengtheners compared to other refractory elements [11,13]. However, at elevated service temperatures of nickel-based superalloys, localized supersaturation of Re atoms leads to formation of deleterious TCP phases [14-16].

### 2.3.3 Coherency-type Strengthening

As given in Equation (2.1), depending on lattice parameters of constituent  $\gamma$  ( $a_\gamma$ ) and  $\gamma'$  phases ( $a_{\gamma'}$ ), the amount of coherency (calculated by lattice misfit parameter,  $\delta$ ) between these two phases induces strain fields which restrict dislocation motion [7]. This phenomenon is defined as coherency-type strengthening which also controls the

coarsening behaviour of  $\gamma'$  precipitates [17-19]. In this mechanism,  $\gamma$  and  $\gamma'$  phases have a cube-on-cube relationship having crystallographic systems of  $(100)_{\text{precipitate}}// (100)_{\text{matrix}}$  and  $[010]_{\text{precipitate}}// [010]_{\text{matrix}}$  [9].

$$\delta = 2 \times \frac{a_{\gamma'} - a_{\gamma}}{a_{\gamma'} + a_{\gamma}} \quad (2.1)$$

### 2.3.4 Grain Boundary Strengthening

Grain boundary strengthening is another strengthening mechanism for polycrystalline nickel-based superalloys. Because, in this mechanism, besides  $\gamma'$  precipitates, grain boundaries also impede dislocation motion. By adjusting alloy compositions (additions of carbon and boron which lead to carbides and borides at grain boundaries) and heat treatment procedures, grain size and correspondingly mechanical properties of these materials can be controlled [1,2].

## 2.4 General Microstructural Features

Depending on different process techniques, general microstructures of nickel-based superalloys may consist of equiaxed grains, columnar grains or single-crystals [1,2]. Considering excellent creep properties, most of the nickel-based superalloys are in single-crystal forms having no grain boundaries acting as damage accumulation sites at elevated service temperatures [1,2]. However, in some certain type of nickel-based superalloys used in the cooler stages of turbine blade and disc applications, equiaxed grains constitute the polycrystalline microstructures of these materials [2]. Polycrystalline nickel-based superalloys may be disadvantageous in terms of creep resistance, however, due to the probabilistic randomness of grain orientations their mechanical properties would most probably have isotropic characteristics [20].

In some certain polycrystalline nickel-based superalloys, annealing twins may form due to growth accidents on  $\{111\}$  propagating steps present on migrating grain

boundaries. Because of these accidents, Shockley partials are created adjacent to the grain boundaries and in the last step, twin boundaries occur since these partials repel each other and cause themselves to glide away from the grain boundaries [21]. In twin boundary formation mechanism, for higher grain boundary velocities, the probability of growth accidents on {111} propagating steps increases. On the other hand, annealing twin boundaries cannot form in high stacking fault energy materials in which Shockley partials are not stable. Therefore, the existence and absence of these boundaries may give some important clues about the stacking fault energy values of related alloy systems [21]. In low stacking fault energy materials, annealing twin boundaries arise that make recrystallization process complicated [22]. In other words, annealing twin boundaries form in low to moderate stacking fault energy materials up to a limited value described by Palumbo et al. [23].

Nickel-based superalloys mainly consist of  $\gamma$  and  $\gamma'$  phases. However, depending on alloy compositions, additional phases may appear at some certain temperatures. In the following parts, general properties of these phases have been mentioned in detail.

#### **2.4.1 $\gamma'$ -Ni<sub>3</sub>Al Precipitates**

Nickel-based superalloys owe their excellent high temperature mechanical properties to the existence of L1<sub>2</sub>-type ordered  $\gamma'$ -Ni<sub>3</sub>Al precipitates in which Al atoms and Ni atoms occupy corner and face-centered sites, respectively (Figure 2.3) [1].  $\gamma'$  precipitates act as obstacles against dislocation motion and alloys containing this phase exhibit yield anomaly with increasing temperature, namely, their yield strength increases up to certain temperatures [2]. The greatest advantage of Ni<sub>3</sub>Al phase compared to  $\gamma$  matrix phase is its resistance capacity to deformation. Ni<sub>3</sub>Al phase may exhibit flow stresses 3-5 times higher than  $\gamma$  matrix phase does [13]. Some physical properties of Ni<sub>3</sub>Al intermetallics are given in Table 2.1 [24]. Besides excellent properties, such as high melting point, low density, high strength, as well as good corrosion-oxidation resistance, Ni<sub>3</sub>Al phase has some drawbacks, such as brittle fracture, deficient ductility and creep resistance at high temperatures [24-27].

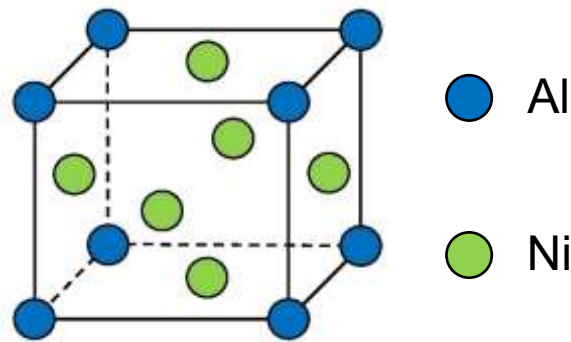


**Figure 2.3** The crystal structure of L1<sub>2</sub>-type ordered  $\gamma'$ -Ni<sub>3</sub>Al precipitates in which Al atoms (blue) and Ni atoms (green) occupy corner and face-centered sites, respectively.

**Table 2.1** Physical properties of Ni<sub>3</sub>Al intermetallics (Adapted from [24]).

Properties	Ni <sub>3</sub> Al phase
Electrical resistivity ( $10^{-8}\Omega\text{m}$ )	32.59
Thermal conductivity (W/m.K)	28.85
Thermal expansion coefficient ( $10^{-6}/\text{K}^{-1}$ )	12.50
Lattice parameter ( $\text{\AA}$ )	3.57 [1,24]
Young's modulus (GPa)	168
Specific heat (J/g.K)	0.54
Melting point ( $^{\circ}\text{C}$ )	1395
Bonding	Covalent/metallic
APB energy ( $\text{mJ m}^{-2}$ )	232 (CALPHAD at 650 $^{\circ}\text{C}$ ), 310 (DFT) [28]
Magnetic moment ( $\mu_{\text{B}}$ )	0.22 [29], 0.23 [30]
Curie temperature (K)	41 [30]
Heat of formation ( $\text{kJ mol}^{-1}$ )	-42 [31]

At low temperatures, deformation in  $\text{Ni}_3\text{Al}$  phase occurs by the activation of  $\langle 110 \rangle \{111\}$  slip systems, whereas at higher temperatures  $\langle 110 \rangle \{100\}$  slip systems lead to deformation [24]. At low temperatures, antiphase domain boundaries (APBs) would be created by the motion of  $\frac{1}{2} \langle 110 \rangle \{111\}$  dislocations due to slip. This boundary will have high energy to make this slip mode unlikely. However, this type of dislocation may move easily within the material since the passage of a  $\langle 110 \rangle \{111\}$  dislocation does not leave any such fault behind it [24].

In nickel-based superalloys, size of  $\gamma'$  precipitates may involve trimodal distribution (i.e. primary, secondary and tertiary  $\gamma'$  precipitates) [32]. Each distinct size of  $\gamma'$  precipitates takes different roles in these alloys. Primary  $\gamma'$  precipitates pin grain boundaries and restrict grain boundary migration, whereas secondary and tertiary  $\gamma'$  precipitates lead to precipitation hardening by interacting with dislocations [32].

#### 2.4.2 $\gamma$ Matrix Phase-Ni Solid Solution

Another phase within the microstructures of nickel-based superalloys is  $\gamma$  matrix phase (Figure 2.4) which is Ni solid solution, indeed [1]. Better mechanical properties can be obtained when this phase is strengthened by alloying elements. Some physical properties of  $\gamma$  matrix phase are shown in Table 2.2.

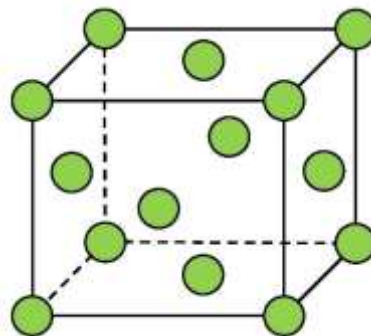


**Figure 2.4** The crystal structure of FCC-type disordered  $\gamma$  matrix phase-Ni solid solution in which Al and Ni atoms randomly occupy any sites.

**Table 2.2** Physical properties of Ni solid solution/Ni.

Properties	Ni solid solution/Ni
Lattice parameter (Å)	3.55 [9]
Curie temperature of Ni (K)	633 [33]
Stacking fault energy of pure Ni (mJ m <sup>-2</sup> )	125 [34]

### 2.4.3 $\gamma''(\delta)$ -Ni<sub>3</sub>(Al,Nb) Phase

When nickel-iron-based superalloys are doped with Nb atoms (e.g. IN718), ordered precipitates,  $\gamma''$ -Ni<sub>3</sub>(Al,Nb), may form.  $\gamma''$  precipitates have D0<sub>22</sub>-type ordered crystal structure which is very close to the crystal structure of  $\gamma'$  precipitates. This phase originates from two L1<sub>2</sub>-type ordered  $\gamma'$  unit cells separated by a conservative (001) antiphase boundary (APB) [1,35,36]. In IN718, lattice parameter of  $\gamma''$  intermetallics is  $a = 3.62 \text{ \AA}$  and  $c = 7.40 \text{ \AA}$  [1]. Similar to the orientation relationship between  $\gamma$  and  $\gamma'$  phases, there is a distinct orientation relationship between  $\gamma$  and  $\gamma''$  phases as well (i.e.  $\langle 001 \rangle_{\gamma} // \langle 001 \rangle_{\gamma''}$  and  $\langle 100 \rangle_{\gamma} // \langle 100 \rangle_{\gamma''}$ ) [1].

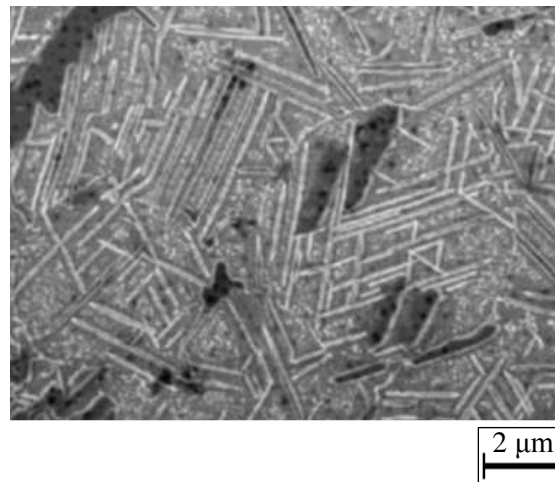


**Figure 2.5** FESEM micrograph showing  $\delta$  phase (white plates) within V207M exposed to heat treatment at 950 °C for 35 minutes (Adapted from [37]).



$\gamma''$  precipitates within superalloy microstructures have disc-like morphology having diameter of  $\sim 50$  nm and thickness of  $\sim 10$  nm [1]. Even if  $\gamma''$  precipitates may lead to better mechanical properties, orthorhombic  $\delta$  phases which evolve from  $\gamma''$  phases at a certain temperature range (650 °C to 980 °C) are detrimental [1,36]. Below this temperature range, formation of these phases occurs at grain boundaries. However, when the alloy is exposed to high temperature levels from 700 °C to 885 °C,  $\delta$  phases occur as  $\gamma''$  precipitates rapidly coarsen at the same time. Above 885 °C,  $\gamma''$  precipitates are no longer stable since  $\delta$  plates form very fast between 840 °C and 950 °C (Figure 2.5) [1,37].

#### **2.4.4 Topologically Close-Packed (TCP) Phases**

At high service temperatures of nickel-based superalloys, i.e.  $> 850$  °C, localized supersaturation of some refractory alloying elements, such as Cr, Mo, Re, Ta and W may start precipitation of topologically closed packed (TCP) phases as a result of atomic size difference in constituent alloying elements [1,14-16,38]. TCP phases are very harmful for mechanical properties since these phases deplete solid solution strengtheners from  $\gamma$  matrix phase, serve as crack initiation sites due to their complex lath- or plate-like shapes (Figure 2.6) and cause void formation at elevated temperatures [1,2,14-16].

Re atoms, as compared to other refractory element atoms, are more effective to initiate TCP phase formation. During solidification, TCP phases preferentially precipitate in dendrite cores (rich with Re concentration) [39,40]. In interdendritic regions, precipitation of TCP phases occurs at later stages [40]. Despite the full solution heat treatment steps, these detrimental phases continue to exist in the microstructures due to low diffusivity of TCP former elements (especially Re) [41]. However, there are also some alloying elements, such as Ir, Pt and Ru which inhibit precipitation rates of TCP phases [1,16,42]. Most particularly, Ru atoms have been proven to influence both nucleation and growth rates of TCP phases, while affecting the interface energy between TCP/ $\gamma$  phases [40,43]. When certain amounts of Ru atoms are added into

nickel-based superalloys, solubility of TCP former elements within  $\gamma$  matrix phase increases, degree of supersaturation behaviour of Re atoms in dendrite cores reduces and partitioning behaviours of TCP former elements may be reversed (i.e. Cr, Mo, Re and W atoms participate into  $\gamma'$  precipitates instead of  $\gamma$  matrix phase) [40,43,44].

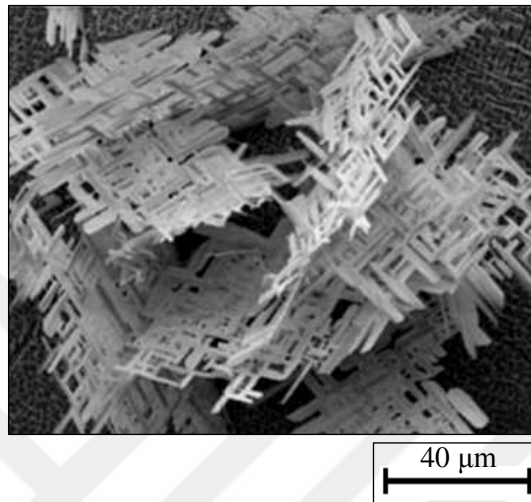


**Figure 2.6** FESEM micrograph showing TCP phase precipitation at 1100 °C for 1000 hr exposure time (Adapted from [16]).

## 2.5 Idealization of Microstructural Characteristics

Better mechanical properties of nickel-based superalloys can be obtained when two phase ( $\gamma$ - $\gamma'$ ) microstructures of these materials are idealized by adjusting volume fraction, size & size distribution, orientation and shape of  $\gamma'$  precipitates; channel width of  $\gamma$  matrix phase; lattice misfit parameter ( $\delta$ ), APB/stacking fault energy of  $\gamma$ - $\gamma'$  interfaces and  $\gamma$ - $\gamma'/\gamma$  phase transformation (solvus) temperatures [2]. Hence, in this part of the thesis, afore mentioned parameters have been examined in detail. In summary, it is important to note that these parameters have already been idealized in the literature as “high volume fraction (approximately 70%) of cuboidal shaped  $\gamma'$  precipitates having edge length of  $\sim 500$  nm which are coherently aligned along the  $\langle 001 \rangle$  directions with quite narrow  $\gamma$  matrix channels ( $\sim 60$  nm)” [9,45,46].

### 2.5.1 Volume Fraction of $\gamma'$ Precipitates

Volume fraction of  $\gamma'$  precipitates has a considerable effect on the achievement of better mechanical properties (i.e. strength is proportional to the product of APB energy and square root of  $\gamma'$  volume fraction,  $E_{APB} \times \sqrt{V_f}$ ) [13,28]. As indicated in many research studies [1-2,9,13], there is an agreement with the optimum value of precipitate volume fraction, i.e. ~ 70% which depends on both alloying element additions and heat treatments.  $\gamma'$  former alloying elements, such as Nb, Ta and Ti are known to increase volume fraction of  $\gamma'$  precipitates [1,2], while strength of alloys rapidly decreases at high temperatures above 1000 °C due to lower precipitate volume fractions [4,5]. In the work of Huang et al. [47], increasing micro-hardness values of some alloy systems have been correlated with their increasing precipitate volume fractions.

### 2.5.2 Size & Size Distribution of $\gamma'$ Precipitates

$\gamma'$ -Ni<sub>3</sub>Al precipitate size is one of the parameters strongly affecting mechanical properties of nickel-based superalloys. By applying different heat treatment procedures and processing steps, it is possible to obtain varying size populations of  $\gamma'$  precipitates which are termed as primary, secondary and tertiary [2]. Cooling rate through solvus temperature is a parameter taking role in the size distribution of Ni<sub>3</sub>Al precipitates. According to Pollock and Tin [2], unimodal distribution of relatively fine  $\gamma'$  precipitates having 300-500 nm size can be obtained when cooling rate is higher than 40 °C/minutes. On the other hand, for slow cooling rates, precipitate size would not be uniform (i.e. appear in different sizes; larger than 500 nm and smaller than 50 nm). Thus, refinement of these different size precipitates into an ideal size is very important for the enhancement of mechanical properties [2,48]. In the works of [1,9,49], Ni<sub>3</sub>Al precipitates having 300-500 nm edge length have been attributed to yield better mechanical properties since this range of precipitate size is more effective for the restriction of dislocation motion in turbine blade applications.

### 2.5.3 Orientation of $\gamma'$ Precipitates

During shape evolution,  $\gamma/\gamma'$  interfaces arrange themselves parallel to the crystallographic orientations having minimal Young's modulus. Due to elastic anisotropy of nickel-based superalloys, these crystallographic orientations are elastically soft  $\langle 001 \rangle$  directions, which make  $\gamma'$  precipitates having 100-type facets [1,9]. Alignment of  $\gamma'$  precipitates along  $\langle 001 \rangle$  directions is related with aging times; randomly distributed precipitates align themselves at long aging times, such as 64 hr [1,9].

### 2.5.4 Shape of $\gamma'$ Precipitates and Lattice Misfit Parameter ( $\delta$ )

Most studies in the literature claim that ideal shape of  $\gamma'$  precipitates for excellent creep properties is "cuboidal" [1,2,50]. However,  $\gamma'$  precipitates are not always in cuboidal forms. This shape of  $\gamma'$  precipitates appears depending on appropriate alloying element additions and heat treatments procedures. Type and content of alloying elements and their atomic radius, site preference and partitioning behaviours in the constituent phases directly affect shape of  $\gamma'$  precipitates and also coarsening phenomenon which comes into prominence at later stages [3,51]. For example, in case of Ni-Al-Cr superalloys, the dominant precipitate shape is spherical or spheroidal, while in Ni-Al superalloys precipitates exist in cuboidal shapes. This shape difference is originated from Cr effect which causes  $\gamma'$  precipitates to become nearly lattice misfit free [52]. On the other hand, cuboidal shaped precipitates are the result of some degree of lattice misfit (i.e.  $\delta = 0.3\%$ ) [2,9]. When lattice misfit is high enough, cuboidal  $\gamma'$  precipitates coarsen into rafts or rods aligned parallel or perpendicular to the applied stress direction depending on stress type (tensile or compressive) and lattice misfit parameter,  $\delta$  (positive or negative) [2]. Secondly, when nickel-based superalloy samples are quenched from a certain temperature above solvus phase transformation to RT, spheroidal shaped precipitates form and depending on aging temperature and times, precipitate shapes evolve from spheroidal to cuboidal [1]. For shorter aging times, randomly distributed  $\gamma'$  precipitates have spheroidal morphology. However, for

longer aging times oriented  $\gamma'$  precipitates (along  $\langle 001 \rangle$  directions) appear in cuboidal morphology [1].

As indicated in Equation 2.1, lattice misfit parameter ( $\delta$ ) depends on lattice parameters of  $\gamma$  and  $\gamma'$  phases and it is arisen from the initial internal stresses associated with high degree of elastic anisotropy which causes spherical coherent precipitates turn into cubes, doublets or octets of smaller size precipitates [2,53]. As indicated in Table 2.3, the relationship between lattice misfit parameter and shape of  $\gamma'$  precipitates is much clear [54]. For low lattice misfit values, precipitates have spheroidal shape which evolve into first cuboidal and then nearly rectangular forms with increasing magnitude of lattice misfit. This shape evolution of  $\gamma'$  precipitates also confirms the work of Fährmann et al. [55]. Similarly, precipitate shape evolution has been determined from spherical to cuboidal, octodendritic or rod-like shapes in other studies as well [48,50].

Morphological evolution of  $\gamma'$  precipitates can be explained as a competition between elastic free energy and interfacial free energy between  $\gamma'$  precipitates and  $\gamma$  matrix phase [50]. As  $\gamma'$  precipitates grow in size, elastic free energy increases in a rate of  $R^3$ , whereas interfacial free energy raises as  $R^2$ . Thus, at later stages of precipitate growth, the elastic free energy becomes dominant over interfacial free energy and causes shape evolution from sphere to cube and coarsening phenomenon which is not beneficial for the mechanical properties of nickel-based superalloys [47,53]. Another feature of elastic free energy is that it acts as driving force for the precipitate alignment occurring at the same time with morphological evolution [53].

Despite the fact that coherency stresses are the main factors for the shape evolution (i.e. when the elastic free energy and interfacial free energy originating from lattice misfit are minimized, and elastic and diffusional interactions between adjacent  $\gamma'$  precipitates control the spatial correlations, precipitate morphologies change [9,53,56]), morphological development of  $\gamma'$  precipitates is also diffusion-controlled. Coherency or low lattice misfit between  $\gamma$  and  $\gamma'$  phases are the results of similar crystal structures and lattice parameters of these phases [1,35]. Cuboidal morphology of  $\gamma'$

precipitates depends on lattice parameter of  $\gamma$  matrix phase regular over the structure which necessitates the alloy becomes chemically homogeneous [57].

**Table 2.3** Lattice misfit parameters ( $\delta$ ) and  $\gamma'$  precipitate morphologies of related alloys (Adapted from [54]).

Alloys	Lattice misfit parameter ( $\delta$ ) at room temperature (%)	Morphology of $\gamma'$ precipitates
Ni - Al	0.60	Nearly rectangular
Ni - Al - Cr	0.65	Nearly rectangular
Ni - Al - Co	0.59	Cuboidal
Ni - Al - Ru	0.42	Spheroidal

Even if cuboidal shape of  $\gamma'$  precipitates is accepted as the most ideal morphology, determination of its degree is important. For this purpose, in the work of Sluytman and Pollock [50], shape parameter ( $\eta$ ) has been defined and measured for the alloy compositions having precipitate volume fractions ranging from 0.45 to 0.70 [50,51]. In these studies [50,51], it has been concluded that precipitates become cuboidal when  $0.4 < \eta < 0.8$  and creep resistance enhancement has been attributed to the optimum value of  $\eta = 0.75$ . Another remarkable result obtained from [50,51] is that there is a relationship between shape parameter ( $\eta$ ) and lattice misfit parameter ( $\delta$ ). When approximate value of  $\delta = 0.4\%$  is obtained, shape parameter reaches its maximum value of  $\eta = 0.75$  which is correlated with better creep properties [50]. For this reason, by considering these microstructural parameters, design and development of high temperature nickel-based superalloys can be attributed to alloying element additions and heat treatment procedures lead to optimum values of  $\eta = 0.75$  and  $\delta = 0.4\%$  [50].

### 2.5.5 Channel Width of $\gamma$ Matrix Phase

As it is previously mentioned, shape of  $\gamma'$  precipitates evolve depending on the competition between elastic free energy and interfacial free energy which strongly

depend on lattice misfit parameter ( $\delta$ ). Channel width between two adjacent precipitates comes into prominence at this point since it influences the magnitude of elastic free energy [9]. In a recent study, optimum value of  $\gamma$  channel width has been determined as  $\sim 60$  nm [9].

### **2.5.6 APB and SF Energy**

When  $\gamma'$  precipitates interact with dislocations, antiphase boundaries (APBs) are created to restrict dislocation motion and therefore improve mechanical properties [7,9,28]. Instead of elastic moduli of the constituent  $\gamma$  and  $\gamma'$  phases (which do not differ greatly from  $\gamma$  to  $\gamma'$ ), APBs and SFs are responsible for better mechanical properties since the magnitudes of these faults strictly inhibit plastic flow [28]. The magnitudes of these faults can be adjusted by the variation of  $\gamma'$ -Ni<sub>3</sub>Al precipitate compositions and heat treatment parameters [58]. At lower temperatures which yield finer microstructures, the energy barrier for the dislocations entering into  $\gamma'$  precipitates leads to classical precipitation strengthening. In this case, yield mechanism occurs as a transition from shearing of precipitates with weakly coupled pair of dislocations into strongly coupled pair of dislocations. Shearing stresses depend on APB energy on the (111) plane [31]. On the other hand, at high temperatures yielding coarser microstructures, that energy barrier decreases and dislocations expose to short range cross slip to the (100) plane which helps the creation of sessile dislocation locks and yield anomaly [1,31].

In literature, since the magnitude of APB energy has such a great effect on better mechanical properties, several techniques and methods have been performed to calculate APB energy of Ni<sub>3</sub>Al-X phases [31]. For this purpose, Paxton [59] and Fu et al. [60] have applied full potential methods, whereas Rosengaard and Skriver [61] have used Green's function technique which is based on linear-muffin-tin orbital (LMTO) method. Furthermore, Guillet et al. [62] have investigated the effects of ternary alloying element additions on the change of APB energy in L1<sub>2</sub>-type ordered crystal structures. Today, APB energy of Ni<sub>3</sub>Al phase can be theoretically determined by

applying density functional theory (DFT). Furthermore, experimental determination of its value can be done by measuring the distance between superlattice partial dislocation pairs of Ni<sub>3</sub>Al phase in transmission electron microscopy (TEM) [28,63,64]. In the work of Crudden et al. [28] and Mignanelli et al. [48], the effects of some ternary alloying elements on APB energy have been investigated and Nb, Ta and Ti elements have been determined to increase APB energy and the overall strength of alloys. For these alloying elements occupying Al sites of Ni<sub>3</sub>Al phase, APB energies for (111) plane have been calculated over 600 mJ m<sup>-2</sup>, while APB energy of the same plane in impurity free Ni<sub>3</sub>Al phase has been found as 181 mJ m<sup>-2</sup> [31]. In the work of [28], according to CALPHAD results, Ti has been determined to have the strongest effect on APB energy. For other alloying elements, such as Mo, Nb, Ta and W, APB energy reaches its maximum value at 5 at.%. For higher concentrations of these elements (> 5 at.%), APB energy is affected negatively. Secondly, in [28], it has been mentioned that Cr is one of the alloying elements reducing APB energy. According to density functional theory (DFT), it has been determined that APB energy is mostly affected by Ta followed by Nb and Ti additions, respectively [28].

### **2.5.7 $\gamma$ - $\gamma'$ / $\gamma$ Phase Transformation (Solvus) Temperature**

In nickel-based superalloys whose operating temperatures are about 1000 °C, phase stability of high volume fraction  $\gamma'$  precipitates is essential. Therefore,  $\gamma'$  solvus temperatures of alloy systems should be high enough to prevent precipitate dissolution in  $\gamma$  matrix phase [51]. According to Hong et al. [65],  $\gamma'$  solvus temperature is determined as the average of  $T_f$  (finishing temperature of  $\gamma'$  dissolution upon heating) and  $T_s$  (starting temperature of  $\gamma'$  precipitation upon cooling). Similarly, as indicated in differential scanning calorimetry (DSC) measurements of the work of [66],  $\gamma'$  solvus temperature refers to minimum of endothermic peak during heating and onset temperature of exothermic peak during cooling. It is assumed that  $\gamma'$  precipitation occurs at a certain amount of undercooling ( $\Delta T$ ) below  $\gamma'$  solvus temperature [67]. Hence, determination of  $\gamma'$  solvus temperature will also lead to appropriate solution heat treatment temperatures at which all existing  $\gamma'$  precipitates in the single  $\gamma$  matrix



phase are dissolved prior to subsequent aging heat treatments. Solution heat treatment temperatures should be selected just above solvus and below solidus temperatures to reduce the risk of incipient melting [48]. Better mechanical properties (i.e. creep resistance) are related with solvus temperature levels since lower  $\gamma'$  solvus temperatures generally yield worse creep resistance. Alloying elements, such as Ta and Ti are known to increase  $\gamma'$  solvus temperatures [1,35].

## 2.6 Coarsening Behaviour of $\gamma'$ Precipitates

At high temperatures, mechanical strength of nickel-based superalloys depends on directional coarsening which takes place via Ostwald ripening process as small  $\gamma'$  precipitates dissolve in  $\gamma$  matrix phase and the subsequent mass transfers into larger  $\gamma'$  precipitates [3]. In Ostwald ripening, mass transfer occurs from high interfacial curvature regions (high chemical potential) to low interfacial curvature regions (low chemical potential) and the total reduction in interfacial area of the system leads to  $\gamma'$  precipitate growth [3,9]. The relationship between precipitate coarsening (diffusion-controlled) and time can be explained via modified Lifshitz-Slyozov-Wagner (LSW) theory. In this theory, coarsening growth kinetics with time depends on  $t^{1/3}$  relationship (considering spherical  $\gamma'$  precipitates without elastic interaction with  $\gamma$  matrix phase and volume fraction close to zero.) [3,9].

Coarsening rate of  $\gamma'$  precipitates can be minimized by alloying elements which strongly participate into  $\gamma'$  precipitates, have low solubility/diffusivity behaviours in  $\gamma$  matrix phase and reduce lattice misfit parameter ( $\delta$ ) [3,9,51,53]. Considerable degree of  $\gamma'$ -Ni<sub>3</sub>Al precipitate coarsening starts at low temperatures, i.e. 645 °C and when refractory alloying elements, such as Mo, Re, Ta and W are added, coarsening can be delayed until 850 °C. However, when temperature is high enough, i.e. > 1000 °C, none of afore mentioned refractory elements can retard further precipitate coarsening [51].

## **2.7 Compositions of Nickel-based Superalloys**

Most of the commercial superalloys used in aircraft applications are nickel-based. However, cobalt-based and iron-nickel-based superalloys are also used in these applications. As indicated in Table 2.4, nickel-based superalloys consist of about ten to fifteen alloying elements each contribute mechanical properties in different manners [1,2]. For example, enhancement of creep properties can be achieved in the following order:  $\text{Co} < \text{Cr} < \text{Ta} < \text{W} < \text{Re}$  [1]. Re addition leads to best creep resistance, while Co addition causes the worst creep properties [1]. Therefore, in the next part, contributions of alloying elements within superalloys have been mentioned in detail.

### **2.7.1 Effects of Alloying Elements**

#### **2.7.1.1 Ni addition**

- Due to its electronic structure, nickel has large solid solubility for many alloying elements which helps solid solution strengthening [68],
- Diffusivity of Ni is higher than some other alloying elements, such as Re and Ru, whereas it is lower than Co [41].

#### **2.7.1.2 Al addition**

- Al increases volume fraction of  $\gamma'$  precipitates [1],
- Shape parameter ( $\eta$ ) can be increased by Al addition and, therefore, precipitate shapes become more cubic [50],
- Al mobility plays a critical role to control coarsening kinetics [69],
- Al helps the formation of dense continuous layers of alumina on the surface of superalloys and enhances oxidation resistance [1,70].

**Table 2.4** Compositions of well-known commercial nickel-based superalloys (wt.%) (Adapted from [2]).

Alloy	Cr	Co	Mo	W	Ta	Re	Nb	Al	Ti	Hf	Zr	Fe
Conventionally Cast Alloys												
Mar-M246	8.30	10.00	0.70	10.00	3.00	-	-	5.50	1.00	1.50	0.05	-
René 80	14.00	9.50	4.00	4.00	-	-	-	3.00	5.00	-	0.03	-
IN-713LC	12.00	-	4.50	-	-	-	2.00	5.90	0.60	-	0.10	-
Directionally Solidified Alloys												
IN792	12.60	9.00	1.90	4.30	4.30	-	-	3.40	4.00	1.00	0.06	-
GTD111	14.00	9.50	1.50	3.80	2.80	-	-	3.00	4.90	-	-	-
First-Generation Single-Crystal Alloys												
PWA 1480	10.00	5.00	-	4.00	12.00	-	-	5.00	1.50	-	-	-
René N4	9.80	7.50	1.50	6.00	4.80	-	0.50	4.20	3.50	0.15	-	-
CMSX-3	8.00	5.00	0.60	8.00	6.00	-	-	5.60	1.00	0.10	-	-
Second-Generation Single-Crystal Alloys												
PWA 1484	5.00	10.00	2.00	6.00	9.00	3.00	-	5.60	-	0.10	-	-
René N5	7.00	7.50	1.50	5.00	6.50	3.00	-	6.20	-	0.15	-	-
CMSX-4	6.50	9.00	0.60	6.00	6.50	3.00	-	5.60	1.00	0.10	-	-
Third-Generation Single-Crystal Alloys												
René N6	4.20	12.50	1.40	6.00	7.20	5.40	-	5.80	-	0.15	-	-
CMSX-10	2.00	3.00	0.40	5.00	8.00	6.00	0.10	5.70	0.20	0.03	-	-
Wrought Superalloys												
IN 718	19.00	-	3.00	-	-	-	5.10	0.50	0.90	-	-	18.50

### 2.7.1.3 Co addition

- Co reduces  $\gamma'$  precipitate solvus temperature [71],
- Since Co reduces the stacking fault energy in  $\gamma$  matrix phase, Co addition improves creep resistance [1],
- In nickel-based superalloys, diffusivity of Co atoms is much faster than other alloying elements, such as Ni, Re and Ru [41].

### 2.7.1.4 Cr addition

- Cr reduces volume fraction and size of  $\gamma'$  precipitates [50],
- In binary Ni-Al system, when Cr is added, lattice misfit parameter ( $\delta$ ) between constituent  $\gamma$  and  $\gamma'$  phases significantly reduces and precipitate shapes become spheroidal [1,9,50],
- Cr reduces APB energy of  $\gamma$  matrix phase [28,72],
- Cr reduces  $\gamma'$  solvus temperature which may cause  $\gamma'$  precipitates to lose their stability [72],
- Cr improves creep properties at elevated temperatures and retards precipitate coarsening [1],
- In addition to ductility, Cr addition enhances oxidation-corrosion properties of nickel-based superalloys by forming protective  $\text{Cr}_2\text{O}_3$  coatings [1,2],
- Because of partitioning behaviour of Cr, addition of this element tends to decrease solubility of Al atoms in  $\gamma'$  precipitates [9],
- Inhibition of TCP phase formation requires low Cr content [1].

### 2.7.1.5 Hf addition

- Hf improves ductility and increases adherence of the protective oxide coatings to the alloys [73],
- As a reactive element, Hf increases anti-oxidation behaviour [1,73].

#### **2.7.1.6 Mo addition**

- Mo reduces lattice misfit parameter ( $\delta$ ) which leads to precipitates having spheroidal morphology [74],
- Mo has a profound effect on APB energy [28],
- Mo improves creep properties and retards coarsening [1],
- Mo leads to TCP phase formation [1].

#### **2.7.1.7 Nb addition**

- Nb increases volume fraction of  $\gamma'$  precipitates [1],
- Nb increases APB energy [28],
- Nb improves creep properties and reduces coarsening rates [75],
- Nb increases hot corrosion resistance of superalloys [76].

#### **2.7.1.8 Pt addition**

- Coarsening can be retarded by addition of Pt [51],
- With small amounts of reactive elements (e.g. Hf), Pt addition remarkably enhances high temperature oxidation resistance of nickel-based superalloys [51,77],
- Pt inhibits TCP phase formation and increases creep resistance [2,42].

#### **2.7.1.9 Re addition**

- Re reduces  $\gamma'$  volume fraction [13,58],
- Re reduces  $\gamma'$  precipitate size [50],
- Re stabilizes cuboidal  $\gamma'$  precipitates up to  $\sim 980$  °C [12],
- Re increases  $\gamma'$  solvus temperature [13],
- Coarsening can be retarded by addition of Re [1,51],

- Creep properties of nickel-based superalloys can be enhanced by Re addition [2,13],
- Re leads to poor oxidation resistance [78],
- Re has very low diffusion coefficient in nickel-based superalloys [79],
- Re leads to TCP phase formation [1,14-16].

#### **2.7.1.10 Ru addition**

- Ru addition reduces  $\gamma'$  volume fraction [13].
- Ru has no effect on the morphology of  $\gamma'$  precipitates [13],
- Ru enhances creep properties and retards coarsening and rafting kinetics [2,13],
- Ru increases oxidation-corrosion resistance [13],
- Ru increases solubility of Re and W atoms within  $\gamma$  matrix phase [16],
- Ru inhibits the formation of TCP phases [1,40,43].

#### **2.7.1.11 Ta addition**

- Ta increases volume fraction of  $\gamma'$  precipitates [1,35,50],
- Ta increases  $\gamma'$  precipitate size [50],
- Shape parameter ( $\eta$ ) is increased by Ta addition which makes  $\gamma'$  precipitates more cubic [50],
- Ta increases APB energy and addition of this element results in better shear resistance [28],
- Ta increases  $\gamma'$  solvus temperature [51],
- Ta reduces coarsening kinetics [1,51],
- Ta leads to better creep strength and good oxidation resistance [80].

#### **2.7.1.12 Ti addition**

- Ti increases volume fraction of  $\gamma'$  precipitates [1],
- Ti increases APB energy [28],
- Ti increases  $\gamma'$  solvus temperature [1].

#### **2.7.1.13 W addition**

- W addition leads to increase in  $\gamma'$  volume fraction [81],
- W reduces  $\gamma'$  precipitate size [81],
- W has a profound effect on APB energy [28],
- W increases  $\gamma'$  solvus temperature [81],
- W increases creep resistance and decreases coarsening rate [1,81],
- W reduces diffusion processes and leads to TCP phase formation [1].

### **2.7.2 Phase Preferences of Alloying Elements**

In addition to alloy compositions, compositions of the constituent  $\gamma$  and  $\gamma'$  phases also impact both mechanical and environmental properties of nickel-based superalloys. For this reason, phase preferences of alloying elements (elemental partitioning) come into prominence in alloy design consideration. Depending on phase preferences of alloying elements, precipitate shapes can be adjusted and thus coarsening kinetics can be controlled [50,51].

In order to reduce coarsening rates of superalloys, the main strategy is the addition of alloying elements tend to participate into  $\gamma'$  precipitates and have low diffusivity and low solubility in  $\gamma$  matrix phase [51]. Besides alloying element additions, heat treatment parameters (aging times and cooling rates following each heat treatment step) also affect phase preferences of alloying elements between  $\gamma$  and  $\gamma'$  phases. In the work of Sudbrack et al. [81], Al concentration in  $\gamma'$  precipitates has been stated to

increase with increasing aging times. In general, alloying elements, such as Nb, Ta and Ti prefer to participate into  $\gamma'$  precipitates, while Co, Cr, Mo, Re and Ru tend to become enrich in  $\gamma$  matrix phase [1,35]. W and Ir atoms have no phase preference, while Ni has a slight tendency to participate into  $\gamma'$  precipitates [56]. On the other hand, in the work of [47], Ni has been stated to participate into  $\gamma$  matrix phase. Phase preference of Hf atoms is still questionable; some atom probe tomography (APT) results have indicated that Hf prefers to be enriched in  $\gamma$  matrix phase, while some first-principles calculations have claimed that it prefers to participate into  $\gamma'$  precipitates [82,83].

Phase preference of impurity alloying “i” elements between the constituent  $\gamma$  and  $\gamma'$  phases can be determined by considering partitioning coefficients of these “i” elements which are calculated by dividing their concentrations in  $\gamma'$  precipitates to the ones in  $\gamma$  matrix phase, Equation 2.2.

$$\kappa_i = \frac{C_i^{\gamma'}}{C_i^{\gamma}} \quad (2.2)$$

where  $\kappa_i$  is the partitioning coefficient of “i” impurity element,  $C_i^{\gamma}$  and  $C_i^{\gamma'}$  are the concentrations of this “i” element in  $\gamma$  and  $\gamma'$  phases, respectively.

Phase preferences of some certain alloying elements also affect phase partitioning and solubility behaviours of other alloying elements in the constituent  $\gamma$  and  $\gamma'$  phases. For instance, in case of W addition, Cr atoms more strongly participate into  $\gamma$  matrix phase, while more Al atoms become enriched in  $\gamma'$  precipitates [9,81]. In the work of [83], it has been justified that Cr addition makes Hf atoms to participate into  $\gamma$  matrix phase. Cr atoms also tend to decrease solubility of Al atoms in  $\gamma'$  precipitates [9]. In addition to experimental APT and theoretical first-principles calculations, phase preference or elemental partitioning characteristics of alloying elements can be determined via another experimental method, electron probe micro-analysis (EPMA).



### 2.7.3 Site Preferences of Alloying Elements

According to Ochiai et al. [84], alloying elements occupying Al sublattice sites of  $\gamma'$ -Ni<sub>3</sub>Al precipitates have much greater strengthening effect rather than those occupying Ni sublattice sites. Similarly, Rawlings and Statonbevan [85] have claimed that yield strength can be enhanced by alloying elements substituting for Al sublattice sites of Ni<sub>3</sub>Al phase and having large lattice misfit in aluminum-rich or stoichiometric compositions of  $\gamma'$  precipitates rather than nickel-rich ones. Because of their important effects on lattice misfit parameter ( $\delta$ ) and mechanical properties of nickel-based superalloys, sublattice site occupancy characteristics of alloying elements in Ni<sub>3</sub>Al phase have drawn attention for many years. For this purpose, Guard and Westbrook [86] have established a phenomenological thermodynamic model by considering electronic structure of ternary alloying element additions into  $\gamma'$  precipitates. Rawlings et al. [85] have tried to set up a relationship between site occupancy characteristics of alloying elements in Ni<sub>3</sub>Al phase and their effects on the mechanical properties. Afterwards, Ochiai et al. [84] have used Miedama model, Tso et al. [87] have applied cluster variation method and Raju et al. [88] have developed pseudopotential orbital radii based structure maps.

#### 2.7.3.1 SRO Parameter Calculations

The excellent mechanical properties of aluminides (i.e. Ni<sub>3</sub>Al) can be attributed to the existence of long range order (LRO) and short range order (SRO) characteristics of these intermetallics [89]. It is possible to determine site preferences of alloying elements by calculating partial short range order parameters of related atomic pairs within Ni<sub>3</sub>Al phase at high temperatures.

#### 2.7.3.2 First-principles Ab Initio Calculations

First-principles based *ab initio* calculations are one of the effective methods to reveal site preferences of alloying elements within a model of Ni<sub>3</sub>Al phase. In these

calculations, VASP is used to carry out density functional theory (DFT) based calculations. *Ab initio* methods can determine some physical properties, such as lattice parameter, lattice misfit, interfacial energy between precipitate and matrix phases, solute diffusivity, solubility and so on. However, all of afore mentioned properties are mostly calculated at 0 Kelvin. Hence, there are also some studies investigating high temperature site preferences of alloying elements by combining first-principles calculations with Wagner-Schottky model [90,91].



## CHAPTER 3

### HIGH TEMPERATURE SITE PREFERENCE AND ATOMIC SHORT RANGE ORDERING CHARACTERISTICS OF TERNARY ALLOYING ELEMENTS IN $\gamma'$ -Ni<sub>3</sub>Al INTERMETALLICS

#### 3.1 Introduction

It has been reported that ordering temperature of Ni<sub>3</sub>Al phase is almost equal to its melting temperature (~ 1375 °C) and depends on the degree of phase stoichiometry as well as impurity concentrations [1]. According to the binary phase diagram of Ni-Al system (Appendix A), the compositional range of Ni<sub>3</sub>Al intermetallics is quite restricted. Besides stoichiometric composition (75 at.% Ni-25 at.% Al), limited non-stoichiometric compositions of Ni<sub>3</sub>Al phase are also available due to some point defects, such as alloying element additions (Appendix B), anti-sites, vacancies and thermal defects [90,91]. In order to state solubility limits of impurity atoms, Ochiai et al. have investigated solubility of some alloying elements in the stoichiometric base composition of Ni<sub>3</sub>Al (whose homogeneity range is 22-27 at.% Al) and determined solubility limits of X = Hf, Mo, Ta and W atoms in Ni<sub>3</sub>Al phase at 1000 °C (along “b” direction of solubility lobe) as 7 at.% <, 5 at.% <, 9 at.% < and 5 at.% <, whereas for X = Co and Pt atoms, solubility limits in “a” direction of solubility lobe have been found as 22 at.% and 19 at.%, respectively (Figure 3.1) [84,92]. However, it has been mentioned that both X = Re and Ru alloying element atoms exhibit very limited solubilities in Ni<sub>3</sub>Al phase [92] which have been further confirmed by isothermal ternary phase diagrams of Ni-Al-Re [93,94] and Ni-Al-Ru [95] alloy systems.

As mentioned in the previous part, many attempts have been made for the prediction of site occupancy characteristics of alloying elements in Ni<sub>3</sub>Al phase by applying

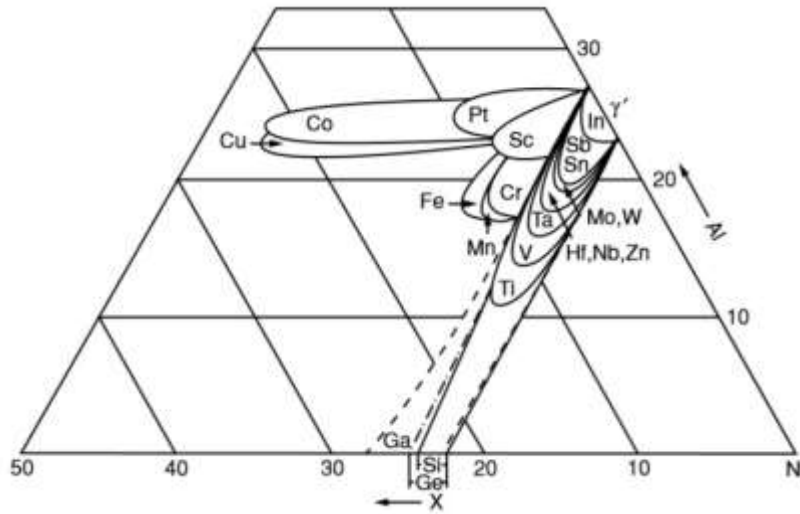


**Figure 3.1** Solubility limits of alloying X elements affecting the extent of  $\gamma'$  phase field in ternary phase diagram of Ni-Al-X systems at 1000 °C (Adapted from [84]).

phenomenological thermodynamic model [86], Miedema model [84], cluster variation method [87] and pseudopotential orbital radii based structure maps [88]. For the last few years, there have been plenty of theoretical and experimental studies dealing with sublattice site occupancy characteristics of substitutional ternary alloying elements in  $\text{Ni}_3\text{Al}$  intermetallics. In this regard, some first-principles based *ab initio* calculations have been performed by applying either anti-site formation-based formalism or substitutional (formation) energy calculations [52,54,82,83,96-103]. Unfortunately, in these studies, calculations have been done at 0 Kelvin which exclude the fact that sublattice site occupancy preferences of ternary alloying elements in  $\text{Ni}_3\text{Al}$  phase could change reversibly with increasing temperature. In order to solve this problem, Jiang and Gleeson [90] and Wu and Li [91] have combined first-principles supercell calculations with Wagner-Schottky model and examined high temperature occupancy characteristics of transition metal elements by considering different compositions of  $\text{Ni}_3\text{Al}$  phase in a wide range of high temperature scale. However, in Wagner-Schottky model, defect concentrations are required to be sufficiently dilute and in regarding temperature effect, only the mean-field configurational entropy is considered, while vibrational entropy is neglected.

In order to support afore mentioned first-principles calculations, sublattice site occupancy characteristics of ternary alloying elements in  $\text{Ni}_3\text{Al}$  phase have also been examined by experimental studies, such as 3D atom probe tomography (APT) [52,54,99,102-105], atom probe field ion microscopy (APFIM) [106-108] and atomic site location by channelling enhanced micro-analysis (ALCHEMI) [109]. It is worth to note that all of these experimental techniques have approved the consequences of previous studies. However, experimental studies, such as APT are very challenging since they require spatial sensitivity which is possible after a careful sample preparation and the experimental devices are operated at very low temperatures like -233 °C (40 K) [105]. Thus, in order to eliminate these deficiencies and considering both service temperatures of nickel-based superalloys, i.e. > 1000 °C, and solubility limits of impurity atoms in  $\text{Ni}_3\text{Al}$  phase, in the current work, high temperature sublattice site occupancy preference (up to 1250 °C which is lower than ordering/melting temperature of  $\text{Ni}_3\text{Al}$  phase [1]) and atomic short range ordering characteristics of ternary alloying X elements (X = Co, Cr, Hf, Mo, Nb, Pt, Re, Ru, Ta and W, respectively) in non-stoichiometric (Ni-rich)  $\text{Ni}_{75}\text{Al}_{21.875}\text{X}_{3.125}$  alloy systems have been studied by combining the statistical theory of ordering and electronic theory of alloys in the pseudopotential approximation. Theory proposed for the calculation of partial short range order (SRO) parameters in ternary intermetallic systems at first coordination sphere (in R space or real space) has been utilized for the first time to evaluate distribution tendencies of constituent atoms in submicro volumes of  $\text{Ni}_3\text{Al}$  phase. Herein, comparisons have been made with other theoretical calculations and experimental studies reported in the literature to validate present modelling approach and simulation results.

### 3.2 Theory

The electronic theory of atomic short range ordering (SRO) in the pseudopotential approximation for ternary alloys has been developed in [110-113] and for the calculation of partial SRO parameters at first coordination sphere,  $R_l$ , following equations have been proposed [113]:

$$\begin{aligned}
& [C_{\text{Ni}} + C_{\text{Al}}\alpha_{\text{Ni-Al}}(R_1) + C_{\text{X}}\alpha_{\text{Ni-X}}(R_1)] \cdot [C_{\text{Al}} + C_{\text{Ni}}\alpha_{\text{Ni-Al}}(R_1) + C_{\text{X}}\alpha_{\text{Al-X}}(R_1)] - \\
& [1 - \alpha_{\text{Ni-Al}}(R_1)]^2 \cdot C_{\text{Ni}}C_{\text{Al}} \cdot \exp\left[-\frac{W_{\text{Ni-Al}}(R_1)}{K_{\text{B}}T}\right] = 0 \\
& [C_{\text{Ni}} + C_{\text{Al}}\alpha_{\text{Ni-Al}}(R_1) + C_{\text{X}}\alpha_{\text{Ni-X}}(R_1)] \cdot [C_{\text{X}} + C_{\text{Ni}}\alpha_{\text{Ni-X}}(R_1) + C_{\text{Al}}\alpha_{\text{Al-X}}(R_1)] - \\
& [1 - \alpha_{\text{Ni-X}}(R_1)]^2 \cdot C_{\text{Ni}}C_{\text{X}} \cdot \exp\left[-\frac{W_{\text{Ni-X}}(R_1)}{K_{\text{B}}T}\right] = 0 \\
& [C_{\text{Al}} + C_{\text{Ni}}\alpha_{\text{Ni-Al}}(R_1) + C_{\text{X}}\alpha_{\text{Al-X}}(R_1)] \cdot [C_{\text{X}} + C_{\text{Ni}}\alpha_{\text{Ni-X}}(R_1) + C_{\text{Al}}\alpha_{\text{Al-X}}(R_1)] - \\
& [1 - \alpha_{\text{Al-X}}(R_1)]^2 \cdot C_{\text{Al}}C_{\text{X}} \cdot \exp\left[-\frac{W_{\text{Al-X}}(R_1)}{K_{\text{B}}T}\right] = 0 \tag{3.1}
\end{aligned}$$

where  $K_{\text{B}}$  is the Boltzmann constant;  $T$  is absolute temperature in Kelvin;  $C_{\text{Ni}}$ ,  $C_{\text{Al}}$  and  $C_{\text{X}}$  are the concentrations of Ni, Al and alloying X atoms in ternary Ni-Al-X systems, respectively. In Equation (3.1),  $W_{\text{Ni-Al}}(R_1)$ ,  $W_{\text{Ni-X}}(R_1)$  and  $W_{\text{Al-X}}(R_1)$  are the pairwise ordering energy values and  $\alpha_{\text{Ni-Al}}(R_1)$ ,  $\alpha_{\text{Ni-X}}(R_1)$  and  $\alpha_{\text{Al-X}}(R_1)$  are the partial SRO parameters of Ni-Al, Ni-X and Al-X atomic pairs at first coordination sphere,  $R_1$ . The pairwise ordering energies,  $W_{\alpha-\alpha'}(R_1)$ , on the base of electronic theory of multicomponent alloys in the pseudopotential approximation can be calculated by using following equations ( $\alpha-\alpha' = \text{Ni-Al, Ni-X and Al-X, respectively}$ ) [110-113].

$$W_{\alpha-\alpha'}(R_1) = \frac{\bar{\Omega}_0}{\pi^2} \int_0^\infty F_{\alpha-\alpha'}(q) \frac{\sin(qR_1)}{qR_1} q^2 dq \tag{3.2}$$

where

$$F_{\alpha-\alpha'}(q) = -\frac{\bar{\Omega}_0}{8\pi} |\omega_\alpha^0(q) - \omega_{\alpha'}^0(q)|^2 q^2 \frac{\varepsilon(q)-1}{\varepsilon^*(q)} + \frac{2\pi}{\bar{\Omega}_0 q^2} |Z_\alpha^* - Z_{\alpha'}^*|^2 \exp\left(-\frac{q^2}{4\xi}\right) \tag{3.3}$$

In Equations (3.2) and (3.3),  $\bar{\Omega}_0$  is the average atomic volume of the ternary alloy;  $\varepsilon(q)$  is the dielectric constant in the Hartree approximation;  $\varepsilon^*(q)$  is the modified dielectric constant which takes into account the correlation and exchange effects;  $\omega_\alpha^0(q)$  and  $\omega_{\alpha'}^0(q)$  are the form factors of unscreened pseudopotentials of  $\alpha$  and  $\alpha'$

component ions ( $\alpha, \alpha' = \text{Ni, Al and X}$ ), respectively;  $Z_\alpha (Z_{\alpha'}^*)$  is the effective valency of the  $\alpha(\alpha')$  component atoms and  $\xi$  is the Ewald parameter.

Equations (3.2) and (3.3) enable one to calculate partial ordering energies as a function of interatomic distance,  $R$ , for any ternary alloy provided that the form factor of unscreened pseudopotentials and effective valences are known for the ions involved. However, unlike simple metal alloys, there are still some difficulties with the utilization of pseudopotential theory for the determination of characteristics of transition metal systems which strongly depends on the full internal energy. The problem has been attributed to the fact that the form-factors of the pseudopotential for transition metals must contain terms responsible for the d-resonance effect. The use of pseudopotential method for the calculation of ordering energies and/or interatomic interaction potentials in transition metal alloy systems has already been discussed in detail elsewhere [111-116]. The non-local bare pseudopotential form factors, proposed by Animalu [117] in which the d-resonance effect has been partly taken into account, were used in quasi-*on the Fermi sphere* approximations and have been screened using a modified dielectric constant. Therefore, the Animalu's model pseudopotential has been successfully applied previously for the evaluation of various characteristics of Ni- and Fe-based binary and multicomponent transition metal systems [111-116,118,119]. In the present study, which deals with the calculation of partial ordering energies, only non-diagonal matrix elements were involved as given in Equations (3.2) and (3.3), in which the contribution of the d-resonance effect is relatively small [117].

### **3.3 Partial Ordering Energy & Partial SRO Parameters**

For  $\text{Ni}_{75}\text{Al}_{21.875}\text{X}_{3.125}$  alloy systems, partial ordering energy variations of related atomic pairs as a function of interatomic distance are given in Figures 3.2 and 3.3 for  $\text{X} = \text{Co, Cr, Hf, Mo, Nb}$  and  $\text{X} = \text{Pt, Re, Ru, Ta}$  and  $\text{W}$ , respectively. In the calculations, the non-local bare pseudopotential form factors, proposed in [117], were used in quasi-*on the Fermi sphere* approximations and have been screened using a modified dielectric constant [120,121]. Moreover, the function proposed by Sham [122] that is

responsible for the exchange and correlation effects in the interacting electron gas was also used. The value of Ewald parameter in Equation (3) was taken as  $\xi = 0.7$ . The radius of first coordination sphere,  $R_1$ , which is equal to  $a\sqrt{2}/2$  in  $L1_2$ -type crystal structure, was derived from lattice parameter of  $Ni_3Al$  phase ( $a = 3.567 \text{ \AA}$ ) [123]. Then,  $R_1$  value was calculated as 4.766 at. u. and put in the graphs (1 at. u. = 0.529177  $\text{\AA}$ ). The position of first coordination sphere, as indicated in the figures, is the same as that calculated for binary  $Ni_3Al$  intermetallics (the effects of low concentration impurity elements and temperature change in the variation of lattice parameter were assumed to be negligible). The ordering energy of Ni-Al atomic pair at first coordination sphere,  $R_1$ , was adapted from the study of Stocks et al. [124], as  $W_{Ni-Al}(R_1) = 7.1 \times 10^{-3}$  at. u. It is evident from Figures 3.2 and 3.3 that the variation of partial ordering energies of Ni-X and Al-X atomic pairs with interatomic distance has quasi-oscillatory and sign changing character which is a well-known feature for metallic interactions. This suggests that the magnitude of partial ordering energies alters for different pairs of atoms and various ternary element additions, not only in terms of quantity but also in terms of sign. The calculated partial ordering energies for all alloying X elements in  $Ni_{75}Al_{21.875}X_{3.125}$  alloy systems are tabulated in Table 3.1.

Short range order parameter ( $\alpha^{ij}$ ) introduced by Cowley [125] can be defined as,

$$\alpha^{ij} = 1 - \frac{P_{AB}^{ij}}{C_B} \quad (3.4)$$

where  $P_{AB}^{ij}$  is the probability of finding an A atom at the lattice site “i” after B atom occupies lattice site “j”, as A-B = Ni-Al, Ni-X and Al-X, respectively. In addition to the determination of partial ordering energies, partial short range order (SRO) parameters for the atomic pairs of ternary  $Ni_{75}Al_{21.875}X_{3.125}$  alloy systems have been calculated at first coordination sphere,  $R_1$ , by using Newton’s method which solves simultaneous non-linear systems of Equation (3.1). In this method, initial values of  $\alpha_{Ni-Al}(R_1)$ ,  $\alpha_{Ni-X}(R_1)$  and  $\alpha_{Al-X}(R_1)$  were put randomly and Jacobian matrix was solved. In the expressions of Equation (3.1), Boltzmann constant was taken as 0.32 x



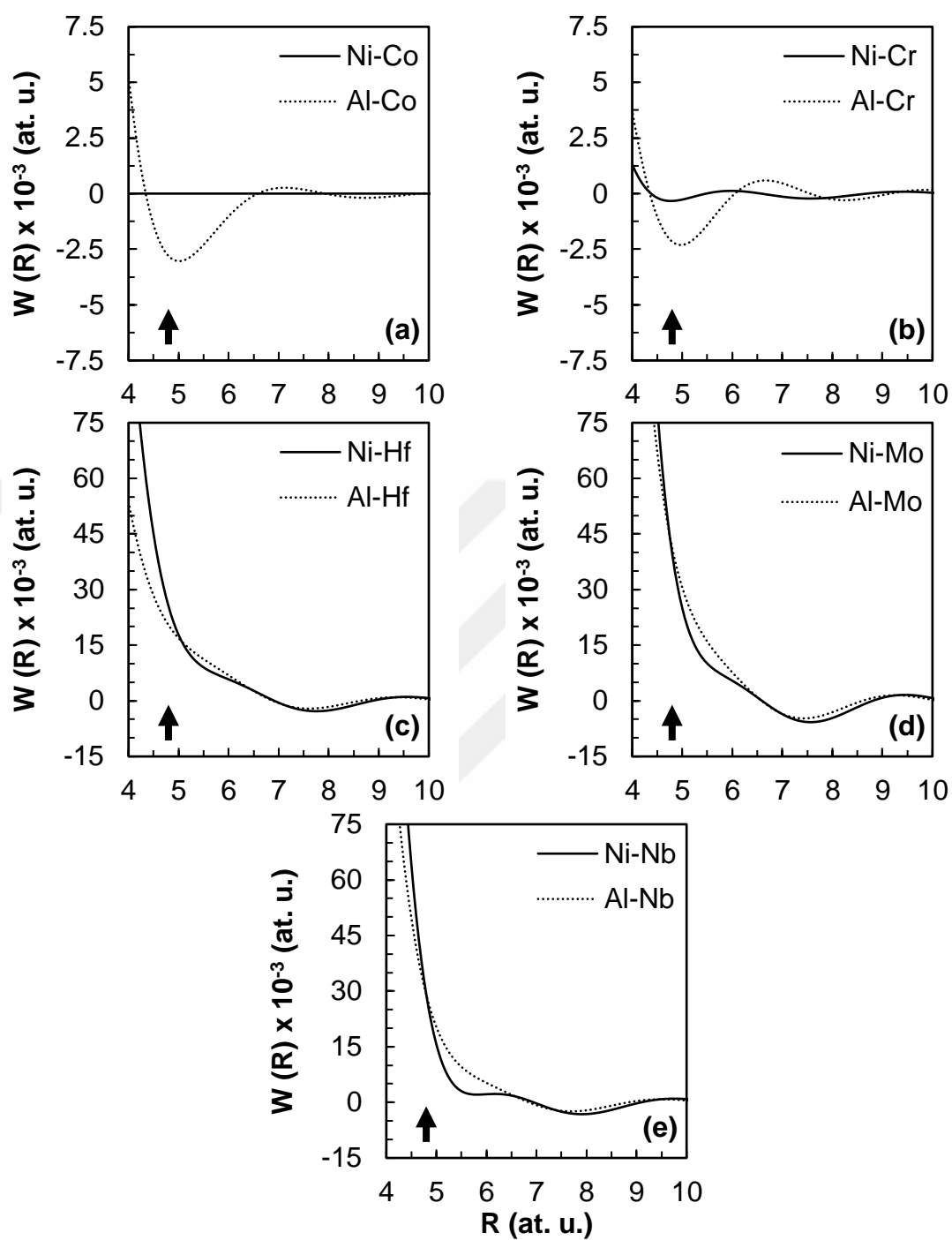


**Figure 3.2** Partial ordering energies of Ni-X (solid curves) and Al-X (dashed curves) atomic pairs as a function of interatomic distance in  $\text{Ni}_{75}\text{Al}_{21.875}\text{X}_{3.125}$  alloy systems where X = (a) Co, (b) Cr, (c) Hf, (d) Mo and (e) Nb, respectively. (1 at. u. (energy) = 2 Ry = 27.2 eV; and 1 at. u. (length) = 0.529177 Å).

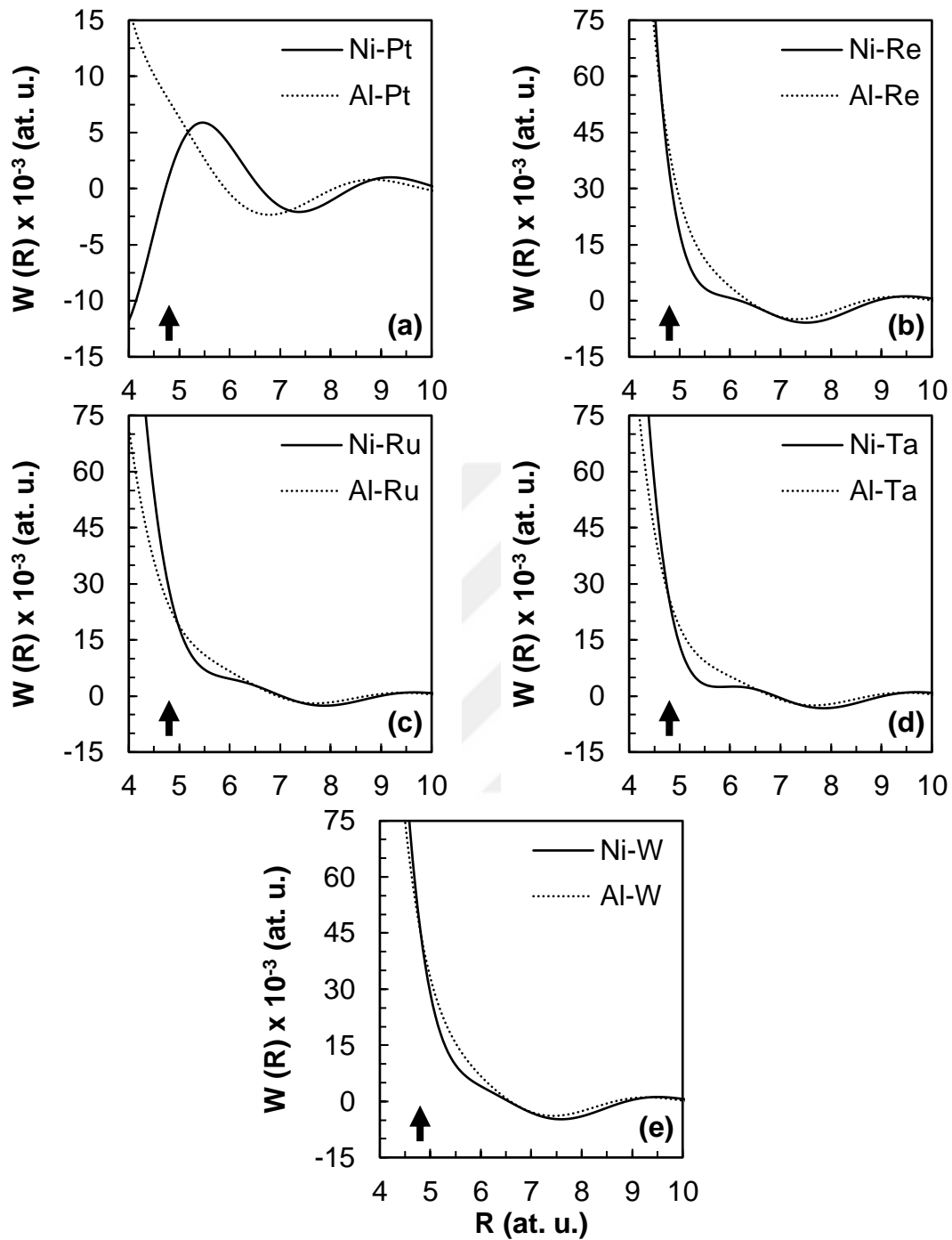


**Figure 3.3** Partial ordering energies of Ni-X (solid curves) and Al-X (dashed curves) atomic pairs as a function of interatomic distance in  $\text{Ni}_{75}\text{Al}_{21.875}\text{X}_{3.125}$  alloy systems where X = (a) Pt, (b) Re, (c) Ru, (d) Ta and (e) W, respectively. (1 at. u. (energy) = 2 Ry = 27.2 eV; and 1 at. u. (length) = 0.529177 Å).

$10^{-5}$  at. u./K ( $K_B = 8.617 \times 10^{-5}$  eV/K, 1 at. u. = 27.2 eV) and temperature dependence of partial SRO parameters has been determined from 800 °C to 1250 °C in 50 °C increments. Final values of partial SRO parameters have been approached by their exact values as the numerical error of the solution was less than  $\varepsilon = 1 \times 10^{-7}$ . Calculated partial SRO parameters of Ni-Al, Ni-X and Al-X atomic pairs of ternary  $\text{Ni}_{75}\text{Al}_{21.875}\text{X}_{3.125}$  alloy systems are presented in Table 3.2.

**Table 3.1** Partial ordering energies of Ni-X and Al-X atomic pairs at first coordination sphere,  $R_1$ , in  $\text{Ni}_{75}\text{Al}_{21.875}\text{X}_{3.125}$  alloy systems.

Alloy systems	Atomic pairs	$W_{\text{Ni-X}}(R_1)$ ( $\times 10^{-3}$ )(at. u.)	Atomic pairs	$W_{\text{Al-X}}(R_1)$ ( $\times 10^{-3}$ )(at. u.)
$\text{Ni}_{75}\text{Al}_{21.875}\text{Co}_{3.125}$	Ni-Co	0	Al-Co	-2.704
$\text{Ni}_{75}\text{Al}_{21.875}\text{Cr}_{3.125}$	Ni-Cr	-0.328	Al-Cr	-2.078
$\text{Ni}_{75}\text{Al}_{21.875}\text{Hf}_{3.125}$	Ni-Hf	27.218	Al-Hf	21.142
$\text{Ni}_{75}\text{Al}_{21.875}\text{Mo}_{3.125}$	Ni-Mo	43.041	Al-Mo	43.577
$\text{Ni}_{75}\text{Al}_{21.875}\text{Nb}_{3.125}$	Ni-Nb	32.107	Al-Nb	30.854
$\text{Ni}_{75}\text{Al}_{21.875}\text{Pt}_{3.125}$	Ni-Pt	0.628	Al-Pt	8.060
$\text{Ni}_{75}\text{Al}_{21.875}\text{Re}_{3.125}$	Ni-Re	38.219	Al-Re	42.865
$\text{Ni}_{75}\text{Al}_{21.875}\text{Ru}_{3.125}$	Ni-Ru	30.719	Al-Ru	25.140
$\text{Ni}_{75}\text{Al}_{21.875}\text{Ta}_{3.125}$	Ni-Ta	28.183	Al-Ta	27.648
$\text{Ni}_{75}\text{Al}_{21.875}\text{W}_{3.125}$	Ni-W	49.949	Al-W	48.309

In binary  $\text{Ni}_3\text{Al}$  intermetallics, according to Equation (3.4), “i” and “j” refer to Ni and Al sublattice sites, respectively, and  $C_B$  is the atomic fraction of B = Al atoms. When there is a preference for unlike neighbours,  $P_{AB}^{ij} > C_B$  and  $\alpha^{ij}$  becomes negative and in case of a preference for like neighbours,  $P_{AB}^{ij} < C_B$  and  $\alpha^{ij}$  becomes positive. For completely randomness,  $P_{AB}^{ij} = C_B$  and  $\alpha^{ij} = 0$ , which is impossible. Hence, negative values of partial SRO parameter of A-B atomic pairs mean that B atoms tend to occupy

**Table 3.2** Partial SRO parameters of Ni-Al, Ni-X and Al-X atomic pairs of  $\text{Ni}_{75}\text{Al}_{21.875}\text{X}_{3.125}$  alloy systems at elevated temperatures.

T (°C)	$\text{Ni}_{75}\text{Al}_{21.875}\text{Co}_{3.125}$		$\text{Ni}_{75}\text{Al}_{21.875}\text{Cr}_{3.125}$		$\text{Ni}_{75}\text{Al}_{21.875}\text{HF}_{3.125}$		$\text{Ni}_{75}\text{Al}_{21.875}\text{Mo}_{3.125}$					
	$\alpha_{\text{Ni-Al}}(\text{R}_1)$	$\alpha_{\text{Ni-Co}}(\text{R}_1)$	$\alpha_{\text{Ni-Al}}(\text{R}_1)$	$\alpha_{\text{Ni-Cr}}(\text{R}_1)$	$\alpha_{\text{Ni-Al}}(\text{R}_1)$	$\alpha_{\text{Ni-Hf}}(\text{R}_1)$	$\alpha_{\text{Ni-Al}}(\text{R}_1)$	$\alpha_{\text{Ni-Mo}}(\text{R}_1)$				
800	-0.254	-0.161	0.620	-0.253	-0.143	0.571	-0.259	-0.259	0.745	-0.246	-0.158	0.398
850	-0.248	-0.156	0.600	-0.246	-0.138	0.551	-0.253	-0.253	0.726	-0.240	-0.152	0.379
900	-0.242	-0.151	0.580	-0.241	-0.134	0.532	-0.247	-0.248	0.707	-0.234	-0.147	0.362
950	-0.237	-0.146	0.562	-0.235	-0.129	0.514	-0.241	-0.242	0.689	-0.229	-0.142	0.346
1000	-0.231	-0.142	0.545	-0.229	-0.125	0.497	-0.235	-0.237	0.671	-0.223	-0.138	0.331
1050	-0.225	-0.138	0.528	-0.224	-0.121	0.481	-0.230	-0.232	0.654	-0.218	-0.134	0.317
1100	-0.220	-0.134	0.513	-0.219	-0.117	0.466	-0.224	-0.227	0.637	-0.213	-0.130	0.303
1150	-0.215	-0.130	0.498	-0.214	-0.114	0.452	-0.219	-0.223	0.621	-0.208	-0.127	0.291
1200	-0.210	-0.126	0.484	-0.209	-0.111	0.438	-0.214	-0.218	0.606	-0.203	-0.123	0.280
1250	-0.206	-0.123	0.470	-0.204	-0.107	0.425	-0.209	-0.214	0.591	-0.199	-0.120	0.269

**Table 3.2 (Continued).**

T (°C)	Ni <sub>75</sub> Al <sub>21.875</sub> Nb <sub>3.125</sub>		Ni <sub>75</sub> Al <sub>21.875</sub> Pt <sub>3.125</sub>		Ni <sub>75</sub> Al <sub>21.875</sub> Re <sub>3.125</sub>				
	$\alpha_{\text{Ni-Al}}(R_1)$	$\alpha_{\text{Ni-Nb}}(R_1)$	$\alpha_{\text{Ni-Al}}(R_1)$	$\alpha_{\text{Ni-Pt}}(R_1)$	$\alpha_{\text{Ni-Al}}(R_1)$	$\alpha_{\text{Ni-Re}}(R_1)$	$\alpha_{\text{Al-Re}}(R_1)$		
800	-0.251	-0.193	0.519	-0.222	0.070	-0.272	-0.233	-0.050	0.027
850	-0.244	-0.187	0.498	-0.217	0.068	-0.264	-0.227	-0.047	0.020
900	-0.238	-0.181	0.479	-0.212	0.066	-0.258	-0.222	-0.045	0.013
950	-0.233	-0.176	0.461	-0.208	0.065	-0.251	-0.217	-0.044	0.007
1000	-0.227	-0.171	0.444	-0.203	0.063	-0.245	-0.212	-0.042	0.002
1050	-0.222	-0.166	0.428	-0.199	0.061	-0.239	-0.207	-0.041	-0.002
1100	-0.217	-0.162	0.412	-0.195	0.060	-0.233	-0.202	-0.040	-0.006
1150	-0.212	-0.158	0.398	-0.190	0.059	-0.227	-0.198	-0.039	-0.010
1200	-0.207	-0.154	0.385	-0.186	0.057	-0.222	-0.193	-0.038	-0.013
1250	-0.202	-0.150	0.372	-0.183	0.056	-0.217	-0.189	-0.037	-0.016

**Table 3.2 (Continued).**

T (°C)	Ni <sub>75</sub> Al <sub>21.875</sub> Ru <sub>3.125</sub>		Ni <sub>75</sub> Al <sub>21.875</sub> Ta <sub>3.125</sub>		Ni <sub>75</sub> Al <sub>21.875</sub> W <sub>3.125</sub>				
	$\alpha_{\text{Ni-Al}}(R_1)$	$\alpha_{\text{Al-Ru}}(R_1)$	$\alpha_{\text{Ni-Al}}(R_1)$	$\alpha_{\text{Al-Ta}}(R_1)$	$\alpha_{\text{Ni-Al}}(R_1)$	$\alpha_{\text{Ni-W}}(R_1)$	$\alpha_{\text{Al-W}}(R_1)$		
800	-0.258	-0.254	0.728	-0.249	-0.180	0.473	-0.251	-0.200	0.542
850	-0.252	-0.248	0.708	-0.243	-0.174	0.453	-0.245	-0.194	0.521
900	-0.246	-0.242	0.689	-0.237	-0.168	0.434	-0.239	-0.188	0.502
950	-0.240	-0.237	0.670	-0.231	-0.163	0.417	-0.234	-0.183	0.483
1000	-0.234	-0.232	0.652	-0.226	-0.158	0.400	-0.228	-0.178	0.466
1050	-0.229	-0.227	0.635	-0.220	-0.154	0.385	-0.223	-0.173	0.450
1100	-0.224	-0.222	0.618	-0.215	-0.150	0.371	-0.217	-0.168	0.434
1150	-0.219	-0.217	0.602	-0.210	-0.146	0.357	-0.212	-0.164	0.420
1200	-0.214	-0.213	0.587	-0.205	-0.142	0.344	-0.207	-0.160	0.406
1250	-0.209	-0.209	0.572	-0.201	-0.138	0.332	-0.203	-0.156	0.393

the nearest neighbour lattice sites of A atoms. For example, for the current ternary  $\text{Ni}_{75}\text{Al}_{21.875}\text{X}_{3.125}$  alloy systems,  $\alpha_{\text{Ni-Al}}(R_1)$  values are expected to be negative since the closest neighbours of Al atoms in  $L1_2$ -type ordered crystal structure of  $\text{Ni}_3\text{Al}$  phase are Ni atoms as indicated in Figure 2.3. Secondly, when  $\alpha_{\text{Ni-X}}(R_1)$  values are negative, X atoms would become the closest neighbours of Ni atoms, namely X atoms would occupy Al sublattice sites of ordered  $\text{Ni}_3\text{Al}$  intermetallics. When  $\alpha_{\text{Al-X}}(R_1)$  values are positive, preference of like neighbours will be dominant and X atoms preferentially occupy Al sublattice sites. Thirdly, when  $\alpha_{\text{Ni-X}}(R_1)$  values are positive and  $\alpha_{\text{Al-X}}(R_1)$  values are negative, X atoms are most likely to occupy Ni sublattice sites rather than Al sublattice sites. Next, when both  $\alpha_{\text{Ni-X}}(R_1)$  and  $\alpha_{\text{Al-X}}(R_1)$  values are negative, X atoms tend to substitute for both Al and Ni sublattice sites. Lastly, in case of both  $\alpha_{\text{Ni-X}}(R_1)$  and  $\alpha_{\text{Al-X}}(R_1)$  values are positive, X atoms would not occupy any sublattice sites of  $\text{Ni}_3\text{Al}$  phase which is not expected at all. Partial short range order parameter of Ni-Al atomic pair,  $\alpha_{\text{Ni-Al}}(R_1)$ , can change in the interval of  $(-0.33, 0)$  [89] but it never reaches zero since unlike atoms always tend to be the closest neighbours at any ambient temperature. Apart from the signs of partial SRO parameters of related atomic pairs, the magnitudes are also quite important which address the fraction of Al and/or Ni sublattice sites of  $\text{Ni}_3\text{Al}$  intermetallics occupied by ternary alloying elements. The site occupancy tendency of ternary alloying elements in  $\text{Ni}_3\text{Al}$  phase and the extent of ordering become more apparent when high magnitudes of partial SRO parameters are attained at lower temperatures. As temperature increases, since ordering progressively disappears and correspondingly  $\alpha^{ij}$  values gradually reduce in magnitude, site occupancy tendency of ternary atoms in  $\text{Ni}_3\text{Al}$  intermetallics diminishes.

### **3.4 Site Occupancy Characteristics of Ternary Alloying Elements and Theoretical Explanation of Possible TCP Phase Formation**

It is evident from Table 3.2 that, ternary alloying elements ( $X = \text{Co}, \text{Cr}, \text{Hf}, \text{Mo}, \text{Nb}, \text{Ru}, \text{Ta}$  and  $\text{W}$ ) revealing  $\alpha_{\text{Ni-X}}(R_1) < 0$  and  $\alpha_{\text{Al-X}}(R_1) > 0$ , mainly occupy Al sublattice sites, whereas alloying elements having  $\alpha_{\text{Ni-X}}(R_1) > 0$  and  $\alpha_{\text{Al-X}}(R_1) < 0$ ,

i.e. X = Pt, predominantly occupy Ni sublattice sites of ordered Ni<sub>3</sub>Al phase at all temperatures. Site occupancy preferences of ternary alloying X elements (X = Co, Cr, Hf, Mo, Nb, Pt, Re, Ru, Ta and W, respectively) in Ni-rich Ni<sub>75</sub>Al<sub>21.875</sub>X<sub>3.125</sub> alloy systems which have been studied in the present work by combining the statistical theory of ordering and electronic theory of alloys in the pseudopotential approximation are mostly consistent with the ones obtained by theoretical first-principles calculations and experimental studies, Table 3.3. However, the occupancy tendency of Co atoms in Ni<sub>3</sub>Al phase is still questionable; some studies have determined that occupancy preference of Co atoms would be Al sites (i.e. for Ni<sub>75</sub>(Al<sub>23</sub>Co<sub>2</sub>) alloy up to ordering temperature [90]), while some works have found that Co atoms preferentially occupy Ni sites (i.e. for (Ni<sub>74</sub>Co<sub>1</sub>)Al<sub>25</sub>, (Ni<sub>75</sub>Co<sub>1</sub>)Al<sub>24</sub> and (Ni<sub>74.25</sub>Co<sub>1</sub>)Al<sub>24.75</sub> alloy systems up to ordering temperature [91]). There are also some studies have claimed that Co atoms substitute for both Al and Ni sites (i.e. at 0 Kelvin [54,90,91] and for Ni<sub>73</sub>Al<sub>25</sub>Co<sub>2</sub> and Ni<sub>73.5</sub>Al<sub>24.5</sub>Co<sub>2</sub> alloy systems up to ordering temperature [90]). The discrepancy of site occupancy tendency of Co atoms reported in the literature may be originated from its high solubility limit in Ni<sub>3</sub>Al intermetallics which depends on both alloy composition and temperature.

It appears that, in addition to temperature, type and content of alloying element additions as well as their solubility limits in Ni<sub>3</sub>Al intermetallics could be very critical in determining the site preference characteristics. In this context, as Re atoms preferentially occupy Al sublattice sites below 1023 °C, both Al and Ni sublattice sites of Ni<sub>3</sub>Al intermetallics are occupied above this particular temperature for Re = 3.125 at.%. Moreover, due to sign changing nature of SRO parameters of Al-Re atomic pairs as a function of composition, as opposed to other X elements, the content of Re atoms in Ni<sub>75</sub>Al<sub>25-x</sub>Re<sub>x</sub> alloys would also play a decisive role for the alteration of the distribution characteristics over Ni<sub>3</sub>Al sublattices. In view of that, sublattice site occupancy characteristics of Re atoms in Ni<sub>75</sub>Al<sub>25-x</sub>Re<sub>x</sub> alloys have also been studied in the current work for x = 1-4 at.% range of composition. As it is evident from Figure 3.4, for the low concentration values of Re atoms (most probably within the solubility limit), i.e. x < 2 at.%, Re atoms favourably occupy Al sublattice sites of Ni<sub>3</sub>Al



**Table 3.3** Site occupancy preferences of ternary alloying X elements (X = Co, Cr, Hf, Mo, Nb, Pt, Re, Ru, Ta and W) in  $\text{Ni}_{75}\text{Al}_{21.875}\text{X}_{3.125}$  alloy systems and the comparison of the current work results with other theoretical first-principles calculations and experimental methods. (<sup>\*</sup>): APFIM studies, (<sup>\*\*</sup>): ALCHEMI works, (<sup>(a)</sup>): at 0 Kelvin, (<sup>(b)</sup>): at lower service temperatures (i.e. < T<sub>c</sub>), (<sup>(c)</sup>): at higher service temperatures (i.e. > T<sub>c</sub>) and (<sup>(d)</sup>): in the studied temperature range (i.e. 800 °C-1250 °C).

Site occupancy preferences of ternary alloying X elements in $\text{Ni}_{75}\text{Al}_{21.875}\text{X}_{3.125}$ alloy systems			
X Elements	Current work	First-principles calculations	APT, APFIM <sup>*</sup> , ALCHEMI <sup>**</sup>
Co	Al <sup>d</sup>	Al <sup>90(d)</sup> , Ni <sup>91(d)</sup> , (Ni-Al) <sup>54(a),91(a),90(a,d)</sup>	Al <sup>105</sup> , (Ni-Al) <sup>54</sup>
Cr	Al <sup>d</sup>	Al <sup>52(a),103(a),90(a,d)</sup>	Al <sup>52,103</sup>
Hf	Al <sup>d</sup>	Al <sup>82(a),83(a),90(a,d)</sup>	Al <sup>108*</sup>
Mo	Al <sup>d</sup>	Al <sup>98(a),99(a),90(a,d),91(a,d)</sup>	Al <sup>99</sup>
Nb	Al <sup>d</sup>	Al <sup>90(a,d),91(a,d)</sup>	-
Pt	Ni <sup>d</sup>	Ni <sup>90(a,d)</sup>	-
Re	Al <sup>b</sup> , (Ni-Al) <sup>c</sup>	Al <sup>98(a),102(a),90(a,d),91(a,d)</sup>	Al <sup>102</sup>
Ru	Al <sup>d</sup>	Al <sup>54(a),102(a),90(c,d),91(d)</sup> , (Ni-Al) <sup>90(a),91(a)</sup>	Al <sup>54,102,109**</sup>
Ta	Al <sup>d</sup>	Al <sup>52(a),98(a),100(a),101(a),90(a,d),91(a,d)</sup>	Al <sup>52,104,106*,107*</sup>
W	Al <sup>d</sup>	Al <sup>52(a),100(a),90(a,d),91(a,d)</sup>	-

intermetallics up to ordering temperature which is consistent with the works of [90,91]. Nevertheless, as the concentration of Re atoms exceeds its unclear low solubility limit [92-94],  $\sim x > 2$  at.%, Re atoms surprisingly have a tendency to occupy both Al and Ni sublattices sites of  $\text{Ni}_3\text{Al}$  phase at critical temperatures,  $T_c$ , where site occupancy characteristics showing alteration, Figure 3.4.

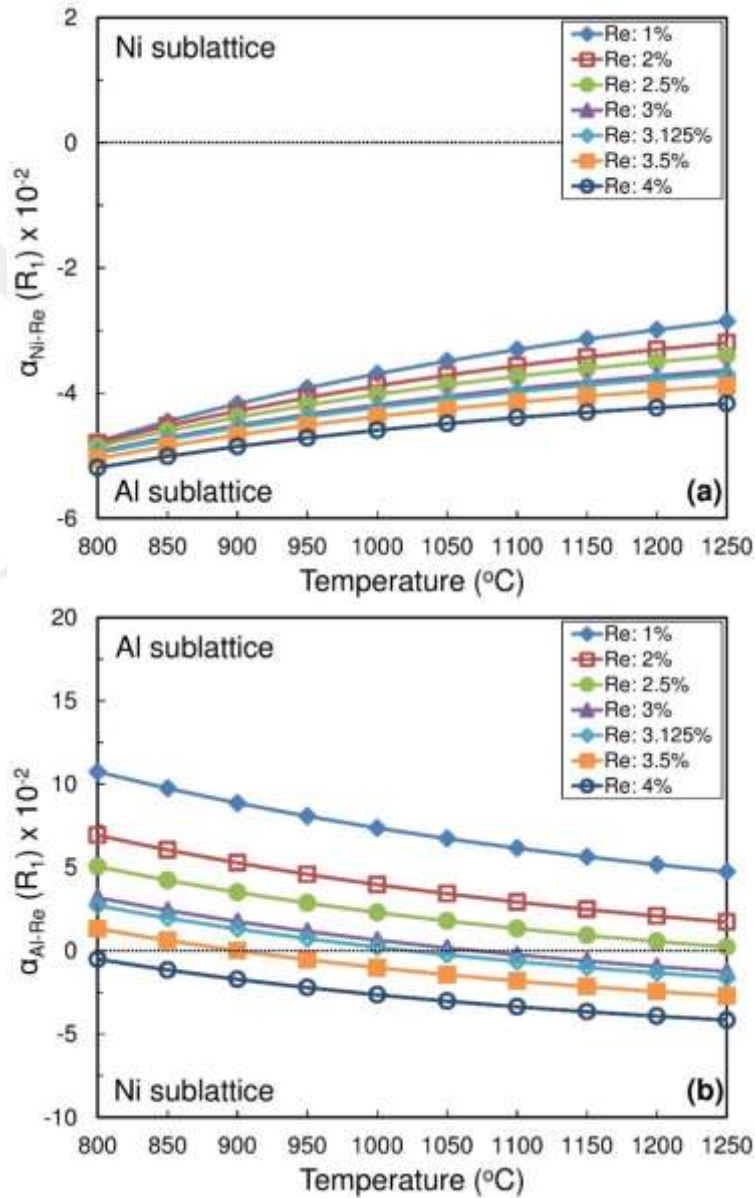


**Figure 3.4** The variation of partial SRO parameters of (a) Ni-Re and (b) Al-Re atomic pairs of  $\text{Ni}_{75}\text{Al}_{25-x}\text{Re}_x$  alloys with increasing temperature where  $x = 1-4$  at.%.

It is of research interest that whether this peculiar behaviour, in contrast to other X alloying element atoms, is a case only for low soluble Re atoms or not. Therefore, attempts have been made for further clarification of site occupancy characteristics of other alloying elements having low solubility in  $\gamma'$ -(Ni<sub>3</sub>Al-X) intermetallics. For this reason, owing to low solubility in Ni<sub>3</sub>Al phase [92,95], Ru alloying element has been selected and studied within the same temperature range for the concentrations believed to exceed the solubility limit (i.e.  $x > 3$  at.%). It is interesting to note that unlike Re atoms, Ru atoms solely occupy Al sublattice sites of Ni<sub>3</sub>Al phase at all temperatures, Table 3.4, and do not display the alteration of site occupancy characteristics with composition and temperature as Re atoms do.

**Table 3.4** Partial SRO parameters of Ni-Al, Ni-Ru and Al-Ru atomic pairs of Ni-rich Ni<sub>75</sub>Al<sub>21</sub>Ru<sub>4</sub> alloy at elevated temperatures ( $W_{\text{Ni-Al}}(R_1) = 7.1 \times 10^{-3}$  at. u.,  $W_{\text{Ni-Ru}}(R_1) = 30.645 \times 10^{-3}$  at. u. and  $W_{\text{Al-Ru}}(R_1) = 25.198 \times 10^{-3}$  at. u.).

T (°C)	Ni <sub>75</sub> Al <sub>21</sub> Ru <sub>4</sub>		
	$\alpha_{\text{Ni-Al}}(R_1)$	$\alpha_{\text{Ni-Ru}}(R_1)$	$\alpha_{\text{Al-Ru}}(R_1)$
800	-0.257	-0.256	0.722
850	-0.251	-0.250	0.702
900	-0.245	-0.244	0.683
950	-0.239	-0.239	0.664
1000	-0.234	-0.234	0.646
1050	-0.228	-0.229	0.629
1100	-0.223	-0.225	0.612
1150	-0.218	-0.220	0.596
1200	-0.213	-0.216	0.581
1250	-0.208	-0.212	0.566

It seems that solubility limit dependency of site occupancy characteristics is unique for Re atoms occupying both Al and Ni sublattice sites of Ni<sub>3</sub>Al phase above certain

critical temperatures,  $T_c$ . The variation of critical temperatures,  $T_c$ , and site occupancy preferences as a function of Re concentration for  $Ni_{75}Al_{25-x}Re_x$  alloys are illustrated in Figure 3.5, for  $x = 1-4$  at.% Re. Based on the site preferences of Re atoms, the demarcation lines in Figure 3.5 separate the regions where different types of predicted phases present. The isotherm at  $\sim 1375$  °C corresponds to order-disorder transformation temperature for binary  $Ni_3Al$  intermetallics below which  $L1_2$ -type ordered  $Ni_3Al$  phase exists. In this region, site preference of Re atoms has been determined as either Al (indicated by down arrows) or both Al and Ni sublattice sites (shown in up arrows). The site occupancy tendencies of Re atoms as a function of concentration and corresponding  $T_c$  values are shown by a solid line.

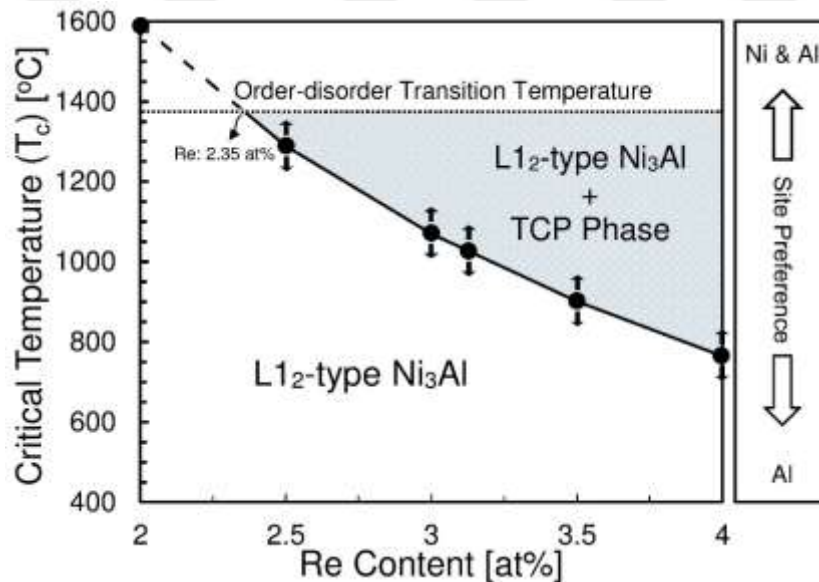


**Figure 3.5** The variation of critical temperatures,  $T_c$ , with respect to Re content at which occupancy preferences of Re atoms in  $L1_2$ -type ordered  $Ni_3Al$  intermetallics showing alteration and lead to phase instability of the parent  $\gamma'$  precipitates and possible formation of TCP phases.

Recent theoretical study [43] based on the calculation of binding energies of low soluble alloying elements (Re and Ru) in nickel-based superalloys has suggested that Re atoms occupying Ni sites of  $\gamma/\gamma'$  interface, lead to phase instability by increasing

binding energy so as to favour TCP phase formation. Consistent with this prediction, the present results show that there is some evidence of possible formation of TCP phase below ordering temperature at a composition  $> 2.35$  at.% Re, where Re atoms occupy both Al and Ni sublattice sites as shown in Figure 3.5. It is evident that, both Al and Ni sublattice sites occupancy of Re atoms for  $x > 2.35$  at.% in  $\text{Ni}_{75}\text{Al}_{25-x}\text{Re}_x$  alloys, may lead to localized supersaturation of the parent  $L1_2$ -type ordered  $\text{Ni}_3\text{Al}$  phase and subsequently makes possible the precipitation/formation of topologically close-packed (TCP) phases below ordering but above critical  $T_c$  temperatures. It is worth to note that, these critical temperatures,  $T_c$ , are compatible with the experimentally determined TCP precipitation/formation temperatures reported to be above  $\sim 850$  °C [14-16]. However, this unusual high temperature behaviour of Re atoms needs a further clarification in terms of the disclosure of the relationship between TCP formation mechanism and sublattice site occupancy characteristics of Re atoms in  $\text{Ni}_3\text{Al}$  phase.

### 3.5 Conclusions

In many studies, improved high temperature mechanical properties of nickel-based superalloys have been attributed to the arrangement of ternary alloying elements in  $\text{Ni}_3\text{Al}$  phase. Therefore, determination of high temperature sublattice site occupancy characteristics of ternary alloying elements in  $\text{Ni}_3\text{Al}$  phase (especially at service temperatures of nickel-based superalloys) is crucial. As opposed to the most of first-principles calculations being done at 0 Kelvin, the present study has shown that statistico-thermodynamical theory of ordering combined with electronic theory of multicomponent alloys can be successfully applied to the qualitative and/or semi-quantitative analysis of the site occupancy tendency and atomic short range ordering characteristics of substitutional X impurity elements ( $X = \text{Co}, \text{Cr}, \text{Hf}, \text{Mo}, \text{Nb}, \text{Pt}, \text{Re}, \text{Ru}, \text{Ta}$  and  $\text{W}$ , respectively) in  $L1_2$ -type ordered  $\text{Ni}_3\text{Al}$  intermetallics at elevated temperatures. In this work, pairwise SRO parameters of Ni-Al, Ni-X and Al-X atomic pairs in  $\text{Ni}_{75}\text{Al}_{25-x}\text{X}_x$  alloy systems have been calculated by taking into account the solubility limits of ternary alloying X elements in  $\text{Ni}_3\text{Al}$  phase. Over a wide

temperature range, the substitution tendencies of ternary X elements in  $\text{Ni}_{75}\text{Al}_{25-x}\text{X}_x$  alloy systems have been classified in three groups:

- 1<sup>st</sup> group: The elements of  $X = \text{Co}, \text{Cr}, \text{Hf}, \text{Mo}, \text{Nb}, \text{Ru}, \text{Ta}$  and  $\text{W}$  which mainly occupy Al sublattice sites of  $\text{Ni}_3\text{Al}$  superlattice at all temperatures, i.e.  $\alpha_{\text{Ni-X}}(R_1) < 0$  and  $\alpha_{\text{Al-X}}(R_1) > 0$ ;
- 2<sup>nd</sup> group: The element of  $X = \text{Pt}$  which mainly occupies Ni sublattice sites at all temperatures, i.e.  $\alpha_{\text{Ni-X}}(R_1) > 0$  and  $\alpha_{\text{Al-X}}(R_1) < 0$ ;
- 3<sup>rd</sup> group: Sublattice site occupancy characteristics of  $X = \text{Re}$  atoms seem to be both composition and temperature dependent. The critical temperatures,  $T_c$ , at which site occupancy characteristics showing alteration also vary with Re content.
  - i. Re atoms predominantly substitute for Al sublattice sites at all temperatures (below ordering temperature) if the composition of  $\text{Re} < 2.35$  at.% or temperatures below  $T_c$  for  $\text{Re} > 2.35$  at.%, i.e.  $\alpha_{\text{Ni-X}}(R_1) < 0$  and  $\alpha_{\text{Al-X}}(R_1) > 0$ ;
  - ii. However, Re atoms occupy both Al and Ni sublattice sites below ordering and above  $T_c$  temperatures for  $\text{Re} > 2.35$  at.%, i.e.  $\alpha_{\text{Ni-X}}(R_1) < 0$  and  $\alpha_{\text{Al-X}}(R_1) < 0$ .

It seems likely that, in contrast to other X elements, this peculiar atomic short range ordering behaviour of Re alloying element atoms distributed at both Al and Ni sublattice sites of  $\text{Ni}_3\text{Al}$  intermetallics above  $T_c$  may lead to localized supersaturation of the parent  $\text{Ni}_3\text{Al}$  phase at certain fraction and makes possible the formation of topologically close-packed (TCP) phases below ordering temperature. By considering above classification, it has been concluded that the results of the current research in terms of site occupancy tendency determination of alloying  $X = \text{Co}, \text{Cr}, \text{Hf}, \text{Mo}, \text{Nb}, \text{Pt}, \text{Re}, \text{Ru}, \text{Ta}$  and  $\text{W}$  element atoms in  $\gamma'-(\text{Ni}_3\text{Al-X})$  intermetallics coincide qualitatively well with other theoretical studies and experimental observations reported in the literature.

## CHAPTER 4

### SITE OCCUPANCY CHARACTERISTICS OF TERNARY ALLOYING ELEMENTS IN $\gamma'$ -Ni<sub>3</sub>Al INTERMETALLICS: FIRST-PRINCIPLES AB INITIO CALCULATIONS AT 0 KELVIN

#### 4.1 Introduction

In this chapter of the thesis, first-principles supercell calculations have been applied to determine sublattice site occupancy behaviours of alloying X elements in a model of Ni<sub>3</sub>Al phase in Vienna ab initio simulation package (VASP) based on density functional theory (DFT).

#### 4.2 Methodology

VASP is a fast and reliable electronic structure method which is applicable to bulk solids, surfaces, interfaces and so on. In these calculations, determination of sufficiently converged values of plane wave cut-off energy and K-mesh (1/K spacing) values, which lead to more accurate total energy and lattice parameter results, is very important. For this purpose, in VASP, automated convergence test has been applied for a 32 atoms 2 x 2 x 2 supercell model of Ni<sub>3</sub>Al phase and optimum values of afore mentioned parameters (considering computation time) have been determined as 315 eV and 9 x 9 x 9, respectively, as shown by down arrows in Figure 4.1. Figure 4.1 shows the variation of energy per atom values (as the computational iterations are done) with respect to plane wave cut-off energy and 1/K spacing. It should be noted that as the magnitudes of plane wave cut-off energy and 1/K spacing values increase, computation time of the total energy and lattice parameter calculations also increases.

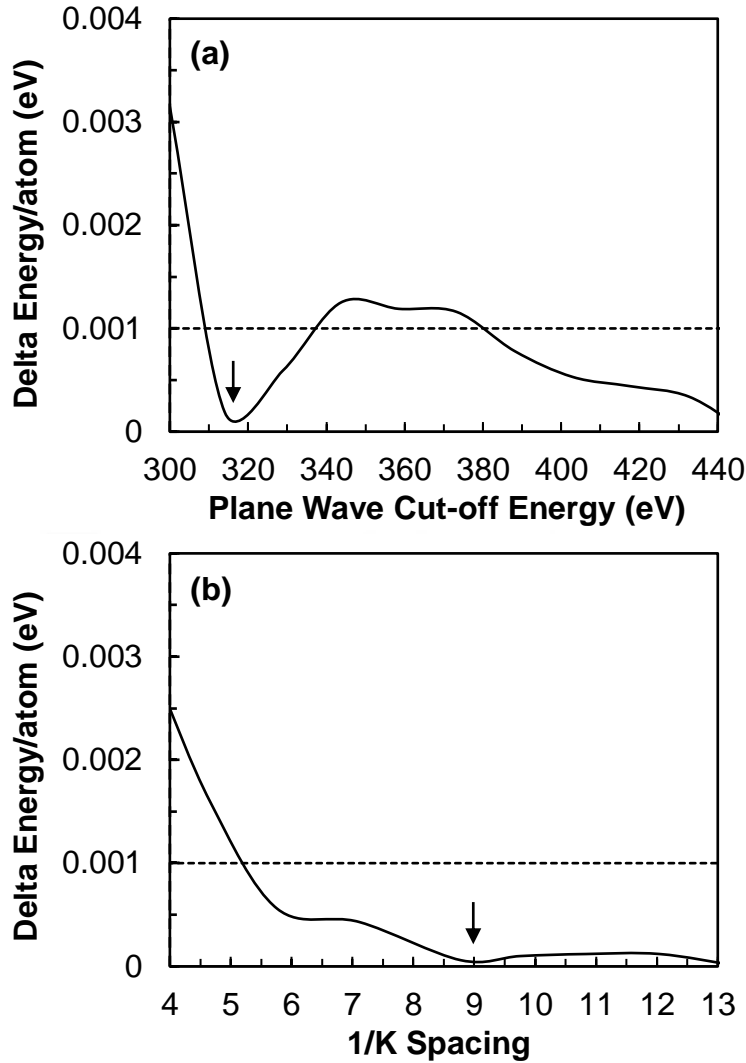


**Figure 4.1** Optimum values of plane wave cut-off energy and 1/K spacing.

In density functional theory solving the Kohn-Sham equations, DFT exchange correlation has been selected as Generalized Gradient Approximation after Perdew, Burke and Ernzerhofer (GGA-PBE) [126]. In the calculations, standard potentials of alloying X elements were treated (except Nb atoms). For Nb atoms, the semi-core 4p electrons were explicitly treated as valence (since standard potential of this element was absent in the simulation program). 32 atoms  $2 \times 2 \times 2$  supercells with plane wave cutoff energy of 315 eV and  $9 \times 9 \times 9$  k-point mesh for Brillouin zone sampling were constructed which give fully converged results (Figure 4.1). In the current work, considering the effects of magnetism, spin-polarized calculations were performed in



real space projection. In order to use time efficiently, structure optimization calculations (i.e. relax atom positions, allow cell volume to change, allow cell shape to change) were done in three steps. In the first step,  $2 \times 2 \times 2$  supercells of all structures (binary and impurity added  $\text{Ni}_3\text{Al}$  phases) were relaxed with all atoms occupying their ideal lattice positions as conjugate gradient convergence was  $0.02 \text{ eV/\text{Ang}}$  and spacing between k-points was  $0.35/\text{Ang}$  which refers to  $3 \times 3 \times 3$  explicit mesh parameter as plane wave cutoff energy was  $315 \text{ eV}$ . In the second step, previous semi-relaxed structures were re-treated to structure optimization by applying the same parameters except conjugate gradient convergence was  $0.01 \text{ eV/\text{Ang}}$ . Finally, fully relaxed structures of all systems were obtained as the previous structures were treated to the same parameters except spacing between k-points was  $0.1/\text{Ang}$  which refers to  $9 \times 9 \times 9$  explicit mesh parameter. In these calculations, type of smearing was Methfessel-Paxton with smearing width of  $0.2 \text{ eV}$  and self-consistent-field (SCF) convergence was  $1 \times 10^{-7} \text{ eV}$ .

### 4.3 Point Defect Formation Enthalpies in $\text{Ni}_3\text{Al}$ Phase

In this part of the supercell calculations, formation enthalpies of point defects (Ni and Al anti-sites) in  $L1_2$ -type ordered  $\text{Ni}_3\text{Al}$  intermetallics have been determined. For this purpose, firstly, 32 atoms  $2 \times 2 \times 2$  supercells of  $\text{Ni}_3\text{Al}$  phase containing one single point defect at their centres have been created as illustrated in Figure 4.2.

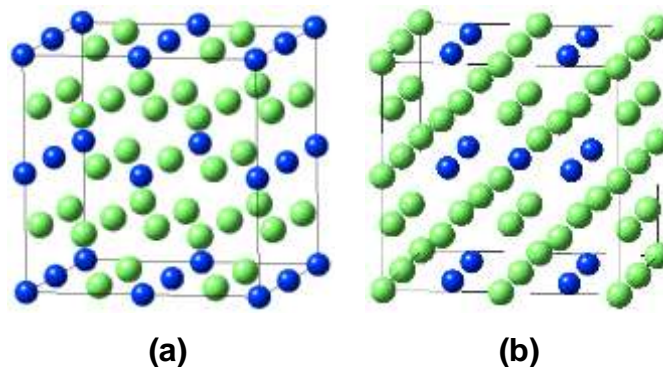


**Figure 4.2** 32 atoms  $2 \times 2 \times 2$  supercells of (a)  $\text{Ni}_{25}\text{Al}_7$  and (b)  $\text{Ni}_{23}\text{Al}_9$  systems in which (a) Ni (green) and (b) Al (blue) anti-sites located at the centres, respectively.

The formation enthalpy of  $\text{Ni}_{32-x-y}\text{Al}_x\text{X}_y$  systems can be calculated by using following equation [90],

$$\Delta H(\text{Ni}_{32-x-y}\text{Al}_x\text{X}_y) = E(\text{Ni}_{32-x-y}\text{Al}_x\text{X}_y) - (32-x-y)E(\text{Ni}) - xE(\text{Al}) - yE(\text{X}) \quad (4.1)$$

where  $E(\text{Ni}_{32-x-y}\text{Al}_x\text{X}_y)$ ,  $E(\text{Ni})$ ,  $E(\text{Al})$  and  $E(\text{X})$  are the total energies (per atom) of the corresponding alloy systems and pure elements of Ni, Al and X, respectively, which have been fully relaxed to their equilibrium geometries in the previous structure optimization part. In Equation (4.1),  $x$  and  $y$  denote the mole fractions of Al and X element atoms in the alloys, respectively. Then, formation enthalpies of the point defects (Ni and Al anti-sites) in a  $\text{Ni}_3\text{Al}$  model can be determined by using [90],

$$H_d = \frac{\partial \Delta H}{\partial x_d} \approx \frac{\Delta H_d - \Delta H_{\text{Ni}_3\text{Al}}}{x_d} \quad (4.2)$$

where  $\Delta H_d$  is the formation enthalpy (per atom) of a 32 atoms  $2 \times 2 \times 2$  supercell of  $\text{Ni}_3\text{Al}$  phase containing one point defect of type  $d$  (anti-site) and  $\Delta H_{\text{Ni}_3\text{Al}}$  is the formation enthalpy of perfectly (defect free) 32 atoms  $2 \times 2 \times 2$  supercell of  $L1_2$ -type ordered  $\text{Ni}_3\text{Al}$  phase. For anti-sites, the value of  $x_d$  is  $1/32$ . In this study, the formation energy of the exchange anti-site defects (both Ni and Al anti-sites) in  $L1_2$ -type  $\text{Ni}_3\text{Al}$  model has been calculated as 1.04 eV which coincides well with other studies [90,91,103,127] as indicated in Table 4.1.

**Table 4.1** Formation enthalpies of exchange anti-site defects.

	$H_{\text{Ni}_{\text{Al}}} \text{ (eV)}$	$H_{\text{Al}_{\text{Ni}}} \text{ (eV)}$	$H_{\text{Ni}_{\text{Al}}} + H_{\text{Al}_{\text{Ni}}} \text{ (eV)}$
Current work	2.01	-0.97	1.04
Wu and Li [91]	2.39	-0.99	1.40
Kim et al. [127]	2.06	-1.00	1.06
Jiang and Gleeson [90]	2.04	-0.92	1.12
Chaudhari et al. [103]	2.10	-1.06	1.04

#### 4.4 Anti-site Formation-based Formalism

At 0 Kelvin, site occupancy preferences of alloying X elements in Ni<sub>3</sub>Al phase can be determined by using anti-site formation-based formalism in which the energy change parameter,  $E_{\text{Ni} \rightarrow \text{Al}}^{\text{X}}$ , describes the energy required to move alloying X element atoms from Ni sublattice sites to the nearest neighbour (NN) Al sublattice sites. Energy change parameter,  $E_{\text{Ni} \rightarrow \text{Al}}^{\text{X}}$ , which equals to  $H_{\text{X}_{\text{Al}}} - H_{\text{X}_{\text{Ni}}} + H_{\text{Al}_{\text{Ni}}}$  [90], can be calculated by considering following equation system,

$$E_{\text{Ni}_{23}\text{XAl}_8} + E_{\text{Ni}_{24}\text{Al}_8} \rightarrow E_{\text{Ni}_{24}\text{XAl}_7} + E_{\text{Ni}_{23}\text{AlAl}_8} \quad (4.3)$$

$$E_{\text{Ni} \rightarrow \text{Al}}^{\text{X}} = E_{\text{Ni}_{24}\text{XAl}_7} + E_{\text{Ni}_{23}\text{AlAl}_8} - E_{\text{Ni}_{23}\text{XAl}_8} - E_{\text{Ni}_{24}\text{Al}_8} \quad (4.4)$$

By looking at the signs and magnitudes of  $E_{\text{Ni} \rightarrow \text{Al}}^{\text{X}}$ , sublattice site occupancy tendencies of alloying X elements in Ni<sub>3</sub>Al phase can be classified into three groups:

- 1<sup>st</sup> group: X element atoms preferentially occupy Al sublattice sites when  $E_{\text{Ni} \rightarrow \text{Al}}^{\text{X}} < 0$ ;
- 2<sup>nd</sup> group: X element atoms tend to occupy Ni sublattice sites when  $E_{\text{Ni} \rightarrow \text{Al}}^{\text{X}} > H_{\text{Ni}_{\text{Al}}} + H_{\text{Al}_{\text{Ni}}} = 1.04 \text{ eV}$ ;
- 3<sup>rd</sup> group: X element atoms may occupy both Al and Ni sublattice sites when  $0 < E_{\text{Ni} \rightarrow \text{Al}}^{\text{X}} < H_{\text{Ni}_{\text{Al}}} + H_{\text{Al}_{\text{Ni}}} = 1.04 \text{ eV}$ .

#### 4.5 Site Preferences of Ternary Alloying Elements at 0 Kelvin

Table 4.2 shows total energy of each system and their corresponding  $E_{\text{Ni} \rightarrow \text{Al}}^{\text{X}}$  values consistent with other first-principles calculations [90,91,127]. According to Table 4.2,  $E_{\text{Ni} \rightarrow \text{Al}}^{\text{X}}$  values of the systems have negative signs for X = Cr, Hf, Mo, Nb, Re, Ta, Ti and W additions, whereas for X = Pt addition,  $E_{\text{Ni} \rightarrow \text{Al}}^{\text{Pt}}$  value equals to 1.27 (greater than 1.04 eV). For X = Co and Ru additions,  $E_{\text{Ni} \rightarrow \text{Al}}^{\text{X}}$  values have positive signs but the

magnitudes are less than 1.04 eV. These results imply that, at 0 Kelvin, aforementioned alloying elements (except Co, Pt and Ru) preferentially occupy Al sublattice sites of Ni<sub>3</sub>Al intermetallics, whereas Pt atoms have a tendency to occupy Ni sublattice sites. Occupancy behaviours of Co and Ru atoms are composition dependent; these atoms may substitute for both Al and Ni sites.

#### **4.6 Theoretical Lattice Parameter Calculations of Ni<sub>3</sub>Al-X Phases**

When impurity alloying X elements (X = Co, Cr, Hf, Mo, Nb, Pt, Re, Ru, Ta, Ti and W, respectively) are placed by a centrally located Al or Ni atoms in 32 atoms 2 x 2 x 2 supercells of Ni<sub>3</sub>Al-X systems (i.e. Ni<sub>24</sub>Al<sub>7</sub>X and Ni<sub>23</sub>Al<sub>8</sub>X, respectively), after full structure optimization, equilibrium lattice parameters of these systems have been calculated (Table 4.3). According to Table 4.3, it is possible to conclude that as most of the alloying X elements occupy Al sublattice sites, lattice parameters of these systems become smaller than the systems in which X atoms occupy Ni sites. However, for X = Pt atoms lattice parameter of Ni<sub>24</sub>Al<sub>7</sub>Pt system looks slightly smaller than Ni<sub>23</sub>Al<sub>8</sub>Pt one. For X = Co and Ru atoms, lattice parameters of Ni<sub>24</sub>Al<sub>7</sub>X systems are smaller than Ni<sub>23</sub>Al<sub>8</sub>X ones but not as much as firstly mentioned alloying elements.

Therefore, by combining the results of occupancy characteristics of alloying X elements and lattice parameters of Ni<sub>3</sub>Al-X systems, it can be concluded that alloying elements preferentially occupy Al sublattice sites of Ni<sub>3</sub>Al phase if the difference between lattice parameters of Ni<sub>24</sub>Al<sub>7</sub>X and Ni<sub>23</sub>Al<sub>8</sub>X systems is big enough (Ni site occupancy probability of these alloying elements leads to considerable amount of lattice distortion). When this difference gets lower, alloying elements may substitute for both sites. However, when the difference is very small, alloying elements tend to occupy Ni sites due to very small amount of lattice distortion. Figure 4.3 illustrates this relationship much clear.

**Table 4.2** Total energy and energy change parameters,  $E_{\text{Ni} \rightarrow \text{Al}}^{\text{X}}$ , of  $\text{Ni}_{32-x-y}\text{Al}_x\text{X}_y$  systems where  $\text{X} = \text{Co}, \text{Cr}, \text{Hf}, \text{Mo}, \text{Nb}, \text{Pt}, \text{Re}, \text{Ru}, \text{Ta}, \text{Ti}$  and  $\text{W}$ , respectively.

Alloying X elements	Total energy of each system (eV)								Site preferences (at 0 Kelvin)
	$\text{Ni}_{24}\text{Al}_7\text{X}$	$\text{Ni}_{23}\text{Al}_8\text{Al}$	$\text{Ni}_{23}\text{Al}_8\text{X}$	$\text{Ni}_{24}\text{Al}_8$	Current work	Wu and Li [91]	Kim et al. [127]	Jiang and Gleeson [90]	
Co	-176.78	-174.53	-176.23	-175.30	0.22	1.25	-	$\sim 0.50$	Al and Ni
Cr	-179.70	-174.53	-178.24	-175.30	-0.70	-0.10	-0.56	$\sim -0.45$	Al
Hf	-181.92	-174.53	-179.91	-175.30	-1.25	-	-1.17	$\sim -1.23$	Al
Mo	-181.64	-174.53	-179.74	-175.30	-1.13	-1.13	-	$\sim -1.07$	Al
Nb	-181.45	-174.53	-179.49	-175.30	-1.19	-1.03	-	$\sim -1.18$	Al
Pt	-175.86	-174.53	-176.36	-175.30	1.27	-	1.30	$\sim 1.40$	Ni
Re	-182.96	-174.53	-181.08	-175.30	-1.11	-1.11	-	$\sim -1.00$	Al
Ru	-178.78	-174.53	-178.13	-175.30	0.11	0.21	-	$\sim 0.25$	Al and Ni
Ta	-183.63	-174.53	-181.56	-175.30	-1.30	-1.06	-	$\sim -1.25$	Al
Ti	-179.65	-174.53	-178.08	-175.30	-0.81	-0.62	-	$\sim -0.78$	Al
W	-183.95	-174.53	-181.88	-175.30	-1.30	-1.26	-	$\sim -1.25$	Al

**Table 4.3** Lattice parameters of  $\text{Ni}_{24}\text{Al}_7\text{X}$  and  $\text{Ni}_{23}\text{Al}_8\text{X}$  systems where  $\text{X} = \text{Co}, \text{Cr}, \text{Hf}, \text{Mo}, \text{Nb}, \text{Pt}, \text{Re}, \text{Ru}, \text{Ta}, \text{Ti}$  and  $\text{W}$ , respectively.

Alloying X elements	Lattice parameter (Å)	
	$\text{Ni}_{24}\text{Al}_7\text{X}$ (Al site is occupied)	$\text{Ni}_{23}\text{Al}_8\text{X}$ (Ni site is occupied)
Co	3.561	3.570
Cr	3.558	3.596
Hf	3.586	3.643
Mo	3.571	3.616
Nb	3.580	3.632
Pt	3.579	3.582
Re	3.568	3.604
Ru	3.569	3.577
Ta	3.578	3.637
Ti	3.570	3.622
W	3.571	3.624

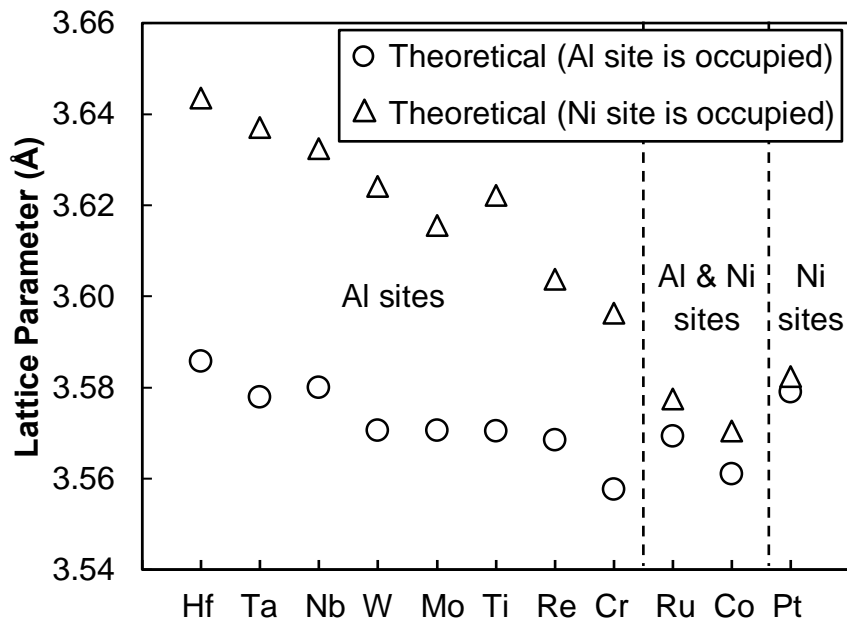


**Figure 4.3** Lattice parameter variations of  $\text{Ni}_{24}\text{Al}_7\text{X}$  (shown in spheres) and  $\text{Ni}_{23}\text{Al}_8\text{X}$  (indicated by triangles) systems where  $\text{X} = \text{Hf}, \text{Ta}, \text{Nb}, \text{W}, \text{Mo}, \text{Ti}, \text{Re}, \text{Cr}, \text{Ru}, \text{Co}$  and  $\text{Pt}$ , respectively.

## 4.7 Atomistic Level Simulations of Ni<sub>3</sub>Al-X Phases

In VASP program, in addition to total energy and equilibrium lattice parameter calculations (which reveal the sublattice site occupancy behaviours of alloying X elements), thanks to some simulation methods, atomic bonding characteristics and hybridization types within the models of Ni<sub>3</sub>Al-X systems can be determined. Hence, in the following parts, charge density difference (CDD), electron localization function (ELF) and density of states (DOS) methods have been applied to both Ni<sub>24</sub>Al<sub>7</sub>X and Ni<sub>23</sub>Al<sub>8</sub>X systems where X = Al(Ni), Co, Cr, Hf, Mo, Nb, Pt, Re, Ru, Ta, Ti and W, respectively.

### 4.7.1 Charge Density Difference (CDD)

The effects of alloying X element additions on the bonding properties of Ni<sub>3</sub>Al-X systems can be determined via charge density difference (CDD) method in which charge (induced by the alloying elements) is redistributed. In this study, the effects of alloying X elements located at either Al or Ni sites of 32 atoms 2 x 2 x 2 models of Ni<sub>3</sub>Al phase on CDD characteristics have been investigated for (010), (110) and (111) planes of the supercells (Figure 4.4). In the simulations, charge distribution characteristics were coloured from red (refers to charge accumulation regions, 0.07) to navy blue (denotes to charge depletion regions, -0.1). In literature [128-130], it has been stated that charge accumulation near alloying X element atoms located at the centre refers to strong bondings (i.e. directional covalent-type bondings) between these X element atoms and their NN atoms. Moreover, it has also been mentioned that as this accumulation region gets more visible in size and/or red colour, bonding strength increases. The CDD characteristics for the additions of X = Al(Ni), Co, Cr, Hf, Mo, Nb, Pt, Re, Ru, Ta, Ti and W atoms located at either Al or Ni sites of Ni<sub>3</sub>Al phase for the afore mentioned planes are given in the following figures starting from Figure 4.5 to Figure 4.10.

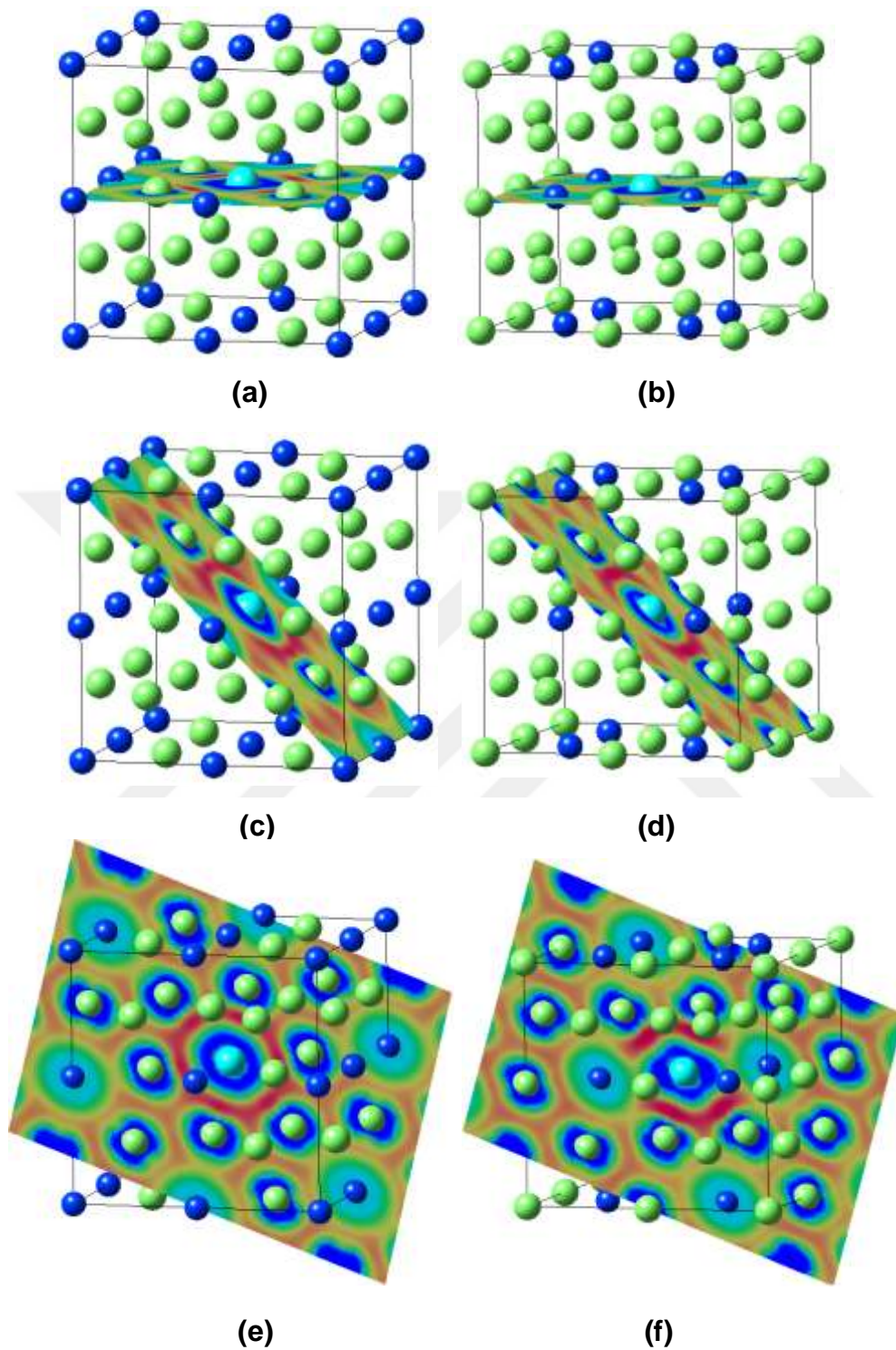


**Figure 4.4** CDD characteristics of centrally located alloying X elements (light blue) at either (a,c,e) Al or (b,d,f) Ni sites of 32 atoms 2 x 2 x 2 model of Ni<sub>3</sub>Al phase for (a,b) (010), (c,d) (110) and (e,f) (111) planes, respectively.



As illustrated in Figure 4.5, for (010) plane CDD simulations, it can be noticed that all ternary X elements located at the centre Al sites cause charge accumulation regions between themselves and their NN Ni atoms denoted as “1”. This accumulation regions can be ordered from the smallest to the largest as Al < Pt < Co < Ru < Ti < Hf < Cr < Nb < Mo < Ta < W < Re. Re atoms lead to the strongest directional covalent bondings with NN Ni atoms, while Pt atoms cause the weakest ones. Secondly, when charge depletion regions of centrally located X elements are examined, it is noticed that the shapes of these depletion regions (shown in navy blue) become different. For most of the alloying elements (except Co, Pt and Ru), NN Ni atoms cause these regions to go inward. However, for Pt atoms, NN Al atoms (instead of NN Ni atoms) seem to lead to the same effect. In this case, NN Ni atoms make these regions to go outward. For X = Co and Ru atoms, both or none of NN Ni and NN Al atoms seem to have effect on this behaviour. The depletion regions of these atoms are nearly spherical; they do not go either inward or outward.

These interesting shape characteristics of the depletion regions around alloying X elements most probably explain their site occupancy preferences (Al and/or Ni) in Ni<sub>3</sub>Al intermetallics. For this purpose, in order to understand better this relationship, the same plane (010) CDD characteristics of centrally located alloying X elements at Ni sites of Ni<sub>3</sub>Al phase have been examined as indicated in Figure 4.6. Interestingly, among these alloying X elements, only Co, Pt and Ru atoms seem to lead to directional covalent bondings with their NN Al atoms, while other alloying elements cause a slight accumulation region (shown in orange colours) towards NN Ni atoms. Therefore, CDD simulation patterns of centrally located alloying X element occupying either Al or Ni sites can also be considered to determine sublattice site occupancy characteristics of these alloying elements. According to CDD simulations, X = Cr, Hf, Mo, Nb, Re, Ta, Ti and W atoms preferentially occupy Al sublattice sites of Ni<sub>3</sub>Al intermetallics, whereas X = Pt atoms tend to substitute for Ni sites. X = Co and Ru atoms occupy both sites. As opposed to other alloying X elements, Re atom located at Ni site creates a thin continuous layer of accumulation region between itself and its NN Al and NN Ni atoms. This peculiar behaviour of Re atoms occupying Ni sites of Ni<sub>3</sub>Al phase would

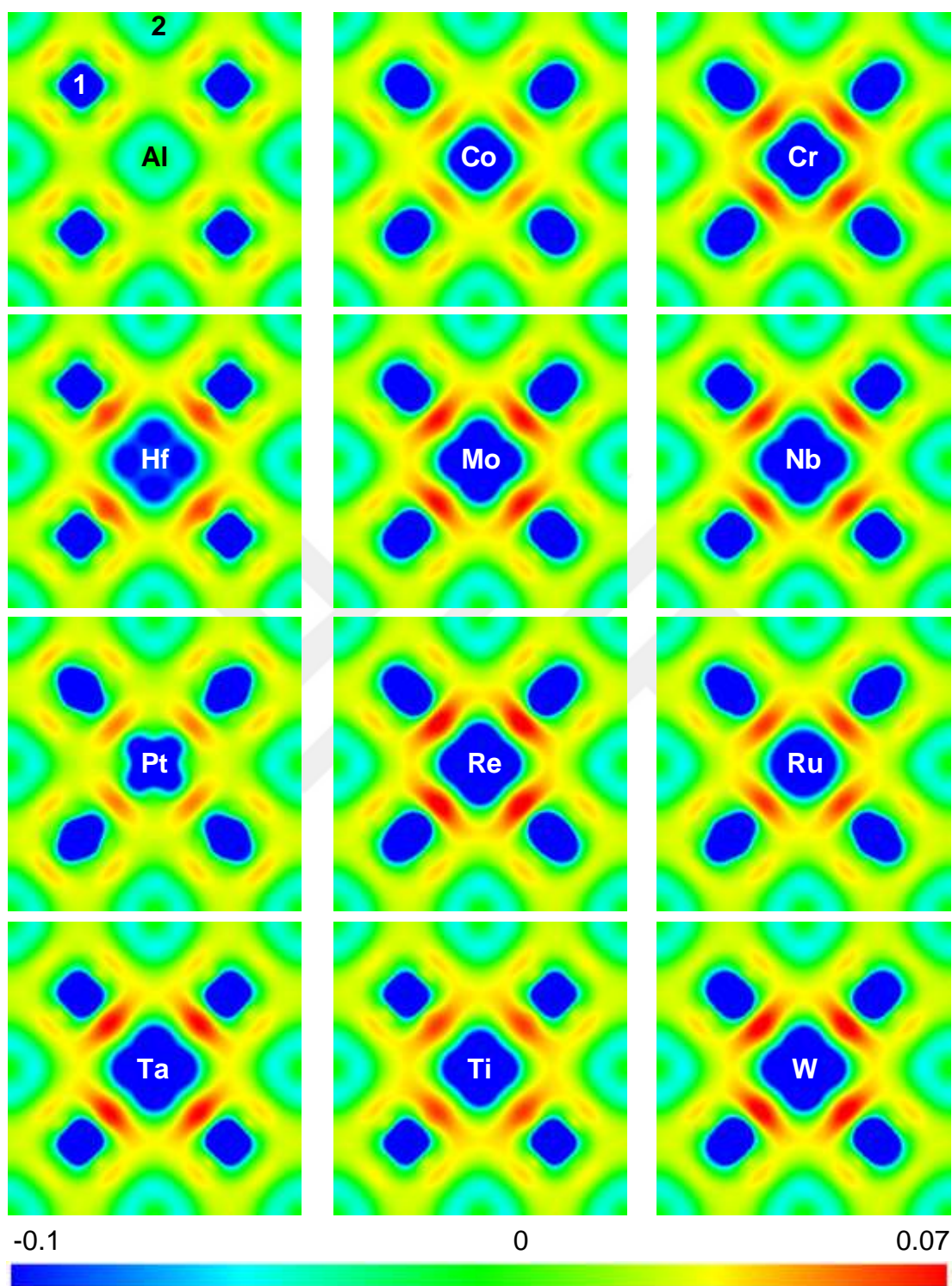


**Figure 4.5** (010) plane CDD characteristics of centrally located alloying X elements at Al sites of  $\text{Ni}_3\text{Al}$  phase where  $X = \text{Al}, \text{Co}, \text{Cr}, \text{Hf}, \text{Mo}, \text{Nb}, \text{Pt}, \text{Re}, \text{Ru}, \text{Ta}, \text{Ti}$  and  $\text{W}$ , respectively (1: NN Ni and 2: NN Al atoms).

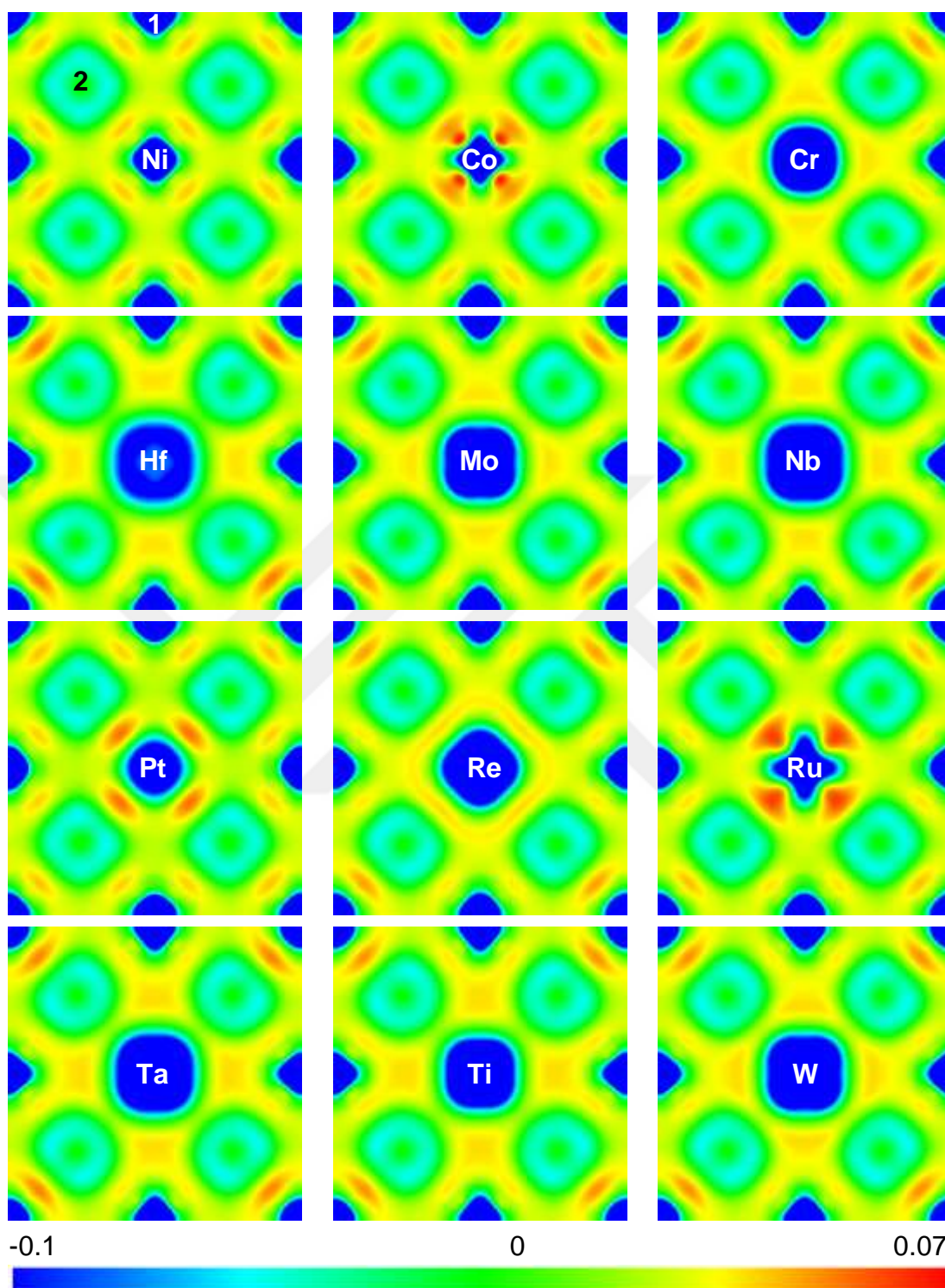


**Figure 4.6** (010) plane CDD characteristics of centrally located alloying X elements at Ni sites of Ni<sub>3</sub>Al phase where X = Ni, Co, Cr, Hf, Mo, Nb, Pt, Re, Ru, Ta, Ti and W, respectively (1: NN Ni and 2: NN Al atoms).

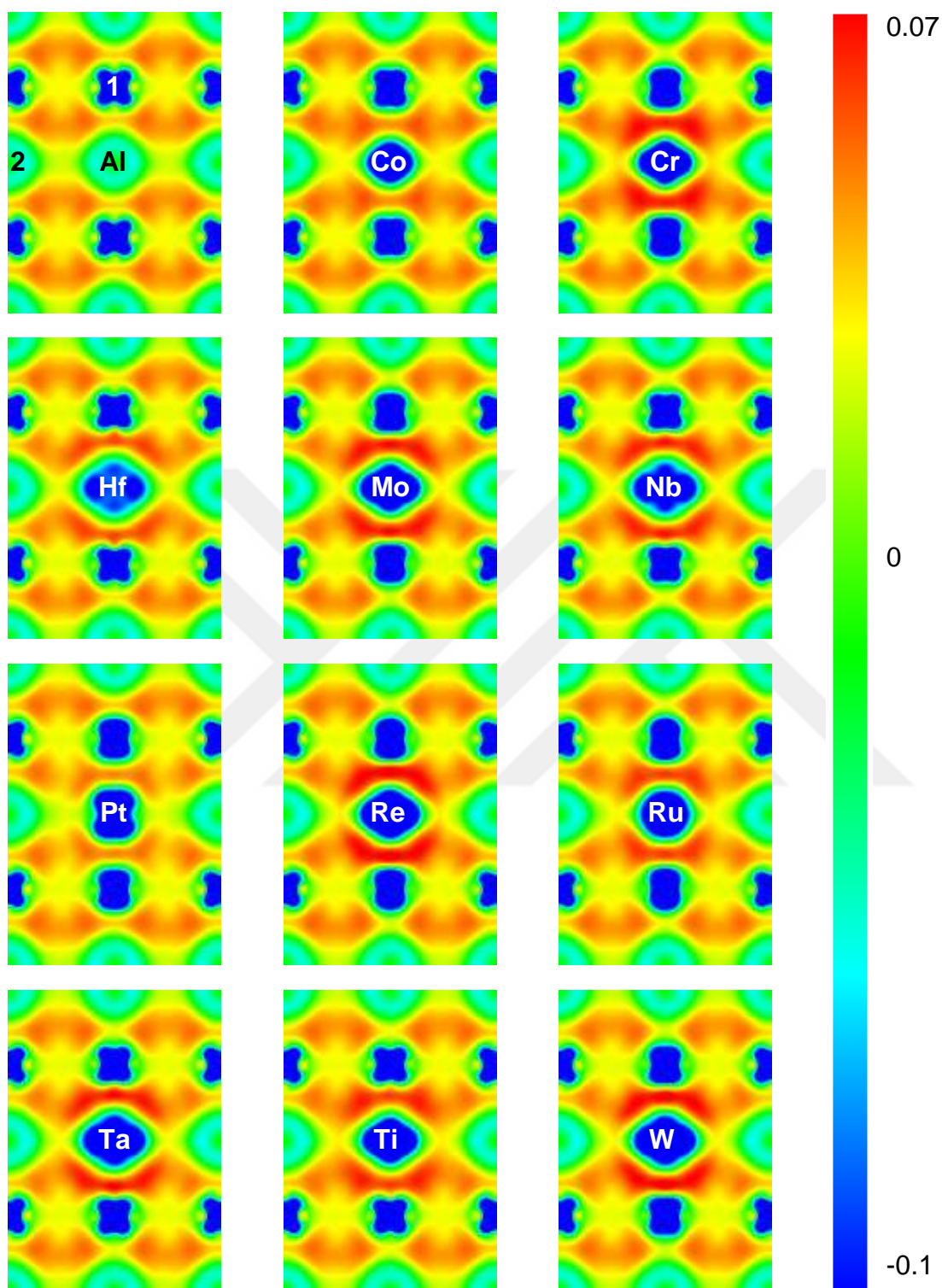


**Figure 4.7** (110) plane CDD characteristics of centrally located alloying X elements at Al sites of  $\text{Ni}_3\text{Al}$  phase where  $X = \text{Al}, \text{Co}, \text{Cr}, \text{Hf}, \text{Mo}, \text{Nb}, \text{Pt}, \text{Re}, \text{Ru}, \text{Ta}, \text{Ti}$  and  $\text{W}$ , respectively (1: NN Ni and 2: NN Al atoms).

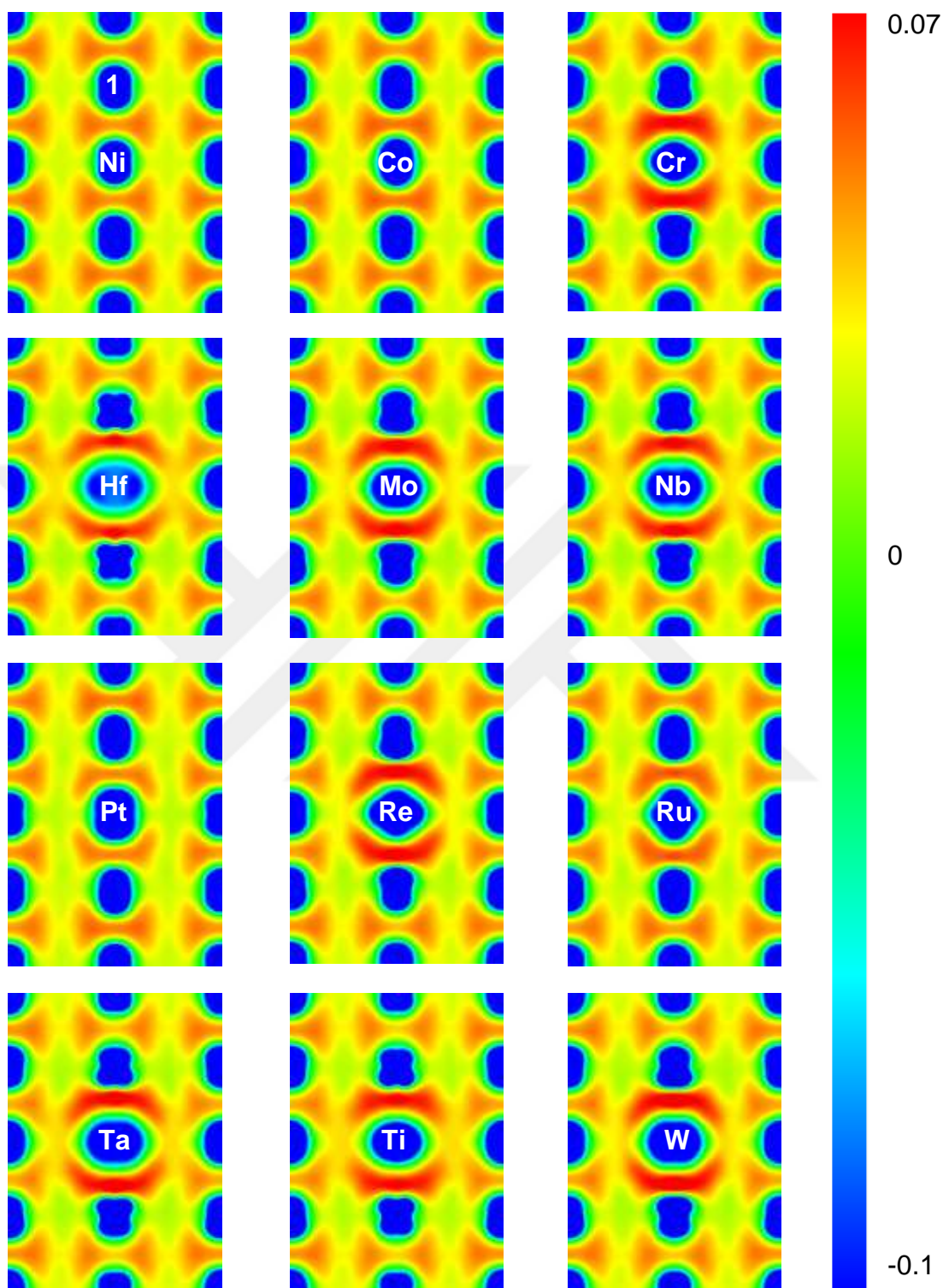


**Figure 4.8** (110) plane CDD characteristics of centrally located alloying X elements at Ni sites of  $\text{Ni}_3\text{Al}$  phase where  $X = \text{Ni}, \text{Co}, \text{Cr}, \text{Hf}, \text{Mo}, \text{Nb}, \text{Pt}, \text{Re}, \text{Ru}, \text{Ta}, \text{Ti}$  and  $\text{W}$ , respectively (1: NN Ni atoms).

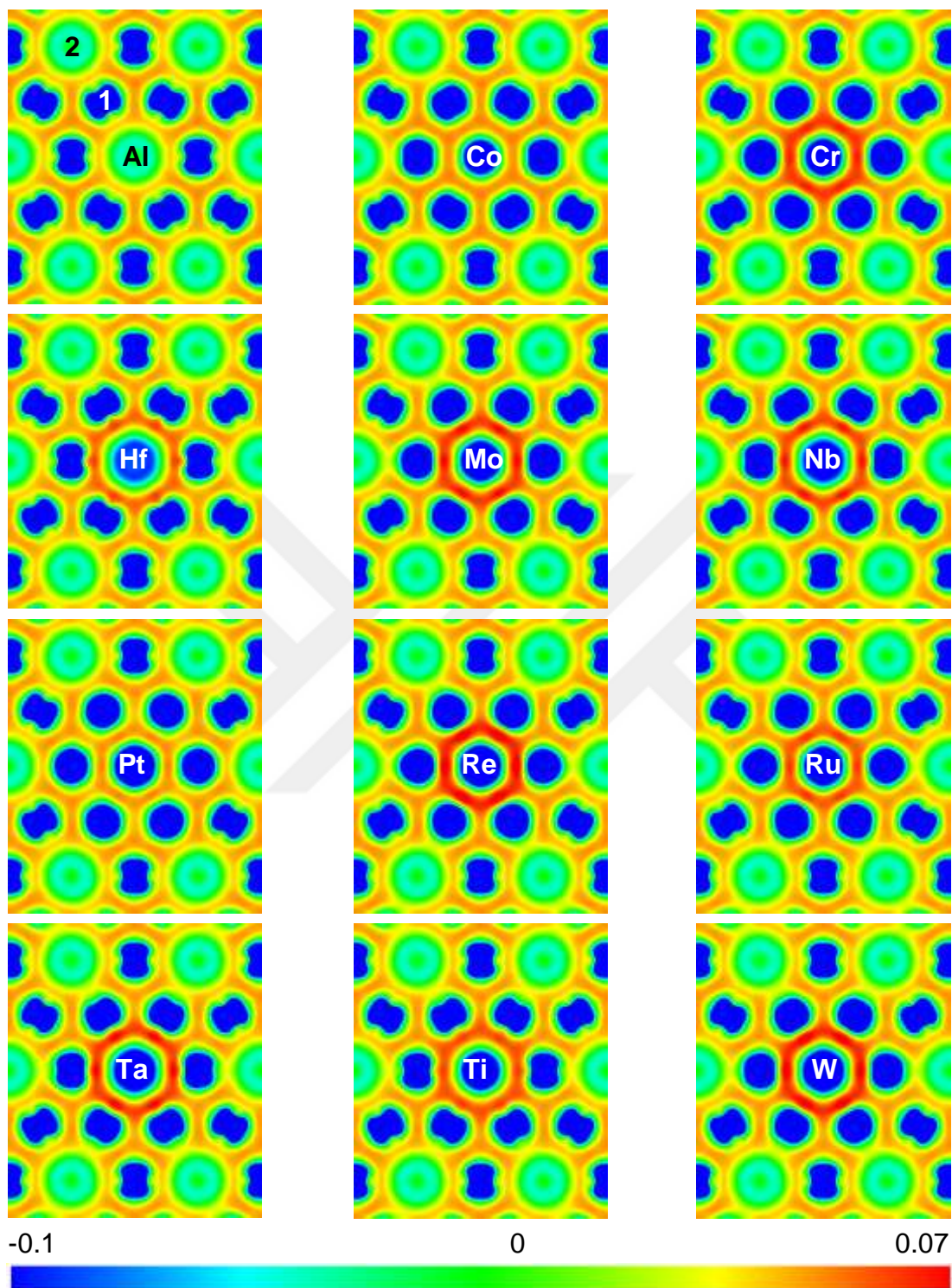


**Figure 4.9** (111) plane CDD characteristics of centrally located alloying X elements at Al sites of  $\text{Ni}_3\text{Al}$  phase where  $X = \text{Al}, \text{Co}, \text{Cr}, \text{Hf}, \text{Mo}, \text{Nb}, \text{Pt}, \text{Re}, \text{Ru}, \text{Ta}, \text{Ti}$  and  $\text{W}$ , respectively (1: NN Ni and 2: NN Al atoms).

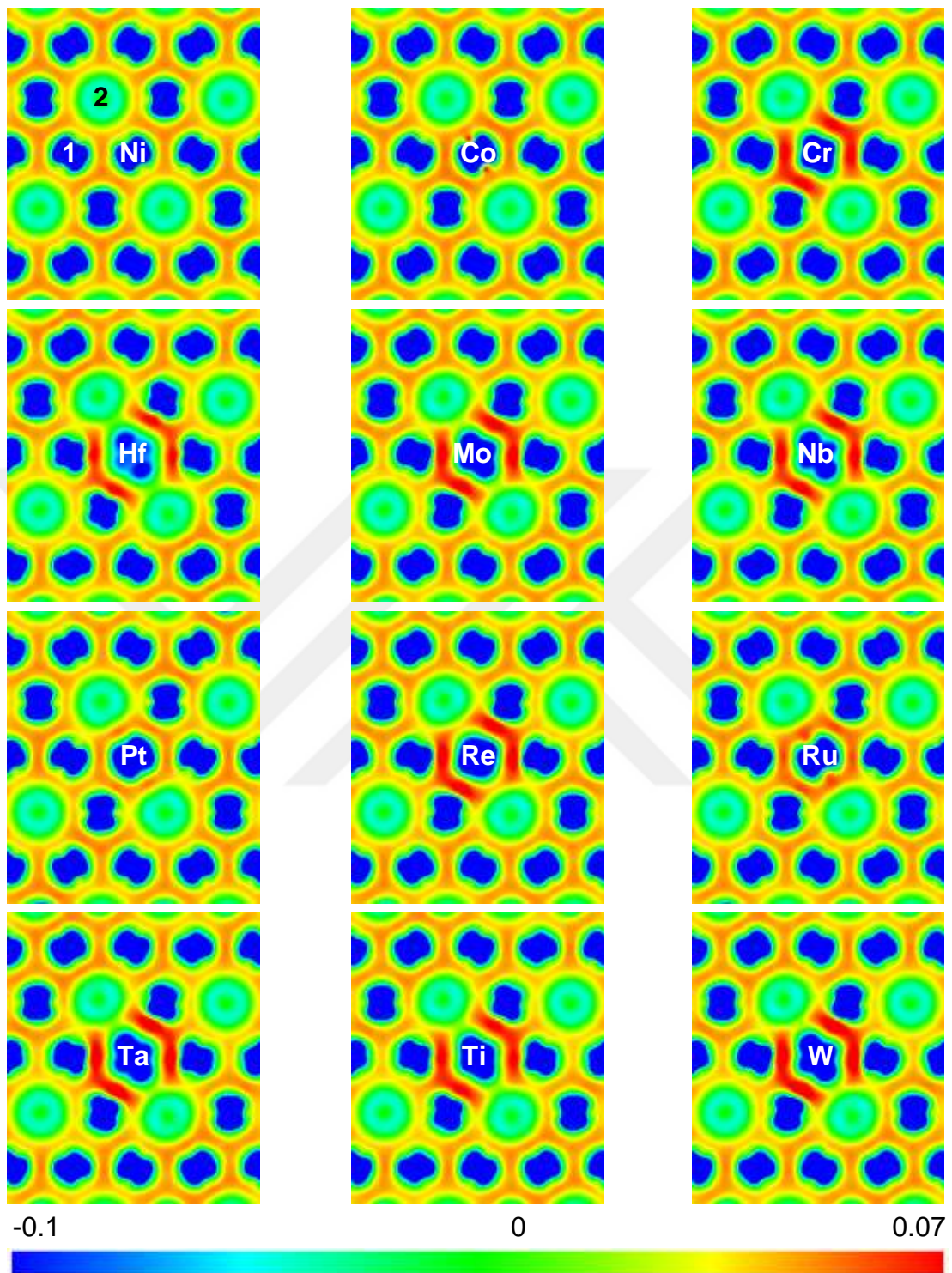


**Figure 4.10** (111) plane CDD characteristics of centrally located alloying X elements at Ni sites of  $\text{Ni}_3\text{Al}$  phase where  $X = \text{Ni}, \text{Co}, \text{Cr}, \text{Hf}, \text{Mo}, \text{Nb}, \text{Pt}, \text{Re}, \text{Ru}, \text{Ta}, \text{Ti}$  and  $\text{W}$ , respectively (1: NN Ni and 2: NN Al atoms).

start charge accumulation/supersaturation and cause TCP phase precipitation as previously mentioned in Figure 3.5 in detail. Secondly, centrally located Pt and Ru atoms, which have been proven to inhibit TCP phase formation by many studies [1,40,42,43], lead to accumulation regions between themselves and their NN Al atoms. Therefore, this behaviour of Pt and Ru atoms would break thin continuous accumulation layers of Re atoms which may help the inhibition of TCP phases. For Co addition, charge accumulation region is visible between Co and its NN Al atoms (similar to Pt and Ru additions); but, unfortunately, there is no information in the literature about the effects of Co atoms on TCP phases. However, it is well known that Co atoms have significant diffusivity in superalloys [41] which may make Co atoms to break afore mentioned accumulation layers introduced by Re atoms having very low diffusion coefficient within superalloys [79].

For (110) planes of  $Ni_{24}Al_7X$  and  $Ni_{23}Al_8X$  systems where  $X \neq Co, Pt$  and  $Ru$ , similar results have been obtained. Since charge accumulation regions represented in red colours dominate along  $\langle 110 \rangle$  directions (along X alloying element atoms and their NN Ni atoms), strengthening can be attributed to occur along this direction instead of  $\langle 001 \rangle$  directions (along X alloying element atoms and their NN Al atoms). Because, along  $\langle 110 \rangle$  directions, covalent bonding characteristics are very clear. However, for  $X = Co, Pt$  and  $Ru$  atoms, there is no such a strong directional covalent bonding nature between these atoms and their NN Ni atoms along  $\langle 110 \rangle$  directions (Figures 4.7-8). Therefore, these alloying elements may be considered to increase ductility rather than strength of  $Ni_3Al$  phase due to possible metallic bondings instead of covalent bondings. In the next part, this possibility is going to be discussed in more detail.

Similarly, for (111) planes of  $Ni_{24}Al_7X$  systems, charge accumulation regions around centrally located alloying X element atoms occupying Al sublattice sites (except Co and Pt) are visible (Figure 4.9). For Ru atoms these regions are not clear enough. However, as shown in Figure 4.10, when alloying X element atoms occupy Ni sublattice sites of (111) plane  $Ni_{23}Al_8X$  systems,  $X = Cr, Hf, Mo, Nb, Re, Ta, Ti$  and  $W$  atoms seem to have directional bondings with NN Ni atoms, whereas  $X = Co, Pt$



and Ru atoms have no directional bondings. Ru atoms lead to more visible accumulation regions rather than Co and Pt atoms do which would make Ru atoms more effective (rather than Co and Pt atoms) to prevent TCP phases.

#### **4.7.2 Electron Localization Function (ELF)**

In order to comprehend the origin of strengthening mechanisms of Ni<sub>3</sub>Al-X phases in atomistic level, electron localization function (ELF) is another way to reveal the bonding characteristics between NN atoms. ELF defines the probability of finding a second electron at a position B, given that a first electron having the same spin is located with certainty at position A and it is considered as more effective to measure the interatomic bonding characteristics rather than electronic charge density maps [100]. In ELF contour plots, directional red regions having high ELF values between adjacent atoms show that covalent bondings are the main bonding types in these areas. However, uniform green regions having low ELF values between adjacent atoms indicate that metallic bondings rather than covalent ones are dominant in these regions.

In this study, ELF characteristics of alloying X elements located at either Al or Ni sites of Ni<sub>3</sub>Al phase have been investigated for (010), (110) and (111) planes of 32 atoms 2 x 2 x 2 supercell models (Figure 4.11). In these simulations, ELF contour plots were coloured from red (0.2) to navy blue (0). The ELF contour plots for X = Co, Cr, Hf, Mo, Nb, Pt, Re, Ru, Ta, Ti and W atoms located at either Al or Ni sites of Ni<sub>3</sub>Al phase for the afore mentioned planes are given in the following figures starting from Figure 4.12 to Figure 4.17. However, it should be noted that for Nb addition, these contour plots would be questionable since the semi-core 4p electrons of this element were explicitly treated as valence as previously mentioned.

ELF simulations of (010) plane for alloying X element atoms located at the centre Al site of Ni<sub>3</sub>Al phase show the effects of these alloying elements on the bonding characteristics (Figure 4.12). Alloying elements, such as X = Re, Ta and W atoms lead to strong directional covalent bondings with NN Ni atoms, while X = Cr and Mo atoms

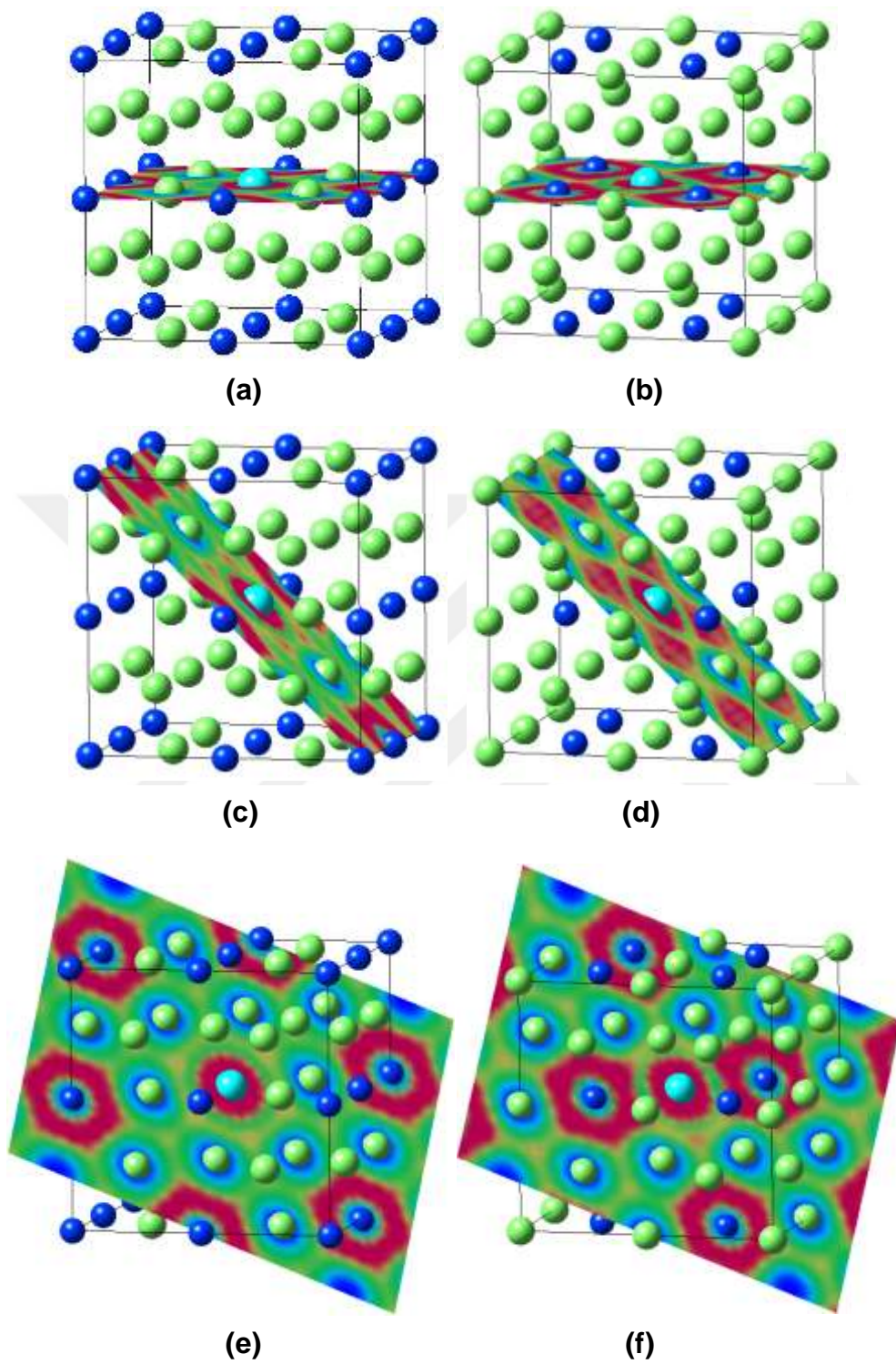


**Figure 4.11** ELF contour plots of centrally located alloying X elements (light blue) at either (a,c,e) Al or (b,d,f) Ni sites of 32 atoms  $2 \times 2 \times 2$  model of  $\text{Ni}_3\text{Al}$  phase for (a,b) (010), (c,d) (110) and (e,f) (111) planes, respectively.

cause moderate ones. Similarly, by the addition of X = Hf, Ru and Ti atoms, very weak covalent bondings are created. However some alloying elements, such as Co and Pt have no any directional accumulation regions around them. For centrally located Co atom, there is a homogeneous green area around it. In case of Pt addition, a continuous (nearly spherical) accumulation region is visible which has no directional character. Therefore, by considering these ELF contour plots, it is possible to suggest that alloying X elements causing directional covalent bondings in the order of Ti < Hf < Ru < Cr < Mo < Ta < W < Re (Re atoms lead to the strongest covalent bondings, while Ti atoms cause the weakest ones) increase strength of Ni<sub>3</sub>Al phase. Secondly, Co and Pt additions seem to have no effect on the strength of this phase. However, these atoms may be attributed to increase ductility of Ni<sub>3</sub>Al intermetallics by creating non-directional (homogeneously distributed or continuous) metallic bondings [98]. ELF contour plots of (110) and (111) planes for alloying X element atoms located at Al or Ni sites of Ni<sub>3</sub>Al phase also confirm that Re addition leads to strength enhancement, while Co addition causes improved ductility of Ni<sub>3</sub>Al phase as illustrated in Figures 4.14-17.

### 4.7.3 Density of States (DOS)

In order to analyse further the interactions between centrally located alloying X elements (either at Al or Ni sites) and their NN Ni(Al) atoms along <110> directions of Ni<sub>3</sub>Al-X systems and correlate electronic structures and energetic states of pure or micro-alloyed Ni<sub>3</sub>Al lattices, partial density of states (pDOS) calculations have been performed where X = Al(Ni), Co, Cr, Hf, Mo, Nb, Pt, Re, Ru, Ta, Ti and W, respectively (Figures 4.18-21). In pDOS diagrams, x axis represents energy values (in eV), whereas y axis indicates the contributions of electron states (i.e. p-states of Al and d-states of Ni/alloying X element atoms) in arbitrary units (a. u.). As it is well known, Al atoms have no d states and Al-p and Ni-d states provide dominant contributions to the total DOSs of Al and Ni atoms [131]. So, in this study, for impurity free Ni<sub>3</sub>Al phase, only Al-p and Ni-d states have been considered and presented. In x axis, the origin refers to Fermi energy level (E<sub>f</sub>). Hence, negative energy values left to

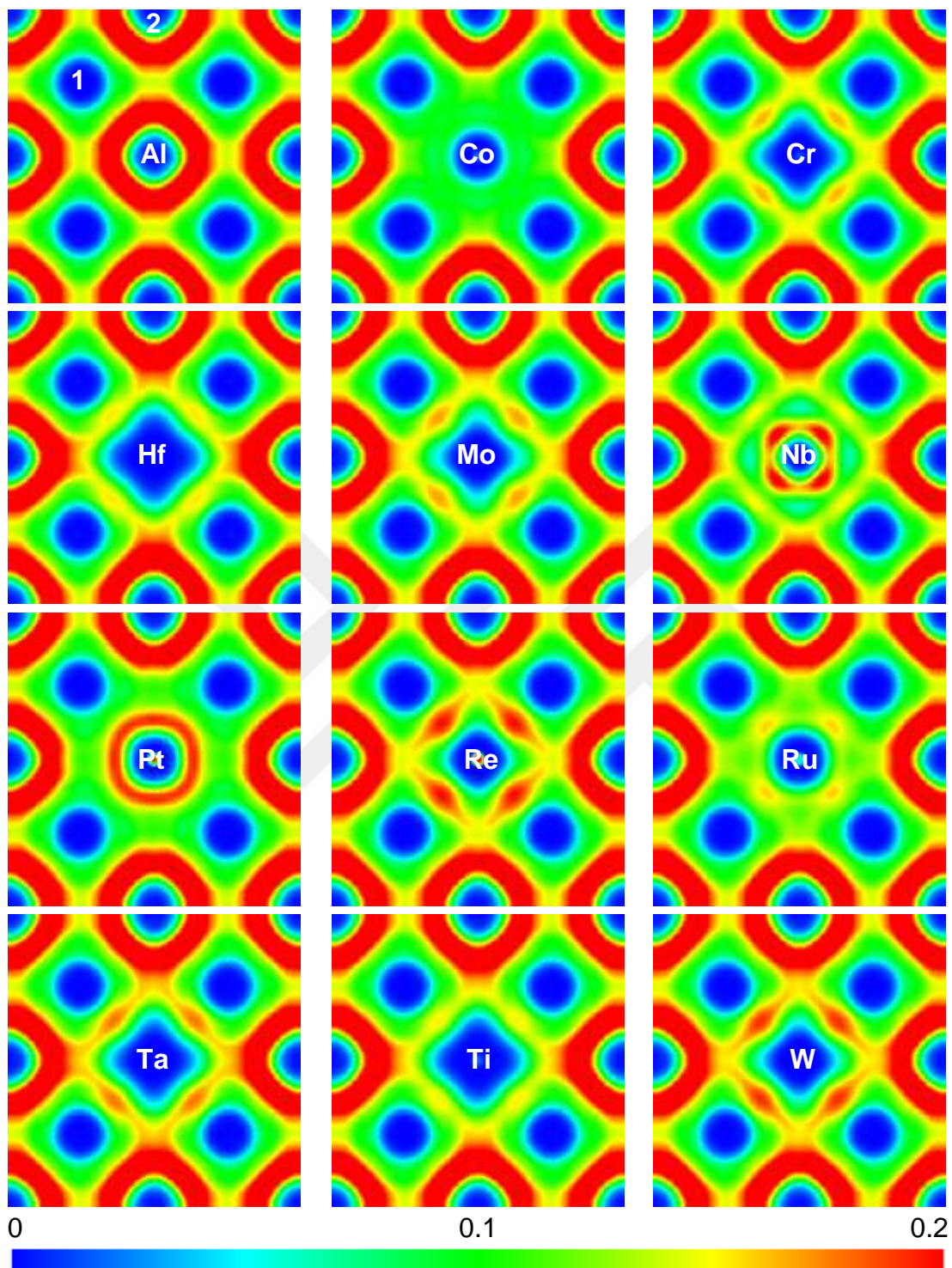


**Figure 4.12** (010) plane ELF contour plots of centrally located alloying X elements at Al sites of  $\text{Ni}_3\text{Al}$  phase where  $X = \text{Al}, \text{Co}, \text{Cr}, \text{Hf}, \text{Mo}, \text{Nb}, \text{Pt}, \text{Re}, \text{Ru}, \text{Ta}, \text{Ti}$  and  $\text{W}$ , respectively (1: NN Ni and 2: NN Al atoms).

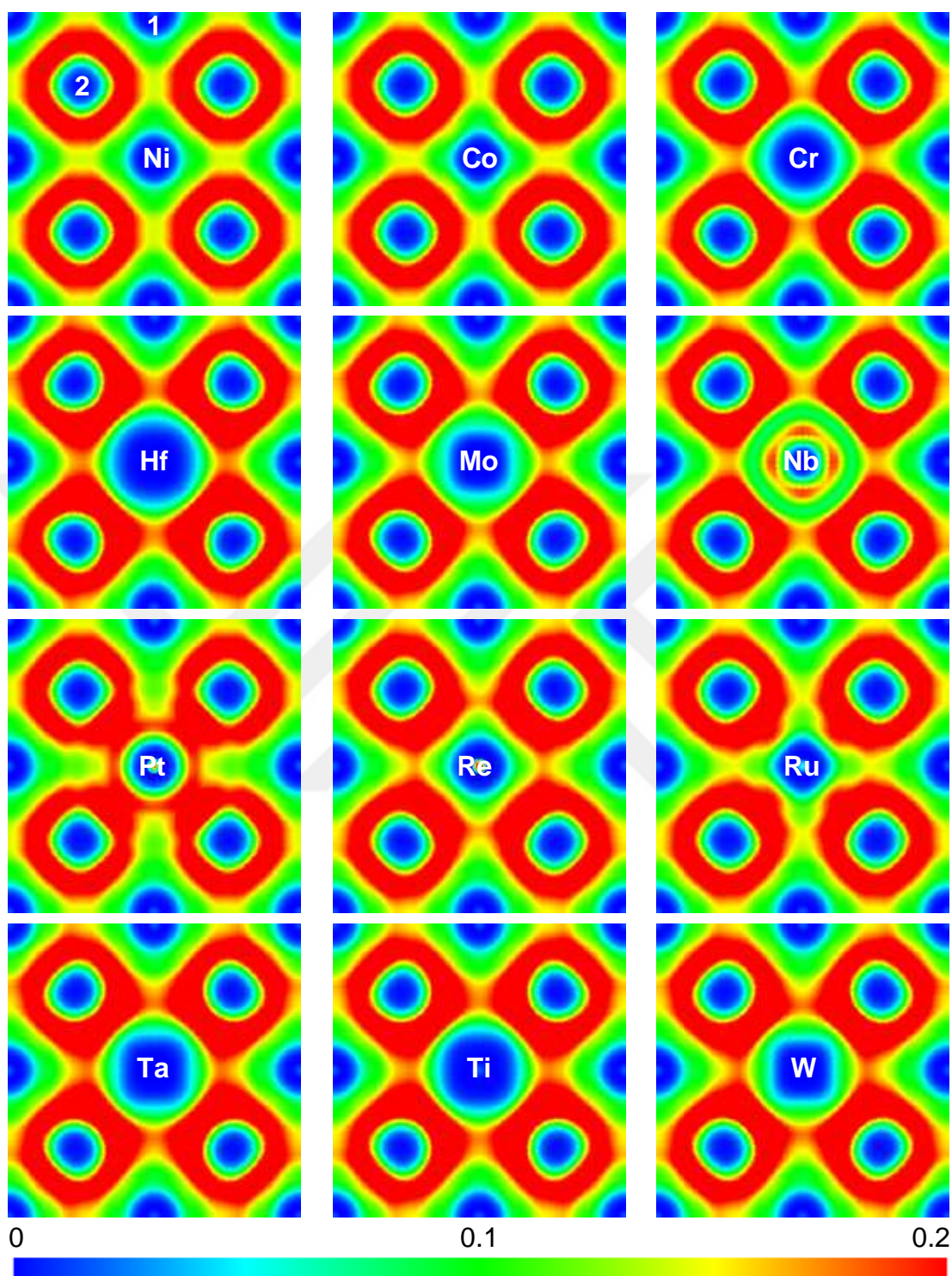


**Figure 4.13** (010) plane ELF contour plots of centrally located alloying X elements at Ni sites of Ni<sub>3</sub>Al phase where X = Ni, Co, Cr, Hf, Mo, Nb, Pt, Re, Ru, Ta, Ti and W, respectively (1: NN Ni and 2: NN Al atoms).

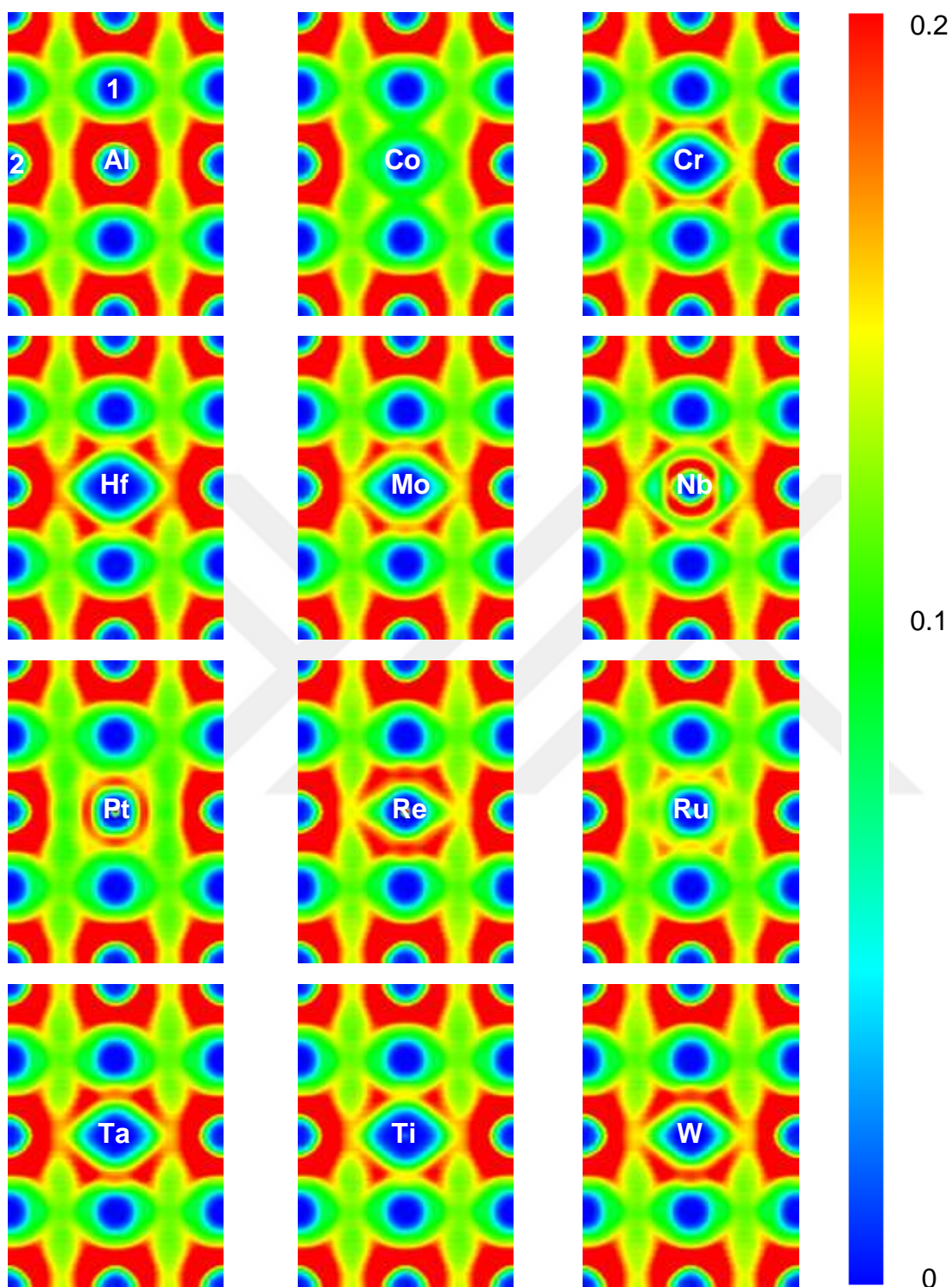


**Figure 4.14** (110) plane ELF contour plots of centrally located alloying X elements at Al sites of Ni<sub>3</sub>Al phase where X = Al, Co, Cr, Hf, Mo, Nb, Pt, Re, Ru, Ta, Ti and W, respectively (1: NN Ni and 2: NN Al atoms).

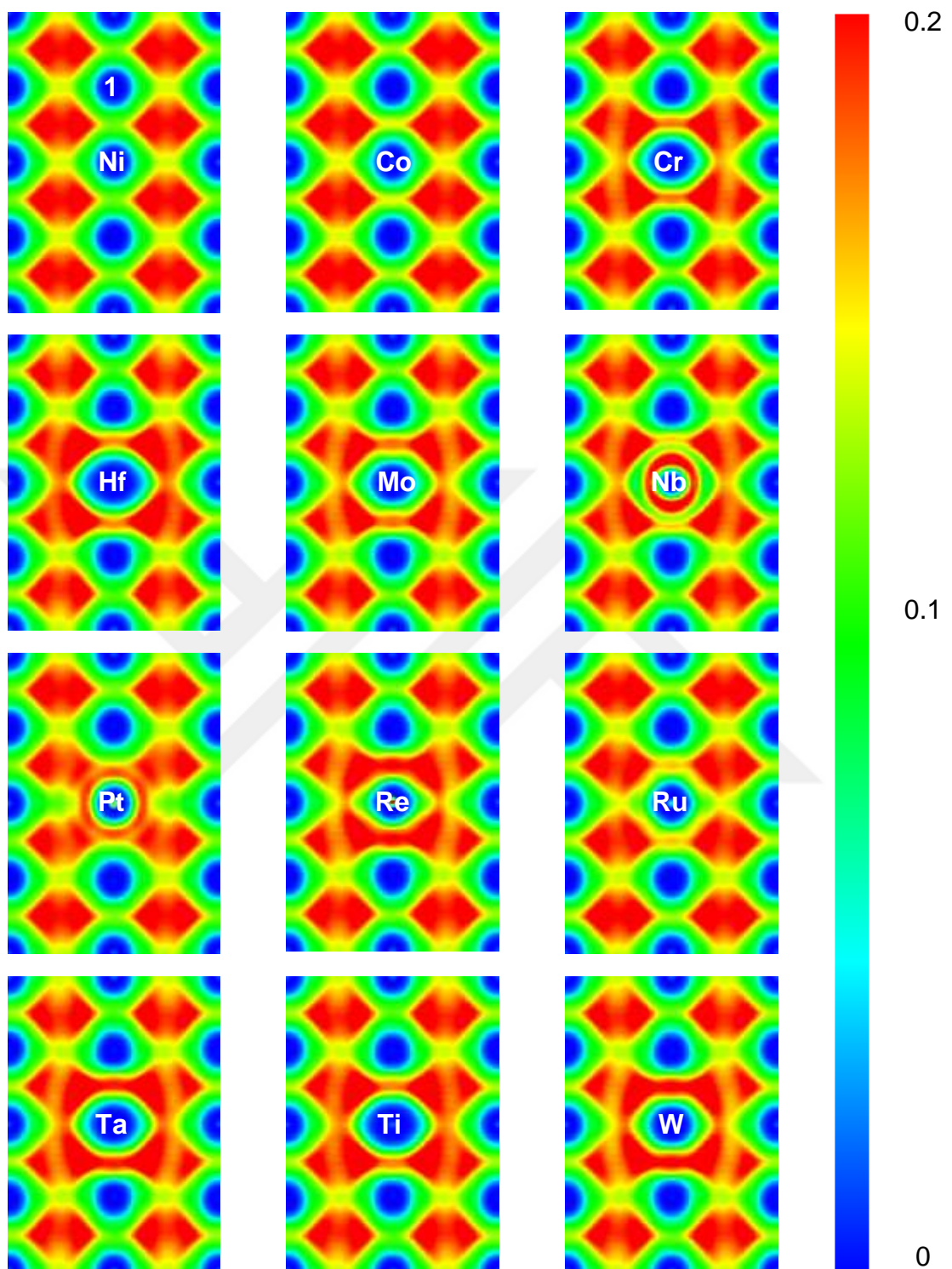


**Figure 4.15** (110) plane ELF contour plots of centrally located alloying X elements at Ni sites of Ni<sub>3</sub>Al phase where X = Ni, Co, Cr, Hf, Mo, Nb, Pt, Re, Ru, Ta, Ti and W, respectively (1: NN Ni atoms).

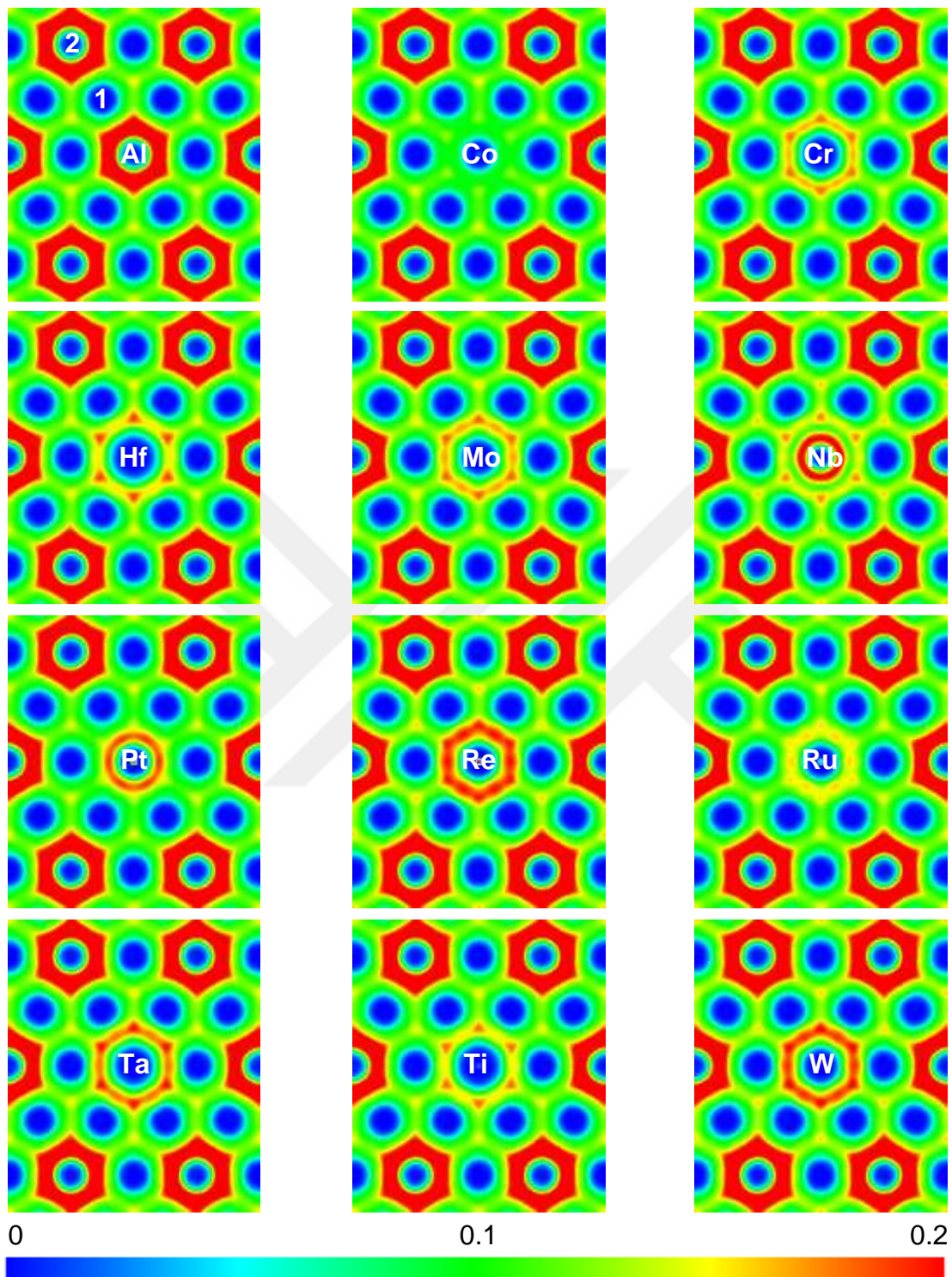


**Figure 4.16** (111) plane ELF contour plots of centrally located alloying X elements at Al sites of  $\text{Ni}_3\text{Al}$  phase where  $X = \text{Al}, \text{Co}, \text{Cr}, \text{Hf}, \text{Mo}, \text{Nb}, \text{Pt}, \text{Re}, \text{Ru}, \text{Ta}, \text{Ti}$  and  $\text{W}$ , respectively (1: NN Ni and 2: NN Al atoms).



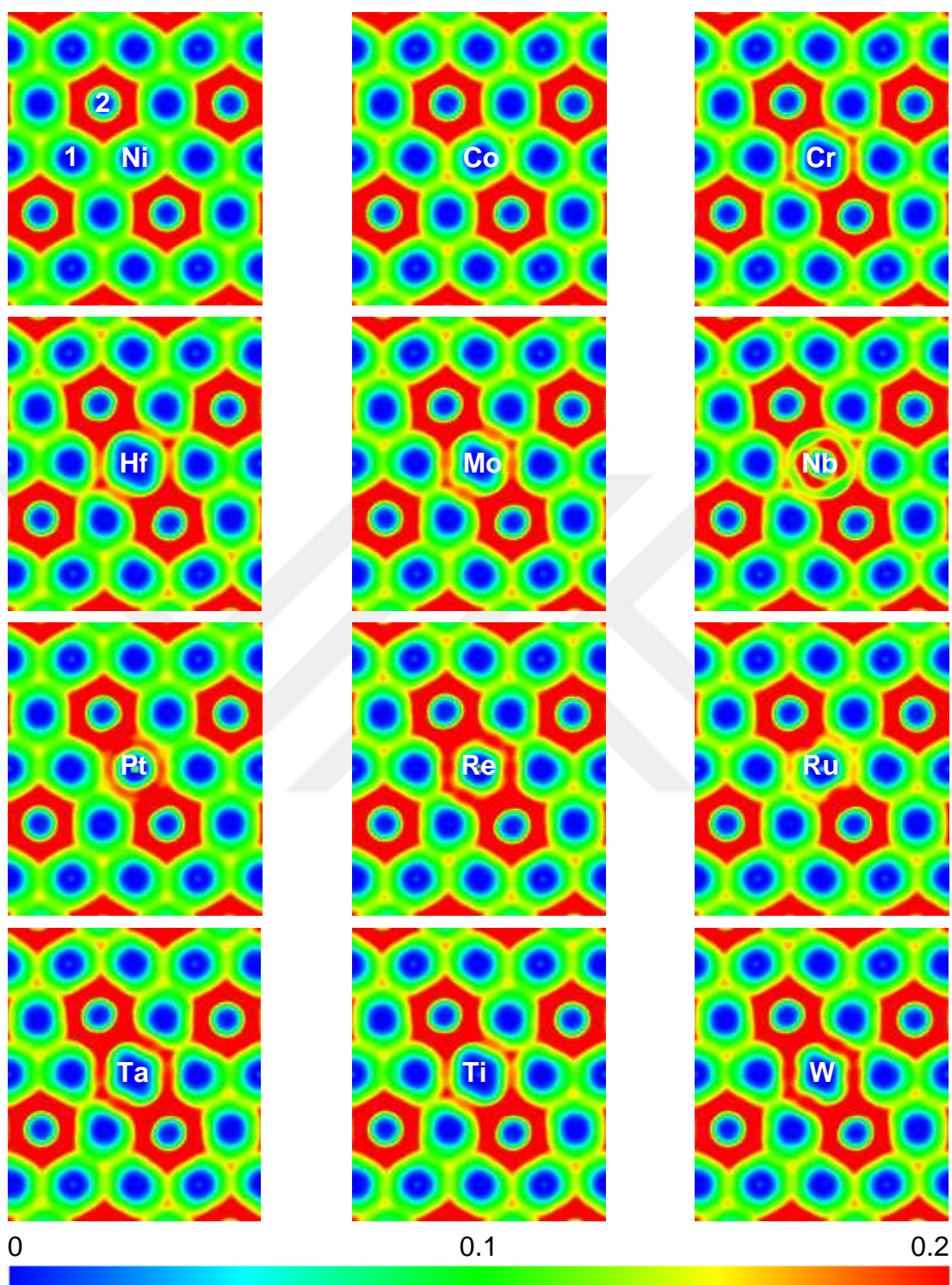


**Figure 4.17** (111) plane ELF contour plots of centrally located alloying X elements at Ni sites of Ni<sub>3</sub>Al phase where X = Ni, Co, Cr, Hf, Mo, Nb, Pt, Re, Ru, Ta, Ti and W, respectively (1: NN Ni and 2: NN Al atoms).

$E_f$  correspond to occupied states, whereas positive energies right to  $E_f$  are the energy values of unoccupied states. Upper part of pDOS diagrams with respect to x axis shows the contributions of spin-up electrons, whereas lower part (which is not shown in Figures 4.18-21) represents the contributions of spin-down electrons, or vice-versa.

One of the most important features of pDOS diagrams determining structural stability is hybridization between Al-p and Ni-d electronic bands [128]. This hybridization forms directional covalent bondings between Al and NN Ni atoms along  $\langle 110 \rangle$  directions as already shown in Figure 4.5. In the first CDD simulation of Figure 4.5, the orange regions between centrally located Al atom and its NN Ni atoms refer to directional bondings along  $\langle 110 \rangle$  directions. In pDOS diagrams, this hybridization is indicated by Al-p/Ni-d peak overlap (Figure 4.18) [100,128]. According to Figure 4.18(a), hybridization between Al-p and Ni-d states is shown by a sharp bonding peak and an anti-bonding peak located near -3 and 1.2 eV, which has also been confirmed by the work of [128]. Other weaker bonding peaks of this system are approximately located at -3.75, -3.2, -2.75, -2.5, -2 and -1 eV, respectively. Another feature of the electronic structure for pure  $Ni_3Al$  system is “a valley” located at about 0.5 eV above the Fermi energy which separates the p-d bonding and anti-bonding states [128]. As shown in Figures 4.18-19, for Co addition, more bonding peaks are visible approximately located at -3.85, -3.65, -3.15, -2.8, -2.25, -2.1, -2, -1.4, -1.1, -0.75 and -0.35 eV. However, there is no any clear anti-bonding peak. In case of Cr addition, bonding peaks and anti-bonding peaks (located at -3.4, -3, -2.75, -1.5, -1, 0.45 and 0.65 eV, respectively) are separated by a narrow pseudogap (valley) which is very close to Fermi energy. For Hf addition, approximate energy values of bonding and anti-bonding peaks are -3.4, -2.25, -1.45, 2.65, 3.1 and 3.6 eV separated by a pseudogap minimum located at nearly 0.5 eV. For Mo addition, these values are approximately -3.7, -3.5, -3.25, -1, 0.55, 0.65, 0.75 and 0.9 eV separated by a narrow valley again. For Nb addition (only the semi-core 4p electrons of this element were explicitly treated as valence as previously mentioned), there are a few peaks nearly located at -3.5, -2.85 and 1.1 eV separated by a valley at about 0.5 eV. For Pt addition, peak distributions are very close to the ones observed in Co addition. In this case, there is no any anti-

bonding peak and bonding peaks are closely located at -3.2, -2.5, -2, -1.75, -1.1, -0.75 and -0.25 eV. However, for Re addition, so many overlapping of bonding and anti-bonding peaks are visible at -4.75, -4, -3.65, -3, -2.5, -1.75, -1.5, -0.5, 0.5, 0.75 and 1.2 eV, respectively. This behaviour between Re-d and Ni-d states imply that there is a strong d-d hybridization which leads to strong covalent bondings between these atoms along  $\langle 110 \rangle$  directions. In case of Ru addition, besides bonding peaks (at -4.6, -4, -3.65, -3, -2.6, -1.85, -1.65, -1, -0.6 eV) there is a weak anti-bonding peak at 0.2 eV. However, these peaks are not separated by a pseudogap valley similar to Co and Pt additions. For Ta addition approximate energy values of bonding and anti-bonding peaks are -3.5, -2.3, -1.5, 1.1 and 2.3 eV separated by a pseudogap minimum located at nearly 0.5 eV. In case of Ti addition, bonding peaks and anti-bonding peaks (located at -3.35, -2.15, -1.5 and 1.1 eV, respectively) are separated by a pseudogap valley which is right to the Fermi energy. Lastly, for W addition, so many overlapping of bonding and anti-bonding peaks (similar to Re addition) are present at -4.5, -3.5, -2.9, -2.3, -1.6, 0.75, 1, 1.2, 1.3 and 1.8 eV, respectively implying that there is a strong W-d/Ni-d hybridization along  $\langle 110 \rangle$  directions which leads to strong covalent bondings.

The stability of a particular system depends on the position of the Fermi energy level in the pDOS plots. Systems are considered to be more stable if the  $E_f$  falls in the pseudogap which separates the bonding states from the anti-bonding states (i.e. stable structures always have low  $N(E_f)$ ) [132]. When the Fermi energy level lies left to the pseudogap minimum, the bonding states become completely occupied. However, when the Fermi energy level lies right to the pseudogap minimum, the bonding states can be considered as incompletely occupied [133]. As it is evident in Figures 4.18-19, for  $X = \text{Cr, Hf, Mo, Nb, Re, Ta, Ti}$  and  $\text{W}$  atoms  $N(E_f)$  values of X-d curves become very low. However, for d states of  $X = \text{Co, Pt}$  and  $\text{Ru}$  atoms,  $N(E_f)$  values are not low. This interesting feature of X-d states at  $E_f$  indicates that when alloying X elements occupy Al sites,  $\text{Ni}_3\text{Al-X}$  phases become stable for the former alloying X elements, whereas they become unstable for the latter alloying X elements. It should be noted that these results have already been confirmed by previous CDD contour plots. Because, strong X-d/Ni-d hybridizations between the former alloying X elements

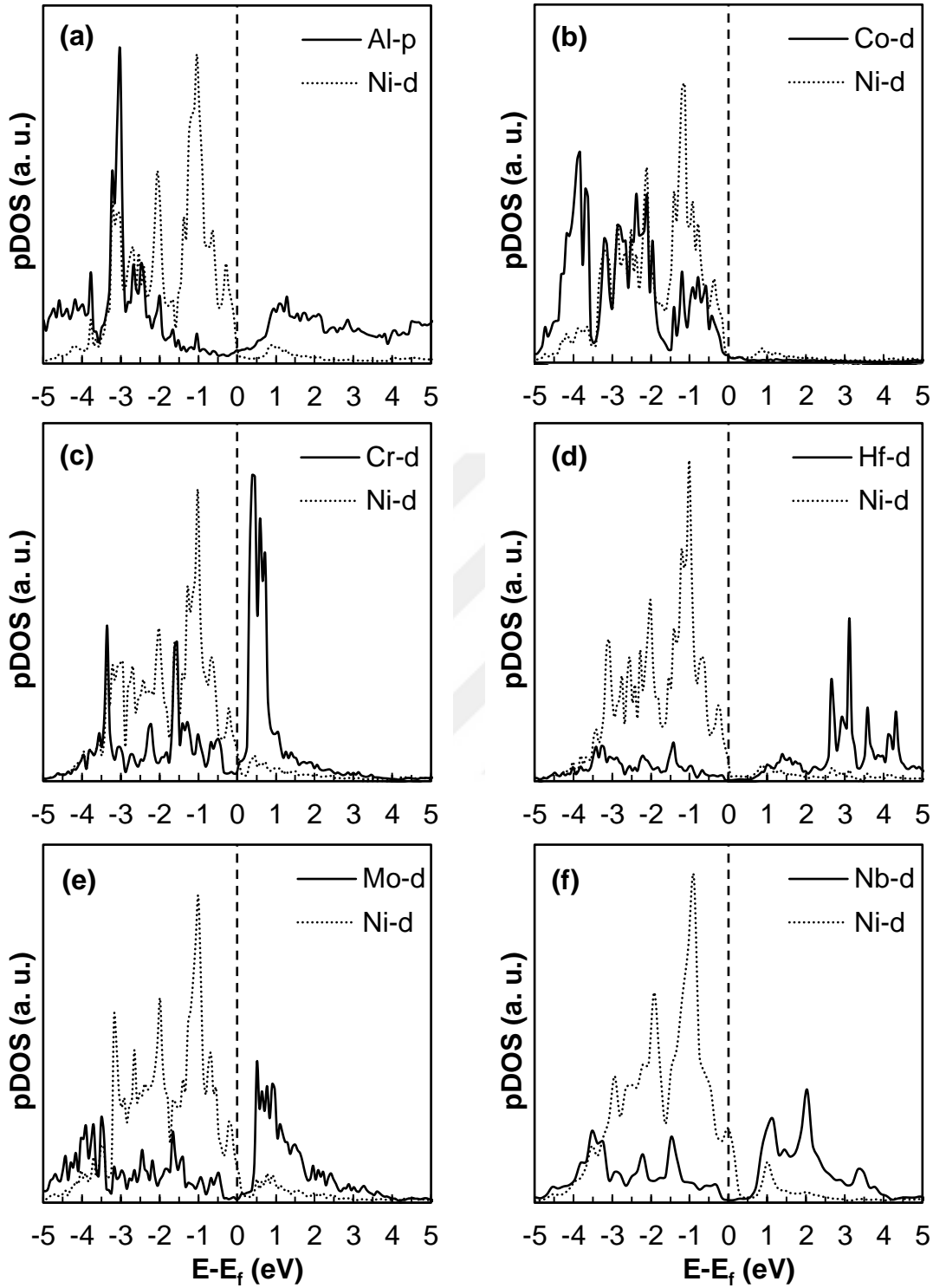


**Figure 4.18** pDOS diagrams of (a) Al-p/Ni-d and (b-f) X-d/Ni-d states showing p-d and d-d hybridizations between centrally located Al(X) and their NN Ni atoms along  $\langle 110 \rangle$  directions where X = Co, Cr, Hf, Mo and Nb, respectively.

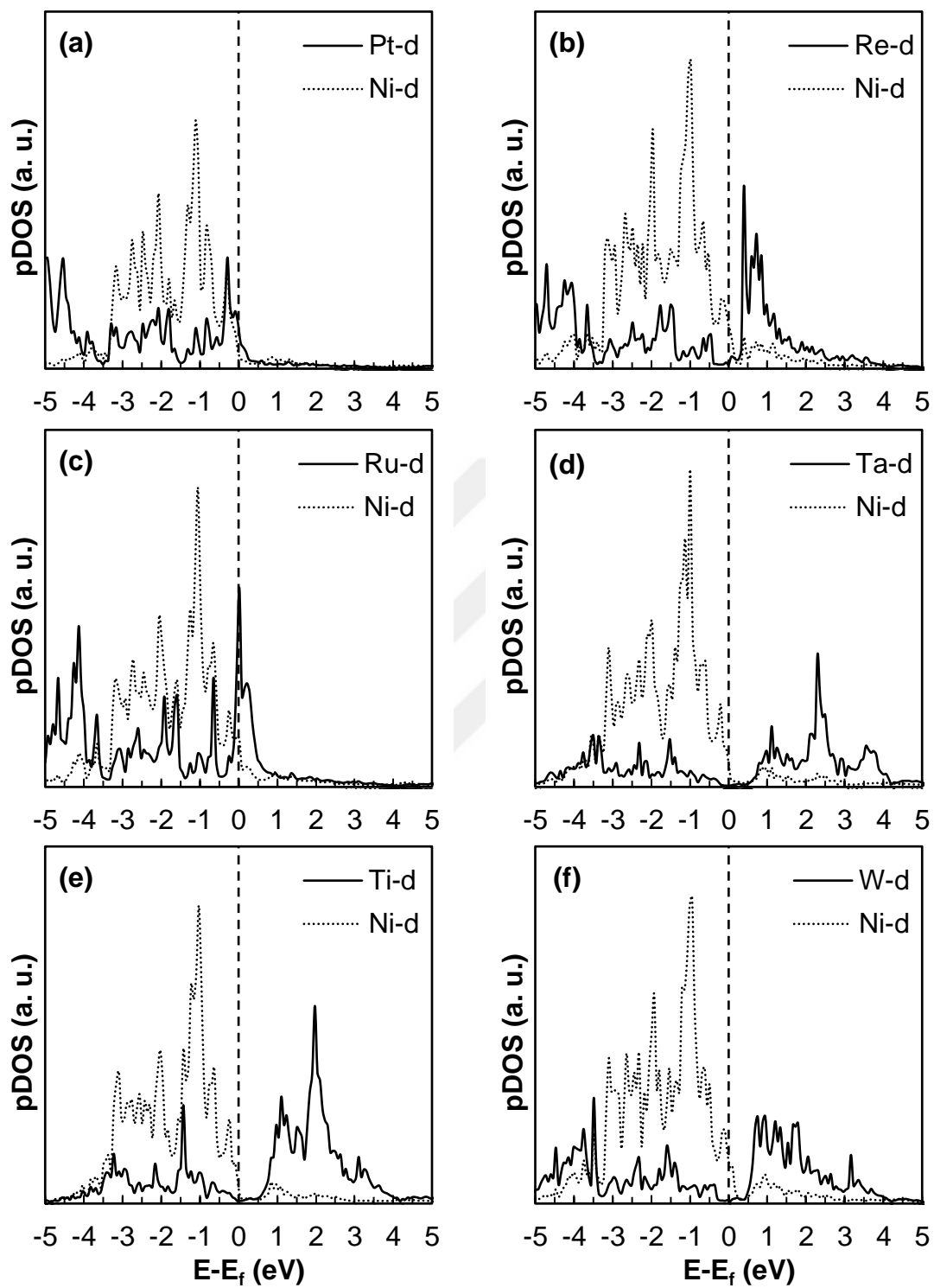


**Figure 4.19** pDOS diagrams of (a-f) X-d/Ni-d states showing d-d hybridizations between centrally located X and their NN Ni atoms along  $\langle 110 \rangle$  directions where X = Pt, Re, Ru, Ta, Ti and W, respectively.

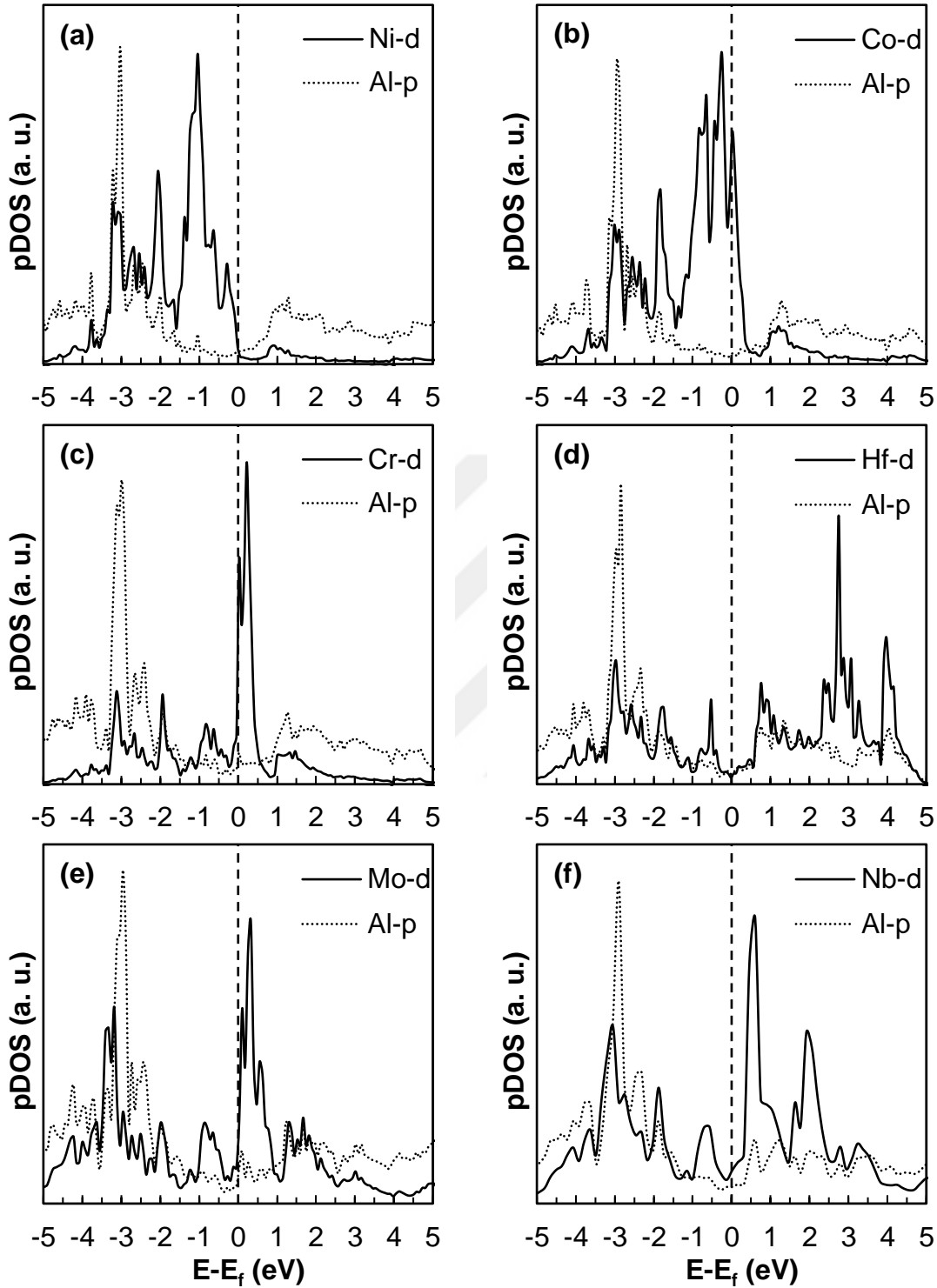


**Figure 4.20** pDOS diagrams of (a) Ni-d/Al-p and (b-f) X-d/Al-p states showing d-p hybridizations between centrally located Ni(X) and their NN Al atoms along  $\langle 110 \rangle$  directions where X = Co, Cr, Hf, Mo and Nb, respectively.

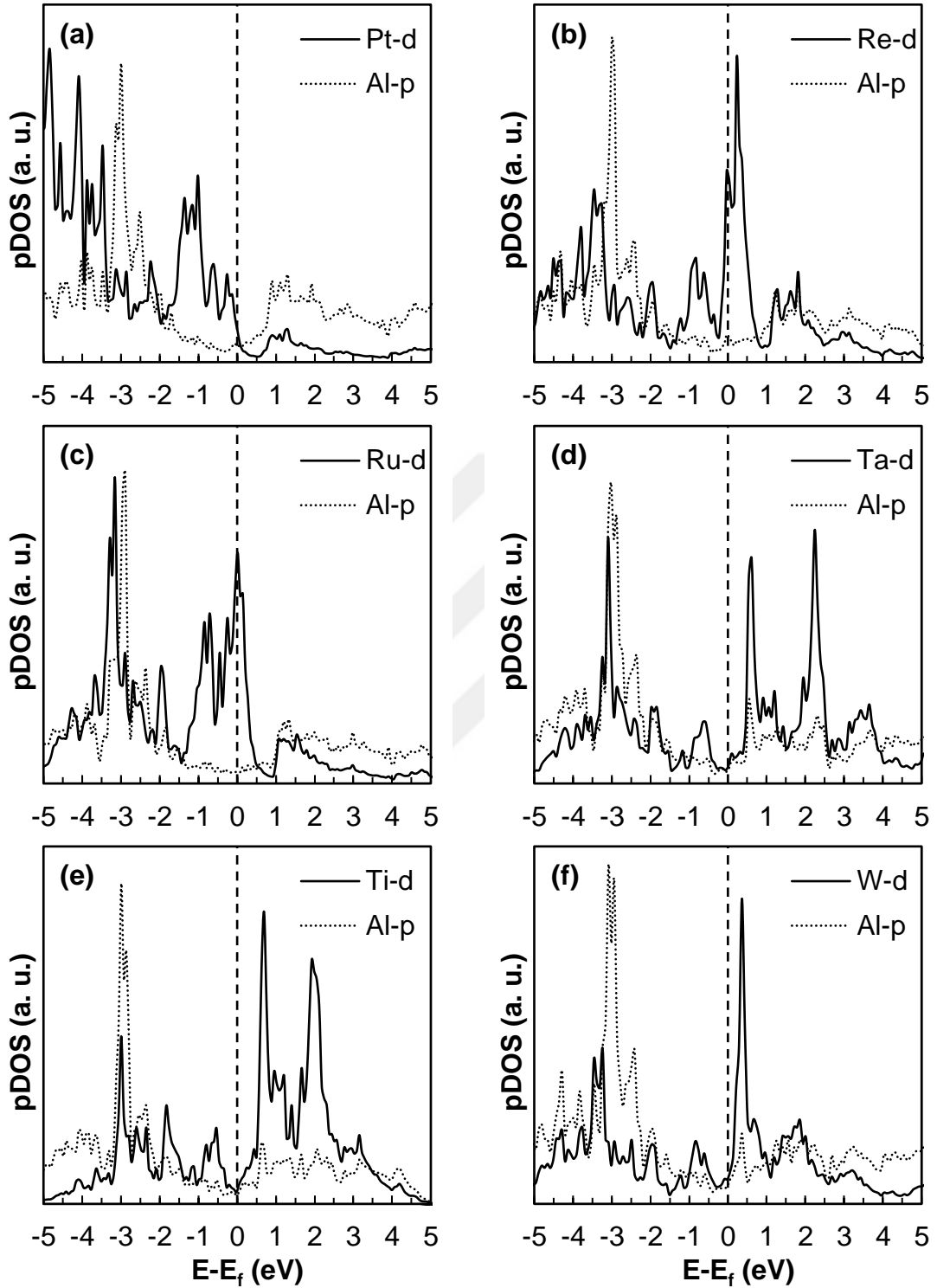


**Figure 4.21** pDOS diagrams of (a-f) X-d/Al-p states showing d-p hybridizations between centrally located X and their NN Al atoms along  $\langle 110 \rangle$  directions where X = Pt, Re, Ru, Ta, Ti and W, respectively.

and their NN Ni atoms along  $\langle 110 \rangle$  directions lead to strong directional covalent bondings which make the  $\text{Ni}_3\text{Al-X}$  phases stable. On the other hand, for the latter alloying X elements, due to lack of anti-bonding peaks and/or some certain amount of  $N(E_f)$  values (which are not low), there is no any hybridization and covalent bondings between these alloying element atoms and their NN Ni atoms. Hence, instead of covalent bondings, metallic bondings may exist between these atoms.

In order to comprehend further the stability of  $\text{Ni}_3\text{Al-X}$  phases, pDOS contour plots of d states of alloying X element atoms occupying Ni sites and p states of their NN Al atoms are given in Figures 4.20-21. As shown in these contour plots, for  $X = \text{Cr}, \text{Hf}^*, \text{Mo}, \text{Nb}, \text{Re}, \text{Ta}^*, \text{Ti}^*$  and  $\text{W}^*$  atoms, there are bonding and anti-bonding peaks but  $N(E_f)$  values are very high (\*: with respect to Figures 4.18-19). However, for  $X = \text{Pt}$  atoms,  $N(E_f)$  is very low. These results, therefore, confirm that most of the afore mentioned alloying X elements preferentially occupy Al sites of  $\text{Ni}_3\text{Al}$  phase, whereas Pt atoms tend to substitute for Ni sites. Interestingly, by looking at high  $N(E_f)$  values of d states of  $X = \text{Co}$  and  $\text{Ru}$  atoms occupying Ni sites of  $\text{Ni}_3\text{Al}$  phase, it is possible to suggest that these high values also lead to unstable structures. Namely, these alloying elements would occupy both sites of  $\text{Ni}_3\text{Al}$  phase as previously determined.

#### 4.8 Conclusions

In conclusion, due to their strong d-d hybridizations with NN Ni atoms along  $\langle 110 \rangle$  directions of  $\text{Ni}_3\text{Al-X}$  phases (i.e. strong covalent bondings), alloying X elements, such as Cr, Hf, Mo, Nb, Re, Ta, Ti and W enhance strength of nickel-based superalloys. The strength enhancement can be understood from the accumulation regions appear in the contour plots of CDD and ELF simulations and overlapping phenomena in pDOS plots. On the other hand, alloying elements, such as Co, Pt and Ru may improve ductility of nickel-based superalloys due to lack of directional bondings. Interestingly, alloying X elements increasing strength preferentially occupy Al sublattice sites of  $\text{Ni}_3\text{Al}$  intermetallics, whereas alloying X elements most probably improving ductility tend to substitute for Ni sites or their site preferences are composition dependent,



namely, they may occupy by Al and Ni sites. Therefore, it is important to note that these results are consistent with the works of Ochiai et al. [84] and Rawlings and Statonbevan [85] which claim that yield strength can be increased by alloying elements occupying Al sublattice sites of  $\text{Ni}_3\text{Al}$  phase instead of Ni ones.





## CHAPTER 5

### PRODUCTION, CHARACTERIZATION AND MICROSTRUCTURAL & MECHANICAL DEVELOPMENT OF $\text{Ni}_{80}\text{Al}_{20}$ AND $\text{Ni}_{80}\text{Al}_{15}\text{X}_5$ ALLOY SYSTEMS

#### 5.1 Introduction

In this chapter, previous theoretical findings, such as site occupancy preferences of alloying X elements (via SRO parameter calculations and first-principles calculations) and effects of these alloying elements on the bonding characteristics of  $\gamma'$ - $\text{Ni}_3\text{Al}$  precipitates (via CDD, ELF and DOS simulation methods) and mechanical properties of nickel-based superalloys have been aimed to be confirmed by experimental studies as well. For this purpose, binary  $\text{Ni}_{80}\text{Al}_{20}$  and ternary  $\text{Ni}_{80}\text{Al}_{15}\text{X}_5$  alloy systems where  $\text{X} = \text{Co}, \text{Cr}, \text{Hf}, \text{Mo}, \text{Nb}, \text{Ta}, \text{Ti}$  and  $\text{W}$ , respectively, have been produced, characterized and microstructural and mechanical development of these alloy systems with increasing aging time have been investigated. Effects of type of alloying element additions and some variations in heat treatment procedures on the microstructural characteristics and mechanical properties of the related alloys have been discussed, correlated and it has been concluded that experimental results coincide well with the literature and theoretical results of this thesis.

#### 5.2 Experimental Procedure

##### 5.2.1 Raw Materials

$\text{Ni}_{80}\text{Al}_{15}\text{X}_5$  samples (where  $\text{X} = \text{Al}, \text{Co}, \text{Cr}, \text{Hf}, \text{Mo}, \text{Nb}, \text{Ta}, \text{Ti}$  and  $\text{W}$ , respectively) were produced by mixing appropriate amount of high purity alloying elements

procured by Alfa Aesar. The high purities of the alloying X elements are given in Table 5.1.

**Table 5.1** Purities of alloying X elements (wt.%).

Alloying X elements	Purity (wt.%)
Ni	99.95
Al	99.90
Co	99.90
Cr	99.20
Hf	99.70
Mo	99.95
Nb	99.90
Ta	99.95
Ti	99.99
W	99.95

### 5.2.2 Production of the Samples

Ni<sub>80</sub>Al<sub>15</sub>X<sub>5</sub> samples were melted and casted into cylindrical ingots via arc melting and suction casting techniques, respectively.

#### 5.2.2.1 Arc Melting

Ni<sub>80</sub>Al<sub>15</sub>X<sub>5</sub> samples were produced by using a non-consumable tungsten electrode on a water-cooled copper tray in arc melting unit which is shown in Figure 5.1. In order to dilute oxygen, firstly, arc melting chamber was vacuumed to  $3.8 \times 10^{-2}$  mbar level by using rotary pump and then vacuum level was increased up to  $1.1 \times 10^{-4}$  mbar level by activating diffusion pump. In addition, a piece of bulk Zr was put in the chamber to reduce oxygen further. Then constituent alloying elements were melted in oxygen-free/inert argon gas environment. In order to achieve homogeneity, samples were remelted three times. After melting processes, the weight loss was negligible.



**Figure 5.1** Edmund Bühler arc melting unit used for the production of samples.

### 5.2.2.2 Suction Casting

After arc melting processes,  $\text{Ni}_{80}\text{Al}_{15}\text{X}_5$  samples were melted one more time and casted into cylindrical rods (with diameter of 3 mm) by applying suction casting technique which enables samples to be exposed to the same cooling rate (Figure 5.2). Furthermore, thanks to this technique, homogeneous rod-like samples were easily cut along the cross sectional directions to see the dendritic as cast microstructures clearly.

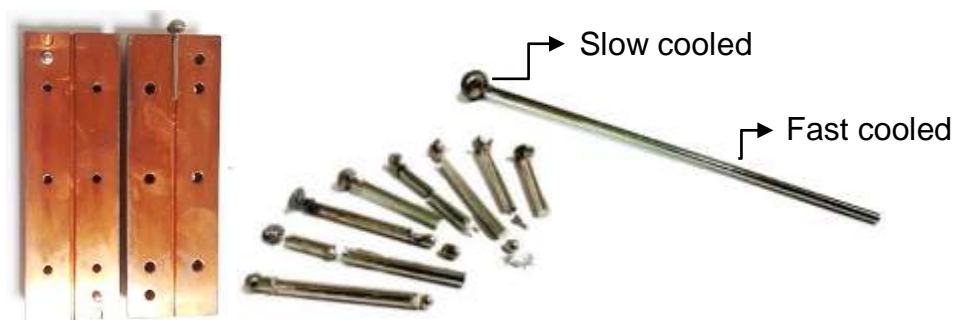


**Figure 5.2** Copper mold and cylindrical rods produced by arc melting and suction casting techniques.

### 5.2.3 ICP-MS Measurements

As cast Ni<sub>80</sub>Al<sub>15</sub>X<sub>5</sub> samples were treated to inductively coupled plasma – mass spectroscopy (ICP-MS) technique to verify the compositions of alloy systems. Comparisons are given in Table 5.2.

**Table 5.2** Verification of alloy compositions by ICP-MS technique.

Systems (as cast)	Nominal compositions (at.%)			ICP-MS (at.%)		
	Ni	Al	X	Ni	Al	X
Ni <sub>80</sub> Al <sub>20</sub>	80	20	-	79.55	20.45	-
Ni <sub>80</sub> Al <sub>15</sub> Co <sub>5</sub>	80	15	5	79.72	15.32	4.96
Ni <sub>80</sub> Al <sub>15</sub> Cr <sub>5</sub>	80	15	5	80.40	14.84	4.76
Ni <sub>80</sub> Al <sub>15</sub> Hf <sub>5</sub>	80	15	5	80.45	14.76	4.79
Ni <sub>80</sub> Al <sub>15</sub> Mo <sub>5</sub>	80	15	5	80.07	15.11	4.82
Ni <sub>80</sub> Al <sub>15</sub> Nb <sub>5</sub>	80	15	5	80.20	15.21	4.59
Ni <sub>80</sub> Al <sub>15</sub> Ta <sub>5</sub>	80	15	5	80.65	14.51	4.84
Ni <sub>80</sub> Al <sub>15</sub> Ti <sub>5</sub>	80	15	5	80.48	14.67	4.85
Ni <sub>80</sub> Al <sub>15</sub> W <sub>5</sub>	80	15	5	80.64	14.47	4.89

### 5.2.4 Heat Treatment

Subsequent to melting and casting, as cast samples were exposed to a series of heat treatment steps to reduce segregation of some alloying elements, adjust  $\gamma'$  precipitate size (primary, secondary and tertiary) and modify dendritic as cast microstructures into grains [1,2]. For this purpose, as cast Ni<sub>80</sub>Al<sub>15</sub>X<sub>5</sub> samples were heat treated according to Table 5.3 (homogenization at 1250 °C for 24 hours, partial solutionizing at 1150 °C for 3 hours, primary aging at 800 °C for 3 hr and aging at 800 °C for 4, 16, 64 and 256 hr, respectively). All samples were furnace cooled to partial-solution heat treatment or

primary aging temperatures after homogenization heat treatment; ice-water quenched to RT after partial solutionizing or primary aging and air cooled to RT after aging heat treatments. These different heat treatment procedures were applied under air/oxygen environment instead of argon (due to heat treatment set-up of argon gas environment which prevents effective ice-water quenching). Oxide layers occurring on the samples were grinded and polished in the subsequent metallographic sample preparation steps.

## **5.2.5 Characterization Techniques**

### **5.2.5.1 X-ray Diffraction (XRD)**

Phase analyses of as cast and heat treated  $\text{Ni}_{80}\text{Al}_{15}\text{X}_5$  samples were performed by X-ray diffraction method using Bruker D8 Advance with  $\text{Cu-K}\alpha$  radiation ( $\lambda = 1.5418 \text{ \AA}$ ) for the angle range of  $2\theta = 20^\circ - 130^\circ$  with a scanning rate of  $2^\circ/\text{minutes}$ .

### **5.2.5.2 Differential Scanning Calorimetry (DSC)**

In order to determine the effects of each X alloying element on the shift of phase transformation temperatures, thermal analysis measurements of as cast  $\text{Ni}_{80}\text{Al}_{15}\text{X}_5$  samples were done by using Setaram Setsys-16/18 differential scanning calorimeter (DSC) (Figure 5.3). The samples of 15-30 mg weight were heated up in alumina crucibles under argon atmosphere from RT to  $1450^\circ\text{C}$  at a constant heating rate of  $20^\circ\text{C}/\text{minutes}$ . After waiting for a while at this temperature, samples were cooled to RT at a constant cooling rate of  $20^\circ\text{C}/\text{minutes}$ .

### **5.2.5.3 Field Emission Scanning Electron Microscopy (FESEM)**

Microstructural characteristics of as cast and heat treated  $\text{Ni}_{80}\text{Al}_{15}\text{X}_5$  samples were examined by using Fei Nova Nano 430 field emission gun model of scanning electron microscope (FESEM). Before that, samples were metallographically prepared; sliced into small cylindrical rods (3 mm diameter and 2 mm height) by sharp cutter, ground

**Table 5.3** A series of heat treatment steps applied to Ni<sub>80</sub>Al<sub>15</sub>X<sub>5</sub> alloy systems (X = Al, Co, Cr, Hf, Mo, Nb, Ta, Ti and W).

Alloy systems	Sample groups	Homogenization		Partial-solutionizing		Primary aging		Aging	
		1250 °C, 24 hr		1150 °C, 3 hr		800 °C, 3 hr		800 °C, 4-16-64-256 hr	
Ni <sub>80</sub> Al <sub>20</sub>	1			x					x
	2		x						x
	3					x			x
	4		x			x			x
Ni <sub>80</sub> Al <sub>15</sub> Co <sub>5</sub>	1			x					x
	2		x						x
Ni <sub>80</sub> Al <sub>15</sub> Cr <sub>5</sub>	1			x					x
	2		x			x			x
Ni <sub>80</sub> Al <sub>15</sub> Hf <sub>5</sub>	1			x					x
	2		x						x
Ni <sub>80</sub> Al <sub>15</sub> Mo <sub>5</sub>	1			x					x
	2		x						x
Ni <sub>80</sub> Al <sub>15</sub> Nb <sub>5</sub>	1			x					x
	2		x						x
Ni <sub>80</sub> Al <sub>15</sub> Ta <sub>5</sub>	1			x					x
	2		x						x
Ni <sub>80</sub> Al <sub>15</sub> Ti <sub>5</sub>	1			x					x
	2		x						x
Ni <sub>80</sub> Al <sub>15</sub> W <sub>5</sub>	1			x					x
	2		x						x



up to 2000 grit, polished with water-based polycrystalline diamond suspension up to 1  $\mu\text{m}$  and etched in the solution of 0.1 mg  $\text{K}_2\text{S}_2\text{O}_5$  + 10 mL HCl and 10 mL distilled water for 10-45 seconds.  $\text{Ni}_{80}\text{Al}_{15}\text{Mo}_5$  and  $\text{Ni}_{80}\text{Al}_{15}\text{W}_5$  samples were etched by using Marble's reagent for 2-3 seconds. Compositions of the samples and each constituent phase were verified through energy dispersive spectroscopy (EDS) method.



**Figure 5.3** Setaram Setsys-16/18 DSC used for thermal analysis measurements.

#### **5.2.5.4 Micro-hardness Measurements**

Vickers micro-hardness measurements were performed on as cast and heat treated  $\text{Ni}_{80}\text{Al}_{15}\text{X}_5$  samples by using a Shimadzu Micro Hardness Tester under a load of 0.5 kg (4.903 N). The average hardness values were calculated by considering ten measurements on each sample.

### **5.3 Characterization of $\text{Ni}_{80}\text{Al}_{20}$ Alloys**

After production of the samples, phase, thermal, microstructural and mechanical properties of binary  $\text{Ni}_{80}\text{Al}_{20}$  alloys have been characterized and discussed in the following parts.

### 5.3.1 Phase Analysis

Phase analyses of binary as cast (fast and slow cooled)  $\text{Ni}_{80}\text{Al}_{20}$  alloys have been carried out by XRD technique. Figure 5.4 shows Miller indices of the constituent phases ( $\gamma$  and  $\gamma'$ ) in white and black spheres, respectively. As shown in Figure 5.4, white and black sphere pairs (denote to (111), (200), (220), (311), (222) and (400) fundamental peaks) confirm the existence of FCC-like  $\gamma$  and  $\gamma'$  phases, while single black spheres (refer to (100), (110), (210) and (211) super-structure peaks of  $L1_2$ -type ordered  $\gamma'$  precipitates) validate the existence of  $\gamma'$  precipitates within two phase microstructures of  $\text{Ni}_{80}\text{Al}_{20}$  alloys.

When fast cooled as cast samples are heat treated according to Table 5.3, following XRD patterns have been obtained, Figures 5.5-8. Figure 5.5 shows the XRD patterns of binary as cast (fast cooled)  $\text{Ni}_{80}\text{Al}_{20}$  alloys partially-solutionized at 1150 °C for 3 hr, ice-water quenched to RT and subsequently aged at 800 °C for different aging times of 4, 16, 64 and 256 hr and air cooled to RT, respectively. Secondly, in Figure 5.6, XRD patterns of the same heat treated  $\text{Ni}_{80}\text{Al}_{20}$  alloys (exceptionally homogenized at 1250 °C for 24 hr before partial solution heat treatment) are given. Next, phase analyses of binary  $\text{Ni}_{80}\text{Al}_{20}$  alloys are demonstrated in Figure 5.7 which are first primarily aged at 800 °C for 3 hr, ice-water quenched to RT and subsequently aged at 800 °C for different aging times following the order of 4, 16, 64 and 256 hr and air cooled to RT, respectively. Lastly, Figure 5.8 indicates the XRD patterns of  $\text{Ni}_{80}\text{Al}_{20}$  alloys homogenized at 1250 °C for 24 hr and primarily aged at 800 °C for 3 hr, ice-water quenched to RT and subsequently aged at 800 °C starting from 4 hr to 256 hr, respectively. It should be noted that fundamental peaks are composed of two individual peaks corresponding to  $\gamma$  and  $\gamma'$  phases. Since the volume fraction of  $\gamma$  matrix phase within the microstructures is very small and lattice parameters of  $\gamma$  and  $\gamma'$  phases are very close to each other, overlapping problem occurs in the fundamental peaks. In order to increase resolution of XRD peaks and eliminate overlapping problem, XRD scanning rate has been reduced from 2°/minutes to 0.01°/minutes. However, fundamental peaks refer to  $\gamma$  and  $\gamma'$  phases could not be separated from each other.

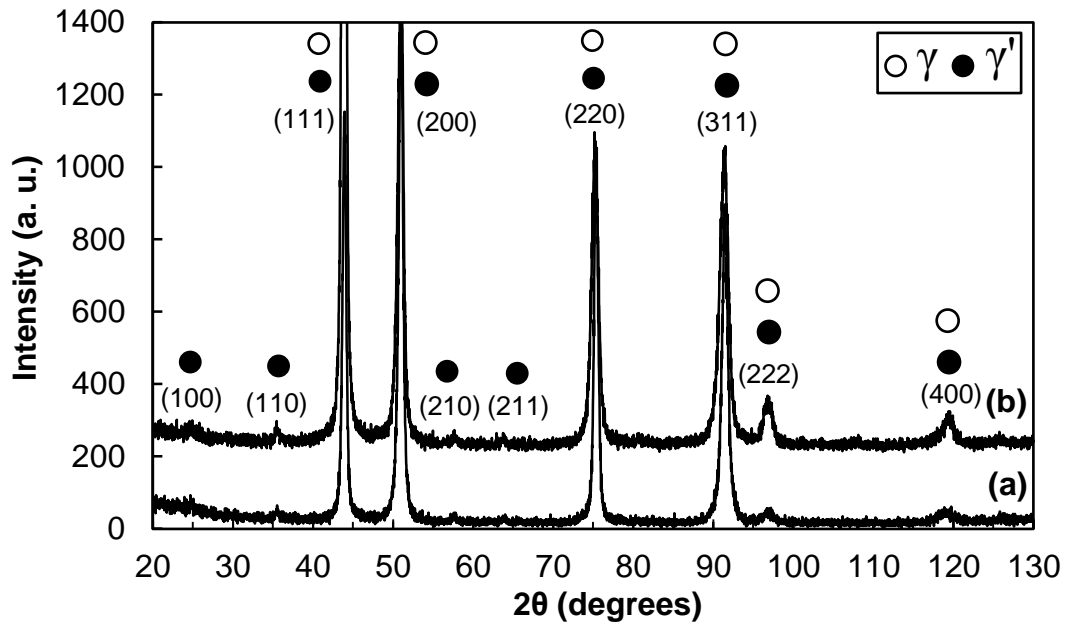


**Figure 5.4** XRD patterns of (a) fast and (b) slow cooled as cast  $\text{Ni}_{80}\text{Al}_{20}$  alloys.

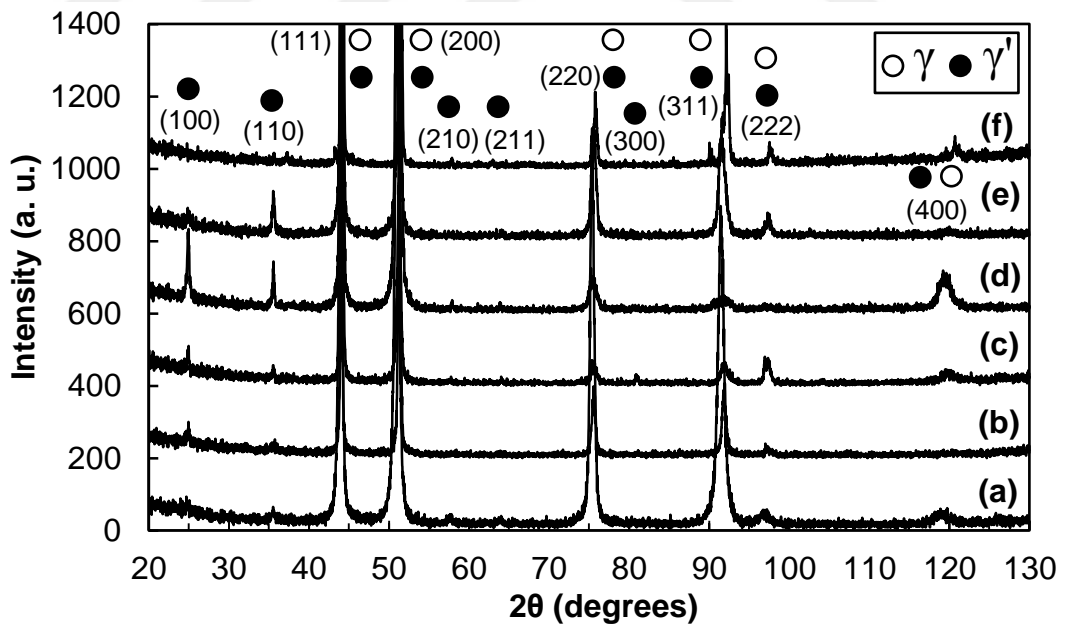


**Figure 5.5** XRD patterns of (a) as cast (fast cooled)  $\text{Ni}_{80}\text{Al}_{20}$  alloys, (b) partially-solutionized at  $1150\text{ }^{\circ}\text{C}$  for 3 hr and subsequently aged at  $800\text{ }^{\circ}\text{C}$  for (c) 4 hr (d) 16 hr (e) 64 hr and (f) 256 hr, respectively.

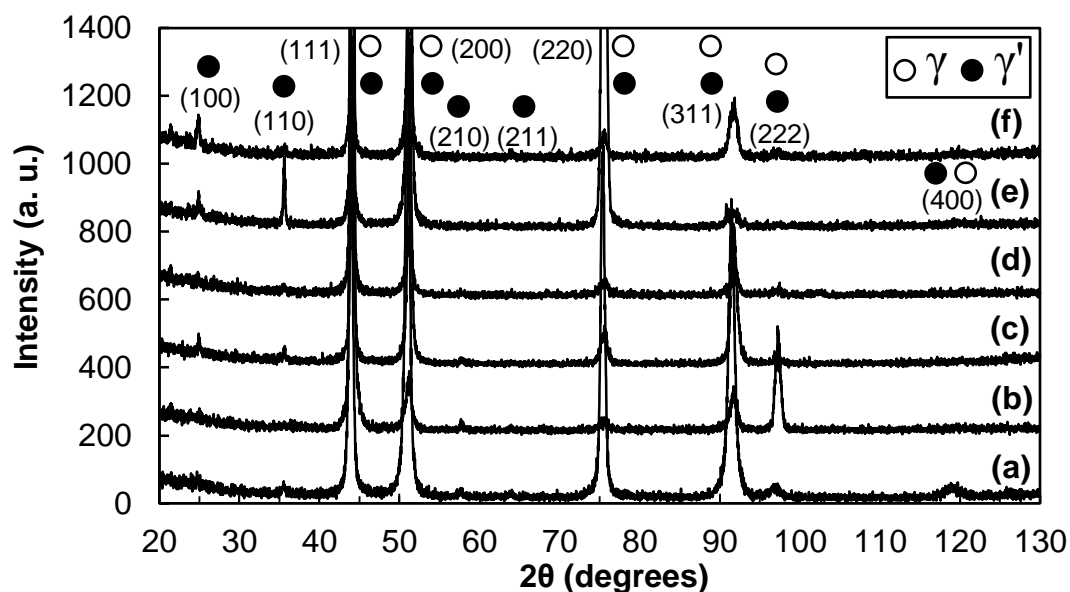


**Figure 5.6** XRD patterns of (a) as cast (fast cooled)  $\text{Ni}_{80}\text{Al}_{20}$  alloys, (b) homogenized at 1250 °C for 24 hr and partially-solutionized at 1150 °C for 3 hr and subsequently aged at 800 °C for (c) 4 hr (d) 16 hr (e) 64 hr and (f) 256 hr, respectively.

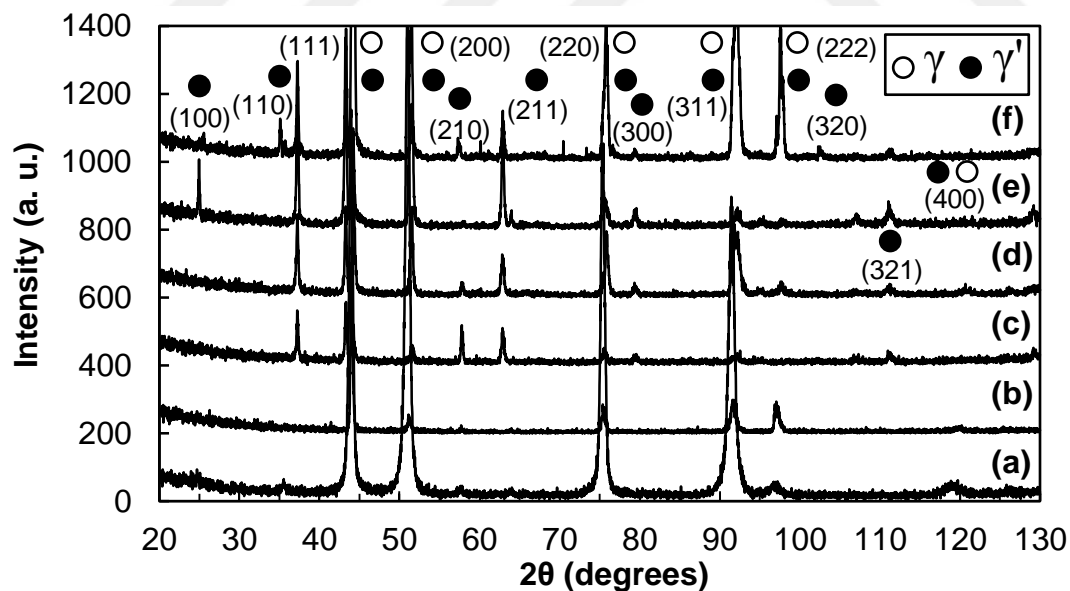


**Figure 5.7** XRD patterns of (a) as cast (fast cooled)  $\text{Ni}_{80}\text{Al}_{20}$  alloys, (b) primarily aged at 800 °C for 3 hr and subsequently aged at 800 °C for (c) 4 hr (d) 16 hr (e) 64 hr and (f) 256 hr, respectively.

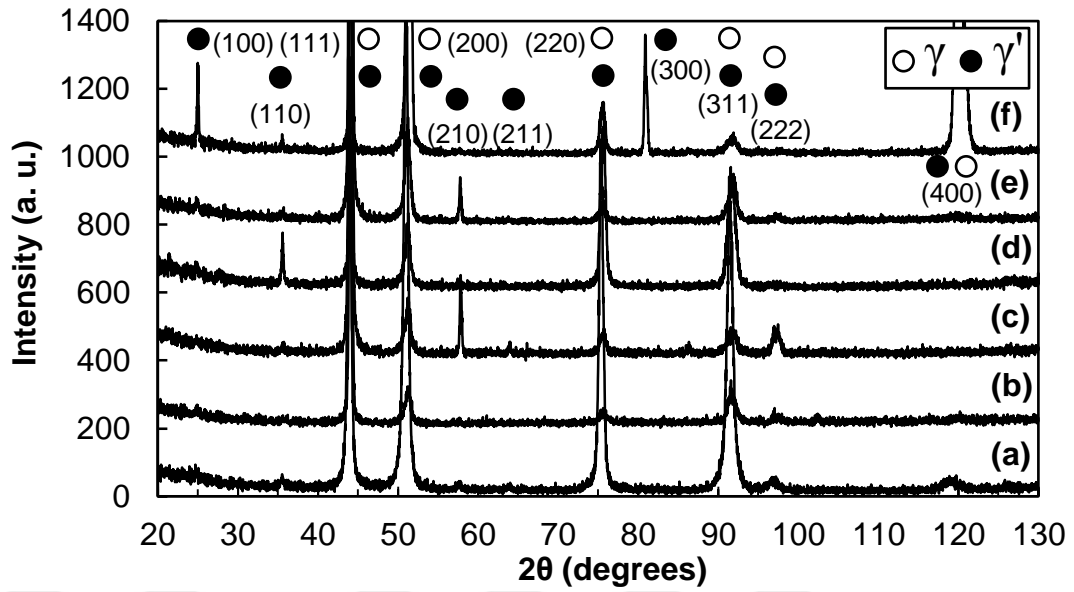


**Figure 5.8** XRD patterns of (a) as cast (fast cooled)  $\text{Ni}_{80}\text{Al}_{20}$  alloys, (b) homogenized at  $1250\text{ }^{\circ}\text{C}$  for 24 hr and primarily aged at  $800\text{ }^{\circ}\text{C}$  for 3 hr and subsequently aged at  $800\text{ }^{\circ}\text{C}$  for (c) 4 hr (d) 16 hr (e) 64 hr and (f) 256 hr, respectively.

### 5.3.2 Determination of Lattice Parameters of $\gamma'$ Precipitates in Binary $\text{Ni}_{80}\text{Al}_{20}$ Alloys

By considering XRD patterns of binary  $\text{Ni}_{80}\text{Al}_{20}$  alloys given in Figures 5.4-8, lattice parameters of the constituent  $\gamma'$  precipitates have been calculated by applying Bragg's Law and the results have been tabulated in Table 5.4 which does not exhibit lattice parameters of  $\gamma$  matrix phase due to previously mentioned overlapping problem in XRD patterns. It is evident from Table 5.4 that lattice parameters of  $\gamma'$  precipitates of as cast (both fast and slow cooled)  $\text{Ni}_{80}\text{Al}_{20}$  alloys coincide well with the literature [123]. Moreover, it is interesting to note that, for each sample group, lattice parameters of  $\gamma'$  precipitates reduce in magnitude and fundamental peaks of individual  $\gamma$  and  $\gamma'$  phases start to separate from each other as aging time is increased from 4 hr to 256 hr which is expected to lead to some significant changes in  $\gamma'$  precipitate shapes and mechanical properties of  $\text{Ni}_{80}\text{Al}_{20}$  alloys (i.e. micro-hardness values).

**Table 5.4** Lattice parameter determination of  $\gamma'$  precipitates in Ni<sub>80</sub>Al<sub>20</sub> alloys.

Ni <sub>80</sub> Al <sub>20</sub> alloys			
Sample groups	Definitions	Heat treatment	Lattice parameter of $\gamma'$ phase (Å)
		Temperature and durations	
0	As cast (fast cooled)	-	3.568
	As cast (slow cooled)	-	3.568
1	Partial solution heat treatment	1150 °C for 3 hr	3.562
		800 °C for 4 hr	3.564
	Aging	800 °C for 16 hr	3.559
		800 °C for 64 hr	3.554
		800 °C for 256 hr	3.548
2	Homogenization and partial solution heat treatment	1250 °C for 24 hr and 1150 °C for 3 hr	3.560
		800 °C for 4 hr	3.561
	Aging	800 °C for 16 hr	3.559
		800 °C for 64 hr	3.559
		800 °C for 256 hr	3.555
3	Primary aging	800 °C for 3 hr	3.564
		800 °C for 4 hr	3.563
	Aging	800 °C for 16 hr	3.563
		800 °C for 64 hr	3.563
		800 °C for 256 hr	3.562
4	Homogenization and primary aging	1250 °C for 24 hr and 800 °C for 3 hr	3.560
		800 °C for 4 hr	3.564
	Aging	800 °C for 16 hr	3.559
		800 °C for 64 hr	3.557
		800 °C for 256 hr	3.554

### 5.3.3 Thermal Properties

It is well known that order-disorder transformation temperature of  $L1_2$ -type ordered stoichiometric  $Ni_3Al$  phase (75 at.% Ni and 25 at.% Al) is in the vicinity of its melting temperature which is about 1375 °C [1]. DSC heating and cooling curves of as cast (fast cooled)  $Ni_{80}Al_{20}$  alloys at a rate of 20 °C/minutes are given in Figure 5.9. By considering this DSC plot, melting/solidification temperatures have been determined as 1388 °C and 1402 °C, respectively. However, for the cooling curve, a small exothermic peak (shown by down arrow) appears left to the main exothermic peak (which refers to solidification) may correspond to order-disorder transformation temperature of  $\gamma'$  precipitates. In addition, for the heating curve, distortion of the main endothermic peak (which refers to melting) confirm that another phase transformation prior to melting is possible (i.e. order-disorder transformation of  $\gamma'$  precipitates). Moreover, in Figure 5.9, other possible peaks which may refer to eutectic and/or peritectic phase transformations are absent. FESEM micrographs in the next part also confirm these predictions.

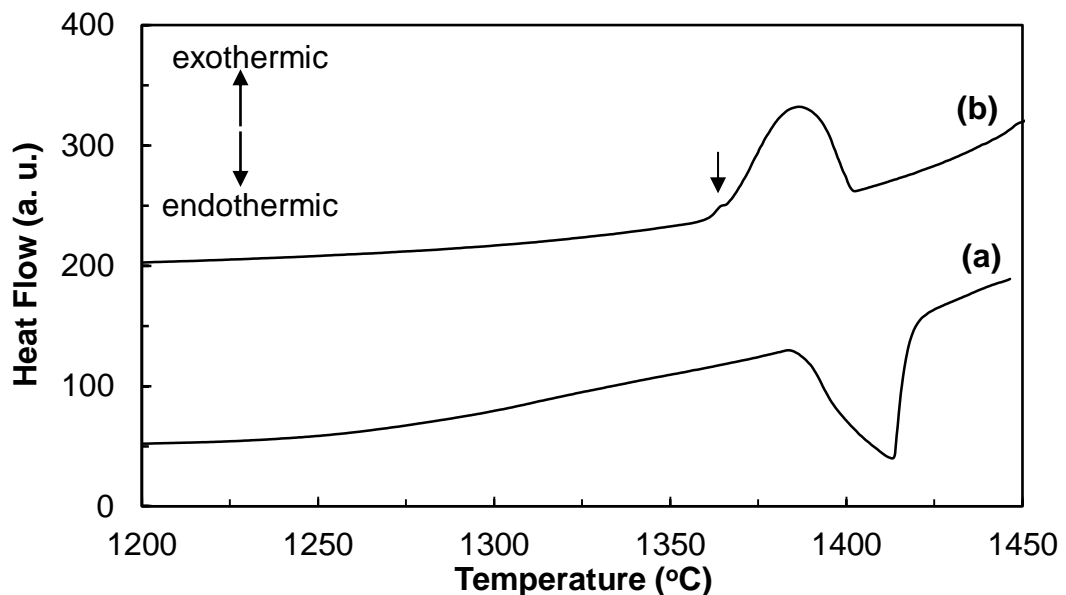


**Figure 5.9** DSC (a) heating and (b) cooling curves of as cast (fast cooled)  $Ni_{80}Al_{20}$  alloys (at a rate of 20 °C/minutes).

### 5.3.4 Microstructural Investigation

In order to investigate microstructural characteristics ( $\gamma'$  precipitate volume fraction, size & size distribution, orientation and shape) of  $\text{Ni}_{80}\text{Al}_{20}$  alloys, FESEM analyses have been performed. For as cast samples, solidification cooling rate has a significant effect on the size distribution of  $\gamma'$  precipitates. When cooling rate is relatively fast, dendrites and  $\gamma'$  precipitates within the dendritic regions have smaller sizes, whereas slow cooling rates lead to larger dendrites and bigger  $\gamma'$  precipitates (Figure 5.10).

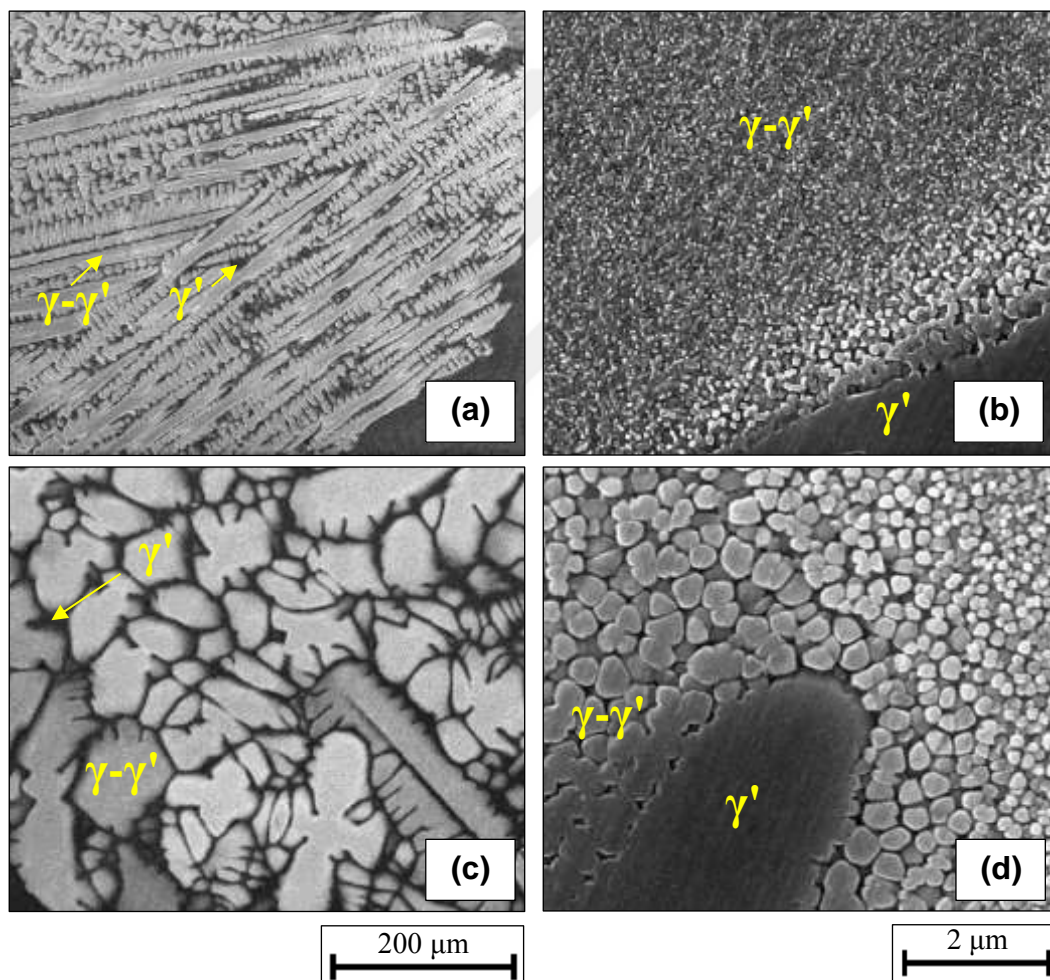


**Figure 5.10** FESEM micrographs of as cast  $\text{Ni}_{80}\text{Al}_{20}$  alloys showing (a) fine and (c) coarse dendritic ( $\gamma-\gamma'$ ) and interdendritic ( $\gamma'$ ) regions due to (a) fast and (c) slow cooling rates, respectively. Micrographs (b,d) show dendrite-interdendrite interface regions of (a,c) where (b) fine and (d) coarse  $\gamma'$  precipitates exist.



As indicated in Figure 5.10, in dendritic regions of both fast and slow cooled as cast  $\text{Ni}_{80}\text{Al}_{20}$  alloys,  $\gamma'$  precipitates have no unimodal distribution. Since in dendritic regions, latter stages of solidification occur at interdendritic interfaces, in this region  $\gamma'$  precipitates have bigger sizes rather than the ones in the interior regions of dendrites.

In order to examine the effects of homogenization, partial solution heat treatment and primary aging as well as aging durations, binary as cast (fast cooled)  $\text{Ni}_{80}\text{Al}_{20}$  alloys have been exposed to four different heat treatment procedures (Figures 5.11-18). In Figures 5.11-12, the first sample group is partially-solutionized at 1150 °C for 3 hr, ice-water quenched to RT and subsequently aged at 800 °C for different aging times of 4, 16, 64 and 256 hr and air cooled to RT, respectively. Secondly, in Figures 5.13-14, FESEM micrographs of the same heat treated (exceptionally homogenized at 1250 °C for 24 hr before partial solution heat treatment)  $\text{Ni}_{80}\text{Al}_{20}$  alloys are given. Next, FESEM micrographs of binary  $\text{Ni}_{80}\text{Al}_{20}$  alloys are indicated in Figures 5.15-16 which are first primarily aged at 800 °C for 3 hr, ice-water quenched to RT and subsequently aged at 800 °C for the aging times following the order of 4, 16, 64 and 256 hr and air cooled to RT, respectively. Lastly, Figures 5.17-18 demonstrate microstructures of  $\text{Ni}_{80}\text{Al}_{20}$  alloys homogenized at 1250 °C for 24 hr and primarily aged at 800 °C for 3 hr, ice-water quenched to RT and subsequently aged at 800 °C starting from 4 hr to 256 hr, respectively.

In Figure 5.11, general microstructures of the first sample group are given. Due to rapid solidification, as cast (fast cooled)  $\text{Ni}_{80}\text{Al}_{20}$  alloys have dendritic and interdendritic regions. As indicated in Figure 5.12, dendritic regions consist of both  $\gamma$  and  $\gamma'$  phases, whereas interdendritic regions are single  $\gamma'$  phases. Since homogenization heat treatment is not applied in this heat treatment procedure, dendritic characteristic of the microstructure (instead of grains) is still visible in the other samples of the first group, Figure 5.11(b-f). When as cast sample is partially-solutionized at 1150 °C for 3 hr, in dendritic region, some of the  $\gamma'$  precipitates dissolve in  $\gamma$  matrix and subsequently lead to higher volume fraction of  $\gamma$  matrix phase and bimodal distribution of  $\gamma'$  precipitates; bigger spheroidal precipitates having

approximately 482 nm size and smaller spherical precipitates (~ 161 nm), Figure 5.12(b). When aging is applied at 800 °C for 4 hr, volume fraction of  $\gamma$  matrix phase within the dendritic region decreases since new  $\gamma'$  precipitates form, Figure 5.12(c). Secondly, previous (bigger) spheroidal precipitates merge with other precipitates and turn into much bigger irregular shaped phases. It is possible to understand this precipitate combination from the serrated surfaces of bigger irregular precipitates. In a similar way, previous (smaller) spherical precipitates become slightly bigger spheroidal precipitates (~ 140 nm). When aging time is increased up to 16 hr, serrated surfaces of big irregular precipitates disappear and previous small spheroidal precipitates turn into bigger cuboidal precipitates (~ 167 nm) aligned in  $\langle 001 \rangle$  directions since these directions are the softest ones in FCC-type phases [1,2]. For 64 hr aging, previous smaller cuboidal precipitates keep their alignment in the same directions and become slightly bigger (~ 212 nm). Lastly, when aging time is increased up to 256 hr, previous cuboidal precipitates lose their shape and they become irregular (elongated) in three specific directions (the angles between these directions are about 51°, 54° and 75°).

In Figure 5.13, general microstructures of the second sample group are given. Since homogenization heat treatment is applied in this heat treatment procedure at 1250 °C for 24 hr, dendritic character of as cast microstructure disappears and equiaxed grains containing annealing twins become visible in the other samples of this group. When as cast sample is subsequently partially-solutionized at 1150 °C for 3 hr, in each grain,  $\gamma'$  precipitates have trimodal distribution; the biggest primary  $\gamma'$  precipitates having serrated surfaces (~ 3.4  $\mu\text{m}$ ), moderate spherical shaped secondary precipitates (~ 158 nm) and between these two types of precipitates tiny tertiary precipitates having spherical shapes (~ 40 nm), Figure 5.14(b). When aging is applied at 800 °C for 4 hr, tertiary precipitates disappear (merged with primary and secondary precipitates) and lead to bigger spheroidal secondary precipitates (~ 160 nm), Figure 5.14(c). When aging time is increased up to 16 hr, previous small spheroidal precipitates turn into bigger spheroidal precipitates (~ 192 nm) aligned in the softest  $\langle 001 \rangle$  directions. For 64 hr aging, previous precipitates become cuboidal and keep their alignment in order,

become bigger (~ 206 nm) and start to elongate. Lastly, when aging time is increased up to 256 hr, slightly elongated precipitates become totally elongated in three specific directions (the angles between these directions are about 39°, 63° and 78°).

For the third group, general microstructures of the samples are given in Figure 5.15. Unlike the first group, in this case, dendrites seem to be much larger. Since homogenization heat treatment is not applied in this heat treatment procedure, dendritic characteristic of the microstructure (instead of grains) is still visible in other samples similar to the first group. However, as opposed to the first group, when as cast sample is primarily aged at 800 °C for 3 hr, in dendritic region, there is no bimodal distribution of  $\gamma'$  precipitates. Figure 5.16(b) shows that primary aging at 800 °C leads to unimodal distribution of  $\gamma'$  precipitates (~ 91 nm). When aging is applied at 800 °C for 4 hr, previous smaller precipitates become slightly bigger (~ 114 nm), Figure 5.16(c). When aging time is increased up to 16 hr, bigger precipitates (~ 139 nm) align along the softest  $\langle 001 \rangle$  directions. For 64 hr aging, previous smaller precipitates become slightly bigger (~ 177 nm) having cuboidal shapes and keep their alignment in order. Lastly, for 256 hr aging, previous cuboidal precipitates lose their shape and become irregular (elongated) mostly in one direction (i.e.  $\langle 001 \rangle$ ).

For the last group of samples, general microstructures are given in Figure 5.17. Since homogenization heat treatment is applied in this heat treatment procedure at 1250 °C for 24 hr, instead of dendritic characteristic of the microstructure equiaxed grains containing annealing twins are visible in the other samples of this group (similar to the second group). When as cast sample is subsequently primarily aged at 800 °C for 3 hr, in each grain,  $\gamma'$  precipitates have bimodal distribution; the biggest irregular shaped  $\gamma'$  precipitates having ~ 2.4  $\mu\text{m}$  in size and tiny spherical precipitates (~ 73 nm), Figure 5.18(b). When aging is applied at 800 °C for 4 hr, tiny spherical precipitates become bigger in size (~ 102 nm). When aging time is increased up to 16 hr, previous small precipitates turn into bigger cuboidal precipitates (~ 131 nm) aligned in the softest  $\langle 001 \rangle$  and  $\langle 010 \rangle$  directions. For 64 hr aging, the number of previous cuboidal precipitates (~ 189 nm) decreases since the volume fraction of  $\gamma$  matrix phase continues

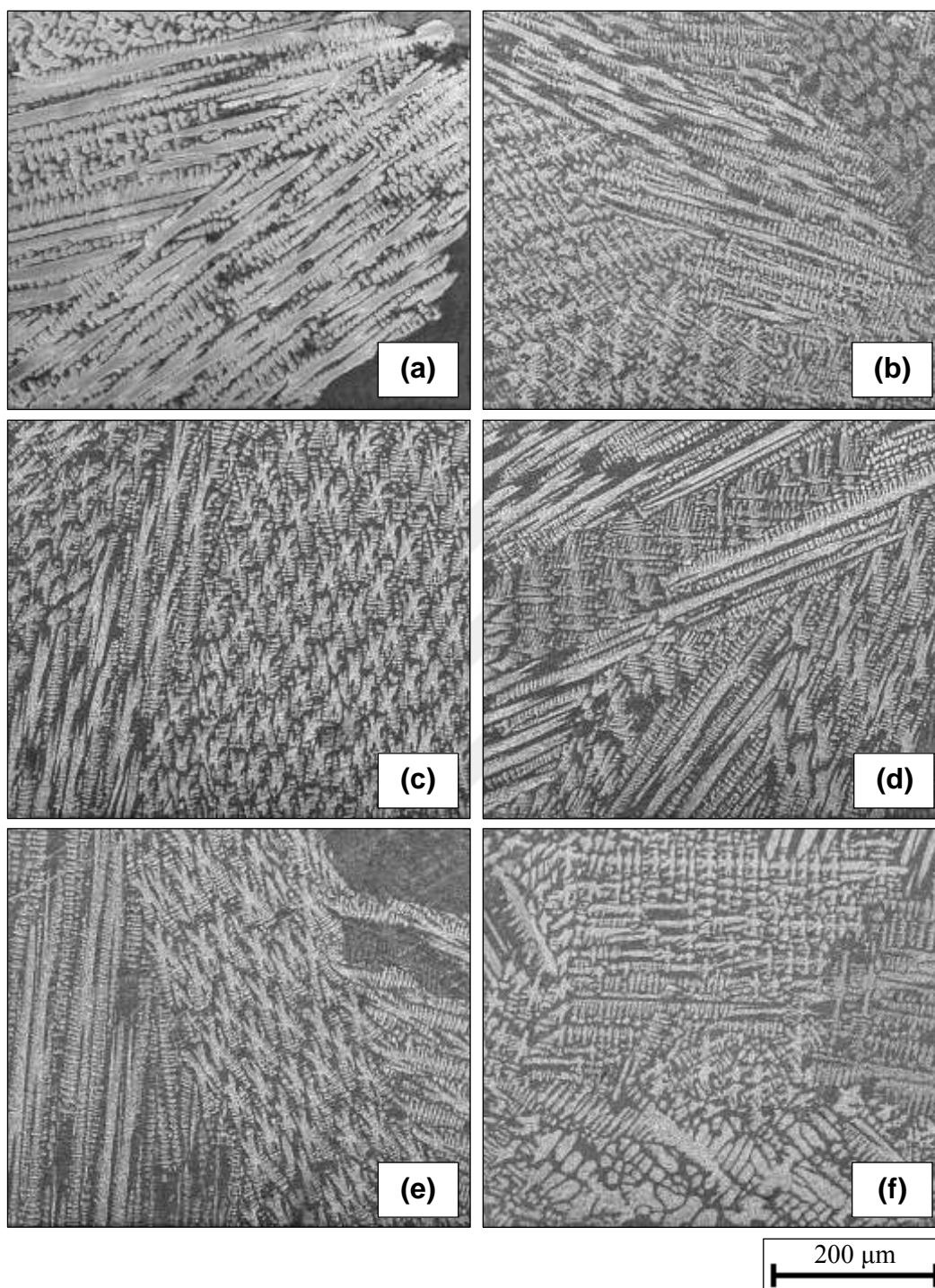


**Figure 5.11** FESEM micrographs showing (a) as cast (fast cooled), (b) partial solution heat treated (at 1150 °C for 3 hr) microstructures and temporal evolution of  $\gamma'$  precipitates in Ni<sub>80</sub>Al<sub>20</sub> alloys as aging time at 800 °C is (c) 4 hr, (d) 16 hr, (e) 64 hr and (f) 256 hr, respectively.

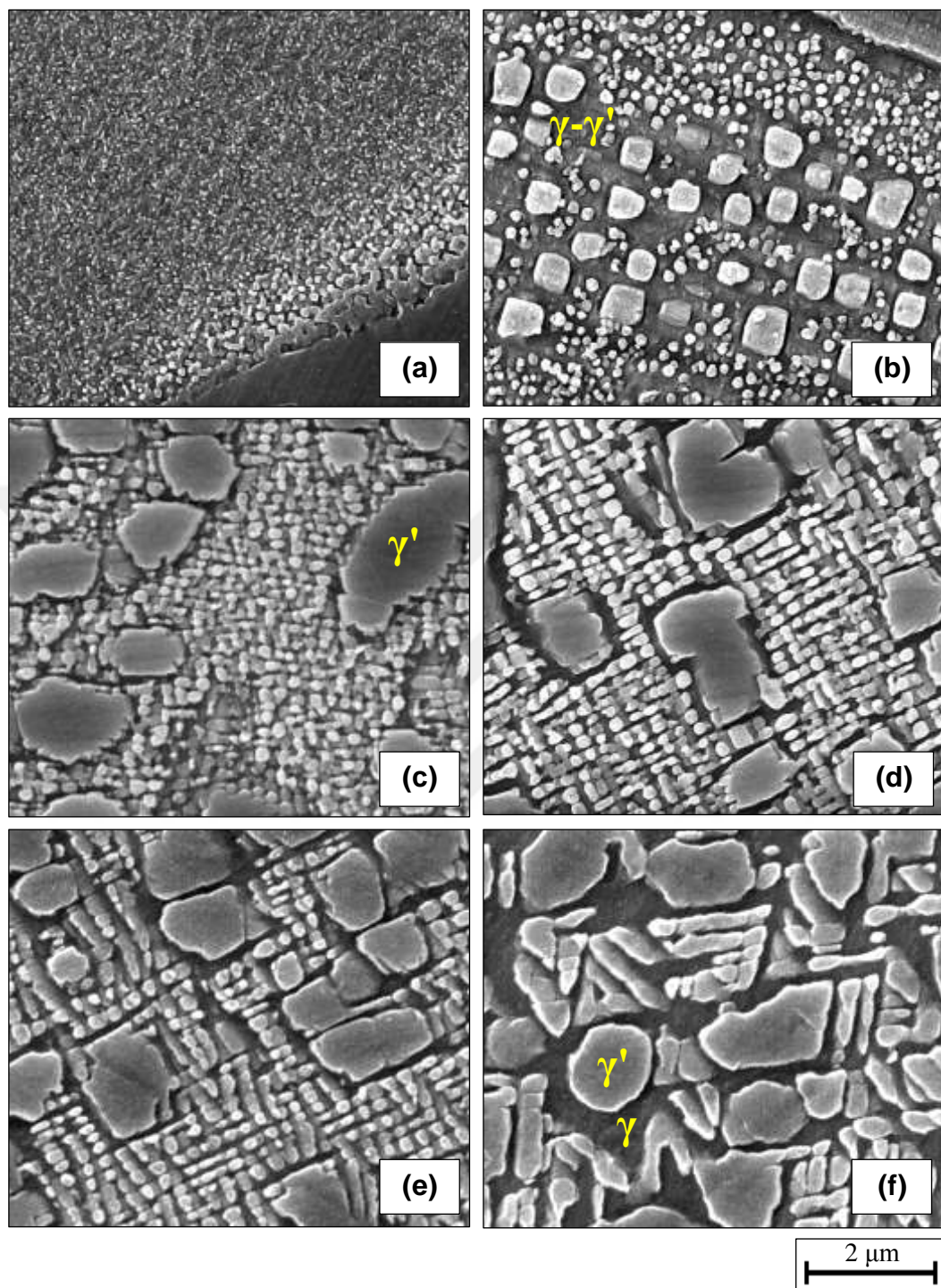


**Figure 5.12** FESEM micrographs showing (a) as cast (fast cooled), (b) partial solution heat treated (at 1150 °C for 3 hr) microstructures and temporal evolution of  $\gamma'$  precipitates in  $\text{Ni}_{80}\text{Al}_{20}$  alloys as aging time at 800 °C is (c) 4 hr, (d) 16 hr, (e) 64 hr and (f) 256 hr, respectively.

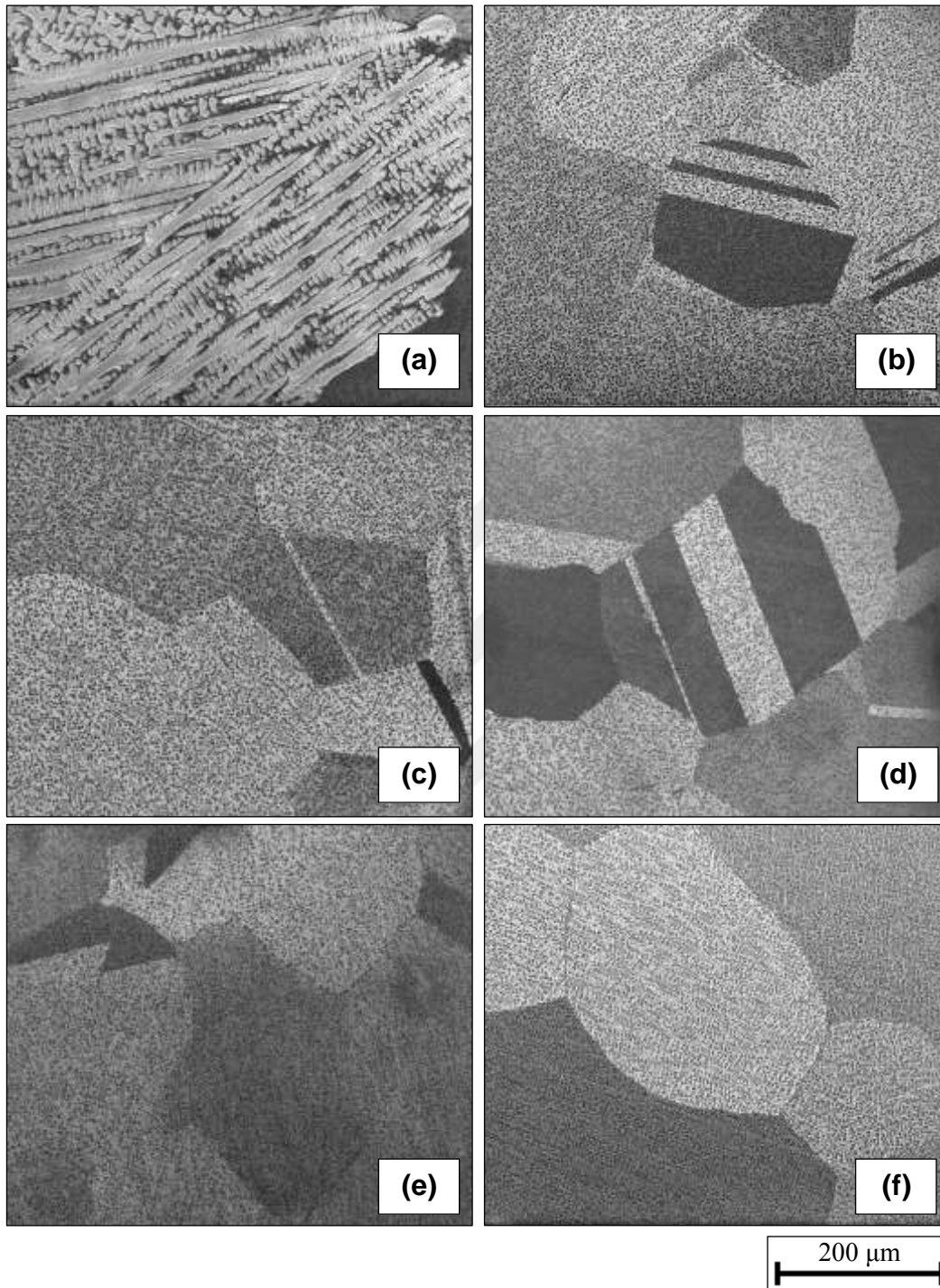


**Figure 5.13** FESEM micrographs showing (a) as cast (fast cooled), (b) homogenized and partial solution heat treated (at 1250 °C for 24 hr and 1150 °C for 3 hr) microstructures and temporal evolution of  $\gamma'$  precipitates in Ni<sub>80</sub>Al<sub>20</sub> alloys as aging time at 800 °C is (c) 4 hr, (d) 16 hr, (e) 64 hr and (f) 256 hr, respectively.

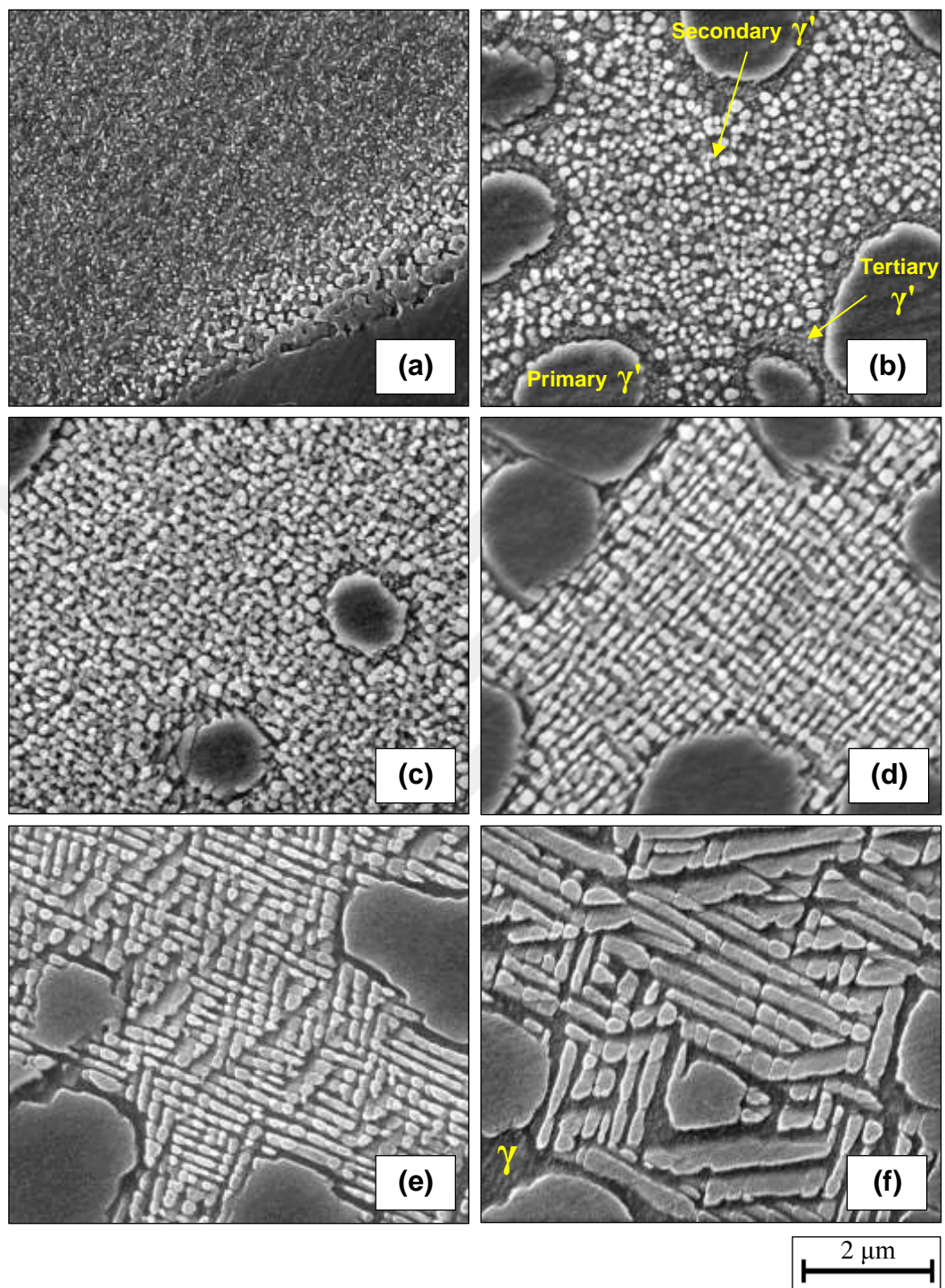


**Figure 5.14** FESEM micrographs showing (a) as cast (fast cooled), (b) homogenized and partial solution heat treated (at 1250 °C for 24 hr and 1150 °C for 3 hr) microstructures and temporal evolution of  $\gamma'$  precipitates in Ni<sub>80</sub>Al<sub>20</sub> alloys as aging time at 800 °C is (c) 4 hr, (d) 16 hr, (e) 64 hr and (f) 256 hr, respectively.

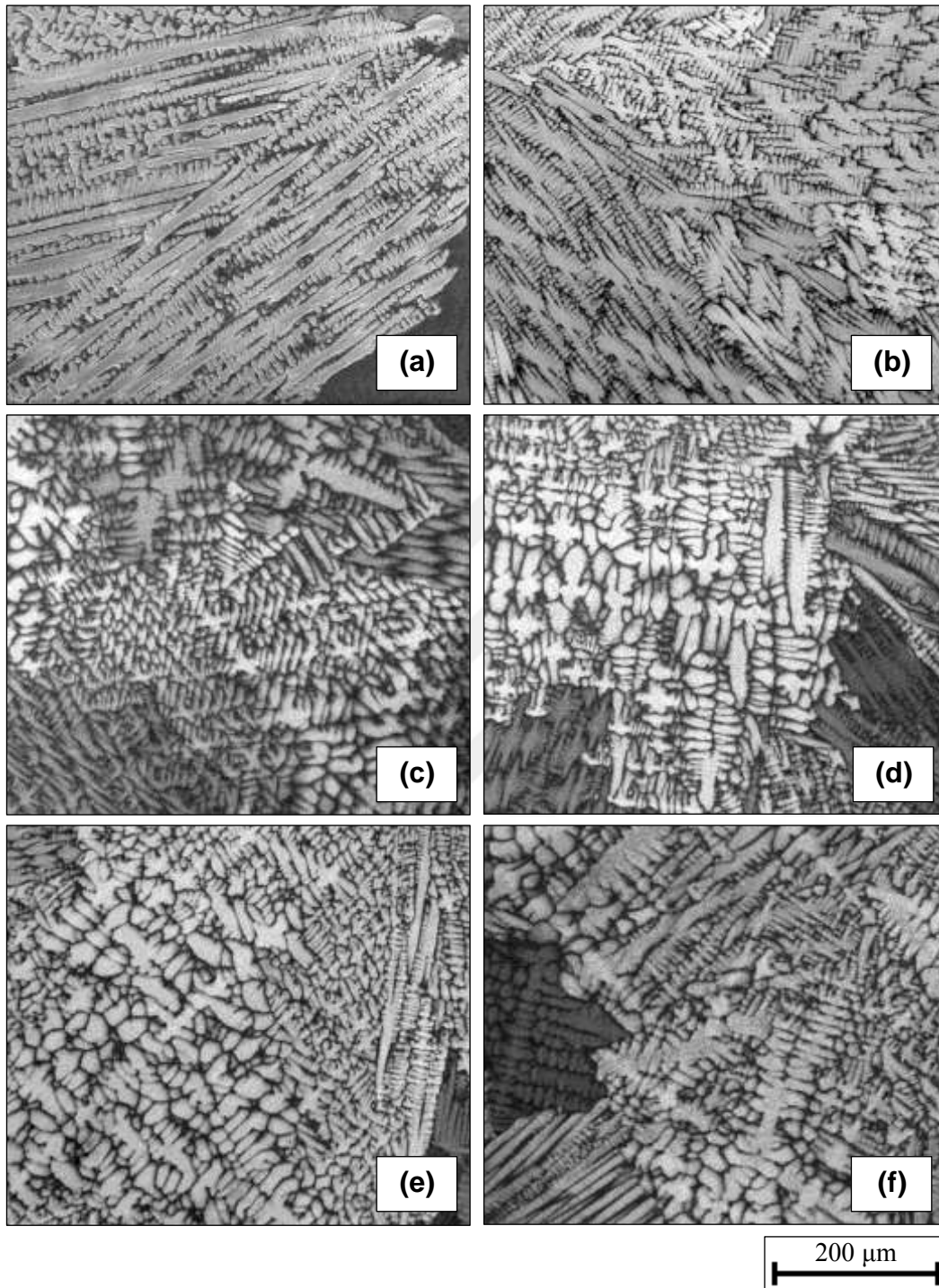


**Figure 5.15** FESEM micrographs showing (a) as cast (fast cooled), (b) primarily aged (at 800 °C for 3 hr) microstructures and temporal evolution of  $\gamma'$  precipitates in  $\text{Ni}_{80}\text{Al}_{20}$  alloys as aging time at 800 °C is (c) 4 hr, (d) 16 hr, (e) 64 hr and (f) 256 hr, respectively.



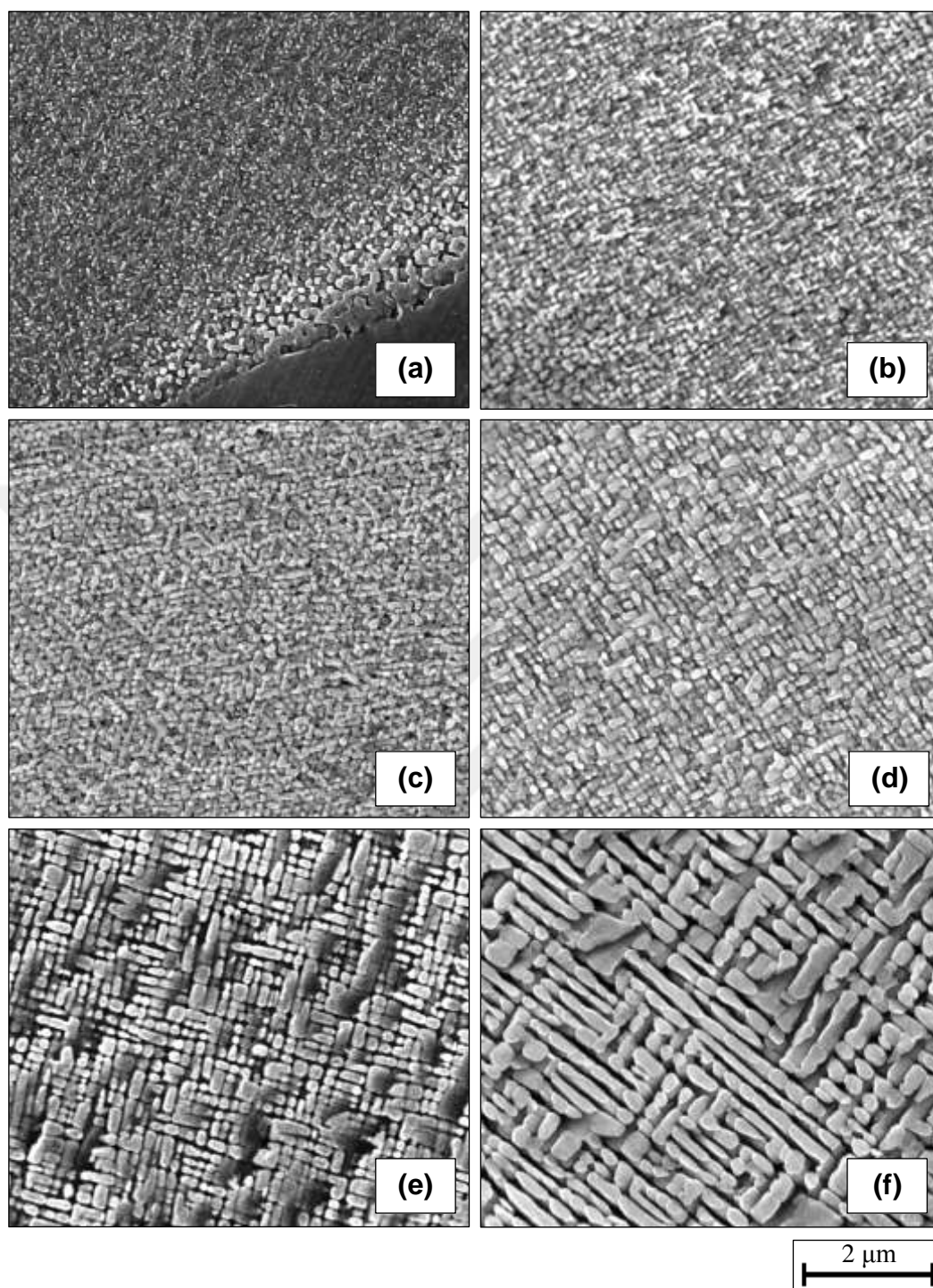


**Figure 5.16** FESEM micrographs showing (a) as cast (fast cooled), (b) primarily aged (at 800 °C for 3 hr) microstructures and temporal evolution of  $\gamma'$  precipitates in Ni<sub>80</sub>Al<sub>20</sub> alloys as aging time at 800 °C is (c) 4 hr, (d) 16 hr, (e) 64 hr and (f) 256 hr, respectively.

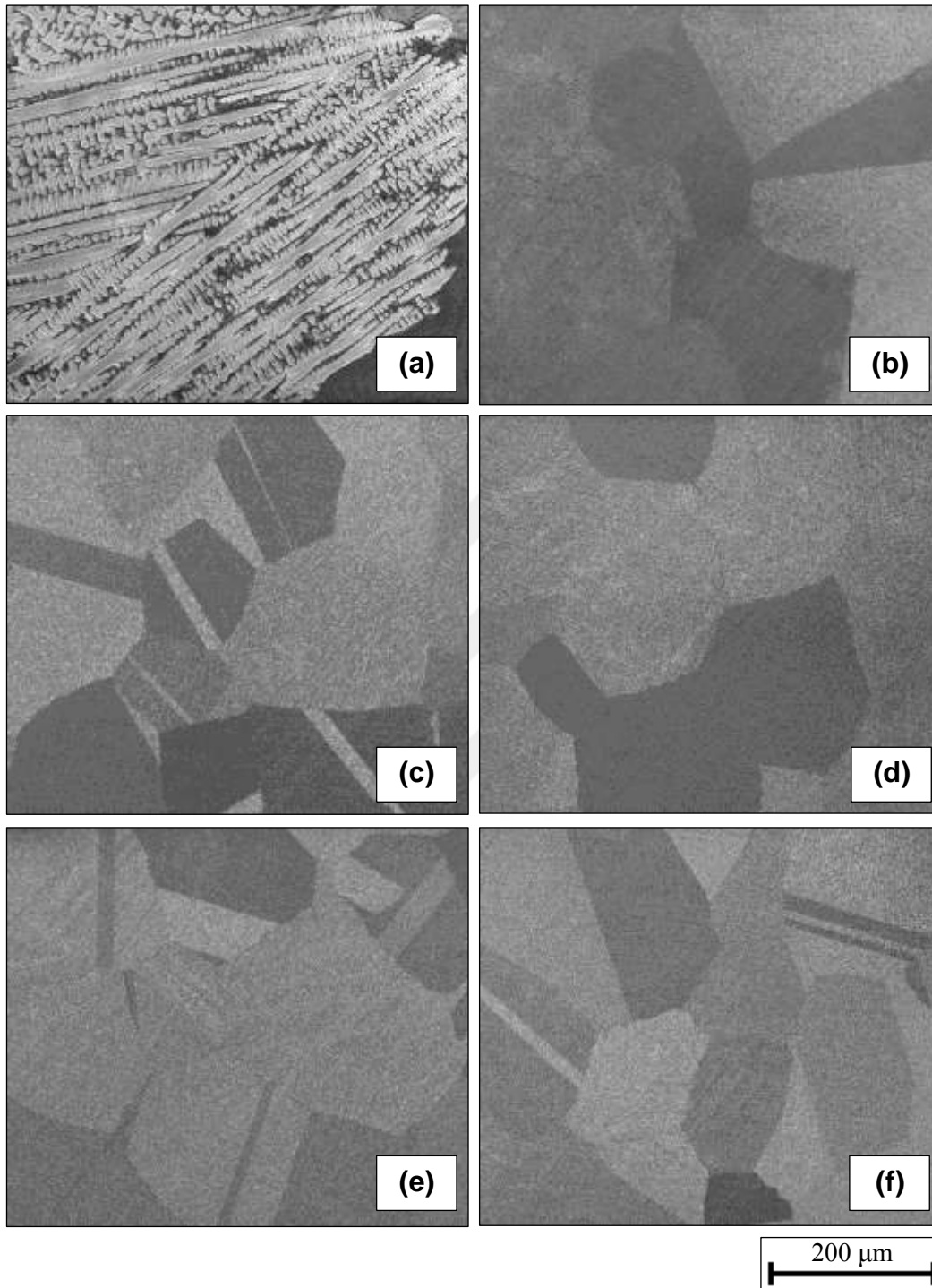


**Figure 5.17** FESEM micrographs showing (a) as cast (fast cooled), (b) homogenized and primarily aged (at 1250 °C for 24 hr and 800 °C for 3 hr) microstructures and temporal evolution of  $\gamma'$  precipitates in  $\text{Ni}_{80}\text{Al}_{20}$  alloys as aging time at 800 °C is (c) 4 hr, (d) 16 hr, (e) 64 hr and (f) 256 hr, respectively.

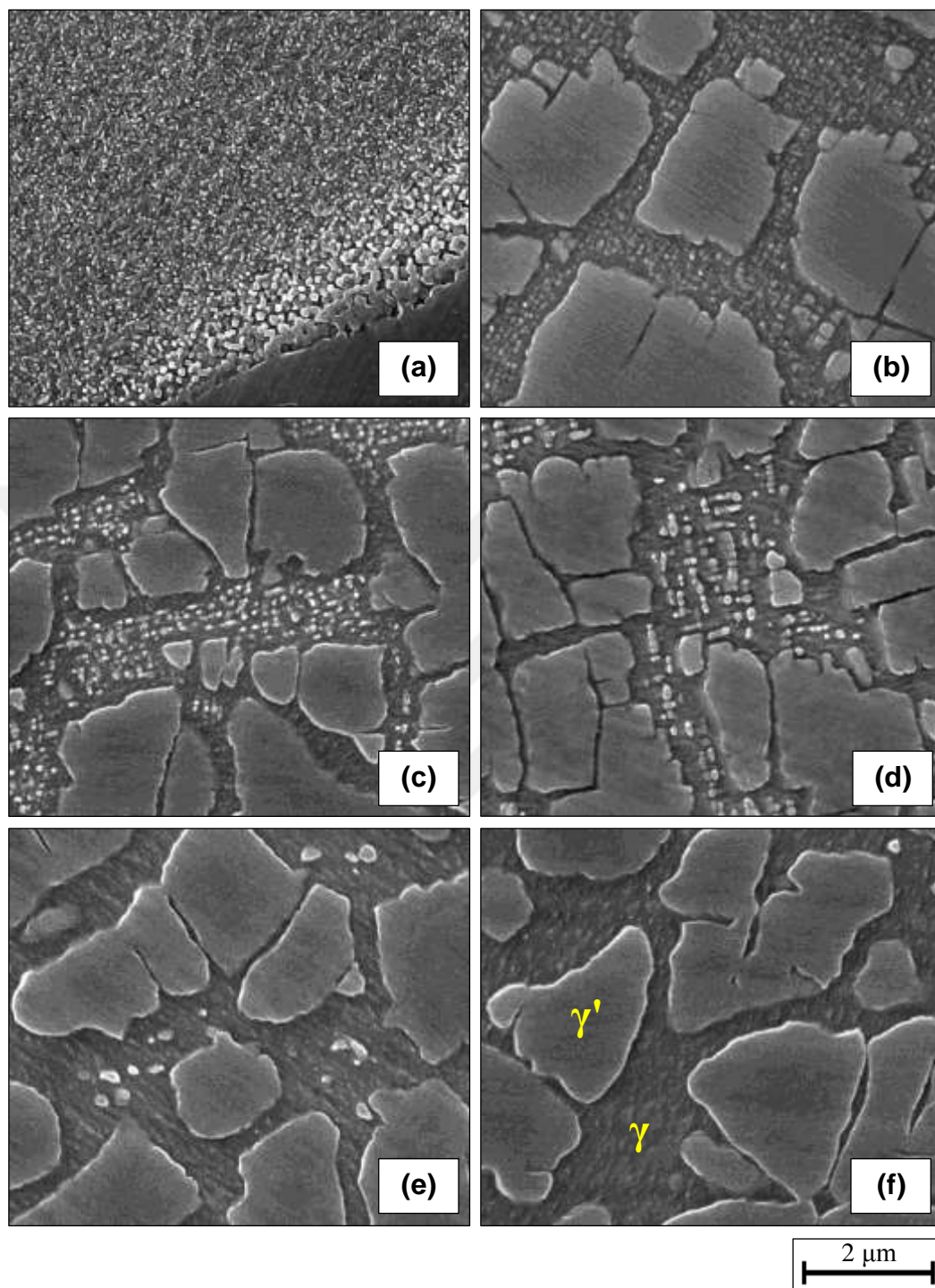


**Figure 5.18** FESEM micrographs showing (a) as cast (fast cooled), (b) homogenized and primarily aged (at 1250 °C for 24 hr and 800 °C for 3 hr) microstructures and temporal evolution of  $\gamma'$  precipitates in  $\text{Ni}_{80}\text{Al}_{20}$  alloys as aging time at 800 °C is (c) 4 hr, (d) 16 hr, (e) 64 hr and (f) 256 hr, respectively.

its increase and precipitate alignment disappears. Lastly, when aging time is increased up to 256 hr, previous precipitates totally dissolve in  $\gamma$  matrix phase which is expected to lead to worsening of mechanical properties, i.e. micro-hardness.

### **5.3.5 Energy Dispersive Spectroscopy (EDS) Measurements**

In order to verify the nominal compositions of as cast and heat treated  $\text{Ni}_{80}\text{Al}_{20}$  alloys and identify the phases visible in FESEM micrographs, energy dispersive spectroscopy measurements have been applied on the general microstructures and constituent  $\gamma$  and  $\gamma'$  phases. In order to get more accurate results, two EDS measurements have been applied on each individual phase and the average results have been tabulated in Table 5.5. In Table 5.5, standard deviation values are not given due to their negligible magnitudes. According to Table 5.5, Ni content of  $\gamma$  matrix phases of as cast and heat treated  $\text{Ni}_{80}\text{Al}_{20}$  alloys is  $\sim > 80$  at.%, whereas  $\gamma'$  precipitates seem to have nearly stoichiometric compositions (75 at.% Ni and 25 at.% Al).

### **5.3.6 Micro-hardness Measurements**

Mechanical responses of as cast and heat treated  $\text{Ni}_{80}\text{Al}_{20}$  alloys have been examined by applying micro-hardness tests. In order to obtain better results, ten measurements have been applied on each sample and the results have been given in Table 5.6. As shown in Table 5.6, low standard deviation values imply that mechanical properties of samples are homogeneously distributed throughout the samples. When the hardness data of as cast samples are compared, it is noticed that fast cooled as cast  $\text{Ni}_{80}\text{Al}_{20}$  alloy is slightly harder than the slow cooled one, Figure 5.19. It is attributed that this result is arisen from the smaller dendrites and  $\gamma'$  precipitates of the fast cooled sample which would lead to more coherency-type strengthening. When pre-aged samples ( partial solution heat treated/primarily aged and both homogenized and partial solution heat treated/primarily aged) are compared, micro-hardness (Vickers) values follow the order of  $292.6 > 238.3 > 233.4 > 226.5$  for the sample groups of  $3 > 4 > 1 > 2$ , respectively, Figure 5.20. These results imply that homogenization and partial solution

**Table 5.5** EDS phase analysis of Ni<sub>80</sub>Al<sub>20</sub> alloys.

Ni <sub>80</sub> Al <sub>20</sub> alloys										
Sample groups	Heat treatment		General (at.%)			γ (at.%)			γ' (at.%)	
	Definitions	Temperature and durations	Ni	Al		Ni	Al		Ni	Al
0	As cast (fast cooled)	-	78.0	22.0	-	-	-	-	76.3	23.7
	As cast (slow cooled)	-	76.0	24.0	78.6	21.4			76.2	23.8
1	Partial solution heat treatment		78.2	21.8	83.0	17.0			74.5	25.5
		1150 °C for 3 hr								
		800 °C for 4 hr	78.1	21.9	83.1	16.9			74.4	25.6
		800 °C for 16 hr	77.5	22.5	79.9	20.1			73.7	26.3
	Aging		77.3	22.7	82.2	17.8			75.3	24.7
		800 °C for 64 hr								
	800 °C for 256 hr		76.3	23.7	82.7	17.3			74.8	25.2
2	Homogenization and partial solution heat treatment		78.7	21.3	81.5	18.5			75.3	24.7
		1250 °C for 24 hr and 1150 °C for 3 hr								
		800 °C for 4 hr	78.5	21.5	83.4	16.6			75.5	24.5
		800 °C for 16 hr	78.4	21.6	82.7	17.3			76.0	24.0
	Aging		78.2	21.8	85.3	14.7			75.4	24.6
		800 °C for 64 hr								
	800 °C for 256 hr		77.6	22.4	83.7	16.3			75.6	24.4
3	Primary aging		77.3	22.7	80.3	19.7			74.6	25.4
		800 °C for 3 hr								
	800 °C for 4 hr		77.2	22.8	84.5	15.5			74.6	25.4
	800 °C for 16 hr		78.4	21.6	78.6	21.4			75.3	24.7
	Aging		75.7	24.3	79.7	20.3			75.2	24.8
		800 °C for 64 hr								
	800 °C for 256 hr		76.1	23.9	80.0	20.0			73.2	26.8
4	Homogenization and primary aging		77.8	22.2	80.4	19.6			74.9	25.1
		1250 °C for 24 hr and 800 °C for 3 hr								
		800 °C for 4 hr	77.6	22.4	84.5	15.5			75.4	24.6
		800 °C for 16 hr	78.4	21.6	81.3	18.7			75.1	24.9
	Aging		78.5	21.5	83.7	16.3			74.4	25.6
		800 °C for 64 hr								
	800 °C for 256 hr		78.4	21.6	84.5	15.5			74.9	25.1

**Table 5.6** Micro-hardness values of Ni<sub>80</sub>Al<sub>20</sub> alloys.

Ni <sub>80</sub> Al <sub>20</sub> alloys		
Sample groups	Heat treatment Definitions	Temperature and durations Micro-hardness (Vickers)
0	As cast (fast cooled)	277.9 ± 4.6
	As cast (slow cooled)	263.3 ± 2.5
1	Partial solution heat treatment	1150 °C for 3 hr
		233.4 ± 5.1
		800 °C for 4 hr
		238.9 ± 5.7
	Aging	800 °C for 16 hr
	236.5 ± 6.1	
	800 °C for 64 hr	247.1 ± 6.9
	800 °C for 256 hr	239.6 ± 4.2
2	Homogenization and partial solution heat treatment	1250 °C for 24 hr and 1150 °C for 3 hr
		226.5 ± 6.2
		800 °C for 4 hr
		257.6 ± 5.2
	Aging	800 °C for 16 hr
	261.3 ± 3.7	
	800 °C for 64 hr	253.3 ± 4.3
	800 °C for 256 hr	242.3 ± 4.9
3	Primary aging	800 °C for 3 hr
		292.6 ± 8.6
		800 °C for 4 hr
		280.9 ± 4.5
	Aging	800 °C for 16 hr
	280.1 ± 3.4	
	800 °C for 64 hr	277.6 ± 3.0
	800 °C for 256 hr	268.3 ± 7.8
4	Homogenization and primary aging	1250 °C for 24 hr and 800 °C for 3 hr
		238.3 ± 5.7
		800 °C for 4 hr
		231.4 ± 6.6
	Aging	800 °C for 16 hr
	228.1 ± 8.2	
	800 °C for 64 hr	226.5 ± 4.9
	800 °C for 256 hr	224.9 ± 6.1

heat treatment procedures yield lower micro-hardness values. Secondly, when heat treated sample groups are compared within themselves, for each sample group, micro-hardness values mostly decrease as aging time is increased from 4 hr to 256 hr, Figure 5.20. These results are attributed to the microstructural characteristics of the samples which will be discussed in the next part in detail.

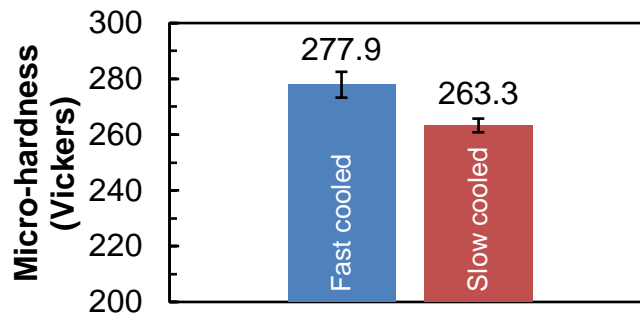


**Figure 5.19** Micro-hardness (Vickers) comparison of fast cooled (left) and slow cooled (right) as cast  $\text{Ni}_{80}\text{Al}_{20}$  alloys.

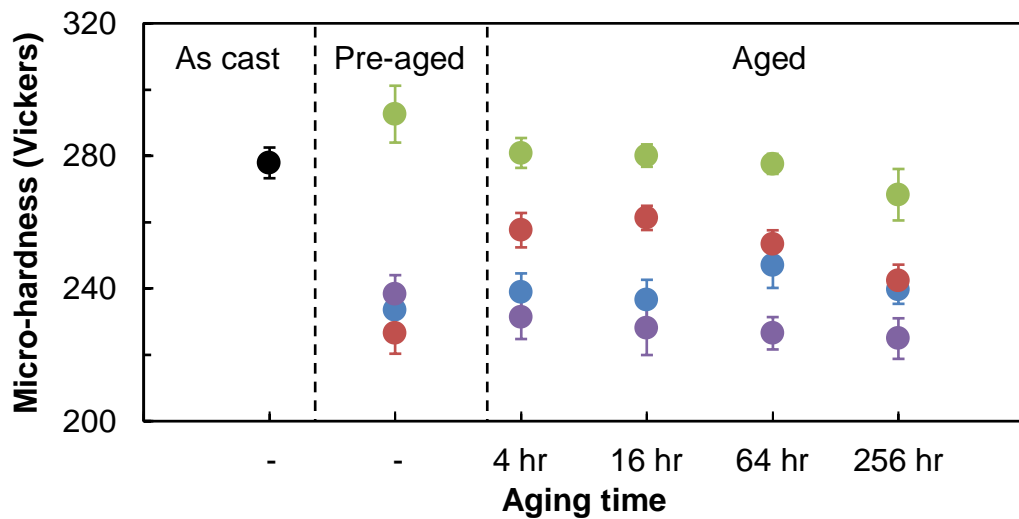


**Figure 5.20** Micro-hardness (Vickers) comparison of heat treated  $\text{Ni}_{80}\text{Al}_{20}$  alloys. Black sphere denotes to fast cooled as cast sample, whereas sample groups (1-4) are represented in 1: blue, 2: red, 3: green and 4: purple spheres, respectively.

### 5.3.7 Effects of Heat Treatment Procedures on the Microstructural and Mechanical Properties of Ni<sub>80</sub>Al<sub>20</sub> Alloys

As previously mentioned in Chapter 2, improved mechanical properties of nickel-based superalloys are strongly related with microstructural characteristics (i.e.  $\gamma'$  precipitate volume fraction, size & size distribution, orientation and shape) of these materials. Hence, in this part, these microstructural properties have been investigated for all sample groups and results have been tabulated in Table 5.7. In terms of being an example, Figures 5.21-22 created by MIPAR software program show the volume fraction, size & size distribution and orientation of  $\gamma'$  precipitates of the second sample group of Ni<sub>80</sub>Al<sub>20</sub> alloys as aging time is increased from 4 hr to 256 hr. According to Figure 5.21, it is easily noticed that as aging time is increased  $\gamma'$  precipitate volume

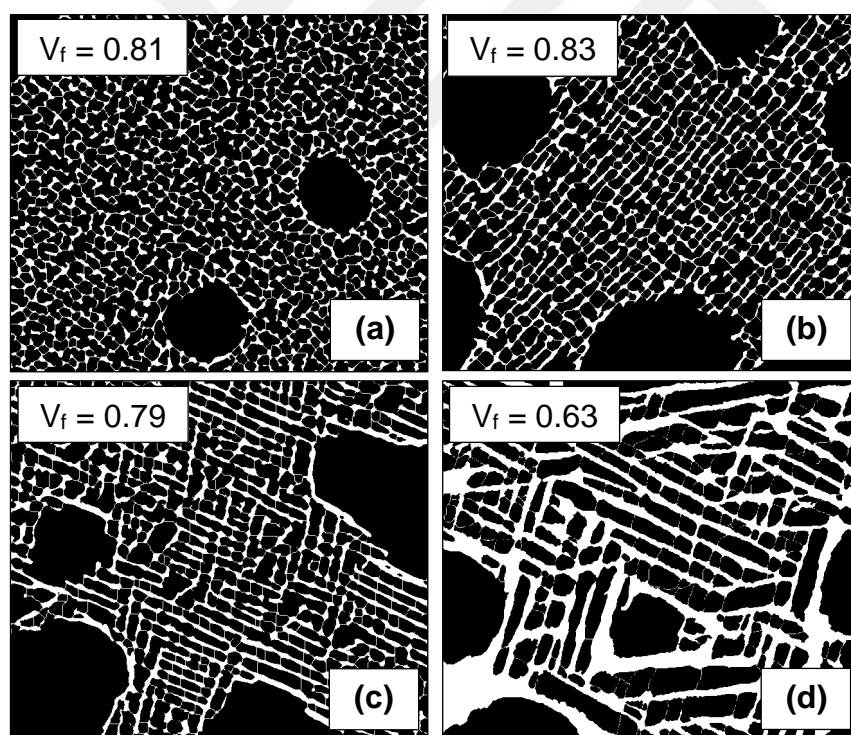


**Figure 5.21**  $\gamma'$  precipitate volume fraction variation of the second sample group of Ni<sub>80</sub>Al<sub>20</sub> alloys as aging time at 800 °C is (a) 4 hr, (b) 16 hr, (c) 64 hr and (d) 256 hr, respectively.



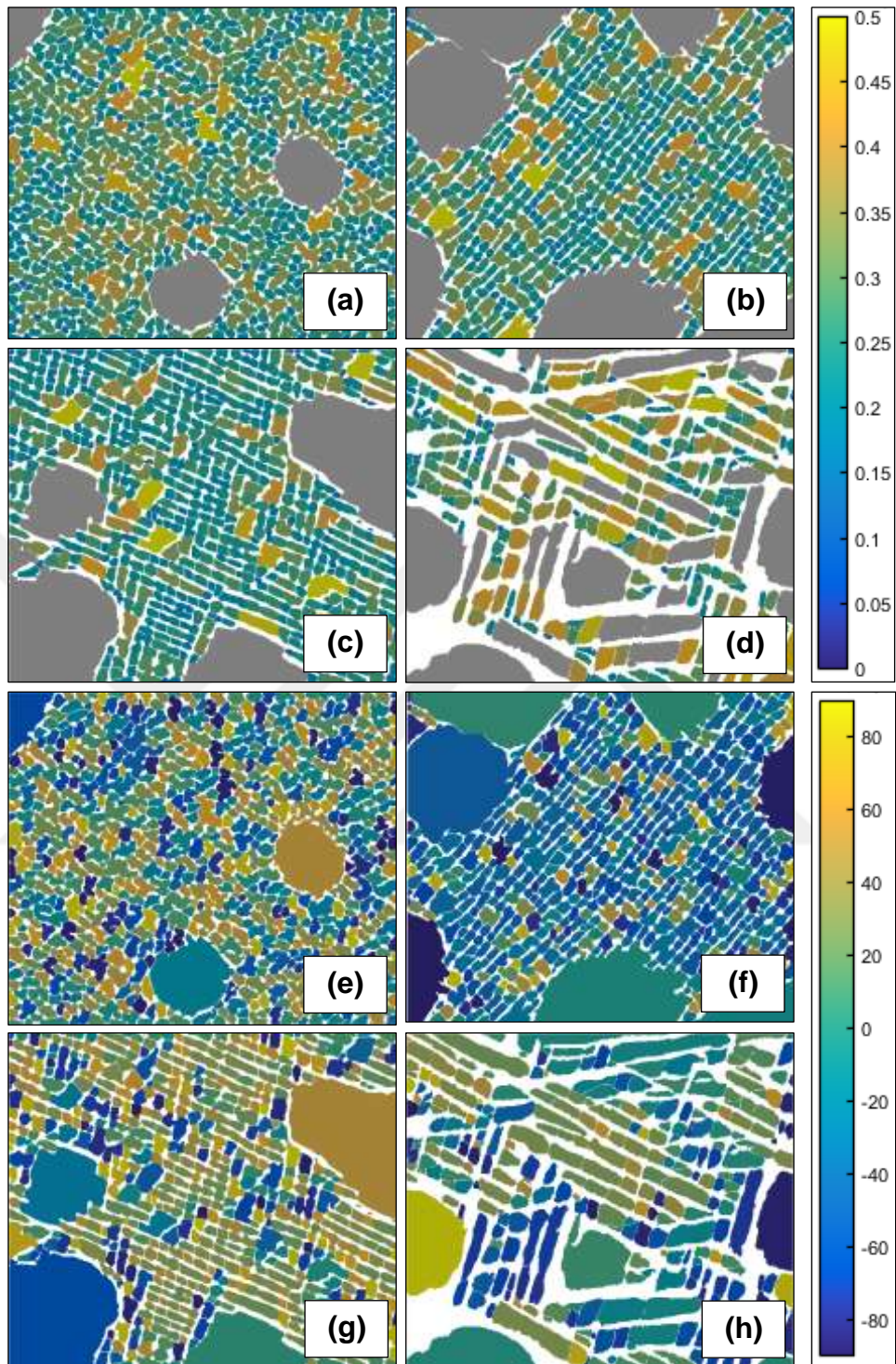


**Figure 5.22** Size & size distribution and orientation of  $\gamma'$  precipitates of the second sample group of  $\text{Ni}_{80}\text{Al}_{20}$  alloys as aging time 800 °C is (a,e) 4 hr, (b,f) 16 hr, (c,g) 64 hr and (d,h) 256 hr, respectively.

fractions of alloys decrease from 0.81 to 0.63. Secondly, as it is given in Figure 5.22(a-d), precipitate sizes increase with increasing aging time. Here, size distribution scale is limited up to 0.5  $\mu\text{m}$ . ( $\gamma'$  precipitates shown in gray colours have bigger sizes than 0.5  $\mu\text{m}$ ). Next, as illustrated in Figure 5.22(e-h), for 4 hr aging time, precipitates are not aligned in order. However, as aging time is increased up to 256 hr, precipitates are mainly aligned in three directions. Here, the orientation scale is coloured from  $-90^\circ$  to  $90^\circ$  relative to the horizontal x axis.

### 5.3.8 Conclusions

In conclusion, as summarized in Table 5.7, with increasing aging time from 4 hr to 256 hr, lattice parameters of  $\gamma'$  precipitates decrease, precipitate volume fractions decrease, precipitate sizes increase and randomly distributed  $\gamma'$  precipitates become aligned in order. As aging time at 800  $^\circ\text{C}$  is increased up to 256 hr, precipitate shapes follow this order: spherical, spheroidal, cuboidal and irregular (elongated). Depending on the variations of afore mentioned microstructural characteristics, micro-hardness values of binary  $\text{Ni}_{80}\text{Al}_{20}$  alloys also decrease. These results imply that micro-hardness values strongly depend on lattice parameter, volume fraction and size of  $\gamma'$  precipitates. In order to have higher strength superalloys, therefore, lattice parameter and volume fraction of  $\gamma'$  precipitates should be increased and increase in precipitate size should be retarded which all lead to an optimum lattice misfit parameter ( $\delta$ ). Due to overlapping problem of  $\gamma$  and  $\gamma'$  phases in XRD technique, in this study, the magnitudes of  $\delta$  parameters could not be calculated. However, it is well known in the literature that  $\delta$  parameter affects shapes of  $\gamma'$  precipitates. When  $\delta = 0$ , precipitates become perfectly spherical and as the magnitude of  $\delta$  parameter increases precipitate shapes evolve in the following order; spheroidal, cuboidal, cubic and irregular (agglomerated and/or elongated). Therefore, at the end of this study, by looking at the shape of  $\gamma'$  precipitates, it can be concluded that elongated shapes observed at higher aging durations are detrimental for the mechanical properties since the magnitudes of  $\delta$  parameters increase too much.

**Table 5.7** Comparison of microstructural characteristics and mechanical properties of Ni<sub>80</sub>Al<sub>20</sub> alloys.

		Ni <sub>80</sub> Al <sub>20</sub> alloys							
Sample groups	Heat treatment		Temperature and durations	Lattice parameter (Å)	V <sub>f</sub>	γ' precipitates		Micro-hardness (Vickers)	
	Definitions					Size (nm)	Orientation		Shape
0	As cast (fast cooled)		-	3.568	0.85	71	NO	Spherical	277.9 ± 4.6
	As cast (slow cooled)		-	3.568	0.88	131	NO	Spherical	263.3 ± 2.5
1	Partial solution heat treatment		1150 °C for 3 hr	3.562	0.88	161	NO	Spherical	233.4 ± 5.1
			800 °C for 4 hr	3.564	0.95	140	NO	Spheroidal	238.9 ± 5.7
	Aging		800 °C for 16 hr	3.559	0.93	167	YES	Cubooidal	236.5 ± 6.1
			800 °C for 64 hr	3.554	0.90	212	YES	Cubooidal	247.1 ± 6.9
			800 °C for 256 hr	3.548	0.88	404	YES	Irregular	239.6 ± 4.2
2	Homogenization and partial solution heat treatment		1250 °C for 24 hr and 1150 °C for 3 hr	3.560	0.84	158	NO	Spherical	226.5 ± 6.2
			800 °C for 4 hr	3.561	0.81	160	NO	Spheroidal	257.6 ± 5.2
	Aging		800 °C for 16 hr	3.559	0.83	192	YES	Spheroidal	261.3 ± 3.7
			800 °C for 64 hr	3.559	0.79	206	YES	Cubooidal	253.3 ± 4.3
		800 °C for 256 hr	3.555	0.63	339	YES	Irregular	242.3 ± 4.9	

**Table 5.7 (Continued).**

Sample groups	Heat treatment		Ni <sub>80</sub> Al <sub>20</sub> alloys						
	Definitions	Temperature and durations	Lattice parameter (Å)	V <sub>f</sub>	Size (nm)	Orientation	Shape	Micro-hardness (Vickers)	
0	As cast (fast cooled)	-	3.568	0.85	71	NO	Spherical	277.9 ± 4.6	
	As cast (slow cooled)	-	3.568	0.88	131	NO	Spherical	263.3 ± 2.5	
3	Primary aging	800 °C for 3 hr	3.564	0.86	91	NO	Spherical	292.6 ± 8.6	
		800 °C for 4 hr	3.563	0.88	114	NO	Spheroidal	280.9 ± 4.5	
	Aging	800 °C for 16 hr	3.563	0.86	139	YES	Spheroidal	280.1 ± 3.4	
		800 °C for 64 hr	3.563	0.85	177	YES	Cuboidal	277.6 ± 3.0	
		800 °C for 256 hr	3.562	0.83	345	YES	Irregular	268.3 ± 7.8	
Homogenization and primary aging	1250 °C for 24 hr and 800 °C for 3 hr	3.560	0.74	73	NO	Spherical	238.3 ± 5.7		
	Aging	800 °C for 4 hr	3.564	0.74	102	NO	Spheroidal	231.4 ± 6.6	
800 °C for 16 hr		3.559	0.68	131	YES	Cuboidal	228.1 ± 8.2		
800 °C for 64 hr		3.557	0.63	189	NO	Irregular	226.5 ± 4.9		
800 °C for 256 hr		3.554	0.58	-	-	-	224.9 ± 6.1		

## 5.4 Characterization of Ni<sub>80</sub>Al<sub>15</sub>X<sub>5</sub> Alloy Systems

After production of samples, phase, thermal, microstructural and mechanical properties of Ni<sub>80</sub>Al<sub>15</sub>X<sub>5</sub> alloy systems have been characterized and discussed in the following parts for X = Co, Cr, Hf, Mo, Nb, Ta, Ti and W additions, respectively.

### 5.4.1 Phase Analysis

When fast cooled as cast samples of ternary Ni<sub>80</sub>Al<sub>15</sub>X<sub>5</sub> alloy systems are heat treated according to Table 5.3, following XRD patterns are obtained (Appendix C). In Appendix C, Figures C.n ( $n = 2k - 1$ ;  $1 \leq k \leq 8$ ;  $k \in \mathbb{N}$ ) show XRD patterns of binary as cast (fast cooled) Ni<sub>80</sub>Al<sub>15</sub>X<sub>5</sub> alloy systems partially-solutionized at 1150 °C for 3 hr, ice-water quenched to RT and subsequently aged at 800 °C for different aging times of 4, 16, 64 and 256 hr and air cooled to RT, respectively. Similarly, in Figures C.n ( $n = 2k$ ;  $1 \leq k \leq 8$ ;  $k \in \mathbb{N}$ ), XRD patterns of the same heat treated Ni<sub>80</sub>Al<sub>15</sub>X<sub>5</sub> alloy systems (exceptionally homogenized at 1250 °C for 24 hr before partial solution heat treatment) are demonstrated.

In Figures C.1-16, Miller indices of the constituent  $\gamma$  and  $\gamma'$  phases are represented in white and black spheres, respectively. White and black sphere pairs which denote to (111), (200), (220), (311), (222) and (400) fundamental peaks confirm the existence of FCC-like  $\gamma$  and  $\gamma'$  phases, while single black spheres refer to super-structure peaks of L1<sub>2</sub>-type ordered  $\gamma'$  precipitates at (100), (110), (210), (211), (221) and (310) indices validate the existence of this phase within the two phase microstructures of Ni<sub>80</sub>Al<sub>15</sub>X<sub>5</sub> alloy systems with  $\gamma$  matrix phase. However, in addition to these two phases, in Ni<sub>80</sub>Al<sub>15</sub>Hf<sub>5</sub> alloys, Ni<sub>5</sub>Hf phase is also present and Miller indices of this phase are shown in white triangles (Figures C.5-6). For other ternary Ni<sub>80</sub>Al<sub>15</sub>X<sub>5</sub> alloy systems (i.e.  $X \neq \text{Hf}$ ), no other phases are present. It is important to note that these phase identifications have been performed by considering isothermal ternary phase diagrams of Ni-Al-X systems demonstrated in Appendix B and EDS results of the constituent phases (to be mentioned later).

#### 5.4.2 Determination of Lattice Parameters of $\gamma'$ Precipitates in $\text{Ni}_{80}\text{Al}_{15}\text{X}_5$ Alloy Systems

By considering XRD patterns of ternary  $\text{Ni}_{80}\text{Al}_{15}\text{X}_5$  alloy systems given in Appendix C, lattice parameters of  $\gamma'$  precipitates have been calculated by applying Bragg's Law and the results have been tabulated in Appendix D. Since the volume fraction of  $\gamma$  matrix phase within the two phase ( $\gamma$ - $\gamma'$ ) microstructures of ternary alloys is very small and lattice parameters of  $\gamma$  and  $\gamma'$  phases are very close to each other, peak overlapping occurs in XRD patterns of these alloy systems. Hence, fundamental peaks refer to  $\gamma$  and  $\gamma'$  phases could not be separated from each other and lattice parameter determination has been carried out only for  $\gamma'$  precipitates which constitute high volume fractions in the microstructures and much more contribute to the formation of fundamental peaks. For Hf addition, lattice parameters of  $\text{Ni}_5\text{Hf}$  phase have been determined and tabulated in Table D.3 which coincide well with the literature [134,135].

#### 5.4.3 Thermal Properties

It is well known that impurity additions in  $\text{L}_{12}$ -type ordered stoichiometric  $\text{Ni}_3\text{Al}$  phase (75 at.% Ni and 25 at.% Al) cause slight changes in its order-disorder transformation temperature. Therefore, depending on type and content of impurity atoms, this phase transformation temperature may slightly increase or decrease in the vicinity of melting temperature of  $\text{Ni}_3\text{Al}$  phase,  $\sim 1375$  °C [1]. For this purpose, DSC measurements have been carried out. Heating/cooling curves of as cast (fast cooled)  $\text{Ni}_{80}\text{Al}_{15}\text{X}_5$  alloy systems at a rate of 20 °C/minutes have been shown in Appendix E and melting/solidification temperatures of these systems have been tabulated in Table 5.8. However, for X = Hf and W additions, melting/solidification temperatures (melting for Hf and both melting and solidification for W additions) could not be obtained since the DSC unit has approached its maximum temperature limit,  $\sim 1450$  °C. However, as it is shown in Figures E.3,8, melting/solidification temperatures of  $\text{Ni}_{80}\text{Al}_{15}\text{Hf}_5$  and  $\text{Ni}_{80}\text{Al}_{15}\text{W}_5$  alloy systems are greater than the ones obtained for binary  $\text{Ni}_{80}\text{Al}_{20}$  alloy.

For the rest of alloying X elements, as it is evident in Appendix E, 5 at.% additions of X = Co and Mo increase melting/solidification temperatures of binary Ni<sub>80</sub>Al<sub>20</sub> alloy, whereas X = Nb, Ta and Ti additions make these temperatures lower. For X = Cr addition, it seems that there is no any dramatic change with respect to binary alloy (when 5 at.% Cr is added, melting temperature slightly increases, whereas solidification temperature slightly decreases).

As demonstrated in Figures E.3,5,7, for X = Hf, Nb and Ti additions, some secondary peaks (shown by down arrows) are visible adjacent to the primary peaks. For Hf addition, the secondary peak refers to eutectic phase transformation, whereas for X = Nb and Ti additions, the existence of these peaks imply that peritectic reactions have occurred in both Ni<sub>80</sub>Al<sub>15</sub>Nb<sub>5</sub> and Ni<sub>80</sub>Al<sub>15</sub>Ti<sub>5</sub> alloy systems. In order to identify these secondary peaks, FESEM investigations of afore mentioned alloy systems have been performed which also validate the current estimations. Similarly, single (primary) peaks of ternary Ni<sub>80</sub>Al<sub>15</sub>X<sub>5</sub> alloy systems (X ≠ Hf, Nb and Ti) explain that solidification occurs without eutectic and/or peritectic reactions that is also verified by FESEM micrographs of as cast Ni<sub>80</sub>Al<sub>15</sub>X<sub>5</sub> alloy systems, Figure 5.23. However, in these peaks additional phase transformations (i.e. order-disorder transformations of  $\gamma'$  precipitates) may be present as in the case of Ni<sub>80</sub>Al<sub>20</sub> alloy.

One of the alloy design considerations in nickel-based superalloys is the determination of  $\gamma$ - $\gamma'$ / $\gamma$  phase transformation (solvus) temperatures. It is known that alloying elements increasing solvus temperature lead to better creep properties since  $\gamma'$  precipitates will start to dissolve in  $\gamma$  matrix phase at higher temperatures (above solvus temperatures). In DSC plots, depending on alloy compositions, solvus phase transformations appear as small endothermic/exothermic peaks in heating/cooling curves. However, in the current study, for both binary Ni<sub>80</sub>Al<sub>20</sub> and ternary Ni<sub>80</sub>Al<sub>15</sub>X<sub>5</sub> alloy systems, these peaks have not been observed (X ≠ Hf and W). As it is evident in equilibrium phase diagram of binary Ni-Al system (Appendix A), binary alloy composition (80 at.% Ni and 20 at.% Al) does not intersect with solvus transformation temperatures at any temperature level. Similarly, additions of very low content impurity X atoms in 5 at.%

would be attributed to not lead to solvus phase transformations to occur. However, as demonstrated by star marks in Figures E.3,8, for X = Hf and W additions small endothermic/exothermic peaks appear at ~ 1210 °C and ~ 1100 °C, respectively. These peaks may refer to solvus temperatures, but it should be noted that any other phase transformations may also become possible. Hence, by considering FESEM micrographs of these alloy systems, identification of these peaks will be carried out in the following parts.

**Table 5.8** Melting/solidification temperatures of heating/cooling curves of as cast (fast cooled) Ni<sub>80</sub>Al<sub>15</sub>X<sub>5</sub> alloy systems where X = Al, Co, Cr, Hf, Mo, Nb, Ta, Ti and W, respectively.

Alloy systems	Melting/solidification temperatures (°C)	
	Heating	Cooling
Ni <sub>80</sub> Al <sub>20</sub>	1388	1402
Ni <sub>80</sub> Al <sub>15</sub> Co <sub>5</sub>	1417	1411
Ni <sub>80</sub> Al <sub>15</sub> Cr <sub>5</sub>	1399	1393
Ni <sub>80</sub> Al <sub>15</sub> Hf <sub>5</sub>	-	1403
Ni <sub>80</sub> Al <sub>15</sub> Mo <sub>5</sub>	1397	1412
Ni <sub>80</sub> Al <sub>15</sub> Nb <sub>5</sub>	1335	1377
Ni <sub>80</sub> Al <sub>15</sub> Ta <sub>5</sub>	1390	1379
Ni <sub>80</sub> Al <sub>15</sub> Ti <sub>5</sub>	1365	1376
Ni <sub>80</sub> Al <sub>15</sub> W <sub>5</sub>	-	-

Since solvus peaks are not visible in DSC plots of most of the Ni<sub>80</sub>Al<sub>15</sub>X<sub>5</sub> alloy systems (Appendix E), firstly, temperature level of solution heat treatment, above which  $\gamma'$  precipitates are aimed to be totally dissolved in  $\gamma$  matrix phase prior to aging, could not be decided. However, in the literature [48,103], for some nickel-based superalloy compositions, solution heat treatment procedures have been carried out at 1150-1200 °C for 30 minutes-48 hr. Therefore, as will be mentioned in the next part, these heat



treatment procedures have been performed at 1150 °C for 3 hr under the name of “partial solution heat treatment”.

#### **5.4.4 Microstructural Investigation**

Microstructural characteristics of as cast and heat treated  $\text{Ni}_{80}\text{Al}_{15}\text{X}_5$  alloy systems ( $\gamma'$  precipitate volume fraction, size & size distribution, orientation and shape) have been investigated by performing field emission scanning electron microscopy analyses (Appendix F). In order to examine the effects of homogenization heat treatment and aging durations, ternary as cast (fast cooled)  $\text{Ni}_{80}\text{Al}_{15}\text{X}_5$  alloy systems have been exposed to two different heat treatment procedures. The first set of samples of  $\text{Ni}_{80}\text{Al}_{15}\text{X}_5$  alloy systems have been partially-solutionized at 1150 °C for 3 hr, ice-water quenched to RT and subsequently aged at 800 °C for different aging times of 4, 16, 64 and 256 hr and air cooled to RT, respectively. Next, the second set of samples have been treated to homogenization heat treatment at 1250 °C for 24 hr before partial solution heat treatment and subsequent aging at 800 °C for the same aging durations.

##### **5.4.4.1 As Cast Microstructures**

Because of rapid solidification, general microstructures of as cast (fast cooled)  $\text{Ni}_{80}\text{Al}_{15}\text{X}_5$  alloy systems consist of different forms of dendrites (Figures 5.23). For  $X = \text{Co}$  and  $\text{Cr}$  additions, some dendrites are still visible at the interior regions of elongated grains. However, for  $X = \text{Hf}$  addition, the general microstructure consists of bigger dendrites whose secondary arms fill the regions between eutectic phase mixture. In this case, existence of eutectic phase regions within as cast microstructure helps the identification of the secondary peak observed in Figure E.3 as eutectic phase transformation. Next, for  $X = \text{Mo}$  addition, even if dendrites turn into small grains, their existence is still visible. For  $X = \text{Nb}$ ,  $\text{Ta}$  and  $\text{Ti}$  additions, dendritic characteristics of the general microstructures are so clear. For instance, in case of  $\text{Nb}$  addition, 3D dendrites can be seen in Figure 5.24(a). For  $\text{Nb}$  and  $\text{Ti}$  additions, as it is evident from Figure 5.24(b) and Figure 5.25(a), some traces of peritectic reactions are observed.

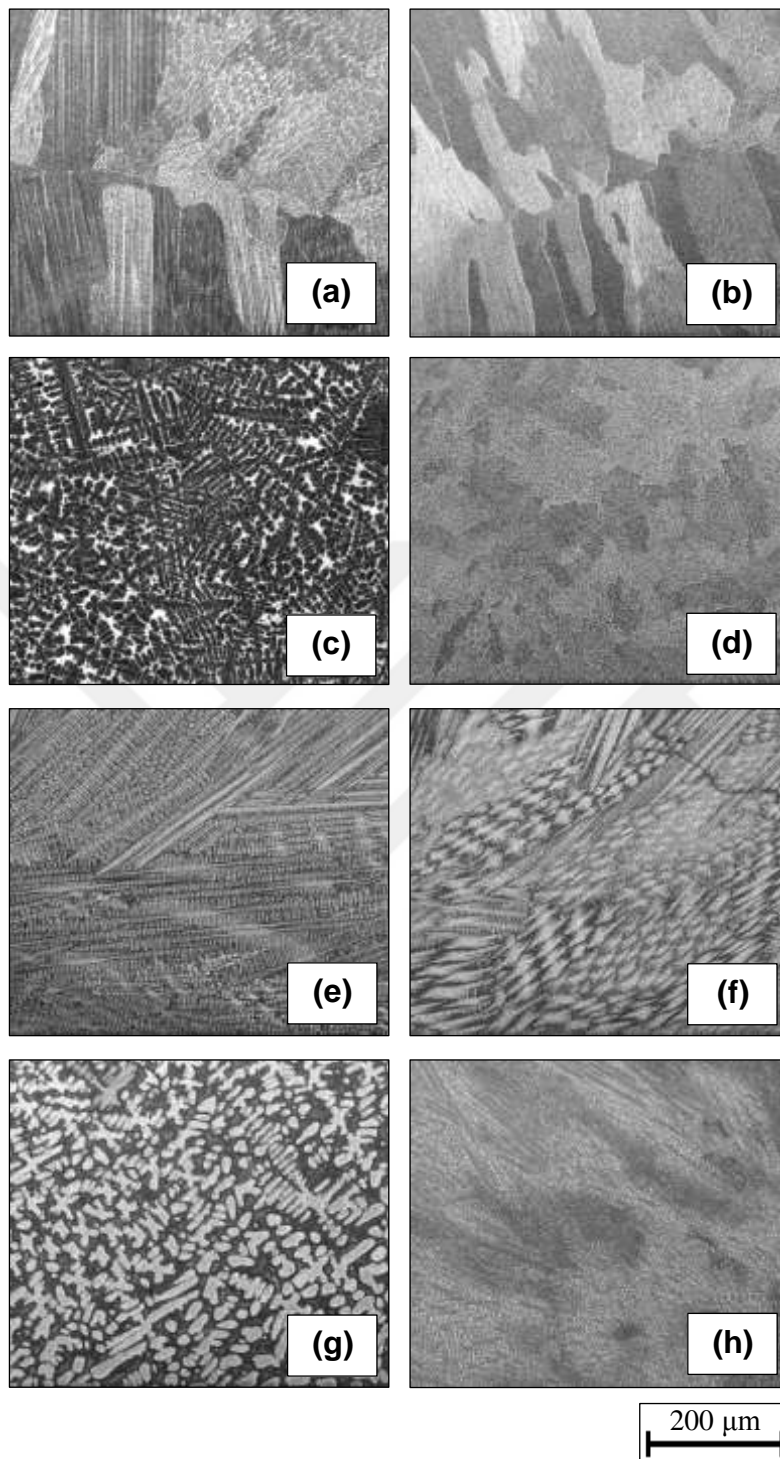


**Figure 5.23** FESEM micrographs showing as cast (fast cooled) microstructures of ternary  $\text{Ni}_{80}\text{Al}_{15}\text{X}_5$  alloy systems where X = (a) Co, (b) Cr, (c) Hf, (d) Mo, (e) Nb, (f) Ta, (g) Ti and (h) W, respectively.

Hence, the existence of these peritectic phases helps the identification of the secondary peaks appear in Figures E.5,7 which refer to peritectic phase transformations. Lastly, For X = W addition, similar to Mo addition, dendrites appear in small grains.

In the light of ternary phase diagrams of Ni-Al-X systems (Appendix B), XRD patterns (Appendix C) and EDS phase analyses (Appendix G), phase identifications have been carried out in FESEM micrographs of as cast Ni<sub>80</sub>Al<sub>15</sub>X<sub>5</sub> alloy systems. For X = Co, Cr, Mo, Ta and W additions, dendritic regions seem to be super-saturated phase mixture of  $\gamma + \gamma'$  phases, whereas interdendritic areas consist of only  $\gamma'$  phases. In case of X = Hf addition, pro regions consist of single  $\gamma'$  phase, Figure 5.26. As it is evident in Figure 5.26(a),  $\gamma'$  precipitates are visible at the pro region-eutectic phase region interfaces. In eutectic phase regions, there are two phases;  $\gamma$  phase (white regions) and Ni<sub>5</sub>Hf phase (black regions), revealing different eutectic phase morphologies: (a,b) lamellar, (c,d,e) rod-like and (f) feathery-like, respectively. For X = Nb addition, peritectic phases are identified in Figure 5.24(c). In ( $\gamma + \gamma'$ ) phase region, narrow channels (black regions) reveal  $\gamma$  matrix phase separating  $\gamma'$  precipitates. However, in the inner regions of single  $\gamma'$  phase, colour becomes lighter. Hence, in these regions, local EDS measurements have been performed. According to the results, Nb atoms seem to segregate in this region (~ 19 at.% Nb). Nb segregation has been further confirmed by BSE micrograph of the same area. In Figure 5.24(d), these regions appear in white colours due to their high amount of Nb content whose atomic mass is much bigger than both Ni and Al. Lastly, for Ti addition, similar to the previous phase characteristics, peritectic phases are visible in Figure 5.25. For as cast Ni<sub>80</sub>Al<sub>15</sub>Ti<sub>5</sub> alloy, Ti segregation (~ 9 at.% Ti) has been detected in peritectic trace regions. This smaller segregation amount of Ti atoms can be attributed to its smaller atomic size with respect to Nb atoms. Another interesting outcome to be drawn from Figure 5.25 is that solidification sequence during peritectic reaction leads to bigger faceted  $\gamma'$  precipitates at  $\gamma'/(\gamma + \gamma')$  interfaces (Figure 5.25(c)) and smaller faceted  $\gamma'$  precipitates in ( $\gamma + \gamma'$ ) phase region (Figure 5.25(d)).

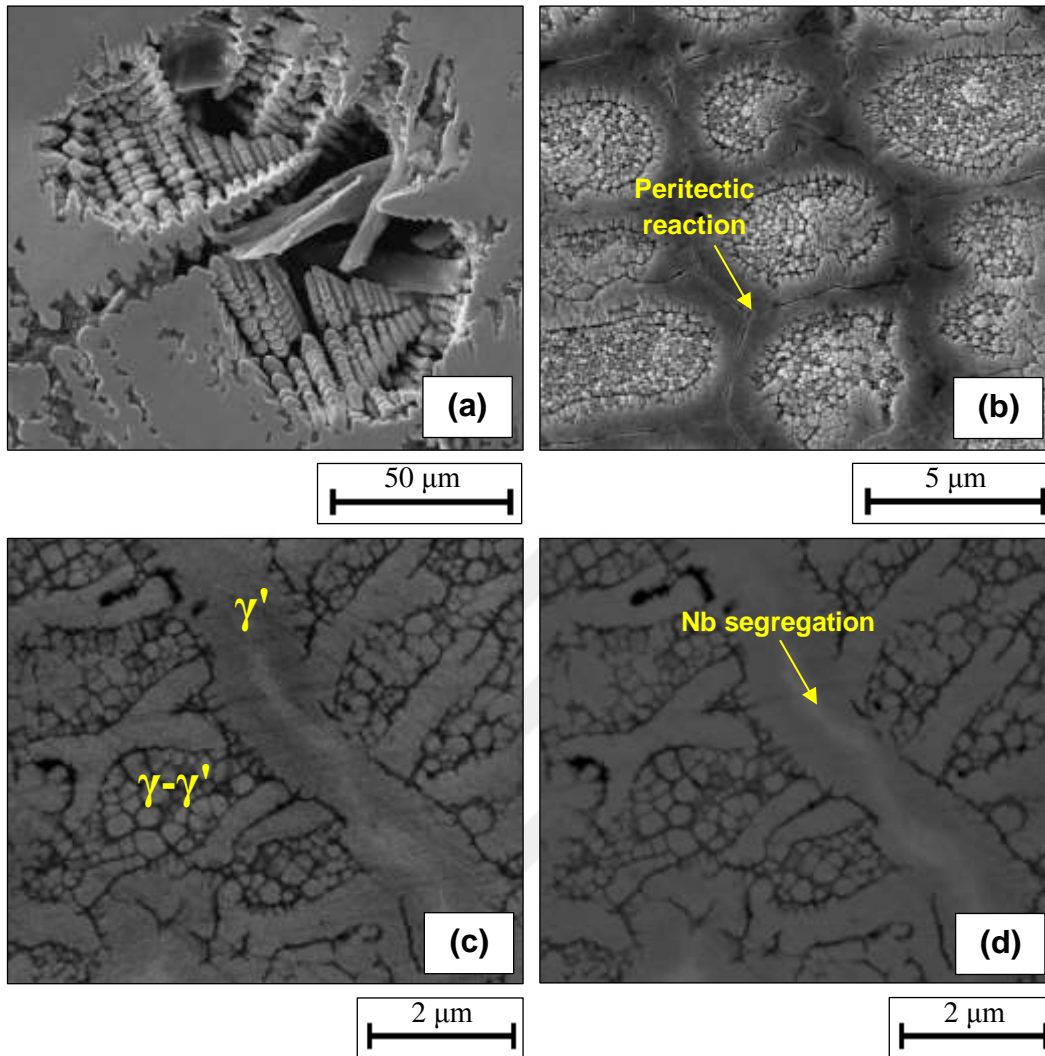


**Figure 5.24** FESEM micrographs of as cast (fast cooled)  $\text{Ni}_{80}\text{Al}_{15}\text{Nb}_5$  alloys showing (a) 3D dendrites, (b) the traces of a peritectic reaction, (c) SEI and (d) BSE micrographs demonstrating peritectic phases and Nb segregation in single  $\gamma'$  phase.

To sum up, microstructural characteristics of as cast  $\text{Ni}_{80}\text{Al}_{15}\text{X}_5$  alloy systems seem to vary with small amount of impurity X element additions (5 at.%). Alloying element additions, such as  $\text{X} = \text{Co}, \text{Cr}, \text{Mo}$  and  $\text{W}$  lead to as cast microstructures of the related alloy systems to reveal in grainy-dendritic characteristics. In these cases, dendrites either lose their original shapes/become more grainy or they appear in grains. On the other hand, in as cast  $\text{Ni}_{80}\text{Al}_{15}\text{X}_5$  alloy systems (where  $\text{X} = \text{Nb}, \text{Ta}$  and  $\text{Ti}$ ), dendritic

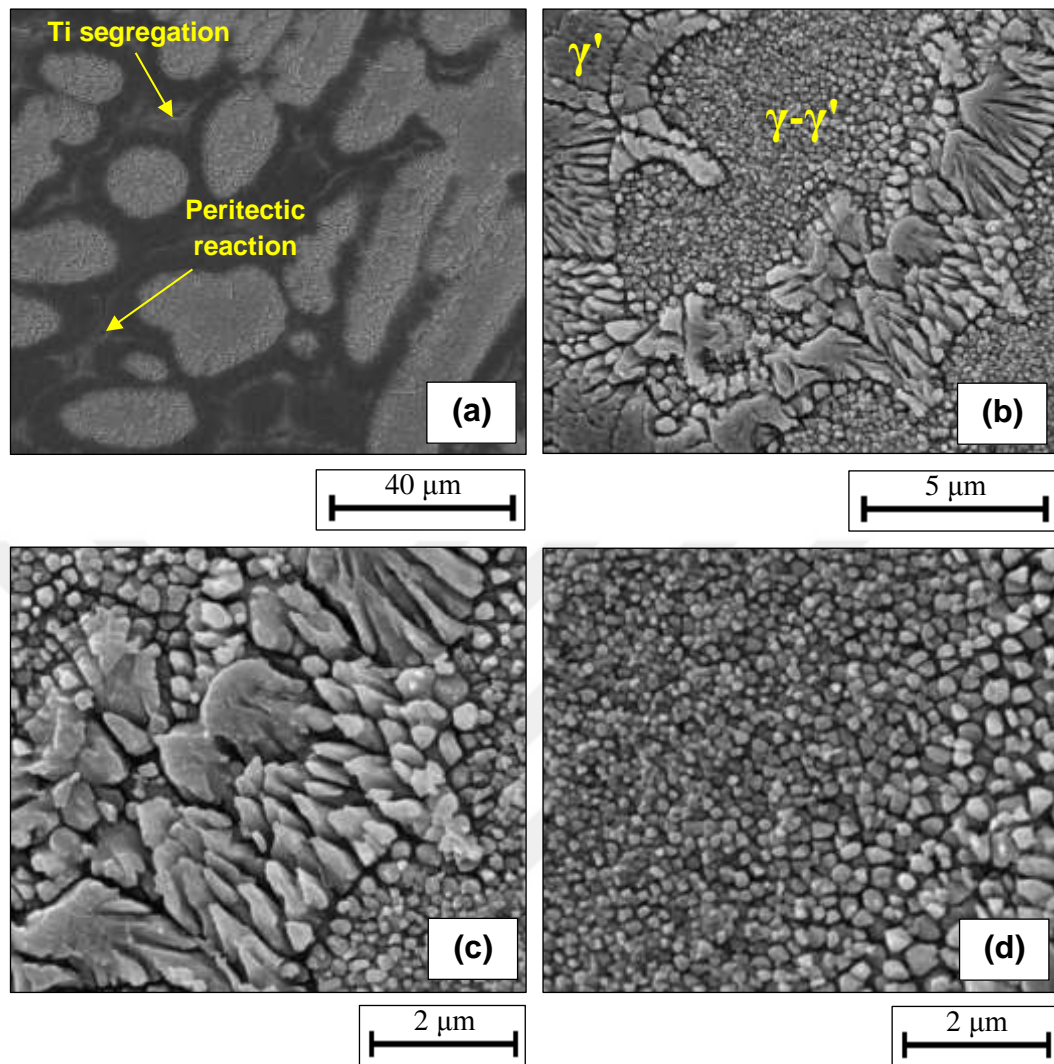


**Figure 5.25** FESEM micrographs of as cast (fast cooled)  $\text{Ni}_{80}\text{Al}_{15}\text{Ti}_5$  alloys showing (a) the traces of a peritectic reaction, (b) peritectic phases (c) bigger and (d) smaller faceted  $\gamma'$  precipitates around and in  $(\gamma + \gamma')$  phase regions, respectively.

characteristics of the microstructures are still dominant similar to the binary as cast  $\text{Ni}_{80}\text{Al}_{20}$  alloy whose as cast microstructural characteristics have been previously mentioned. For  $X = \text{Hf}$  addition, it seems that secondary arms of dendrites lead to pro regions to occur between eutectic phases. Therefore, for each alloying  $X$  element addition, by considering these as cast microstructural characteristics and melting/solidification temperatures determined in the previous part, it is anticipated that 5 at.% additions of  $X = \text{Co}, \text{Cr}, \text{Hf}, \text{Mo}$  and  $\text{W}$  atoms shift the composition of

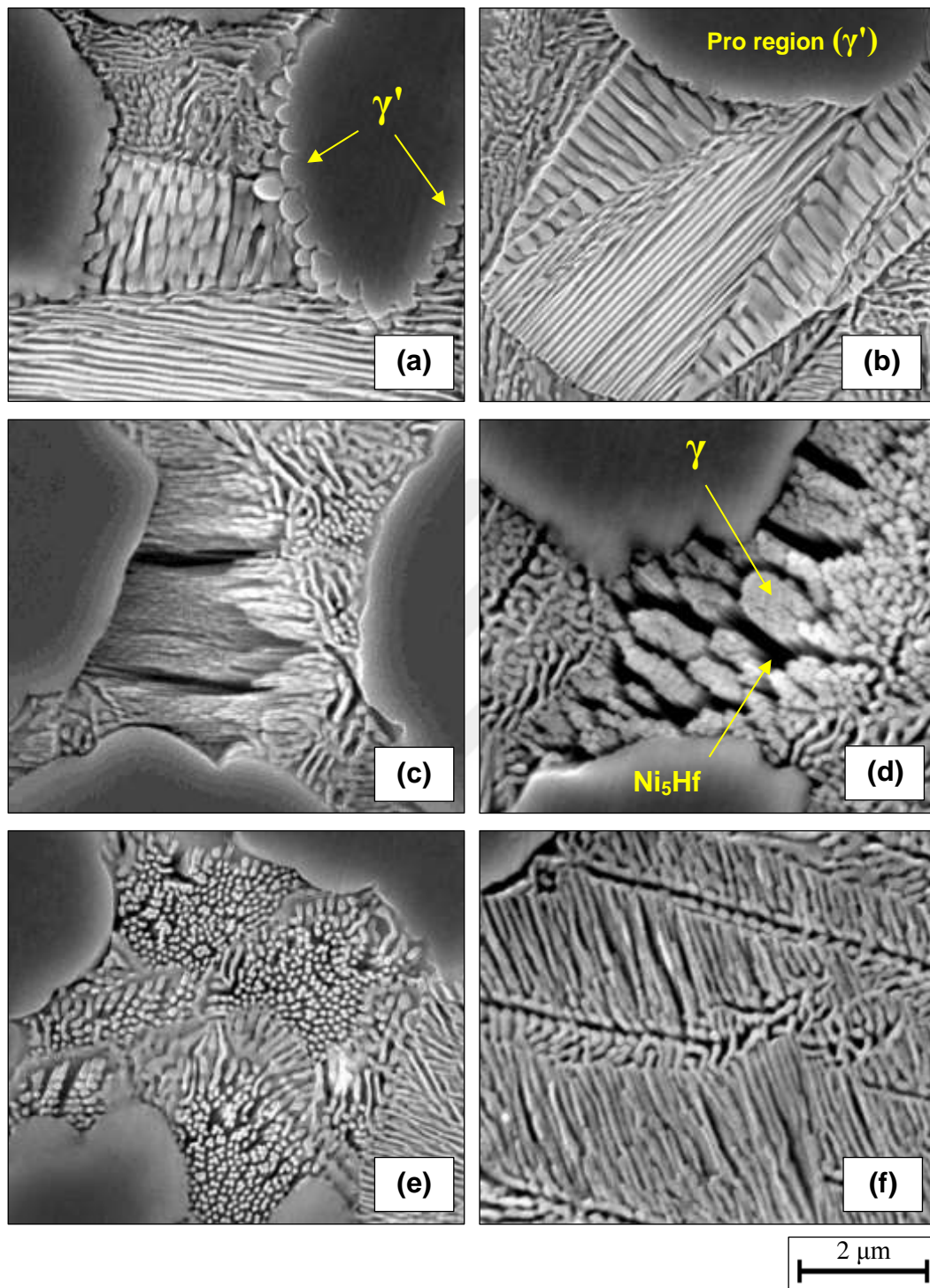


**Figure 5.26** FESEM micrographs showing different eutectic morphologies of as cast (fast cooled)  $\text{Ni}_{80}\text{Al}_{15}\text{Hf}_5$  alloys: (a,b) lamellar, (c,d,e) rod-like and (f) feathery-like.

Ni<sub>80</sub>Al<sub>20</sub> alloy to the Ni-rich side of binary Ni-Al phase diagram (Appendix A) and lead to grainy-dendritic as cast microstructures, whereas 5 at.% additions of X = Nb, Ta and Ti atoms cause this shift to the Al-rich side and lead to pure dendritic as cast microstructures.

It is well known in the literature that alloying elements, such as X = Co, Cr, Mo and W tend to participate into  $\gamma$  matrix phase, whereas X = Nb, Ta and Ti preferentially participate into  $\gamma'$  precipitates. Therefore, in this study, it is introduced that alloying X elements shifting the composition of Ni<sub>80</sub>Al<sub>20</sub> alloy system to the Ni-rich side of Ni-Al phase diagram and correspondingly reducing the fraction of  $\gamma'$  precipitates (according to Lever rule) are  $\gamma$ -former elements (e.g. Co, Cr, Mo and W), whereas alloying X elements causing this shift to the Al-rich side and correspondingly increasing the fraction of  $\gamma'$  precipitates are  $\gamma'$ -former elements (e.g. Nb, Ta and Ti). Furthermore, partitioning coefficients of afore mentioned alloying elements (which will be mentioned in the following parts) also confirm these predictions. As previously mentioned, in literature, phase preference of Hf atoms is still questionable; APT investigations have claimed that Hf atoms prefer to be enriched in  $\gamma$  matrix phase, while first-principles calculations have suggested that Hf atoms prefer  $\gamma'$  precipitates to be involved in [82,83]. Similarly, by looking at DSC heating and cooling plots of Ni<sub>80</sub>Al<sub>15</sub>Hf<sub>5</sub> alloy and comparing melting/solidification temperatures of this alloy with respect to binary system, it is possible to suggest that Hf preferentially participate into  $\gamma$  matrix phase. However, by considering partitioning coefficient of Hf atoms it is possible to suggest that Hf atoms are more likely to participate into  $\gamma'$  precipitates. It is anticipated that formation of additional phases (i.e. Ni<sub>5</sub>Hf) in as cast microstructure of Ni<sub>80</sub>Al<sub>15</sub>Hf<sub>5</sub> alloy affect this phase preference discrepancy of Hf atoms. Since Hf atoms participate into both  $\gamma$  matrix phase and Ni<sub>5</sub>Hf phase in eutectic phase mixture region, partitioning coefficient of this element may become greater than unity, namely, it seems to prefer  $\gamma'$  precipitates. If additional Ni<sub>5</sub>Hf phase would not occur, partitioning coefficient of Hf would be smaller than unity and it would tend to participate into  $\gamma$  matrix phase as it is expected from its afore mentioned “shift” behaviour.

Another interesting conclusion to be drawn from this study is that when X = Nb, Ta and Ti added as cast  $\text{Ni}_{80}\text{Al}_{15}\text{X}_5$  alloy systems are compared within themselves, all of them lead to dendritic microstructures. In case of X = Ta addition, there is no eutectic- or peritectic-type reactions. However, for X = Nb and Ti additions, peritectic reactions occur subsequent to initial solidifications. As it is evident from Figures 5.24,25, peritectic character of as cast  $\text{Ni}_{80}\text{Al}_{15}\text{Nb}_5$  alloy is more obvious than as cast  $\text{Ni}_{80}\text{Al}_{15}\text{Ti}_5$  alloy. Interestingly, melting/solidification temperatures of these alloys follow this order; Ta > Ti > Nb (from higher to lower). Therefore, it is interpreted that alloying elements (i.e. Nb and Ti) lead to significant shifts of the composition of  $\text{Ni}_{80}\text{Al}_{20}$  alloy system to the Al-rich side in binary Ni-Al phase diagram cause peritectic phases to appear within the microstructures. This suggestion is also supported by Ni-Al phase diagram which has a peritectic reaction at  $\sim 1395$  °C (Appendix A).

#### **5.4.4.2 Pre-aged Microstructures**

Prior to aging at 800 °C, ternary as cast (fast cooled)  $\text{Ni}_{80}\text{Al}_{15}\text{X}_5$  alloy systems have been exposed to different pre-aging heat treatments. The first set of samples have been partially-solutionized at 1150 °C for 3 hr, whereas the second set of samples have been firstly homogenized at 1250 °C for 24 hr and then partially-solutionized at 1150 °C for 3 hr. The purpose of this procedure is to realize the effects of homogenization heat treatment on as cast microstructures of these alloys. FESEM micrographs of afore mentioned heat treated  $\text{Ni}_{80}\text{Al}_{15}\text{X}_5$  alloy systems are demonstrated in Appendix F. As it is evident in the micrographs, for X = Co, Cr and Mo additions, afore mentioned heat treatment procedures cause their microstructures to consist of grains. In these grains, dendrites are no longer visible. In case of X = Hf addition, big dendrites of as cast microstructure turn into grains, Figure 5.27. However, without homogenization heat treatment, these grains are small and some of them (darker ones) are  $\gamma$  matrix phase and the others (gray ones) are  $\gamma'$  phase. On the other hand, when homogenization is applied at 1250 °C, grains compose of only  $\gamma$  matrix phase and due to higher heat treatment temperature level (for a long time), grain sizes are much bigger than the ones in the previous case. Hence, the small endothermic peak appear in heating curve of



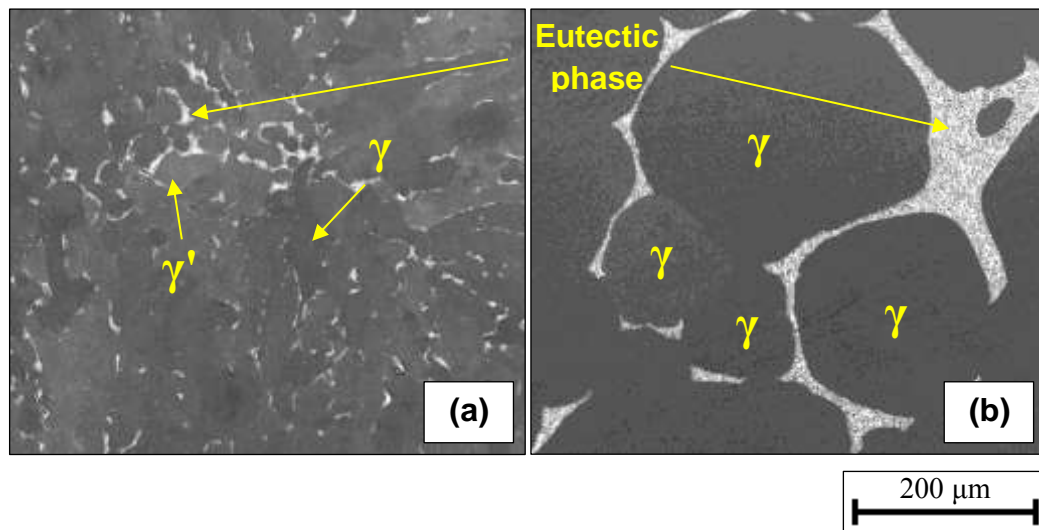


**Figure 5.27** FESEM micrographs showing (a) partially-solution heat treated (at 1150 °C for 3 hr) and (b) homogenized and partially-solution heat treated (at 1250 °C for 24 hr and 1150 °C for 3 hr) microstructures of  $\text{Ni}_{80}\text{Al}_{15}\text{Hf}_5$  alloys.

as cast  $\text{Ni}_{80}\text{Al}_{15}\text{Hf}_5$  alloy at about 1210 °C most probably refer to a “solvus” transformation. Because, as it is evident in Figure 5.27, when as cast  $\text{Ni}_{80}\text{Al}_{15}\text{Hf}_5$  alloy (whose pro region is  $\gamma'$  phase) is exposed to the first heat treatment procedure at 1150 °C for 3 hr, since this temperature level is below solvus, some of the pro  $\gamma'$  phase regions partially turn into  $\gamma$  matrix phase. On the other hand, for the latter case, since homogenization temperature is slightly higher than solvus, each pro  $\gamma'$  phase region transforms into single  $\gamma$  matrix phase. Therefore, this solvus peak also explains previously mentioned “shift” phenomenon. For  $X = \text{Hf}$  addition, the “shift” into Ni-rich direction is too much to allow solvus peak to appear. For other  $X$  element additions, since their shifts along Ni-rich direction are not too much or their shifts are into the Al-rich direction, solvus peaks do not appear in DSC plots of these alloy systems. For  $X = \text{Nb}$ , Ta and Ti additions, the former heat treatment procedure leads to dendritic microstructures of these alloy systems (similar to their as cast counterparts), whereas the latter one causes dendrites turn into grains. However, for  $X = \text{Ta}$  addition, homogenization heat treatment does not result in homogeneous (either dendrites or grains) microstructure. As it is evident in Figure 5.28 that both dendrites

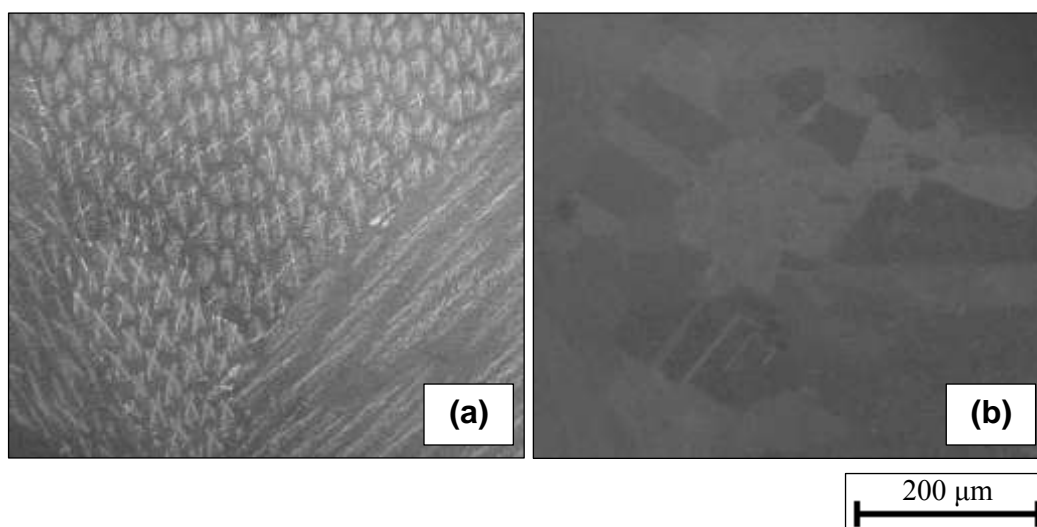


**Figure 5.28** FESEM micrographs showing homogenized and partially-solution heat treated (at 1250 °C for 24 hr and 1150 °C for 3 hr) microstructures of  $\text{Ni}_{80}\text{Al}_{15}\text{Ta}_5$  alloys containing both (a) dendritic regions and (b) grains within the same sample.

and grains are visible in different regions of  $\text{Ni}_{80}\text{Al}_{15}\text{Ta}_5$  alloy for the latter heat treatment. This result may be originated from solidification characteristics of this alloy having different cooling rates in different regions of the sample. Lastly, for  $X = \text{W}$  addition, without homogenization dendritic microstructure becomes dominant. However, when homogenization heat treatment is applied at 1250 °C for 24 hr, extremely reactive W and Al atoms at high temperatures lead to formation of oxide particles. Therefore, for  $X = \text{W}$  addition, clear FESEM micrographs for the latter case could not be obtained. It should be noted that, in NOVALAB, homogenization heat treatment of the samples could be performed in argon atmosphere in quartz tubes. However, due to requirement of ice-water quenching after this heat treatment, this heat treatment has been done under open atmosphere which enables a quick cooling rate.

#### 5.4.4.3 Aged Microstructures

Subsequent to pre-aging heat treatment procedures, ternary  $\text{Ni}_{80}\text{Al}_{15}\text{X}_5$  alloy systems have been exposed to aging at 800 °C for different aging times; 4, 16, 64 and 256 hr. The main reason to select these different aging durations is to observe temporal

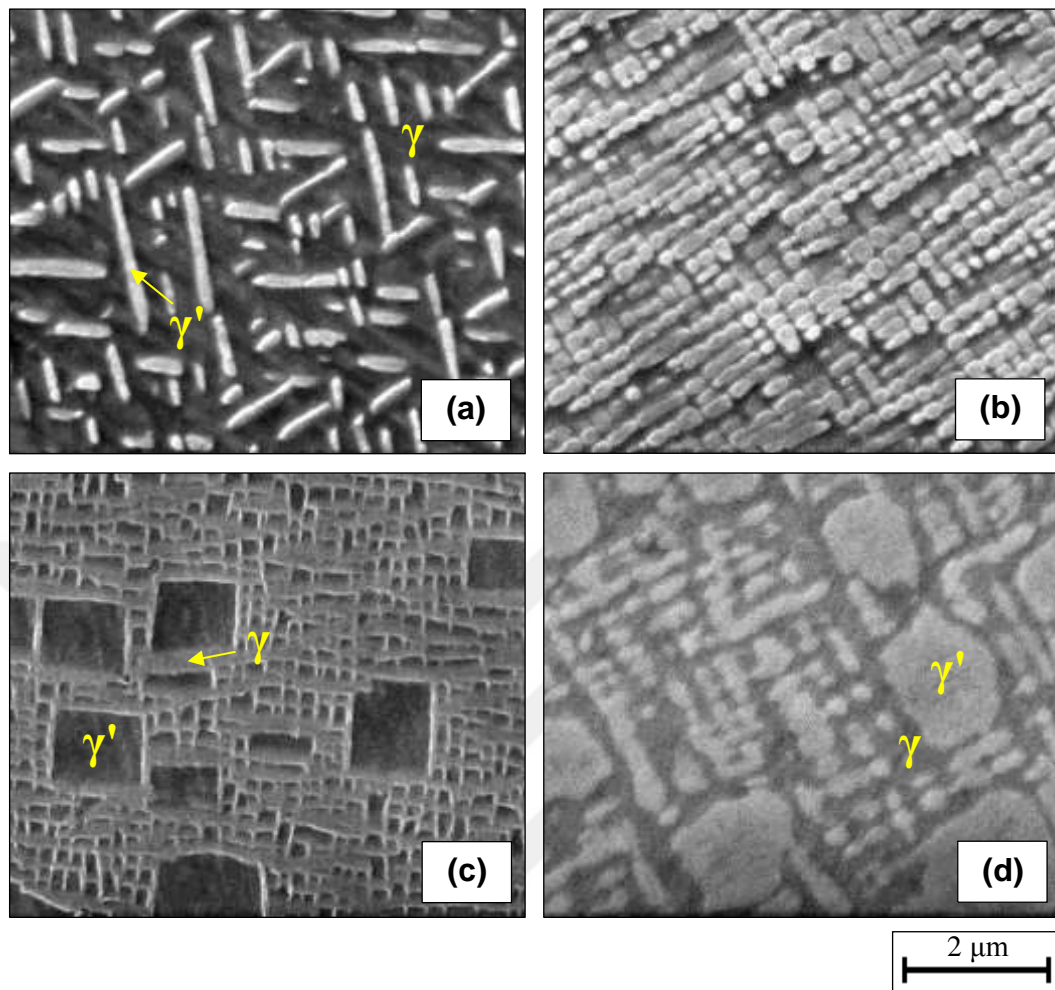


**Figure 5.29** FESEM micrographs showing homogenized and partial solution heat treated (at 1250 °C for 24 hr and 1150 °C for 3 hr) and aged (at 800 °C for 256 hr) microstructures of  $\text{Ni}_{80}\text{Al}_{15}\text{X}_5$  alloy systems where X = (a) Co, (b) Cr, (c) Mo and (d) Nb, respectively.

evolution of  $\gamma'$  precipitates. FESEM micrographs of  $\text{Ni}_{80}\text{Al}_{15}\text{X}_5$  alloy systems aged at 800 °C are demonstrated in Appendix F. As it is evident in the micrographs, type of alloying X elements and different aging durations lead to distinct  $\gamma'$  precipitate volume fractions, size & size distributions, orientations and shapes. For instance, when the second sample groups of  $\text{Ni}_{80}\text{Al}_{15}\text{X}_5$  alloy systems (where X = Co, Cr, Mo and Nb, respectively) are homogenized, partially-solutionized and subsequently aged at 800 °C for 256 h, FESEM micrographs represented in Figure 5.29 are obtained. As shown in

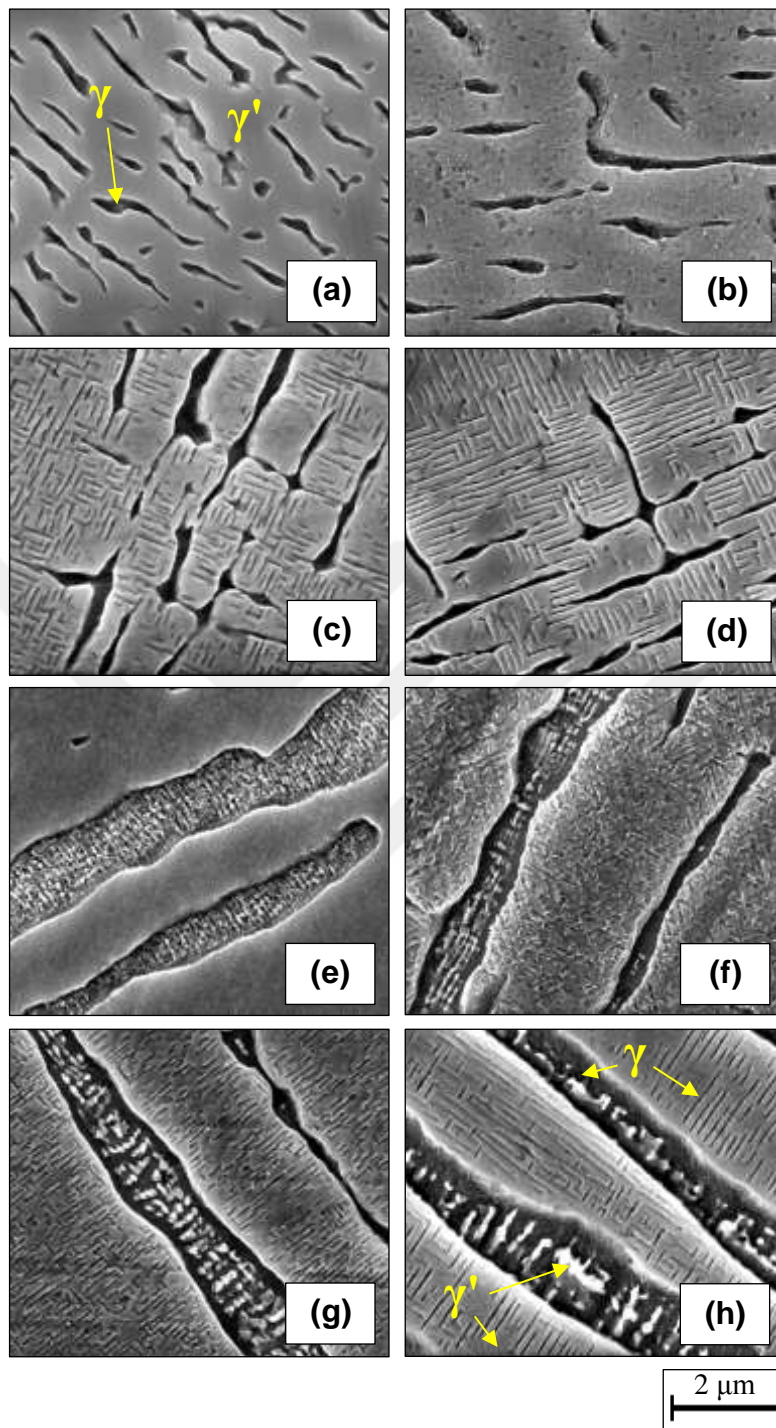


**Figure 5.30** FESEM micrographs showing  $\text{Ni}_{80}\text{Al}_{15}\text{Ta}_5$  alloys aged at 800 °C for (a,e) 4 hr, (b,f) 16 hr, (c,g) 64 hr and (d,h) 256 hr subsequent to either (a-d) partial solution heat treatment (at 1150 °C for 3 hr) or (e-h) homogenization and partial solution heat treatment (at 1250 °C for 24 hr and 1150 °C for 3 hr), respectively.

Figure 5.29, it seems that even if all heat treatment parameters are the same, each distinct type of alloying X elements leads to dramatic variations in afore mentioned microstructural characteristics. When the  $\gamma'$  precipitate volume fractions are compared, following order is obtained: Cr (= 0.69) > Nb (= 0.68) > Mo (= 0.60) > Co (= 0.25). When the alloy systems are compared in terms of size & size distribution, it is noticed that Cr addition leads to more uniform  $\gamma'$  precipitates in size, followed by Co addition. However, for X = Mo and Nb additions,  $\gamma'$  precipitates appear in bimodal (bigger and smaller) size distribution. Orientation characteristics of these alloying X element additions are also different; Co addition causes  $\gamma'$  precipitates to become aligned in three specific directions, whereas  $\gamma'$  precipitates align in only one direction for Cr addition. For X = Mo and Nb additions, even if orientation directions are not clear, their  $\gamma'$  precipitates seem to be aligned in one direction. Lastly,  $\gamma'$  precipitate shapes of these alloy systems are totally different from each other. It is obvious in Figure 5.29 that X = Co, Cr, Mo and Nb additions lead to elongated, cuboidal, cubic and irregular (agglomerated/elongated) shaped  $\gamma'$  precipitates, respectively.

In addition to type of alloying X elements, some variations in heat treatment procedures also affect microstructural characteristics. For this purpose, for X = Ta addition, effects of homogenization heat treatment and aging durations ( up to 256 hr) have been examined. As it is clear in Figure 5.30, without homogenization, size of  $\gamma$  matrix phase regions are small and these regions do not involve  $\gamma'$  precipitates. On the other hand, when homogenization is applied,  $\gamma$  matrix phase regions become larger and filled with  $\gamma'$  precipitates. Secondly, as indicated in Figure 5.30(a,e), for 4 hr aging time, there is no any other phase in  $\gamma'$  phase region. For 16 hr aging time, for both cases,  $\gamma$  matrix phase starts to nucleate in  $\gamma'$  phase region and evolve in labyrinth-like shapes for longer aging times (i.e. 64 and 256 hr). Lastly, afore mentioned microstructural characteristics of  $\gamma'$  precipitates within  $\gamma$  matrix phase change with increasing aging time (Figure 5.30(e,h)). As aging time is approached to 256 hr, volume fraction of  $\gamma'$  precipitates decrease, precipitate sizes increase, randomly distributed  $\gamma'$  precipitates become aligned and precipitate shapes become irregular (agglomerated/elongated) as observed for other alloy systems as well (Appendix F).

In conclusion, microstructural characteristics of  $\text{Ni}_{80}\text{Al}_{15}\text{X}_5$  alloy systems (where X = Co, Cr, Hf, Mo, Nb, Ta, Ti and W, respectively) strongly depend on both type of alloying X elements and aging durations. Depending on their phase preferences ( $\gamma$  and/or  $\gamma'$ ), site preferences in  $\gamma'$  precipitates (Al and/or Ni), atomic radius and correspondingly effects on lattice misfit parameter ( $\delta$ ), each distinct alloying X element leads to different  $\gamma'$  precipitate volume fractions, size & size distributions, orientations and shapes. However, with increasing aging times, these microstructural characteristics follow nearly the same trend; precipitate volume fractions decrease, precipitate sizes increase, randomly distributed precipitates become aligned and their shape evolution follows this order: spherical > spheroidal > cuboidal > cubic > irregular (agglomerated/elongated). For all  $\text{Ni}_{80}\text{Al}_{15}\text{X}_5$  alloy systems, effect of alloying X element additions and heat treatment procedures on their microstructural characteristics and mechanical properties will be examined later in detail. However, before that, in the following parts, EDS and micro-hardness measurements are going to be carried out.

#### **5.4.5 Energy Dispersive Spectroscopy (EDS) Measurements**

In order to verify the nominal compositions of as cast and heat treated  $\text{Ni}_{80}\text{Al}_{15}\text{X}_5$  alloy systems (where X = Co, Cr, Hf, Mo, Nb, Ta, Ti and W, respectively) and identify the phases visible in FESEM micrographs, energy dispersive spectroscopy (EDS) measurements have been applied on the general microstructures of alloys and their constituent  $\gamma$  and  $\gamma'$  phases. In order to get more accurate results, two EDS measurements have been applied on each individual phase. Average results without (negligible) standard deviations are tabulated in Appendix G which also indicates the partitioning coefficients of alloying X elements for each step of heat treatments. For instance, as it is clear in Figure 5.31, partitioning coefficients (defined in Equation 2.2) of X = Co, Mo and W atoms are less than unity, whereas these values for X = Hf, Nb, Ta and Ti atoms are greater than unity. For X = Cr atoms, it is slightly less than unity. Considering partitioning coefficients of alloying X elements, it has been concluded that X = Co, Mo and W atoms prefer to participate into  $\gamma$  matrix phase,

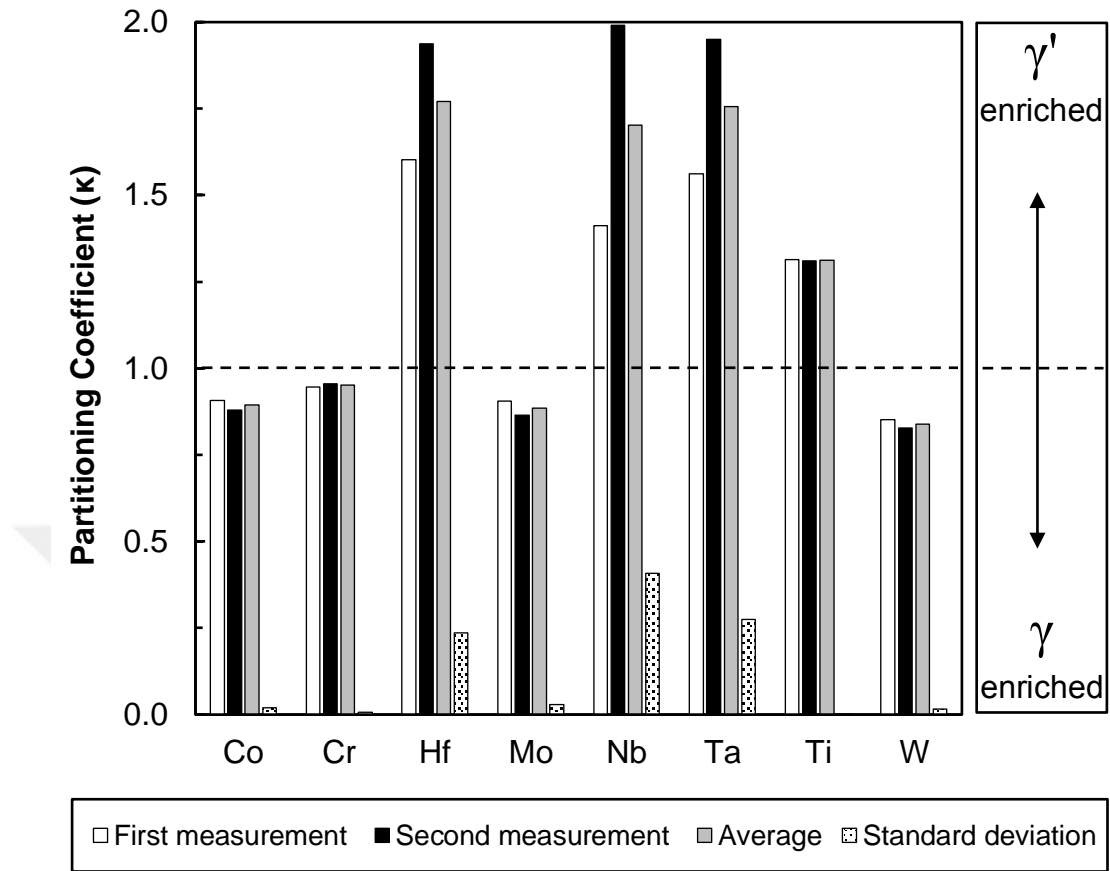


**Figure 5.31** Phase partitioning coefficients of alloying X elements (X = Co, Cr, Hf, Mo, Nb, Ta, Ti and W) in  $Ni_{80}Al_{15}X_5$  alloy systems homogenized, partially solutionized and aged for 64 hr. First two columns (white and black) represent two individual measurements, whereas third and fourth columns (gray and pattern filled) are for their average values and standard deviations, respectively.

whereas X = Hf, Nb, Ta and Ti atoms strongly involve in  $\gamma'$  precipitates. Similarly, X = Cr atoms slightly prefer to participate into  $\gamma$  matrix phase. These results are consistent with the literature [1,35].

#### 5.4.6 Micro-hardness Measurements

Mechanical responses of as cast and heat treated  $Ni_{80}Al_{15}X_5$  alloy systems have been examined by applying micro-hardness tests. In order to obtain better results, ten

measurements have been applied on each sample and the results have been tabulated in Appendix H. It seems that micro-hardness values strongly depend on both type of alloying element additions and heat treatment variations. For instance, when as cast sample groups of alloying X element additions are compared within themselves, micro-hardness values decrease from Hf addition to Co addition in the following order;  $Hf > Ta > Nb > W > Mo > Ti > Cr > Co$ . Secondly, when pre-aged sample groups (partial solution heat treated and homogenized/partial solution heat treated) are compared, micro-hardness values of the latter group are greater than the former group of each alloying X element addition ( $X \neq Hf$  and  $W$ ). These results may imply that as a consequence of homogenization heat treatment, homogeneous distribution of alloying X elements within the microstructures leads to this increase. On the contrary, for  $X = Hf$  and  $W$  additions, micro-hardness values decrease because of oxidation problem occurred during homogenization heat treatment. It is anticipated that extremely reactive behaviours of these alloying elements have caused oxide layers on the samples which deteriorate mechanical properties (i.e. micro-hardness). Hence, in order to get more accurate results, homogenization heat treatment of  $Ni_{80}Al_{15}Hf_5$  and  $Ni_{80}Al_{15}W_5$  alloys should be performed under argon atmosphere. Next, when aged sample groups of  $Ni_{80}Al_{15}X_5$  alloy systems are compared, it is noticed that micro-hardness values of the sample groups under examination change in different ways as aging time is increased from 4 hr to 256 hr, Appendix I. These results have been attributed to the microstructural characteristics of the samples (i.e.  $\gamma'$  precipitate volume fraction, size & size distribution, orientation and shape).

#### **5.4.7 Effects of Alloying X element Additions and Heat Treatment Procedures on the Microstructural Characteristics and Mechanical Properties of $Ni_{80}Al_{15}X_5$ Alloy Systems**

In order to obtain desired mechanical properties of  $Ni_{80}Al_{15}X_5$  alloy systems, it is very important to have some information about candidate alloying X elements. For this purpose, in this part of the thesis, effects of alloying X elements (where  $X = Co, Cr, Hf, Mo, Nb, Ta, Ti$  and  $W$ , respectively) and heat treatment procedures on the



microstructural characteristics (i.e.  $\gamma'$  precipitate volume fraction, size & size distribution, orientation and shape) and mechanical properties (micro-hardness) have been examined in detail and the results have been tabulated in Appendices J, K and L.

#### 5.4.7.1 Effects of Alloying X Elements on the Mechanical Properties

As mentioned in the previous parts, with increasing aging time (from 4 hr to 256 hr) micro-hardness values of  $\text{Ni}_{80}\text{Al}_{15}\text{X}_5$  alloys change in different manners (Appendix I). For instance, for  $\text{X} = \text{Co}$  addition, micro-hardness values of aged  $\text{Ni}_{80}\text{Al}_{15}\text{Co}_5$  alloys (both unhomogenized and homogenized sample groups) decrease as aging time is increased up to 256 hr. In case of  $\text{X} = \text{Cr}$  and  $\text{Ti}$  additions, micro-hardness values tend to decrease as well. However, for the second sample group of  $\text{Ni}_{80}\text{Al}_{15}\text{Cr}_5$  alloys, it seems that 64 hr aging leads to a slight increase in micro-hardness value with respect to the previous 16 hr aged one. Similarly, for  $\text{X} = \text{Ti}$  addition, another slight increase occurs for the first sample group of  $\text{Ni}_{80}\text{Al}_{15}\text{Ti}_5$  alloys for 256 hr aging. On the other hand, for  $\text{X} = \text{Mo}$ ,  $\text{Nb}$  and  $\text{Ta}$  additions, variations of micro-hardness values show different characteristics. For instance, while second sample groups of  $\text{Ni}_{80}\text{Al}_{15}\text{Nb}_5$  and

**Table 5.9** Atomic radius of alloying X elements from the biggest to the smallest where  $\text{X} = \text{Hf}$ ,  $\text{Ta}$ ,  $\text{Nb}$ ,  $\text{W}$ ,  $\text{Mo}$ ,  $\text{Ti}$ ,  $\text{Cr}$  and  $\text{Co}$ , respectively (Adapted from [136]).

Alloying X elements	Atomic radius (Å)
Hf	2.08
Ta	2.00
Nb	1.98
W	1.93
Mo	1.90
Ti	1.76
Cr	1.66
Co	1.52

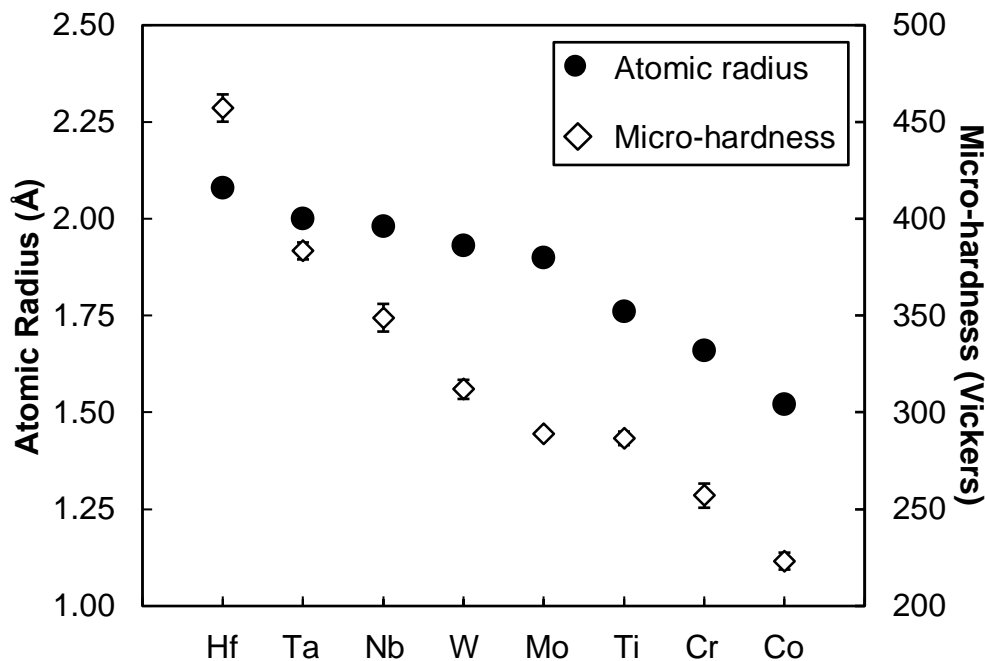


**Figure 5.32** Atomic radius of alloying X elements (represented in black spheres) and micro-hardness values of as cast  $\text{Ni}_{80}\text{Al}_{15}\text{X}_5$  alloy systems (shown in white marks) where X = Hf, Ta, Nb, W, Mo, Ti, Cr and Co, respectively.

$\text{Ni}_{80}\text{Al}_{15}\text{Ta}_5$  alloys gradually lose their strength with increasing aging time, micro-hardness values of their first group counterparts seem to have both increasing and decreasing manners between 4-256 hr aging time interval. On the contrary, for X = Mo addition; their first sample group alloys gradually become weakened, whereas micro-hardness values of second sample group of  $\text{Ni}_{80}\text{Al}_{15}\text{Mo}_5$  alloys first decrease and then increase. Because of oxidation problem, micro-hardness values of second sample groups of  $\text{Ni}_{80}\text{Al}_{15}\text{X}_5$  alloy systems (X = Hf and W) are not shown in Figures I.3,8. However, it is apparent that first sample groups of Hf and W additions gradually become weakened and strengthened, respectively. Therefore, it is of research interest to determine the main reasons behind of these different micro-hardness variations depending on both type of alloying X elements and heat treatment procedures.

In periodic table, each element has its distinct atomic radius. For afore mentioned alloying X elements, their atomic radius values have been tabulated in Table 5.9. As it

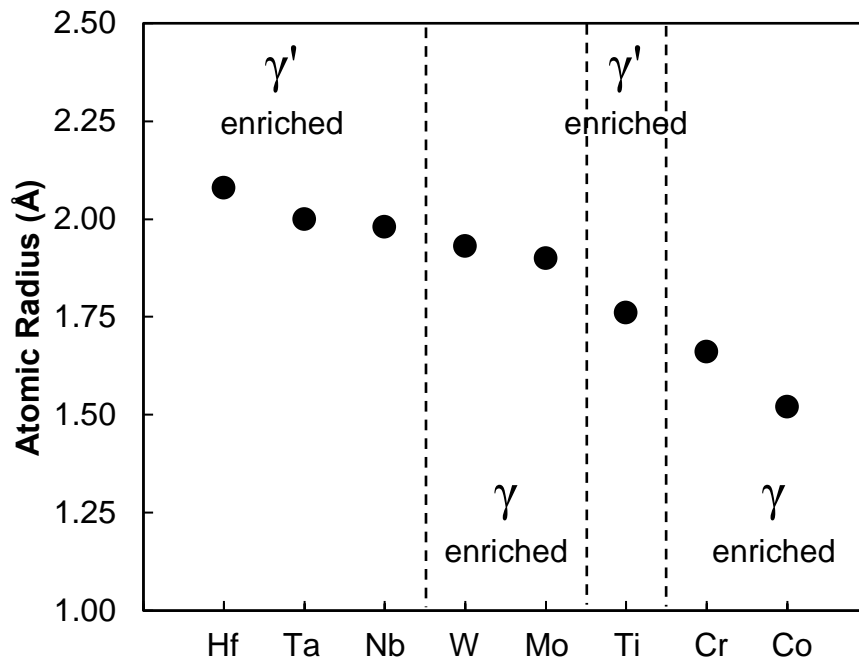


**Figure 5.33** Atomic radius of alloying X elements (represented in black spheres) and phase preferences of these alloying elements where X = Hf, Ta, Nb, W, Mo, Ti, Cr and Co, respectively.

evident in Table 5.9, Hf atoms have the biggest atomic radius, whereas Co atoms have the smallest one. Interestingly, as it is much clear in Figure 5.32, there is a relationship between atomic radius of alloying X elements and micro-hardness values of as cast  $\text{Ni}_{80}\text{Al}_{15}\text{X}_5$  alloy systems. It seems that, in order to have higher strength levels, alloying X element additions having higher atomic radius values would be helpful. Besides atomic radius, phase and sublattice site preferences of alloying X elements also affect mechanical properties. As it is mentioned in previous parts, alloying X elements, such as Co, Cr, Mo and W prefer to participate into  $\gamma$  matrix phase, whereas Hf, Nb, Ta and Ti atoms tend to become enriched in  $\gamma'$  precipitates. Hence, another interesting result may be arisen from the relationship between atomic sizes of alloying X elements and their phase preferences. Figure 5.33 illustrates this relationship clearly. According to Figure 5.33, it seems that smaller size alloying X elements tend to be involved in  $\gamma$  matrix phase, whereas bigger size ones prefer to participate into  $\gamma'$  precipitates. As it

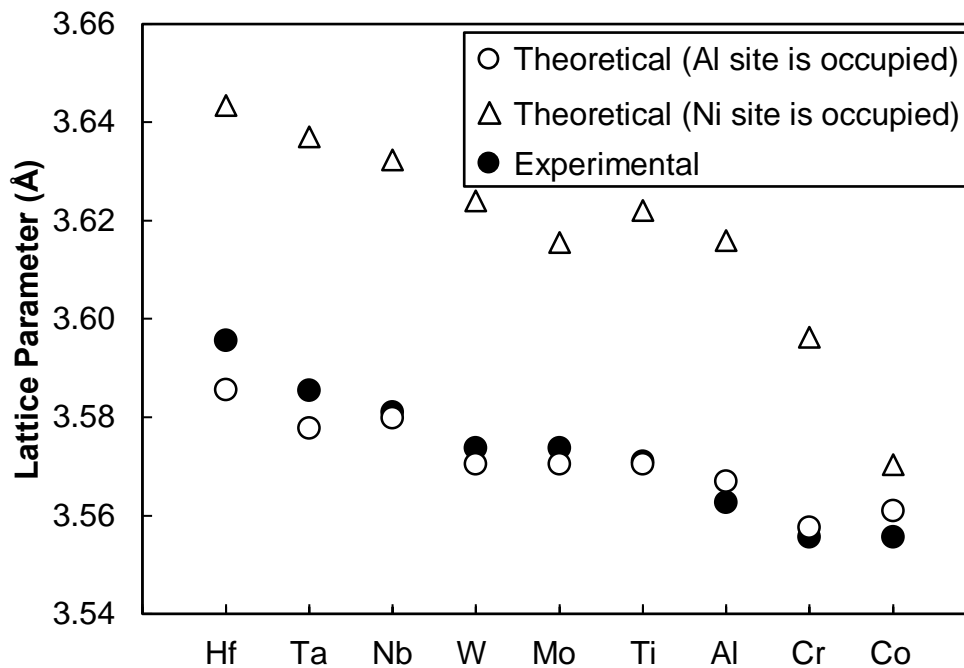


**Figure 5.34** Lattice parameter variations of  $\text{Ni}_3\text{Al-X}$  phases; theoretically determined ones in  $\text{Ni}_{24}\text{Al}_7\text{X}$  (indicated in white spheres) and  $\text{Ni}_{23}\text{Al}_8\text{X}$  (represented by triangles) systems where alloying X elements occupy either Al or Ni sublattice sites, respectively and experimentally determined lattice parameters of  $\gamma'$  precipitates in as cast  $\text{Ni}_{80}\text{Al}_{15}\text{X}_5$  alloy systems (shown in black spheres) where  $X = \text{Hf, Ta, Nb, W, Mo, Ti, Al, Cr}$  and  $\text{Co}$ , respectively.

is well known,  $\gamma'$  precipitates are actually  $L1_2$ -type ordered  $\text{Ni}_3\text{Al}$  intermetallics, whereas  $\gamma$  matrix phase is Ni solid solution, indeed. According to [136], atomic radius of Ni atoms ( $r_{\text{Ni}} = 1.49 \text{ \AA}$ ) is bigger than Al atoms ( $r_{\text{Al}} = 1.18 \text{ \AA}$ ). Therefore, another reason for bigger atomic radius alloying X elements ( $X = \text{Hf, Ta}$  and  $\text{Nb}$ ) to not participate into  $\gamma$  matrix phase would be originated from bigger atomic radius of Ni atoms with respect to Al atoms. If these alloying X elements would participate into Ni solid solution, lattice distortion would become much bigger due to bigger atomic radius of both Ni and these X atoms. However, as shown in Figure 5.33, smaller size Ti atoms prefer to be enriched in  $\gamma'$  precipitates instead of  $\gamma$  matrix phase violate this prediction.

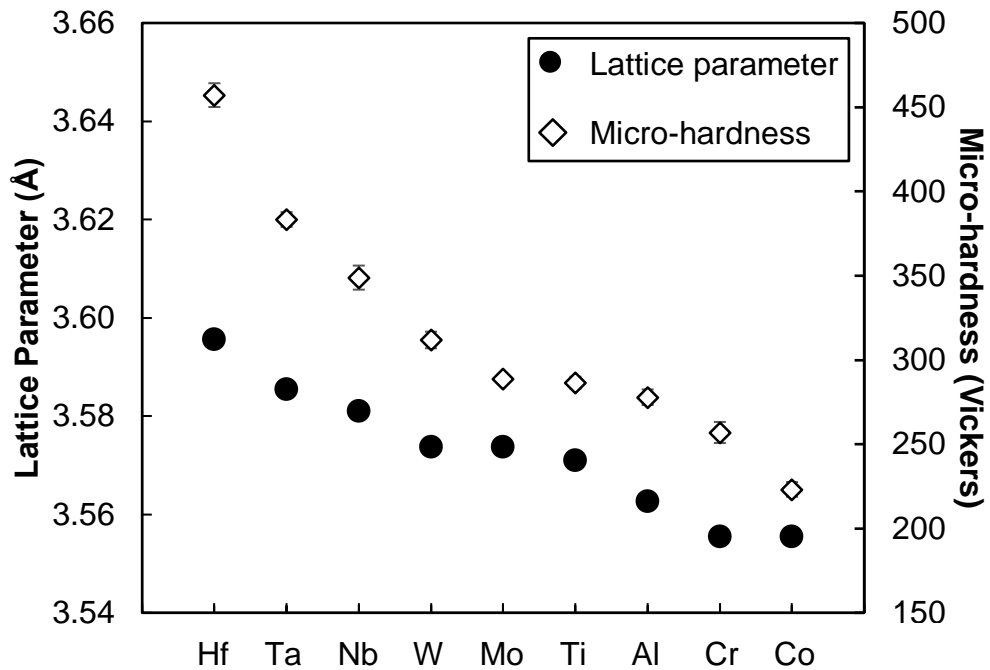


**Figure 5.35** Experimentally determined lattice parameters of  $\gamma'$  precipitates ( $\text{Ni}_3\text{Al-X}$ ) (represented in black spheres) and micro-hardness values of as cast  $\text{Ni}_{80}\text{Al}_{15}\text{X}_5$  alloy systems (shown in white marks) where  $X = \text{Hf, Ta, Nb, W, Mo, Ti, Cr}$  and  $\text{Co}$ , respectively.

In Chapters 3 and 4, site occupancy preferences of alloying X elements within  $\gamma'$ - $\text{Ni}_3\text{Al}$  precipitates have been theoretically determined at elevated temperatures (by applying SRO parameter calculations) and at 0 Kelvin (by performing first-principles calculations), respectively. According to these studies, alloying  $X = \text{Cr, Hf, Mo, Nb, Ta, Ti}$  and  $\text{W}$  elements (except  $X = \text{Co}$ ) tend to occupy Al sublattice sites, whereas  $\text{Co}$  atoms have been found to preferentially occupy Al sublattice sites at high temperatures and both Al and Ni sublattice sites at 0 Kelvin. Figure 5.34 shows lattice parameters of  $\text{Ni}_3\text{Al-X}$  systems (theoretical lattice parameters when alloying X elements occupy either Al or Ni sublattice sites and experimental lattice parameters (determined via XRD technique)). As it is evident in Figure 5.34, experimentally determined lattice parameters of  $\text{Ni}_3\text{Al-X}$  precipitates perfectly overlap with the theoretical ones in which alloying X element atoms substitute for Al sublattice sites. On the other hand, theoretical lattice parameters for alloying X elements occupying

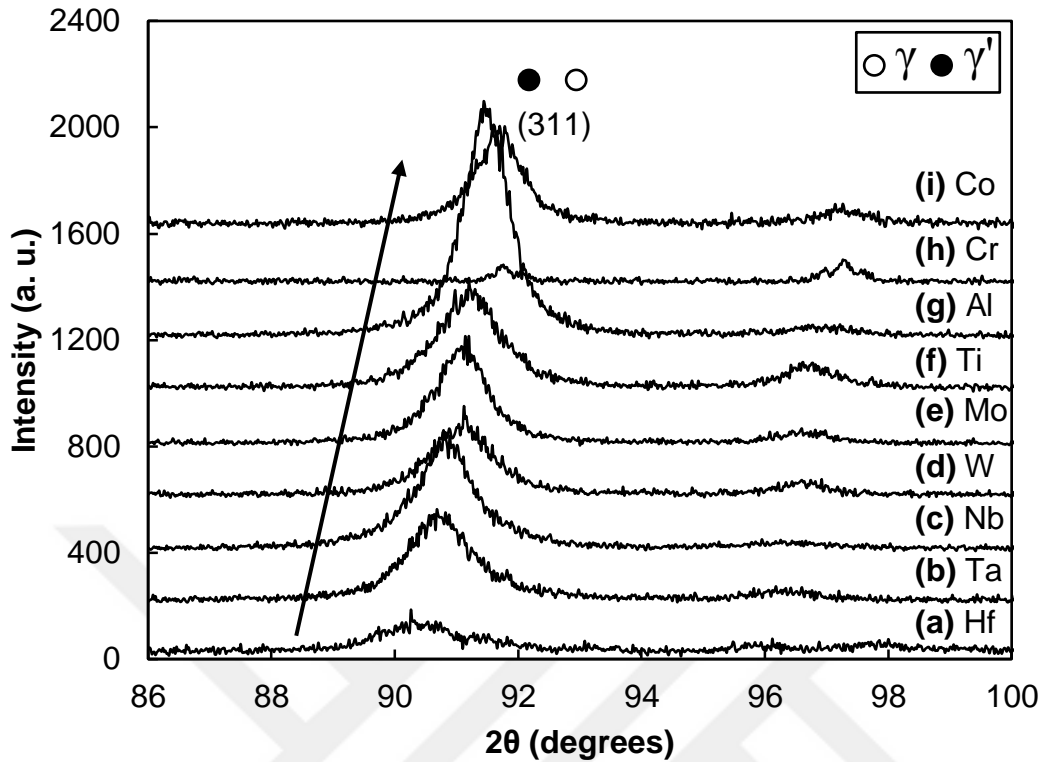


**Figure 5.36** XRD patterns of as cast (fast cooled)  $\text{Ni}_{80}\text{Al}_{15}\text{X}_5$  alloy systems where X = (a) Hf, (b) Ta, (c) Nb, (d) W, (e) Mo, (f) Ti, (g) Al, (h) Cr and (i) Co, respectively.

Ni sublattice sites are much bigger than these two ones. Therefore, by applying XRD technique, considering lattice parameters of  $\gamma'$  precipitates in as cast  $\text{Ni}_{80}\text{Al}_{15}\text{X}_5$  alloy systems and combining the results with theoretical first-principles calculations, site occupancy characteristics of alloying X elements in  $\text{Ni}_3\text{Al}$  phase have been determined in semi-experimental/semi-theoretical way. For X = Co atoms, experimental lattice parameter is much closer to the theoretical one (occupying Al sites instead of Ni sites) implying that Co atoms preferentially occupy Al sublattice sites of  $\gamma'$  precipitates in as cast  $\text{Ni}_{80}\text{Al}_{15}\text{Co}_5$  alloy as theoretically predicted by SRO parameter calculations. However, in this case, close positions of both theoretical lattice parameters (in which Al or Ni sublattice sites are occupied, respectively) also approve the consequences of first-principles calculations implying that Co atoms may occupy both Al and Ni sublattice sites of  $\text{Ni}_3\text{Al}$  phase.

Hence, by considering both atomic radius of alloying X elements and their Al site preferences in Ni<sub>3</sub>Al phase, experimental lattice parameters of Ni<sub>3</sub>Al-X phases have been demonstrated and compared with micro-hardness values of as cast Ni<sub>80</sub>Al<sub>15</sub>X<sub>5</sub> alloy systems, Figure 5.35. As it is expected, from X = Hf to Co additions, micro-hardness values gradually decrease parallel to reducing lattice parameters of  $\gamma'$  precipitates. This decrease of lattice parameters (from Hf addition to Co addition) can be understood from the shift of  $2\theta$  values of (311) fundamental peaks of Ni<sub>3</sub>Al-X phases to the right as demonstrated in Figure 5.36.

In conclusion, depending on their phase preferences ( $\gamma$  and/or  $\gamma'$ ) and site occupancy characteristics (Al and/or Ni) in  $\gamma'$ -Ni<sub>3</sub>Al phase, atomic radius of each alloying X element directly affects alloy strengths (i.e. micro-hardness) by adjusting lattice parameters of  $\gamma$  and  $\gamma'$  phases and correspondingly lattice misfit parameter ( $\delta$ ). In the next part, temporal evolutions of  $\gamma'$  precipitates with increasing aging time will be examined in Ni<sub>80</sub>Al<sub>15</sub>X<sub>5</sub> alloy systems. For each alloying X element addition, the variation of micro-hardness values is going to be explained in terms of microstructural characteristics.

#### **5.4.7.2 Effects of Heat Treatment Procedures on the Microstructural Characteristics**

In the earlier parts of this chapter, microstructural evolution of Ni<sub>80</sub>Al<sub>15</sub>Ta<sub>5</sub> alloys have been examined briefly. In this part, for Ni<sub>80</sub>Al<sub>15</sub>X<sub>5</sub> alloy systems (X  $\neq$  Hf and W), all changing microstructural characteristics (i.e.  $\gamma'$  precipitate volume fraction, size & size distribution, orientation and shape) with increasing aging time have been investigated in detail by using MIPAR software program. Because of eutectic phases of Ni<sub>80</sub>Al<sub>15</sub>Hf<sub>5</sub> alloys and oxidation problem for X = W addition, microstructural characteristics have not been determined for these alloying X element additions.

#### 5.4.7.2.1 Volume Fraction of $\gamma'$ Precipitates

For each alloying X element addition, as aging time is increased from 4 hr to 256 hr, volume fraction of  $\gamma'$  precipitates change in different ways. In terms of being an example, for the second sample groups of  $\text{Ni}_{80}\text{Al}_{15}\text{X}_5$  alloys ( $\text{X} \neq \text{Hf}$  and  $\text{W}$ ), volume fractions of  $\gamma'$  precipitates have been calculated (Appendix J). Appendix L tabulates all precipitate volume fraction data after doing the same job for the first sample groups as well. As it is apparent in Figures J.1-6, in case of Co and Ti additions,  $\gamma'$  precipitate volume fractions of aged alloys (both sample groups) decrease as aging time is increased from 4 hr up to 256 hr. For  $\text{X} = \text{Cr}$  addition, precipitate volume fractions tend to decrease as well. However, for the second sample group of  $\text{Ni}_{80}\text{Al}_{15}\text{Cr}_5$  alloys, 64 hr aging leads to a slight increase in precipitate volume fraction with respect to the previous 16 hr aged one. However, for  $\text{X} = \text{Mo}$ , Nb and Ta additions, precipitate volume fractions vary differently. While precipitate volume fractions of second sample groups of  $\text{Ni}_{80}\text{Al}_{15}\text{Nb}_5$  and  $\text{Ni}_{80}\text{Al}_{15}\text{Ta}_5$  alloys gradually decrease with increasing aging time, for their first group counterparts precipitate volume fractions seem to have an oscillating behaviour (both increasing and decreasing manners between 4-256 hr aging time interval). On the other hand, for  $\text{Ni}_{80}\text{Al}_{15}\text{Mo}_5$  alloys, precipitate volume fractions of the first sample group gradually decrease, whereas precipitate volume fractions of the second sample group first decrease and then increase.

#### 5.4.7.2.2 Size & Size Distribution of $\gamma'$ Precipitates

With increasing aging time,  $\gamma'$  precipitate sizes tend to increase. For the second sample groups of  $\text{Ni}_{80}\text{Al}_{15}\text{X}_5$  alloy systems ( $\text{X} \neq \text{Hf}$  and  $\text{W}$ ), size & size distributions of  $\gamma'$  precipitates have been determined and shown in Appendix K. Appendix L tabulates average precipitate sizes of  $\text{Ni}_{80}\text{Al}_{15}\text{X}_5$  alloy systems after doing the same job for the first sample groups. As it is apparent in Figures K.1-6,  $\gamma'$  precipitate sizes increase as aging time follows its 4-16-64-256 hr order. For higher aging times, precipitates are not in uniform sizes any longer. In Figures K.1-6, size distribution scale is limited up to  $0.5 \mu\text{m}$  ( $\gamma'$  precipitates shown in gray colours have bigger sizes than  $0.5 \mu\text{m}$ ).



### 5.4.7.2.3 Orientation of $\gamma'$ Precipitates

Parallel to the evolution of other microstructural characteristics, as aging time is increased from 4 hr to 256 hr,  $\gamma'$  precipitates align in specific directions. For the second sample groups of  $\text{Ni}_{80}\text{Al}_{15}\text{X}_5$  alloy systems ( $\text{X} \neq \text{Hf}$  and  $\text{W}$ ), orientation characteristics of  $\gamma'$  precipitates are demonstrated in Appendix K. Here, the orientation scales are coloured from  $90^\circ$  to  $-90^\circ$  relative to the horizontal x axis. After doing the same job for the first sample groups, all orientation data of  $\text{Ni}_{80}\text{Al}_{15}\text{X}_5$  alloys have been tabulated in Appendix L.

As it is evident in Figures K.1-6,  $\gamma'$  precipitates of 4 hr aged  $\text{Ni}_{80}\text{Al}_{15}\text{X}_5$  alloy systems are randomly oriented. When aging time is increased up to 16 hr, for most of the alloying X element additions, precipitates start to become oriented. For 64 hr aging time, this orientation becomes much clear and when aging time is increased up to 256 hr, it seems that each distinct alloying X element addition leads to different orientation characteristics. For instance,  $\text{X} = \text{Co}$  addition leads to trimodal orientation distribution of  $\gamma'$  precipitates (mainly aligned in three directions shown by yellow, blue and green colours). The angles between these orientations have been calculated as  $33^\circ$ ,  $70^\circ$  and  $77^\circ$ , respectively. In case of  $\text{X} = \text{Cr}$  addition,  $\gamma'$  precipitates seem to be aligned in one direction, i.e.  $\langle 001 \rangle$ . For other alloying X element additions (i.e.  $\text{X} = \text{Mo}$ ,  $\text{Nb}$ ,  $\text{Ta}$  and  $\text{Ti}$ ), orientation characteristics are not clear due to irregular (agglomerated/elongated) shapes of  $\gamma'$  precipitates. However, it is still possible to mention alignments for the 256 hr aged samples of these alloy systems when the orientation characteristics are compared with 4 hr aged ones.

### 5.4.7.2.4 Shape of $\gamma'$ Precipitates

In Chapter 2, the relationship between shape of  $\gamma'$  precipitates and lattice misfit parameter ( $\delta$ ) has been explained in detail. It is well known that as the magnitude of  $\delta$  parameter increases precipitate shapes follow this order: spherical > spheroidal > cuboidal > cubic > irregular (agglomerated/elongated). As it is obvious in Appendix

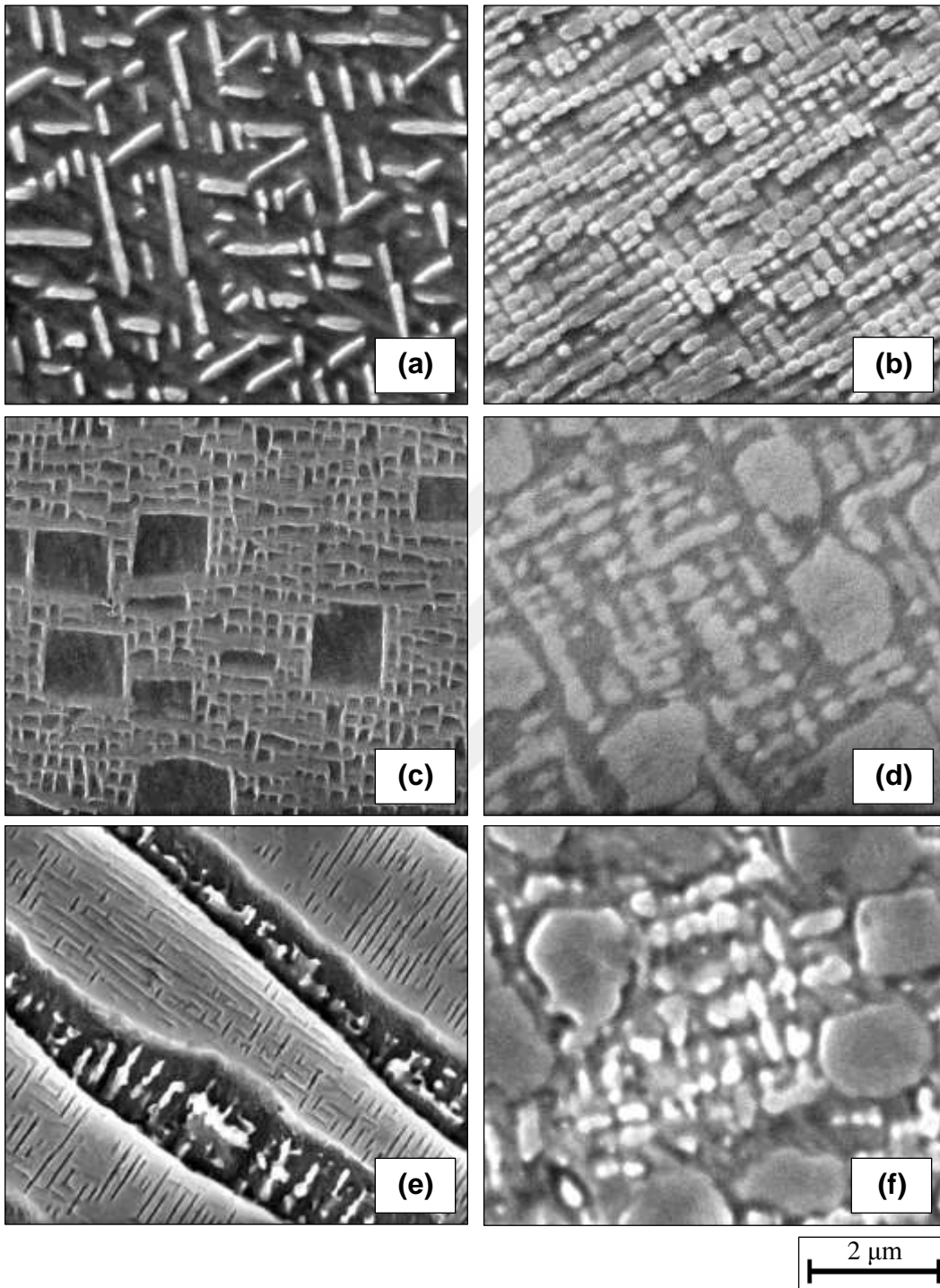


**Figure 5.37** FESEM micrographs showing (a) elongated, (b) cuboidal, (c) cubic, (d-f) irregular (agglomerated/elongated) shapes of  $\gamma'$  precipitates of the second sample groups of  $\text{Ni}_{80}\text{Al}_{15}\text{X}_5$  alloy systems aged at  $800\text{ }^\circ\text{C}$  for 256 hr where  $X =$  (a) Co, (b) Cr, (c) Mo, (d) Nb, (e) Ta and (f) Ti, respectively.

F, shape of  $\gamma'$  precipitates of  $\text{Ni}_{80}\text{Al}_{15}\text{X}_5$  alloy systems follow the same order when aging time is increased up to 256 hr. For instance, in case of  $\text{X} = \text{Nb}$  addition, spherical  $\gamma'$  precipitates of as cast  $\text{Ni}_{80}\text{Al}_{15}\text{Nb}_5$  alloy evolve in spheroidal forms in pre-aged condition, Figure F.21. When aging is applied for 4-16-64 hr, spheroidal precipitates turn into cuboidal and cubic ones, respectively. Lastly, for 256 hr aging time,  $\gamma'$  precipitates become irregular (agglomerated/elongated). In addition to  $\text{X} = \text{Nb}$  addition, similar shape (temporal) evolution characteristics have also been observed for other alloying  $\text{X}$  element additions. Appendix L demonstrates all data related with precipitate shapes.

In previous parts, phase partitioning coefficients of alloying  $\text{X}$  elements have been calculated and it has been determined that  $\text{X} = \text{Co}, \text{Cr}, \text{Mo}$  and  $\text{W}$  atoms tend to become enriched in  $\gamma$  matrix phase, whereas  $\text{X} = \text{Hf}, \text{Nb}, \text{Ta}$  and  $\text{Ti}$  atoms preferentially participate  $\gamma'$  precipitates. As it is evident in Figure 5.37, these different partitioning behaviours of alloying  $\text{X}$  elements may strongly affect shape of  $\gamma'$  precipitates especially for higher aging durations, i.e. 256 hr. In case of  $\gamma$ -former alloying element additions (i.e.  $\text{Cr}$  and  $\text{Mo}$ ), for higher aging times, precipitate shapes are cuboidal and cubic, respectively. However, for  $\gamma'$ -former ones (i.e.  $\text{Nb}, \text{Ta}$  and  $\text{Ti}$ ) precipitates seem to be in irregular (agglomerated/elongated) shapes. Therefore, it is anticipated that phase preferences of alloying  $\text{X}$  elements would affect shape of  $\gamma'$  precipitates at higher aging times;  $\gamma$ -former alloying elements lead to regular-shaped precipitates, whereas  $\gamma'$ -former ones cause precipitates to form in irregular shapes. So, additions of  $\gamma'$ -former alloying elements would be helpful for nickel-based superalloys exposed to shorter high service temperature times, whereas the ones subjected to longer high service temperatures need to be micro-alloyed by  $\gamma$ -former alloying elements as well to keep  $\gamma'$  precipitates stable (having regular shapes).

#### **5.4.8 Conclusions**

As tabulated in Figures L.1-8, the variations of microstructural characteristics (i.e.  $\gamma'$  precipitate volume fraction, size & size distribution, orientation and shape) with

respect to increasing aging time from 4 hr to 256 hr and phase/site preferences of different atomic radius alloying X elements lead to enhancement or worsening in mechanical properties (i.e. micro-hardness) of  $\text{Ni}_{80}\text{Al}_{15}\text{X}_5$  alloy systems where X = Co, Cr, Hf, Mo, Nb, Ta, Ti and W, respectively. By considering all theoretical and experimental data obtained from the previous chapters, it has been concluded that higher micro-hardness values strongly depend on higher atomic radius alloying X element additions, higher precipitate lattice parameters, higher precipitate volume fractions and lower precipitate sizes cause optimum lattice misfit parameters ( $\delta$ ). For most of the alloy systems, since precipitate shapes become more irregular with increasing aging time it is anticipated that  $\delta$  parameters of the related alloy systems become very distant from their optimum values and lead to decrease in micro-hardness values. Decrease in precipitate lattice parameters and volume fractions and increase in precipitate sizes with increasing aging times validate these predictions.

## CHAPTER 6

### CONCLUSIONS

This master thesis has focused on design and development of  $\text{Ni}_{80}\text{Al}_{20}$  and  $\text{Ni}_{80}\text{Al}_{15}\text{X}_5$  alloy systems where  $\text{X} = \text{Co}, \text{Cr}, \text{Hf}, \text{Mo}, \text{Nb}, \text{Ta}, \text{Ti}$  and  $\text{W}$ , respectively. For this purpose, in theoretical calculations part, sublattice site occupancy preferences of aforementioned alloying  $\text{X}$  elements in  $\gamma'$ - $\text{Ni}_3\text{Al}$  precipitates have been determined by performing both SRO parameter calculations at high temperatures (from 800 °C up to 1250 °C) and first-principles calculations at 0 Kelvin. Next, by simulating atomic bonding characteristics between alloying  $\text{X}$  elements and their NN Ni(Al) atoms along  $\langle 110 \rangle$  directions via CDD, ELF and DOS methods, mechanical responses of  $\text{Ni}_3\text{Al-X}$  phases have been predicted. In the light of these theoretical calculations, aforementioned binary and ternary alloy systems have been produced by arc melting and suction casting techniques. Then each as cast sample has been treated to different heat treatment procedures to realize the effects of homogenization, partial solution heat treatment and primary aging heat treatments as well as aging durations on the microstructural characteristics and temporal evolutions of  $\gamma'$  precipitates. After phase, thermal and microstructural characterizations, mechanical properties of these alloys have been determined by micro-hardness tests.

To sum up, in this study, the reasons behind enhanced mechanical properties of nickel-based superalloys have been both theoretically and experimentally examined and many results have been achieved. From these results, the most interesting and important ones are as follows:

- According to SRO parameter calculations, at elevated temperatures,  $\text{X} = \text{Co}, \text{Cr}, \text{Hf}, \text{Mo}, \text{Nb}, \text{Ru}, \text{Ta}$  and  $\text{W}$  atoms preferentially occupy Al sublattice sites

of Ni<sub>3</sub>Al phase, whereas X = Pt atoms tend to substitute for Ni sites.

- Sublattice site occupancy characteristics of X = Re atoms seem to both composition and temperature dependent. Site occupancy preference of Re atoms switches from Al to both Al and Ni sites at critical temperatures, T<sub>c</sub>, for Re > 2.35 at.%. Distribution of Re atoms at both Al and Ni sublattice sites above T<sub>c</sub> may lead to localized supersaturation of the parent Ni<sub>3</sub>Al phase and makes possible the formation of topologically close-packed (TCP) phases.
- According to first-principles calculations, at 0 Kelvin, X = Cr, Hf, Mo, Nb, Re, Ta, Ti and W atoms preferentially occupy Al sublattice sites of Ni<sub>3</sub>Al phase, whereas X = Pt atoms tend to substitute for Ni sites. X = Co and Ru atoms may occupy both Al and Ni sites.
- Site occupancy behaviours of alloying X elements can be determined from theoretical lattice parameters of Ni<sub>3</sub>Al-X phases. If lattice parameters of (Ni<sub>3</sub>,X)Al phases (in which alloying X elements occupy Ni sites) are bigger than lattice parameters of Ni<sub>3</sub>(Al,X) phases (in which alloying X elements occupy Al sites), these alloying X elements tend to occupy Al sites (i.e. X = Cr, Hf, Mo, Nb, Re, Ta, Ti and W). However, if there is no such a big difference in lattice parameters of Ni<sub>3</sub>Al-X phases (in which alloying X elements occupy either Al or Ni sites), these alloying elements prefer to occupy Ni sites (i.e. X = Pt). If there is a slight difference in favour of lattice parameters of (Ni<sub>3</sub>,X)Al phases, these alloying X elements substitute for both Al and Ni sites (i.e. X = Co and Ru).
- As it is evident in (010) plane CDD and ELF simulation plots of Ni<sub>3</sub>Al-X phases, alloying X elements lead to directional covalent bondings with their NN Ni atoms along <110> directions and increase strength of Ni<sub>3</sub>Al phase in the order of Ti < Hf < Cr < Mo < Ta < W < Re (The strongest covalent bondings are created by the addition of X = Re atoms whereas the weakest ones are obtained by X = Ti addition). X = Co, Pt and Ru atoms may lead to metallic bondings instead of directional covalent bondings and enhance ductility of Ni<sub>3</sub>Al phase. These theoretical predictions are also confirmed by pDOS plots showing the X-d/Ni-d hybridizations for alloying X element additions (i.e. X ≠

Co, Pt and Ru). Due to their strong d-d hybridizations with NN Ni atoms along  $\langle 110 \rangle$  directions of  $\text{Ni}_3\text{Al-X}$  phases, alloying X elements, such as Mo, Re, Ta and W improve the mechanical properties (strength) of nickel-based superalloys.

- According to DSC heating and cooling plots, it seems that alloying X element additions (i.e. X = Co, Cr, Hf, Mo and W) increase melting/solidification temperatures of binary  $\text{Ni}_{80}\text{Al}_{20}$  alloy, whereas some other alloying X element additions (i.e. X = Nb, Ta and Ti) decrease its melting/solidification temperatures. Interestingly, it is well known in the literature that former alloying X elements preferentially participate into  $\gamma$  matrix phase, whereas the latter ones tend to become enriched in  $\gamma'$  precipitates. Therefore, it is anticipated that the addition of former alloying X elements into binary  $\text{Ni}_{80}\text{Al}_{20}$  alloy shift its composition to the Ni-rich side in Ni-Al phase diagram and addition of latter ones shift it to the Al-rich side. Among the former alloying X elements X = Hf and W additions lead to appearance of solvus peaks in DSC plots, whereas solvus peaks do not appear for other alloying X element additions. This behaviour explains that X = Hf and W additions contribute this shift into Ni-rich side more than other former alloying X elements which is also confirmed by their (Hf and W) highest melting/solidification temperatures.
- Afore mentioned “shift” phenomenon can be confirmed by Lever Rule. Since former alloying X elements shift binary composition to the Ni-rich side, according to Lever Rule,  $\gamma'$  precipitate volume fractions of related alloy systems decrease. Similarly, since the latter ones shift it to the Al-rich side (towards  $\text{Ni}_3\text{Al}$  phase),  $\gamma'$  precipitate volume fractions increase.
- These findings can also be validated by as cast microstructures of  $\text{Ni}_{80}\text{Al}_{15}\text{X}_5$  alloy systems. For the former alloying X element additions, as cast microstructures consist of dendrites (lose their shapes or visible in grains), whereas in case of latter alloying X element additions and binary  $\text{Ni}_{80}\text{Al}_{20}$  alloy, pure dendrites appear in their original characteristics.
- By applying EDS analyses, phase partitioning coefficients of alloying X elements can be calculated. According to the results, X = Co, Cr, Mo and W

atoms preferentially participate into  $\gamma$  matrix phase, whereas X = Hf, Nb, Ta and Ti atoms tend to become enriched in  $\gamma'$  precipitates. As opposed to the previous “shift” characteristic of X = Hf atoms (implying that Hf atoms tend to participate into  $\gamma$  matrix phase), its partitioning coefficient shows that Hf atoms prefer  $\gamma'$  precipitates to be involved in. This questionable result is also arised in the literature; APT studies indicate that Hf atoms prefer to be enriched in  $\gamma$  matrix phase, while first-principles calculations claim that  $\gamma'$  precipitates are the preferable phases of Hf atoms. It is anticipated that, this conflict is due to existence of other phase ( $\text{Ni}_3\text{Hf}$  phase involves in eutectic phase mixture) in  $\text{Ni}_{80}\text{Al}_{15}\text{Hf}_5$  alloys.

- Enhanced mechanical properties of  $\text{Ni}_{80}\text{Al}_{15}\text{X}_5$  alloy systems (where X = Co, Cr, Hf, Mo, Nb, Ta, Ti and W, respectively) strongly depend on higher atomic radius alloying X element additions, higher precipitate lattice parameters, higher precipitate volume fractions and lower precipitate sizes lead to optimum lattice misfit parameters ( $\delta$ ).
- Better mechanical properties (i.e. micro-hardness) of  $\text{Ni}_{80}\text{Al}_{15}\text{X}_5$  alloy systems are mostly influenced by higher atomic radius alloying X element additions lead to higher precipitate lattice parameters. For as cast samples, micro-hardness values of alloying X element additions can be ordered from the highest to the smallest as Hf > Ta > Nb > W > Mo > Ti > Binary (Al) > Cr > Co. Similar sequence has been obtained in the work of Crudden et al. [28]. In this work [28], by performing both CALPHAD and DFT calculations, effects of alloying elements on the APB energies of  $\text{Ni}_3\text{Al-X}$  phases have been determined. According to CAPHAD results, it has been concluded that Mo, Nb, Ta, Ti and W additions increase APB energy, whereas Cr addition decreases it. For DFT calculations, it has been noticed that Ta is the leading alloying element increasing APB energy followed by Nb and Ti, respectively. So, in the light of this information, it can ben suggested that alloying element additions, such as Hf, Mo, Nb, Ta, Ti and W (which yield higher precipitate lattice parameters due to their higher atomic radii) increase micro-hardness values, whereas alloying element additions, such as Co and Cr (which yield lower precipitate lattice



parameters due to their lower atomic radii) decrease micro-hardness values by increasing and decreasing APB energies of the alloy systems, respectively. These results can also be confirmed by the general microstructures of  $\text{Ni}_{80}\text{Al}_{15}\text{X}_5$  alloy systems. For  $\text{X} = \text{Hf}, \text{Mo}, \text{Nb}, \text{Ta}, \text{Ti}$  and  $\text{W}$  additions, general microstructures of these alloy systems do not contain clear annealing twins, whereas for  $\text{X} = \text{Al}, \text{Co}$  and  $\text{Cr}$  additions, annealing twins are visible throughout the samples which imply that former alloying  $\text{X}$  elements increase APB/SF energy, whereas latter ones decrease it [21-23].

- As aging time is increased from 4 hr to 256 hr, micro-hardness values of most of the alloy systems tend to gradually decrease since lattice parameters of  $\gamma'$  precipitates also gradually decrease and  $\gamma'$  precipitates evolve from spherical to irregular (agglomerated/elongated) shapes in the order of spherical > spheroidal > cuboidal > cubic > irregular which imply  $\delta$  parameters lose their optimum values. For some alloying  $\text{X}$  element additions (i.e.  $\text{X} = \text{Mo}$  and  $\text{Nb}$ ), micro-hardness values of these alloy systems show oscillating behaviour in the aging time interval of 4-16-64-256 hr. Interestingly, for these alloy systems,  $\gamma'$  precipitate volume fraction variations also exhibit the same oscillating characteristics which imply that precipitate volume fraction is also one of the leading parameters to be concerned in design and development of high temperature nickel-based superalloys.
- Phase preferences of alloying  $\text{X}$  elements would affect shape of  $\gamma'$  precipitates especially at higher aging times;  $\gamma$ -former alloying elements, such as  $\text{Cr}$  and  $\text{Mo}$  lead to regular-shaped (cuboidal and cubic) precipitates, whereas  $\gamma'$ -former ones, such as  $\text{Nb}, \text{Ta}$  and  $\text{Ti}$  cause precipitates to form in irregular (agglomerated/elongated) shapes. Even if  $\text{Co}$  is a  $\gamma$ -former alloying element, its addition also leads to irregular shaped  $\gamma'$  precipitates which may be the result of extremely low precipitate volume fractions of  $\text{Ni}_{80}\text{Al}_{15}\text{Co}_5$  alloys.



## CHAPTER 7

### FUTURE SUGGESTIONS

- Site occupancy characteristics of ternary alloying X elements can be experimentally verified by Rietveld refinement analyses.
- By applying in-situ XRD analyses of  $\text{Ni}_{75}\text{Al}_{25-x}\text{Re}_x$  alloy systems (where  $x = 1, 2, 3$  or  $4$ ) below/at/above  $T_c$  temperatures,  $\gamma'$  precipitate and possible TCP phase formation temperatures can be determined and by using in-situ XRD patterns of these alloy systems, sublattice site occupancy characteristics of  $X = \text{Re}$  atoms can be studied by Rietveld refinement analyses. Hence, the current theoretical explanation of TCP phase formation mechanism would be totally clarified.
- In order to enhance mechanical properties of the current  $\text{Ni}_{80}\text{Al}_{15}\text{X}_5$  alloy systems, in the light of theoretical first-principles simulations, such as CDD, ELF and DOS, quaternary  $\text{Ni}_{80}\text{Al}_{20-x-y}\text{X}_x\text{Y}_y$  alloy systems can be produced and characterized.



## REFERENCES

- [1] R.C. Reed, *The Superalloys: Fundamentals and Applications*, Cambridge University Press, Cambridge, 2006.
- [2] T.M. Pollock, and S. Tin, *Nickel-based superalloys for advanced turbine engines: Chemistry, microstructure, and properties*, *Journal of Propulsion and Power*, 22 (2006), pp. 361-374.
- [3] N. Cayetano-Castro, M.L. Saucedo-Muñoz, H.J. Dorantes-Rosales, Jorge L. Gonzalez-Velazquez, J.D. Villegas-Cardenas, and V.M. Lopez-Hirata, *Ostwald ripening process of coherent  $\beta'$  precipitates during aging in  $Fe_{0.75}Ni_{0.10}Al_{0.15}$  and  $Fe_{0.74}Ni_{0.10}Al_{0.15}Cr_{0.01}$  alloys*, *Advances in Materials Science and Engineering*, 485626 (2015), pp. 1-7.
- [4] B. Roebuck, D. Cox, and R. Reed, *The temperature dependence of  $\gamma'$  volume fraction in a Ni-based single crystal superalloy from resistivity measurements*, *Scripta Materialia*, 44 (2001), pp. 917-921.
- [5] F. Cao, B. Tryon, C.J. Torbet, and T.M. Pollock, *Microstructural evolution and failure characteristics of a NiCoCrAlY bond coat in “hot spot” cyclic oxidation*, *Acta Materialia*, 57 (2009), pp. 3885-3894.
- [6] A.J. Ardell, *Precipitation hardening*, *Metallurgical and Materials Transactions A*, 16 (1985), pp. 2131-2165.
- [7] C. Sun, M. Kirk, M. Li, K. Hattar, Y. Wang, O. Anderoglu, J. Valdez, B.P. Uberuaga, R. Dickerson, and S.A. Maloy, *Microstructure, chemistry and*

- mechanical properties of Ni-based superalloy Rene N4 under irradiation at room temperature*, Acta Materialia, 95 (2015), pp. 357-365.
- [8] S. Antonov, M. Detrois, R.C. Helmink, and S. Tin, *Precipitate phase stability and compositional dependence on alloying additions in  $\gamma$ - $\gamma'$ - $\delta$ - $\eta$  Ni-base superalloys*, Journal of Alloys and Compounds, 626 (2015), pp. 76-86.
- [9] Chantal K. Sudbrack, *Decomposition Behavior in Model Ni-Al-Cr-X Superalloys: Temporal Evolution and Compositional Pathways on a Nanoscale*, PhD Thesis, Northwestern University, Evanston, Illinois, 2004.
- [10] A. Vattré, B. Devincere, and A. Roos, *Dislocation dynamics simulation of precipitation hardening in Ni-based superalloys with high  $\gamma'$  volume fraction*, Intermetallics, xxx (2009), pp. 1-7.
- [11] E. Fleischmann, M.K. Miller, E. Affeldt, and U. Glatzel, *Quantitative experimental determination of the solid solution hardening potential of rhenium, tungsten and molybdenum in single-crystal nickel-based superalloys*, Acta Materialia, 87 (2015), pp. 350-356.
- [12] A.F. Giamei, and D.L. Anton, *Rhenium additions to a Ni-base superalloy: Effects on microstructure*, Metallurgical and Materials Transactions A, 16 (1985), pp. 1997-2005.
- [13] A.C. Yeh, and S. Tin, *Effects of Ru and Re additions on the high temperature flow stresses of Ni-base single crystal superalloys*, Scripta Materialia, 52 (2005), pp. 519-524.
- [14] C.M.F. Rae, and R.C. Reed, *The precipitation of topologically close packed phases in rhenium-containing superalloys*, Acta Materialia, 49 (2001), pp. 4113-4125.

- [15] S. Tin, and T.M. Pollock, *Phase instabilities and carbon additions in single-crystal nickel-base superalloys*, Materials Science and Engineering A, 348 (2003), pp. 111-121.
- [16] R.A. Hobbs, L. Zhang, C.M.F. Rae, and S. Tin, *Mechanisms of topologically close-packed phase suppression in an experimental ruthenium-bearing single-crystal nickel-base superalloy at 1100 °C*, Metallurgical and Materials Transactions A, 39 (2008), pp. 1014-1025.
- [17] M.V. Nathal, R.A. MacKay, and R.V. Miner, *Influence of precipitate morphology on intermediate temperature creep properties of a nickel-base superalloy single crystal*, Metallurgical and Materials Transactions A, 20 (1989), pp. 133-141.
- [18] M. Ott, and H. Mughrabi, *Dependence of the high-temperature low-cycle fatigue behaviour of the monocrystalline nickel-base superalloys CMSX-4 and CMSX-6 on the  $\gamma/\gamma'$ -morphology*, Materials Science and Engineering A, 272 (1999) pp. 24–30.
- [19] H. Mughrabi, M. Ott, and U. Tetzlaff, *New microstructural concepts to optimize the high-temperature strength of  $\gamma'$ -hardened monocrystalline nickel-based superalloys*, Materials Science and Engineering A, 234-236 (1997) pp. 434–437.
- [20] Y.W. Ma, K.B. Yoon, and A. Saxena, *Creep crack growth data reduction of directionally solidified Ni base superalloy using  $C_t$  estimation scheme for anisotropic materials*, Materials at High Temperatures, 32 (2015), pp. 289-292.
- [21] S. Mahajan, C.S. Pande, M.A. Imam, and B.B. Rath, *Formation of annealing twins in f.c.c. crystals*, Acta Materialia, 45 (1997), pp. 2633-2638.

- [22] D.P. Field, L.T. Bradford, M.M. Nowell, and T.M. Lillo, *The role of annealing twins during recrystallization of Cu*, Acta Materialia, 55 (2007), pp. 4233-4241.
- [23] G. Palumbo, K.T. Aust, U. Erb, P.J. King, A.M. Brennenstuhl, and P.C. Lichtenberger, *On annealing twins and CSL distributions in F.C.C. polycrystals*, Physica Status Solidi A, 131 (1992), pp. 425-428.
- [24] G.K. Dey, *Physical metallurgy of nickel aluminides*, Sadhana-academy Proceedings in Engineering Sciences, 28 (2003), pp. 247-262.
- [25] N.S. Stoloff, C.T. Liu, and S.C. Deevi, *Emerging applications of intermetallics*, Intermetallics, 8 (2000), pp. 1313-1320.
- [26] V.K. Sikka, S.C. Deevi, S. Viswanathan, R.W. Swindeman, and M.L. Santella, *Advances in processing of Ni<sub>3</sub>Al-based intermetallics and applications*, Intermetallics, 8 (2000), pp. 1329-1337.
- [27] S.C. Deevi, and V.K. Sikka, *Nickel and iron aluminides: An overview on properties, processing, and applications*, Intermetallics, 4(1996), pp. 357-375.
- [28] D.J. Crudden, A. Mottura, N. Warnken, B. Raeisinia, and R.C. Reed, *Modelling of the influence of alloy composition on flow stress in high-strength nickel-based superalloys*, Acta Materialia, 75 (2014), pp. 356-370.
- [29] M.H.F. Sluiter, M. Takahashi, and Y. Kawazoe, *The effect of magnetism on the site preference in Ni<sub>3</sub>Al*, Acta Materialia, 44 (1996), pp. 209-215.
- [30] F.R. De Boer, C.J. Schinkel, J. Biesterbos, and S. Proost, *Exchange-enhanced paramagnetism and weak ferromagnetism in the Ni<sub>3</sub>Al and Ni<sub>3</sub>Ga phases; giant moment inducement in Fe doped Ni<sub>3</sub>Ga*, Journal of Applied Physics, 40 (1969),



pp. 1049-1055.

- [31] M. Chandran, and S.K. Sondhi, *First-principle calculation of APB energy in Ni-based binary and ternary alloys*, Modelling and Simulation in Materials Science and Engineering, 19 (2011), 025008.
- [32] D.M. Collins, L. Yan, E.A. Marquis, L.D. Connor, J.J. Ciardiello, A.D. Evans, and H.J. Stone, *Lattice misfit during ageing of a polycrystalline nickel-base superalloy*, Acta Materialia, 61 (2013), pp. 7791-7804.
- [33] J.C. Glueckstein, and L.E. Klebanoff, *Temperature-dependent study of 3s multiplet splitting in ferromagnetic Ni*, Physical Review B, 68 (2003), 052407.
- [34] S.L. Shang, C.L. Zacherl, H.Z. Fang, Y. Wang, Y. Du, and Z.K. Liu, *Effects of alloying element and temperature on the stacking fault energies of dilute Ni-base superalloys*, Journal of Physics: Condensed Matter, 24 (2012), 505403.
- [35] M. Durand-Charre, *The Microstructure of Superalloys*, CRC Press, Boca Raton, Florida, 1998.
- [36] D. Blavette, E. Cadel, C. Pareige, B. Deconihout, and P. Caron, *Phase transformation and segregation to lattice defects in Ni-base superalloys*, Microscopy and Microanalysis, 13 (2007), pp. 464-483.
- [37] P.M. Mignanelli, N.G. Jones, K.M. Perkins, M.C. Hardy, and H.J. Stone, *Microstructural evolution of a delta containing nickel-base superalloy during heat treatment and isothermal forging*, Materials Science and Engineering A, 621 (2015), pp. 265-271.
- [38] H. Murakami, T. Honma, Y. Koizumi, and H. Harada, in *Proceedings of the Ninth International Symposium on Superalloys*, Seven Springs, PA, 2000, pp.

747–756.

- [39] M.S.A. Karunaratne, C.M.F. Rae, and R.C. Reed, *On the microstructural instability of an experimental nickel-based single-crystal superalloy*, Metallurgical and Materials Transactions A, 32 (2001), pp. 2409-2421.
- [40] K. Matuszewski, R. Rettig, H. Matysiak, Z. Peng, I. Povstugar, P. Choi, J. Muller, D. Raabe, E. Spiecker, and K.J. Kurydlowski, *Effect of ruthenium on the precipitation of topologically close packed phases in Ni-based superalloys of 3rd and 4th generation*, Acta Materialia, 95 (2015), pp. 274-283.
- [41] X.M. Zhang, H.Q. Deng, S.F. Xiao, Z. Zhang, J.F. Tang, L. Deng, and W.Y. Hu, *Diffusion of Co, Ru and Re in Ni-based superalloys: A first-principles study*, Journal of Alloys and Compounds, 588 (2014), pp. 163-169.
- [42] S. Gao, Y. Zhou, C.F. Li, Z.Q. Liu, and T. Jin, *Effects of platinum group metals addition on the precipitation of topologically close-packed phase in Ni-base single crystal superalloys*, Journal of Alloys and Compounds, 671 (2016), pp. 458-464.
- [43] Y.J. Wang, and C.Y. Wang, *The alloying mechanisms of Re, Ru in the quaternary  $\gamma/\gamma'$  interface: A first principles calculation*, Materials Science and Engineering A, 490 (2008), pp. 242-249.
- [44] R.A. Hobbs, S. Tin, C.M.F. Rae, R.W. Broomfield, and C.J. Humphreys, *Solidification characteristics of advanced nickel-base single crystal superalloys*, edited by K.A. Green et al., TMS, 2004.
- [45] M.V. Nathal, J.O. Diaz, and R.V. Miner, *High temperature creep behaviour of single crystal gamma prime and gamma alloys*, edited by C.T. Liu et al., MRS, Pittsburg, PA, 133 (1989), pp. 269-274.

- [46] H. Mughrabi,  *$\gamma/\gamma'$  rafting and its effect on the creep and fatigue behaviour of monocrystalline superalloys*, edited by R.J. Arsenault et al., MRS, Warrendale, PA, 133 (1996), pp. 267-278.
- [47] Y. Huang, Z. Mao, R.D. Noebe, and D.N. Seidman, *The effects of refractory elements on Ni-excesses and Ni-depletions at  $\gamma$ (f.c.c.)/ $\gamma'$ ( $L1_2$ ) interfaces in model Ni-based superalloys: Atom-probe tomographic experiments and first-principles calculations*, *Acta Materialia*, 121 (2016), pp. 288-298.
- [48] P.M. Mignanelli, N.G. Jones, M.C. Hardy, and H.J. Stone, *The influence of Al:Nb ratio on the microstructure and mechanical response of quaternary Ni–Cr–Al–Nb alloys*, *Materials Science & Engineering A*, 612 (2014), pp. 179-186.
- [49] T. Murakumo, T. Kobayashi, Y. Koizumi, and H. Harada, *Creep behaviour of Ni-base single-crystal superalloys with various  $\gamma'$  volume fraction*, *Acta Materialia* 52 (2004), pp. 3737–3744.
- [50] J.S. Van Sluytman, and T.M. Pollock, *Optimal precipitate shapes in nickel-base  $\gamma$ - $\gamma'$  alloys*, *Acta Materialia*, 60 (2012), pp. 1771-1783.
- [51] J.S. Van Sluytman, C.J. Mocerri, and T.M. Pollock, *A Pt-modified Ni-base superalloy with high temperature precipitate stability*, *Materials Science & Engineering A*, 639 (2015), pp. 747-754.
- [52] C. Booth-Morrison, Z.G. Mao, R.D. Noebe, and D.N. Seidman, *Chromium and tantalum site substitution patterns in  $Ni_3Al$  ( $L1_2$ )  $\gamma'$ -precipitates*, *Applied Physics Letters*, 93 (2008), 033103.
- [53] C.K. Sudbrack, T.D. Ziebell, R.D. Noebe, and D.N. Seidman, *Effects of a tungsten addition on the morphological evolution, spatial correlations and*

- temporal evolution of a model Ni-Al-Cr superalloy*, Acta Materialia, 56 (2008), pp. 448-463.
- [54] S.H. Liu, C.P. Liu, W.Q. Liu, X.N. Zhang, P. Yan, and C.Y. Wang, *Investigation of the elemental partitioning behaviour and site preference in ternary model nickel-based superalloys by atom probe tomography and first-principles calculations*, Philosophical Magazine, 96 (2016), pp. 2204-2218.
- [55] M. Fährmann, P. Fratzl, O. Paris, E. Fährmann, and W.C. Johnson, *Influence of coherency stress on microstructural evolution in model Ni-Al-Mo alloys*, Acta Metallurgica and Materialia, 43(3) (1995), pp. 1007-1022.
- [56] F. Pyczak, B. Devrient, F.C. Neuner, and H. Mughrabi, *The influence of different alloying elements on the development of  $\gamma/\gamma'$  microstructure of nickel-base superalloys during high-temperature annealing and deformation*, Acta Materialia, 53 (2005), pp. 3879-3891.
- [57] R. Vilar, and A. Almeida, *Repair and manufacturing of single crystal Ni-based superalloys components by laser powder deposition-A review*, Journal of Laser Applications, 27 (2015), S17004.
- [58] M. Segersäll, P. Kontis, S. Pedrazzini, P.A.J. Bagot, M.P. Moody, J.J. Moverare, and R.C. Reed, *Thermal-mechanical fatigue behaviour of a new single crystal superalloy: Effects of Si and Re alloying*, Acta Materialia, 95 (2015), pp. 456-467.
- [59] A.T. Paxton, *Electron Theory in Alloy Design*, edited by D.G. Pettifor and A.H. Cottrell, The Institute of Materials, London, 1992.
- [60] C.L. Fu, Y.Y. Ye, and M.H. Yoo, *High-temperature ordered intermetallic alloys V*, edited by I. Baker et al., MRS, 288, Pittsburgh, PA, 1993.

- [61] N.M. Rosengaard, and H.L. Skriver, *Ab-initio study of antiphase boundaries and stacking-faults in  $L1_2$  and  $D0_{22}$  compounds*, Physical Review B, 50 (1992), pp. 4848-4858.
- [62] F. Guillet, Y. Calvayrac, and P. Cénédèse, *Thermodynamic study of the effect of a ternary addition on antiphase boundaries in fcc alloys*, Journal of Physics-Condensed Matter, 5 (1993), pp. 6787-6800.
- [63] H.P. Karnthaler, E.T. Muhlbacher, and C. Rentenberger, *The influence of the fault energies on the anomalous mechanical behaviour of  $Ni_3Al$  alloys*, Acta Materialia, 44 (1996), pp. 547-560.
- [64] K.J. Hemker, and M.J. Mills, *Measurements of antiphase boundary and complex stacking fault energies in binary and B-doped  $Ni_3Al$  using TEM*, Philosophical Magazine, 68 (1993), pp. 305-324.
- [65] Y.M. Hong, H. Nakajima, Y. Mishima, and T. Suzuki, *The  $\gamma$  solvus surface in  $Ni-Al-X$  ( $X$ : Cr, Mo, and W) ternary systems*, ISIJ International, 29 (1989), pp. 78-84.
- [66] T. Maciag, K. Rzyman, and R. Przeliorz, *DSC analysis of order-disorder transition in  $Ni_3Al$  based alloys from Ni-Al-Cr system*, Archives of Metallurgy and Materials, 60 (2015), pp. 1871-1876.
- [67] M.P. Jackson, M.J. Starink, and R.C. Reed, *Determination of the precipitation kinetics of  $Ni_3Al$  in the Ni-Al system using differential scanning calorimetry*, Materials Science and Engineering, 264 (1999), pp. 26-38.
- [68] Y. Mishima, S. Ochai, N. Hamao, M. Yodogawa, and T. Suzuki, *Solid solution hardening of nickel-role of transition-metal and B-subgroup solutes*, Transactions of the Japan Institute of Metals, 27: 9 (1986), pp. 656-664.

- [69] C. Pareige, F. Soisson, G. Martin, and D. Blavette, *Ordering and phase separation in Ni-Cr-Al: Monte Carlo simulations vs three-dimensional atom probe*, *Acta Materialia*, 47 (1999), pp. 1889-1899.
- [70] J.T. Lu, S.L. Zhu, and F.H. Wang, *High temperature corrosion behavior of an AlP NiCoCrAlY coating modified by aluminizing*, *Surface & Coatings Technology*, 205 (2011), pp. 5053-5058.
- [71] M. Nathal, and L. Ebert, *The influence of cobalt, tantalum, and tungsten on the microstructure of single crystal nickel-base superalloys*, *Metallurgical and Materials Transactions A*, 16(10) (1985), pp. 1849–1862.
- [72] D.N. Duhl, and A.D. Cetel, *Advanced high strength single crystal superalloy compositions*, US Patent 4,719,080, Jan 12, 1988.
- [73] T. Izumi, N. Mu, L. Zhang, and B. Gleeson, *Effects of targeted  $\gamma$ -Ni +  $\gamma'$ -Ni<sub>3</sub>Al-based coating compositions on oxidation behavior*, *Surface & Coatings Technology*, 202 (2007), pp. 628-631.
- [74] R.A. Mackay, M.V. Nathal, and D.D. Pearson, *Influence of molybdenum on the creep-properties of nickel-base superalloy single-crystals*, *Metallurgical and Materials Transactions A*, 21(2) (1990), pp. 381-388.
- [75] A.K. Jena, and M.C. Chaturvedi, *The role of alloying elements in the design of nickel-base superalloys*, *Journal of Materials Science*, 10 (1984), pp. 3121-3139.
- [76] F. Weng, H. Yu, C. Chen, and K. Wan, *Influence of Nb and Y on Hot Corrosion Behavior of Ni-Cr-based Superalloys*, *Materials and Manufacturing Processes*, 30 (2015), pp. 677-684.

- [77] B. Gleeson, W. Wang, S. Hayashi, and D. Sordelet, *Effects of platinum on the interdiffusion and oxidation behavior of Ni-Al-based alloys*, Materials Science Forum, 461-464 (2004), pp. 213-222.
- [78] K. Kawagishi, H. Harada, A. Sato, A. Sato, and T. Kobayashi, *The oxidation properties of fourth generation single-crystal nickel-based superalloys*, JOM, 58 (2006), pp. 43-46.
- [79] R.A. Hobbs, M.S.A. Karunaratne, S. Tin, R.C. Reed, and C.M.F. Rae, *Uphill diffusion in ternary Ni-Re-Ru alloys at 1000 and 1100 °C*, Materials Science and Engineering A, 460 (2007), pp. 587-594.
- [80] M.K. Miller, *Contributions of atom probe tomography to the understanding of nickel-based superalloys*, Micron, 32 (2001), pp. 757-764.
- [81] C.K. Sudbrack, D. Isheim, R.D. Noebe, N.S. Jacobson, and D.N. Seidman, *The influence of tungsten on the chemical composition of a temporally evolving nanostructure of a model Ni-Al-Cr superalloy*, Microscopy and Microanalysis, 10 (2004), pp. 355-365.
- [82] Y.X. Wu, J. Guo, J.S. Hou, W.L. Zhang, R.Z. Huang, X.G. Liu, X.F. Ma, and Q.F. Zhang, *First-principles study of the influence of lattice misfit on the behavior and the ductility effect of hafnium in Ni-Ni<sub>3</sub>Al system*, Acta Metallurgica Sinica-English Letters, 27(1) (2014), pp. 87-94.
- [83] Y. Amouyal, Z.G. Mao, and D.N. Seidman, *Phase partitioning and site-preference of hafnium in the  $\gamma'$  ( $L1_2$ ) /  $\gamma$  (fcc) system in Ni-based superalloys: An atom-probe tomographic and first-principles study*, Applied Physics Letters, 95 (2009), 161909.

- [84] S. Ochiai, Y. Oya, and T. Suzuki, *Alloying behaviour of Ni<sub>3</sub>Al, Ni<sub>3</sub>Ga, Ni<sub>3</sub>Si and Ni<sub>3</sub>Ge*, Acta Metallurgica, 32 (1984), pp. 289-298.
- [85] R.D. Rawlings, and A.E. Statonbevan, *Alloying behavior and mechanical-properties of polycrystalline Ni<sub>3</sub>Al ( $\gamma'$  phase) with ternary additions*, Journal of Materials Science, 10 (1975), pp. 505-514.
- [86] R.W. Guard, and J.H. Westbrook, *Alloying behavior of Ni<sub>3</sub>Al (gamma-phase)*, Transactions of the American Institute of Mining and Metallurgical Engineers, 215 (1959), pp. 807-814.
- [87] N.C. Tso, and J. M. Sanchez, *Thermodynamic modeling of site occupation in the  $\gamma'$  phase of the Ni-Al-Hf system*, Materials Science and Engineering A-Structural Materials Properties Microstructure and Processing, 108 (1989), pp. 159-164.
- [88] S. Raju, E. Mohandas, and V.S. Raghunathan, *A study of ternary element site substitution in Ni<sub>3</sub>Al using pseudopotential orbital radii based structure maps*, Scripta Materialia, 34 (1996), pp. 1785-1790.
- [89] A.O. Mekhrabov, and M.V. Akdeniz, *Modelling and Monte Carlo simulation of the atomic ordering processes in Ni<sub>3</sub>Al intermetallics*, Modelling and Simulation in Materials Science and Engineering, 15 (2007), pp. 1–12.
- [90] C. Jiang, and B. Gleeson, *Site preference of transition metal elements in Ni<sub>3</sub>Al*, Scripta Materialia, 55 (2006), pp. 433-436.
- [91] Q. Wu, and S. Li, *Alloying element additions to Ni<sub>3</sub>Al: Site preferences and effects on elastic properties from first-principles calculations*, Computational Materials Science, 53 (2012), pp. 436-443.



- [92] S. Ochiai, Y. Oya, and T. Suzuki, *Solubility data in Ni<sub>3</sub>Al with ternary additions*, Bull. P.M.E. (T.I.T.), 52 (1983), pp. 1-16.
- [93] E.V. Kozlov, E.L. Nikonenko, N.A. Koneva, N.A. Popova, N.R. Sizonenko, Y.R. Kolobov, G.P. Grabovetskaya, and V.P. Buntushkin, *Effect of Re content on structure and phase composition of Ni-Al alloys*, Bull. Russ. Acad. Sci., Phys. Ser., 69 (2005), pp. 1116-1120.
- [94] V. Raghavan, *Al-Ni-Re (Aluminum-Nickel-Rhenium)*, JPEDAV, 27 (2006), pp. 499-500.
- [95] B. Tryon, and T.M. Pollock, *Experimental assessment of the Ru-Al-Ni ternary phase diagram at 1000 and 1100 °C*, Materials Science and Engineering A, 430 (2006), pp. 266-276.
- [96] Y.P. Wu, N.C. Tso, J.M. Sanchez, and J.K. Tien, *Modeling of ternary site occupation in L1<sub>2</sub> ordered intermetallics*, Acta Metallurgica, 37 (1989), pp. 2835-2840.
- [97] A. Fujita, T. Matsumoto, M. Nakamura, and Y. Takeda, *In high-temperature ordered intermetallic alloys III*, edited by C.T. Liu et al., MRS, Pittsburgh, PA, 1989.
- [98] W. Zhao, Z. Sun, and S. Gong, *Synergistic effect of co-alloying elements on site preferences and elastic properties of Ni<sub>3</sub>Al: A first-principles study*, Intermetallics, 65 (2015), pp. 75-80.
- [99] Y. Tu, Z.G. Mao, and D.N. Seidman, *Phase-partitioning and site-substitution patterns of molybdenum in a model Ni-Al-Mo superalloy: An atom-probe tomographic and first-principles study*, Applied Physics Letters, 101 (2012), pp. 121910.

- [100] Y. Amouyal, Z.G. Mao, and D.N. Seidman, *Effects of tantalum on the partitioning of tungsten between the  $\gamma$ - and  $\gamma'$ -phases in nickel-based superalloys: Linking experimental and computational approaches*, Acta Materialia, 58 (2010), pp. 5898-5911.
- [101] Y. Amouyal, Z.G. Mao, C. Booth-Morrison, and D.N. Seidman, *On the interplay between tungsten and tantalum atoms in Ni-based superalloys: An atom-probe tomographic and first-principles study*, Applied Physics Letters, 94 (2009), 041917.
- [102] Y. Zhou, Z.G. Mao, C. Booth-Morrison, and D.N. Seidman, *The partitioning and site preference of rhenium or ruthenium in model nickel-based superalloys: An atom-probe tomographic and first-principles study*, Applied Physics Letters, 93 (2008), 171905.
- [103] M. Chaudhari, A. Singh, P. Gopal, S. Nag, G.B. Viswanathan, J. Tiley, R. Banerjee, and J. Du, *Site occupancy of chromium in the  $\gamma'$ -Ni<sub>3</sub>Al phase of nickel-based superalloys: A combined 3D atom probe and first-principles study*, Philosophical Magazine Letters, 92(9) 2012, pp. 495-506.
- [104] D. Blavette, and A. Bostel, *Phase-composition and long-range order in  $\gamma'$ -phase of a nickel-base single-crystal superalloy CMSX2 - An atom probe study*, Acta Metallurgica, 32 (1984), pp. 811-816.
- [105] S. Meher, T. Rojhirunsakool, P. Nandwana, J. Tiley, and R. Banerjee, *Determination of solute site occupancies within  $\gamma'$  precipitates in nickel-base superalloys via orientation-specific atom probe tomography*, Ultramicroscopy, 159 (2015), pp. 272-277.
- [106] M.K. Miller, R. Jayaram, L.S. Lin, and A.D. Cetel, *APFIM characterization of single-crystal PWA-1480 nickel-base superalloy*, Applied Surface Science, 76

(1994), pp. 172-176.

- [107] K.L. More, and M.K. Miller, *Microstructural characterization of Udimet 720 - A nickel-base alloy*, Journal de Physique, 49 (1988), pp. 391-396.
- [108] M.K. Miller, and J.A. Horton, *Site occupation determinations by APFIM for Hf, Fe, and Co in Ni<sub>3</sub>Al*, Scripta Metallurgica, 20 (1986), pp. 1125–1130.
- [109] A.P. Ofori, C.J. Rossouw, and C.J. Humphreys, *Determining the site occupancy of Ru in the L1<sub>2</sub> phase of a Ni-base superalloy using ALCHEMI*, Acta Materialia, 53 (2005), pp. 97-110.
- [110] A.A. Katsnelson, A.O. Mekhrabov, and V.M. Silonov, *Electron theory of short order of 3-component alloys in pseudopotential approximation*, Fizika Metallov I Metallovedenie, 52 (1981), pp. 661-662.
- [111] A.O. Mekhrabov, and M. Doyama, *Electronic theory of atomic short-range order for ternary alloys using the pseudopotential approximation and its comparison with experiments*, Physica Status Solidi B-Basic Research, 126 (1984), pp. 453-458.
- [112] A.O. Mekhrabov, *Pseudopotential calculations of short-range atomic order characteristics of 3-component Ni<sub>3</sub>(Fe,Me) alloys*, Fizika Metallov I Metallovedenie, 62 (1986), pp. 1023-1025.
- [113] A.O. Mekhrabov, *A study of short-range order in ternary alloys in the pseudopotential approximation*, Tr. J. of Engineering and Environmental Sciences, 18 (1994), pp. 349-356.
- [114] A.O. Mekhrabov, and M.V. Akdeniz, *Effect of ternary alloying elements*

- addition on atomic ordering characteristics of Fe-Al intermetallics*, Acta Materialia, 47 (1999), pp. 2067-2075.
- [115] A.O. Mekhrabov, M.V. Akdeniz, and M.M. Arer, *Atomic ordering characteristics of Ni<sub>3</sub>Al intermetallics with substitutional ternary additions*, Acta Materialia, 45 (1997), pp. 1077-1083.
- [116] M.V. Akdeniz, and A.O. Mekhrabov, *The effect of substitutional impurities on the evolution of Fe-Al diffusion layer*, Acta Materialia, 46 (1998), pp. 1185-1192.
- [117] A.O.E. Animalu, *Electronic-structure of transition-metals. 1. Quantum defects and model potential*, Physical Review B, 8 (1973), pp. 3542-3554.
- [118] Z.M. Babayev, Z.A. Matysina, and A.O. Mekhrabov, *Ordering temperatures and order parameters of Ni<sub>3</sub>Fe alloys with Mn and Cr impurities*, Fizika Metallov I Metallovedenie, 64 (1987), pp. 202-205.
- [119] M. Yıldırım, M.V. Akdeniz, and A.O. Mekhrabov, *Effect of ternary alloying elements addition on the order-disorder transformation temperatures of B2-type ordered Fe-Al-X intermetallics*, Metallurgical and Materials Transactions A, 43 (2012), pp. 1809-1816.
- [120] J. Hubbard, *The description of collective motions in terms of many-body perturbation theory*, Proceedings of the Royal Society of London Series A-Mathematical and Physical Sciences, 240 (1957), pp. 539-560.
- [121] J. Hubbard, *The description of collective motions in terms of many-body perturbation theory. 2. The correlation energy of a free-electron gas*, Proceedings of the Royal Society of London Series A-Mathematical and Physical Sciences, 243 (1958), pp. 336-352.

- [122] L.J. Sham, *A calculation of phonon frequencies in sodium*, Proceedings of the Royal Society of London Series A-Mathematical and Physical Sciences, 283 (1965), pp. 33-&.
- [123] N.I. Kourov, S.Z. Nazarova, A.V. Korolev, Y.A. Dorofeev, N.V. Volkova, and E.V. Belozеров, *Magnetic properties of  $Ni_3Al_xMn_{1-x}$  alloys*, Physics of Metals and Metallography, 110 (2010), pp. 1-4.
- [124] G.M. Stocks, D.M. Nicholson, F.J. Pinski, W.H. Butler, P. Sterne, W.M. Temmerman, B.L. Gyorffy, D.D. Johnson, A. Gonis, X.G. Zhang, and P.E.A. Turchi, *In high temperature ordered intermetallic alloys II*, edited by N.S. Stoloff et al., MRS, Pittsburg, PA, 1987.
- [125] J.M. Cowley, *An approximate theory of order in alloys*, Physical Review, 77 (1950), pp. 669-675.
- [126] J.P. Perdew, K. Burke, and M. Ernzerhof, *Generalized gradient approximation made simple*, Physical Review Letters, 77 (1996), pp. 3865-3868.
- [127] D.E. Kim, S.L. Shang, and Z.K. Liu, *Effects of alloying elements on elastic properties of  $Ni_3Al$  by first-principles calculations*, Intermetallics, 18 (2010), pp. 1163-1171.
- [128] C.Y. Geng, C.Y. Wang, and T. Yu, *Site preference and alloying effect of platinum group metals in  $\gamma'$ - $Ni_3Al$* , Acta Materialia, 52 (2004), pp. 5427-5433.
- [129] F. Sun, S.C. Mao, and J.X. Zhang, *Identification of the partitioning characteristics of refractory elements in  $\sigma$  and  $\gamma$  phases of Ni-based single crystal superalloys based on first principles*, Materials Chemistry and Physics, 147 (2014), pp. 483-487.

- [130] Y.J. Wang, and C.Y. Wang, *Influence of the alloying element Re on the ideal tensile and shear strength of  $\gamma'$ -Ni<sub>3</sub>Al*, Scripta Materialia, 61 (2009), pp. 197-200.
- [131] C.Y. Geng, C.Y. Wang, J.T. Wang, and T. Yu, *First-principles study of the electronic properties of  $\gamma/\gamma'$  Interface in Ni based superalloys*, Materials Transactions, 46 (2005), pp. 1122-1126.
- [132] P. Ravindran, G. Subramoniam, and R. Asokamani, *Ground-state properties and relative stability between the L1<sub>2</sub> and DO<sub>a</sub> phases of Ni<sub>3</sub>Al by Nb substitution*, Physical Review B, 53 (1996), pp. 1129-1137.
- [133] G. Ghosh, and G.B. Olson, *Integrated design of Nb-based superalloys: Ab initio calculations, computational thermodynamics and kinetics, and experimental results*, Acta Materialia, 55 (2007), pp. 3281-3303.
- [134] A. Umicevic, H.E. Mahnke, B. Cekic, J. Grbovic, V. Koteski, and J. Belosevic-Cavor, *SEM and XRD characterization of Ni-Hf alloys at low Hf concentration*, edited by D.P. Uskokovic et al., Recent Developments in Advanced Materials and Processes, 518 (2006), pp. 325-330.
- [135] P. Nash, and D.R.F. West, *Phase-equilibria in Ni-rich region of Ni-Al-Hf system*, Metal Science, 15 (1981), pp. 347-352.
- [136] *Crystal and Molecular Structures Modelling & Diffraction*, [www.crystalmaker.com](http://www.crystalmaker.com), last visited on June 2017.
- [137] P.Y. Li, S.D. Li, Z.J. Tian, Z.G. Huang, F.M. Zhang, and Y.W. Du, *Effect of Ni-Al atomic ratio on glass formation in La-Al-Cu-Ni bulk metallic glasses*, Journal of Alloys and Compounds, 478 (2009), pp. 193-196.

- [138] H. Harada, K. Ohno, T. Yamagata, T. Yokokawa, and M. Yamazaki, *Phase calculation and its use in alloy design program for nickel-base superalloys*, Superalloys 1988, The Metallurgical Society, 1988, pp. 733-741.
- [139] W. Huang, and Y.A. Chang, *Thermodynamic properties of the Ni-Al-Cr system*, Intermetallics, 7 (1999), pp. 863-874.
- [140] C. Zhang, J. Zhu, Y. Yang, H.B. Cao, F. Zhang, W.S. Cao, and Y.A. Chang, *Thermodynamic modeling and experimental investigation of the Ni-rich corner of the Ni-Al-Hf system*, Intermetallics, 16 (2008), pp. 139-147.
- [141] V. Raghavan, *Al-Hf-Ni (Aluminum-Hafnium-Nickel)*, Journal of Phase Equilibria and Diffusion, 30 (2009), pp.64-66.
- [142] X.G. Lu, Y.W. Cui, and Z.P. Jin, *Experimental and thermodynamic investigation of the Ni-Al-Mo system*, Metallurgical and Materials Transactions A, 30 (1999), pp. 1785-1795.
- [143] Y. Du, Y.A. Chang, W.P. Gong, B.Y. Huang, H.H. Xu, Z.P. Jin, F. Zhang, and S.L. Chen, *Thermodynamic properties of the Al-Nb-Ni system*, Intermetallics, 11 (2003), pp. 995-1013.
- [144] M. Palm, W. Sanders, and G. Sauthoff, *Phase equilibria in the Ni-Al-Ta system*, Zeitschrift Fur Metallkunde, 87 (1996), pp. 390-398.
- [145] R. Kainuma, K. Urushiyama, K. Ishikawa, C.C. Jia, I. Ohnuma, and K. Ishida, *Ordering and phase separation in bcc aluminides of the Ni-Fe-Al-Ti system*, Materials Science and Engineering A, 240 (1997), pp. 235-244.
- [146] P. Broz, J. Bursik, and Z. Stara, *Phase equilibria in the Ni-Al-W system at 900 °C*, Monatshefte Fur Chemie, 136 (2005), pp. 1915-1920.





APPENDIX A

BINARY PHASE DIAGRAM OF Ni-Al SYSTEM

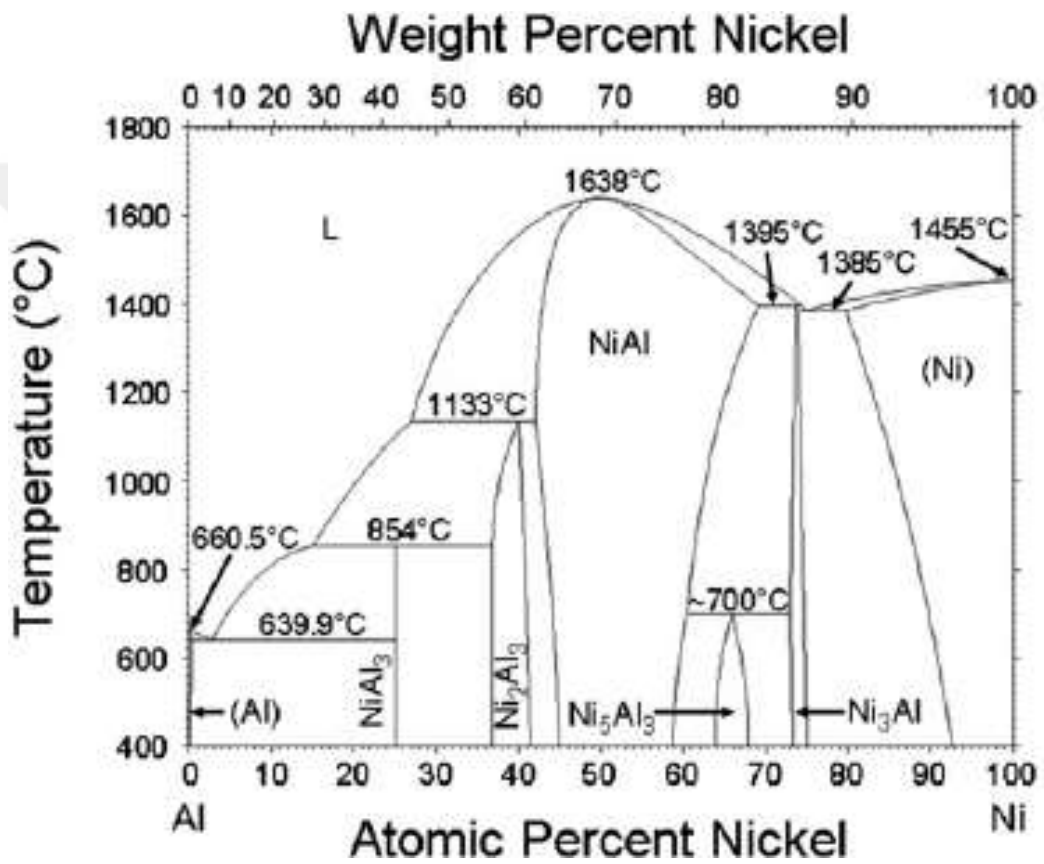
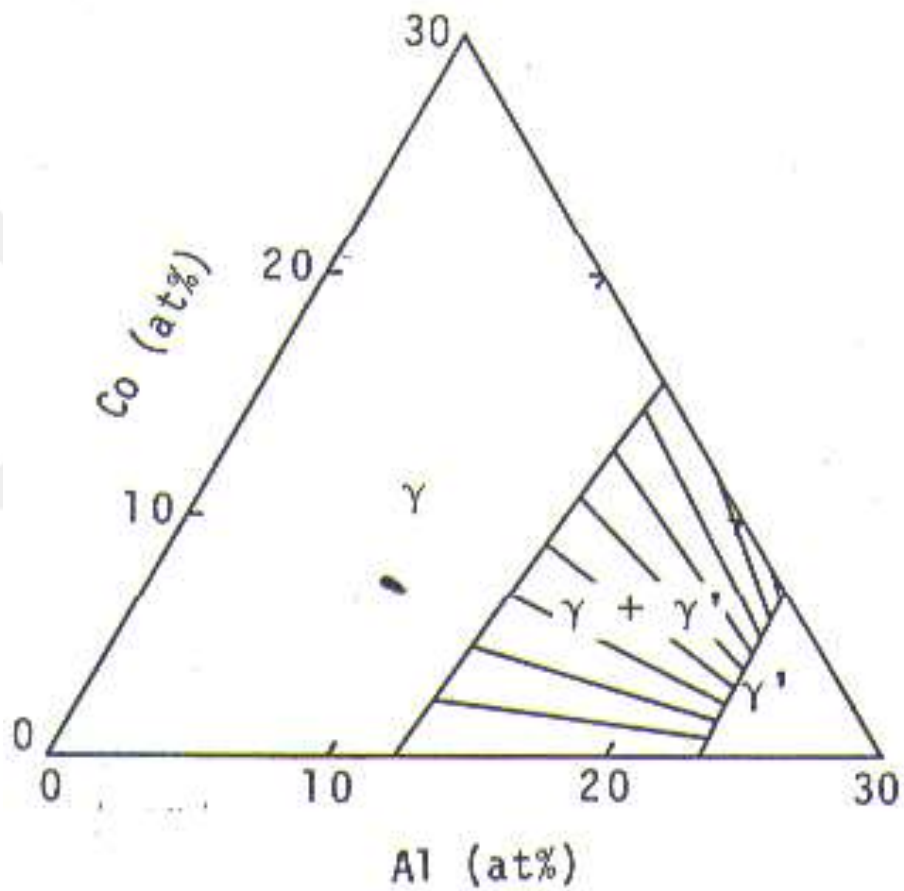


Figure A.1 Binary phase diagram of Ni-Al system (Adapted from [137]).



## APPENDIX B

### TERNARY PHASE DIAGRAMS OF Ni-Al-X SYSTEMS



**Figure B.1** Isothermal (900 °C) ternary phase diagram of Ni-Al-Co system  
(Adapted from [138]).

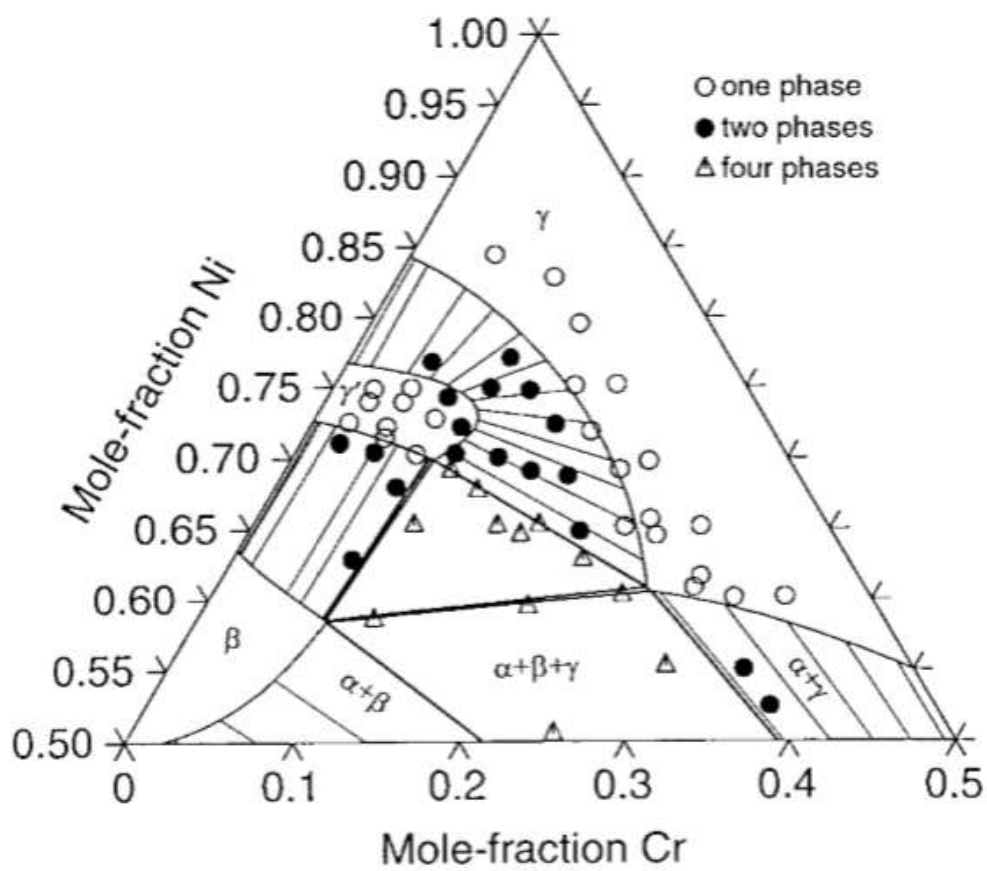


**Figure B.2** Isothermal (1000 °C) ternary phase diagram of Ni-Al-Cr system  
(Adapted from [139]).

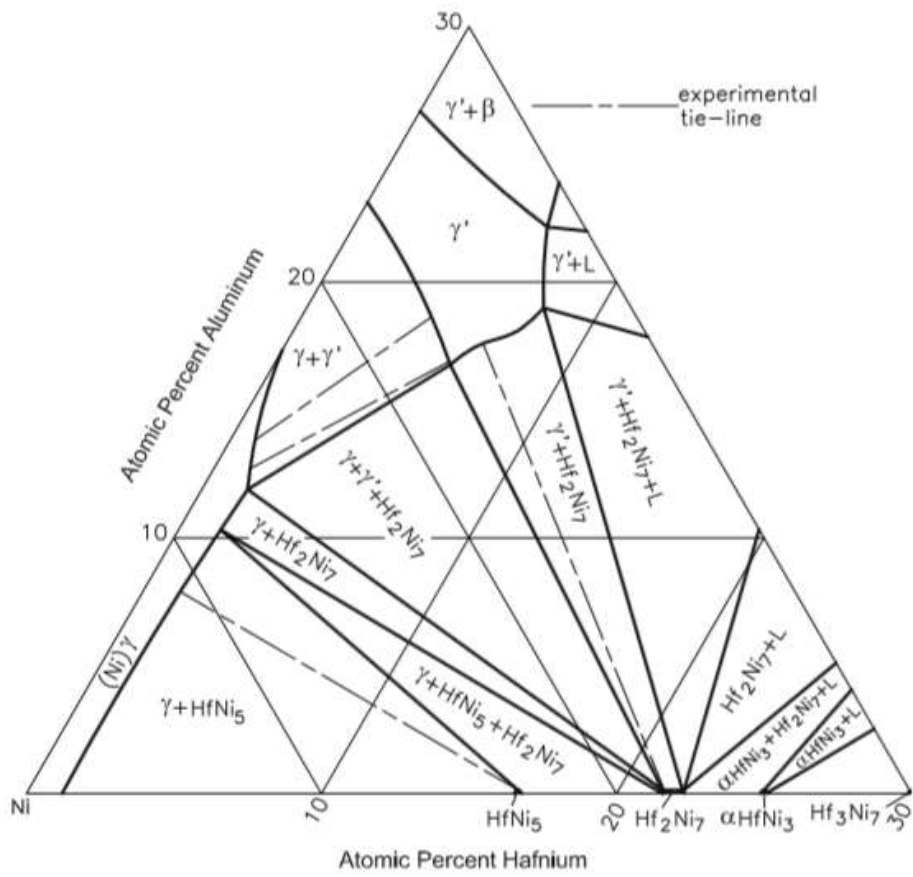


**Figure B.3** Isothermal (1160 °C) ternary phase diagram of Ni-Al-Hf system (Adapted from [140]).

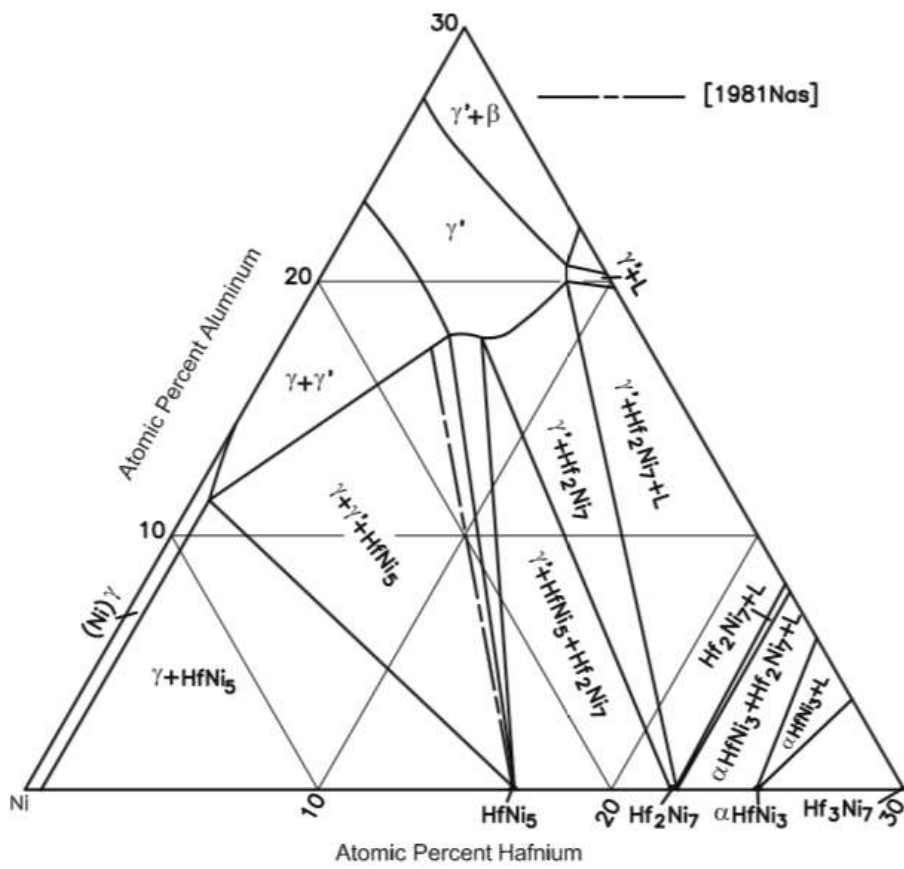


**Figure B.4** Isothermal (1000 °C) ternary phase diagram of Ni-Al-Hf system (Adapted from [140]).

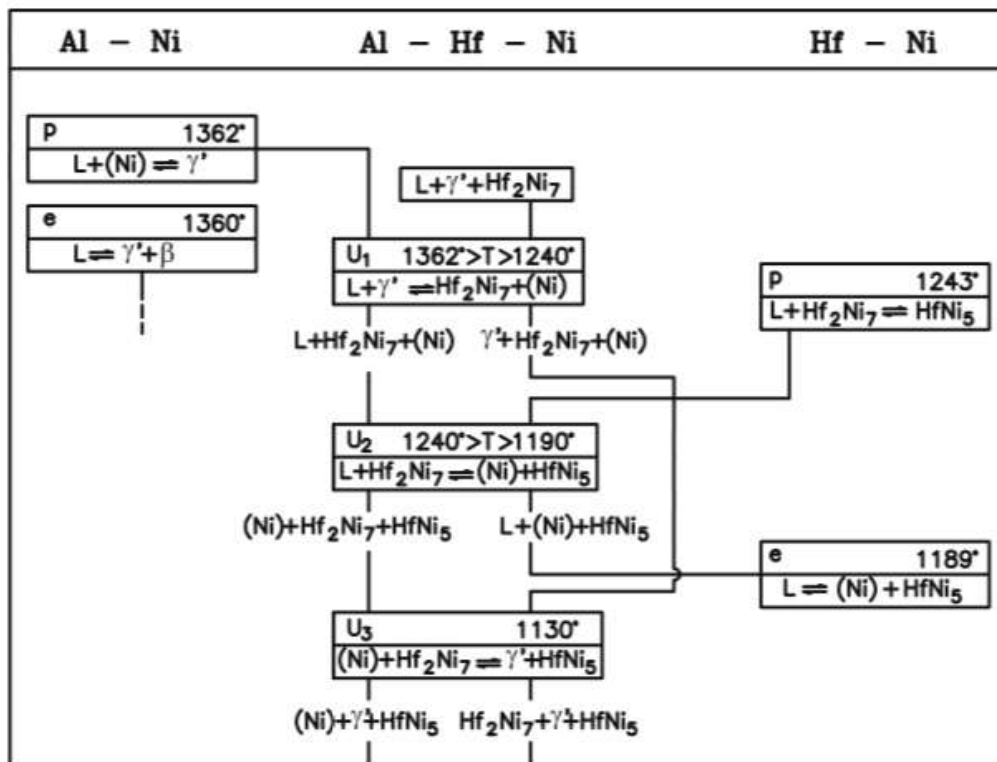


**Figure B.5** Partial reaction sequence of Ni-Al-Hf system (Adapted from [141]).

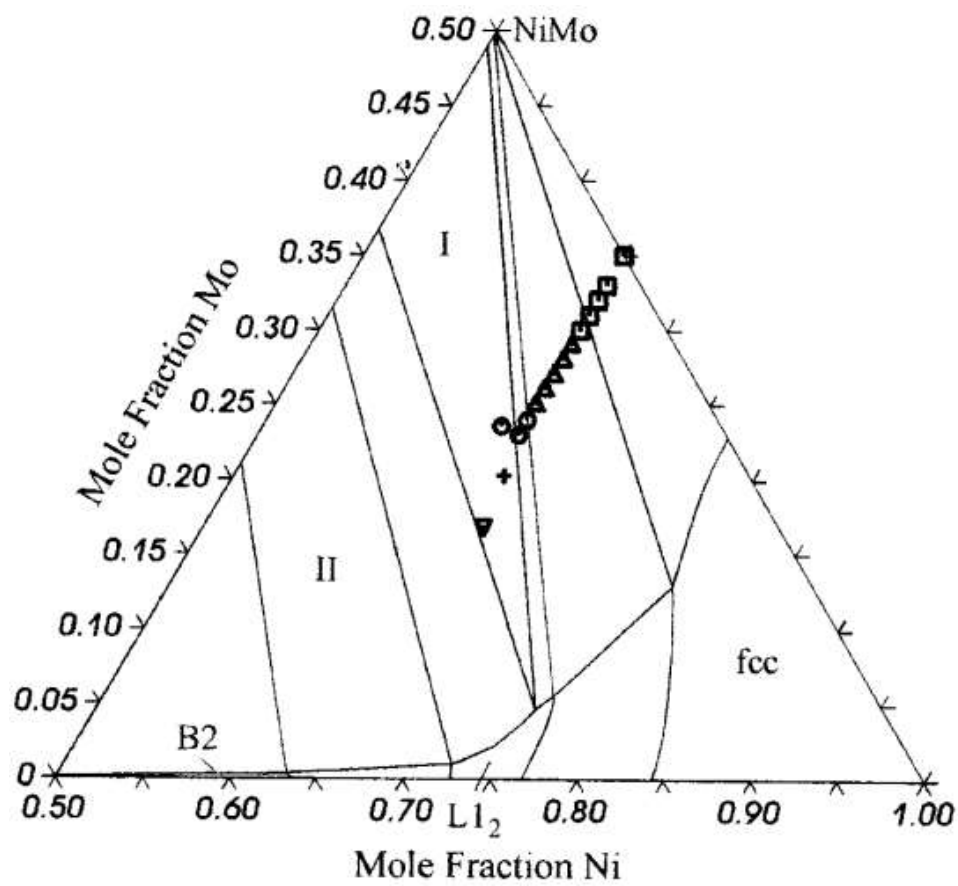


**Figure B.6** Isothermal (1000 °C) ternary phase diagram of Ni-Al-Mo system  
 (Adapted from [142]).



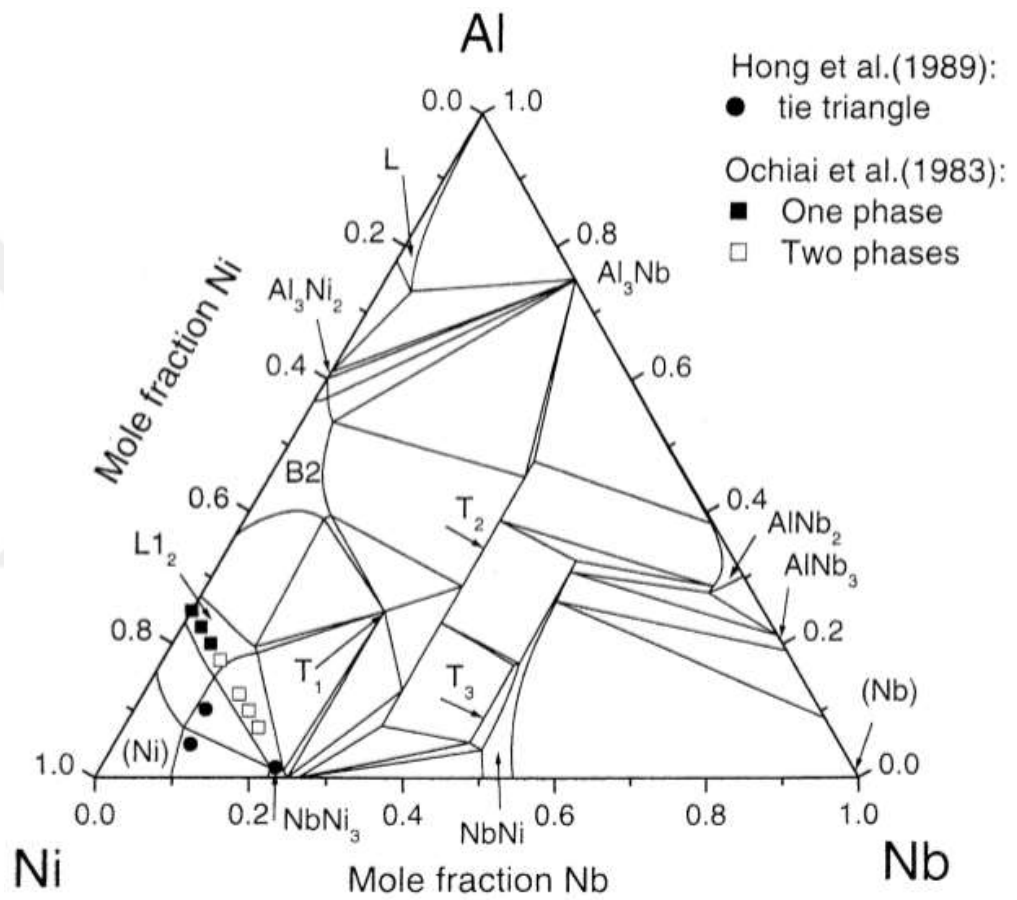


**Figure B.7** Isothermal (1027 °C) ternary phase diagram of Ni-Al-Nb system (Adapted from [143]).

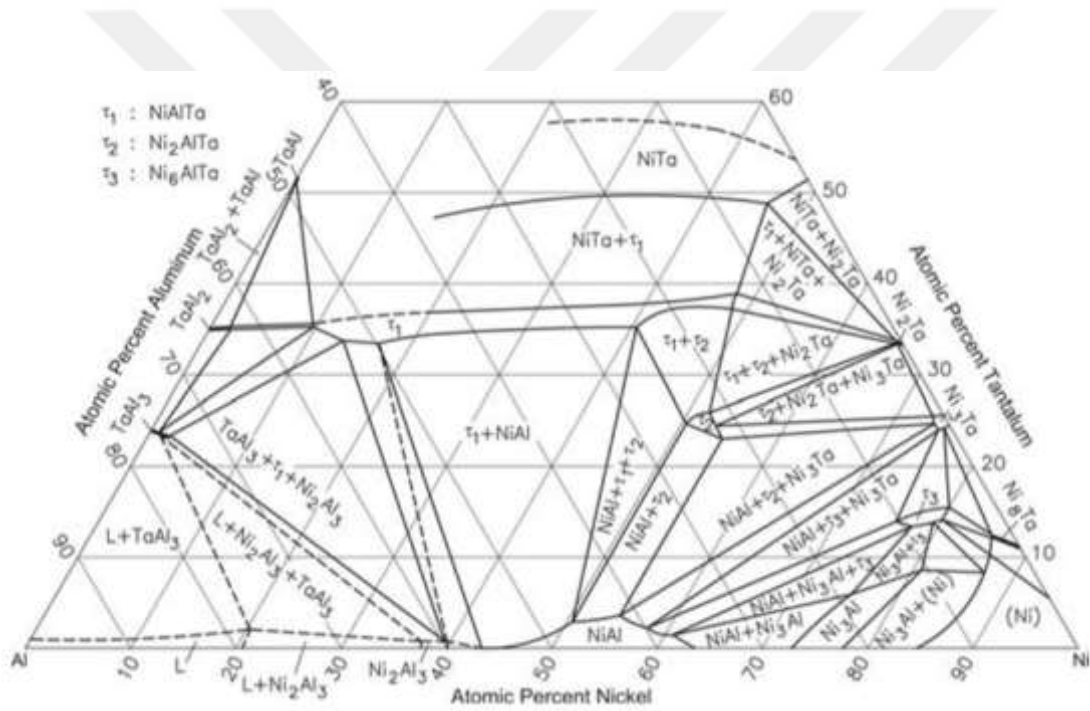


**Figure B.8** Isothermal (1000 °C) ternary phase diagram of Ni-Al-Ta system (Adapted from [144]).

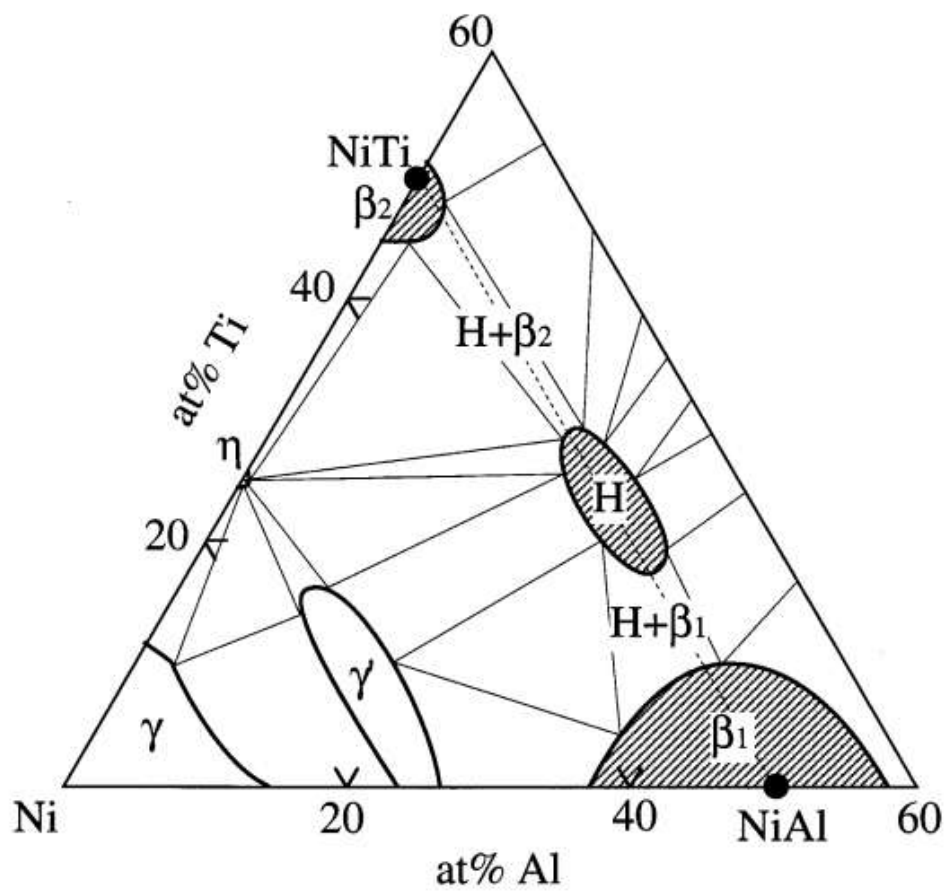


**Figure B.9** Isothermal (900 °C) ternary phase diagram of Ni-Al-Ti system  
 (Adapted from [145]).



## APPENDIX C

### XRD PATTERNS OF $\text{Ni}_{80}\text{Al}_{15}\text{X}_5$ ALLOY SYSTEMS

In Appendix C, XRD patterns of as cast (fast cooled), partial solution heat treated (1150 °C for 3 hr), homogenized/partial solution heat treated (1250 °C for 24 hr/1150 °C for 3 hr) and aged (800 °C for 4, 16, 64 and 256 hr, respectively)  $\text{Ni}_{80}\text{Al}_{15}\text{X}_5$  alloy systems ( $X = \text{Co}, \text{Cr}, \text{Hf}, \text{Mo}, \text{Nb}, \text{Ta}, \text{Ti}$  and  $\text{W}$ , respectively) have been demonstrated. Miller indices of  $\gamma$  matrix phase,  $\gamma'$  precipitates and  $\text{Ni}_5\text{Hf}$  phase have been shown in white spheres, black spheres and white triangles, respectively. In Figure C.16, extra peaks refer to oxides formed during homogenization heat treatment at high temperatures.

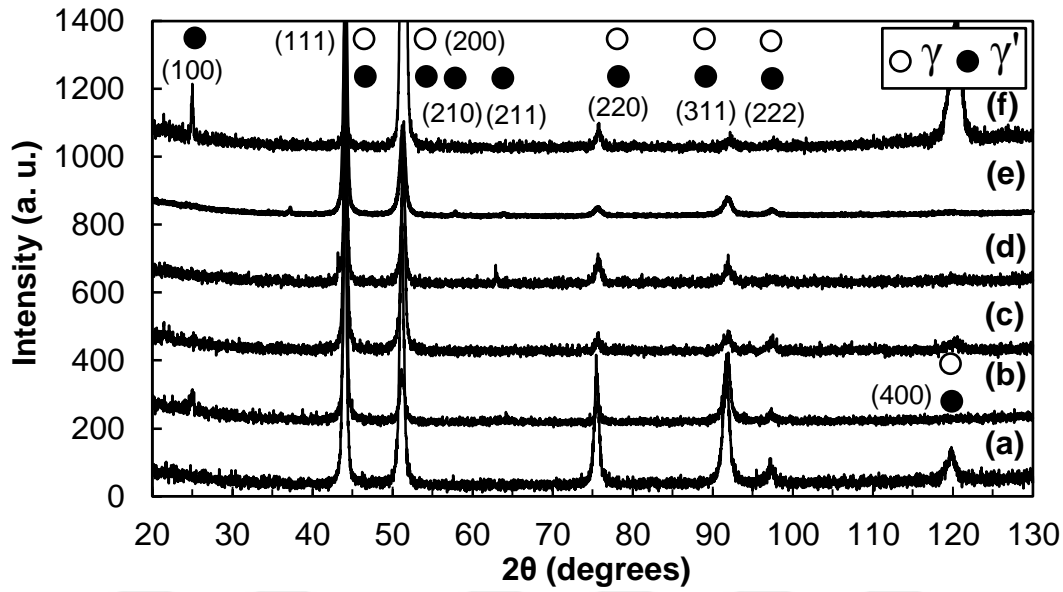


**Figure C.1** XRD patterns of (a) as cast (fast cooled)  $\text{Ni}_{80}\text{Al}_{15}\text{Co}_5$  alloys, (b) partially-solutionized at 1150 °C for 3 hr and subsequently aged at 800 °C for (c) 4 hr (d) 16 hr (e) 64 hr and (f) 256 hr, respectively.

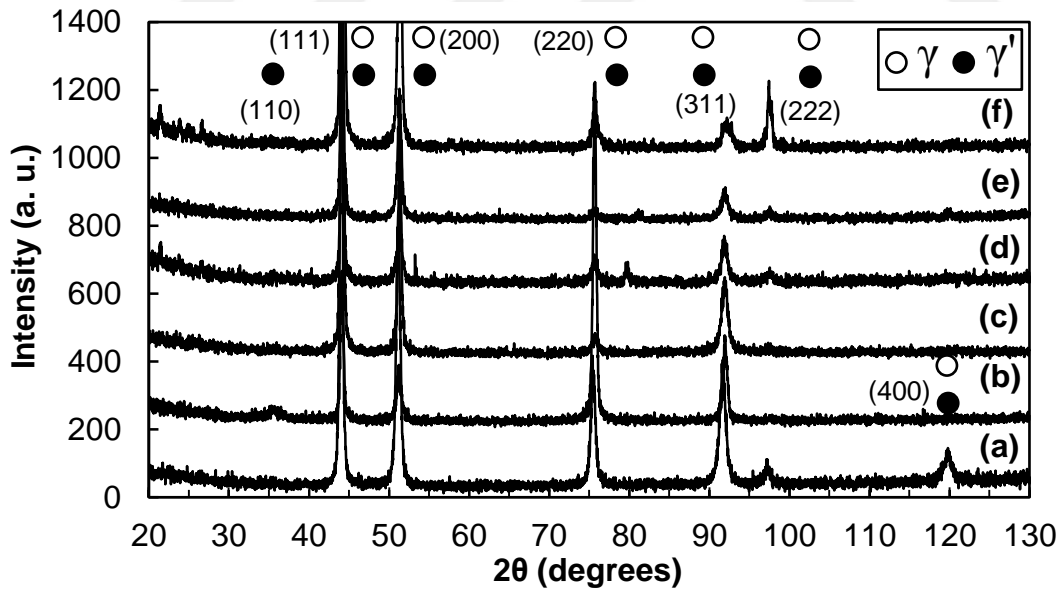


**Figure C.2** XRD patterns of (a) as cast (fast cooled)  $\text{Ni}_{80}\text{Al}_{15}\text{Co}_5$  alloys, (b) homogenized at 1250 °C for 24 hr and partially-solutionized at 1150 °C for 3 hr and subsequently aged at 800 °C for (c) 4 hr (d) 16 hr (e) 64 hr and (f) 256 hr, respectively.

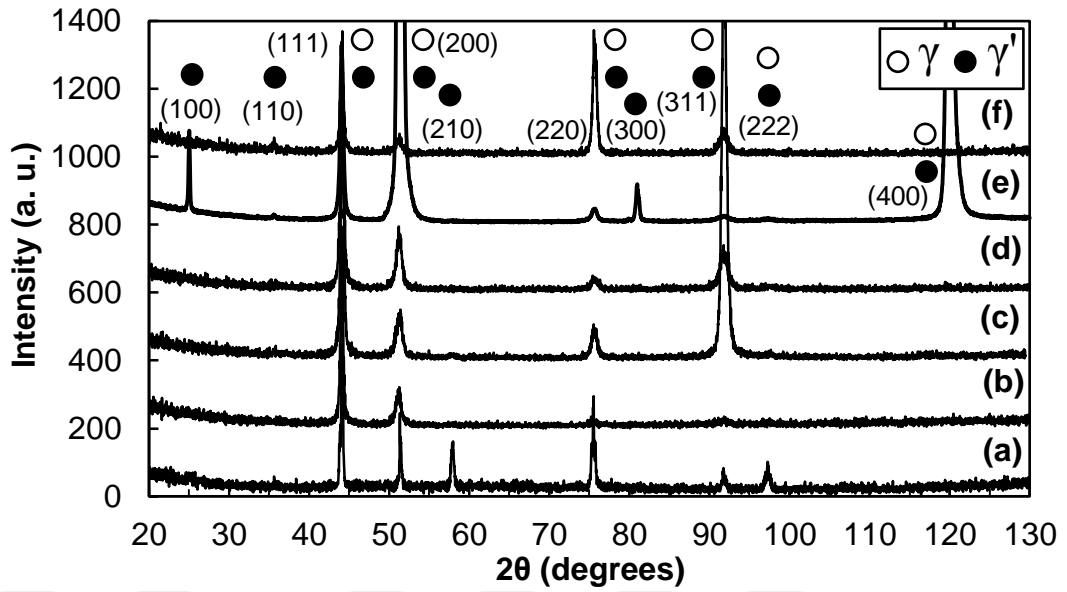


**Figure C.3** XRD patterns of (a) as cast (fast cooled)  $\text{Ni}_{80}\text{Al}_{15}\text{Cr}_5$  alloys, (b) partially-solutionized at 1150 °C for 3 hr and subsequently aged at 800 °C for (c) 4 hr (d) 16 hr (e) 64 hr and (f) 256 hr, respectively.

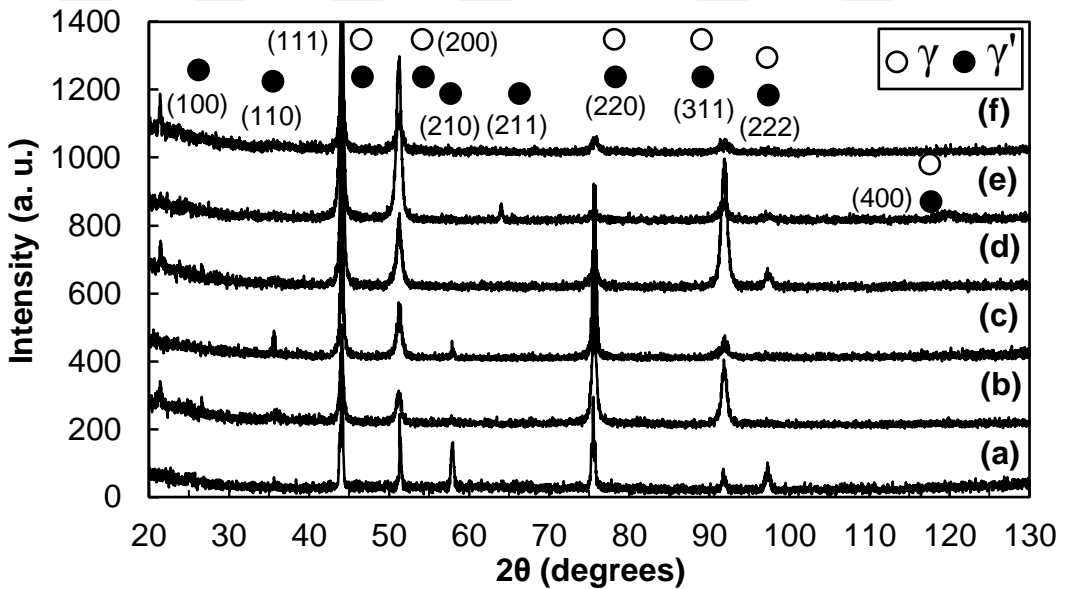


**Figure C.4** XRD patterns of (a) as cast (fast cooled)  $\text{Ni}_{80}\text{Al}_{15}\text{Cr}_5$  alloys, (b) homogenized at 1250 °C for 24 hr and partially-solutionized at 1150 °C for 3 hr and subsequently aged at 800 °C for (c) 4 hr (d) 16 hr (e) 64 hr and (f) 256 hr, respectively.

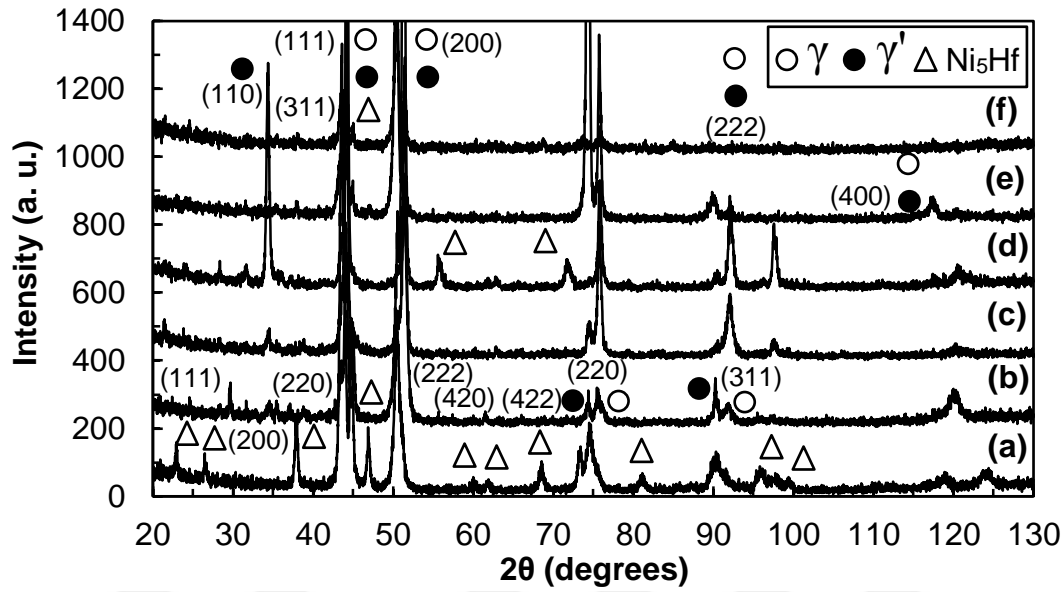


**Figure C.5** XRD patterns of (a) as cast (fast cooled)  $\text{Ni}_{80}\text{Al}_{15}\text{Hf}_5$  alloys, (b) partially-solutionized at 1150 °C for 3 hr and subsequently aged at 800 °C for (c) 4 hr (d) 16 hr (e) 64 hr and (f) 256 hr, respectively.

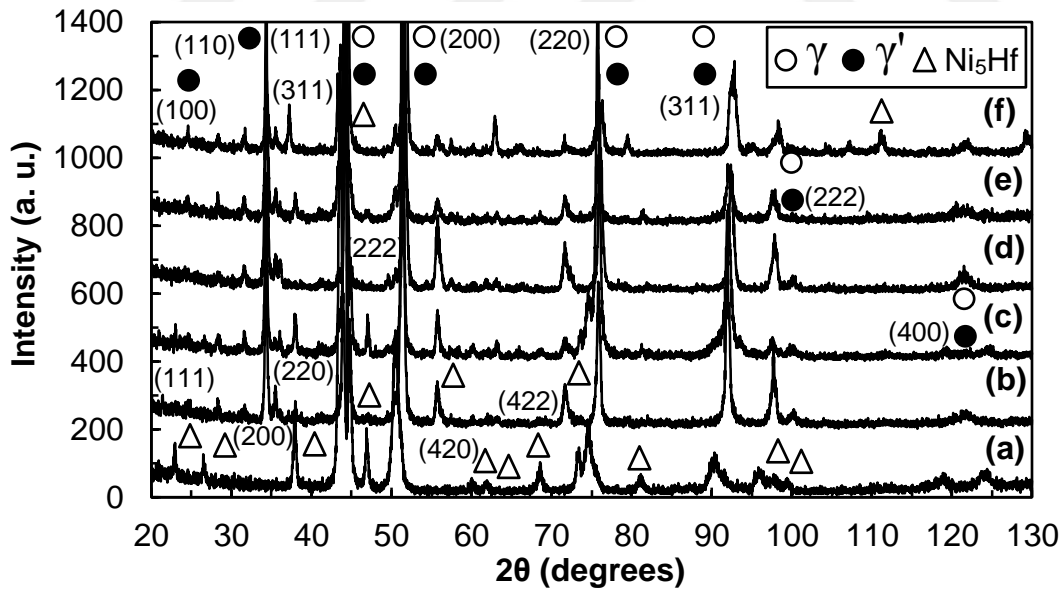


**Figure C.6** XRD patterns of (a) as cast (fast cooled)  $\text{Ni}_{80}\text{Al}_{15}\text{Hf}_5$  alloys, (b) homogenized at 1250 °C for 24 hr and partially-solutionized at 1150 °C for 3 hr and subsequently aged at 800 °C for (c) 4 hr (d) 16 hr (e) 64 hr and (f) 256 hr, respectively.



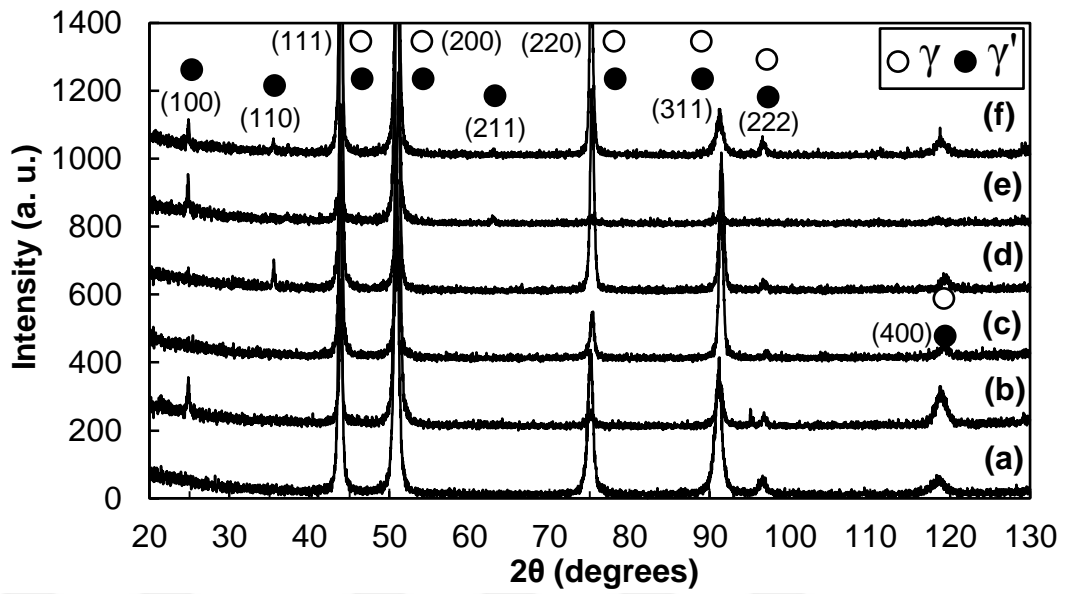


**Figure C.7** XRD patterns of (a) as cast (fast cooled)  $\text{Ni}_{80}\text{Al}_{15}\text{Mo}_5$  alloys, (b) partially-solutionized at  $1150^\circ\text{C}$  for 3 hr and subsequently aged at  $800^\circ\text{C}$  for (c) 4 hr (d) 16 hr (e) 64 hr and (f) 256 hr, respectively.

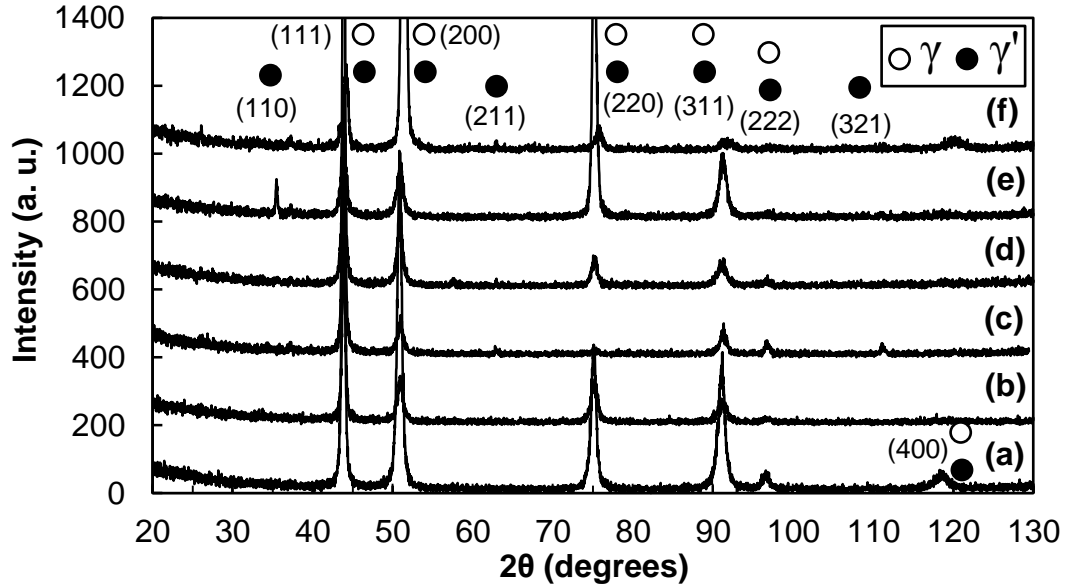


**Figure C.8** XRD patterns of (a) as cast (fast cooled)  $\text{Ni}_{80}\text{Al}_{15}\text{Mo}_5$  alloys, (b) homogenized at  $1250^\circ\text{C}$  for 24 hr and partially-solutionized at  $1150^\circ\text{C}$  for 3 hr and subsequently aged at  $800^\circ\text{C}$  for (c) 4 hr (d) 16 hr (e) 64 hr and (f) 256 hr, respectively.

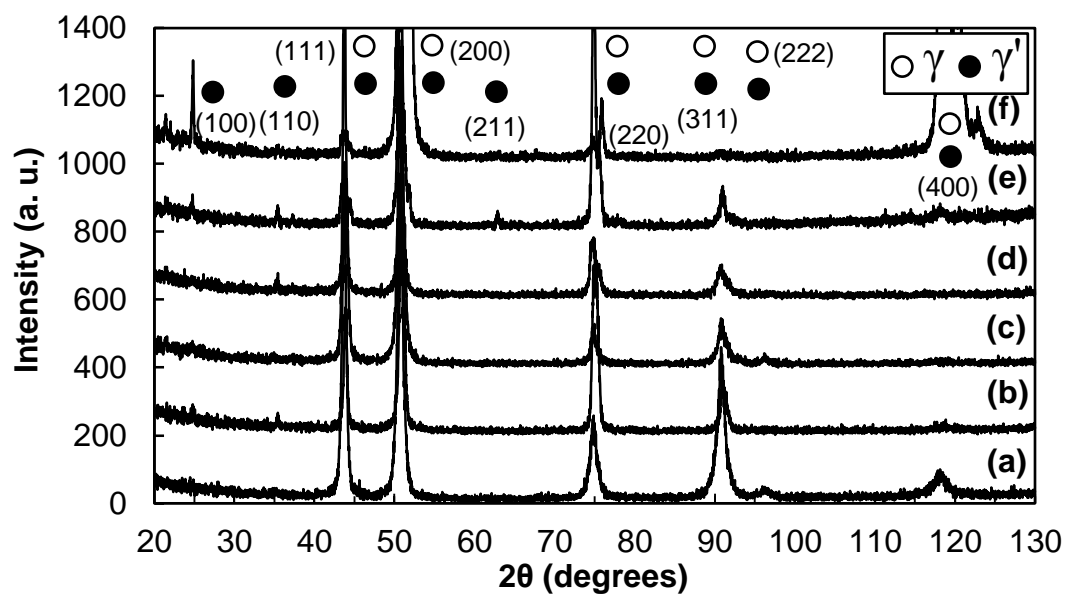


**Figure C.9** XRD patterns of (a) as cast (fast cooled)  $\text{Ni}_{80}\text{Al}_{15}\text{Nb}_5$  alloys, (b) partially-solutionized at  $1150^\circ\text{C}$  for 3 hr and subsequently aged at  $800^\circ\text{C}$  for (c) 4 hr (d) 16 hr (e) 64 hr and (f) 256 hr, respectively.

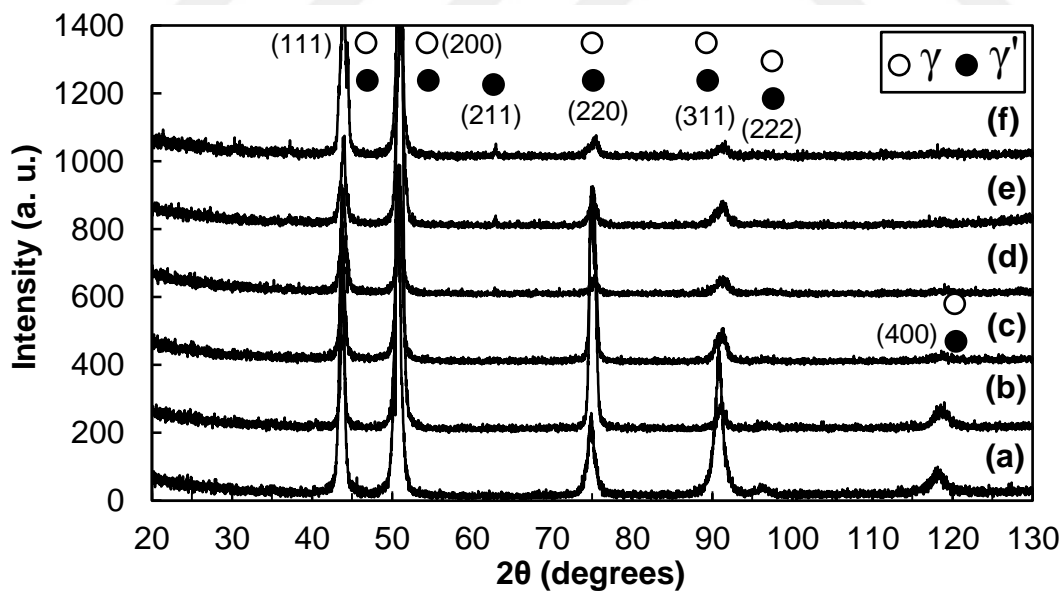


**Figure C.10** XRD patterns of (a) as cast (fast cooled)  $\text{Ni}_{80}\text{Al}_{15}\text{Nb}_5$  alloys, (b) homogenized at  $1250^\circ\text{C}$  for 24 hr and partially-solutionized at  $1150^\circ\text{C}$  for 3 hr and subsequently aged at  $800^\circ\text{C}$  for (c) 4 hr (d) 16 hr (e) 64 hr and (f) 256 hr, respectively.

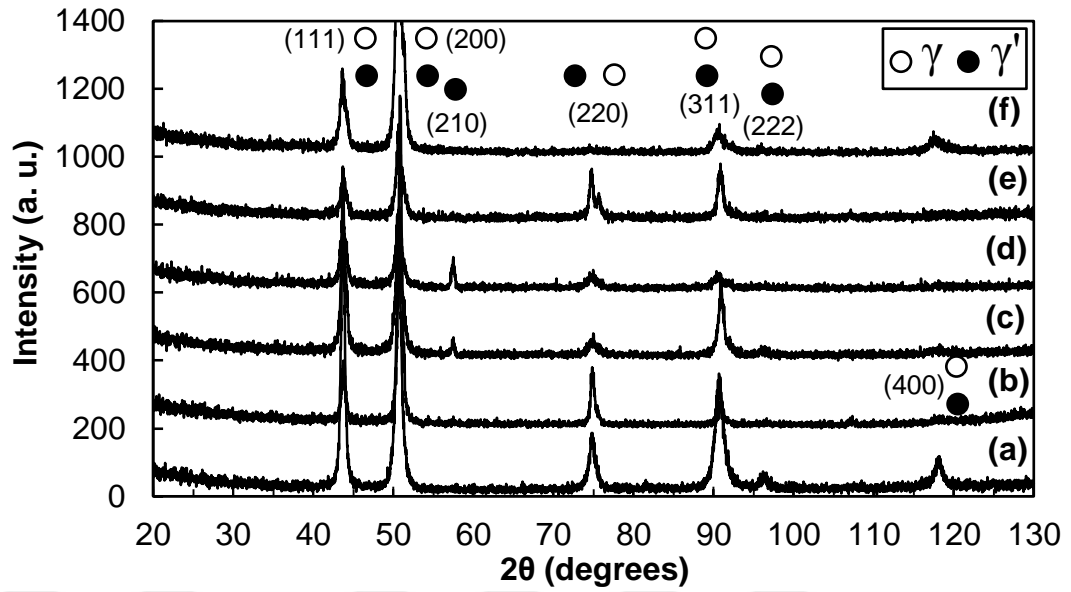


**Figure C.11** XRD patterns of (a) as cast (fast cooled)  $\text{Ni}_{80}\text{Al}_{15}\text{Ta}_5$  alloys, (b) partially-solutionized at 1150 °C for 3 hr and subsequently aged at 800 °C for (c) 4 hr (d) 16 hr (e) 64 hr and (f) 256 hr, respectively.

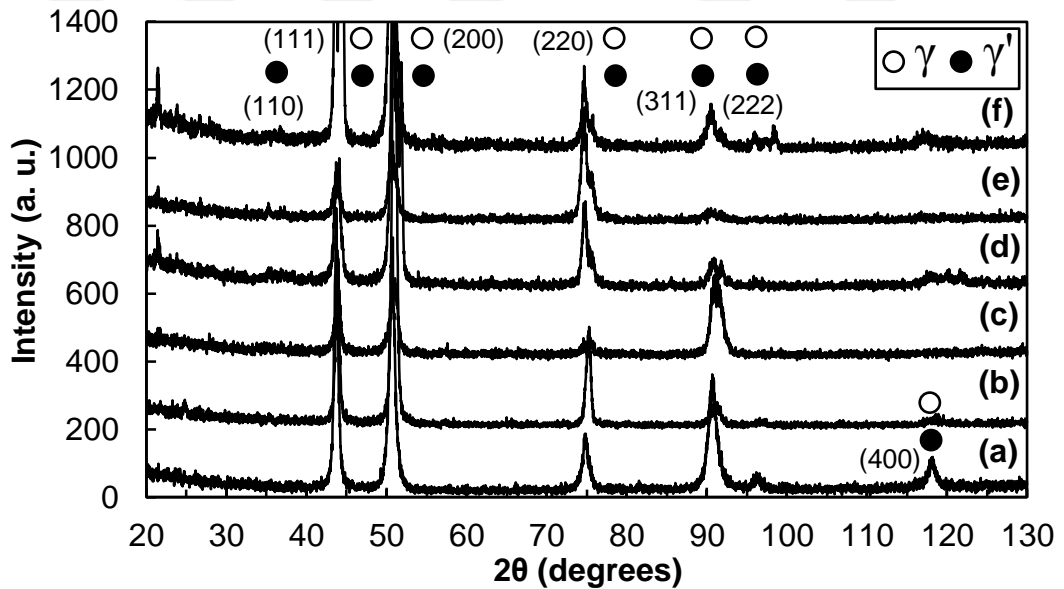


**Figure C.12** XRD patterns of (a) as cast (fast cooled)  $\text{Ni}_{80}\text{Al}_{15}\text{Ta}_5$  alloys, (b) homogenized at 1250 °C for 24 hr and partially-solutionized at 1150 °C for 3 hr and subsequently aged at 800 °C for (c) 4 hr (d) 16 hr (e) 64 hr and (f) 256 hr, respectively.

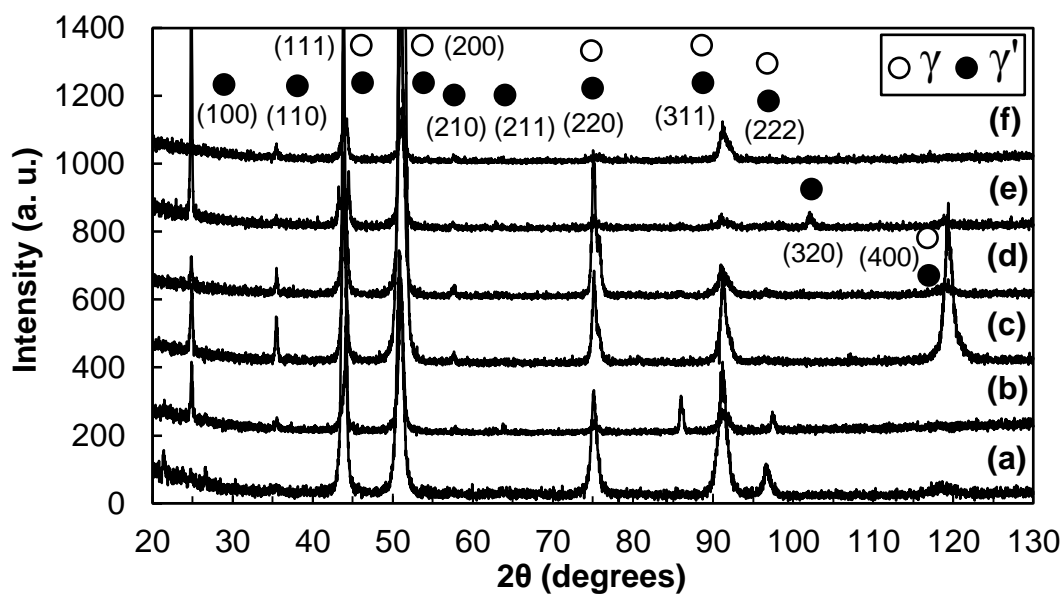


**Figure C.13** XRD patterns of (a) as cast (fast cooled)  $\text{Ni}_{80}\text{Al}_{15}\text{Ti}_5$  alloys, (b) partially-solutionized at 1150 °C for 3 hr and subsequently aged at 800 °C for (c) 4 hr (d) 16 hr (e) 64 hr and (f) 256 hr, respectively.

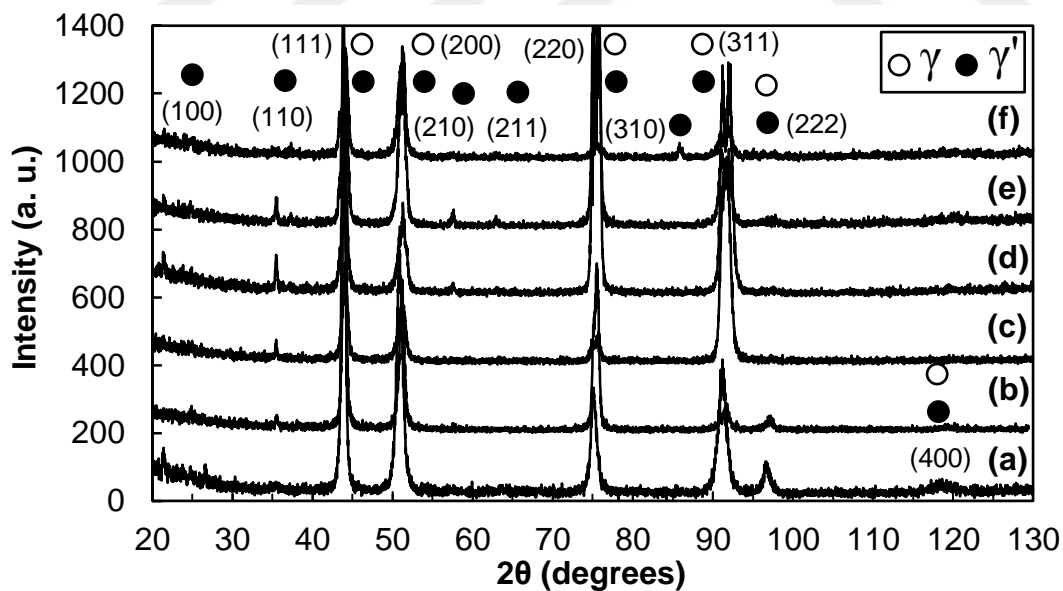


**Figure C.14** XRD patterns of (a) as cast (fast cooled)  $\text{Ni}_{80}\text{Al}_{15}\text{Ti}_5$  alloys, (b) homogenized at 1250 °C for 24 hr and partially-solutionized at 1150 °C for 3 hr and subsequently aged at 800 °C for (c) 4 hr (d) 16 hr (e) 64 hr and (f) 256 hr, respectively.

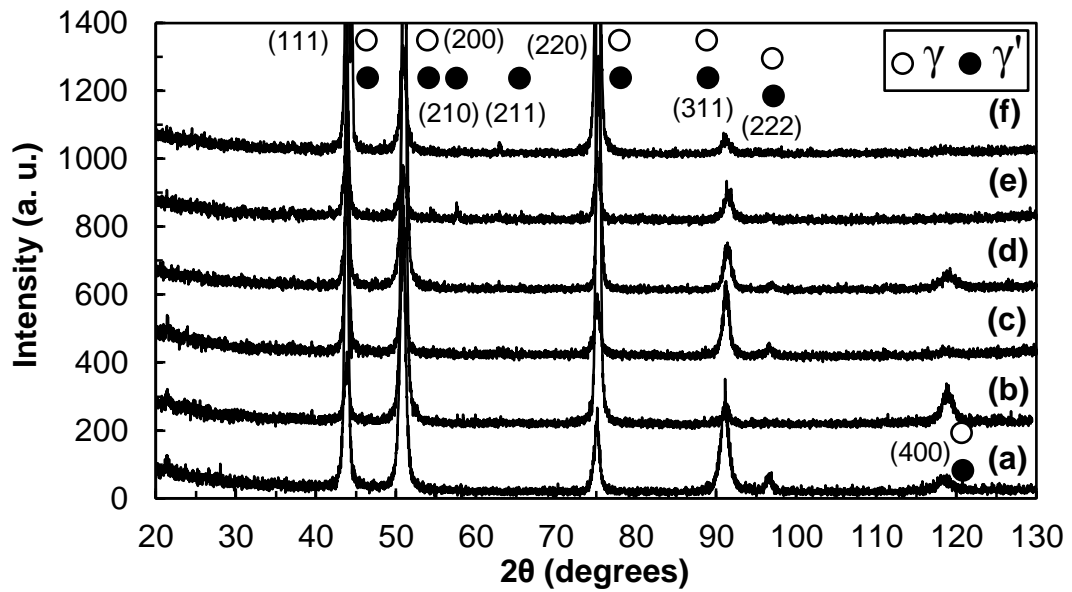


**Figure C.15** XRD patterns of (a) as cast (fast cooled)  $\text{Ni}_{80}\text{Al}_{15}\text{W}_5$  alloys, (b) partially-solutionized at 1150 °C for 3 hr and subsequently aged at 800 °C for (c) 4 hr (d) 16 hr (e) 64 hr and (f) 256 hr, respectively.

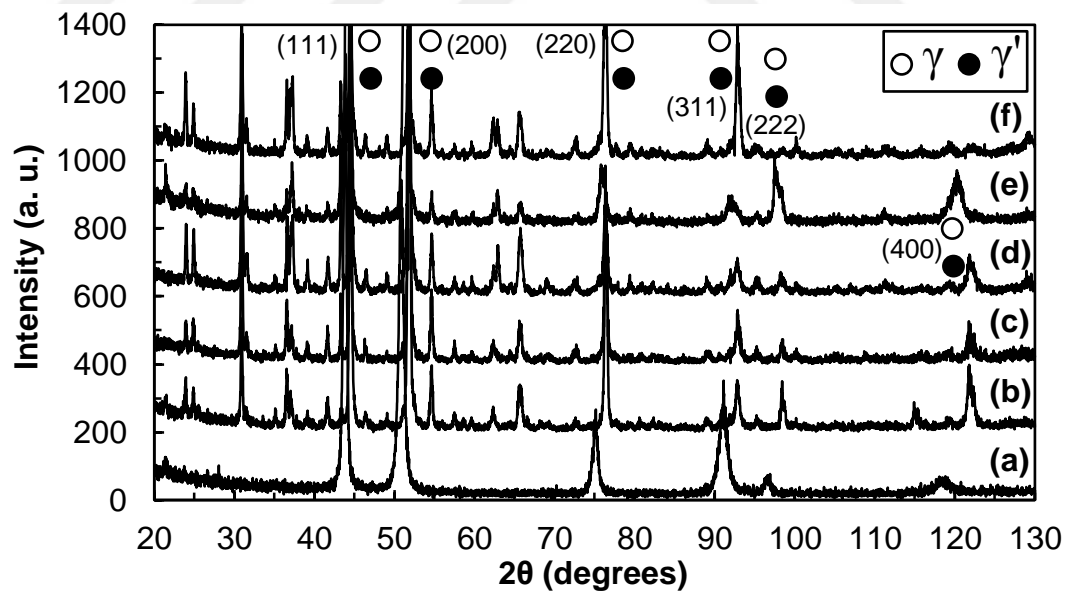


**Figure C.16** XRD patterns of (a) as cast (fast cooled)  $\text{Ni}_{80}\text{Al}_{15}\text{W}_5$  alloys, (b) homogenized at 1250 °C for 24 hr and partially-solutionized at 1150 °C for 3 hr and subsequently aged at 800 °C for (c) 4 hr (d) 16 hr (e) 64 hr and (f) 256 hr, respectively.



## APPENDIX D

### DETERMINATION OF LATTICE PARAMETERS OF $\gamma'$ PRECIPITATES IN $\text{Ni}_{80}\text{Al}_{15}\text{X}_5$ ALLOY SYSTEMS

**Table D.1** Lattice parameter determination of  $\gamma'$  precipitates in  $\text{Ni}_{80}\text{Al}_{15}\text{X}_5$  alloy systems where X = Co, Cr, Hf and Mo, respectively.

Sample groups	Heat treatment		X = Co	X = Cr	X = Hf	X = Mo	
	Definitions	Temperature and durations					
0	As cast (fast cooled)	-	3.559	3.559	3.602	3.579	
	As cast (slow cooled)	-	-	-	-	-	
1	Partial solution heat treatment	1150 °C for 3 hr	3.558	3.557	3.605	3.577	
		800 °C for 4 hr	3.549	3.557	3.591	3.571	
	Aging	800 °C for 16 hr	3.554	3.558	3.590	3.568	
		800 °C for 64 hr	3.553	3.557	3.605	3.575	
		800 °C for 256 hr		3.546	3.554	3.608	3.574
Homogenization and partial solution heat treatment	1250 °C for 24 hr and 1150 °C for 3 hr		3.554	3.557	-	3.569	
2	Aging	800 °C for 4 hr	3.553	3.553	-	3.571	
		800 °C for 16 hr	3.555	3.554	-	3.573	
	800 °C for 64 hr		3.551	3.556	-	3.575	
			3.545	3.553	-	3.557	

**Table D.2** Lattice parameter determination of  $\gamma'$  precipitates in  $\text{Ni}_{80}\text{Al}_{15}\text{X}_5$  alloy systems where X = Nb, Ta, Ti and W, respectively.

Sample groups	Definitions	Heat treatment				
		Temperature and durations	X = Nb	X = Ta	X = Ti	X = W
0	As cast (fast cooled)	-	3.586	3.590	3.576	3.578
	As cast (slow cooled)	-	-	-	-	-
1	Partial solution heat treatment	1150 °C for 3 hr	3.583	3.584	3.579	3.576
		800 °C for 4 hr	3.589	3.584	3.574	3.575
	Aging	800 °C for 16 hr	3.589	3.588	3.578	3.569
		800 °C for 64 hr	3.585	3.586	3.580	3.572
		800 °C for 256 hr	3.583	3.596	3.576	3.575
Homogenization and partial solution heat treatment	1250 °C for 24 hr and 1150 °C for 3 hr	3.577	3.577	3.566	-	
	Aging	800 °C for 4 hr	3.589	3.575	3.558	-
800 °C for 16 hr		3.572	3.585	3.575	-	
800 °C for 64 hr		3.572	3.597	3.579	-	
800 °C for 256 hr		3.563	3.595	3.581	-	



**Table D.3** Lattice parameter determination of Ni<sub>5</sub>Hf phase in Ni<sub>80</sub>Al<sub>15</sub>Hf<sub>5</sub> alloys.

Sample groups	Heat treatment		Ni <sub>5</sub> Hf
	Definitions	Temperature and durations	
0	As cast (fast cooled)	-	6.707
	As cast (slow cooled)	-	-
1	Partial solution heat treatment	1150 °C for 3 hr	-
		800 °C for 4 hr	-
	Aging	800 °C for 16 hr	-
		800 °C for 64 hr	6.692
		800 °C for 256 hr	6.692
2	Homogenization and partial solution heat treatment	1250 °C for 24 hr and 1150 °C for 3 hr	-
		800 °C for 4 hr	6.685
	Aging	800 °C for 16 hr	6.708
		800 °C for 64 hr	6.700
		800 °C for 256 hr	-



## APPENDIX E

### DSC HEATING AND COOLING CURVES OF $\text{Ni}_{80}\text{Al}_{15}\text{X}_5$ ALLOY SYSTEMS

In Appendix E, DSC heating and cooling plots of as cast (fast cooled)  $\text{Ni}_{80}\text{Al}_{15}\text{X}_5$  alloy systems ( $X = \text{Co}, \text{Cr}, \text{Hf}, \text{Mo}, \text{Nb}, \text{Ta}, \text{Ti}$  and  $\text{W}$ , respectively) have been shown. Secondary peaks (indicated by down arrows) observed in Figure E.3 and Figures E.5,7 refer to eutectic and peritectic reactions, respectively. In Figures E.3,8, peaks denoted by star marks may correspond to solvus phase transformations.

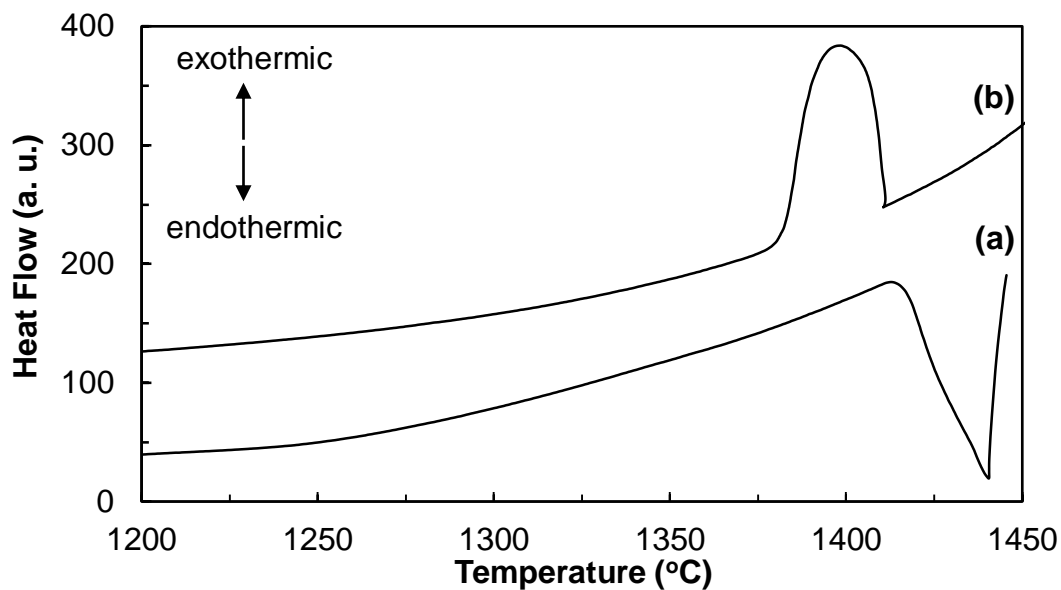


**Figure E.1** DSC (a) heating and (b) cooling curves of as cast (fast cooled)  $\text{Ni}_{80}\text{Al}_{15}\text{Co}_5$  alloys (at a rate of 20  $^{\circ}\text{C}/\text{minutes}$ ).

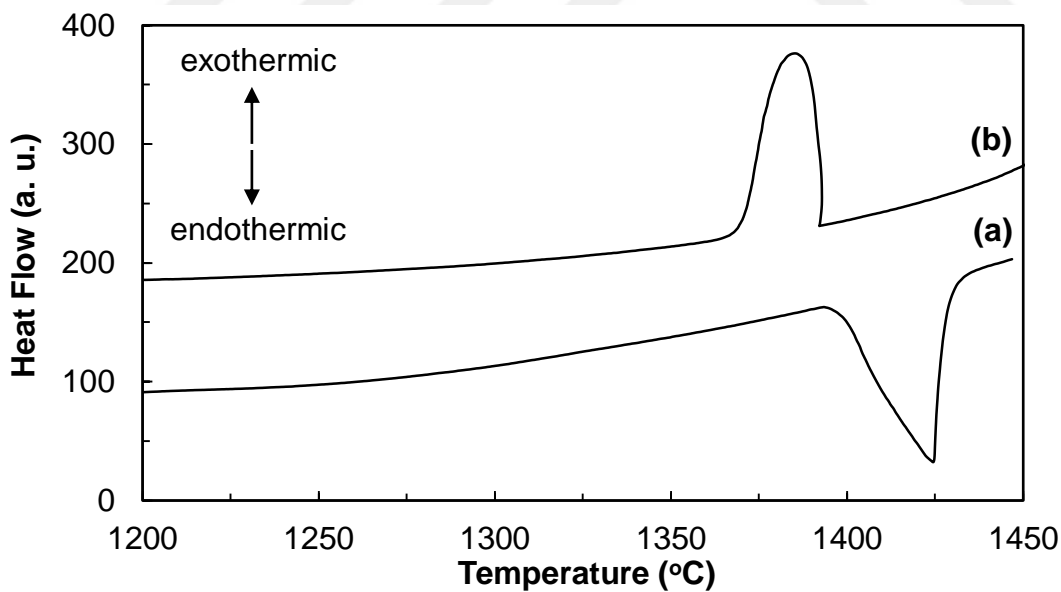


**Figure E.2** DSC (a) heating and (b) cooling curves of as cast (fast cooled)  $\text{Ni}_{80}\text{Al}_{15}\text{Cr}_5$  alloys (at a rate of 20  $^{\circ}\text{C}/\text{minutes}$ ).

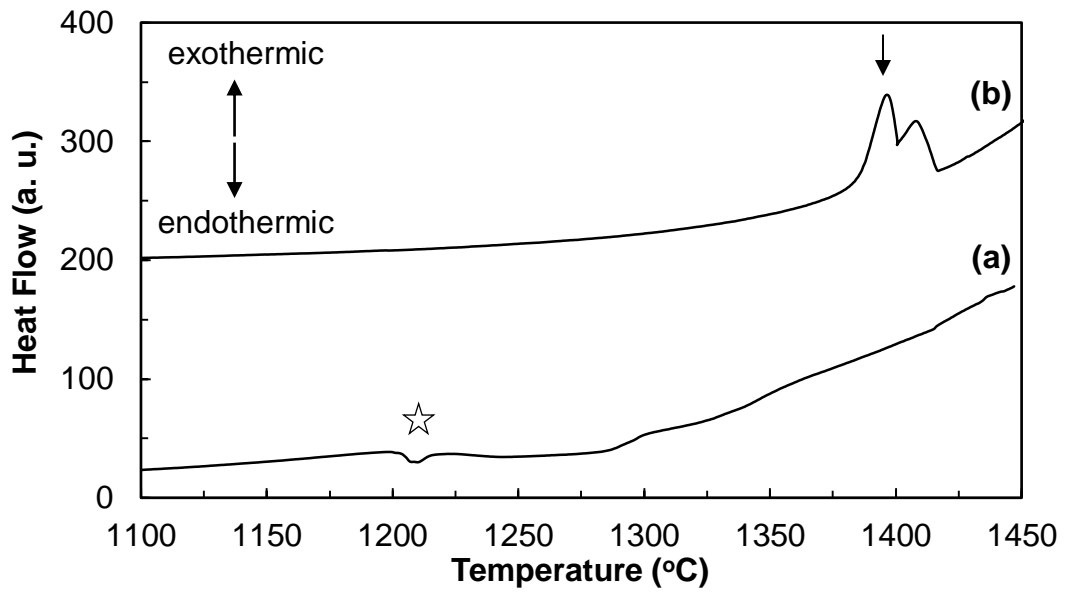


**Figure E.3** DSC (a) heating and (b) cooling curves of as cast (fast cooled)  $\text{Ni}_{80}\text{Al}_{15}\text{Hf}_5$  alloys (at a rate of 20 °C/minutes).

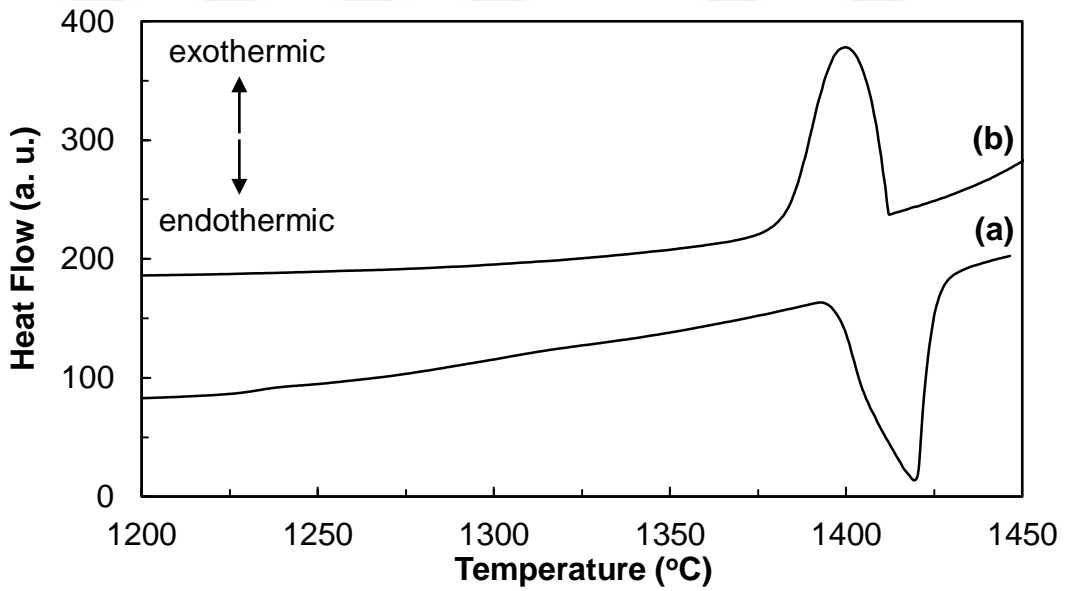


**Figure E.4** DSC (a) heating and (b) cooling curves of as cast (fast cooled)  $\text{Ni}_{80}\text{Al}_{15}\text{Mo}_5$  alloys (at a rate of 20 °C/minutes).

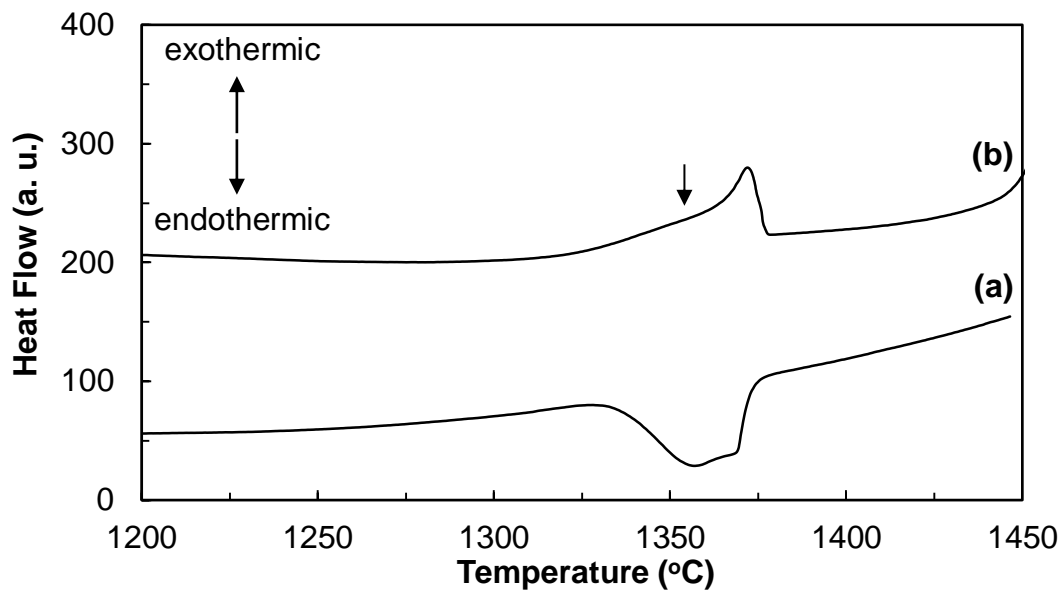


**Figure E.5** DSC (a) heating and (b) cooling curves of as cast (fast cooled)  $\text{Ni}_{80}\text{Al}_{15}\text{Nb}_5$  alloys (at a rate of 20  $^{\circ}\text{C}/\text{minutes}$ ).

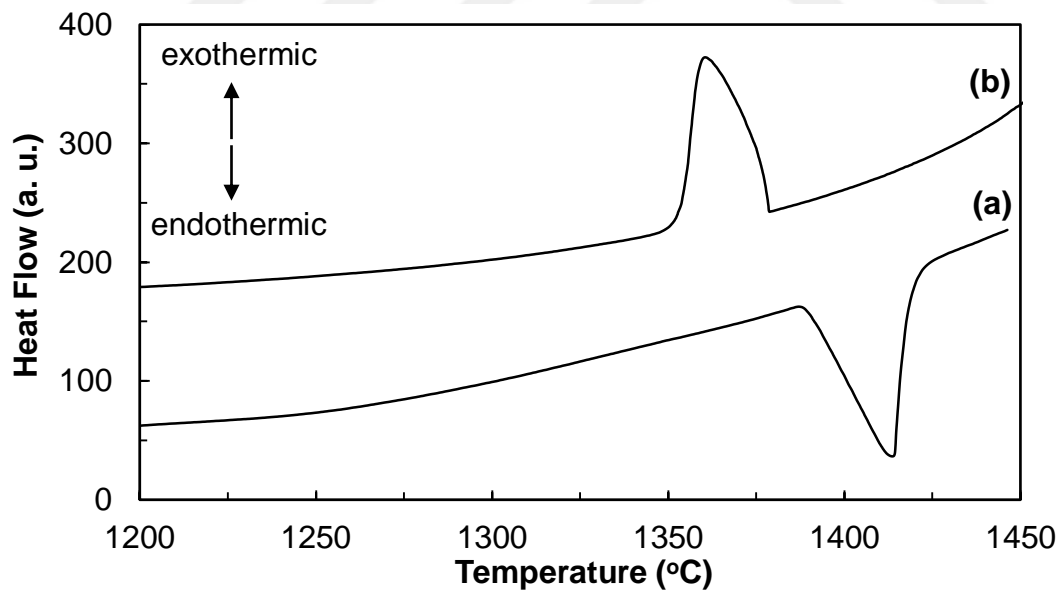


**Figure E.6** DSC (a) heating and (b) cooling curves of as cast (fast cooled)  $\text{Ni}_{80}\text{Al}_{15}\text{Ta}_5$  alloys (at a rate of 20  $^{\circ}\text{C}/\text{minutes}$ ).

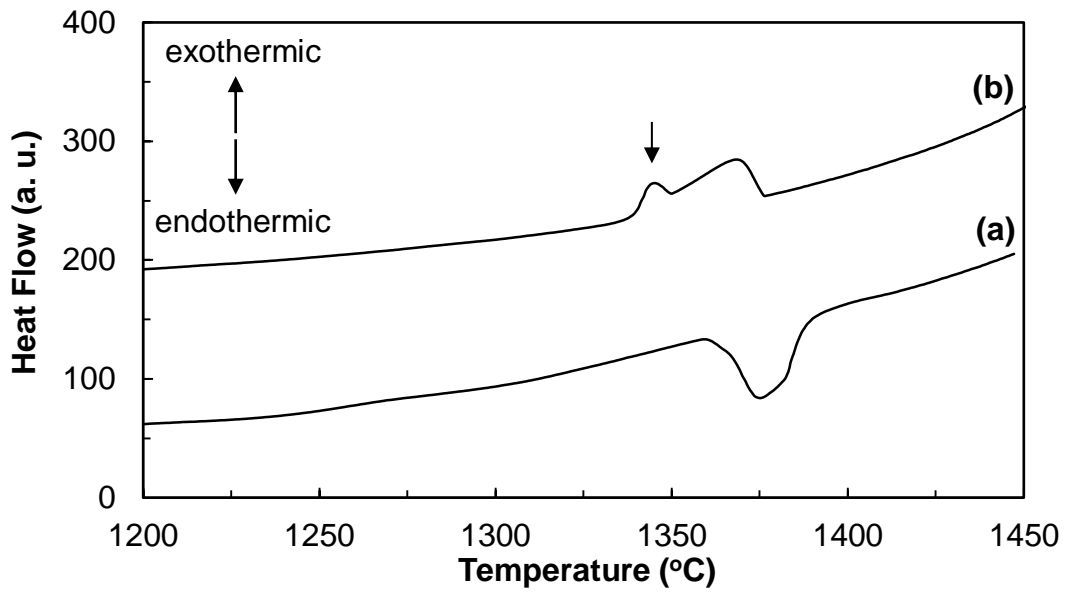


**Figure E.7** DSC (a) heating and (b) cooling curves of as cast (fast cooled)  $\text{Ni}_{80}\text{Al}_{15}\text{Ti}_5$  alloys (at a rate of 20  $^{\circ}\text{C}/\text{minutes}$ ).

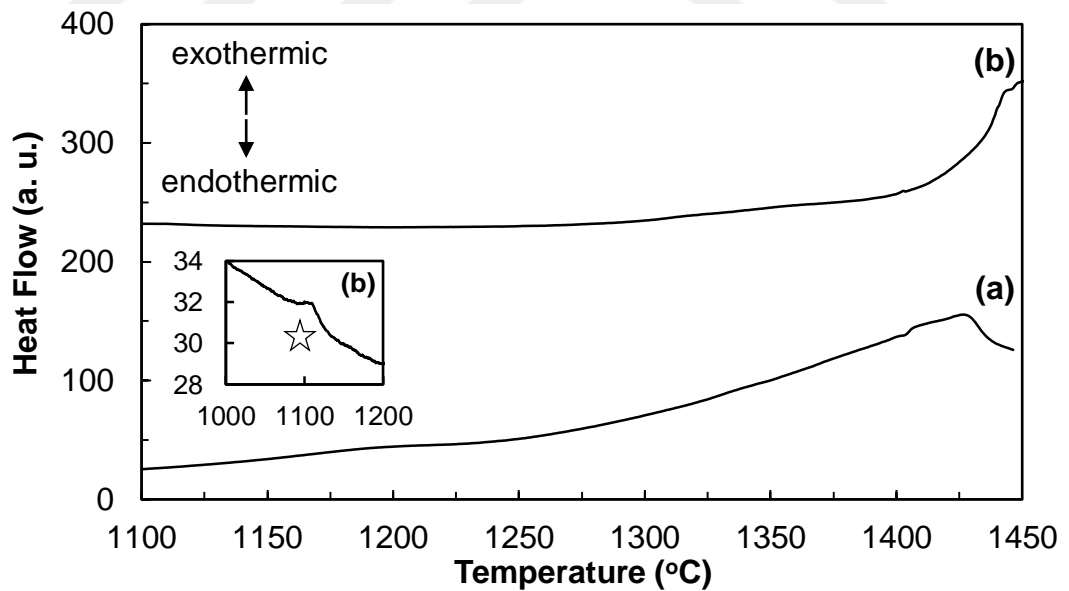


**Figure E.8** DSC (a) heating and (b) cooling curves of as cast (fast cooled)  $\text{Ni}_{80}\text{Al}_{15}\text{W}_5$  alloys (at a rate of 20  $^{\circ}\text{C}/\text{minutes}$ ).





## APPENDIX F

### FESEM MICROGRAPHS OF $\text{Ni}_{80}\text{Al}_{15}\text{X}_5$ ALLOY SYSTEMS

Appendix F demonstrates FESEM micrographs of as cast (fast cooled), partial solution heat treated (1150 °C for 3 hr) and homogenized/partial solution heat treated (1250 °C for 24 hr/1150 °C for 3 hr) microstructures and temporal evolution of  $\gamma'$  precipitates in  $\text{Ni}_{80}\text{Al}_{15}\text{X}_5$  alloy systems ( $X = \text{Co}, \text{Cr}, \text{Hf}, \text{Mo}, \text{Nb}, \text{Ta}$  and  $\text{Ti}$ , respectively) as aging time at 800 °C is 4, 16, 64 and 256 hr, respectively. For the second sample group of  $\text{Ni}_{80}\text{Al}_{15}\text{Hf}_5$  alloys, microstructures belong to 256 hr aging time are absent due to oxidation problem. Similarly, FESEM micrographs of  $X = \text{W}$  addition are also missing due to some problems related with etching and oxide layer formation at 1250 °C.

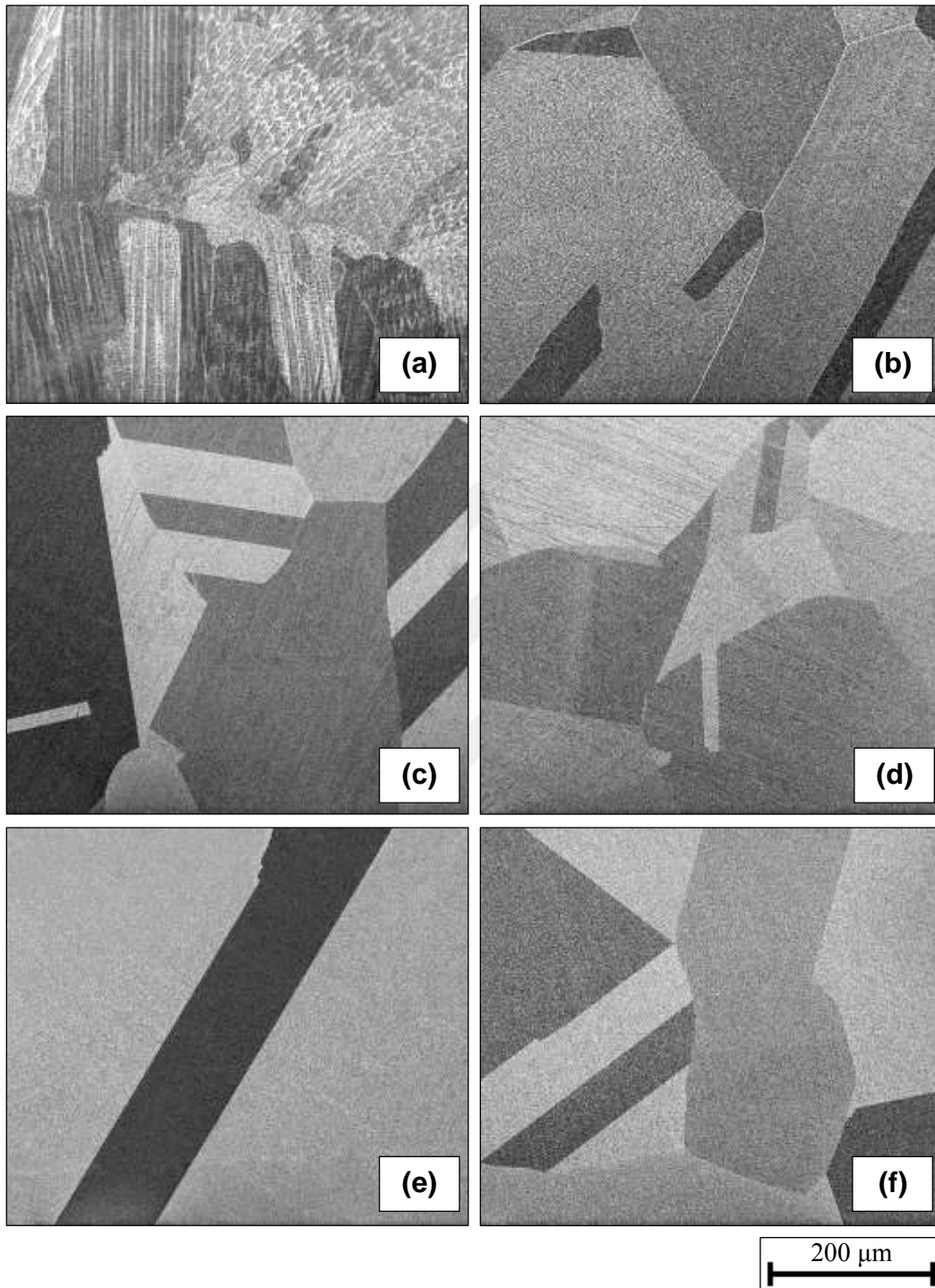


**Figure F.1** FESEM micrographs of (a) as cast, (b) partial solution heat treated microstructures and temporal evolution of  $\gamma'$  precipitates in  $\text{Ni}_{80}\text{Al}_{15}\text{Co}_5$  alloys as aging time is (c) 4 hr, (d) 16 hr, (e) 64 hr and (f) 256 hr, respectively.

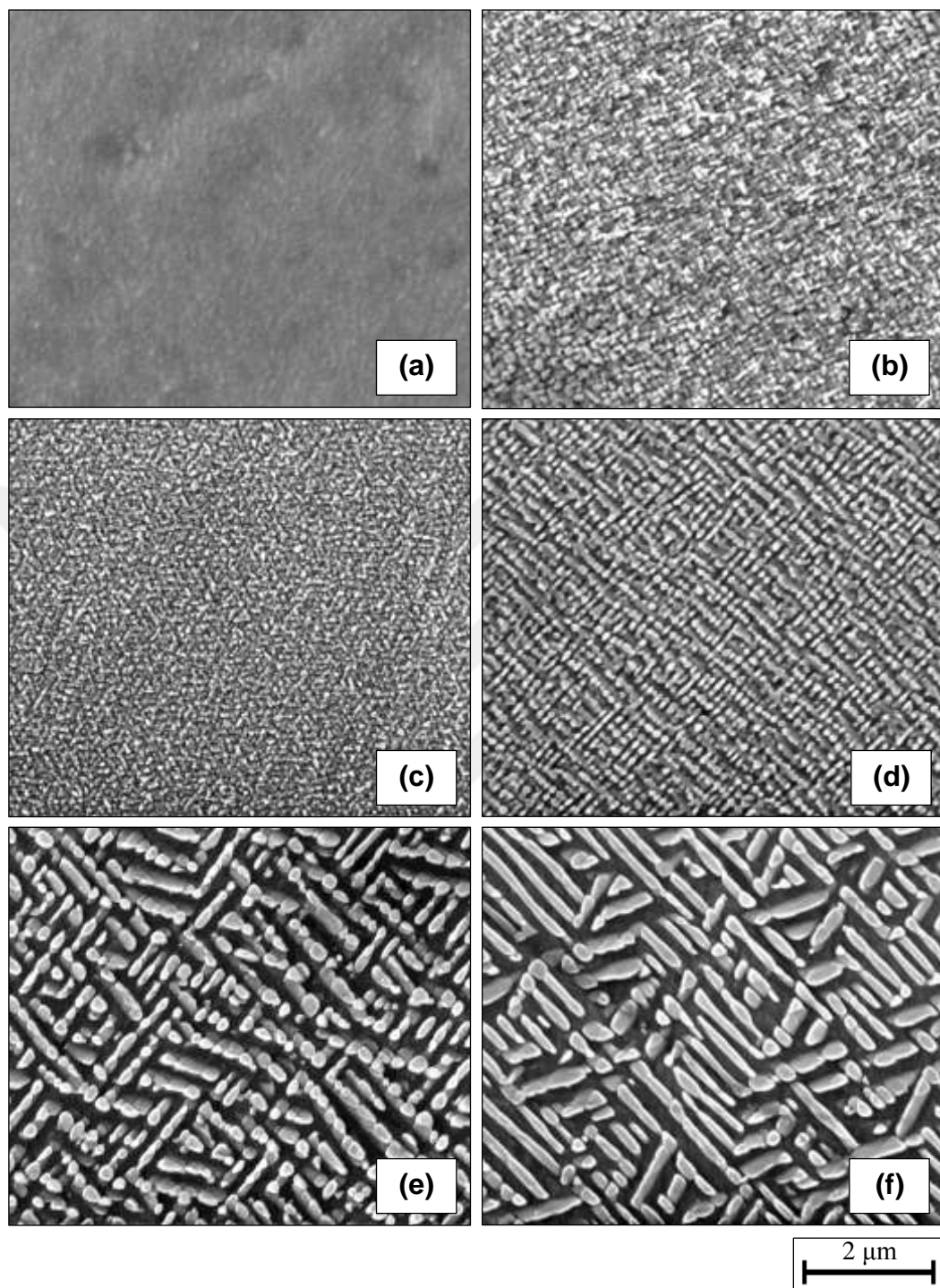


**Figure F.2** FESEM micrographs of (a) as cast, (b) partial solution heat treated microstructures and temporal evolution of  $\gamma'$  precipitates in  $\text{Ni}_{80}\text{Al}_{15}\text{Co}_5$  alloys as aging time is (c) 4 hr, (d) 16 hr, (e) 64 hr and (f) 256 hr, respectively.

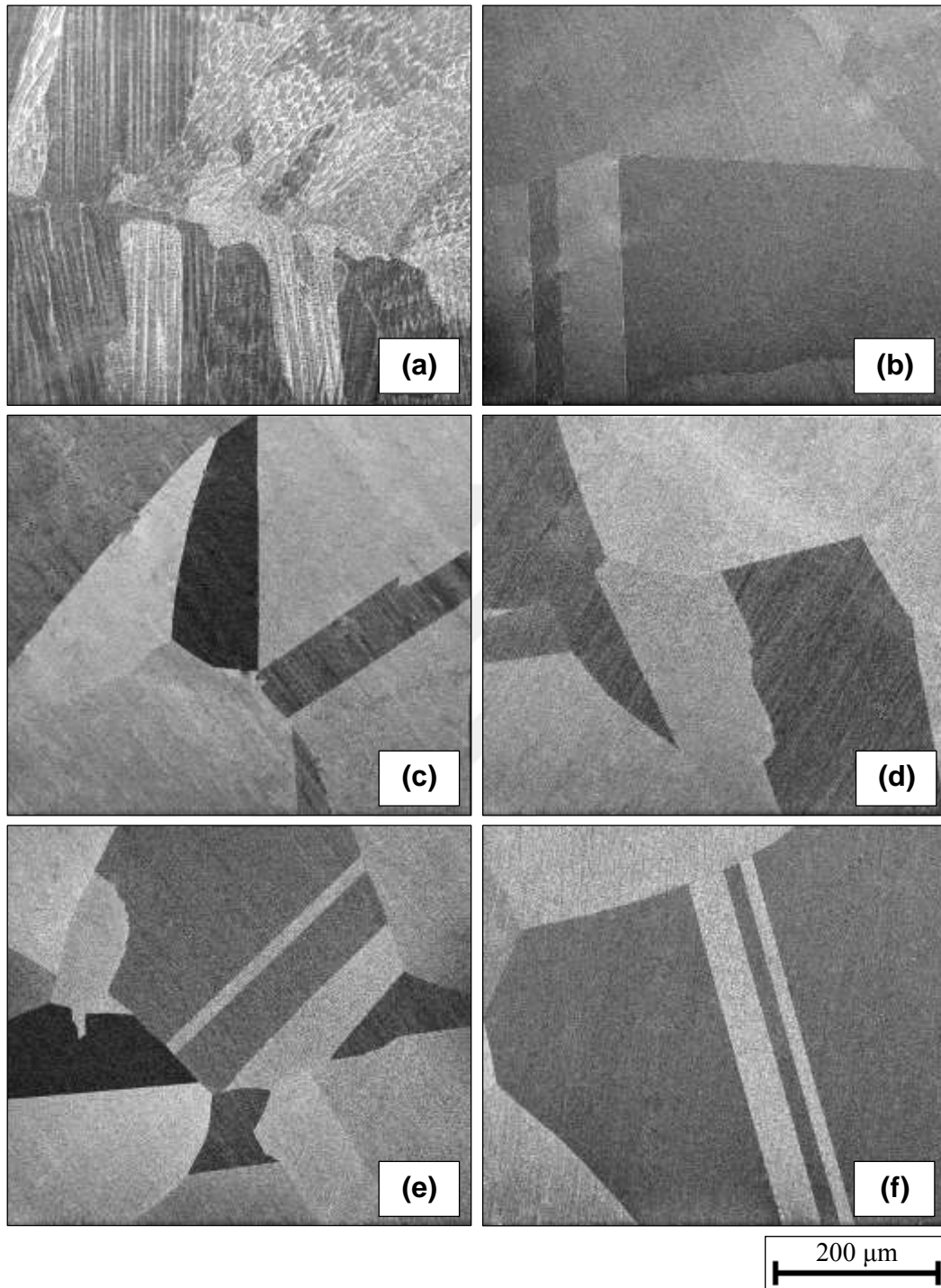


**Figure F.3** FESEM micrographs of (a) as cast, (b) homogenized/partial solution heat treated microstructures and temporal evolution of  $\gamma'$  precipitates in  $\text{Ni}_{80}\text{Al}_{15}\text{Co}_5$  alloys as aging time is (c) 4 hr, (d) 16 hr, (e) 64 hr and (f) 256 hr, respectively.

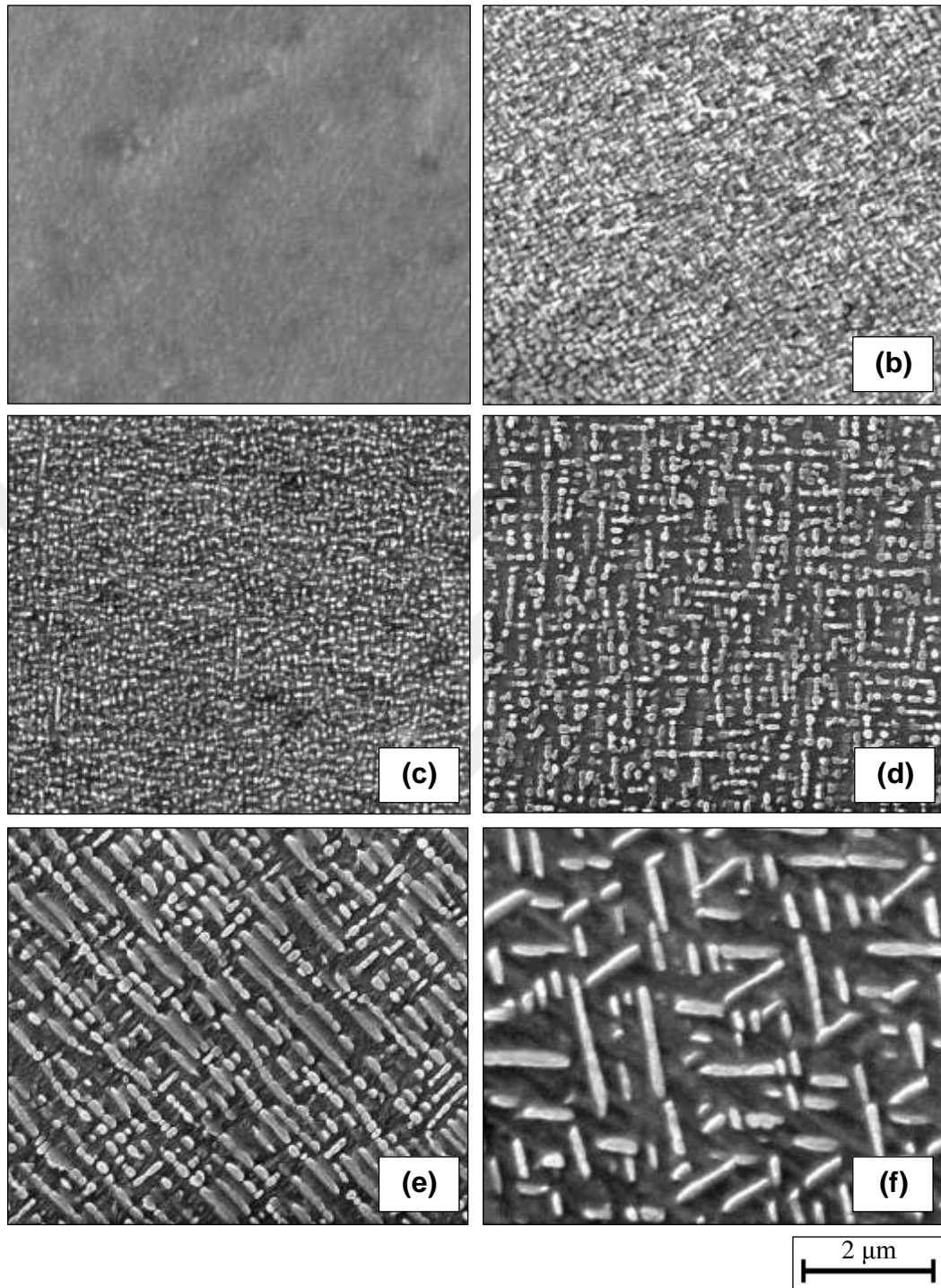


**Figure F.4** FESEM micrographs of (a) as cast, (b) homogenized/partial solution heat treated microstructures and temporal evolution of  $\gamma'$  precipitates in  $\text{Ni}_{80}\text{Al}_{15}\text{Co}_5$  alloys as aging time is (c) 4 hr, (d) 16 hr, (e) 64 hr and (f) 256 hr, respectively.

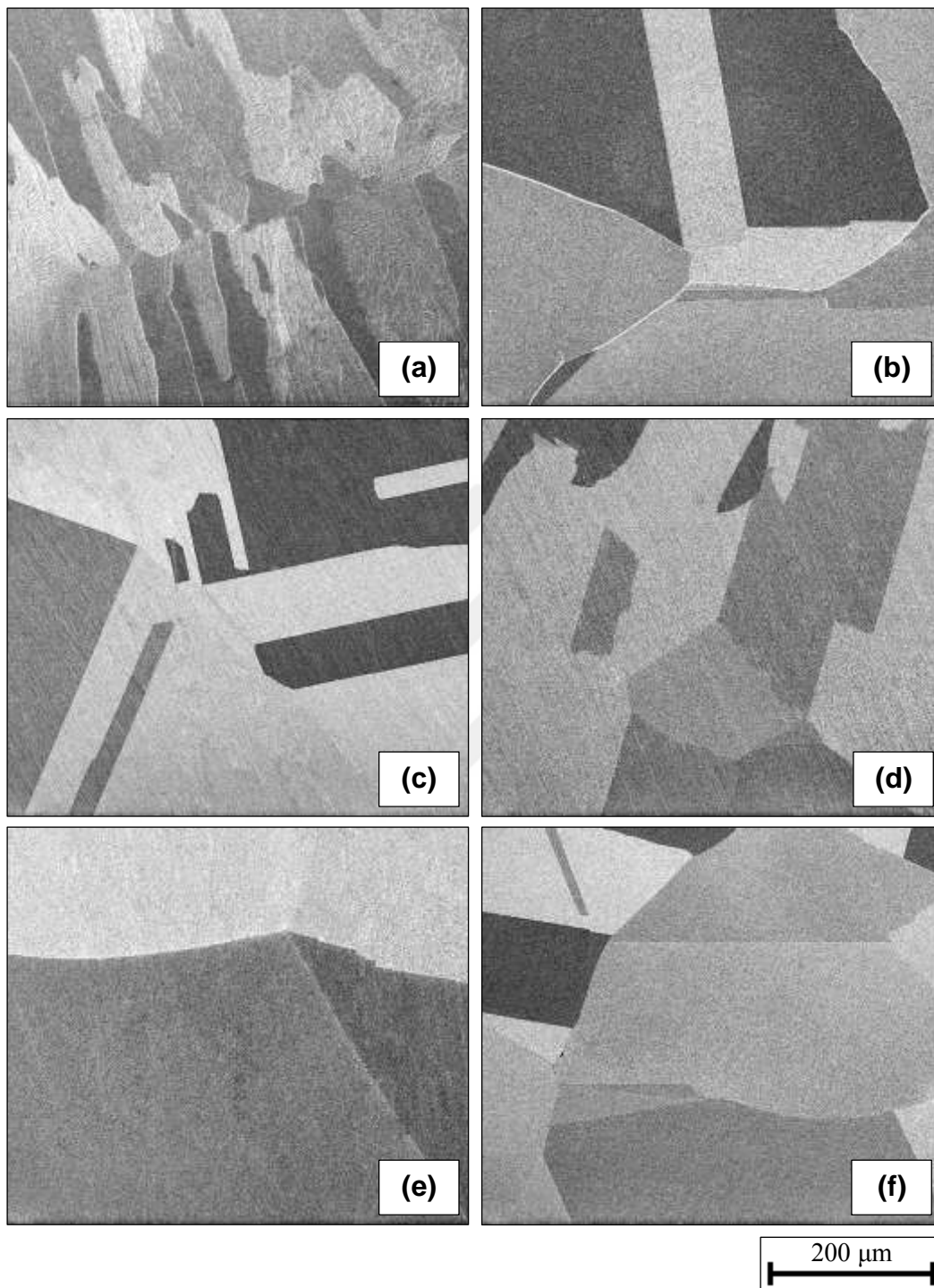


**Figure F.5** FESEM micrographs of (a) as cast, (b) partial solution heat treated microstructures and temporal evolution of  $\gamma'$  precipitates in Ni<sub>80</sub>Al<sub>15</sub>Cr<sub>5</sub> alloys as aging time is (c) 4 hr, (d) 16 hr, (e) 64 hr and (f) 256 hr, respectively.

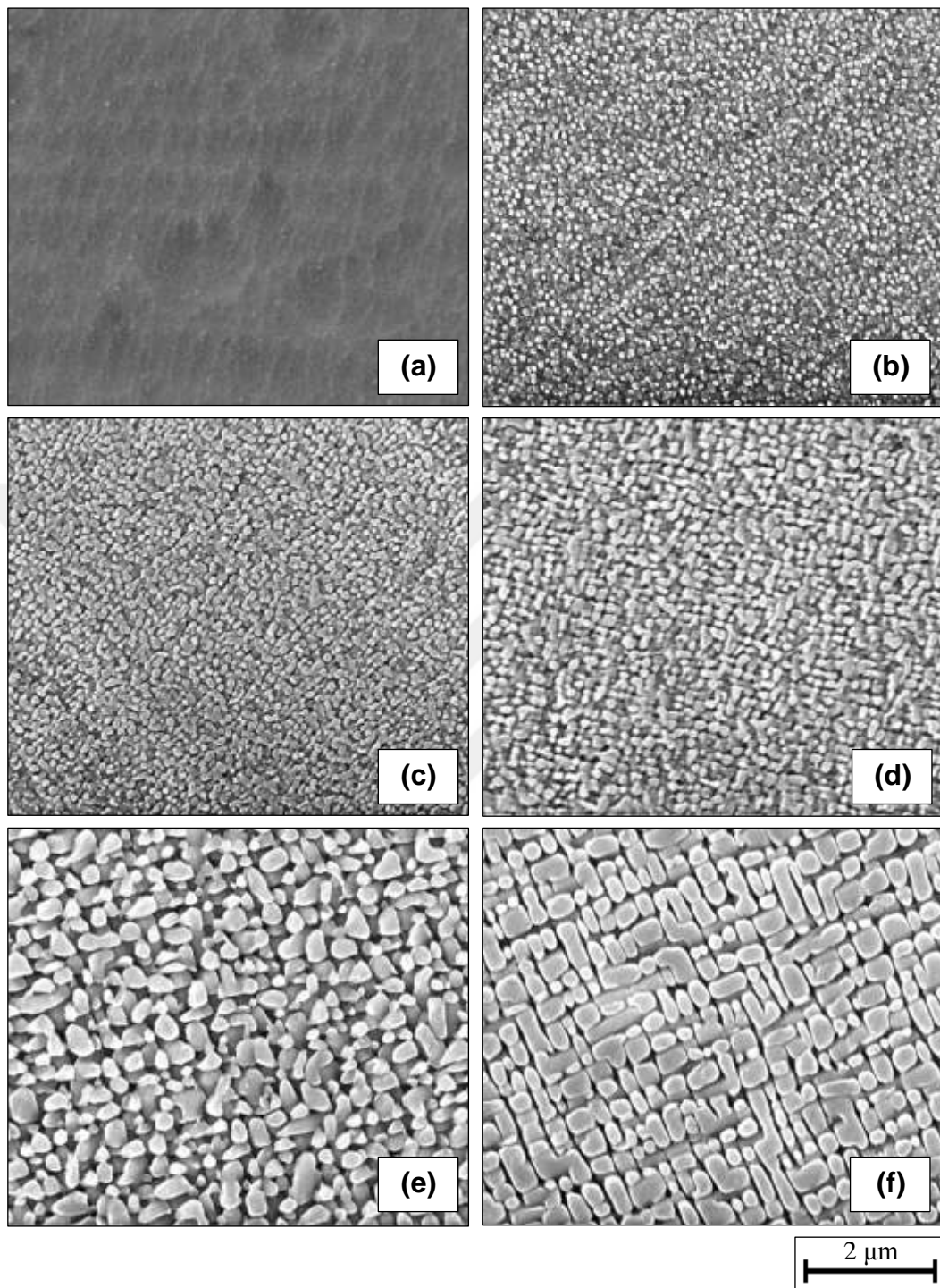


**Figure F.6** FESEM micrographs of (a) as cast, (b) partial solution heat treated microstructures and temporal evolution of  $\gamma'$  precipitates in  $\text{Ni}_{80}\text{Al}_{15}\text{Cr}_5$  alloys as aging time is (c) 4 hr, (d) 16 hr, (e) 64 hr and (f) 256 hr, respectively.

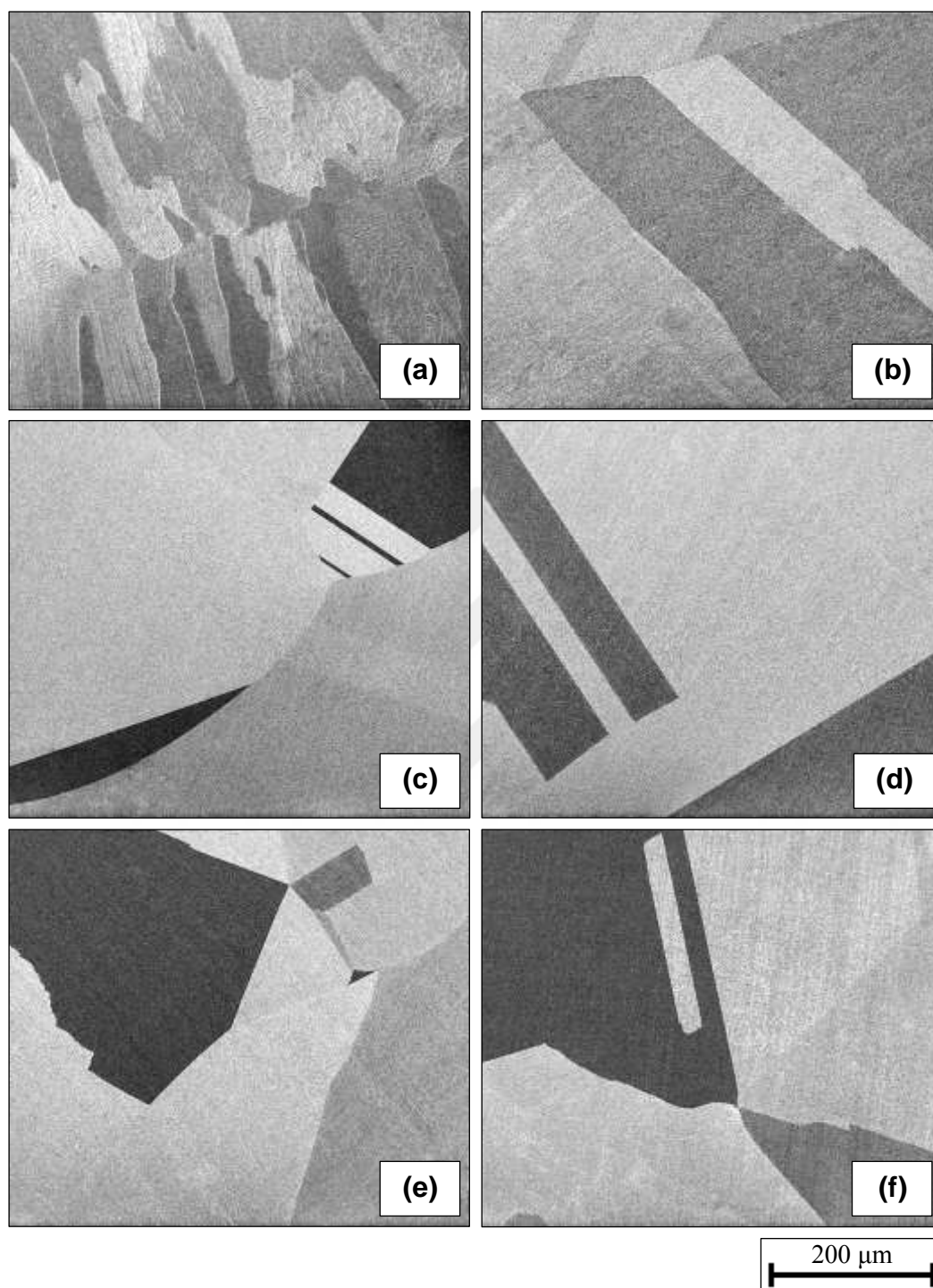


**Figure F.7** FESEM micrographs of (a) as cast, (b) homogenized/partial solution heat treated microstructures and temporal evolution of  $\gamma'$  precipitates in  $\text{Ni}_{80}\text{Al}_{15}\text{Cr}_5$  alloys as aging time is (c) 4 hr, (d) 16 hr, (e) 64 hr and (f) 256 hr, respectively.



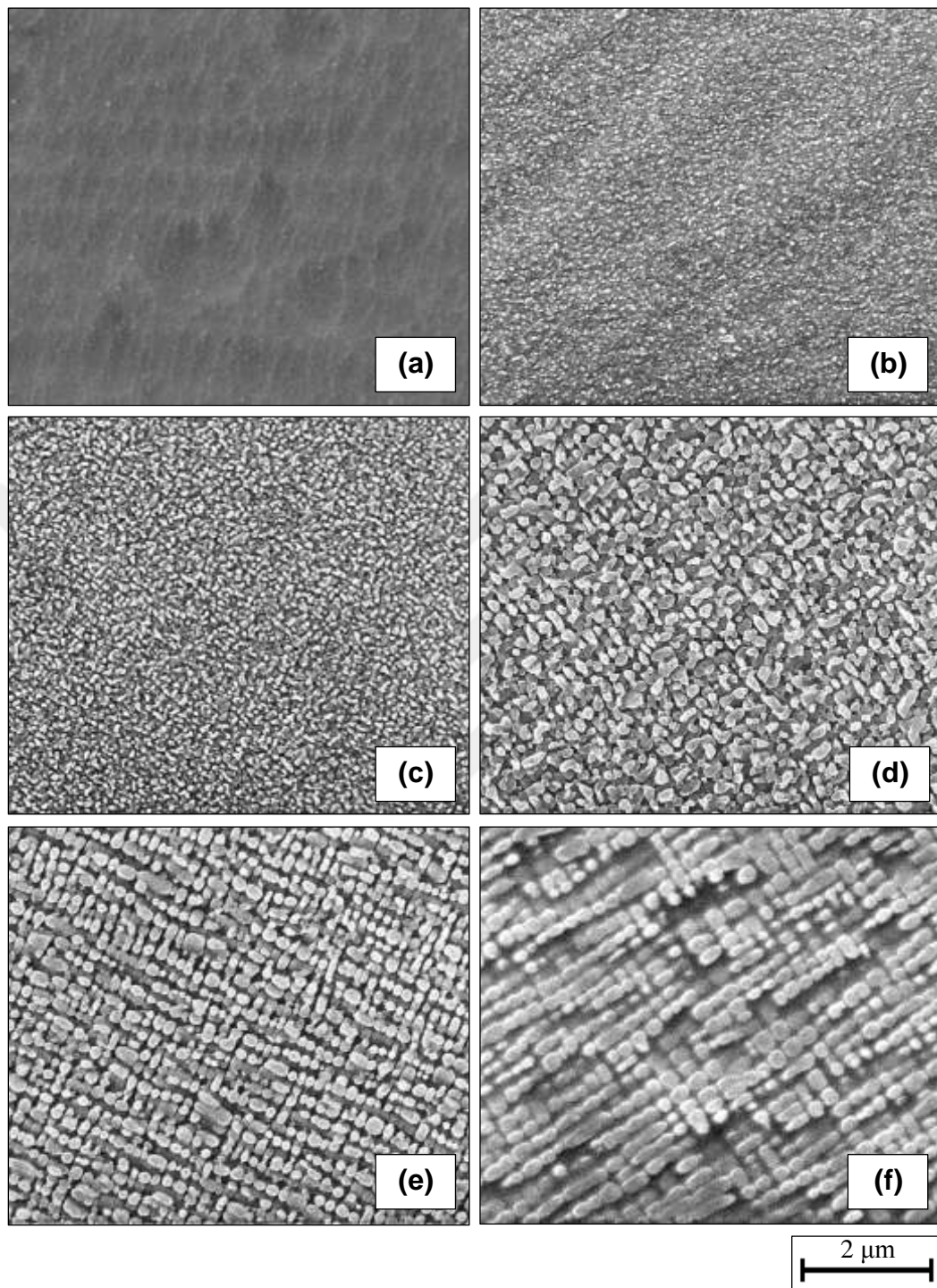


**Figure F.8** FESEM micrographs of (a) as cast, (b) homogenized/partial solution heat treated microstructures and temporal evolution of  $\gamma'$  precipitates in  $\text{Ni}_{80}\text{Al}_{15}\text{Cr}_5$  alloys as aging time is (c) 4 hr, (d) 16 hr, (e) 64 hr and (f) 256 hr, respectively.

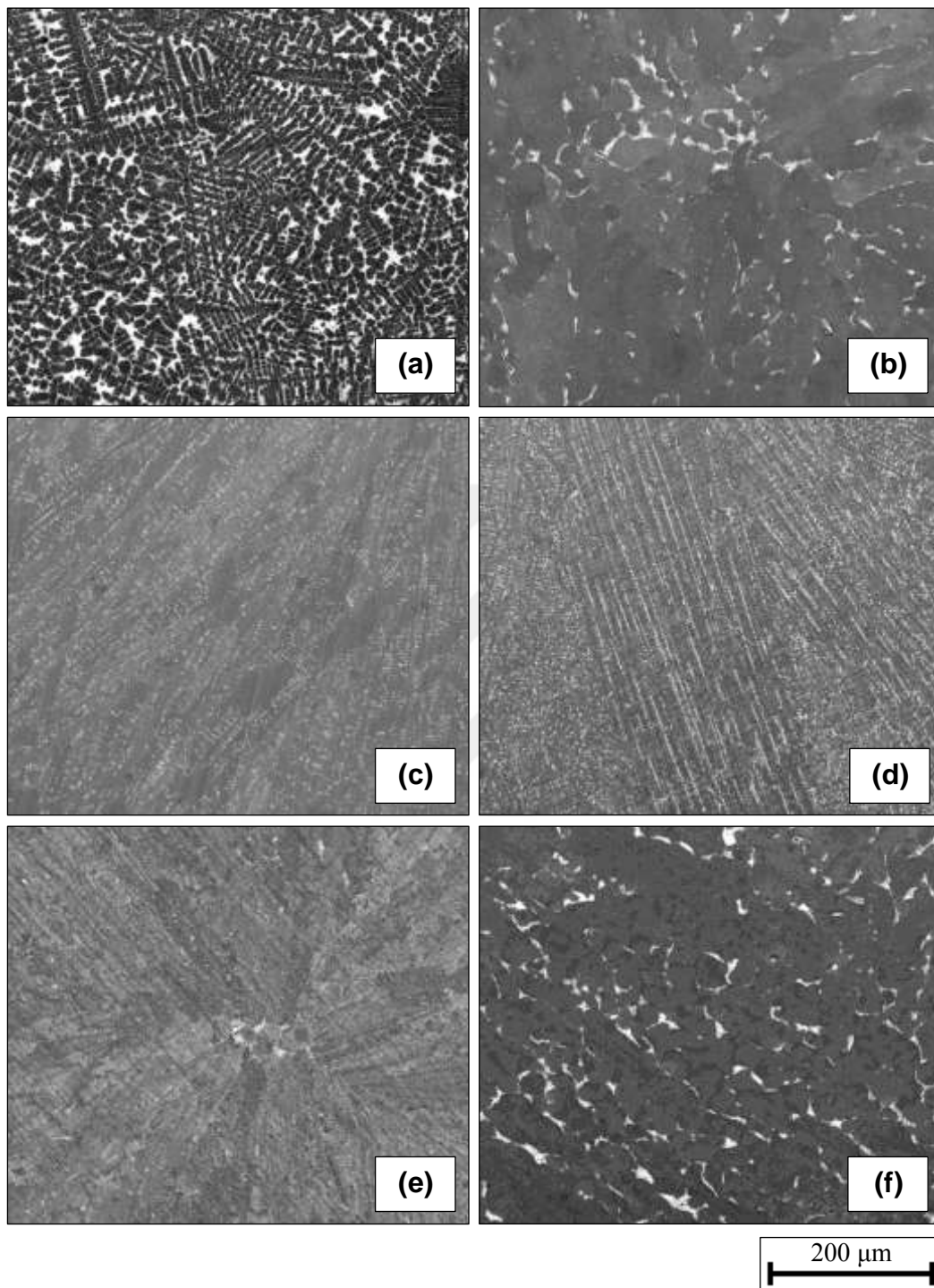


**Figure F.9** FESEM micrographs of (a) as cast, (b) partial solution heat treated microstructures and temporal evolution of  $\gamma'$  precipitates in  $\text{Ni}_{80}\text{Al}_{15}\text{Hf}_5$  alloys as aging time is (c) 4 hr, (d) 16 hr, (e) 64 hr and (f) 256 hr, respectively.

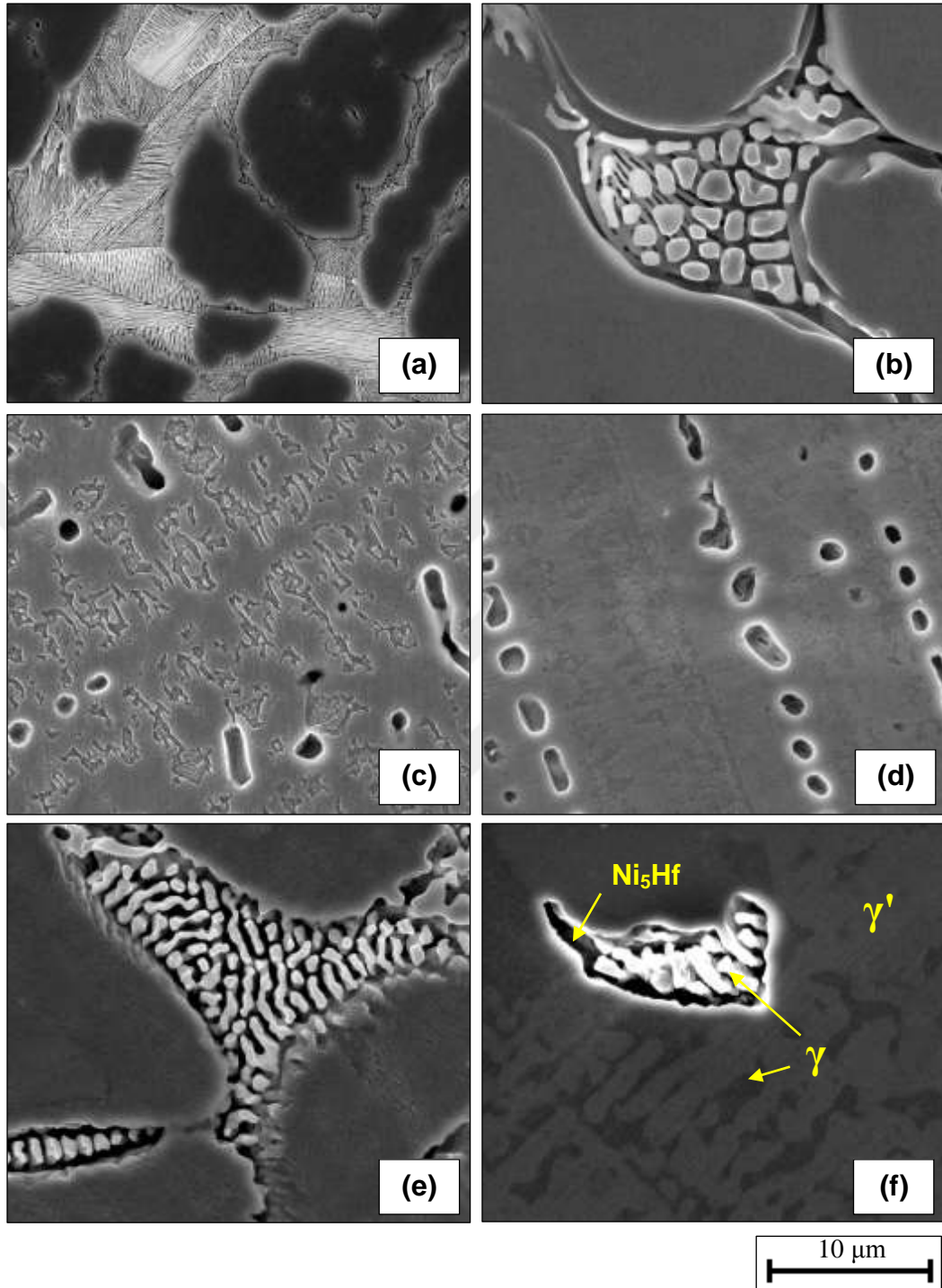


**Figure F.10** FESEM micrographs of (a) as cast, (b) partial solution heat treated microstructures and temporal evolution of  $\gamma'$  precipitates in  $\text{Ni}_{80}\text{Al}_{15}\text{Hf}_5$  alloys as aging time is (c) 4 hr, (d) 16 hr, (e) 64 hr and (f) 256 hr, respectively.

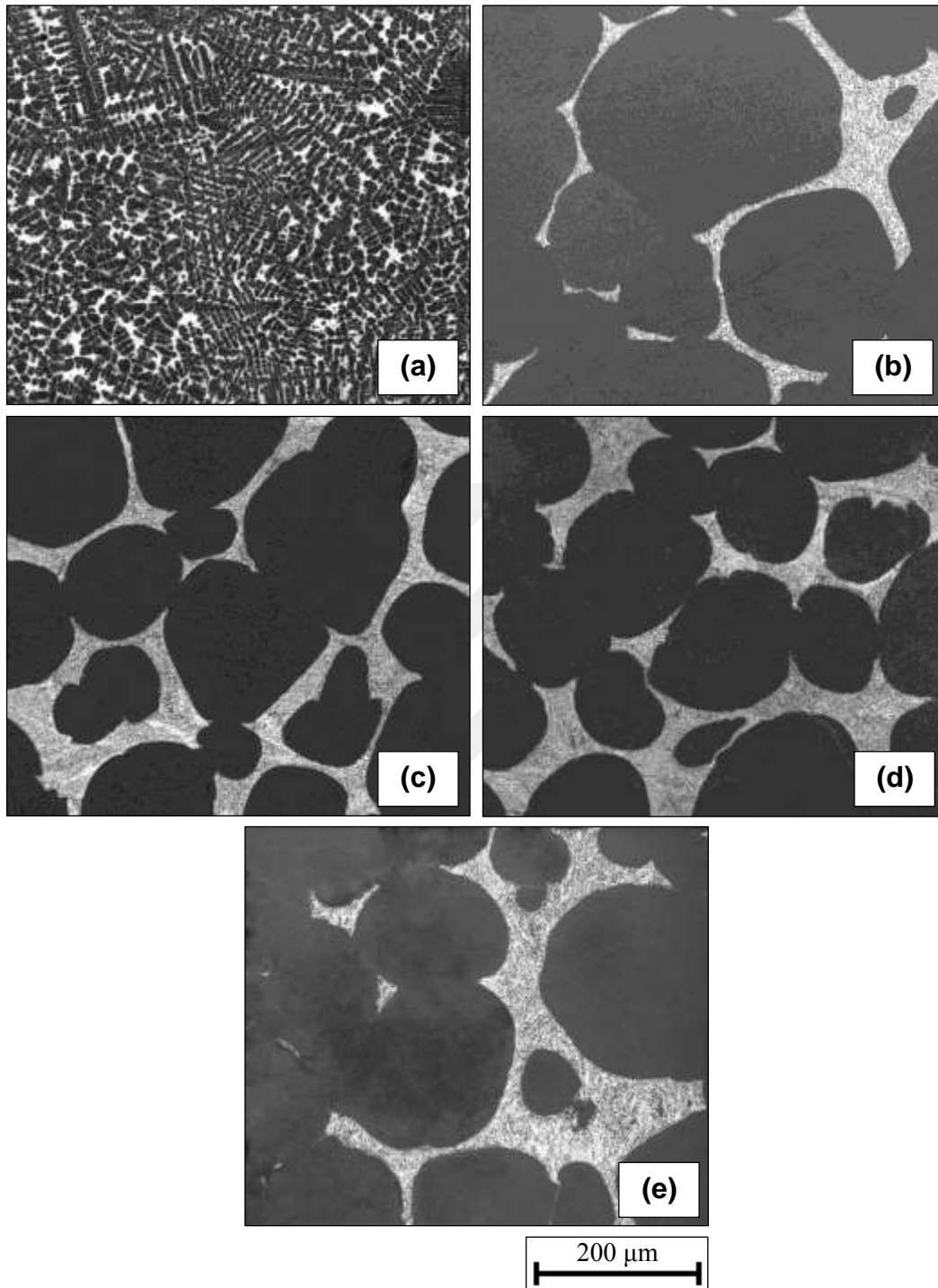


**Figure F.11** FESEM micrographs of (a) as cast, (b) homogenized/partial solution heat treated microstructures and temporal evolution of  $\gamma'$  precipitates in  $\text{Ni}_{80}\text{Al}_{15}\text{Hf}_5$  alloys as aging time is (c) 4 hr, (d) 16 hr and (e) 64 hr, respectively.

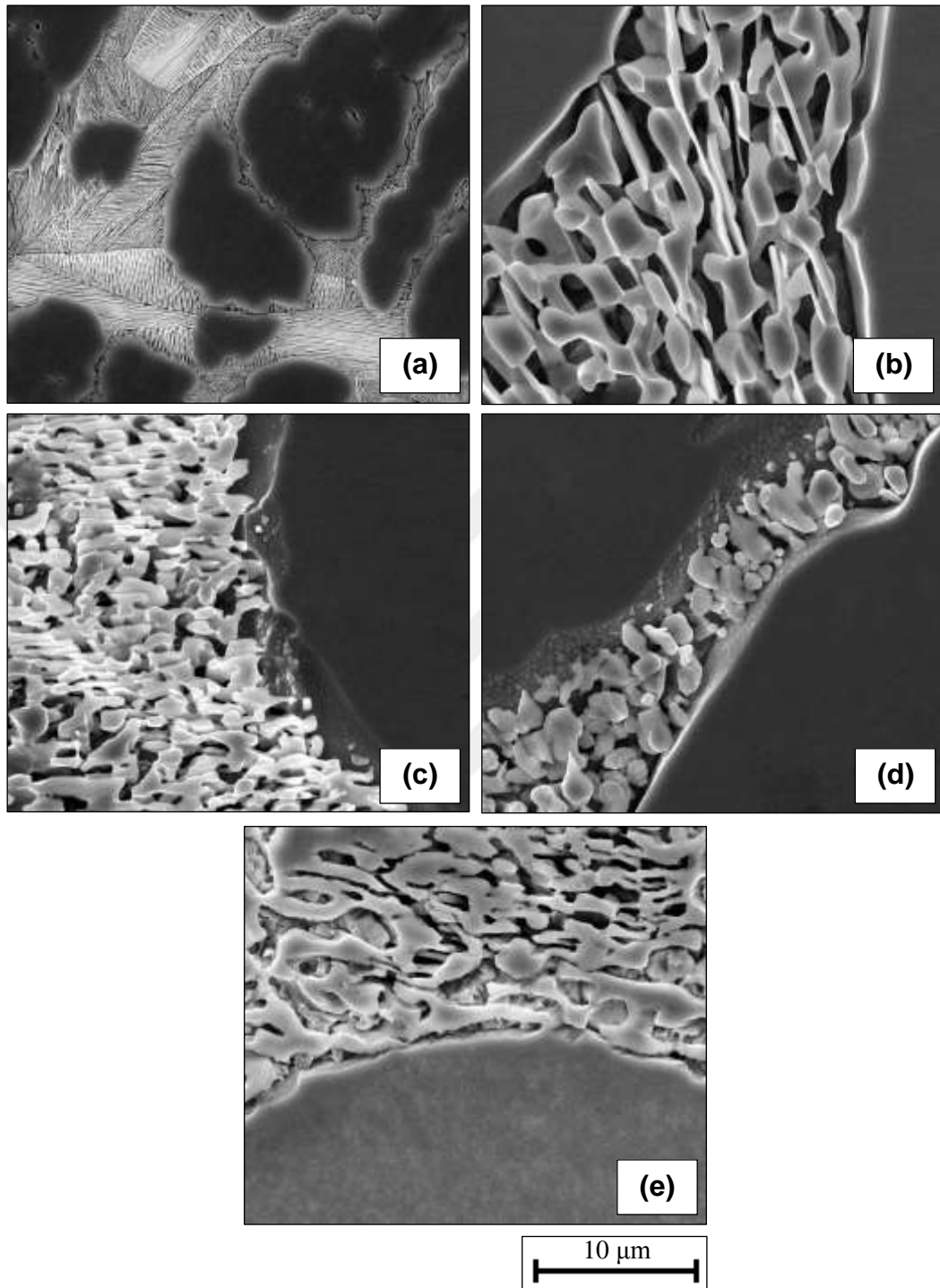


**Figure F.12** FESEM micrographs of (a) as cast, (b) homogenized/partial solution heat treated microstructures and temporal evolution of  $\gamma'$  precipitates in  $\text{Ni}_{80}\text{Al}_{15}\text{Hf}_5$  alloys as aging time is (c) 4 hr, (d) 16 hr and (e) 64 hr, respectively.

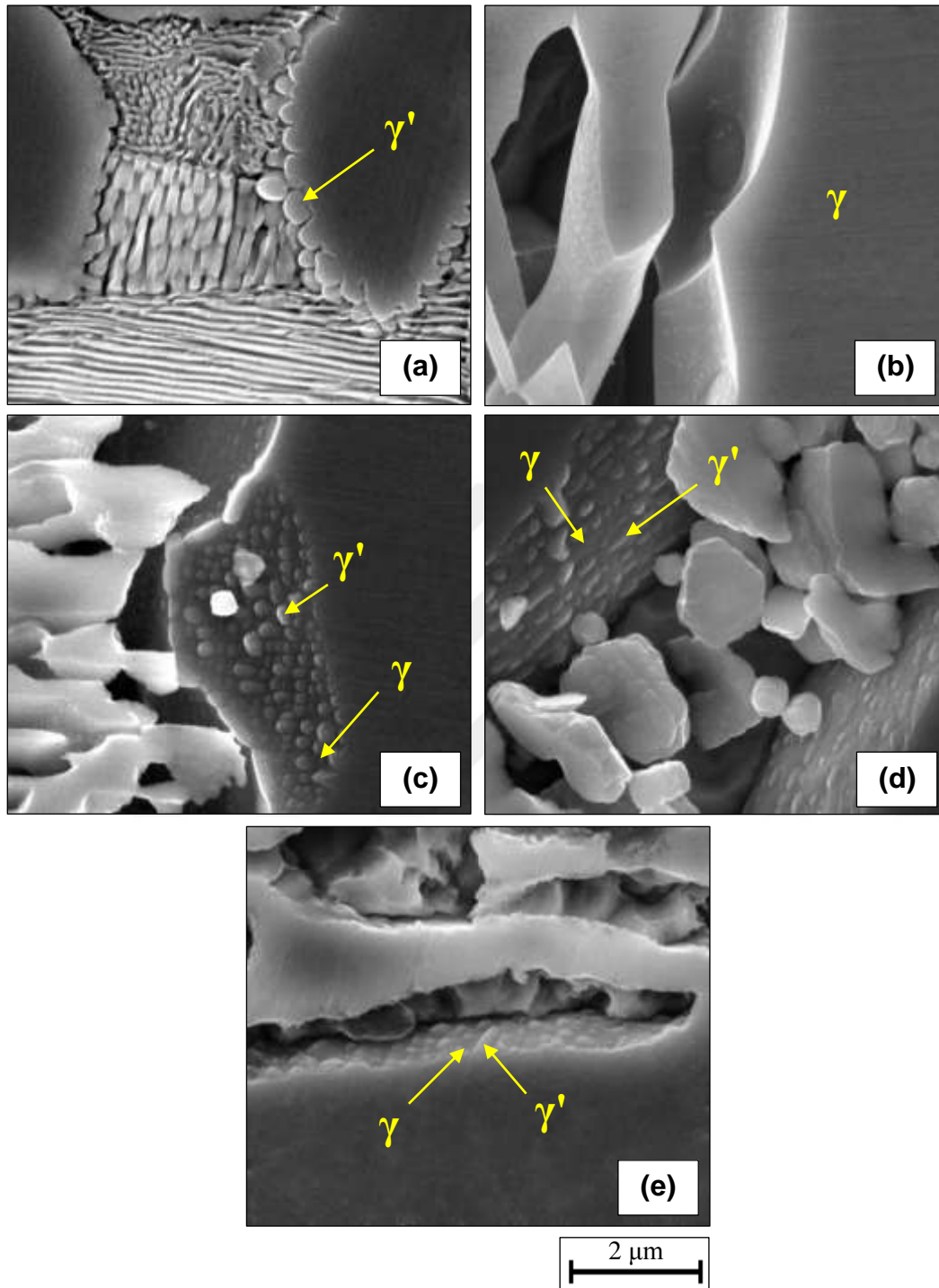


**Figure F.13** FESEM micrographs of (a) as cast, (b) homogenized/partial solution heat treated microstructures and temporal evolution of  $\gamma'$  precipitates in  $\text{Ni}_{80}\text{Al}_{15}\text{Hf}_5$  alloys as aging time is (c) 4 hr, (d) 16 hr and (e) 64 hr, respectively.

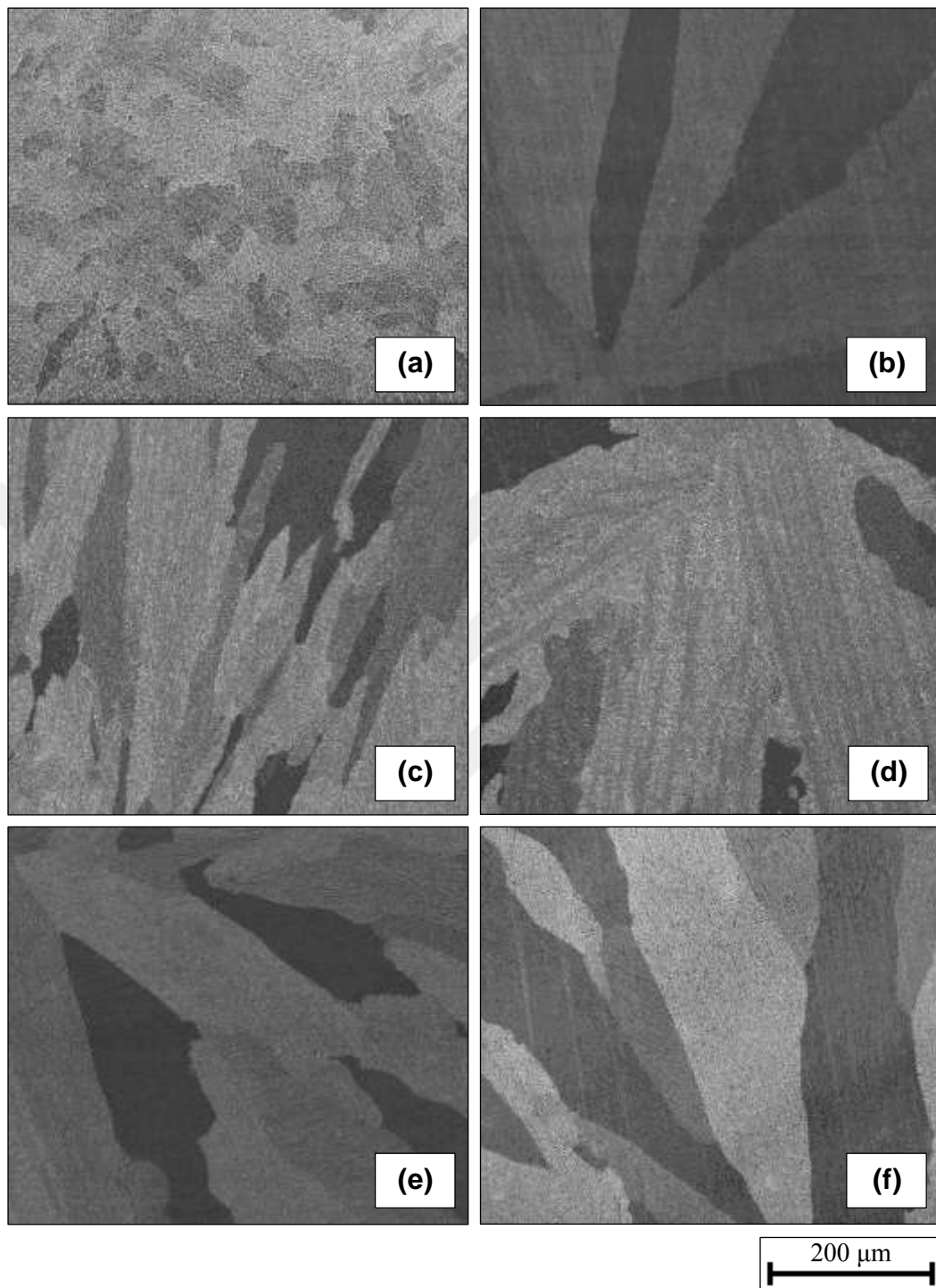


**Figure F.14** FESEM micrographs of (a) as cast, (b) partial solution heat treated microstructures and temporal evolution of  $\gamma'$  precipitates in Ni<sub>80</sub>Al<sub>15</sub>Mo<sub>5</sub> alloys as aging time is (c) 4 hr, (d) 16 hr, (e) 64 hr and (f) 256 hr, respectively.

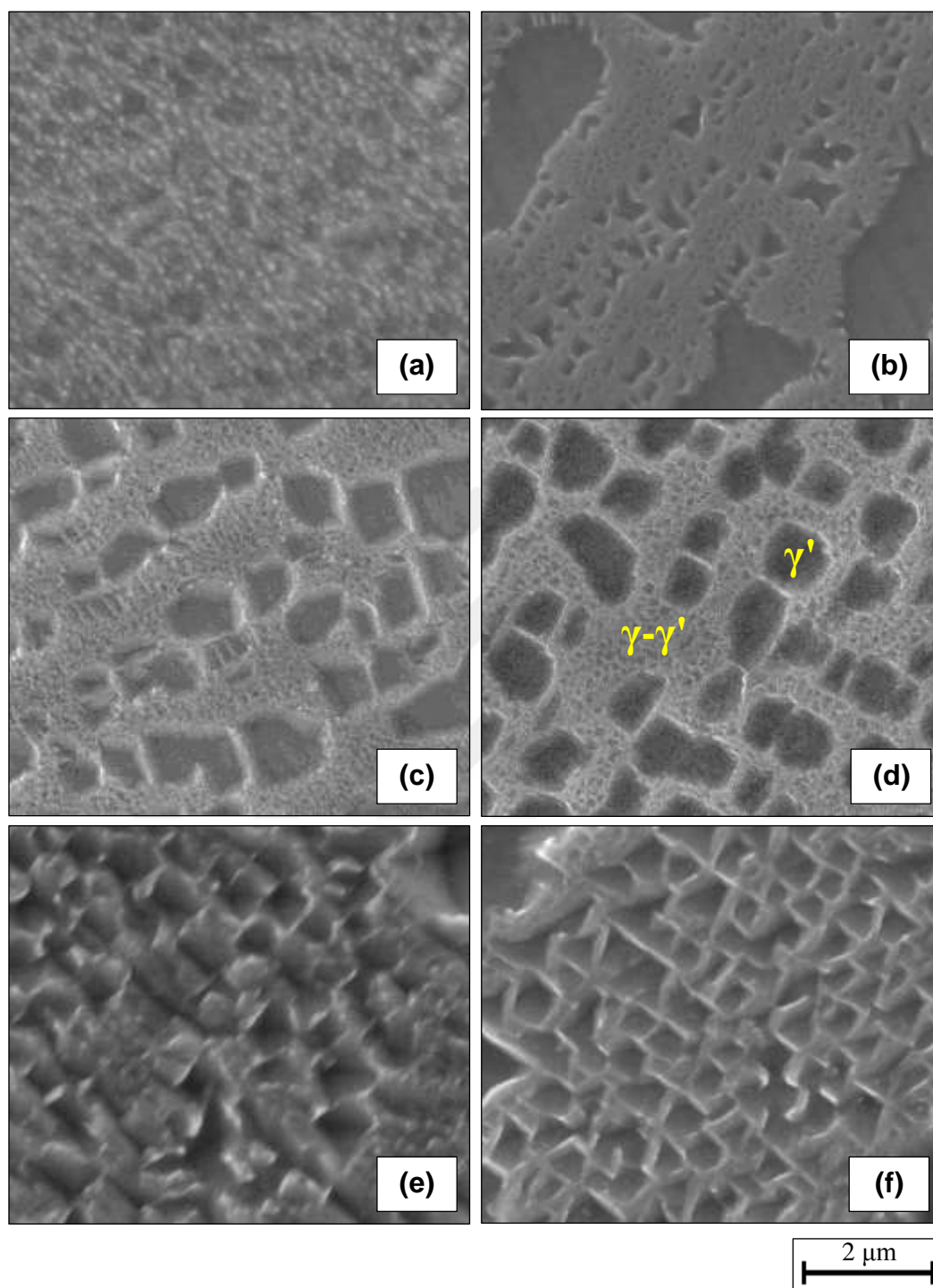


**Figure F.15** FESEM micrographs of (a) as cast, (b) partial solution heat treated microstructures and temporal evolution of  $\gamma'$  precipitates in Ni<sub>80</sub>Al<sub>15</sub>Mo<sub>5</sub> alloys as aging time is (c) 4 hr, (d) 16 hr, (e) 64 hr and (f) 256 hr, respectively



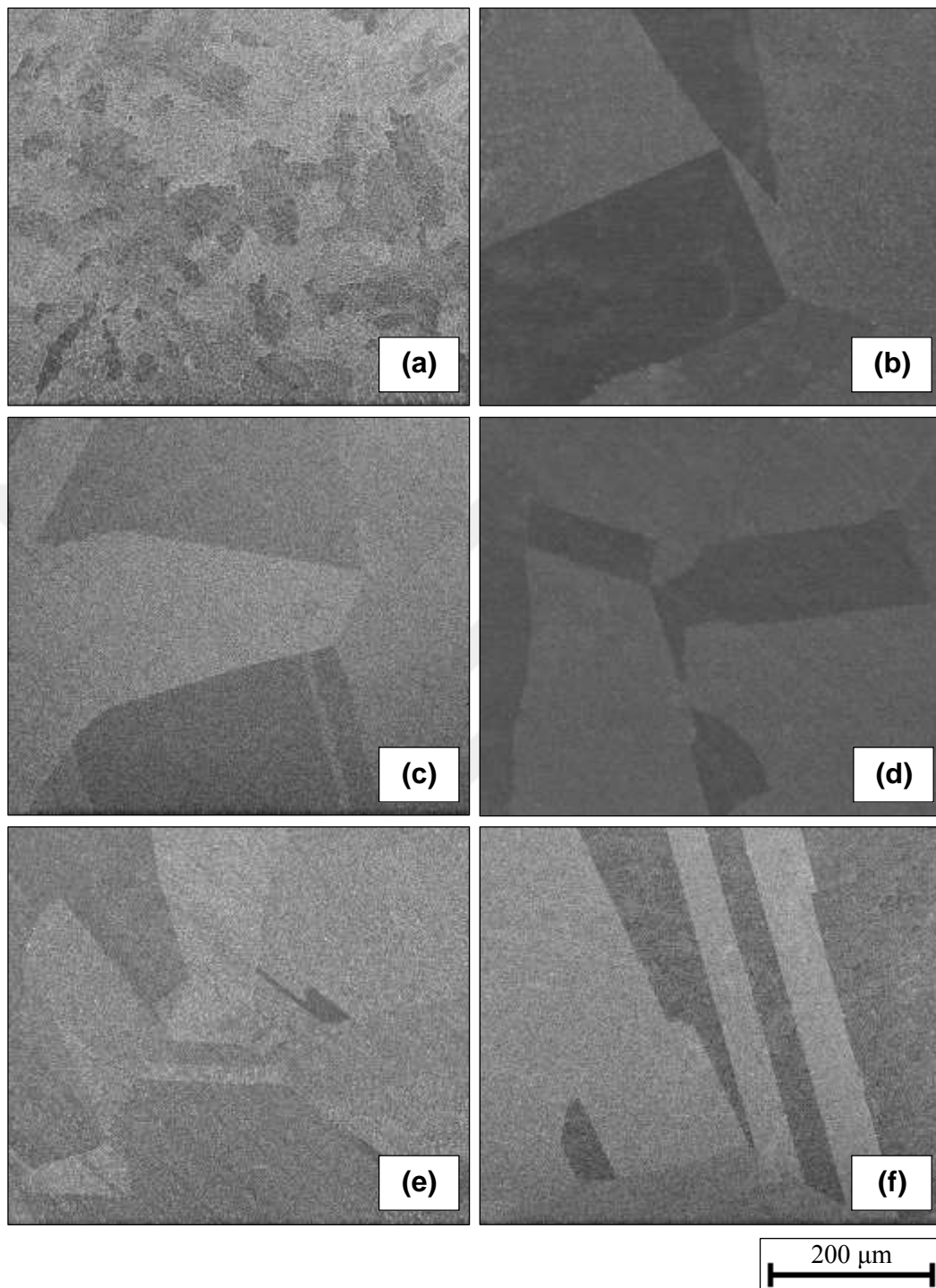


**Figure F.16** FESEM micrographs of (a) as cast, (b) homogenized/partial solution heat treated microstructures and temporal evolution of  $\gamma'$  precipitates in  $\text{Ni}_{80}\text{Al}_{15}\text{Mo}_5$  alloys as aging time is (c) 4 hr, (d) 16 hr, (e) 64 hr and (f) 256 hr, respectively.

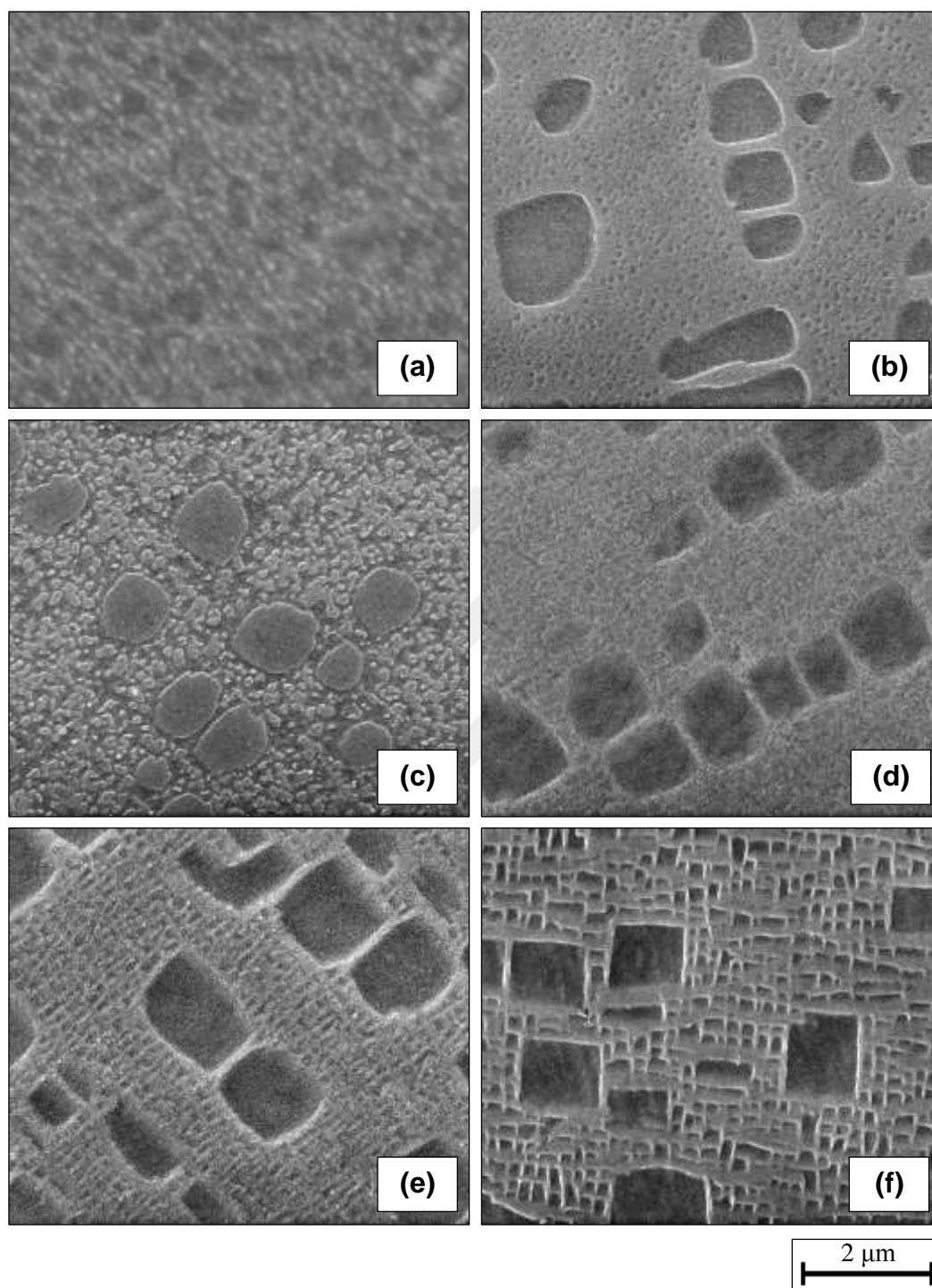


**Figure F.17** FESEM micrographs of (a) as cast, (b) homogenized/partial solution heat treated microstructures and temporal evolution of  $\gamma'$  precipitates in  $\text{Ni}_{80}\text{Al}_{15}\text{Mo}_5$  alloys as aging time is (c) 4 hr, (d) 16 hr, (e) 64 hr and (f) 256 hr, respectively.

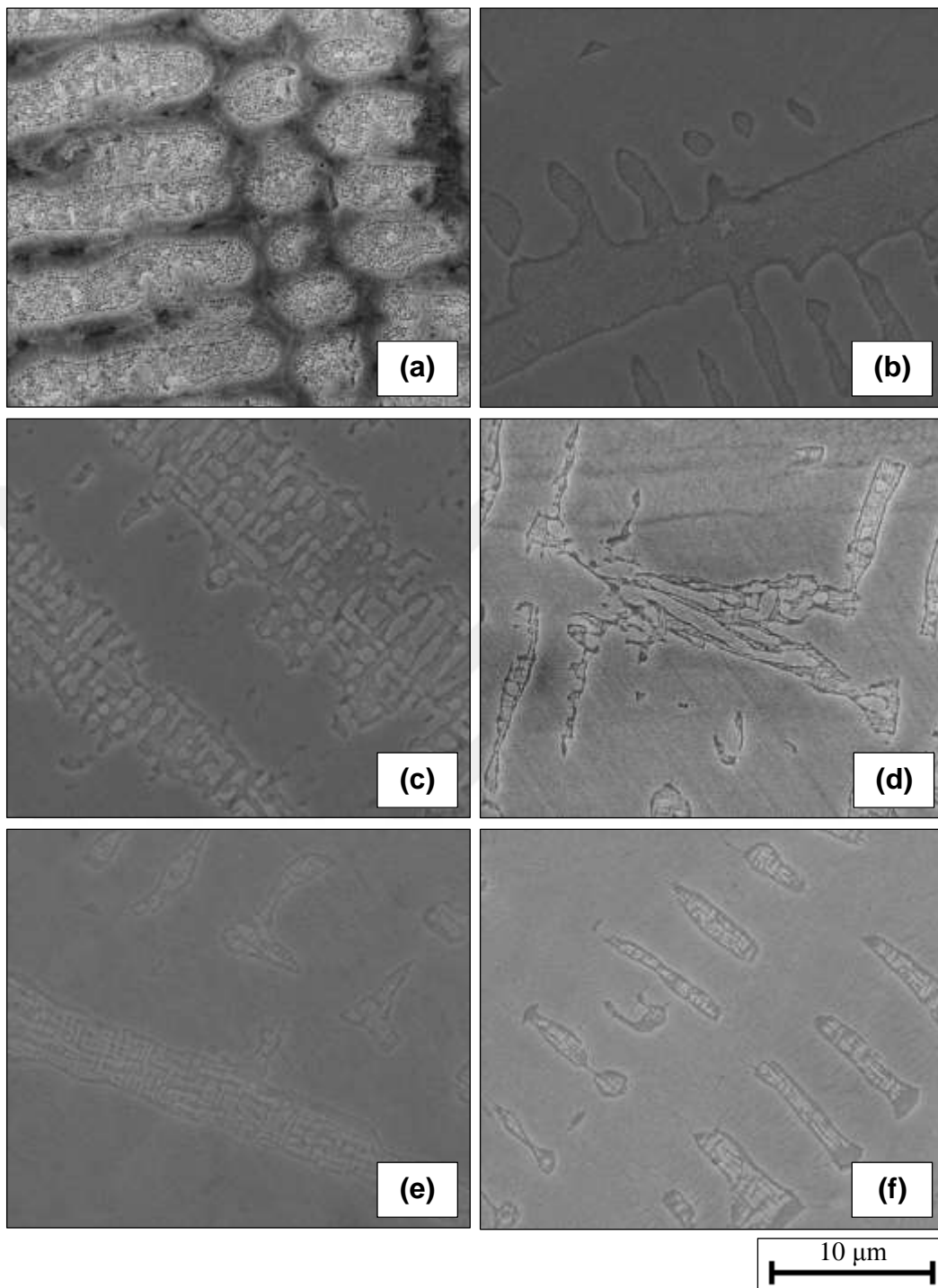


**Figure F.18** FESEM micrographs of (a) as cast, (b) partial solution heat treated microstructures and temporal evolution of  $\gamma'$  precipitates in Ni<sub>80</sub>Al<sub>15</sub>Nb<sub>5</sub> alloys as aging time is (c) 4 hr, (d) 16 hr, (e) 64 hr and (f) 256 hr, respectively.

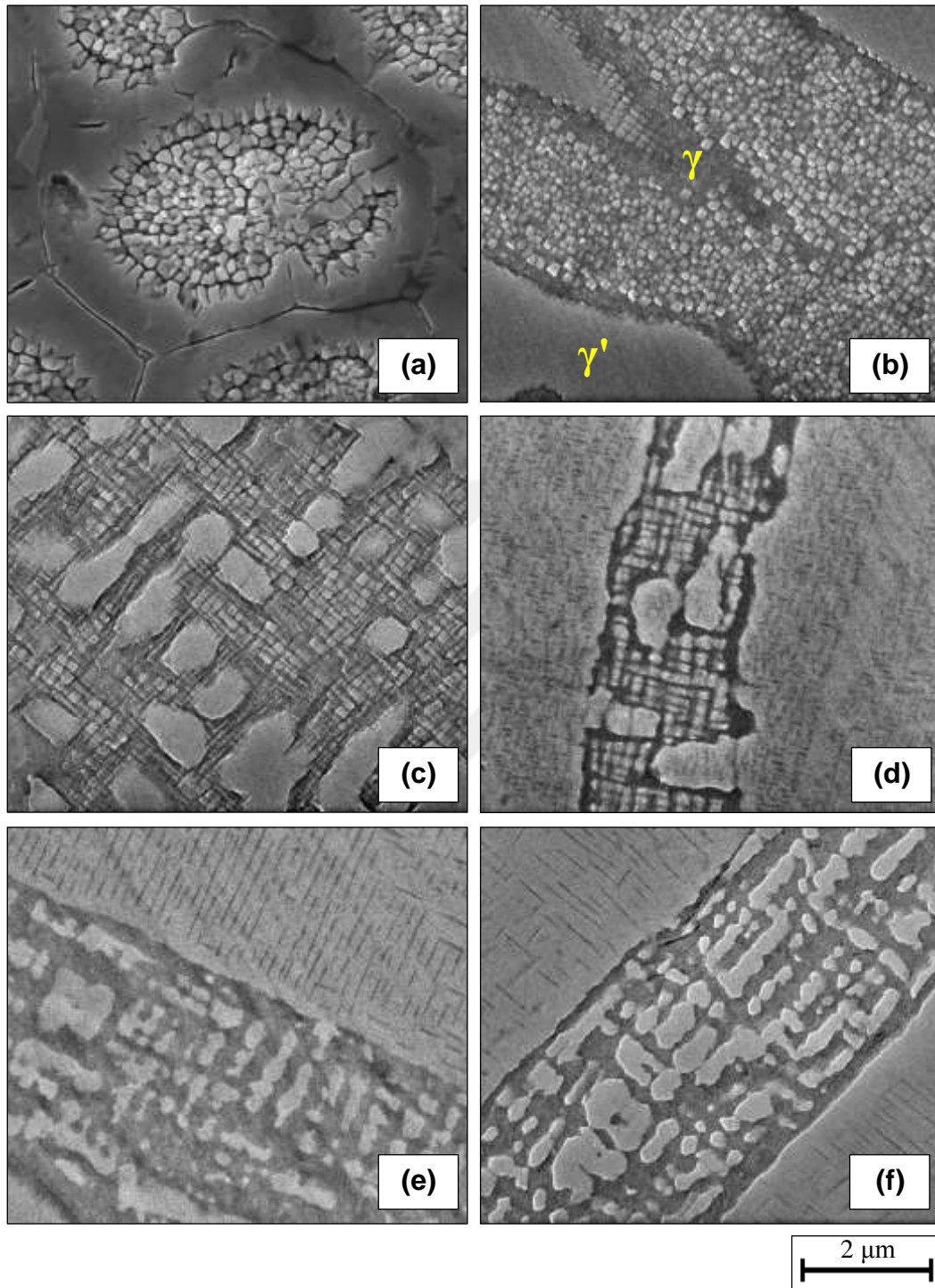


**Figure F.19** FESEM micrographs of (a) as cast, (b) partial solution heat treated microstructures and temporal evolution of  $\gamma'$  precipitates in  $\text{Ni}_{80}\text{Al}_{15}\text{Nb}_5$  alloys as aging time is (c) 4 hr, (d) 16 hr, (e) 64 hr and (f) 256 hr, respectively.

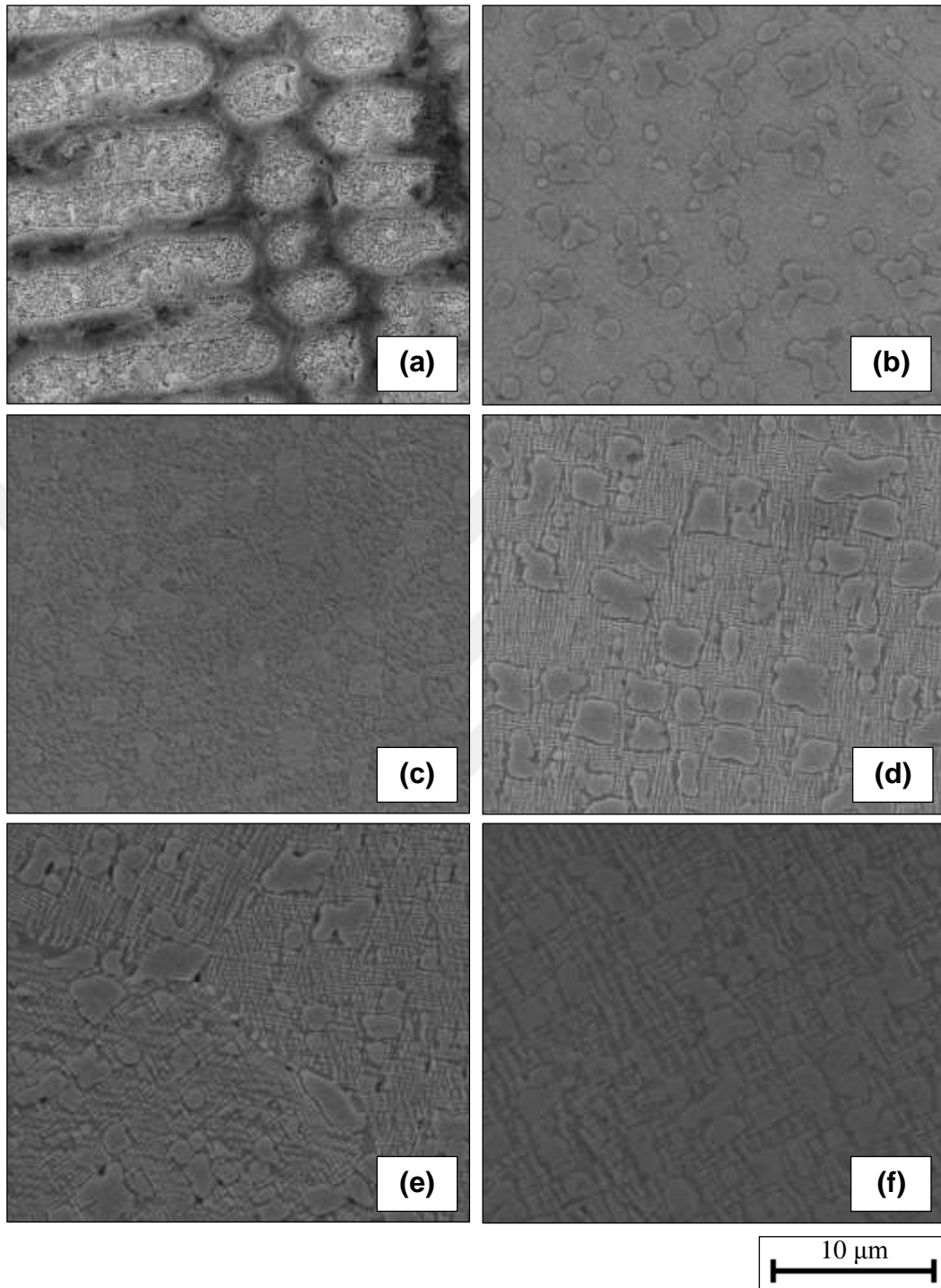


**Figure F.20** FESEM micrographs of (a) as cast, (b) homogenized/partial solution heat treated microstructures and temporal evolution of  $\gamma'$  precipitates in  $\text{Ni}_{80}\text{Al}_{15}\text{Nb}_5$  alloys as aging time is (c) 4 hr, (d) 16 hr, (e) 64 hr and (f) 256 hr, respectively.

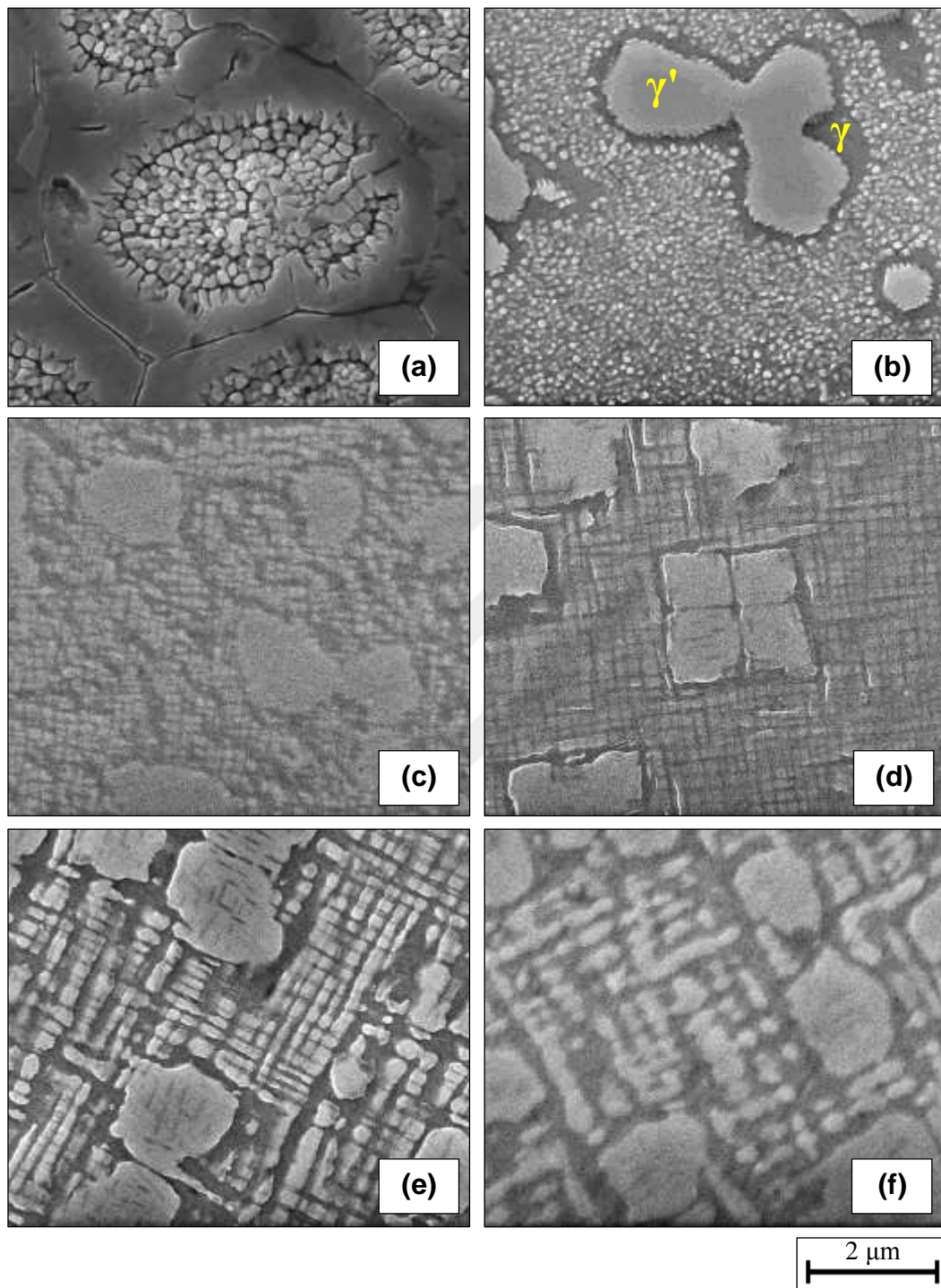


**Figure F.21** FESEM micrographs of (a) as cast, (b) homogenized/partial solution heat treated microstructures and temporal evolution of  $\gamma'$  precipitates in  $\text{Ni}_{80}\text{Al}_{15}\text{Nb}_5$  alloys as aging time is (c) 4 hr, (d) 16 hr, (e) 64 hr and (f) 256 hr, respectively.

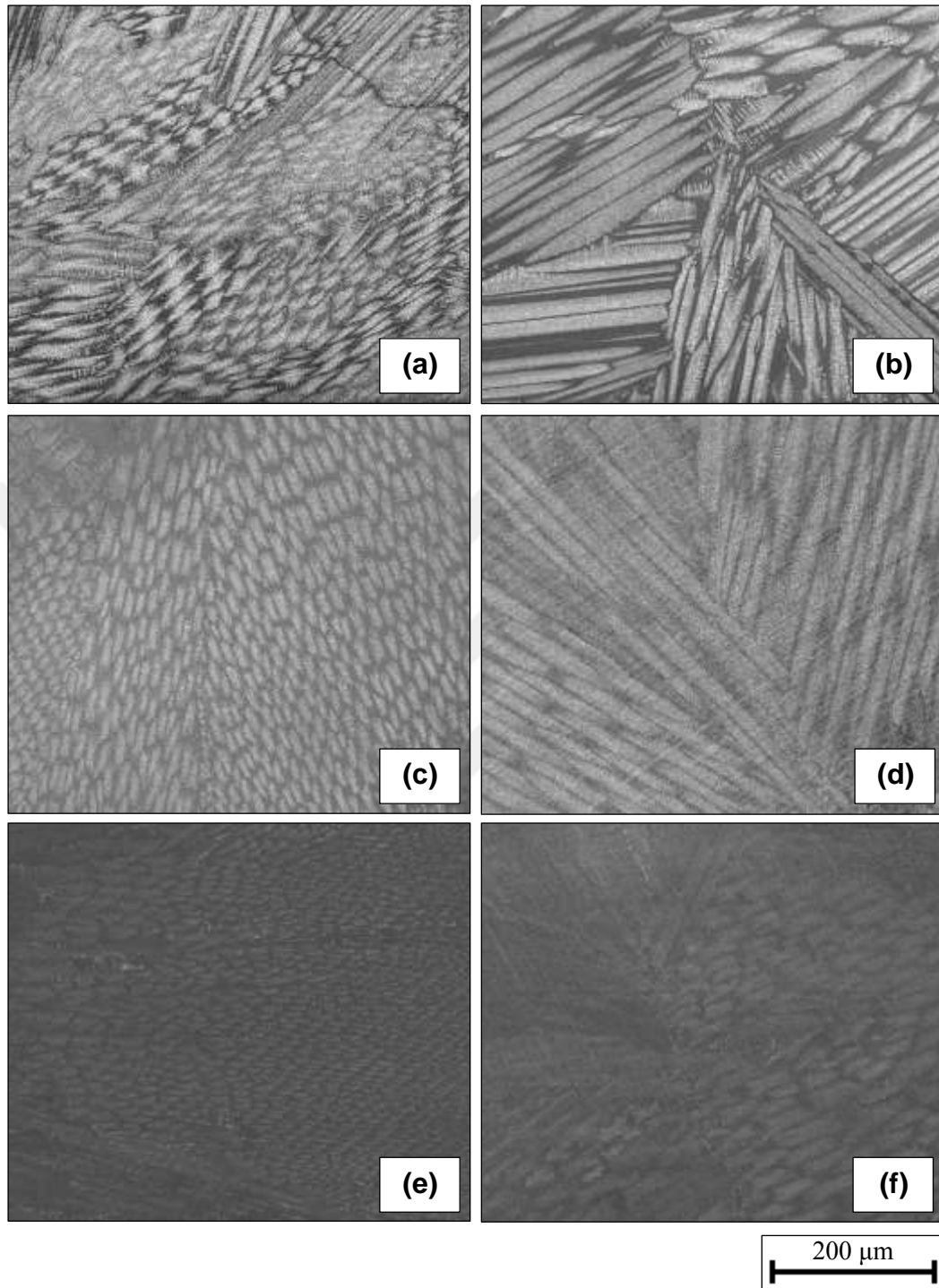


**Figure F.22** FESEM micrographs of (a) as cast, (b) partial solution heat treated microstructures and temporal evolution of  $\gamma'$  precipitates in  $\text{Ni}_{80}\text{Al}_{15}\text{Ta}_5$  alloys as aging time is (c) 4 hr, (d) 16 hr, (e) 64 hr and (f) 256 hr, respectively.

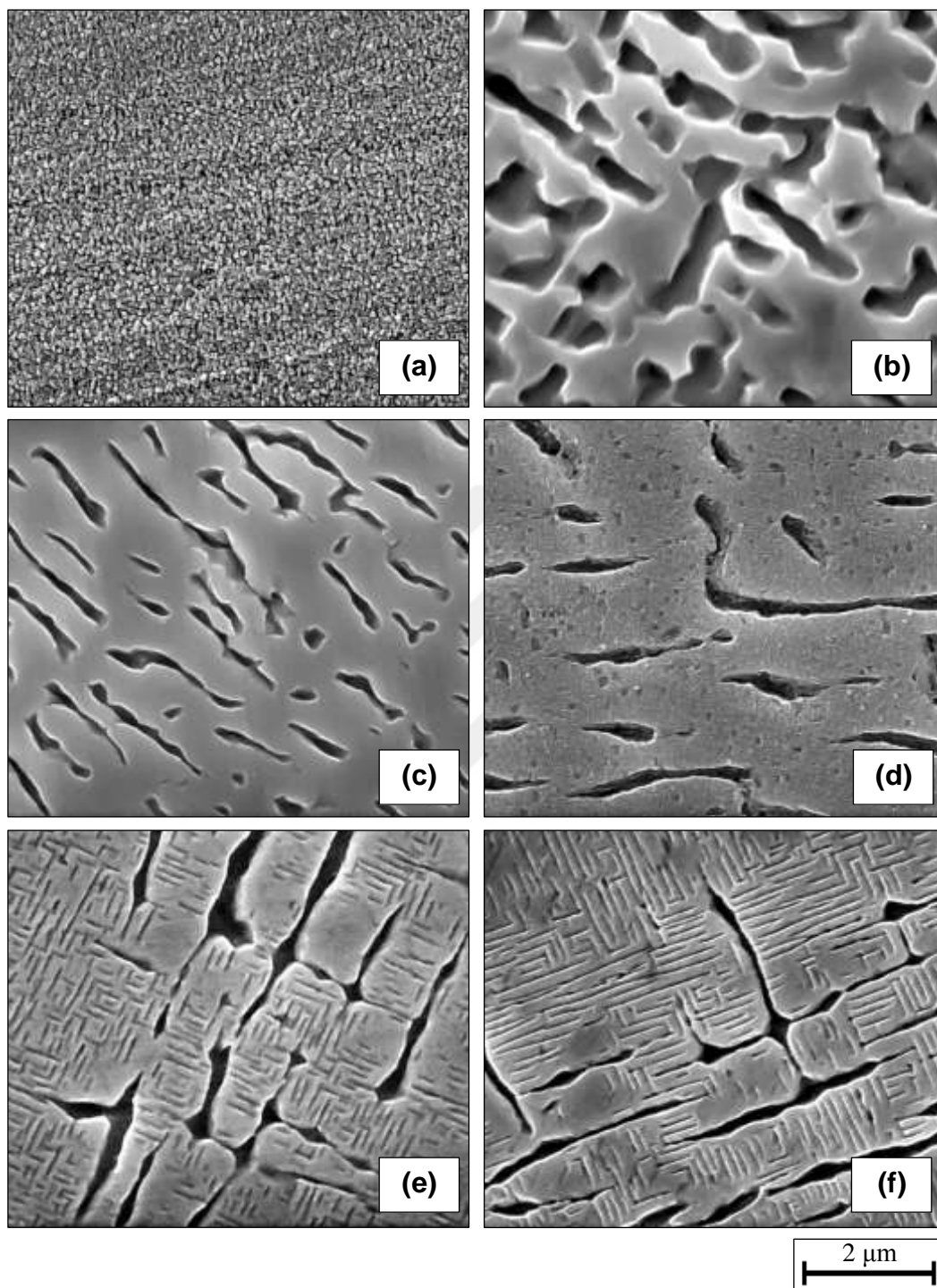


**Figure F.23** FESEM micrographs of (a) as cast, (b) partial solution heat treated microstructures and temporal evolution of  $\gamma'$  precipitates in  $\text{Ni}_{80}\text{Al}_{15}\text{Ta}_5$  alloys as aging time is (c) 4 hr, (d) 16 hr, (e) 64 hr and (f) 256 hr, respectively.



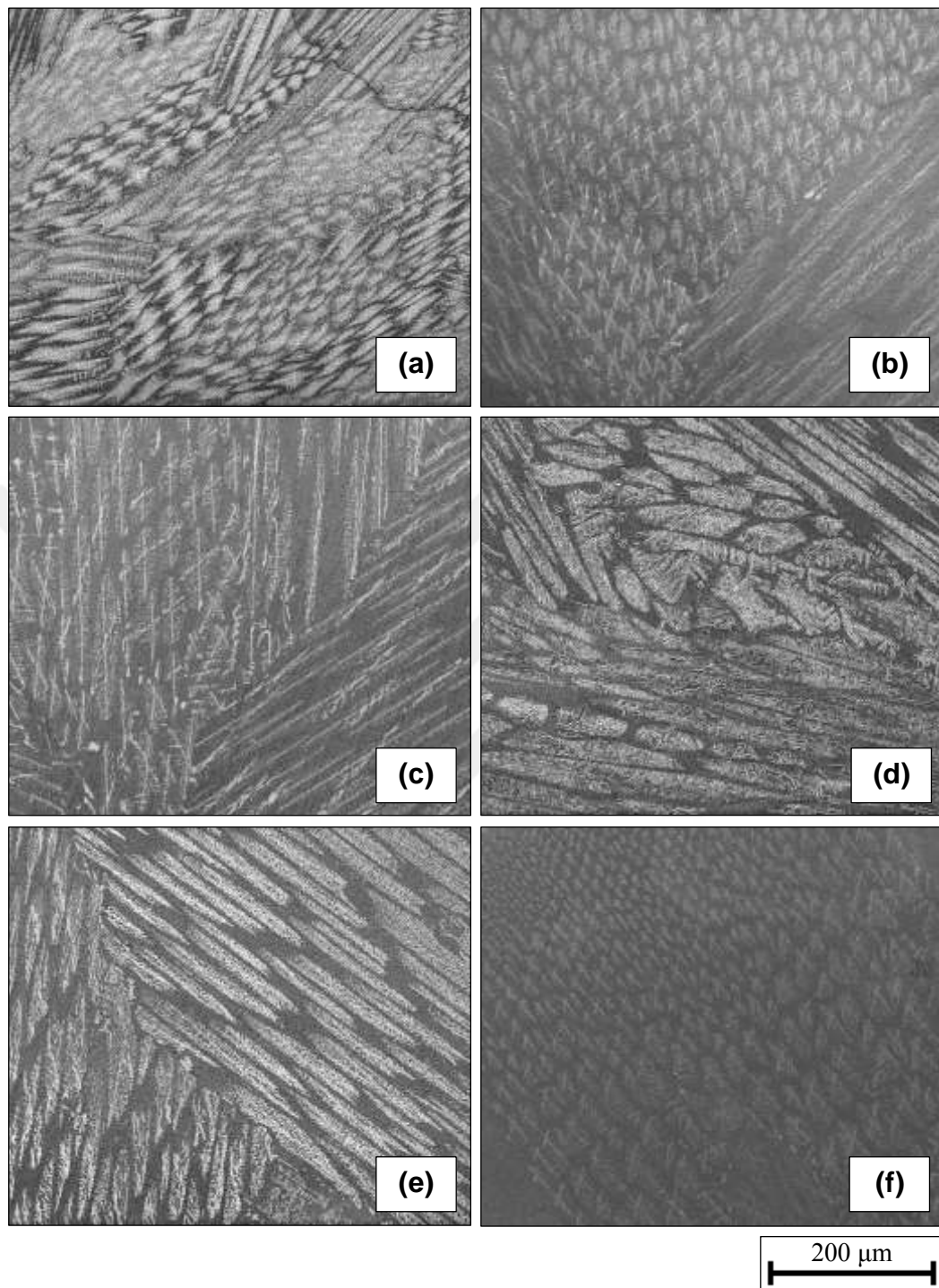


**Figure F.24** FESEM micrographs of (a) as cast, (b) homogenized/partial solution heat treated microstructures and temporal evolution of  $\gamma'$  precipitates in  $\text{Ni}_{80}\text{Al}_{15}\text{Ta}_5$  alloys as aging time is (c) 4 hr, (d) 16 hr, (e) 64 hr and (f) 256 hr, respectively.

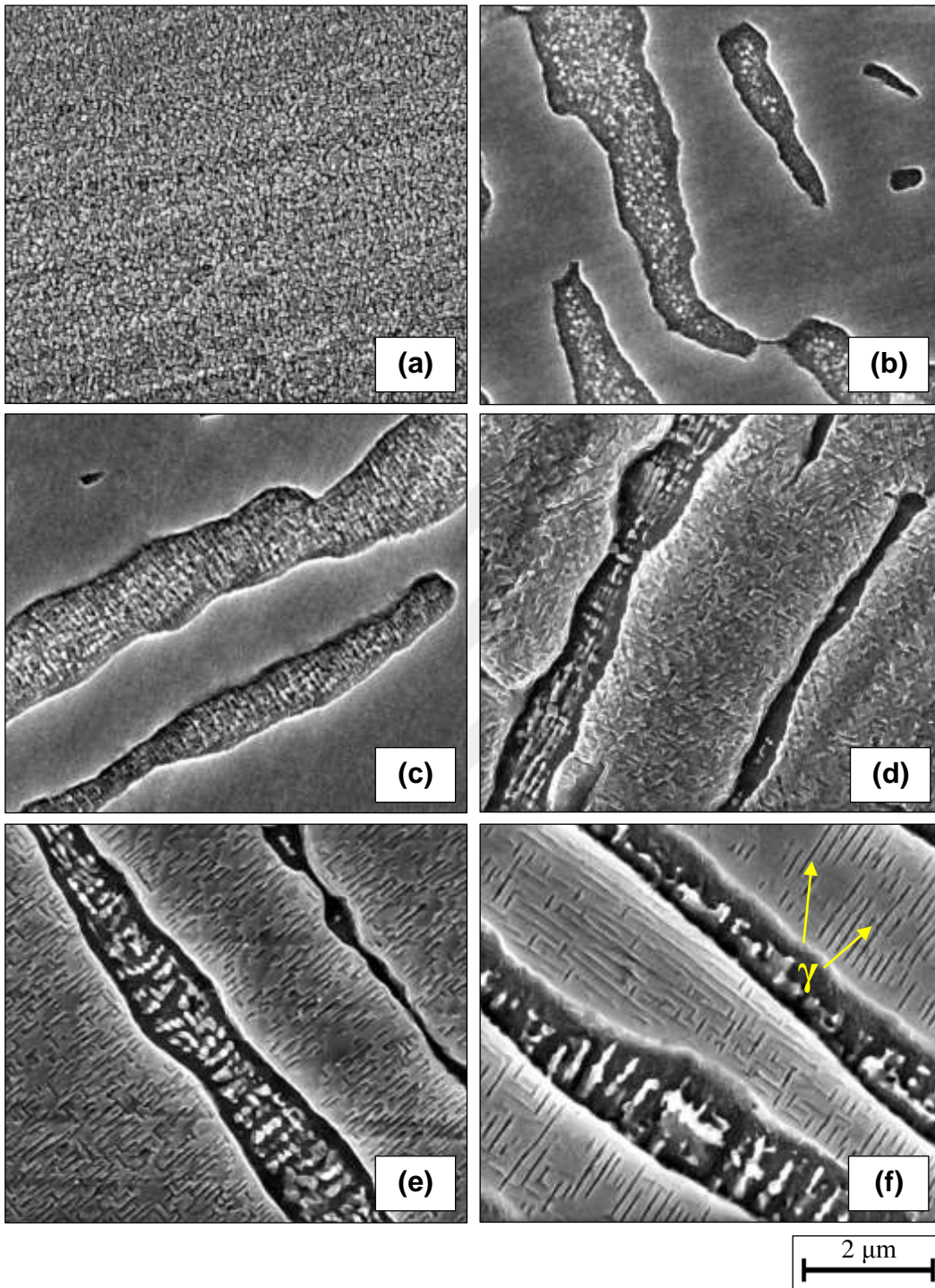


**Figure F.25** FESEM micrographs of (a) as cast, (b) homogenized/partial solution heat treated microstructures and temporal evolution of  $\gamma'$  precipitates in  $\text{Ni}_{80}\text{Al}_{15}\text{Ta}_5$  alloys as aging time is (c) 4 hr, (d) 16 hr, (e) 64 hr and (f) 256 hr, respectively.

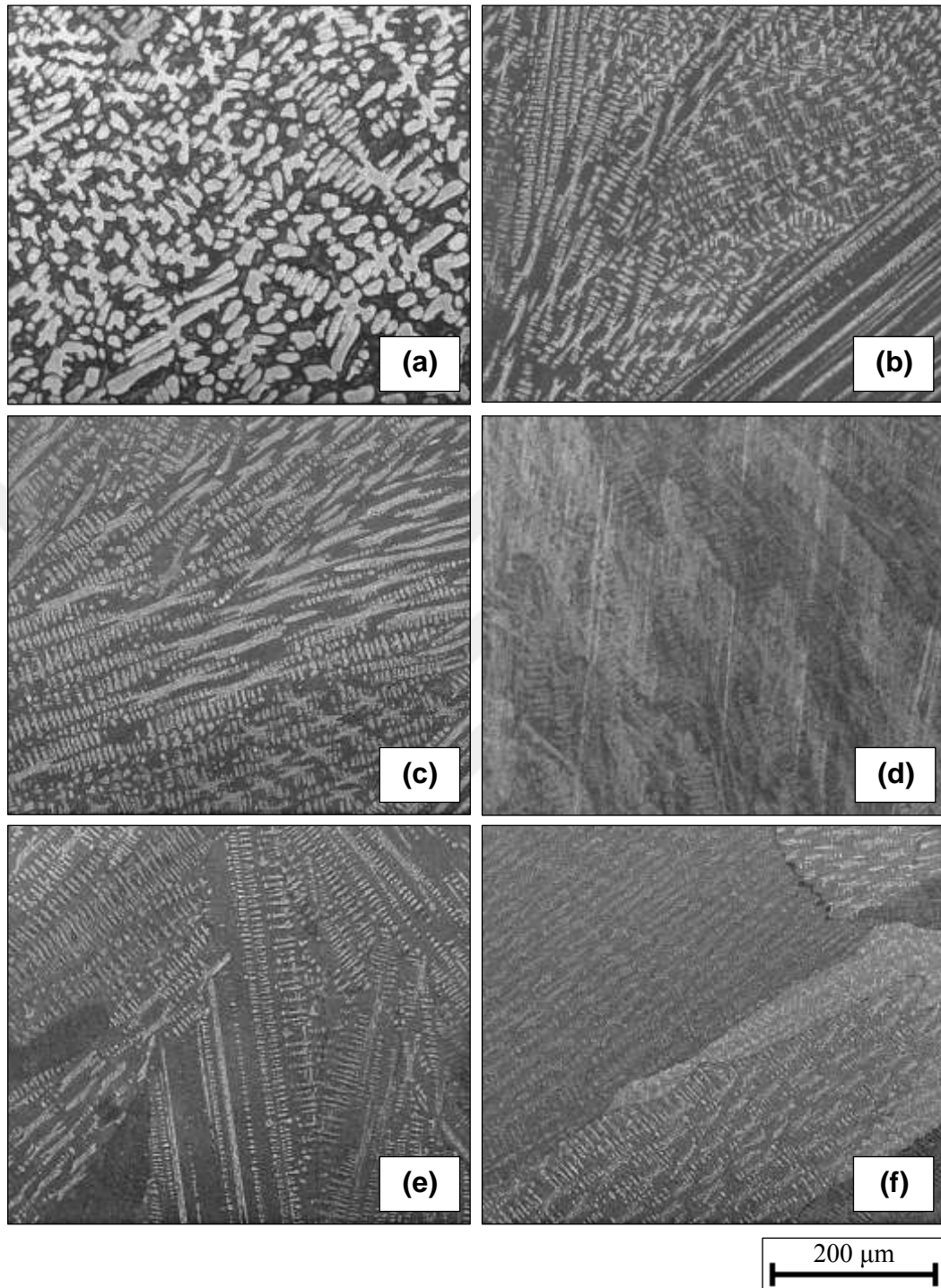


**Figure F.26** FESEM micrographs of (a) as cast, (b) partial solution heat treated microstructures and temporal evolution of  $\gamma'$  precipitates in  $\text{Ni}_{80}\text{Al}_{15}\text{Ti}_5$  alloys as aging time is (c) 4 hr, (d) 16 hr, (e) 64 hr and (f) 256 hr, respectively.

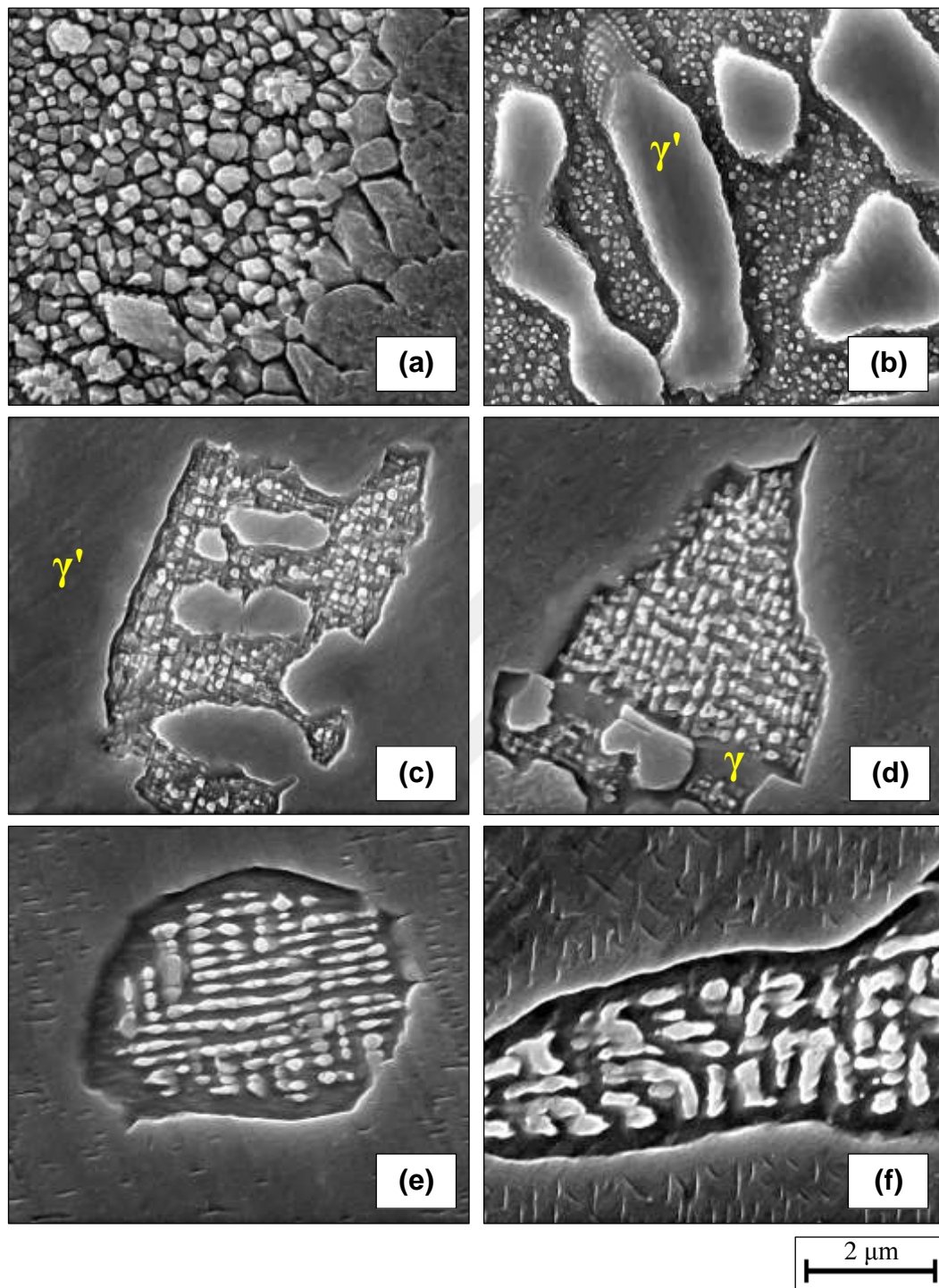


**Figure F.27** FESEM micrographs of (a) as cast, (b) partial solution heat treated microstructures and temporal evolution of  $\gamma'$  precipitates in  $\text{Ni}_{80}\text{Al}_{15}\text{Ti}_5$  alloys as aging time is (c) 4 hr, (d) 16 hr, (e) 64 hr and (f) 256 hr, respectively.

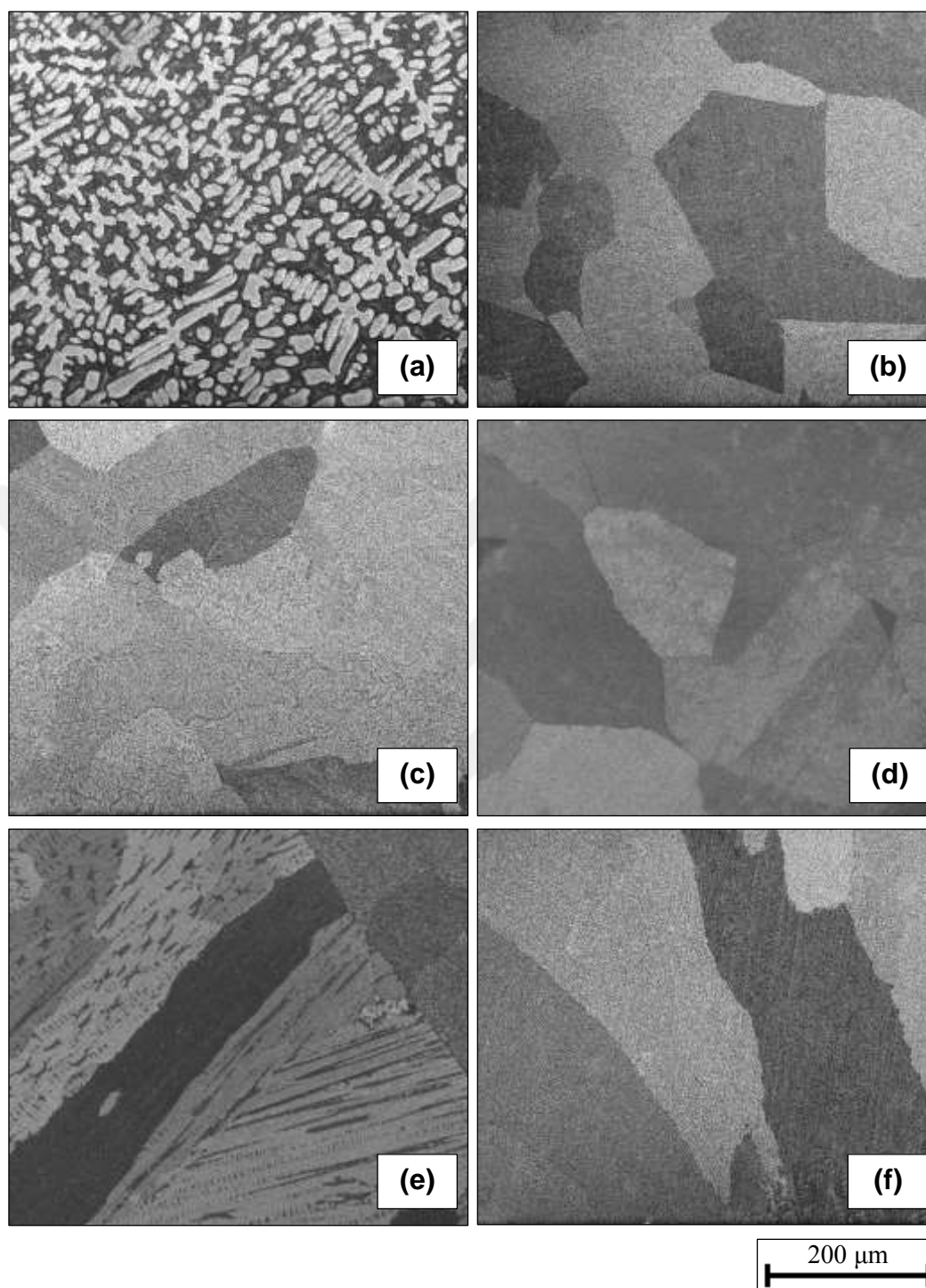


**Figure F.28** FESEM micrographs of (a) as cast, (b) homogenized/partial solution heat treated microstructures and temporal evolution of  $\gamma'$  precipitates in Ni<sub>80</sub>Al<sub>15</sub>Ti<sub>5</sub> alloys as aging time is (c) 4 hr, (d) 16 hr, (e) 64 hr and (f) 256 hr, respectively.

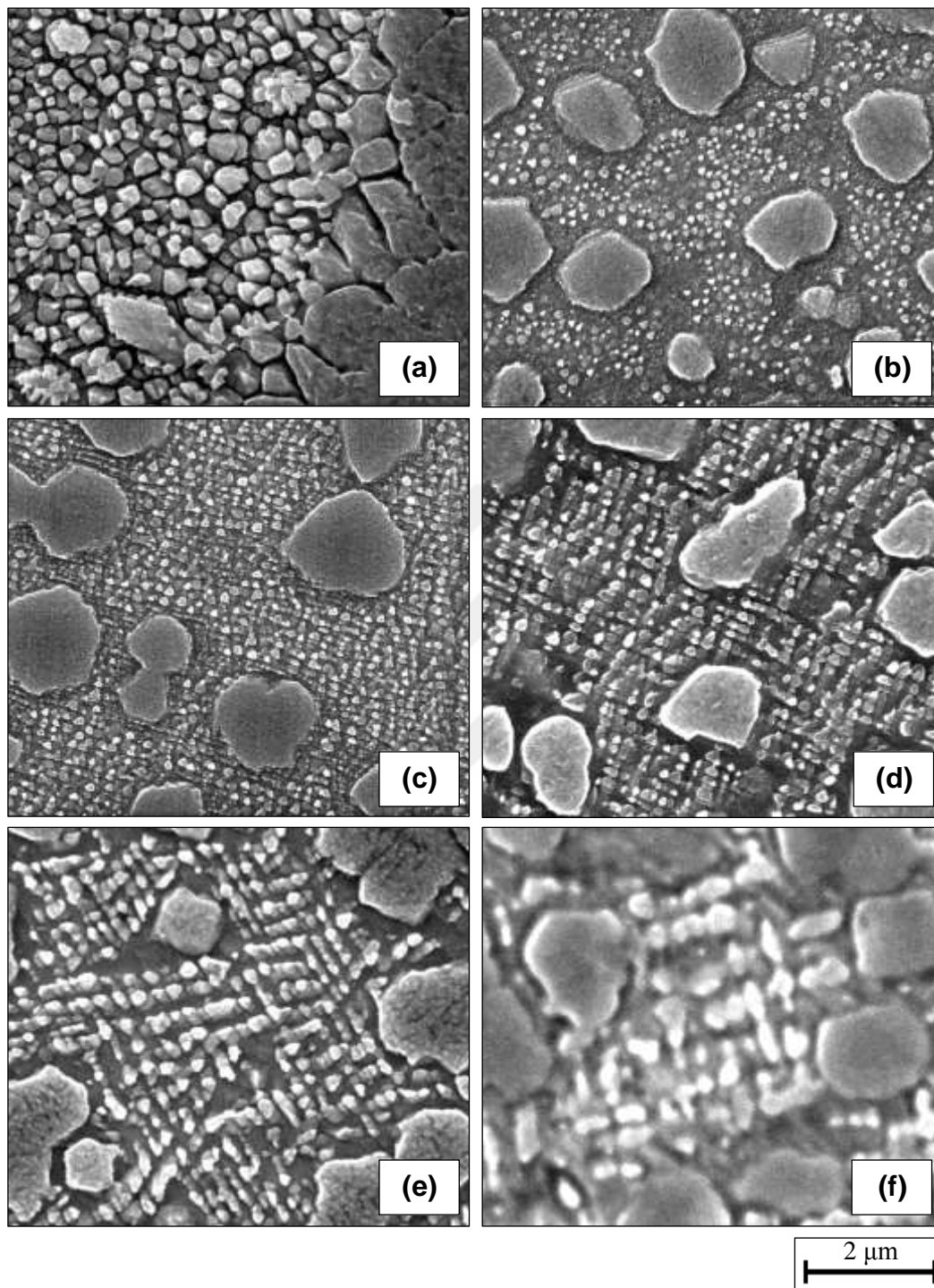


**Figure F.29** FESEM micrographs of (a) as cast, (b) homogenized/partial solution heat treated microstructures and temporal evolution of  $\gamma'$  precipitates in  $\text{Ni}_{80}\text{Al}_{15}\text{Ti}_5$  alloys as aging time is (c) 4 hr, (d) 16 hr, (e) 64 hr and (f) 256 hr, respectively.

## APPENDIX G

### EDS PHASE ANALYSIS AND DETERMINATION OF PHASE PARTITIONING COEFFICIENTS OF ALLOYING X ELEMENTS IN $\text{Ni}_{80}\text{Al}_{15}\text{X}_5$ ALLOY SYSTEMS

Appendix G shows EDS phase analysis and phase partitioning coefficients of alloying X elements in  $\text{Ni}_{80}\text{Al}_{15}\text{X}_5$  alloy systems (X = Co, Cr, Hf, Mo, Nb, Ta, Ti and W, respectively).

**Table G.1** EDS phase analysis and determination of phase partitioning coefficients of X = Co atoms in Ni<sub>80</sub>Al<sub>15</sub>Co<sub>5</sub> alloys.

Ni <sub>80</sub> Al <sub>15</sub> Co <sub>5</sub> alloys													
Sample groups	Definitions	Heat treatment		General (at.%)					γ (at.%)			K <sub>Co</sub>	
		Temperature and durations		Ni	Al	Co	Ni	Al	Co	Ni	Al		Co
	As cast (fast cooled)	-		74.7	20.4	4.9	78.2	16.3	5.5	75.8	19.1	5.1	0.94
	As cast (slow cooled)	-		-	-	-	-	-	-	-	-	-	-
1	Partial solution heat treatment	1150 °C for 3 hr		78.0	16.8	5.2	-	-	-	-	-	-	-
	Aging	800 °C for 4 hr		76.5	18.0	5.5	78.2	16.2	5.6	76.0	19.1	4.9	0.88
		800 °C for 16 hr		77.4	17.4	5.2	78.0	16.9	5.1	74.8	20.4	4.8	0.93
		800 °C for 64 hr		76.3	18.2	5.5	79.5	15.2	5.3	72.3	22.9	4.8	0.90
		800 °C for 256 hr		76.8	18.0	5.2	78.0	16.3	5.7	73.4	21.8	4.8	0.84
2	Homogenization and partial solution heat treatment	1250 °C for 24 hr and 1150 °C for 3 hr		77.9	16.4	5.7	-	-	-	-	-	-	-
		800 °C for 4 hr		77.9	16.5	5.6	78.5	15.9	5.6	76.7	18.1	5.2	0.93
	Aging	800 °C for 16 hr		77.7	16.9	5.4	79.8	14.7	5.5	74.0	21.2	4.8	0.86
		800 °C for 64 hr		78.0	16.2	5.8	79.5	14.9	5.6	76.4	18.6	5.0	0.89
		800 °C for 256 hr		79.2	15.2	5.6	80.2	14.3	5.5	75.0	20.2	4.8	0.87



**Table G.2** EDS phase analysis and determination of phase partitioning coefficients of X = Cr atoms in Ni<sub>80</sub>Al<sub>15</sub>Cr<sub>5</sub> alloys.

Ni <sub>80</sub> Al <sub>15</sub> Cr <sub>5</sub> alloys														
Sample groups	Definitions	Heat treatment		General (at.%)					γ (at.%)			κ <sub>Cr</sub>		
		Temperature and durations		Ni	Al	Cr	Ni	Al	Cr	Ni	Al	Cr	Al	Cr
	As cast (fast cooled)	-		77.0	18.1	4.9	-	-	-	-	-	-	-	-
	As cast (slow cooled)	-		-	-	-	-	-	-	-	-	-	-	-
1	Partial solution heat treatment	1150 °C for 3 hr		76.5	18.4	5.1	-	-	-	-	-	-	-	-
		800 °C for 4 hr		78.0	17.0	5.0	80.2	14.6	5.3	77.9	17.1	5.0	0.96	
	Aging	800 °C for 16 hr		77.8	17.1	5.0	78.8	16.0	5.3	74.9	20.0	5.1	0.97	
		800 °C for 64 hr		76.9	17.9	5.2	80.4	14.3	5.2	75.8	19.3	4.9	0.95	
		800 °C for 256 hr		78.1	16.9	5.0	81.3	13.5	5.2	75.6	19.6	4.8	0.92	
2	Homogenization and partial solution heat treatment	1250 °C for 24 hr and 1150 °C for 3 hr		78.2	16.8	5.0	-	-	-	-	-	-	-	-
		800 °C for 4 hr		79.3	15.6	5.1	78.9	15.8	5.2	77.6	17.3	5.2	0.99	
	Aging	800 °C for 16 hr		78.1	16.5	5.4	81.0	13.7	5.3	76.4	18.3	5.2	0.98	
		800 °C for 64 hr		78.4	16.7	5.0	80.5	14.4	5.1	76.6	18.6	4.8	0.95	
		800 °C for 256 hr		79.0	16.0	5.0	81.7	12.9	5.4	75.9	19.4	4.8	0.89	

**Table G.3** EDS phase analysis and determination of phase partitioning coefficients of X = Hf atoms in Ni<sub>80</sub>Al<sub>15</sub>Hf<sub>5</sub> alloys.

Ni <sub>80</sub> Al <sub>15</sub> Hf <sub>5</sub> alloys															
Sample groups	Definitions	Heat treatment	General (at.%)						γ (at.%)			γ' (at.%)			κ <sub>Hf</sub>
			Ni	Al	Hf	Ni	Al	Hf	Ni	Al	Hf	Ni	Al	Hf	
	As cast (fast cooled)	-	76.9	17.3	5.7	81.5	14.0	4.5	75.3	20.0	4.8	1.07	-	-	
	As cast (slow cooled)	-	-	-	-	-	-	-	-	-	-	-	-	-	
1	Partial solution heat treatment	1150 °C for 3 hr	76.8	17.9	5.3	82.9	14.7	2.4	75.2	18.2	6.6	2.77	-	-	
		800 °C for 4 hr	77.5	17.1	5.5	82.3	14.3	3.4	75.0	18.5	6.5	1.91	-	-	
	Aging	800 °C for 16 hr	76.3	18.6	5.1	83.1	14.8	2.0	75.1	18.2	6.6	3.28	-	-	
		800 °C for 64 hr	76.6	18.2	5.3	82.4	15.1	2.5	74.6	19.0	6.5	2.57	-	-	
	Homogenization and partial solution heat treatment	800 °C for 256 hr	77.4	17.0	5.5	81.8	15.7	2.5	75.1	18.6	6.3	2.47	-	-	
		1250 °C for 24 hr and 1150 °C for 3 hr	86.2	11.8	2.0	85.8	12.2	2.0	-	-	-	-	-	-	
2	Aging	800 °C for 4 hr	84.7	13.2	2.2	80.7	17.9	1.4	77.6	20.7	1.7	1.20	-	-	
		800 °C for 16 hr	83.8	13.4	2.8	83.4	14.8	1.8	77.1	20.1	2.8	1.54	-	-	
	Aging	800 °C for 64 hr	86.3	12.0	1.7	85.2	12.9	1.9	78.0	18.6	3.4	1.79	-	-	
		800 °C for 256 hr	88.3	10.6	1.2	-	-	-	-	-	-	-	-	-	

**Table G.4** EDS phase analysis and determination of phase partitioning coefficients of X = Mo atoms in Ni<sub>80</sub>Al<sub>15</sub>Mo<sub>5</sub> alloys.

Ni <sub>80</sub> Al <sub>15</sub> Mo <sub>5</sub> alloys														
Sample groups	Definitions	Heat treatment		General (at.%)						γ (at.%)			κ <sub>Mo</sub>	
		Temperature and durations		Ni	Al	Mo	Ni	Al	Mo	Ni	Al	Mo		
	As cast (fast cooled)	-	-	76.2	18.0	5.8	-	-	-	-	-	-	-	-
	As cast (slow cooled)	-	-	-	-	-	-	-	-	-	-	-	-	-
	Partial solution heat treatment	1150 °C for 3 hr		77.2	17.5	5.3	81.0	13.3	5.7	76.0	19.6	4.4	0.78	
1		800 °C for 4 hr		78.8	15.9	5.3	78.1	15.9	6.0	75.6	19.7	4.7	0.79	
		800 °C for 16 hr		78.0	16.5	5.6	78.9	15.3	5.9	74.7	20.8	4.5	0.77	
		800 °C for 64 hr		77.6	17.2	5.3	81.1	13.5	5.4	75.5	19.5	5.0	0.92	
		800 °C for 256 hr		77.5	17.0	5.5	79.0	15.2	5.7	75.0	20.4	4.6	0.81	
	Homogenization and partial solution heat treatment	1250 °C for 24 hr and 1150 °C for 3 hr		78.5	16.0	5.5	78.9	15.3	5.8	76.0	19.2	4.7	0.81	
2		800 °C for 4 hr		78.5	16.0	5.5	79.2	15.2	5.7	75.4	19.9	4.8	0.84	
		800 °C for 16 hr		79.1	15.7	5.3	79.5	14.9	5.6	77.0	18.6	4.5	0.80	
		800 °C for 64 hr		79.1	15.5	5.4	79.8	14.6	5.7	75.5	19.5	5.0	0.88	
		800 °C for 256 hr		79.4	15.0	5.6	78.3	15.9	5.8	76.4	18.9	4.7	0.80	

**Table G.5** EDS phase analysis and determination of phase partitioning coefficients of  $X = \text{Nb}$  atoms in  $\text{Ni}_{80}\text{Al}_{15}\text{Nb}_5$  alloys.

		$\text{Ni}_{80}\text{Al}_{15}\text{Nb}_5$ alloys														
Sample groups	Definitions	Heat treatment		General (at.%)					$\gamma$ (at.%)			$\gamma'$ (at.%)		$k_{\text{Nb}}$		
		Temperature and durations	Ni	Al	Nb	Ni	Al	Nb	Ni	Al	Nb	Ni	Al	Nb	Ni	Nb
	As cast (fast cooled)	-	76.9	17.5	5.6	80.7	15.3	4.0	75.1	18.7	6.2	1.54	-	-	-	-
	As cast (slow cooled)	-	-	-	-	-	-	-	-	-	-	-	-	-	-	-
1	Partial solution heat treatment	1150 °C for 3 hr	76.6	17.4	6.0	81.8	13.9	4.3	76.3	18.1	5.6	1.29	-	-	-	-
		800 °C for 4 hr	77.6	16.6	5.8	83.2	12.8	4.0	76.7	17.6	5.8	1.42	-	-	-	-
	Aging	800 °C for 16 hr	78.0	16.6	5.5	82.8	13.1	4.1	76.3	17.9	5.9	1.43	-	-	-	-
		800 °C for 64 hr	77.3	17.0	5.6	82.9	13.2	3.9	75.7	18.2	6.1	1.56	-	-	-	-
2	Homogenization and partial solution heat treatment	1250 °C for 24 hr and 1150 °C for 3 hr	81.1	13.0	5.9	82.0	12.3	5.7	77.1	16.1	6.9	1.20	-	-	-	-
		800 °C for 4 hr	80.9	13.1	6.0	81.1	12.9	6.0	76.9	16.4	6.7	1.11	-	-	-	-
	Aging	800 °C for 16 hr	81.2	12.7	6.1	84.0	10.4	5.5	77.6	15.9	6.5	1.18	-	-	-	-
		800 °C for 64 hr	81.6	12.5	5.9	86.5	8.9	4.6	76.0	16.3	7.7	1.67	-	-	-	-
		800 °C for 256 hr	78.5	15.7	5.8	84.6	10.9	4.5	76.6	16.8	6.6	1.46	-	-	-	-

**Table G.6** EDS phase analysis and determination of phase partitioning coefficients of X = Ta atoms in Ni<sub>80</sub>Al<sub>15</sub>Ta<sub>5</sub> alloys.

Ni <sub>80</sub> Al <sub>15</sub> Ta <sub>5</sub> alloys														
Sample groups	Definitions	Heat treatment		General (at.%)					γ (at.%)			κ <sub>Ta</sub>		
		Temperature and durations		Ni	Al	Ta	Ni	Al	Ta	Ni	Al		Ta	
	As cast (fast cooled)	-	-	75.6	18.3	6.1	-	-	-	-	-	-	-	-
	As cast (slow cooled)	-	-	-	-	-	-	-	-	-	-	-	-	-
1	Partial solution heat treatment	1150 °C for 3 hr		75.5	16.4	8.1	82.2	13.3	4.5	76.4	18.2	5.4	1.20	
		800 °C for 4 hr		76.6	16.8	6.6	85.1	10.2	4.7	76.3	18.2	5.5	1.16	
		800 °C for 16 hr		76.0	17.3	6.6	83.0	11.3	5.7	76.2	17.6	6.2	1.09	
	Aging	800 °C for 64 hr		77.5	18.1	4.3	84.6	12.0	3.4	76.0	19.0	5.0	1.48	
2		800 °C for 256 hr		77.3	16.7	6.1	82.2	12.6	5.2	75.7	17.6	6.7	1.29	
	Homogenization and partial solution heat treatment	1250 °C for 24 hr and 1150 °C for 3 hr		79.0	15.6	5.4	82.7	13.4	3.9	76.6	17.7	5.8	1.50	
		800 °C for 4 hr		76.6	18.1	5.4	83.9	11.4	4.8	77.0	16.2	6.8	1.43	
		800 °C for 16 hr		76.9	17.3	5.8	83.0	12.3	4.8	75.8	18.2	6.1	1.27	
	Aging	800 °C for 64 hr		77.8	15.9	6.3	85.6	10.5	3.9	75.4	17.8	6.8	1.72	
		800 °C for 256 hr		76.9	17.2	5.9	86.4	9.6	4.0	75.8	18.4	5.8	1.44	

**Table G.7** EDS phase analysis and determination of phase partitioning coefficients of X = Ti atoms in Ni<sub>80</sub>Al<sub>15</sub>Ti<sub>5</sub> alloys.

		Ni <sub>80</sub> Al <sub>15</sub> Ti <sub>5</sub> alloys										
Sample groups	Definitions	Heat treatment		General (at.%)			γ (at.%)			γ' (at.%)		κ <sub>Ti</sub>
		Temperature and durations	Ni	Al	Ti	Ni	Al	Ti	Ni	Al	Ti	
	As cast (fast cooled)	-	77.2	17.6	5.2	79.8	16.2	4.0	75.7	18.9	5.4	1.34
	As cast (slow cooled)	-	-	-	-	-	-	-	-	-	-	-
1	Partial solution heat treatment	1150 °C for 3 hr	77.1	17.8	5.1	80.8	14.9	4.4	75.1	19.4	5.5	1.26
	Aging	800 °C for 4 hr	77.5	17.5	4.9	82.6	13.5	3.9	76.1	18.2	5.7	1.46
		800 °C for 16 hr	77.1	17.8	5.2	83.3	12.7	4.0	76.0	19.0	5.0	1.23
		800 °C for 64 hr	76.6	17.9	5.5	83.9	12.8	3.3	75.7	18.4	5.9	1.77
		800 °C for 256 hr	77.0	17.6	5.4	87.3	10.1	2.7	76.0	18.4	5.6	2.07
2	Homogenization and partial solution heat treatment	1250 °C for 24 hr and 1150 °C for 3 hr	81.5	13.7	4.8	83.9	12.1	4.0	80.0	14.6	5.3	1.32
		800 °C for 4 hr	80.0	14.8	5.2	83.2	12.4	4.4	76.9	16.8	6.3	1.43
2	Aging	800 °C for 16 hr	80.9	13.7	5.4	84.4	11.3	4.3	77.2	16.7	6.1	1.42
		800 °C for 64 hr	78.0	16.5	5.6	83.3	11.9	4.9	75.8	17.8	6.4	1.31
		800 °C for 256 hr	79.5	15.4	5.1	84.6	11.7	3.7	75.3	17.9	6.8	1.82

**Table G.8** EDS phase analysis and determination of phase partitioning coefficients of X = W atoms in Ni<sub>80</sub>Al<sub>15</sub>W<sub>5</sub> alloys.

Ni <sub>80</sub> Al <sub>15</sub> W <sub>5</sub> alloys													
Sample groups	Definitions	Heat treatment		General (at.%)					γ (at.%)			κ <sub>w</sub>	
		Temperature and durations		Ni	Al	W	Ni	Al	W	Ni	Al		W
1	As cast (fast cooled)	-	-	75.2	16.8	8.0	-	-	-	-	-	-	-
	As cast (slow cooled)	-	-	-	-	-	-	-	-	-	-	-	-
	Partial solution heat treatment	1150 °C for 3 hr	-	-	-	-	-	-	-	-	-	-	-
	Aging	800 °C for 4 hr 800 °C for 16 hr 800 °C for 64 hr 800 °C for 256 hr	77.8 77.2 76.6 77.3	16.9 17.1 16.6 17.3	5.3 5.7 6.8 5.4	80.5 81.7 80.7 80.1	12.7 12.2 12.9 13.4	6.8 6.1 6.4 6.5	75.2 76.2 76.1 74.8	19.3 18.9 18.6 19.3	5.5 4.9 5.3 5.9	0.80 0.80 0.83 0.91	
2	Homogenization and partial solution heat treatment	1250 °C for 24 hr and 1150 °C for 3 hr	-	-	-	-	-	-	-	-	-	-	-
	Aging	800 °C for 4 hr 800 °C for 16 hr 800 °C for 64 hr 800 °C for 256 hr	-	-	-	-	-	-	-	-	-	-	-





## APPENDIX H

### MICRO-HARDNESS VALUES OF $\text{Ni}_{80}\text{Al}_{15}\text{X}_5$ ALLOY SYSTEMS

Appendix H tabulates micro-hardness values of  $\text{Ni}_{80}\text{Al}_{15}\text{X}_5$  alloy systems ( $\text{X} = \text{Co}, \text{Cr}, \text{Hf}, \text{Mo}, \text{Nb}, \text{Ta}, \text{Ti}$  and  $\text{W}$ , respectively).



**Table H.1.1** Micro-hardness values of Ni<sub>80</sub>Al<sub>15</sub>X<sub>5</sub> alloy systems where

X = Co, Cr, Hf and Mo, respectively.

Sample groups	Heat treatment		X = Co	X = Cr	X = Hf	X = Mo
	Definitions	Temperature and durations				
0	As cast (fast cooled)	-	223.2 ± 4.4	257.0 ± 6.2	457.2 ± 7.1	289.0 ± 1.8
	As cast (slow cooled)	-	-	-	-	-
1	Partial solution heat treatment	1150 °C for 3 hr	199.9 ± 8.6	220.2 ± 4.2	440.3 ± 6.1	254.4 ± 9.1
	Aging	800 °C for 4 hr	250.3 ± 9.2	258.8 ± 5.8	422.5 ± 10.9	275.9 ± 8.4
		800 °C for 16 hr	238.0 ± 5.2	253.4 ± 8.9	415.9 ± 10.8	267.2 ± 7.8
		800 °C for 64 hr	234.3 ± 3.7	251.7 ± 3.7	412.7 ± 6.4	249.5 ± 10.8
		800 °C for 256 hr	215.9 ± 9.4	247.1 ± 10.2	414.1 ± 9.3	246.7 ± 3.0
2	Homogenization and partial solution heat treatment	1250 °C for 24 hr and 1150 °C for 3 hr	219.8 ± 9.9	234.8 ± 7.2	-	267.0 ± 8.9
		800 °C for 4 hr	235.7 ± 13.1	258.3 ± 6.3	-	303.3 ± 5.3
	Aging	800 °C for 16 hr	217.8 ± 10.6	247.0 ± 6.4	-	279.4 ± 9.6
		800 °C for 64 hr	205.6 ± 12.3	252.1 ± 7.6	-	294.8 ± 5.8
		800 °C for 256 hr	189.1 ± 6.2	235.2 ± 9.0	-	300.2 ± 10.7

**Table H.2** Micro-hardness values of Ni<sub>80</sub>Al<sub>15</sub>X<sub>5</sub> alloy systems where

X = Nb, Ta, Ti and W, respectively.

Micro-hardness (Vickers) values of Ni <sub>80</sub> Al <sub>15</sub> X <sub>5</sub> alloy systems							
Sample groups	Definitions	Heat treatment		X = Nb	X = Ta	X = Ti	X = W
		Temperature	and durations				
0	As cast (fast cooled)	-	-	348.9 ± 7.1	383.4 ± 4.4	286.6 ± 3.5	311.9 ± 4.9
	As cast (slow cooled)	-	-	-	-	-	-
1	Partial solution heat treatment	1150 °C for 3 hr		259.3 ± 6.6	303.4 ± 6.2	211.7 ± 5.2	245.9 ± 7.0
		800 °C for 4 hr		306.8 ± 8.7	377.9 ± 6.2	274.2 ± 4.0	279.1 ± 4.5
	800 °C for 16 hr		328.7 ± 9.4	380.6 ± 8.4	270.0 ± 4.6	282.3 ± 6.8	
	800 °C for 64 hr		290.7 ± 5.6	389.3 ± 6.6	238.3 ± 6.0	285.9 ± 4.1	
	800 °C for 256 hr		306.2 ± 5.8	363.8 ± 6.1	241.7 ± 5.3	304.7 ± 9.2	
Homogenization and partial solution heat treatment	1250 °C for 24 hr and 1150 °C for 3 hr			306.1 ± 8.7	331.6 ± 11.6	264.2 ± 3.0	-
	800 °C for 4 hr			365.3 ± 7.8	418.9 ± 12.2	320.3 ± 5.5	-
2	Aging	800 °C for 16 hr		339.3 ± 10.3	376.8 ± 9.4	266.6 ± 7.9	-
		800 °C for 64 hr		317.6 ± 8.4	373.3 ± 14.8	259.4 ± 6.0	-
		800 °C for 256 hr		307.6 ± 7.9	357.0 ± 7.4	242.2 ± 7.5	-



## APPENDIX I

### MICRO-HARDNESS VARIATIONS OF $\text{Ni}_{80}\text{Al}_{15}\text{X}_5$ ALLOY SYSTEMS

Appendix I shows micro-hardness variations of  $\text{Ni}_{80}\text{Al}_{15}\text{X}_5$  alloy systems ( $\text{X} = \text{Co}, \text{Cr}, \text{Hf}, \text{Mo}, \text{Nb}, \text{Ta}, \text{Ti}$  and  $\text{W}$ , respectively) as aging time is increased from 4 hr to 256 hr. In Figures I.3,8, micro-hardness data is absent since for the second sample groups of  $\text{Ni}_{80}\text{Al}_{15}\text{Hf}_5$  and  $\text{Ni}_{80}\text{Al}_{15}\text{W}_5$  alloys, homogenization heat treatment has lead to excessive amount of oxide layers which deteriorate micro-hardness properties.

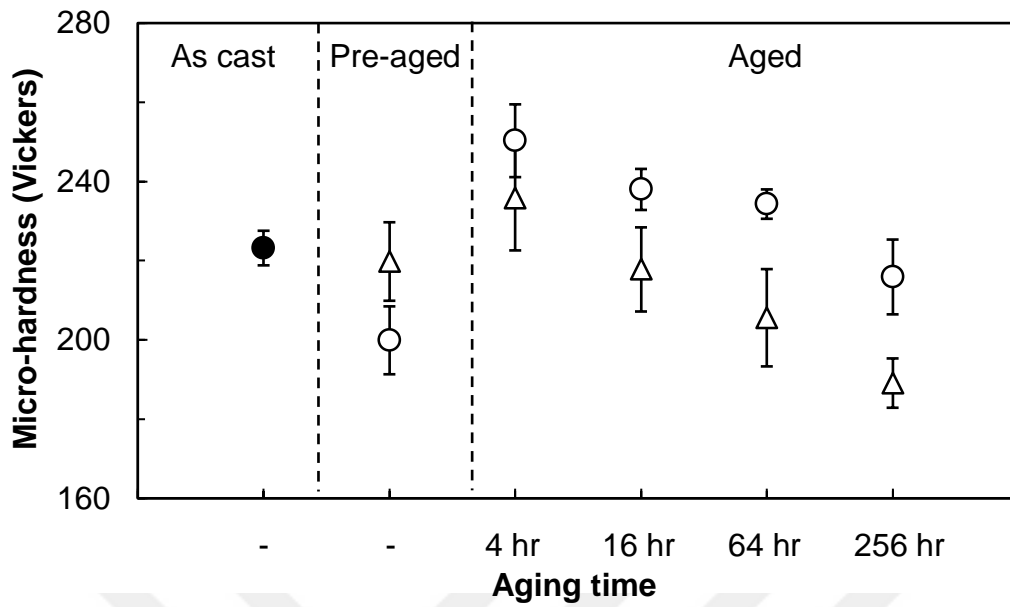


**Figure I.1** Micro-hardness (Vickers) comparison of heat treated Ni<sub>80</sub>Al<sub>15</sub>Co<sub>5</sub> alloys. Black sphere denotes to fast cooled as cast sample, whereas sample groups (1-2) are represented in 1: open spheres and 2: open triangles, respectively.

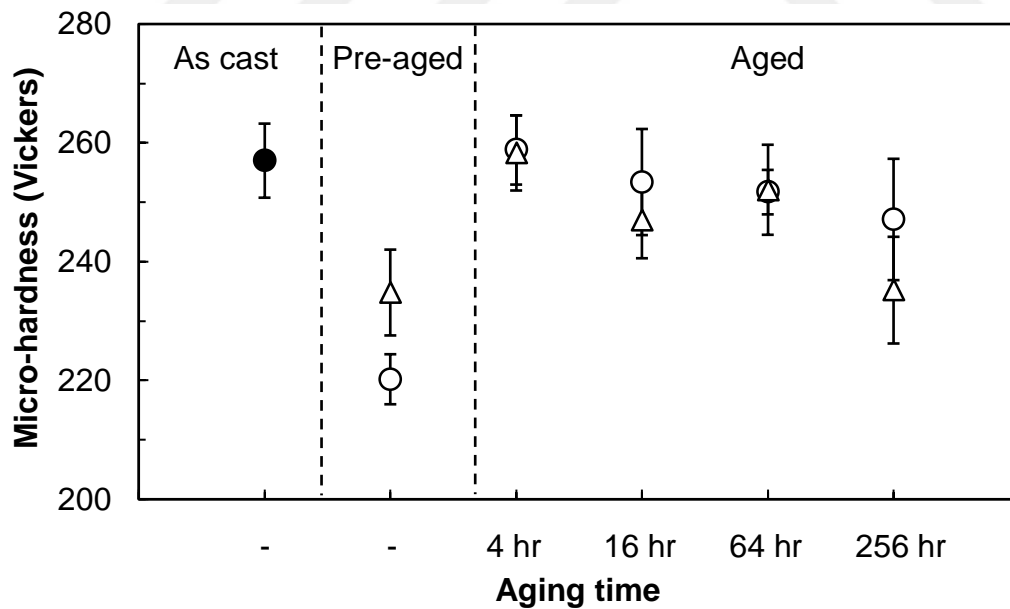


**Figure I.2** Micro-hardness (Vickers) comparison of heat treated Ni<sub>80</sub>Al<sub>15</sub>Cr<sub>5</sub> alloys. Black sphere denotes to fast cooled as cast sample, whereas sample groups (1-2) are represented in 1: open spheres and 2: open triangles, respectively.

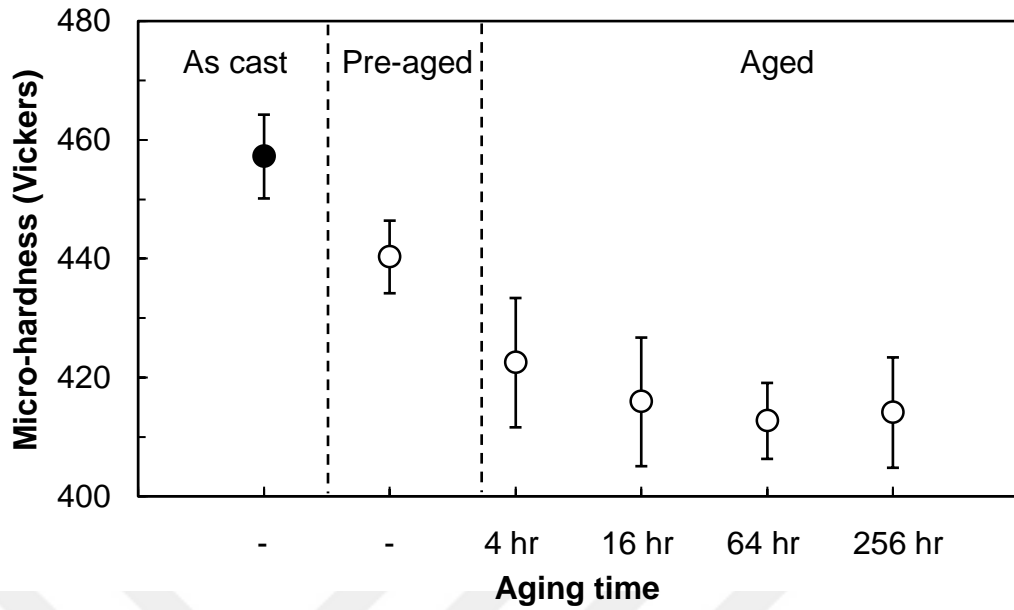


**Figure I.3** Micro-hardness (Vickers) comparison of heat treated Ni<sub>80</sub>Al<sub>15</sub>Hf<sub>5</sub> alloys. Black sphere denotes to fast cooled as cast sample, whereas first sample group is represented in open spheres.

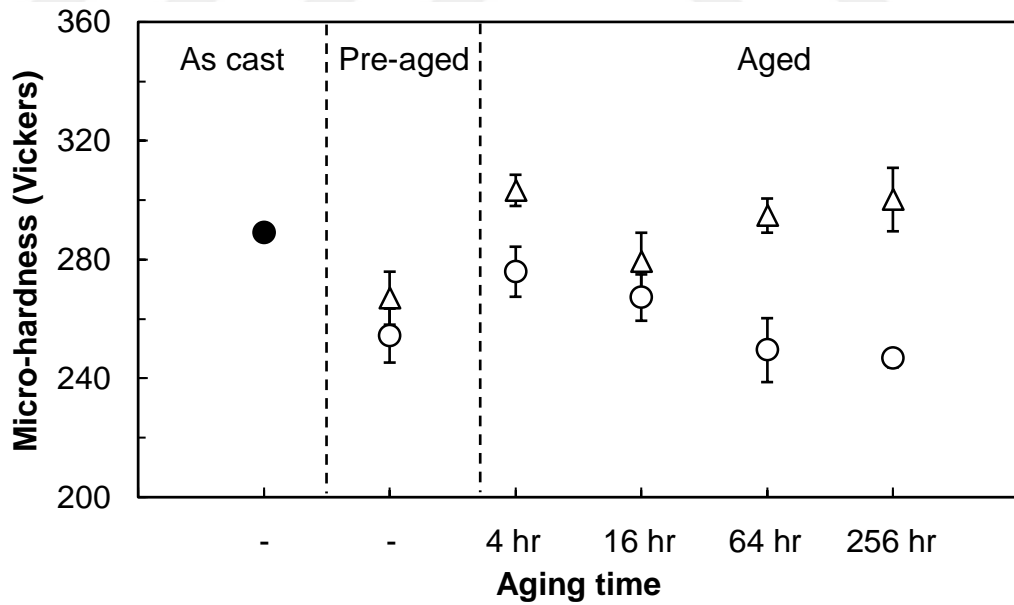


**Figure I.4** Micro-hardness (Vickers) comparison of heat treated Ni<sub>80</sub>Al<sub>15</sub>Mo<sub>5</sub> alloys. Black sphere denotes to fast cooled as cast sample, whereas sample groups (1-2) are represented in 1: open spheres and 2: open triangles, respectively.

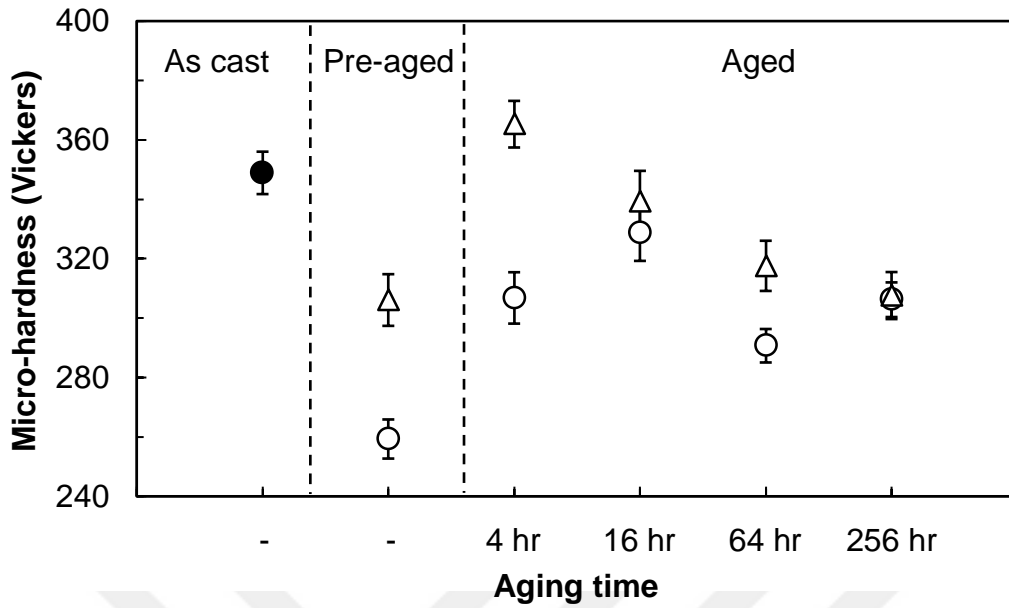


**Figure I.5** Micro-hardness (Vickers) comparison of heat treated Ni<sub>80</sub>Al<sub>15</sub>Nb<sub>5</sub> alloys. Black sphere denotes to fast cooled as cast sample, whereas sample groups (1-2) are represented in 1: open spheres and 2: open triangles, respectively.

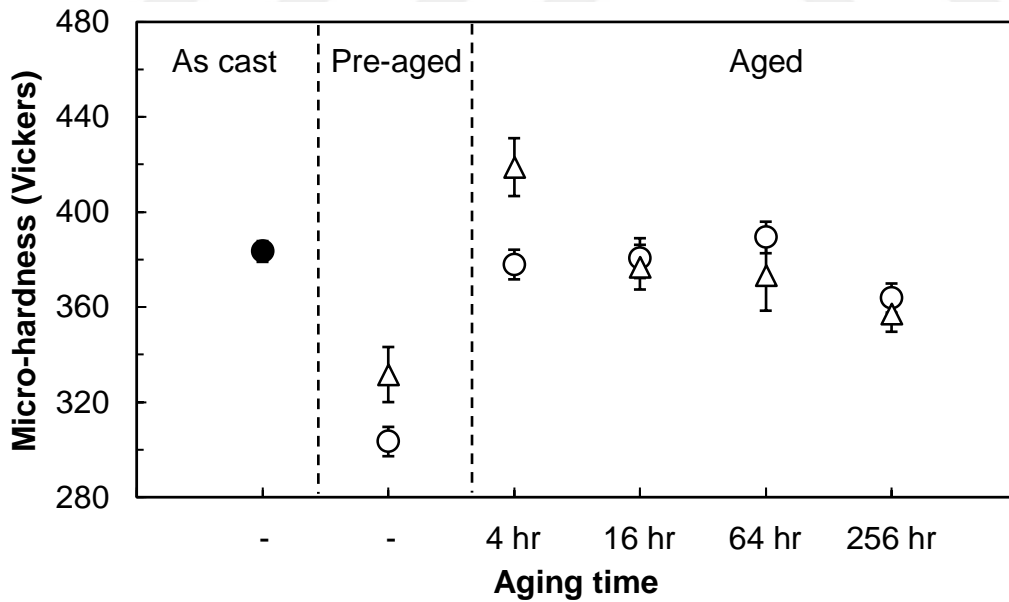


**Figure I.6** Micro-hardness (Vickers) comparison of heat treated Ni<sub>80</sub>Al<sub>15</sub>Ta<sub>5</sub> alloys. Black sphere denotes to fast cooled as cast sample, whereas sample groups (1-2) are represented in 1: open spheres and 2: open triangles, respectively.



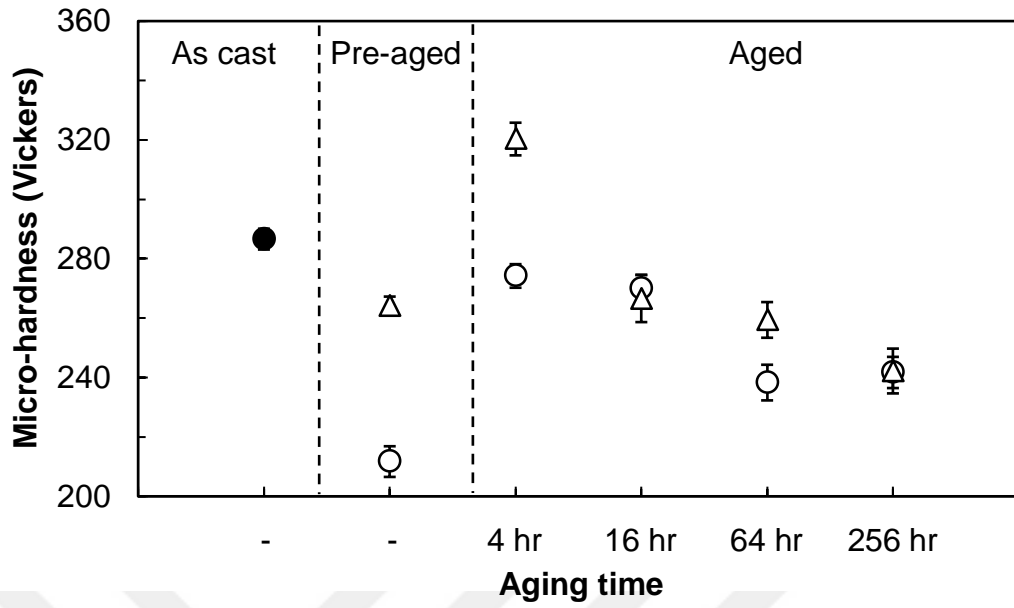


**Figure I.7** Micro-hardness (Vickers) comparison of heat treated Ni<sub>80</sub>Al<sub>15</sub>Ti<sub>5</sub> alloys. Black sphere denotes to fast cooled as cast sample, whereas sample groups (1-2) are represented in 1: open spheres and 2: open triangles, respectively.

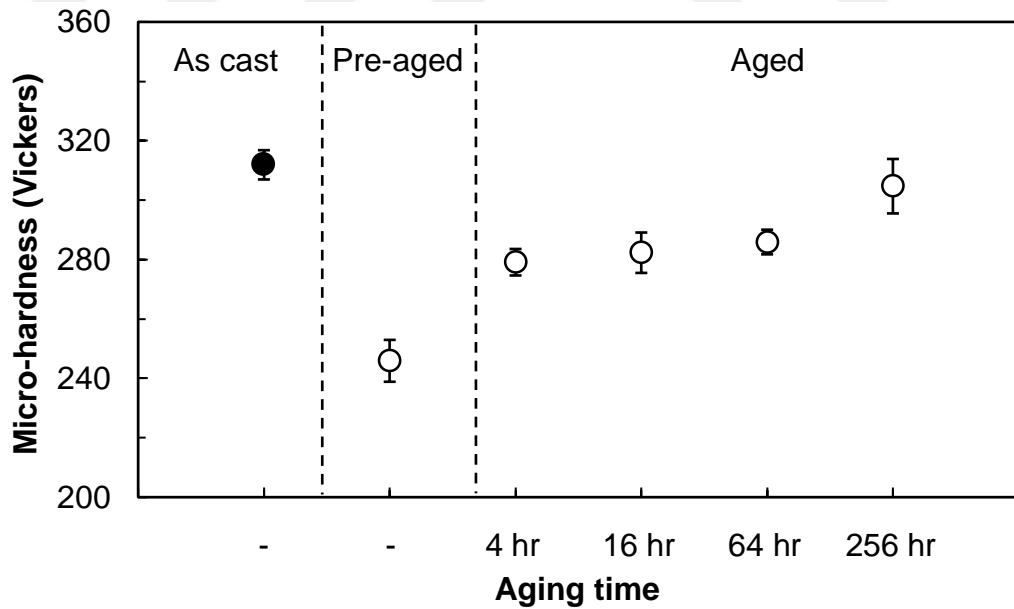


**Figure I.8** Micro-hardness (Vickers) comparison of heat treated Ni<sub>80</sub>Al<sub>15</sub>W<sub>5</sub> alloys. Black sphere denotes to fast cooled as cast sample, whereas first sample group is represented in open spheres.



## APPENDIX J

### $\gamma'$ PRECIPITATE VOLUME FRACTIONS OF Ni<sub>80</sub>Al<sub>15</sub>X<sub>5</sub> ALLOY SYSTEMS

Appendix J represents volume fractions of  $\gamma'$  precipitates in the second sample groups of Ni<sub>80</sub>Al<sub>15</sub>X<sub>5</sub> alloy systems (X = Co, Cr, Mo, Nb, Ta and Ti, respectively) as aging time is increased from 4 hr to 256 hr. Volume fractions of  $\gamma'$  precipitates in Ni<sub>80</sub>Al<sub>15</sub>Hf<sub>5</sub> and Ni<sub>80</sub>Al<sub>15</sub>W<sub>5</sub> alloys could not be calculated due to unclear FESEM micrographs arising from oxidation problem. For Ni<sub>80</sub>Al<sub>15</sub>Hf<sub>5</sub> alloys,  $\gamma'$  precipitates are only visible at  $\gamma$  matrix phase/eutectic phase mixture interfaces which obstruct volume fraction calculations.

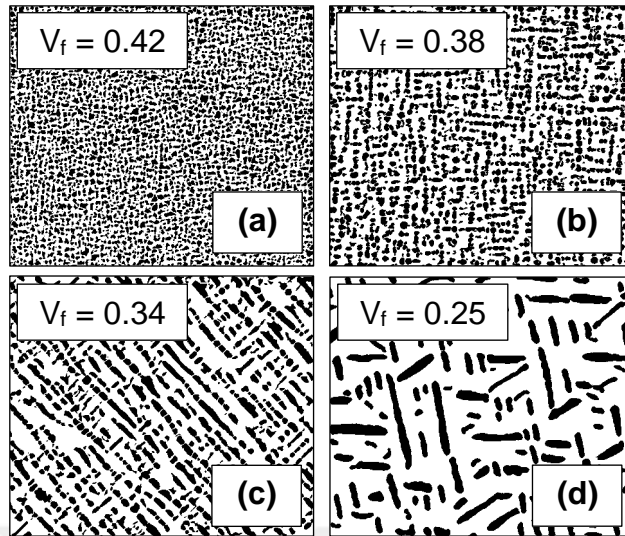


**Figure J.1**  $\gamma'$  precipitate volume fraction variation of the second sample group of  $\text{Ni}_{80}\text{Al}_{15}\text{Co}_5$  alloys as aging time at  $800\text{ }^\circ\text{C}$  is (a) 4 hr, (b) 16 hr, (c) 64 hr and (d) 256 hr, respectively.

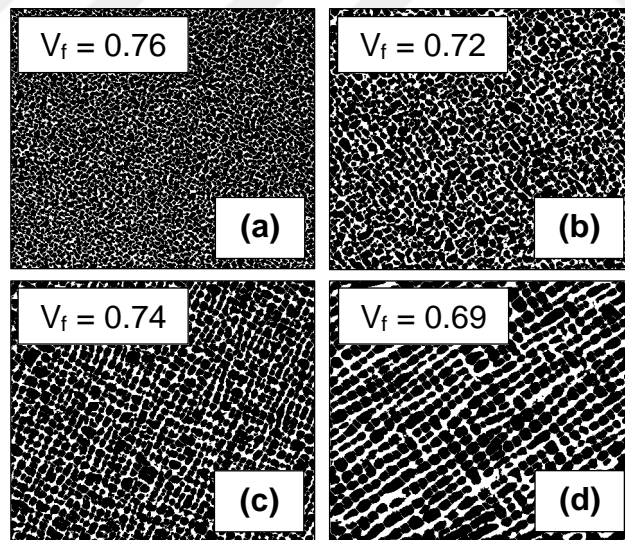


**Figure J.2**  $\gamma'$  precipitate volume fraction variation of the second sample group of  $\text{Ni}_{80}\text{Al}_{15}\text{Cr}_5$  alloys as aging time at  $800\text{ }^\circ\text{C}$  is (a) 4 hr, (b) 16 hr, (c) 64 hr and (d) 256 hr, respectively.

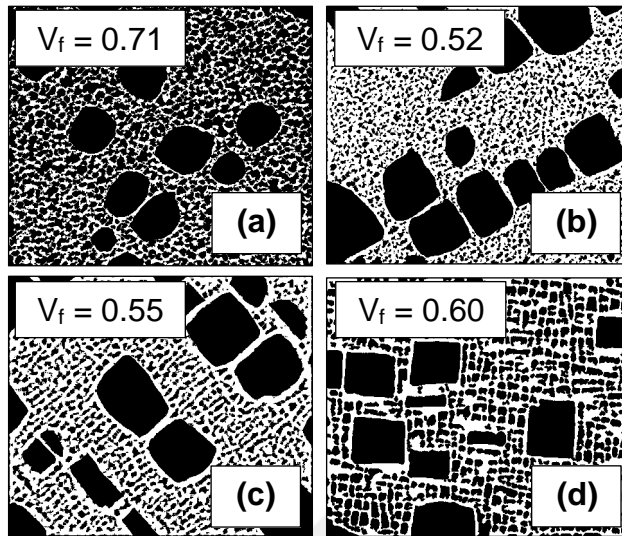


**Figure J.3**  $\gamma'$  precipitate volume fraction variation of the second sample group of  $\text{Ni}_{80}\text{Al}_{15}\text{Mo}_5$  alloys as aging time at  $800\text{ }^\circ\text{C}$  is (a) 4 hr, (b) 16 hr, (c) 64 hr and (d) 256 hr, respectively.

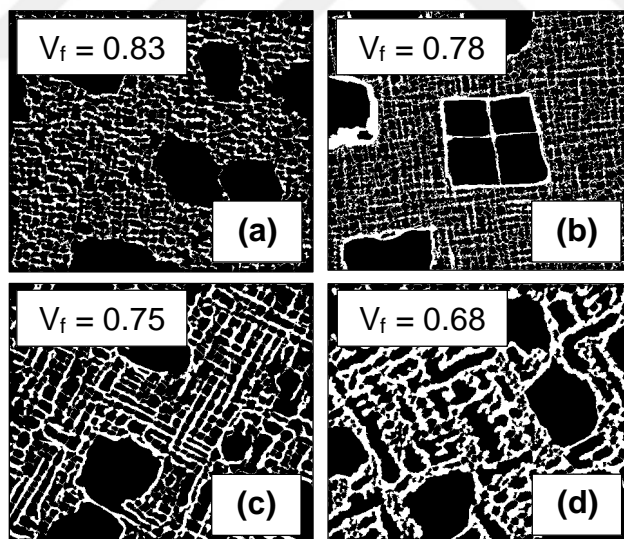


**Figure J.4**  $\gamma'$  precipitate volume fraction variation of the second sample group of  $\text{Ni}_{80}\text{Al}_{15}\text{Nb}_5$  alloys as aging time at  $800\text{ }^\circ\text{C}$  is (a) 4 hr, (b) 16 hr, (c) 64 hr and (d) 256 hr, respectively.

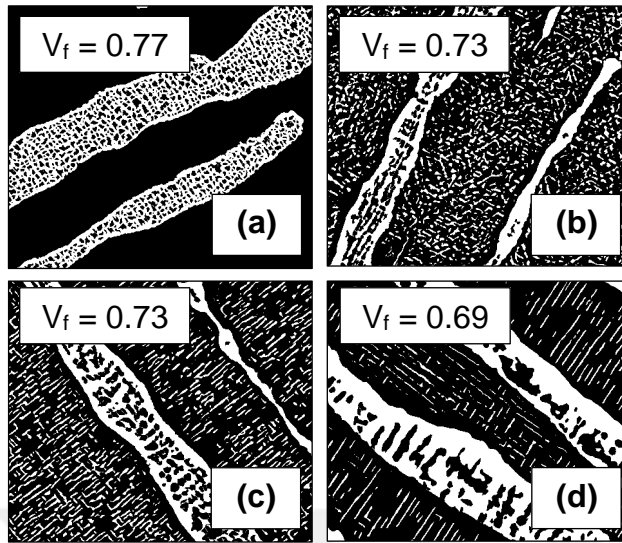


**Figure J.5**  $\gamma'$  precipitate volume fraction variation of the second sample group of  $\text{Ni}_{80}\text{Al}_{15}\text{Ta}_5$  alloys as aging time at  $800\text{ }^\circ\text{C}$  is (a) 4 hr, (b) 16 hr, (c) 64 hr and (d) 256 hr, respectively.

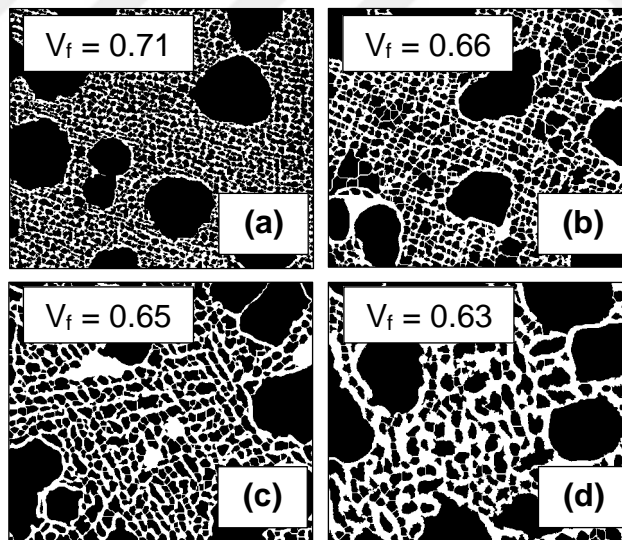


**Figure J.6**  $\gamma'$  precipitate volume fraction variation of the second sample group of  $\text{Ni}_{80}\text{Al}_{15}\text{Ti}_5$  alloys as aging time at  $800\text{ }^\circ\text{C}$  is (a) 4 hr, (b) 16 hr, (c) 64 hr and (d) 256 hr, respectively.

## APPENDIX K

### $\gamma'$ PRECIPITATE SIZE & SIZE DISTRIBUTION AND ORIENTATION CHARACTERISTICS OF $\text{Ni}_{80}\text{Al}_{15}\text{X}_5$ ALLOY SYSTEMS

Appendix K shows size & size distribution and orientation characteristics of  $\gamma'$  precipitates in the second sample groups of  $\text{Ni}_{80}\text{Al}_{15}\text{X}_5$  alloy systems ( $X = \text{Co}, \text{Cr}, \text{Mo}, \text{Nb}, \text{Ta}$  and  $\text{Ti}$ , respectively) as aging time is increased from 4 hr to 256 hr. Size & size distribution and orientation characteristics of  $\gamma'$  precipitates in  $\text{Ni}_{80}\text{Al}_{15}\text{Hf}_5$  and  $\text{Ni}_{80}\text{Al}_{15}\text{W}_5$  alloys could not be calculated due to the same reasons mentioned in Appendix J.

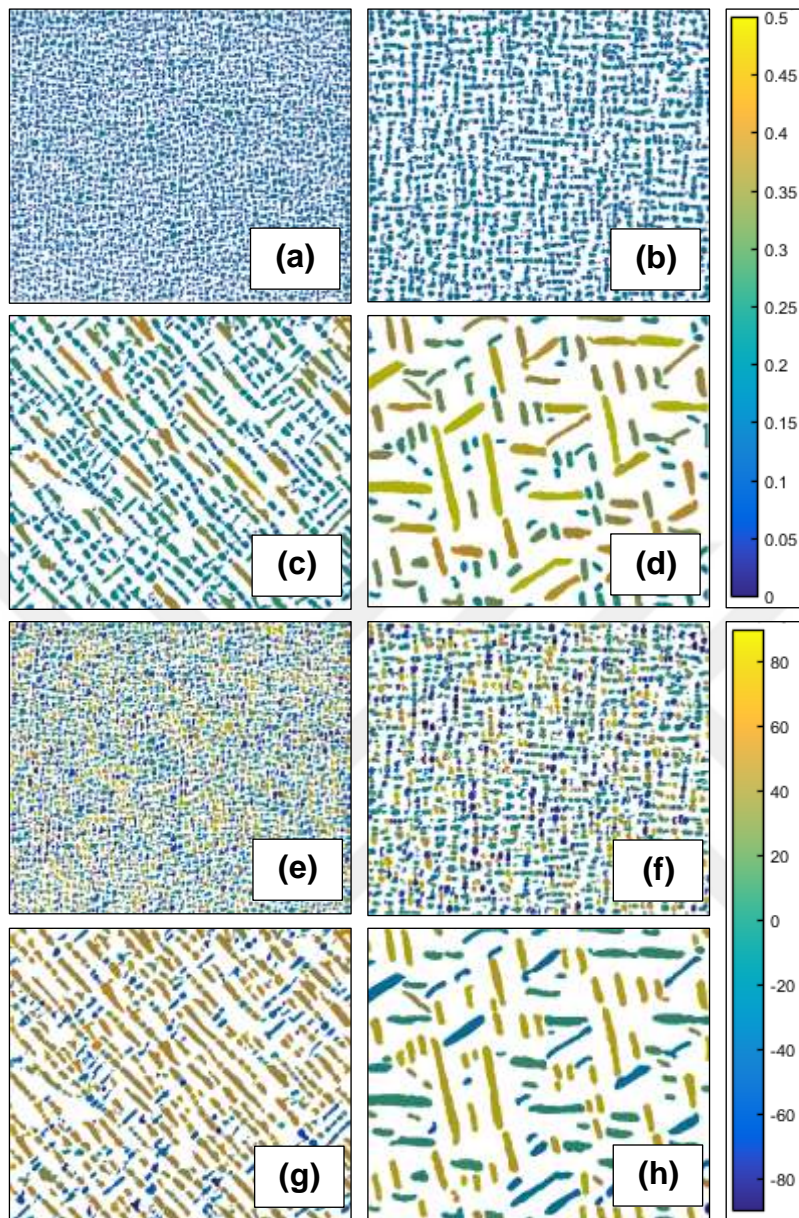


**Figure K.1** Size & size distribution and orientation of  $\gamma'$  precipitates of the second sample group of  $\text{Ni}_{80}\text{Al}_{15}\text{Co}_5$  alloys as aging time at  $800\text{ }^\circ\text{C}$  is (a,e) 4 hr, (b,f) 16 hr, (c,g) 64 hr and (d,h) 256 hr, respectively.



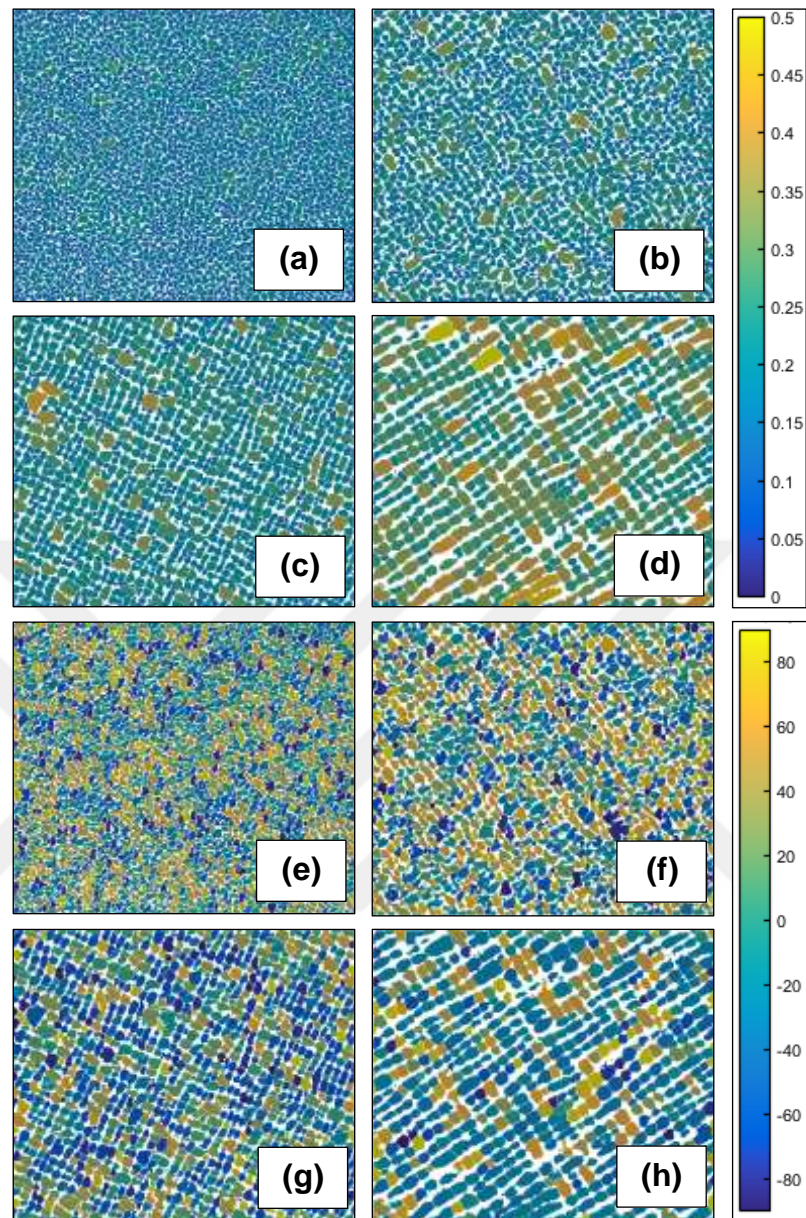


**Figure K.2** Size & size distribution and orientation of  $\gamma'$  precipitates of the second sample group of  $\text{Ni}_{80}\text{Al}_{15}\text{Cr}_5$  alloys as aging time at 800 °C is (a,e) 4 hr, (b,f) 16 hr, (c,g) 64 hr and (d,h) 256 hr, respectively.

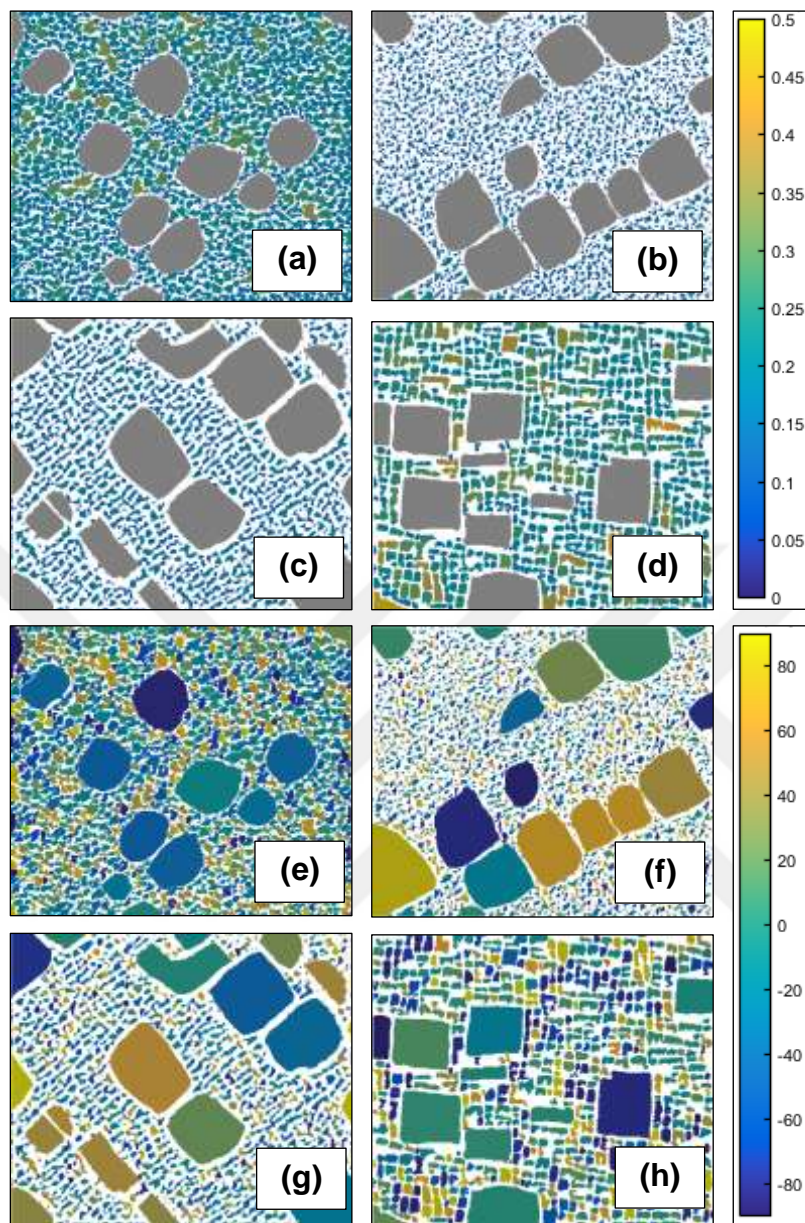


**Figure K.3** Size & size distribution and orientation of  $\gamma'$  precipitates of the second sample group of  $\text{Ni}_{80}\text{Al}_{15}\text{Mo}_5$  alloys as aging time at  $800\text{ }^\circ\text{C}$  is (a,e) 4 hr, (b,f) 16 hr, (c,g) 64 hr and (d,h) 256 hr, respectively.

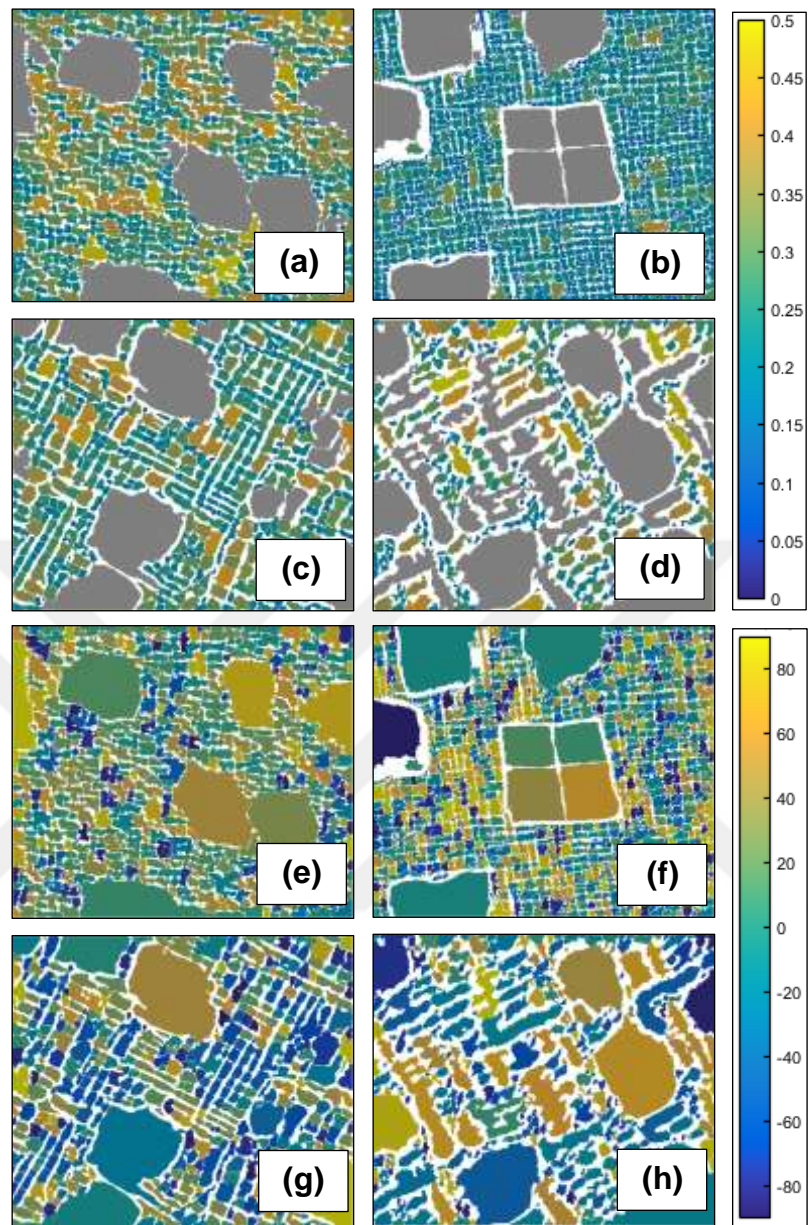


**Figure K.4** Size & size distribution and orientation of  $\gamma'$  precipitates of the second sample group of  $\text{Ni}_{80}\text{Al}_{15}\text{Nb}_5$  alloys as aging time at  $800\text{ }^\circ\text{C}$  is (a,e) 4 hr, (b,f) 16 hr, (c,g) 64 hr and (d,h) 256 hr, respectively.

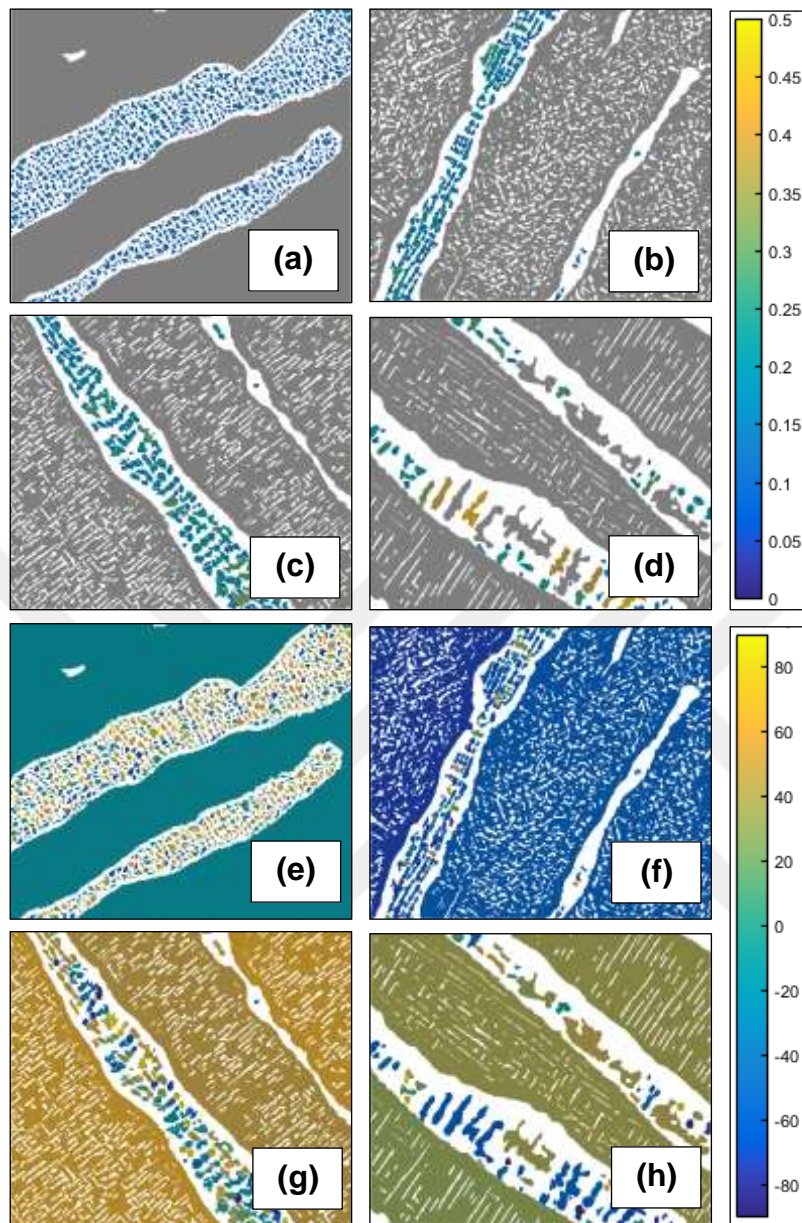


**Figure K.5** Size & size distribution and orientation of  $\gamma'$  precipitates of the second sample group of  $\text{Ni}_{80}\text{Al}_{15}\text{Ta}_5$  alloys as aging time at 800 °C is (a,e) 4 hr, (b,f) 16 hr, (c,g) 64 hr and (d,h) 256 hr, respectively.

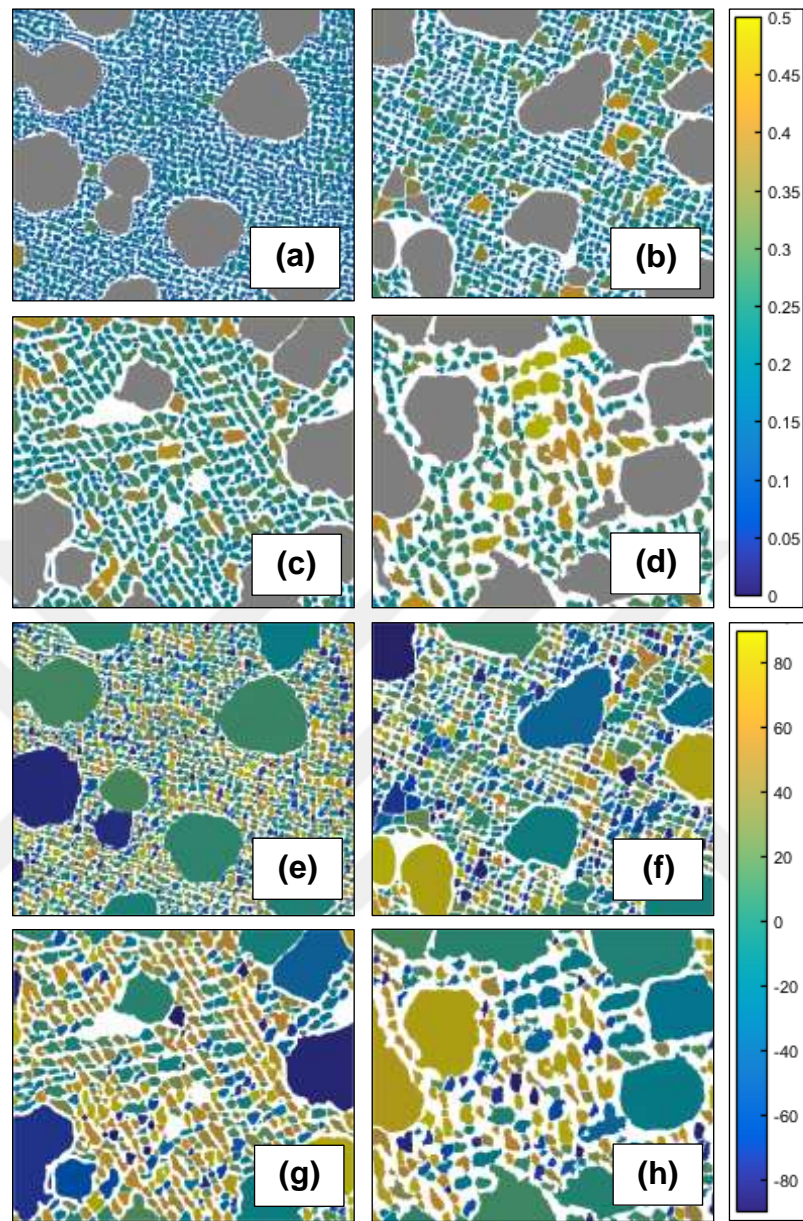


**Figure K.6** Size & size distribution and orientation of  $\gamma'$  precipitates of the second sample group of  $\text{Ni}_{80}\text{Al}_{15}\text{Ti}_5$  alloys as aging time at 800 °C is (a,e) 4 hr, (b,f) 16 hr, (c,g) 64 hr and (d,h) 256 hr, respectively.



## APPENDIX L

### COMPARISON OF MICROSTRUCTURAL CHARACTERISTICS AND MECHANICAL PROPERTIES OF $\text{Ni}_{80}\text{Al}_{15}\text{X}_5$ ALLOY SYSTEMS

Appendix L compares the microstructural characteristics ( $\gamma'$  precipitate volume fraction, size & size distribution, orientation and shape) and mechanical properties (i.e. micro-hardness) of  $\text{Ni}_{80}\text{Al}_{15}\text{X}_5$  alloy systems ( $\text{X} = \text{Co}, \text{Cr}, \text{Hf}, \text{Mo}, \text{Nb}, \text{Ta}, \text{Ti}$  and  $\text{W}$ , respectively) as aging time is increased from 4 hr to 256 hr.

**Table L.1** Comparison of microstructural characteristics and mechanical properties of Ni<sub>80</sub>Al<sub>15</sub>Co<sub>5</sub> alloys.

Sample groups	Heat treatment		Lattice parameter (Å)	V <sub>f</sub>	γ' precipitates			Micro-hardness (Vickers)
	Definitions	Temperature and durations			Size (nm)	Orientation	Shape	
0	As cast (fast cooled)	-	3.559	-	-	-	-	223.2 ± 4.4
	As cast (slow cooled)	-	-	-	-	-	-	-
1	Partial solution heat treatment	1150 °C for 3 hr	3.558	-	-	-	-	199.9 ± 8.6
	Aging	800 °C for 4 hr	3.549	0.78	66	NO	Spheroidal	250.3 ± 9.2
		800 °C for 16 hr	3.554	0.71	109	YES	Spheroidal	238.0 ± 5.2
		800 °C for 64 hr	3.553	0.62	243	YES	Irregular	234.3 ± 3.7
		800 °C for 256 hr	3.546	0.52	288	YES	Irregular	215.9 ± 9.4
2	Homogenization and partial solution heat treatment	1250 °C for 24 hr and 1150 °C for 3 hr	3.554	-	-	-	-	219.8 ± 9.9
	Aging	800 °C for 4 hr	3.553	0.42	92	NO	Spheroidal	235.7 ± 13.1
800 °C for 16 hr		3.555	0.38	121	YES	Cuboidal	217.8 ± 10.6	
800 °C for 64 hr		3.551	0.34	158	YES	Irregular	205.6 ± 12.3	
800 °C for 256 hr		3.545	0.25	175	YES	Irregular	189.1 ± 6.2	



**Table L.2** Comparison of microstructural characteristics and mechanical properties of Ni<sub>80</sub>Al<sub>15</sub>Cr<sub>5</sub> alloys.

Sample groups	Heat treatment		Lattice parameter (Å)	V <sub>f</sub>	γ precipitates		Micro-hardness (Vickers)	
	Definitions	Temperature and durations			Size (nm)	Orientation		Shape
0	As cast (fast cooled)	-	3.559	-	-	-	257.0 ± 6.2	
	As cast (slow cooled)	-	-	-	-	-	-	
1	Partial solution heat treatment	1150 °C for 3 hr	3.557	0.74	85	NO	Spherical	220.2 ± 4.2
		800 °C for 4 hr	3.557	0.91	112	NO	Spheroidal	258.8 ± 5.8
	Aging	800 °C for 16 hr	3.558	0.89	148	NO	Spheroidal	253.4 ± 8.9
		800 °C for 64 hr	3.557	0.88	329	YES	Cuboidal	251.7 ± 3.7
		800 °C for 256 hr	3.554	0.86	410	YES	Cuboidal	247.1 ± 10.2
Homogenization and partial solution heat treatment	1250 °C for 24 hr and 1150 °C for 3 hr	3.557	-	-	-	-	234.8 ± 7.2	
	Aging	800 °C for 4 hr	3.553	0.76	112	NO	Spheroidal	258.3 ± 6.3
800 °C for 16 hr		3.554	0.72	150	NO	Spheroidal	247.0 ± 6.4	
800 °C for 64 hr		3.556	0.74	176	YES	Cuboidal	252.1 ± 7.6	
800 °C for 256 hr		3.553	0.69	274	YES	Cuboidal	235.2 ± 9.0	

**Table L.3** Comparison of microstructural characteristics and mechanical properties of Ni<sub>80</sub>Al<sub>15</sub>Hf<sub>5</sub> alloys.

Sample groups	Heat treatment		Lattice parameter (Å)	V <sub>t</sub>	γ precipitates			Micro-hardness (Vickers)
	Definitions	Temperature and durations			Size (nm)	Orientation	Shape	
0	As cast (fast cooled)	-	3.602	-	-	-	457.2 ± 7.1	
	As cast (slow cooled)	-	-	-	-	-	-	
1	Partial solution heat treatment	1150 °C for 3 hr	3.605	-	-	-	440.3 ± 6.1	
		800 °C for 4 hr	3.591	-	-	-	422.5 ± 10.9	
	Aging	800 °C for 16 hr	3.590	-	-	-	415.9 ± 10.8	
		800 °C for 64 hr	3.605	-	-	-	412.7 ± 6.4	
		800 °C for 256 hr	3.608	-	-	-	414.1 ± 9.3	
Homogenization and partial solution heat treatment	1250 °C for 24 hr and 1150 °C for 3 hr	-	-	-	-	-		
	Aging	800 °C for 4 hr	-	-	-	-	-	
800 °C for 16 hr		-	-	-	-	-		
800 °C for 64 hr		-	-	-	-	-		
800 °C for 256 hr		-	-	-	-	-		

**Table L.4** Comparison of microstructural characteristics and mechanical properties of Ni<sub>80</sub>Al<sub>15</sub>Mo<sub>5</sub> alloys.

		Ni <sub>80</sub> Al <sub>15</sub> Mo <sub>5</sub> alloys						
Sample groups	Heat treatment		Lattice parameter (Å)	V <sub>f</sub>	γ' precipitates		Micro-hardness (Vickers)	
	Definitions	Temperature and durations			Size (nm)	Orientation		Shape
0	As cast (fast cooled)	-	3.579	-	-	-	289.0 ± 1.8	
	As cast (slow cooled)	-	-	-	-	-	-	
1	Partial solution heat treatment	1150 °C for 3 hr	3.577	-	-	-	254.4 ± 9.1	
	Aging	800 °C for 4 hr	3.571	-	-	-	275.9 ± 8.4	
		800 °C for 16 hr	3.568	-	-	-	267.2 ± 7.8	
		800 °C for 64 hr	3.575	-	-	-	249.5 ± 10.8	
		800 °C for 256 hr	3.574	-	-	-	246.7 ± 3.0	
Homogenization and partial solution heat treatment	1250 °C for 24 hr and 1150 °C for 3 hr	3.569	0.38	82	NO	Spherical	267.0 ± 8.9	
	Aging	800 °C for 4 hr	3.571	0.71	176	NO	Spherical	303.3 ± 5.3
800 °C for 16 hr		3.573	0.52	174	NO	Spheroidal	279.4 ± 9.6	
800 °C for 64 hr		3.575	0.55	173	YES	Cuboidal	294.8 ± 5.8	
800 °C for 256 hr		3.557	0.60	225	YES	Cubic	300.2 ± 10.7	

**Table L.5** Comparison of microstructural characteristics and mechanical properties of Ni<sub>80</sub>Al<sub>15</sub>Nb<sub>5</sub> alloys.

Sample groups	Heat treatment		Lattice parameter (Å)	V <sub>f</sub>	γ' precipitates			Micro-hardness (Vickers)
	Definitions	Temperature and durations			Size (nm)	Orientation	Shape	
0	As cast (fast cooled)	-	3.586	0.91	107	NO	Spherical	348.9 ± 7.1
	As cast (slow cooled)	-	-	-	-	-	-	-
1	Partial solution heat treatment	1150 °C for 3 hr	3.583	0.66	176	NO	Cubic	259.3 ± 6.6
		800 °C for 4 hr	3.589	0.78	144	YES	Cubic	306.8 ± 8.7
	Aging	800 °C for 16 hr	3.589	0.81	169	YES	Cubic	328.7 ± 9.4
		800 °C for 64 hr	3.585	0.58	247	YES	Irregular	290.7 ± 5.6
		800 °C for 256 hr	3.583	0.64	269	YES	Irregular	306.2 ± 5.8
Homogenization and partial solution heat treatment	1250 °C for 24 hr and 1150 °C for 3 hr	3.577	0.70	114	NO	Spheroidal	306.1 ± 8.7	
	Aging	800 °C for 4 hr	3.589	0.83	176	YES	Cuboidal	365.3 ± 7.8
800 °C for 16 hr		3.572	0.78	182	YES	Cubic	339.3 ± 10.3	
800 °C for 64 hr		3.572	0.75	206	YES	Cubic	317.6 ± 8.4	
800 °C for 256 hr		3.563	0.68	297	YES	Irregular	307.6 ± 7.9	

**Table L.6** Comparison of microstructural characteristics and mechanical properties of Ni<sub>80</sub>Al<sub>15</sub>Ta<sub>5</sub> alloys.

Sample groups	Heat treatment		Ni <sub>80</sub> Al <sub>15</sub> Ta <sub>5</sub> alloys					Micro-hardness (Vickers)
	Definitions	Temperature and durations	Lattice parameter (Å)	V <sub>f</sub>	Size (nm)	Orientation	Shape	
0	As cast (fast cooled)	-	3.590	-	-	-	-	383.4 ± 4.4
	As cast (slow cooled)	-	-	-	-	-	-	-
1	Partial solution heat treatment	1150 °C for 3 hr	3.584	-	-	-	-	303.4 ± 6.2
	Aging	800 °C for 4 hr	3.584	-	-	-	-	377.9 ± 6.2
		800 °C for 16 hr	3.588	-	-	-	-	380.6 ± 8.4
		800 °C for 64 hr	3.586	-	-	-	-	389.3 ± 6.6
		800 °C for 256 hr	3.596	-	-	-	-	363.8 ± 6.1
Homogenization and partial solution heat treatment	1250 °C for 24 hr and 1150 °C for 3 hr	3.577	-	71	NO	Spherical	331.6 ± 11.6	
2	Aging	800 °C for 4 hr	3.575	0.77	67	NO	Spheroidal	418.9 ± 12.2
		800 °C for 16 hr	3.585	0.73	132	YES	Cuboidal	376.8 ± 9.4
		800 °C for 64 hr	3.597	0.73	187	YES	Irregular	373.3 ± 14.8
		800 °C for 256 hr	3.595	0.69	257	YES	Irregular	357.0 ± 7.4

**Table L.7** Comparison of microstructural characteristics and mechanical properties of Ni<sub>80</sub>Al<sub>15</sub>Ti<sub>5</sub> alloys.

Ni <sub>80</sub> Al <sub>15</sub> Ti <sub>5</sub> alloys									
Sample groups	Heat treatment		Lattice parameter (Å)			γ' precipitates			Micro-hardness (Vickers)
	Definitions	Temperature and durations	V <sub>f</sub>	Size (nm)	Orientation	Shape			
0	As cast (fast cooled)	-	3.576	0.92	140	NO	Faceted	286.6 ± 3.5	
	As cast (slow cooled)	-	-	-	-	-	-	-	
1	Partial solution heat treatment	1150 °C for 3 hr	3.579	0.89	137	NO	Spherical	211.7 ± 5.2	
		800 °C for 4 hr	3.574	0.88	154	NO	Spheroidal	274.2 ± 4.0	
	Aging	800 °C for 16 hr	3.578	0.88	186	YES	Spheroidal	270.0 ± 4.6	
		800 °C for 64 hr	3.580	0.86	184	YES	Irregular	238.3 ± 6.0	
		800 °C for 256 hr	3.576	0.81	257	YES	Irregular	241.7 ± 5.3	
Homogenization and partial solution heat treatment	1250 °C for 24 hr and 1150 °C for 3 hr	3.566	0.56	118	NO	Spherical	264.2 ± 3.0		
	Aging	800 °C for 4 hr	3.558	0.71	142	NO	Spheroidal	320.3 ± 5.5	
800 °C for 16 hr		3.575	0.66	157	YES	Spheroidal	266.6 ± 7.9		
800 °C for 64 hr		3.579	0.65	206	YES	Cuboidal	259.4 ± 6.0		
800 °C for 256 hr		3.581	0.63	303	YES	Irregular	242.2 ± 7.5		

**Table L.8** Comparison of microstructural characteristics and mechanical properties of Ni<sub>80</sub>Al<sub>15</sub>W<sub>5</sub> alloys.

Sample groups	Heat treatment		Lattice parameter (Å)	V <sub>f</sub>	γ' precipitates		Micro-hardness (Vickers)
	Definitions	Temperature and durations			Size (nm)	Orientation	
0	As cast (fast cooled)	-	3.578	-	-	-	311.9 ± 4.9
	As cast (slow cooled)	-	-	-	-	-	-
1	Partial solution heat treatment	1150 °C for 3 hr	3.576	-	-	-	245.9 ± 7.0
		800 °C for 4 hr	3.575	-	-	-	279.1 ± 4.5
	Aging	800 °C for 16 hr	3.569	-	-	-	282.3 ± 6.8
		800 °C for 64 hr	3.572	-	-	-	285.9 ± 4.1
		800 °C for 256 hr	3.575	-	-	-	304.7 ± 9.2
2	Homogenization and partial solution heat treatment	1250 °C for 24 hr and 1150 °C for 3 hr	-	-	-	-	-
		800 °C for 4 hr	-	-	-	-	-
	Aging	800 °C for 16 hr	-	-	-	-	-
		800 °C for 256 hr	-	-	-	-	-





## CURRICULUM VITAE

**Rasim ERİŞ**

M.S. Student

Department of Metallurgical and Materials Engineering,  
Novel Alloys Design and Development Laboratory (NOVALAB), Room D-312,  
Middle East Technical University, 06800, Ankara, Turkey

Research Assistant

METU Central Laboratory,  
Mechanical Testing Laboratory (MTL), Room 111,  
Middle East Technical University, 06800, Ankara, Turkey

E-mail: rasim.eris@metu.edu.tr, Telephone: +90 5066208418, +90 3122106441

## EDUCATION

2015-2017 M.S. Student, Metallurgical and Materials Engineering, Middle East Technical University

- The most successful M.S. student with GPA of 3.64/4.00
- Thesis Title: Design and Development of High Temperature Nickel-based Superalloys, Supervisor: Prof. Dr. M. Vedat Akdeniz, Co-supervisor: Prof. Dr. Amdulla O. Mekhrabov

January 2014-June 2014 Erasmus exchange student, Materials Science and Engineering, Tampere University of Technology, Tampere, Finland

2010-2014 B.S. Student, Metallurgical and Materials Engineering, Middle East Technical University

- GPA of 2.81/4.00

### **RESEARCH INTEREST**

- Nickel-based superalloys,
- Intermetallics (based on aluminides),
- First-principles *ab initio* calculations including CDD, ELF and DOS simulations,
- Solidification, phase transformations and microstructural evolution.

### **PUBLICATIONS**

R. Eriş, A.O. Mekhrabov, and M.V. Akdeniz (2017), High-temperature Site Preference and Atomic Short-range Ordering Characteristics of Ternary Alloying Elements in  $\gamma'$ -Ni<sub>3</sub>Al Intermetallics, Philosophical Magazine, DOI: 10.1080/14786435.2017.1344787.

### **CONGRESS PROCEEDINGS**

R. Eriş, A.O. Mekhrabov, and M.V. Akdeniz (2016), The Effects of Cr Addition on the Atomic Ordering Properties of Ni-based Superalloys, 18<sup>th</sup> International Metallurgy & Materials Congress (IMMC 2016), 29 September-1 October 2016, Istanbul, Turkey, pp. 689-692.

R. Eriş, A.O. Mekhrabov, and M.V. Akdeniz (2016), The Effects of Nb Element Addition on the Short Range Order Characteristics of Nickel-based Superalloys, Modern Problems of Physics of Metals, V International Scientific-Practical Conference, 10-11 June 2016, Baku, Azerbaijan, pp. 48-52.

## CONGRESS PRESENTATIONS

R. Eriş, M.V. Akdeniz, and A.O. Mekhrabov (2017), The Effects of Refractory Element Addition on the Long Term Stability and Microstructural Characteristics of Nickel-based Superalloys, TMS 2017: 146<sup>th</sup> Annual Meeting & Exhibition, 26 February-2 March 2017, San Diego, USA.

R. Eriş, M.V. Akdeniz, and A.O. Mekhrabov (2017), The Effects of Transition Metal Element Addition on the Temporal Evolution and Microstructural Characteristics of Nickel-based Superalloys, TMS 2017: 146<sup>th</sup> Annual Meeting & Exhibition, 26 February-2 March 2017, San Diego, USA.

## SKILLS

- First-principles *ab initio* calculations (VASP, CDD, ELF, DOS),
- Arc melting & suction casting, X-ray diffraction (XRD), Thermal analysis (DSC), Scanning electron microscopy (SEM), Vibrating sample magnetometer experiments (VSM),
- Mechanical testing (tensile test, compression test, 3 point bending test, micro-hardness, macro-hardness and impact test).

## SCHOLARSHIPS

- TÜBİTAK, National Scholarship Programme for Graduate Students (2211),
- TÜBİTAK, Scholarship Program for Participation in Scientific Activities Abroad (2224-A).

## HOBBIES

- Tennis, hiking, travelling, photography, canvas painting, reading.